Lecture Notes in Physics

Springer
Berlin
Heidelberg
New York
Barcelona
Hong Kong
London
Milan
Paris
Singapore
Tokyo

Physics and Astronomy ONLINE LIBRARY
http://www.springer.de/phys/

The Editorial Policy for Proceedings

The series Lecture Notes in Physics reports new developments in physical research and teaching – quickly, informally, and at a high level. The proceedings to be considered for publication in this series should be limited to only a few areas of research, and these should be closely related to each other. The contributions should be of a high standard and should avoid lengthy redraftings of papers already published or about to be published elsewhere. As a whole, the proceedings should aim for a balanced presentation of the theme of the conference including a description of the techniques used and enough motivation for a broad readership. It should not be assumed that the published proceedings must reflect the conference in its entirety. (A listing or abstracts of papers presented at the meeting but not included in the proceedings could be added as an appendix.)

When applying for publication in the series Lecture Notes in Physics the volume's editor(s) should submit sufficient material to enable the series editors and their referees to make a fairly accurate evaluation (e.g. a complete list of speakers and titles of papers to be presented and abstracts). If, based on this information, the proceedings are (tentatively) accepted, the volume's editor(s), whose name(s) will appear on the title pages, should select the papers suitable for publication and have them refereed (as for a journal) when appropriate. As a rule discussions will not be accepted. The series editors and Springer-Verlag will normally not interfere with the detailed editing except in fairly obvious cases or on technical matters.

Final acceptance is expressed by the series editor in charge, in consultation with Springer-Verlag only after receiving the complete manuscript. It might help to send a copy of the authors' manuscripts in advance to the editor in charge to discuss possible revisions with him. As a general rule, the series editor will confirm his tentative acceptance if the final manuscript corresponds to the original concept discussed, if the quality of the contribution meets the requirements of the series, and if the final size of the manuscript does not greatly exceed the number of pages originally agreed upon. The manuscript should be forwarded to Springer-Verlag shortly after the meeting. In cases of extreme delay (more than six months after the conference) the series editors will check once more the timeliness of the papers. Therefore, the volume's editor(s) should establish strict deadlines, or collect the articles during the conference and have them revised on the spot. If a delay is unavoidable, one should encourage the authors to update their contributions if appropriate. The editors of proceedings are strongly advised to inform contributors about these points at an early stage.

The final manuscript should contain a table of contents and an informative introduction accessible also to readers not particularly familiar with the topic of the conference. The contributions should be in English. The volume's editor(s) should check the contributions for the correct use of language. At Springer-Verlag only the prefaces will be checked by a copy-editor for language and style. Grave linguistic or technical shortcomings may lead to the rejection of contributions by the series editors. A conference report should not exceed a total of 500 pages. Keeping the size within this bound should be achieved by a stricter selection of articles and not by imposing an upper limit to the length of the individual papers. Editors receive jointly 30 complimentary copies of their book. They are entitled to purchase further copies of their book at a reduced rate. As a rule no reprints of individual contributions can be supplied. No royalty is paid on Lecture Notes in Physics volumes. Commitment to publish is made by letter of interest rather than by signing a formal contract. Springer-Verlag secures the copyright for each volume.

The Production Process

The books are hardbound, and the publisher will select quality paper appropriate to the needs of the author(s). Publication time is about ten weeks. More than twenty years of experience guarantee authors the best possible service. To reach the goal of rapid publication at a low price the technique of photographic reproduction from a camera-ready manuscript was chosen. This process shifts the main responsibility for the technical quality considerably from the publisher to the authors. We therefore urge all authors and editors of proceedings to observe very carefully the essentials for the preparation of camera-ready manuscripts, which we will supply on request. This applies especially to the quality of figures and halftones submitted for publication. In addition, it might be useful to look at some of the volumes already published. As a special service, we offer free of charge LaTeX and TeX macro packages to format the text according to Springer-Verlag's quality requirements. We strongly recommend that you make use of this offer, since the result will be a book of considerably improved technical quality. To avoid mistakes and time-consuming correspondence during the production period the conference editors should request special instructions from the publisher well before the beginning of the conference. Manuscripts not meeting the technical standard of the series will have to be returned for improvement.

For further information please contact Springer-Verlag, Physics Editorial Department II, Tiergartenstrasse 17, D-69121 Heidelberg, Germany

Series homepage – http://www.springer.de/phys/books/lnpp

Christoph Egbers Gerd Pfister (Eds.)

Physics of Rotating Fluids

Selected Topics of the 11th International
Couette–Taylor Workshop
Held at Bremen, Germany, 20-23 July 1999

Springer

Editors

Christoph Egbers
Lehrstuhl Aerodynamik und Strömungslehre
Fakultät Maschinenbau, Elektrotechnik
und Wirtschaftsingenieurwesen
Brandenburgisch Technische Universität Cottbus
03013 Cottbus

Gerd Pfister
Institut für Experimentelle und Angewandte Physik
Universität Kiel
Olshausenstrasse 40
24098 Kiel, Germany

Cover picture: Plots of the velocity vectors of the spiral TG vortex flow, see K.Nakabayashi, W. Sha, *Spiral and wavy vortices in the spherical Couette Flow,* this issue.

Library of Congress Cataloging-in-Publication Data applied for.

Die Deutsche Bibliothek - CIP-Einheitsaufnahme

Physics of rotating fluids : selected topics of the 11th International
Couette Taylor Workshop, held at Bremen, Germany, 20 - 23 July 1999 /
Christoph Egbers ; Gerd Pfister (ed.). - Berlin ; Heidelberg ; New
York ; Barcelona ; Hong Kong ; London ; Milan ; Paris ; Singapore ;
Tokyo : Springer, 2000
(Lecture notes in physics ; Vol. 549)
(Physics and astronomy online library)
ISBN 3-540-67514-0

ISSN 0075-8450
ISBN 3-540-67514-0 Springer-Verlag Berlin Heidelberg New York

Typesetting: Camera-ready by the authors/editors
Cover design: *design & production*, Heidelberg

Printed on acid-free paper
SPIN: 10719300 55/3144/du - 5 4 3 2 1 0

Preface

"Lecture Notes in Physics", having a strong publishing history in fundamental physics research, has devoted a special volume to recent developments in the field of physics of rotating fluids and related topics. The present volume will comprise 23 contributed papers on the different aspects of rotating fluids, i.e. Taylor–Couette flow, spherical Couette flow, plane Couette flow, as well as rotating annulus flow.

In the seminal paper by G.I. Taylor, a powerful combination of theory and experiment was brought to bear on the stability of flow between rotating cylinders, now referred to as Taylor–Couette flow. The significance of his work lies in the fact that here, for the first time, an experiment in fluid dynamics and the theory, using the Navier–Stokes equations, could be compared and led to excellent agreement. Since that time ideas associated with rotating flows have been extended and have resulted in classic texts such as Greenspan's "The theory of rotating fluids".

In this present book we report on modern developments in the field where new mathematical ideas have been applied to experimental observations on a variety of related flow fields.

The aim of this volume is to provide the reader with a comprehensive overview of the current state of the art and possible future directions of the Taylor–Couette community and to include related topics and applications.

The first part of this volume is devoted to several new results in the classical Taylor–Couette problem covering diverse theoretical, experimental and numerical works on bifurcation theory, the influence of boundary conditions, counter-rotating flows, spiral vortices, time-periodic flows, low dimensional dynamics, axial effects, secondary bifurcations, spatiotemporal intermittency, Taylor–Couette flows with axial and radial flow, Taylor vortices at different geometries and transport phenomena in magnetic fluids.

The second part of this volume focuses on spherical Couette flows, including isothermal flows, vortical structures, spiral and wavy vortices, the influence of throughflow, thermal convective motions, intermittency at the onset of convection, as well as magneto-hydrodynamics in spherical shells.

Further parts are devoted to Goertler vortices and flows along curved surfaces, rotating annulus flows, as well as superfluid Couette flows, tertiary and quarternary solutions for plane Couette flows with thermal stratification and rotating disk flows.

We hope that the readers will find this volume useful, giving an overview of the latest experimental and theoretical studies on the physics of rotating fluids.

It is a pleasure for us to thank all those who contributed to the conference "11th International Couette–Taylor Workshop" and, by the same token, to this volume. We would like to thank the Dipl. Phys. Oliver Meincke, Markus Junk, Arne Schulz and Jan Abshagen for their invaluable and indispensable help in editing this book.

Last, but not least, we are grateful to Dr. Christian Caron for offering to publish this volume in the Springer Series "Lecture Notes in Physics" and for the patient assistance of Mrs. Brigitte Reichel-Mayer.

Bremen, Kiel
August 2000

Christoph Egbers
Gerd Pfister

List of Contributors

Jan Abshagen
Universität Kiel
Institut für Experimentelle und Angewandte Physik
Olshausenstrasse 40
24098 Kiel
Germany
jan@ang-physik.uni-kiel.de

Eberhard Bänsch
Zentrum für Technomathematik
Universität Bremen
Postfach 33 04 40
28334 Bremen
Germany
baensch@math.uni-bremen.de

Carlo F. Barenghi
Dept. of Mathematics and Statistics
The University of Newcastle Upon Tyne
Newcastle Upon Tyne NE1 7RU
United Kingdom
C.F.Barenghi@newcastle.ac.uk

John H. Bolstad
Laurence Livermore National Laboratory
L-23, University of California
POB 808
Livermore, CA 94550
USA
bolstad@lll-crg.llnl.gov

Friedrich Busse
Universität Bayreuth
Physikalisches Institut
95440 Bayreuth
Germany
busse@uni-bayreuth.de

Pascal Chossat
Université de Nice
Sophia Antipolis
I.N.L.N.
1361, route des lucioles
06560 Sophia Antipoli
France
chossat@inln.cnrs.fr

R.M. Clever
Institute of Geophysics and Planetary Physics
University of California
Los Angeles
USA

Antonio Delgado
TU München
Lehrstuhl für Fluidmechanik und Prozessautomation
Weihenstephaner Steig 23
85350 Freising
Germany
delgado@lfp.blm.tu-muenchen.de

Christoph Egbers
ZARM
Universität Bremen
Am Fallturm
28359 Bremen
Germany
egbers@zarm.uni-bremen.de

Afshin Goharzadeh
Université du Havre
Laboratoire de Mécanique
Groupe d'Energétique et Mécanique
25, rue Philippe Lebon, B.P. 540
76058 Le Havre Cedex
France
goharzadeh@univ-lehavre.fr

Genrich R. Grek
Russian Academy of Sciences,
Siberian Division
Institute of Theoretical and Applied Mechanics
630090 Novosibirsk
Russia
grek@itam.nsc.ru

Christoph Hartmann
TU München
Lehrstuhl für Fluidmechanik und Prozessautomation
Weihenstephaner Steig 23
85350 Freising
Germany
hartmann@lfp.blm.tu-muenchen.de

Rainer Hollerbach
University of Glasgow
Department of Mathematics
15 University Gardens
Glasgow G12 8QW
United Kingdom
rainer@maths.gla.ac.uk

Markus Junk
ZARM
Universität Bremen
Am Fallturm
28359 Bremen
Germany
junk@zarm.uni-bremen.de

Victor V. Kozlov
Russian Academy of Sciences,
Siberian Division
Institute of Theoretical
and Applied Mechanics
630090 Novosibirsk
Russia
kozlov@itam.nsc.ru

Patrice Laure
Institut Non-Linéaire de Nice
UMR 129 CNRS-Université de Nice,
1361, route des Lucioles
06560 Valbonne
France
laure@inln.cnrs.fr

Ming Liu
ZARM
Universität Bremen
Am Fallturm
28359 Bremen
Germany
ming.liu@promis.com

Manfred Lücke
Institut für Theoretische Physik
Universität des Saarlandes
66041 Saarbrücken
Germany
luecke@lusi.uni-sb.de

Richard M. Lueptow
Northwestern University
Dept. of Mechanical Engineering
2145 Sheridan Road
Evanston, IL 60208-3111
USA
r-lueptow@nwu.edu

Francesc Marquès
Universitat Politècnica de Catalunya
Departamenta de Física Aplicada
Jordi Girona Salgado s/n
Mòdul B4 Campus Nord
08034 Barcelona, Spain
Spain
marques@chandra.upc.es

Oliver Meincke
ZARM
Universität Bremen
Am Fallturm
28359 Bremen
Germany
meincke@zarm.uni-bremen.de

Álvaro Meseguer
Oxford University
Computing Laboratory
Numerical Analysis Group
Wolfson Building, Parks Road
Oxford OX1 3QD
United Kingdom
alvaro@comlab.ox.ac.uk

Rita Meyer-Spasche
MPI für Plasmaphysik
EURATOM-Association
85748 Garching
Germany
meyer-spasche@ipp-garching.mpg.de

Innocent Mutabazi
Université du Havre
Laboratoire de Mécanique
Groupe d'Energétique et Mécanique
25, rue Philippe Lebon, B.P. 540
76058 Le Havre Cedex
France
mutabazi@univ-lehavre.fr

Tom Mullin
Department of Physics and Astronomy
The University of Manchester
Manchester M13 9PL
United Kingdom
tom@reynolds.ph.man.ac.uk

Koichi Nakabayashi
Nagoya Institute of Technology
Department of Mechanical
Engineering
Gokiso-Cho, Showa-Ku
Nagoya, 466-8555
Japan
nakabaya@cfd.mech.nitech.ac.jp

Christiane Normand
C.E.A/Saclay,
Service de Physique Théorique
91191 Gif-sur-Yvette Cedex
France
normand@spht.saclay.cea.fr

Stefan Odenbach
ZARM
Universität Bremen
Am Fallturm
28359 Bremen
Germany
odenbach@zarm.uni-bremen.de

Gerd Pfister
Universität Kiel
Institut für Experimentelle und
Angewandte Physik
Olshausenstrasse 40
24098 Kiel
Germany
pfister@ang-physik.uni-kiel.de

Frank Pohl
MPI für Plasmaphysik
EURATOM-Association
85748 Garching
Germany

Doug Satchwell
Department of Physics and Astronomy
The University of Manchester
Manchester M13 9PL
United Kingdom
satch@reynolds.ph.man.ac.uk

Arne Schulz
Universität Kiel
Institut für Experimentelle
und Angewandte Physik
Olshausenstrasse 40
24098 Kiel

Germany
arne@ang-physik.uni-kiel.de

Nicoleta Dana Scurtu
Zentrum für Technomathematik
Universität Bremen
Postfach 33 04 40
28334 Bremen
Germany
scurtu@math.uni-bremen.de

Weiming Sha
Geophysical Institute
Graduate School of Science
Tohoku University
Aoba-Ku, Sendai, 980-8578
Japan
sha@wind.geophys.tohoku.ac.jp

Bernd Sitte
ZARM
Universität Bremen
Am Fallturm
28359 Bremen
Germany
sitte@zarm.uni-bremen.de

Yorinobu Toya
Nagano National College of Technology
Department of Mechanical Engineering
716 Tokuma
Nagano, 381-8550
Japan
toya@me.nagano-nct.ac.jp

Manfred Wimmer
Universität Karlsruhe
Fachgebiet Strömungsmaschinen
Kaiserstr. 12
76128 Karlsruhe
Germany
manfred.wimmer@mach.uni-karlsruhe.de

Contents

Part IV Rotating annulus

Part V Plane Couette flow

Pitchfork bifurcations in small aspect ratio Taylor–Couette flow

Tom Mullin[1], Doug Satchwell[1], and Yorinobu Toya[2]

[1] Department of Physics and Astronomy,
The University of Manchester,
Manchester M15 9PL, UK
[2] Department of Mechanical Engineering, Nagano National College of Technology,
Nagano,
381–8550, Japan

Abstract. We present a discussion of steady bifurcation phenomena in Taylor–Couette flow. The emphasis is on the role of pitchfork bifurcations in mathematical models and their relevance to the physical problem. The general features of such bifurcations are reviewed before we discuss the numerical and experimental techniques used to explore their properties. New results are then presented for a wide-gap small aspect ratio version of Taylor–Couette flow. We find good agreement between numerical and experimental results and show that the qualitative features of the bifurcation sequence are the same as those found with other radius ratios.

1 Introduction

The application of ideas from singularity theory to bifurcation phenomena in viscous fluid flows was pioneered by Benjamin[1,2]. He decided to focus his study on a well established hydrodynamic stability problem and hence selected the flow between concentric cylinders which is commonly called Taylor–Couette flow. The brilliant pioneering work of Taylor [22] on this problem is regarded as a milestone in the subject of hydrodynamic stability theory. Taylor used the powerful combination of theory and experiment to test the viscous formulation of Rayleigh's stability criterion for circulating flows. He established the principle of exchange of stability between two fluid states and obtained remarkable agreement between theory and experiment for stability limits. His success spawned a new subject area and to this date there have been over one thousand papers written on the subject. A comprehensive listing of references on the topic can be found in [20,21].

The onset of cells in the Taylor–Couette problem is widely believed to be an example of a simple planar pitchfork bifurcation. While evidence suggests that this is a good description, the connection between mathematical models and observations was shown by Benjamin to be very subtle. In particular, the symmetry of the abstract model is one of translation of the cellular pattern and this is not readily achievable in the physical system. As a result the onset of cells remains sharp but the second branch of the pitchfork is removed to Reynolds numbers far in excess of those required for the first appearance of cells. We will

C. Egbers and G. Pfister (Eds.): LNP 549, pp. 3–21, 2000.

discuss these issues below and also review other important simple geometrical symmetry breaking bifurcations in the problem.

A pitchfork bifurcation is so named because of its shape i.e. it resembles a three pronged hayfork. The handle and central prong correspond to the trivial solution or zero state and the outer prongs relate to the bifurcating branches. A familiar physical example of this mathematical entity is the Euler strut where an initially straight elastic beam is buckled by the action of a compressive load. The straight configuration is the trivial solution which loses stability to a pair of buckled states as the load is increased. This phenomenon can readily be demonstrated by applying an end loading to a plastic ruler using your hands. The ruler will bend up or down (say) above a critical compression. Here we have an example of a simple symmetry breaking pitchfork bifurcation where the symmetry of the originally straight ruler is destroyed above a critical load. It will soon become apparent to anyone who tries this demonstration that the ruler will prefer to buckle in a particular direction. This is because the ruler and the application of the load is not symmetric. In fact it can never be so even in a laboratory where a high precision version of the plastic ruler experiment could be made. This important aspect of the physical system can be modelled by including an imperfection term in the model equations as discussed by Golubitsky and Schaeffer[12]. The result is that there is a smoothly evolving state together with a disconnected branch which is terminated at its lower end by a saddle–node bifurcation.

We will now consider the Taylor–Couette problem in the context of pitchfork bifurcations. In the Taylor–Couette geometry the region between the surfaces of two concentric cylinders is filled with fluid. We consider the case where flow is driven by the inner cylinder which rotates with a constant angular velocity, while the outer cylinder is held stationary. In the configuration of interest here the flow is terminated with fixed horizontal plates which span the gap between the cylinders at the ends of the fluid annulus. A sketch of the Taylor–Couette geometry is presented in Fig. 1. The coordinates system is cylindrical polar (r, θ, z) with the origin located along the central axis and midway between the end boundaries.

The Reynolds number for this system is :

$$Re = \frac{\Omega r_i d}{\nu} \tag{1}$$

where ν is the kinematic viscosity of the fluid.
Two further independent dimensionless parameters may be defined for the Taylor–Couette geometry. These are the ratio of the length l of the fluid annulus to the gap width d, known as the *aspect ratio* :

$$\Gamma = \frac{l}{d}, \tag{2}$$

and the *radius ratio* of the cylinders :

$$\eta = \frac{r_i}{r_o}. \tag{3}$$

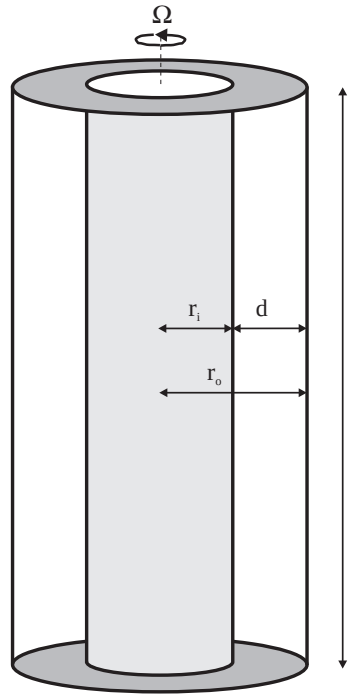

Fig. 1. The Taylor–Couette geometry. Fluid contained between the surfaces of two concentric cylinders is driven by a rotating inner cylinder.

The Reynolds number and aspect ratio are continuously variable parameters. The radius ratio, on the other hand, is not easily adjusted and is therefore fixed throughout an experiment. At small Re the flow is observed to be mainly featureless along most of the cylindrical gap except for some three dimensional motion at the ends. In practice, the laboratory flow appears to provide a reasonable approximation to rotary Couette flow where the principal action is shear between the rotating cylinders. It is this flow that is often considered to be related to the trivial state of the mathematical model where the cylinders are taken to be infinitely long. The connection is appealing since it appears reasonable that the distant ends in a long apparatus will act as small perturbations. This suggests that the pitchfork in the model will be disconnected by a small amount. Hence one branch would be continuously connected and show a sharp change in gradient close to the bifurcation point of the perfect system while the other branch would be disconnected and have a lower limit defined by a saddle–node. However, experimental evidence gathered over the last twenty years suggests that this view is misleading.

It is an experimental fact that when Re is increased above a certain well defined value then cellular motion sets in rather quickly. This is found to be the case even when the aspect ratio of the system is as small as four. If we consider the onset of cells as a bifurcation then we must ask if it can be described as a simple disconnected pitchfork. One fact which would test this idea is an observation of the second branch of the pitchfork and a measure of its lower limit of stability. Surprisingly, Benjamin appears to be the first person to have attempted this and in doing so he discovered that the second branch exists but it is far away from the first onset of cells. He termed these new solutions 'anomalous modes' and they have been the subject of a great deal of subsequent study [3,10]. Included in these investigations is direct numerical evidence [7] of the connection between the 'periodic' model and experimental observations using the Schaeffer [19] homotopy parameter. This clearly elucidates the origin and role of anomalous modes.

The range of Re between the saddle-node and that for the onset of cells can be as much as an order of magnitude and appears to be independent of aspect ratio. This suggests that 'end effects' are dominant in the Taylor–Couette problem in practice no matter what the aspect ratio is. One half of a simple planar pitchfork appears to provide a good model of the onset of cells. However, the symmetry involved is one of translation [1] and since the physical system does not easily permit this action the other half of the pitchfork is far removed from the mathematical idealisation of the model. This finding has important consequences for the onset of low–dimensional chaos and in particular codimension–2 organising centres [16,17].

Pitchfork bifurcations which give rise to pairs of solutions that break the mirror plane $\mathbf{Z}_2$ symmetry are now known to be important in the organisation of the dynamics found at higher Re [17]. These are found on nontrivial symmetric cellular flows where one half of the pattern grows at the expenses of the other as Re is varied. As in any physical system the effects of imperfections are present but, unlike the onset of cells, the disconnection is small and is generally of the order of a few percent of the range of the control parameter.

A feature of the Taylor–Couette experiment which can be readily observed is that there is a large multiplicity in the steady solution set [4]. This feature was highlighted in the time–dependent regime by Coles [11] and also commented on in [5] for steady flows. Thus if one wishes to explore important details of the bifurcation structure it can be difficult if the aspect ratio is large. Since 'end effects' are important for all aspect ratios it seems appropriate to carry out such investigations at small or modest aspect ratios where the solution set is manageable. This strategy has been adopted in several investigations which have provided an exacting challenge for comparison between the results of numerical calculation and experiment [9].

The simplest example of a symmetry breaking pitchfork bifurcation in the Taylor–Couette problem is found when the aspect ratio is $\mathbf{O}(1)$. In this case it was shown [3] that a two-cell state can bifurcate into a pair of single-cell anomalous modes. This is the only known example of a continuously connected anomalous

mode and has been the subject of a great deal of subsequent numerical and experimental study, as discussed in [18,23]. We will use this flow as our example to highlight a numerical bifurcation approach used to explore these and related problems. Then, we will present some new experimental results on a wide gap version of the problem which shows the robustness of the basic mechanisms.

2 A numerical bifurcation method

Before proceeding to discuss the equations of motion and a numerical bifurcation method used in their study we will first discuss those symmetries which are important in the physical system. The Taylor–Couette problem is invariant under reflections about the midplane or rotations through the azimuthal angle. These symmetries are embodied in the symmetry groups $\mathbf{Z}_2$ and $\mathbf{SO}_2$, respectively, that map :

$$(r, \theta, z) \rightarrow (r, \theta, -z) \tag{4}$$

and

$$(r, \theta, z) \rightarrow (r, \theta + \phi, z) \tag{5}$$

where ϕ is an arbitrary phase.

The numerical methods used to calculate the Taylor–Couette flow make full use of these symmetries. The $\mathbf{SO}_2$ symmetry is used implicitly since all calculations are performed over the two-dimensional vertical cross-section. The $\mathbf{Z}_2$ symmetry, on the other hand, is used to reduce the computational effort by approximately half using a half-grid discretisation.

2.1 Governing equations

The velocity components $(u_r^*, u_\theta^*, u_z^*)$, where * denotes dimensional quantities, are made non-dimensional by scaling with the inner cylinder velocity :

$$(u_r, u_\theta, u_z) = \frac{(u_r^*, u_\theta^*, u_z^*)}{\Omega r_i}. \tag{6}$$

Dimensionless quantities r, z, p and t are similarly defined :

$$r = \frac{r^*}{d} - \beta, z = \frac{z^*}{l}, p = \frac{dp^*}{\mu \Omega r_i}, t = \frac{\nu t^*}{d^2}. \tag{7}$$

where β is the ratio of inner cylinder radius to gap width :

$$\beta = \frac{r_i}{d} = \frac{\eta}{1 - \eta}. \tag{8}$$

With this notation, the dimensionless Navier–Stokes equations for an incompressible Newtonian fluid are :

$$\frac{\partial u_r}{\partial t} + Re\left\{u_r\frac{\partial u_r}{\partial r} + u_z\frac{\partial u_r}{\partial z} - \frac{u_\theta^2}{(r+\beta)}\right\} + \frac{\partial p}{\partial r}$$
$$-\frac{1}{(r+\beta)}\frac{\partial}{\partial r}\left((r+\beta)\frac{\partial u_r}{\partial r}\right) - \frac{1}{\Gamma^2}\frac{\partial^2 u_r}{\partial z^2} + \frac{u_r}{(r+\beta)^2} = 0 \tag{9a}$$

$$\frac{\partial u_\theta}{\partial t} + Re\left\{u_r\frac{\partial u_\theta}{\partial r} + u_z\frac{\partial u_\theta}{\partial z} + \frac{u_r u_\theta}{(r+\beta)}\right\}$$
$$-\frac{1}{(r+\beta)}\frac{\partial}{\partial r}\left((r+\beta)\frac{\partial u_\theta}{\partial r}\right) - \frac{1}{\Gamma^2}\frac{\partial^2 u_\theta}{\partial z^2} + \frac{u_\theta}{(r+\beta)^2} = 0 \tag{9b}$$

$$\frac{\partial u_z}{\partial t} + Re\left\{u_r\frac{\partial u_z}{\partial r} + u_z\frac{\partial u_z}{\partial z}\right\} + \frac{1}{\Gamma^2}\frac{\partial p}{\partial z}$$
$$-\frac{1}{(r+\beta)}\frac{\partial}{\partial r}\left((r+\beta)\frac{\partial u_z}{\partial r}\right) - \frac{1}{\Gamma^2}\frac{\partial^2 u_z}{\partial z^2} = 0 \tag{9c}$$

$$\frac{1}{(r+\beta)}\frac{\partial}{\partial r}\left((r+\beta)u_r\right) + \frac{\partial u_z}{\partial z} = 0 \tag{9d}$$

Equations (9a) - (9d) hold in the region of vertical cross-section D :

$$D = \left\{(r,z) \mid 0 \le r \le 1, -\frac{1}{2} \le z \le \frac{1}{2}\right\}. \tag{10}$$

The boundary conditions for domain D are :

$$u_r = u_z = 0 \text{ on } r = 0, 1 \text{ and on } z = \pm\tfrac{1}{2} \tag{11}$$

and

$$u_\theta = \begin{cases} 1 & \text{on } r = 0 \\ 0 & \text{on } r = 1 \\ F(r) & \text{on } z = \pm\frac{1}{2} \end{cases} \tag{12}$$

Thus u_r and u_z are zero on the entire boundary, and $u_\theta = 1$ at the inner cylinder and $u_\theta = 0$ at the outer cylinder. At the ends of the annulus u_θ has the dependence $F(r)$ shown in Fig. 2. This is the smooth function originally suggested [3] as a model for the corner singularity at $(r,z) = (0, \pm\frac{1}{2})$ where the rotating inner cylinder meets a stationary end-boundary. The dissipation rate in the fluid resulting from the singularity would otherwise be infinite, and therefore physically unrealistic. The particular form for $F(r)$ used in this case is a quadratic fitted to u_θ from $r = 0$ to $r = \epsilon$. Cliffe and Spence[8] report their numerical results to be insensitive to the precise value of ϵ, and conclude that any sufficiently small value is adequate.

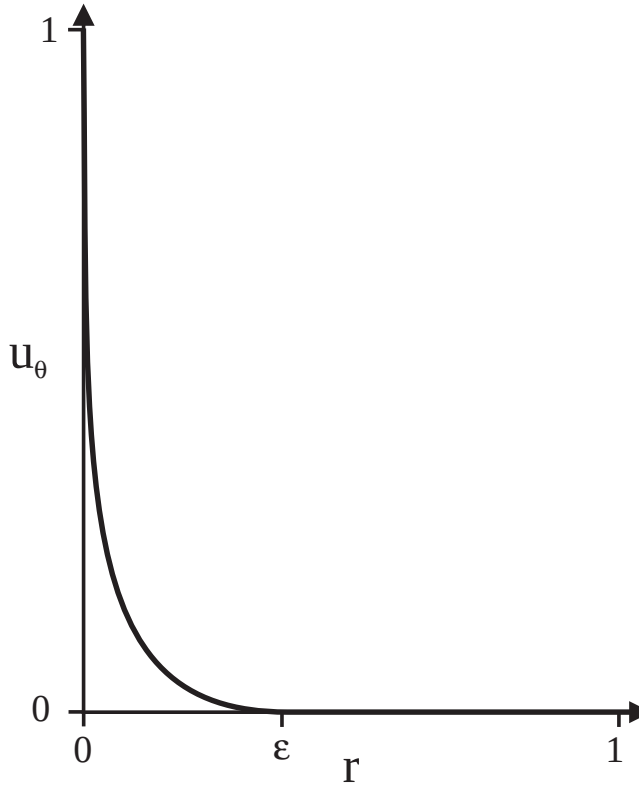

Fig. 2. The continuous function $F(r)$ used as a model for the corner singularities.

2.2 The finite element technique

The discrete two-dimensional version of the Navier–Stokes equations for the Taylor–Couette flow were calculated on a Silicon Graphics Power Challenge using the numerical bifurcation package ENTWIFE. This is the same technique originally used by Cliffe [9] to calculate the 4/6 cell exchange mechanism for a Newtonian fluid at radius ratios $\eta = 0.6$ and $\eta = 0.507$. he found good agreement with experimental results and also showed the importance of symmetry breaking bifurcations. We now present an overview of the techniques used to calculate these bifurcations and details of the basic numerical method may be found in Cliffe and Spence [8] and Jepson and Spence [13].

The steady version of equations (9a) - (9d) is solved using a primitive variable Galerkin formulation. The pressure terms p are required to lie in the space $L^2(D)$, the space of functions that are square integrable over the domain D. Similarly the velocity components u_r, u_θ and u_z are each required to lie in the space $W^{1,2}(D)$, the space of functions whose generalised first derivatives lie in $L^2(D)$. $\boldsymbol{W}^{1,2}(D)^3$

is then the space of three-dimensional vector valued functions with components existing in $W^{1,2}(D)$. This space is a natural setting for the problem, since the total rate of viscous dissipation by the fluid is incorporated in the square of the norm of the vector (u_r, u_θ, u_z).

On the boundary of D the elements of $\boldsymbol{W}^{1,2}(D)^3$ must vanish, and the subspace with this property is written $\boldsymbol{W}_0^{1,2}(D)^3$. We therefore seek an axisymmetric solution $\boldsymbol{U} + \hat{\boldsymbol{U}}$ where $\boldsymbol{U} = (u_r, u_z, u_\theta, p) \in \boldsymbol{H} \equiv \boldsymbol{W}_0^{1,2}(D)^3 \times L^2(D)$ and the function $\hat{\boldsymbol{U}} = (0, \hat{u}_\theta, 0, 0) \in \boldsymbol{W}^{1,2}(D)^3 \times L^2(D)$ matches the boundary conditions on the azimuthal component of velocity.

The domain D is covered with a finite-element mesh, the length of the longest edge of which is denoted h. $\boldsymbol{W}_h$ and M_h are two finite-dimensional subspaces such that $\boldsymbol{W}_h \in \boldsymbol{W}^{1,2}(D)^3$ and $M_h \in L^2(D)$. The continuous solution $\boldsymbol{U} \in \boldsymbol{H}$ is then approximated to a finite-dimensional $\boldsymbol{U}_h \in \boldsymbol{H}_h$, where the finite-dimensional Hilbert space $\boldsymbol{H}_h = \boldsymbol{W}_{h,0} \times M_h$, $\boldsymbol{W}_{h,0} \subset \boldsymbol{W}_0^{1,2}(D)^3$.

The steady finite-dimensional weak form of the Navier–Stokes equations are expressed in D as a nonlinear operator $\boldsymbol{f}$ in finite-dimensional Hilbert space :

$$\boldsymbol{f}(\boldsymbol{x}; Re, \Gamma, \eta) = \boldsymbol{0};\ \boldsymbol{f} : \boldsymbol{X} \times R \times R \times R \to \boldsymbol{X} \tag{13}$$

where $\boldsymbol{x}$ is a vector containing all the velocity and pressure degrees of freedom. The space $\boldsymbol{X}$ is the set of all possible $\boldsymbol{x}$ and is equivalent to R^N, where N is the total number of degrees of freedom. Solutions to (13) are known as weak solutions.

In principle equations (13) may be solved directly using Euler-Newton continuation. However, in practice numerical problems are associated with this method when a turning point is encountered, as the equations become singular. To avoid this difficulty the arclength continuation process proposed by Keller[14] is used. Consider the problem of solving a one parameter equation :

$$\boldsymbol{g}(\boldsymbol{u}, \lambda) = \boldsymbol{0}; \boldsymbol{u} \in R^n, \lambda \in R. \tag{14}$$

If an arclength s is used to parametrise the solution then equation (14) may be written :

$$\begin{cases} \boldsymbol{g}(\boldsymbol{u}(s); \lambda(s)) = \boldsymbol{0} \\ N(\boldsymbol{u}(s); \lambda(s), s) = 0 \end{cases} \tag{15}$$

where

$$N(\boldsymbol{u}(s); \lambda(s), s) = \frac{\partial \boldsymbol{u}}{\partial s}(s_0)^T (\boldsymbol{u}(s) - \boldsymbol{u}(s_0)). \tag{16}$$

The augmented system (15) is not singular at a turning point, and therefore allows continuation of a solution around a limit point. Euler's method supplies a prediction at each step s_i, and Newton's method is used to locate the solution accurately. The same parametrisation applies equally to the continuation of solutions in Re, Γ or η. In this way paths of limit points in parameter space may be computed. The continuation procedure also extends naturally to the computation of bifurcations using the extended systems to be introduced in section 2.5.

2.3 Spatial discretisation and symmetry

The finite-dimensional space $\boldsymbol{W}_{h,0}$ is generated using the nine-node isoparametric quadrilateral elements shown in Fig. 3. Each element has three components of velocity at each node, totalling 27 velocity degrees of freedom in all, with each component of velocity being approximated by biquadratic polynomials. M_h is generated by piecewise linear interpolation on the same elements. In addition, three pressure degrees of freedom p, p_x and p_y are associated with the central node and the interpolation is, in general, discontinuous across element boundaries.

In order to compensate for the rapid variation in velocity experienced near $(r, z) = (0, \pm\frac{1}{2})$, the corner elements are refined, as shown in Fig. 4. The main element is successively subdivided into smaller elements as the corner is approached. Cliffe [6] shows that the numerical results are insensitive to any number of subdivisions greater than four. Here the number of subdivisions used for the calculations is five.

The full domain D was discretised using a 24×40 mesh. The mesh is symmetrical about the line $z = 0$ and, with the the exception of the corners, is uniform over the domain. As Cliffe and Spence [8] point out, this is an important consideration if the symmetry of the physical problem is to be correctly modelled. It has already been noted that the Taylor–Couette geometry is $\boldsymbol{Z}_2$ symmetric, and therefore the Navier–Stokes equations in D are invariant under the following operation $\underline{\underline{\boldsymbol{S}}}$:

$$\begin{aligned} &\underline{\underline{\boldsymbol{S}}}\{u_r(r,z), u_\theta(r,z), u_z(r,z), p(r,z)\} \\ &= \{u_r(r,-z), u_\theta(r,-z), u_z(r,-z), p(r,-z)\} \end{aligned} \tag{17}$$

The effect of $\underline{\underline{\boldsymbol{S}}}$ is to partition the Hilbert space $\boldsymbol{H}$ into symmetric and antisymmetric subspaces :

$$\boldsymbol{H} = \boldsymbol{H}^s \oplus \boldsymbol{H}^a \tag{18}$$

where $\boldsymbol{U} \in \boldsymbol{H}^s$ if $\underline{\underline{\boldsymbol{S}}}\boldsymbol{U} = \boldsymbol{U}$ and $\boldsymbol{U} \in \boldsymbol{H}^a$ if $\underline{\underline{\boldsymbol{S}}}\boldsymbol{U} = -\boldsymbol{U}$. $\hat{\boldsymbol{U}}$ is such that $\underline{\underline{\boldsymbol{S}}}\hat{\boldsymbol{U}} = \hat{\boldsymbol{U}}$.

Cliffe and Spence [8] calculate the form for the symmetry operator $\underline{\underline{\boldsymbol{S}}}^*$, as the discretised analogue of the continuous symmetry operator $\underline{\underline{\boldsymbol{S}}}$, and obtain the relation

$$\underline{\underline{\boldsymbol{S}}}^* \boldsymbol{f}(\boldsymbol{x}; Re, \Gamma, \eta) = \boldsymbol{f}(\underline{\underline{\boldsymbol{S}}}^* \boldsymbol{x}; Re, \Gamma, \eta) \tag{19}$$

where $\underline{\underline{\boldsymbol{S}}}^* \neq \underline{\underline{\boldsymbol{I}}}$ and $\underline{\underline{\boldsymbol{S}}}^{*2} = \underline{\underline{\boldsymbol{I}}}$.

Just as the symmetry operator $\underline{\underline{\boldsymbol{S}}}$ partitions Hilbert space into symmetric and antisymmetric subspaces $\boldsymbol{H}^s$ and $\boldsymbol{H}^a$ in the continuous case, the symmetry operator $\underline{\underline{\boldsymbol{S}}}^*$ partitions the space $\boldsymbol{X}$ into symmetric and antisymmetric subspaces $\boldsymbol{X}^s$ and $\boldsymbol{X}^a$ in the discrete case :

$$\boldsymbol{X} = \boldsymbol{X}^s \oplus \boldsymbol{X}^a \tag{20}$$

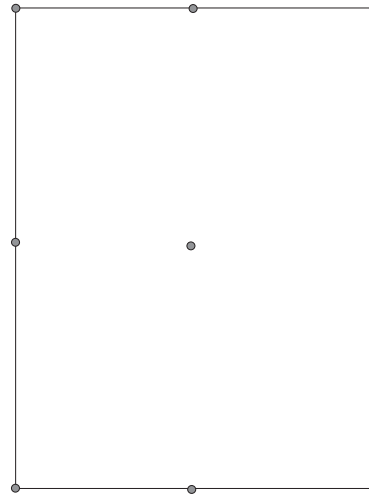

Fig. 3. A nine-node quadrilateral element.

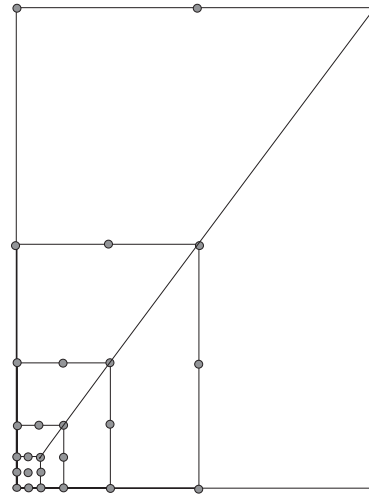

Fig. 4. The five-fold corner refinement.

where

$$\boldsymbol{X}^s := \left\{\boldsymbol{x} \in \boldsymbol{X} | \underline{\underline{\boldsymbol{S}}}^* \boldsymbol{x} = \boldsymbol{x}\right\}, \boldsymbol{X}^a := \left\{\boldsymbol{x} \in \boldsymbol{X} | \underline{\underline{\boldsymbol{S}}}^* \boldsymbol{x} = -\boldsymbol{x}\right\}, \tag{21}$$

The symmetry of the problem may be utilised in order to reduce the computational effort. Flows that are *symmetric* about $z = 0$ can be calculated more efficiently using the half domain :

$$D^+ = \left\{(r, z) \mid 0 \leq r \leq 1, 0 \leq z \leq \frac{1}{2}\right\}. \tag{22}$$

Thus two cell flows and symmetry breaking bifurcations from them are calculated on half domains. The full two-dimensional flow field is obtained upon reflection of the half-grid solution about $z = 0$. The result is a reduction in the number of degrees of freedom from 19124 for the full grid to just 9562 for the half grid.

2.4 Stability

The weak form of the Navier–Stokes equations in D may be expressed as a set of differential equations in t, with the pressure and velocity degrees of freedom as dependent variables. They are written in the form :

$$\underline{\underline{\boldsymbol{M}}} \frac{d\boldsymbol{x}}{dt} + \boldsymbol{f}(\boldsymbol{x}(t); Re, \Gamma, \eta) = \boldsymbol{0} \tag{23}$$

where $\underline{\underline{\boldsymbol{M}}}$ is the mass matrix.

If a small axisymmetric perturbation $\boldsymbol{\xi}$ is introduced then the behaviour is governed to first order by :

$$\underline{\underline{\boldsymbol{M}}} \dot{\boldsymbol{\xi}} + \underline{\underline{\boldsymbol{f}_{\boldsymbol{x}}}}(\boldsymbol{x}; Re, \Gamma, \eta)\boldsymbol{\xi} = \boldsymbol{0}. \tag{24}$$

where $\underline{\underline{\boldsymbol{f}_{\boldsymbol{x}}}} \equiv \dfrac{\partial \boldsymbol{f}}{\partial \boldsymbol{x}}$ is the Jacobian matrix. Solving the differential equation using characteristic functions, let :

$$\boldsymbol{\xi} = \boldsymbol{\epsilon} e^{-\gamma t} \tag{25}$$

where $\boldsymbol{\epsilon} \in \boldsymbol{X}$ and $\gamma = \sigma + i\omega$. Substituting into equation (23) :

$$-\gamma \underline{\underline{\boldsymbol{M}}} \boldsymbol{\epsilon} + \underline{\underline{\boldsymbol{f}_{\boldsymbol{x}}}}(\boldsymbol{x}; Re, \Gamma, \eta)\boldsymbol{\epsilon} = \boldsymbol{0} \tag{26}$$

Thus the linear stability of solutions $\boldsymbol{x}$ to (13) is dependent upon solutions of the generalised eigenproblem :

$$\underline{\underline{\boldsymbol{f}_{\boldsymbol{x}}}}(\boldsymbol{x}; Re, \Gamma, \eta)\boldsymbol{\epsilon} = \gamma \underline{\underline{\boldsymbol{M}}} \boldsymbol{\epsilon} \tag{27}$$

where γ is the generalised eigenvalue and $\boldsymbol{\epsilon}$ the corresponding eigenvector.

If $\sigma > 0$ the perturbation $\boldsymbol{\xi}$ decays with time, otherwise if $\sigma < 0$ the perturbation $\boldsymbol{\xi}$ grows. For the solution to be stable all generalised eigenvalues γ of (27) must have positive real part. However, the Jacobian matrix can in practice be very large and it is not efficient to calculate all the generalised eigenvalues. The sign of the determinant of the Jacobian matrix, though, may be calculated with very little additional computational cost. A necessary but not sufficient condition for stability, then, is that the sign of the determinant of the Jacobian matrix $\underline{\underline{\boldsymbol{f}_{\boldsymbol{x}}}}$ is positive. On the other hand, a solution is necessarily unstable if the determinant of $\underline{\underline{\boldsymbol{f}_{\boldsymbol{x}}}}$ is negative.

For symmetric solutions $\boldsymbol{x} \in \boldsymbol{X}^s$, the Jacobian $\underline{\underline{\boldsymbol{f}_{\boldsymbol{x}}}}$ maps $\boldsymbol{X}^s \to \boldsymbol{X}^s$ and $\boldsymbol{X}^a \to \boldsymbol{X}^a$. Therefore the Jacobian matrix $\underline{\underline{\boldsymbol{f}_{\boldsymbol{x}}}}$ evaluated at $\boldsymbol{x} \in \boldsymbol{X}^s$ may be written in the block diagonal form :

$$\underline{\underline{\boldsymbol{f}_{\boldsymbol{x}}}}|_{\boldsymbol{f}_{\boldsymbol{x}} \in \boldsymbol{X}^s} = \begin{bmatrix} \underline{\underline{\boldsymbol{f}_{\boldsymbol{x}}}}^s & 0 \\ 0 & \underline{\underline{\boldsymbol{f}_{\boldsymbol{x}}}}^a \end{bmatrix}. \tag{28}$$

The eigenvectors are exclusively elements of $\boldsymbol{X}^s$ or $\boldsymbol{X}^a$:

$$\boldsymbol{\epsilon} = \begin{pmatrix} \boldsymbol{\epsilon}^s \\ \boldsymbol{\epsilon}^a \end{pmatrix}. \tag{29}$$

For the symmetric solution to be stable, it must be stable to both symmetric and antisymmetric disturbances. Thus all the generalised eigenvalues γ^s corresponding to eigenvectors $\boldsymbol{\epsilon}^s \in \boldsymbol{X}^s$ must have positive real part, and therefore the sign of the determinant $\underline{\underline{\boldsymbol{f}_{\boldsymbol{x}}}}^s$ must be positive. In addition, all the generalised eigenvalues γ^a corresponding to eigenvectors $\boldsymbol{\epsilon}^a \in \boldsymbol{X}^a$ must have positive real part, and therefore the determinant of $\underline{\underline{\boldsymbol{f}_{\boldsymbol{x}}}}^a$ must also be positive.

Thus for symmetric solutions the determinants of $\underline{\underline{\boldsymbol{f}_{\boldsymbol{x}}}}^s$ and $\underline{\underline{\boldsymbol{f}_{\boldsymbol{x}}}}^a$ are calculated on the half grid at each step of the continuation procedure. The sign of the determinant indicates the stability of the solution with respect to symmetric and antisymmetric disturbances respectively. For asymmetric solutions $\boldsymbol{x} \in \boldsymbol{X}^a$, however, the Jacobian $\underline{\underline{\boldsymbol{f}_{\boldsymbol{x}}}}$ does not map $\boldsymbol{X}^s \to \boldsymbol{X}^s$ nor $\boldsymbol{X}^a \to \boldsymbol{X}^a$, since eigenvectors are not exclusively elements of $\boldsymbol{X}^s$ or $\boldsymbol{X}^a$, and $\underline{\underline{\boldsymbol{f}_{\boldsymbol{x}}}}$ cannot be partitioned into block diagonal form. Thus the stability of these solutions cannot be obtained by finding the determinant of $\underline{\underline{\boldsymbol{f}_{\boldsymbol{x}}}}^s$ and $\underline{\underline{\boldsymbol{f}_{\boldsymbol{x}}}}^a$, since these matrices do not exist. The asymmetric solutions must therefore be computed on the full grid.

For asymmetric solutions the Jacobian $\underline{\underline{\boldsymbol{f}_{\boldsymbol{x}}}}$ may be expressed in the Jordan form :

$$\underline{\underline{\boldsymbol{f}_{\boldsymbol{x}}}} = \begin{bmatrix} \underline{\underline{\boldsymbol{B}}} & 0 \\ 0 & \underline{\underline{\boldsymbol{C}}} \end{bmatrix} \tag{30}$$

where $\underline{\underline{\boldsymbol{B}}}$ is a (2×2) matrix and $\underline{\underline{\boldsymbol{C}}}$ is a $((N-2) \times (N-2))$ matrix with positive eigenvalues. The eigenvalues of $\underline{\underline{\boldsymbol{B}}}$ are those closest to the imaginary axis. This is a useful construct since the stability of the solution is dependent upon the eigenvalues of $\underline{\underline{\boldsymbol{B}}}$ alone, and it is therefore used to indicate the stability of asymmetric solution branches.

2.5 Bifurcation points and extended systems

The linear stability analysis (24) fails whenever $\sigma = 0$. This occurs, for example, at a simple singular point $\boldsymbol{x}_0$ where the Jacobian matrix $\underline{\underline{\boldsymbol{f}_{\boldsymbol{x}}}}$ has a single real eigenvalue $\gamma_0 = \sigma_0 + i\omega_0$ such that $\sigma_0 = \omega_0 = 0$. At such a point there exists a unique null eigenvector $\boldsymbol{\phi}_0$. If $\boldsymbol{x}_0 \in \boldsymbol{X}^s$ then the null eigenvector $\boldsymbol{\phi}_0$ is either an element of $\boldsymbol{X}^s$ or an element of $\boldsymbol{X}^a$. Thus if the determinant of $\underline{\underline{\boldsymbol{f}_{\boldsymbol{x}}}}^s$ is zero then the bifurcation is symmetry-*preserving*, otherwise if the determinant of $\underline{\underline{\boldsymbol{f}_{\boldsymbol{x}}}}^a$ is zero then the bifurcation is symmetry-*breaking*.

In order to compute such bifurcation points it is necessary to use extended versions of the equations. Moore and Spence [15] show that a limit point may be characterised as an isolated solution of the following extended system :

$$\boldsymbol{F}(\boldsymbol{y}; \Gamma, \eta) \equiv \begin{pmatrix} \boldsymbol{f}(\boldsymbol{x}; Re, \Gamma, \eta) \\ \underline{\underline{\boldsymbol{f}_{\boldsymbol{x}}}}(\boldsymbol{x}; Re, \Gamma, \eta)\boldsymbol{\phi} \\ \boldsymbol{l}\boldsymbol{\phi} - 1 \end{pmatrix} = \boldsymbol{0} \tag{31}$$

where $\boldsymbol{y} = (\boldsymbol{x}, \boldsymbol{\phi}, Re) \in \boldsymbol{X} \times \boldsymbol{X} \times R$ and $\boldsymbol{l} \in \boldsymbol{X}'$ (the dual of $\boldsymbol{X}$). In order to calculate a path of limit points in the two-dimensional space (Re, Γ) for instance the Keller arc-length continuation method (15) is applied to (31) with $\boldsymbol{u} = \boldsymbol{y}$, $\lambda = \Gamma$ and $\boldsymbol{g}(.,.) = \boldsymbol{F}(.,.)$.

Werner and Spence [24] show that a pitchfork bifurcation may be characterised as an isolated solution of the extended system :

$$\boldsymbol{F}(\boldsymbol{y}; \Gamma, \eta) \equiv \begin{pmatrix} \boldsymbol{f}(\boldsymbol{x}; Re, \Gamma, \eta) \\ \underline{\underline{\boldsymbol{f}_{\boldsymbol{x}}}}(\boldsymbol{x}; Re, \Gamma, \eta)\boldsymbol{\phi} \\ \boldsymbol{l}\boldsymbol{\phi} - 1 \end{pmatrix} = \boldsymbol{0} \tag{32}$$

where $\boldsymbol{y} = (\boldsymbol{x}, \boldsymbol{\phi}, Re) \in \boldsymbol{X}^s \times \boldsymbol{X}^a \times R$. This is similar to equation (31) but there is an essential difference since now $\boldsymbol{x}$ must belong to $\boldsymbol{X}^s$ and $\boldsymbol{\phi}$ must belong to $\boldsymbol{X}^a$. Thus the basic solution is symmetric but the eigenvector, and thus the bifurcating branch, is asymmetric. Other symmetry-breaking points include the C^+ and C^- coalescence points and quartic bifurcation points which can occur at certain singularities of the system (32). Extended systems for these singularities may be found in Cliffe and Spence [8].

The numerical problem is such that all of the symmetry-breaking bifurcations are perfect, and therefore on perfectly symmetric boundary conditions there is no possibility of distinguishing between asymmetric solution branches. One practical point here is that it is possible to step on to an asymmetric solution branch by perturbing the pitchfork bifurcation so that all solutions become slightly asymmetric. It is then possible to step along the connected solution branch through the point at which the pitchfork occurs in the symmetric case. This solution is used as a first approximation to the perfectly symmetric problem, which converges to the true value when the boundary conditions are reset to their original configuration. In this way the paths of fold bifurcations along asymmetric solution branches may be computed.

Since both $\underline{\underline{\boldsymbol{M}}}$ and $\underline{\underline{\boldsymbol{f_x}}}$ are real matrices it follows that the eigenvalues γ_0 are either real or exist as complex conjugate pairs. If at a simple singular point $\boldsymbol{x}_0$ the real part σ_0 is zero and the imaginary part ω_0 is non-zero, then a purely imaginary pair of eigenvalues and corresponding complex conjugate eigenvectors must exist. In this case $\boldsymbol{x}_0$ is a Hopf bifurcation point.

At a Hopf bifurcation point $\gamma = \pm i\omega$ and equation (27) becomes :

$$\underline{\underline{\boldsymbol{f_x}}}\boldsymbol{\epsilon} = i\omega\underline{\underline{\boldsymbol{M}}}\boldsymbol{\epsilon}. \tag{33}$$

Letting $\boldsymbol{\epsilon} = \boldsymbol{a} + i\boldsymbol{b}$, and equating real and imaginary parts :

$$\begin{aligned} \underline{\underline{\boldsymbol{f_x}}}\boldsymbol{a} + \omega\underline{\underline{\boldsymbol{M}}}\boldsymbol{b} &= \boldsymbol{0} \\ \underline{\underline{\boldsymbol{f_x}}}\boldsymbol{b} - \omega\underline{\underline{\boldsymbol{M}}}\boldsymbol{a} &= \boldsymbol{0}. \end{aligned} \tag{34}$$

Then, Hopf bifurcation points are isolated solutions of the following extended system :

$$\boldsymbol{F}(\boldsymbol{y}; \Gamma, \eta) \equiv \begin{pmatrix} \boldsymbol{f}(\boldsymbol{x}; Re, \Gamma) \\ \underline{\underline{\boldsymbol{f_x}}}(\boldsymbol{x}; Re, \Gamma, \eta)\boldsymbol{a} + \omega\underline{\underline{\boldsymbol{M}}}\boldsymbol{b} \\ \underline{\underline{\boldsymbol{f_x}}}(\boldsymbol{x}; Re, \Gamma, \eta)\boldsymbol{b} - \omega\underline{\underline{\boldsymbol{M}}}\boldsymbol{a} \\ \boldsymbol{c}^T\boldsymbol{a} - 1 \\ \boldsymbol{c}^T\boldsymbol{b} \end{pmatrix} = \boldsymbol{0} \tag{35}$$

where $\boldsymbol{y} = (\boldsymbol{x}, Re, \omega, \boldsymbol{a}, \boldsymbol{b}) \in (\boldsymbol{X} \times R \times R \times \boldsymbol{X} \times \boldsymbol{X})$.

We will not calculate Hopf bifurcations here but refer the reader to [18] where a discussion of Hopf bifurcations in small aspect ratio Taylor–Couette flows is given.

3 Results

We will now discuss the application of the numerical techniques discussed above to the study of pitchfork bifurcations in a wide-gap Taylor–Couette system. Our results are concerned with two-cell and single-cell flows and the exchange of stability between these flows as the aspect ratio is varied. We will first present a brief description of the experimental apparatus before discussing the numerical and experimental results.

3.1 Experimental apparatus

The fluid was contained in the annular gap between two concentric cylinders. The outer cylinder was a precision bore glass tube with inner diameter $74.6 \pm 0.02mm$. The inner cylinder was machined stainless steel with a diameter $25.3 \pm 0.02mm$ so that the radius ratio was 0.339. It was located in bearings and driven round by a stepping motor via a gear box and belt drive system. The motor speed was controlled by an oscillator and its speed was monitored. The ends of the annular

gap were defined by two stationary PTFE collars which bridged the annular gap. The upper collar was attached to a pair of posts so that it could be moved accurately up and down. The aspect ratio was measured using a cathetometer which was also used to measure the flow structure.

The fluid used was a water glycerol mixture whose viscosity was measured to be 5.69 cSt. The cylinders were surrounded by a water bath whose temperature was controlled to 0.02^oC by fluid pumped through commercial temperature controller. The flow was visualised using Mearlmaid AA pearlessence and illumination was provided by a plane of light from a slide projector. The cellular structure was then clearly visible and the respective heights of cells were used to distinguish between flow states. Estimates of the symmetry breaking bifurcation points were obtained by measuring the saddle–node points where the asymmetric states collapsed to the symmetric ones by reduction in Re. All other bifurcation points correspond to catastrophic changes in the flow structure with change in Re and so reliable estimates could be obtained.

3.2 Numerical and experimental bifurcation set

We show in Fig. 5 the bifurcation set in the (Re,Γ) plane for the one-cell, two-cell interaction.The solid lines have been calculated using the methods discussed above and the crosses are the measured points. In general, there is very good agreement between the numerical and experimental results. Some 'typical' streamline plots for these flows are shown in Fig. 6 where we show both symmetric and asymmetric flows. As discussed in [3] we call the asymmetric states single cell flows since this the form they would have in a model problem where the end boundary conditions match Couette flow. In the laboratory and in the numerical calculations with stationary end–conditions there are always weak recirculations present in the corners. Since these will be present for all cellular flows on finite domains we choose to define the flow states in this way.

We next show in Fig. 7 a sequence of schematic bifurcation diagrams which we will now use in our discussion of Fig. 5. In Fig. 5 AB is the locus of symmetry breaking bifurcations from the two-cell state to a pair of single cell flows. The corresponding bifurcation diagram is given in Fig. 7(a) where we see a simple pitchfork. A 'typical' pair of streamline plots for such states are presented in Fig. 6 (a) and (c) respectively. As the aspect ratio is increased towards B there is an interaction with a second pitchfork which restabilises the two-cell branch. This second pitchfork is shown in Fig. 7(b) where it can be seen that the bifurcation to the pair of one single-cell states has become quartic. The path of second pitchforks is denoted by BC in Fig. 5.

As the aspect ratio is increased further the interaction increases such that there is hysteresis in the development of the single-cell states as shown schematically in Fig. 7(c). The hysteresis is very small and is hardly detectable on the numerical results on the scale used in Fig. 5. The influence of imperfections in the experiment may be clearly seen in Fig. 5 for the hysteresis is larger than in the numerics and all points lie below the calculated ones. Nevertheless, the

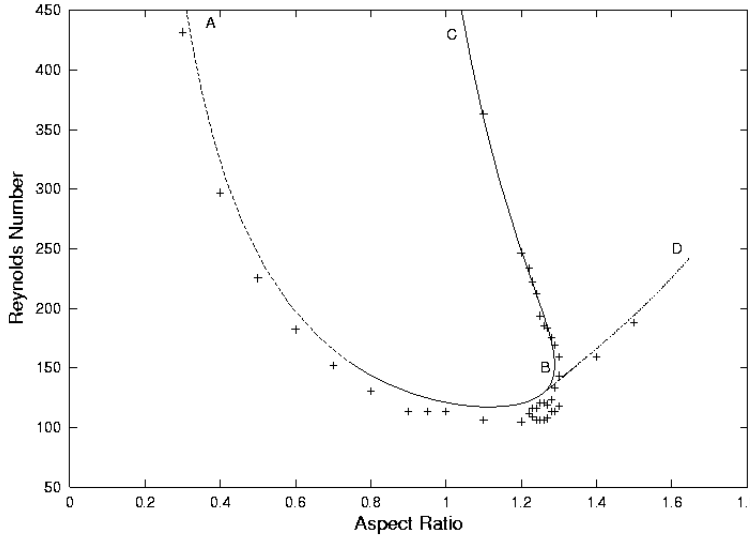

Fig. 5. Comparison between experimental and numerical results for the bifurcation set for one and two steady cell flows. ABC is a locus of symmetry breaking bifurcation points and BD is a path of saddle–nodes.

qualitative nature of the events is clear and we attribute the quantitative difference to the sensitivity of this feature to experimental imperfections. Yet further increase in aspect ratio causes the disconnection of the single-cell states through a coalescence of the pitchforks between Figs. 7 (c) and (d). Thus along BD in Fig. 5 the pair of single-cell states are disconnected and this is the locus of limit points for these states.

4 Discussion

The bifurcation sequence described above is consistent with those previously discussed by [3,6,18] for other values of the radius ratio. These new results therefore confirm that these qualitative features are robust when the radius ratio is varied. It is known [16] that pitchfork symmetry breaking bifurcations form organising centres for complicated dynamical motion in the Taylor–Couette problem and hence the robustness of the underpinning steady solution structure gives hope that features such as Silnikov dynamics may also be relevant over a wide parameter range.

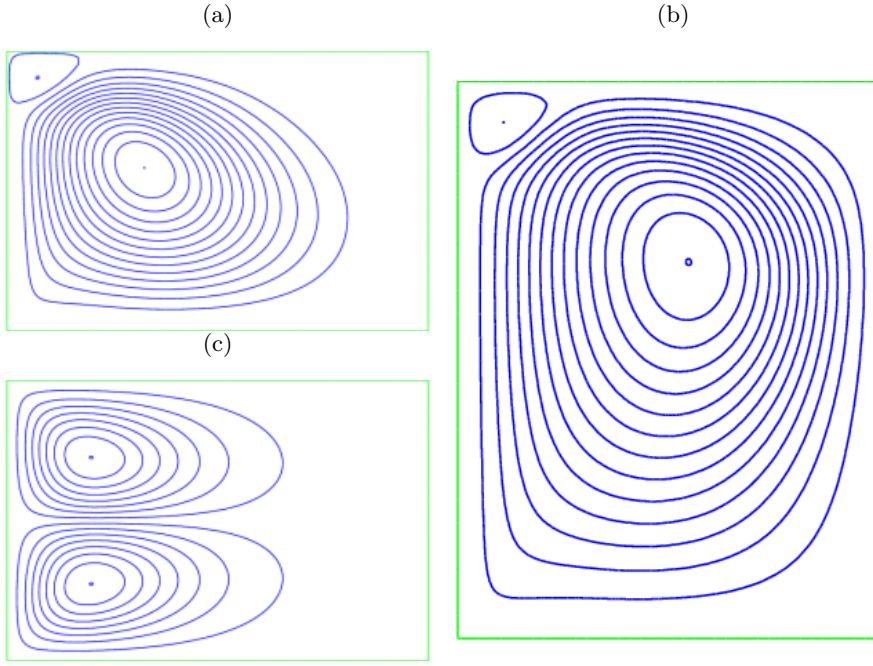

Fig. 6. Streamline plots for single and two-cell states. a) Re = 420 $\Gamma = 0.66$, b) Re = 420 $\Gamma = 1.30$ c) Re = 150 $\Gamma = 0.66$

References

1. T. B. Benjamin 1978*a* Bifurcation phenomena in steady flows of a viscous liquid. Part 1. Theory. *Proc. R. Soc. Lond.* A **359**, 1–26.
2. T. B. Benjamin 1978*b* Bifurcation phenomena in steady flows of a viscous liquid. Part 2. Experiments. *Proc. R. Soc. Lond.* A **359**, 27–43.
3. T. B. Benjamin and T. Mullin 1981 Anomalous modes in the Taylor experiment. *Proc. R. Soc. Lond.* A **377**, 221–249.
4. T. B. Benjamin and T. Mullin 1982 Notes on the multiplicity of flows in the Taylor–Couette experiment.
5. J. E. Burkhalter and E. L. Koschmieder 1973 Steady supercritical Taylor vortex flow. *J. Fluid Mech.* **58**, 547–560.
6. K. A. Cliffe 1983 Numerical calculations of two–cell and single–cell Taylor flows. *J. Fluid Mech.* **135**, 219–233.
7. K. A. Cliffe and T. Mullin 1985 A numerical and experimental study of anomalous modes in the Taylor experiment. *J. Fluid Mech.* **153**, 243–258.
8. K. A. Cliffe, and Spence A. 1986 Numerical calculations of bifurcations in the finite Taylor problem. In *Numerical Methods for Bifurcation Problems* (ed. T. Kupper, H.D. Mittleman and H. Weber), pp 129–144. Birkhauser:ISNM..
9. K. A. Cliffe 1988 Primary–flow exchange process in the Taylor problem. *J. Fluid Mech.* **197**, 57–79.
10. K. A. Cliffe, J. J. Kobine and T. Mullin 1992 The role of anomalous modes in Taylor–Couette flow. *Proc. R. Soc. Lond.* A **439**, 341–357.

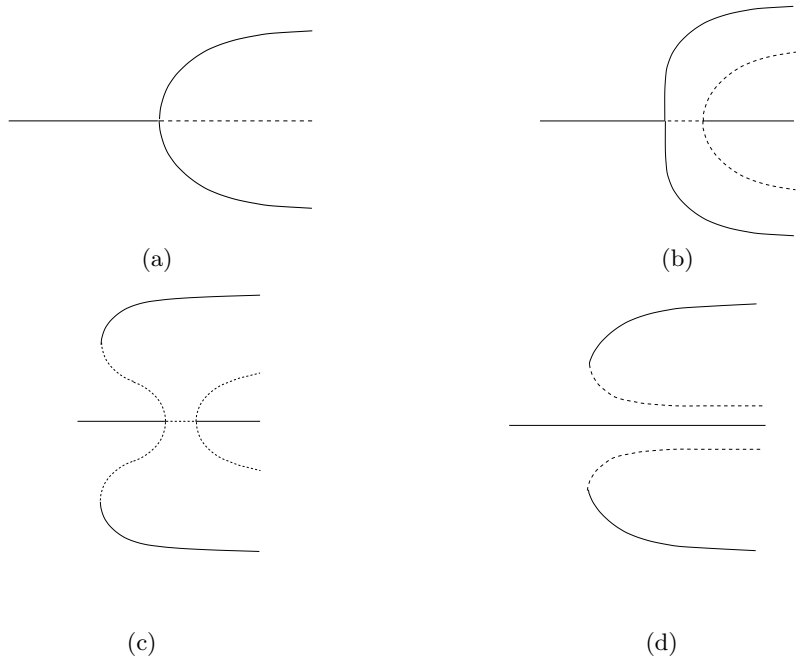

Fig. 7. A set of schematic bifurcation diagrams portraying the interaction between the two-cell and pair of single-cell states. Solid lines denote stable solutions and dashed lines unstable. a)The pitchfork at small aspect ratios corresponding to AB in fig 5 b) The pitchfork becomes quartic when there is interaction with a second pitchfork (BC in fig 5) near B in fig 5 c) hysteresis in the development of the single cell pair near b in fig 5 d) the single-cell pair are disconnected along BD in Fig. 5

11. D. Coles 1965 Transition in circular Couette flow. *J. Fluid Mech.* **21**, 385–425.
12. M. Golubitsky and D. G. Schaeffer 1985 *Singularities and Groups in Bifurcation Theory.* Vol. 1. Applied Mathematical Sciences **51**. Springer.
13. A. Jepson and A. Spence 1985 Folds in solutions of two parameter systems. *SIAM J. Numer. Anal.* **22**, 347–368.
14. H. B. Keller 1977 Numerical solutions of bifurcation and nonlinear eigenvalue problems. In *Applications of Bifurcation Theory* (ed. P. H. Rabinowitz), pp. 359–384, Academic.
15. G. Moore and A. Spence 1980 The calculation of turning points of nonlinear equations. *SIAM J. Numer. Anal.* **17**, 567–576.
16. T. Mullin 1991 Finite-dimensional dynamics in Taylor–Couette flow. *IMA J. App. Math.* **46**, 109-120.
17. T. Mullin 1993 *The Nature of Chaos.* Oxford University Press.
18. G. Pfister, H. Schmidt, K. A. Cliffe and T. Mullin 1988 Bifurcation phenomena in Taylor–Couette flow in a very short annulus. *J. Fluid Mech.* **191**, 1–18.
19. D. G. Schaeffer 1980 Analysis of a model in the Taylor problem. *Math. Proc. Camb. Phil. Soc.* **87**, 307–337.
20. H.Ł. Swinney and J. P. Gollub 1981 *Hydrodynamic Instabilities and the Transition to Turbulence* Topics in Applied Physics, Vol. **45**. Springer.

21. R. Tagg 1994 The Couette–Taylor problem. *Nonlinear Science Today* **4**, 1–25.
22. G. I. Taylor 1923 Stability of a viscous liquid contained between two rotating cylinders. *Phil. Trans. R. Soc. Lond.* A **223**, 289–343.
23. Y. Toya, L. Nakamura, S. Yamashita and Y. Ueki 1994 An experiment on a Taylor vortex flow in a gap with small aspect ratio. *Acta Mechanica* **102**, 137–148.
24. B. Werner and A. Spence 1984 The computation of symmetry–breaking bifurcation points. *SIAM J. Numer. Anal.* **21**, 388–399.

Taylor–Couette system with asymmetric boundary conditions

Oliver Meincke[1], Christoph Egbers[1], Nicoleta Scurtu[2], and Eberhard Bänsch[2]

[1] ZARM, Center of Applied Space Technology and Microgravity, University of Bremen, Am Fallturm, 28359 Bremen, Germany
[2] Center of Technomathematics, University of Bremen, Postfach 33 04 40, 28334 Bremen, Germany

Abstract. We report on a study on stability, bifurcation scenarios and routes into chaos in Taylor–Couette flow. By increasing the Reynolds number with the angular velocity of the driving inner cylinder, the flow bifurcates from laminar mid-plane-symmetric basic flow via a pitchfork bifurcation to mid-plane-symmetric Taylor vortex flow. Both flow states are rotationally symmetric. We now compare the dynamical behaviour in a system with symmetric boundary conditions with the effects in an asymmetric system. We also could vary the gap widths. The different flow states can be detected by visualization with small aluminium flakes and also measured by Laser Doppler Velocimetry (LDV) and Particle Image Velocimetry (PIV). The dynamical behaviour of the rotating flow is discussed by time series analysis methods and velocity bifurcation diagrams and then compared with numerical calculations.

1 Introduction

The subject of hydrodynamic instabilities and the transition to turbulence is important for the understanding of nonlinear dynamic systems. A classical system to investigate such instabilities is besides the Rayleigh–Bénard system the Taylor–Couette system. It consists of two concentric cylinders where the so formed gap is filled with the working fluid. The system was first examined theoretically and experimentally by Taylor [16]. Here, only rotation of the inner cylinder is considered and the outer one is held at rest. By increasing the speed of the inner cylinder, the azimuthal Couette flow becomes unstable and is replaced by a cellular pattern in which the fluid travels in helical paths around the cylinder in layers of vortices (Taylor vortex flow). By a further increase of the rotation speed the system undergoes several bifurcations before the flow structure becomes more complicated. Different routes to chaos are possible by further increasing the rotation rate. One model was described by Ruelle & Takens [13]. Benjamin [3], [4] showed the importance of the finite size of the cylinders and its effects upon the bifurcation phenomena. A summary of the current state of research was published by Ahlers [1], Chossat [6], Koschmieder [9], Meyer–Spasche [10] and Tagg [15].

In this work, short systems are investigated to reduce the multiplicity of possible solutions. Some new aspects of the dynamical behaviour of the Taylor–Couette flow during the transition to turbulence for the case of symmetric and

C. Egbers and G. Pfister (Eds.): LNP 549, pp. 22–36, 2000.

asymmetric boundary conditions and the small ($\eta = 0.85$) and the wide gap width ($\eta = 0.5$) are presented in this study.

2 Experimental setup

Most of our experiments were carried out by increasing the Reynolds number of the inner cylinder in a quasistationary way from rest. However, since the occuring flow structures could depend on initial conditions, it is possible to vary the acceleration rate for the cylinder. The temperature was precisely controlled and measured to allow the determination of a well defined Reynolds number of the flow. The Taylor–Couette flow is characterized by the following three control parameters: The aspect-ratio ($\Gamma = H/d$), the radius ratio ($\eta = R_i/R_a$) and the Reynolds number $Re = \frac{R_i d \Omega_i}{\nu}$, where H, d, R_i, R_a, Ω_i and ν are the height, the gap width, the inner and outer radii, the angular velocity of the inner cylinder and the kinematic viscosity respectively. The symmetric experimental setup is illustrated in Fig. 1a. It is only possible to obtain different aspect ratios by integrating different inner cylinders due to the constant length of the system. The radius ratios we used during this work were ($\eta = 0.5$) to realize a wide cylindrical gap and ($\eta = 0.85$) a small one. To realize asymmetric boundary conditions, a new setup consisting of an inner cylinder with an attached bottom plate is available (Fig. 1b). In this system the radius ratio is ($\eta = 0.5$) and the aspect ratio is variable.

3 Measurement techniques

To observe the behaviour of the flow, two different techniques were used. Using the PIV-technique one gets a 2–D vector map of the flow field whereas LDV leads to time series with high resolution containing information about one component of velocity at a special location in the working fluid depending on time.

3.1 PIV

In our system a pulsed double cavity, frequency doubled Nd:YAG-Laser is used for the **P**article **I**mage **V**elocimetry. The second cavity is required to get a very short time delay between the two pulses. A single laser achieves only a repetition frequency of about 15Hz. This time delay is too long for high flow rates and no correlation between the records would be achieved. The emitted laser beam is frequency doubled and then spread with a cylindrical lense to get a green light sheet, because the original wavelength of a Nd:YAG-Laser is in the infrared. To get two images in a short time-interval, a fast CCD-camera is used. In Fig. 2 a sketch of the Taylor–Couette system with the applied PIV-setup is shown. With the two recorded images one gets a light intensity distribution which shows the particles suspended into the measuring fluid. The recorded images are divided into smaller subareas, so called ‘interrogation areas’. The cross correlation

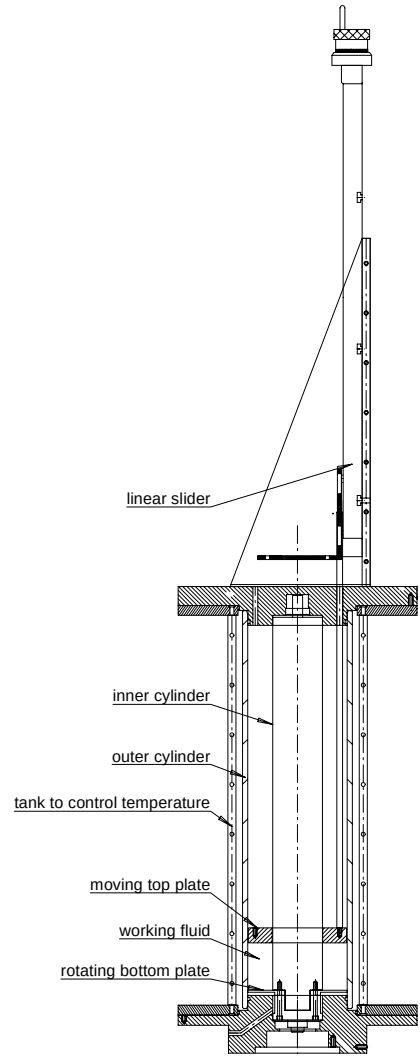

a) photograph of the symmetric experimental setup

b) principle sketch of the asymmetric setup with rotating bottom plate

Fig. 1. The two different experimental setups which were used during this work

algorithm (see Eqn. 1) calculates for every interrogation area a vector of the movement of the particles so that at least a 2–D vector map of the flow in the

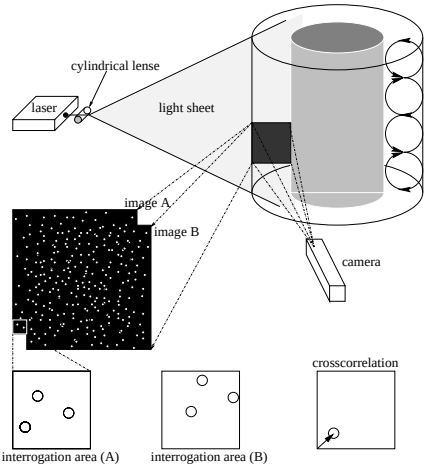

Fig. 2. Taylor–Couette system with the applied PIV-setup

gap is displayed.

$$\sum\sum I(m,n)I^{\star}(m+i,n+j) = \mathcal{C}(i,j) \tag{1}$$

I and $I^{\star}$ describe the light intensities within the interrogation areas at the time t and Δt due to the spatial coordinates m and n. The cross correlation $\mathcal{C}(i,j)$ has its maximum, if many particles correlate with their spatial shifted equivalent $\rightarrow$ true correlation. To get more information about the PIV-technique the reader is refered to the book by Raffel et al. [11].

3.2 LDV

Laser-**D**oppler-**V**elocimetry is a widely accepted tool for fluid dynamic investigations, as it gives information about flow velocity without influencing the fluid. For the application of the Laser-Doppler-Velocimetry on the rotating system a special traversing system has been constructed, which allows the traversing of the LDV-system in axial direction. Figure 3 shows a principle sketch of a LDV-system. The LDV-system used in our experiments consists of a He-Ne-Laser, whose beam is split and then one laser beam is shifted in its frequency. Suspended particles create a signal by scattering light when passing the interference fringes formed by the intersected beams in the measuring volume. From these Doppler bursts information of the direction and the quantity of the velocity can be obtained. As tracer particles for the LDV-measurements polysterene spheres with a diameter of 1.6µm were used. By using different algorithms, for example described in [18], it is possible to calculate the power spectrum, the attractors and bifurcation diagrams out of the obtained time series, measured with the LDV-system. Both systems we used are distributed by DANTEC–Electronics, Denmark

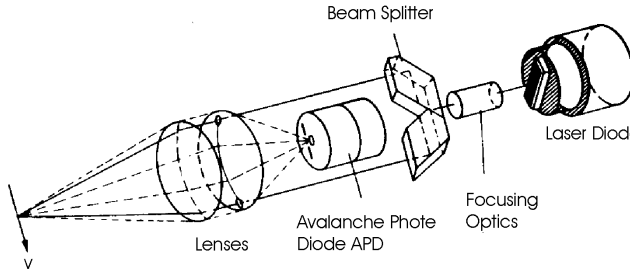

Fig. 3. Sketch of LDV, [12]

4 Numerical method

The mathematical model to describe the system are the incompressible Navier–Stokes equations. Since we are mainly interested in the first bifurcations and to limit the required cpu–times, we use a 2.5–D approach. This means we assume that all dependent variables are constant in the azimuthal direction φ. Numerical computations for the full 3–D problem will be reported in a forthcoming paper.

The 2.5–D incompressible Navier–Stokes equations read in dimensionless form: We are looking for a velocity field $\boldsymbol{u} = u_r \boldsymbol{e}_r + u_z \boldsymbol{e}_z + u_\varphi \boldsymbol{e}_\varphi$ and a pressure field p fulfilling

$$\begin{aligned}
\partial_t u_r + u_r \partial_r u_r + u_z \partial_z u_r - \frac{1}{r} u_\varphi^2 &= -\partial_r p + \frac{1}{Re}\Big(\frac{1}{r}\partial_r(r\partial_r u_r) + \partial_z^2 u_r - \frac{1}{r^2} u_r\Big) \\
\partial_t u_z + u_r \partial_r u_z + u_z \partial_z u_z &= -\partial_z p + \frac{1}{Re}\Big(\frac{1}{r}\partial_r(r\partial_r u_z) + \partial_z^2 u_z\Big) \\
\partial_t u_\varphi + u_r \partial_r u_\varphi + u_z \partial_z u_\varphi + \frac{1}{r} u_r u_\varphi &= \frac{1}{Re}\Big(\frac{1}{r}\partial_r(r\partial_r u_\varphi) + \partial_z^2 u_\varphi - \frac{1}{r^2} u_\varphi\Big)
\end{aligned}$$

$$\frac{1}{r}\partial_r(r u_r) + \partial_z u_z = 0$$

for $t > 0$, $\frac{\eta}{1-\eta} = r_i < r < r_a = \frac{1}{1-\eta}$, $0 < z < \Gamma$ and $0 \le \varphi < 2\pi$ together with the no–slip boundary conditions

$$\begin{aligned}
u_r = u_z = 0, \quad u_\varphi = 1 \qquad & \text{at} \quad r_i = \frac{\eta}{1-\eta} \\
u_r = u_z = u_\varphi = 0 \qquad & \text{at} \quad r_a = \frac{1}{1-\eta} \\
u_r = u_z = 0 \qquad & \text{at} \quad z = 0 \quad \text{and } z = \Gamma
\end{aligned}$$

and either

$$u_\varphi = 0 \qquad \text{at } z = 0 \quad \text{and } z = \Gamma \qquad \text{(symmetric case)}$$

or

$$u_\varphi = r\frac{1-\eta}{\eta} \quad \text{at } z = 0 \quad \text{and } u_\varphi = 0 \quad \text{at } z = \Gamma \qquad \text{(asymmetric case)}.$$

Here we have used dimensionless velocities, pressures and coordinates.

To solve this problem numerically, we use a code based on the method described in [2] and in [17] for the 2.5–D case. The method uses the so called *fractional step θ–scheme* for the time discretization in a variant as an operator splitting to decouple the incompressibility condition from the nonlinearity, see also [8]. For the space discretization the *Taylor–Hood* element, i.e. piecewise quadratic finite elements for the velocity and piecewise linear ones for the pressure, are used.

5 Results

5.1 Symmetric system

In this section the influence of the gap width on the flow is investigated. On this account experiments on bifurcation scenarios in the Taylor–Couette system were carried out for two different radius ratios, $\eta = 0.85$ (small gap) and $\eta = 0.5$ (wide gap). The velocity bifurcation diagrams as illustrated in Fig. 4 and 5 were obtained by collecting the extrema of the velocity time series measured with the LDV-technique with a quasi-stationary increase of the Reynolds number. As it can be seen from the bifurcation diagram (Fig. 4), the flow undergoes a bifurcation from the laminar basic state to a steady Taylor vortex flow via a pitchfork bifurcation. This is an imperfect pitchfork bifurcation perturbed by the boundary conditions. By smoothly increasing the Reynolds number only one branch is reachable, which is the normal mode with inward flow adjacent to the end plates. The anomalous mode may be reached by changing the Reynolds number instantaneously. After this pitchfork bifurcation, the flow bifurcates via a Hopf bifurcation into the Wavy–Mode. With a further increase of the Reynolds number, the flow bifurcates via a second Hopf bifurcation into the modulated wavy mode before chaotic motion occurs. The second critical Reynolds number for the onset of the wavy mode is about 2.5 times higher as the first critical one. In contrast to small cylindrical gaps ($\eta = 0.85$) just mentioned, the experiments on bifurcation scenarios in the wide gap Taylor–Couette system $\eta = 0.5$ show a different bifurcation scenario and a different route into chaos, which is illustrated in Fig. 5. The basic flow bifurcates via a pitchfork bifurcation into Taylor vortex flow. The onset of the Wavy–Mode is shifted to higher Reynolds numbers in comparison to $\eta = 0.85$ because the vortices at the end-plates cannot oscillate due to the boundary conditions. This state is only stable over a small range of Reynolds numbers and it seems that the flow bifurcates directly into chaotic motion.

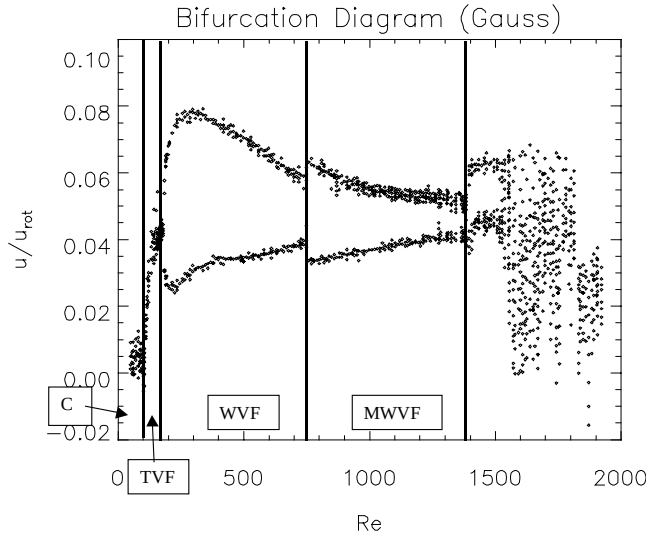

Fig. 4. Bifurcation diagram in the Taylor–Couette system as a function of the Reynolds number. The meridional velocities are normalized by the velocity of rotation ($\eta = 0.85$, $\Gamma = 13.2$, $z = 0.40L$, $(r - R_i)/(R_a - R_i) = 0.6$)
C: Couette flow TVF: Taylor vortex flow WVF: Wavy vortex flow
MWVF: Modulated Wavy vortex flow

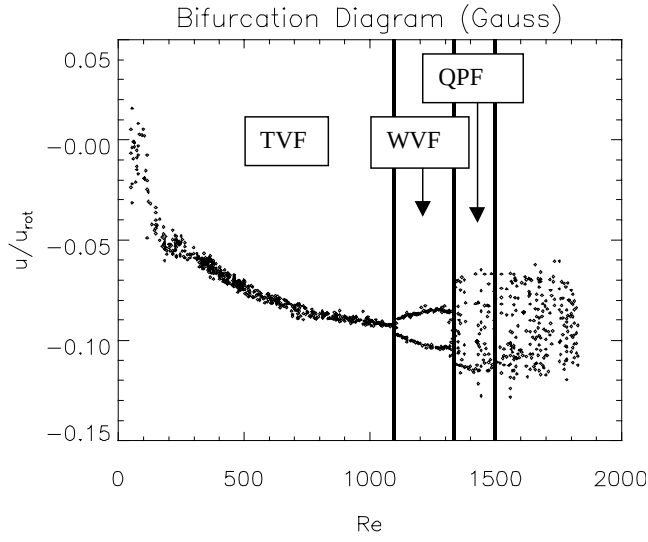

Fig. 5. Bifurcation diagram in the Taylor–Couette system as a function of the Reynolds number. The meridional velocities are normalized by the velocity of rotation.
($\eta = 0.5$, $\Gamma = 3.97$, $z = 0.37L$, $(r - R_i)/(R_a - R_i) = 0.91$)
TVF: Taylor vortex flow WVF: Wavy vortex flow
QPF: Quasiperiodic flow

a)

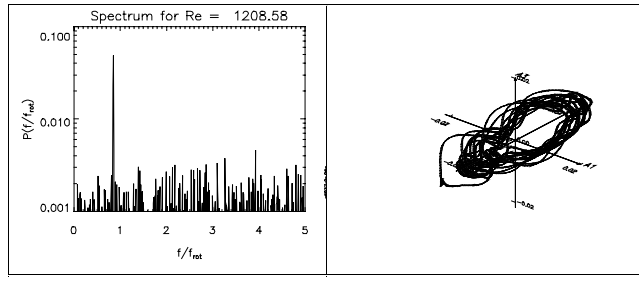

$Re = 1220$

b)

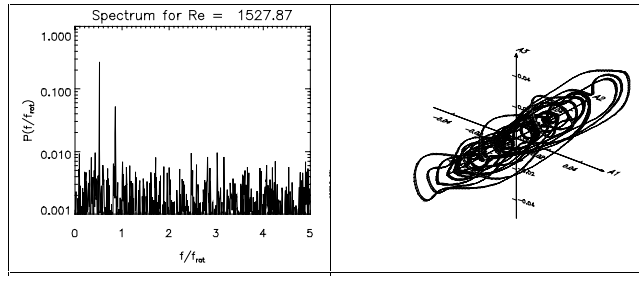

$Re = 1500$

Fig. 6. Power spectrum and attractor in case of two different Reynolds numbers ($\eta = 0.5$, $\Gamma = 3.97$, $z = 0.37L$, $(r - R_i)/(R_a - R_i) = 0.91$)

Figure 6 shows the frequency spectrum and the attractor for two different Reynolds numbers. The spectrum of Fig. 6a shows one characteristic frequency. All diagrams correspond to the Wavy vortex flow state. The reconstruction of the flow yields a limit cycle which is perturbed by noise. In the flow state in Fig. 6b a second frequency occurs at higher Reynolds numbers. The attractor is not a limit cycle anymore. It is pointed out that it is a quasiperiodic flow state and not a chaotic one. The further research is now focussed on the exact investigation of the dynamics of Reynolds numbers higher than Re = 1500.

In Fig. 7 three experimental flow states obtained with the PIV-technique are shown. Fig. 7b shows the normal 4-vortex state which could be reached by increase the Reynolds number in a quasistationary way. Figures 7c and 7d represent the two different anomalous modes which could be obtained in this system with a constant $\Gamma = 3.97$. These two flow states could be adjusted by a sudden increasing of the Reynolds number. In contrast to the stretched 3-vortex state the 5 vortices are squeezed into the system. In comparison with the experimental results a normal flow state is calculated and shown in 7a. The cores of the vortices are shifted to the outer cylinder but not as much as in the experimental result. In the experiment the cores seem to be closer to

the outer cylinder due to the optical way through curved surfaces with different refraction indices. This distortion is reduced in the new experimental setup using a rectangular tank filled with silicon oil enclosing the whole setup, which in addition keeps the working temperature constant.

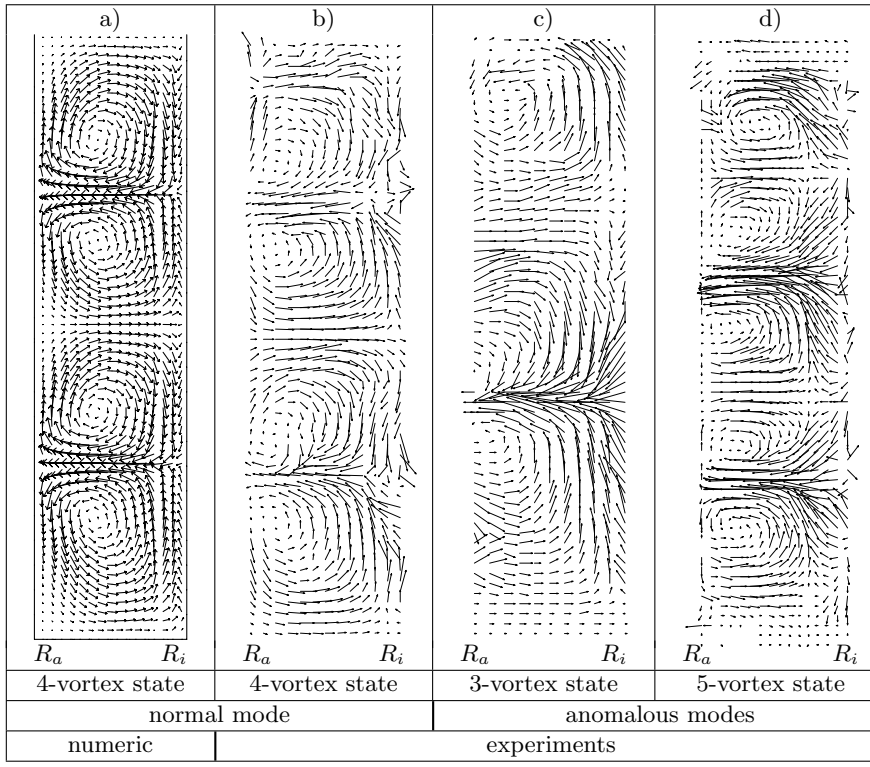

Fig. 7. Experimental and numerical results in case of the following parameters: $\eta = 0.5$, $\Gamma = 3.97$ and $Re = 500$. Experimental results obtained by using different acceleration rates.

To investigate the influence of the boundary conditions in the Taylor–Couette system an asymmetric experimental setup with a rotating bottom plate was constructed. First results are described in Section 5.2.

5.2 Asymmetric system

In this section we also only consider the situation where the outer cylinder is held at rest and the inner rotates. In this part of our research the effects of end conditions should be investigated. In contrast to the previous section the bottom end plate is allowed to rotate with the inner cylinder. As a result of

the rotating bottom plate always outward flow is found adjacent to the rotating plate, whereas at the stationary top plate inward flow occurs. This leads to an odd number of cells in such an experimental setup, when only normal modes are considered.

In 1986, Cliffe & Mullin [7] investigated both experimentally and numerically the interaction between 5-cell and 3-cell modes in the asymmetric system. They investigated the stability of the flow states in a range of $\Gamma = 4.2 - 5.0$ and $Re = 50 - 300$.

Stability of 3-cell and one cell modes

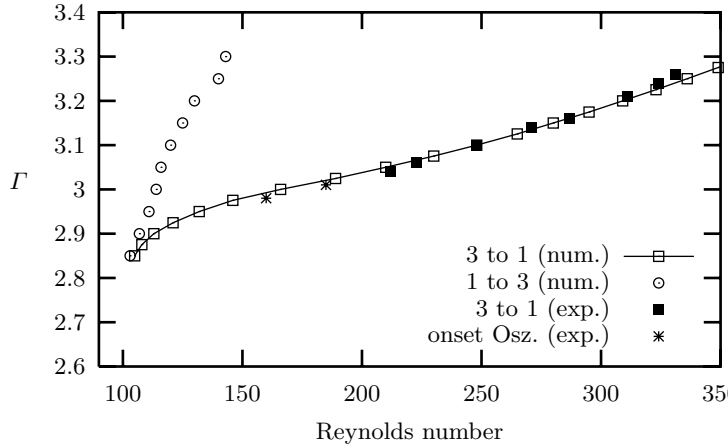

Fig. 8. *Numerical and experimental stability diagram. Squares represent the transition from three vortices to one vortex by increasing the Reynolds number. Stars point out an onset of a oscillation (exp.). Circles indicate the change from 1-cell state to 3-cell state when decreasing the Reynolds number (only numerical).*

In this section the investigations were focussed on the 3-cell and 1-cell modes. A result of this work is the stability diagram of steady solutions shown in Fig. 8. The bordered squares represent the transition from steady 3-cell flow to steady one cell flow by numerical calculations using the numerical method described in Sect. 4. In consideration of the fact that a 2.5–D-Code was used, no transitions to time dependent states were found. The experimental stability limit (filled squares) was investigated by smoothly increasing the Reynolds number at a fixed Γ. The two stares at lower Γ indicate a transition from steady 3-cell flow to a time dependent 1-cell state. A transition from steady 1-cell to steady 3-cell flow by decreasing the Reynolds number was found numerically at the line consists of circles. Experimentally, time dependence occurs by decreasing the Reynolds number at higher values so that this line could not be found in the

experiments [5]. In 1997, Blohm [5] in cooperation with Mullin obtained similar results.

As an example of the two occuring flow states the calculated 3-vortex- and 1-vortex states are shown in Fig. 9 for $\Gamma = 3.2$ and two different Reynolds numbers. The visualization of the numerical results was realized with GRAPE [14]. The arrows represent the velocity components in r- and z-direction in the whole cylindrical gap. The inner cylinder on the left side and the bottom plate are rotating. The top plate and the outer cylinder on the right side are fixed.

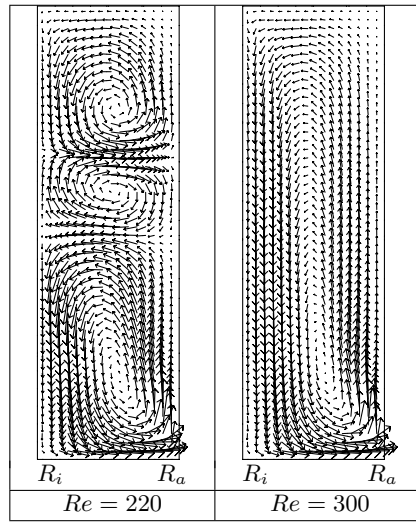

Fig. 9. Numerical results for $\Gamma = 3.2$ Left side and bottom are rotating. The velocity components in r- and z-direction in the whole cylindrical gap are shown respectively.

Growth of bottom vortex

During these investigations it was found numerically that the size of the cell adjacent to the rotating bottom plate is depending on the Reynolds number. For different Γ the size of the bottom vortex in percent of the height of the cylinder was investigated depending on the Reynolds number. The results are shown in Fig. 10. The effect of the growing bottom vortex could be seen clearer in the case of higher values of Γ. At the time these predictions are verified experimentally. Blohm [5] in cooperation with Mullin obtained qualitative similar results experimentally during his diploma thesis. To illustrate these results, different flow states depending on the Reynolds number for two different Γ were calculated. Figure 11 and Fig. 12 show the development of the bottom vortex in the case of $\Gamma = 2.975$ and $\Gamma = 3.225$. These calculations confirm that in the case of a large Γ the effect of growing is considerably more noticeable.

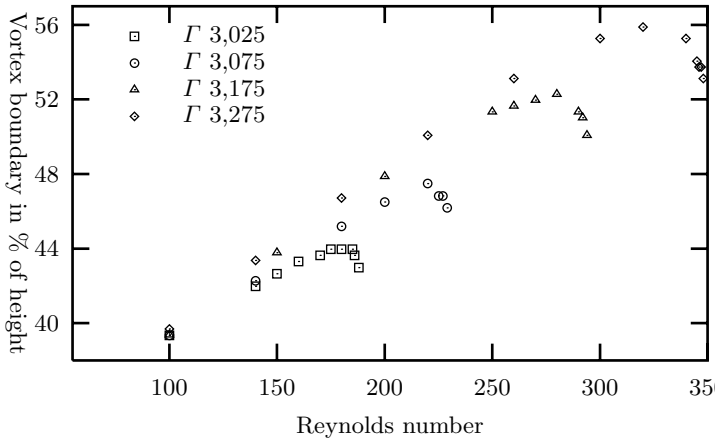

Fig. 10. Numerical results for the growth of the bottom vortex depending on the Reynolds number due to different values of Γ.

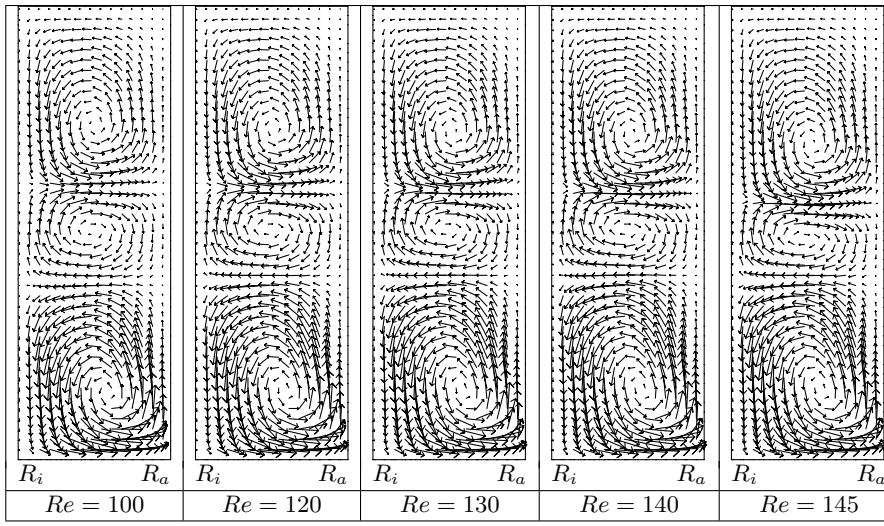

Fig. 11. *Numerical results for $\Gamma = 2.975$ depending on Re.*

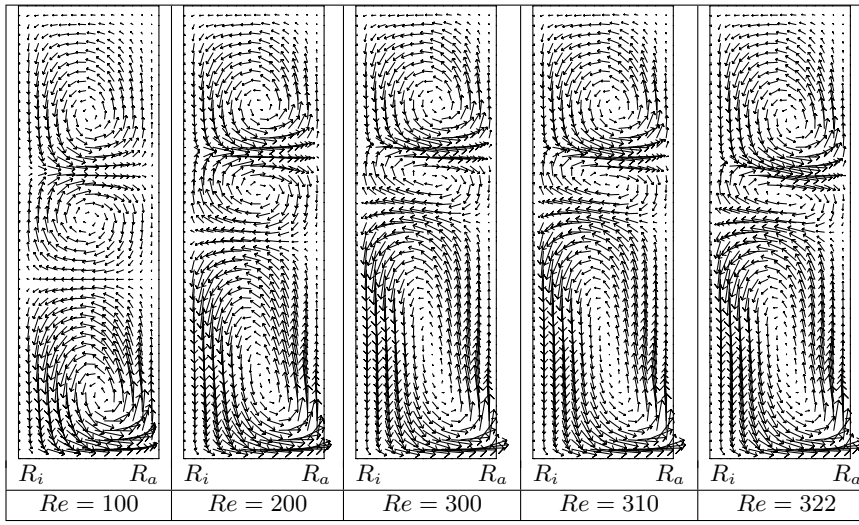

Fig. 12. *Numerical results for $\Gamma = 3.225$ depending on Re.*

Results by decreasing Re: $\Gamma = 3.15$

In this Section an example for the onset of a time dependent flow in the numerical calculations by decreasing the Reynolds number in the case of $\Gamma = 3.15$ is shown. The two graphics in Fig. 13 represent the difference in the flow state in arbitrary units (a.u.) for consecutive time steps. Calculations at $Re = 173$ converge straightly so that a steady state is reached very fast. At $Re = 172$ the flow shows an oscillating behaviour in the difference which is an indication for an oscillating flow in the system although only a 2.5–D-Code was used. Blohm found these oscillations by decreasing the Reynolds number in his experiments.

6 Conclusions

In this work experimental and numerical investigations considering different boundary conditions for the Taylor–Couette system are presented. First the experimental results in a very short annulus due to two different aspect ratios in the symmetric system were described. It could be shown that the gap width influences the dynamic of the flow, which could be seen in the measured bifurcation scenarios.

Then the effect of a rotating bottom plate was investigated. The numerical and the experimental stability boundaries show a very good agreement. The results measured by Blohm and calculated by Mullin [5] are in accordance with our results. Both calculations show a stability limit by decreasing the Reynolds number, which could not be found in the experiments due to a occuring time dependence.

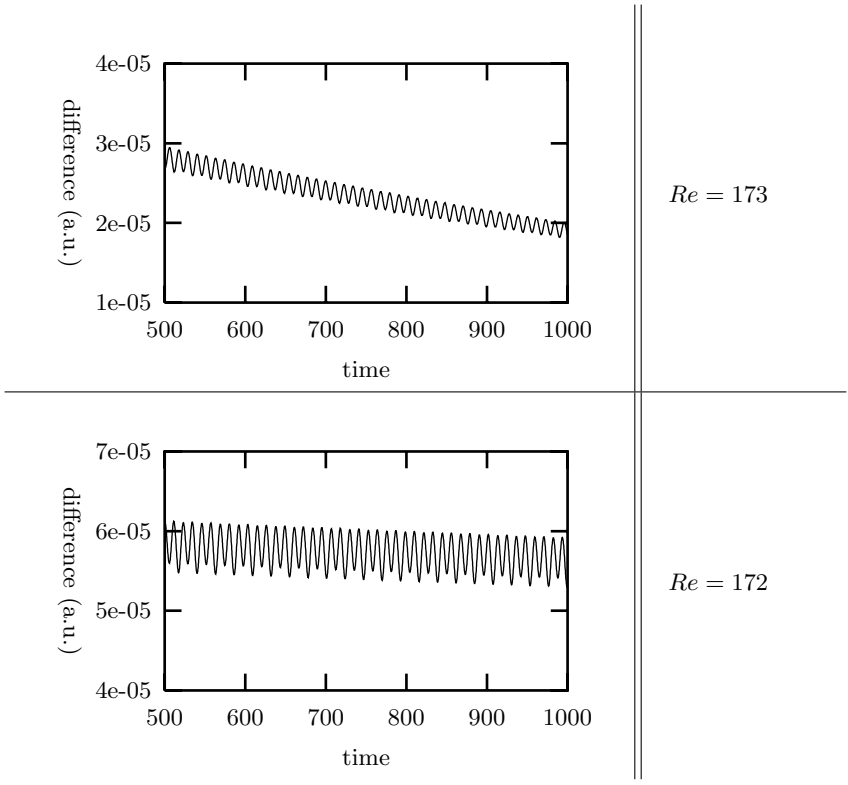

Fig. 13. Difference between two calculated flow states at t and $t + \Delta t$ depending on time for two different Reynolds numbers

The measurements to distinguish the growth of the bottom vortex show qualitatively a good agreement with our calculation. It could be pointed out that the effect depends on the value of Γ.

Indications for the onset of an oscillation were found in our numerical calculations by decreasing the Reynolds number as much as in the experimental investigations of Blohm, [5].

Now we focus our work on comparative experimental investigations with the new built setup and on numerical calculations for the full 3–D problem.

Acknowledgements. The financial support of Deutsche Forschungsgemeinschaft (DFG) is gratefully acknowledged. The authors want to thank Wolfgang Beyer, Rüdiger Maier and Klaus Franke for their assistance during this work.

References

1. Ahlers, G.: *Experiments on Bifurcations and One-Dimensional Patterns in Nonlinear Systems far from Equilibrium*; Complex Systems, SFI Studies in the Sciences of

Complexity, Ed. D. Stein, Addison–Wesley Longman Publishing Group Ltd.,(1989)
2. Bänsch, E.: *Simulation of instationary incompressible flows*; Acta Math. Univ. Comenianae, volume [**LXVII**], pp101-114 (1998)
3. Benjamin, T. B.: *Bifurcation Phenomena in steady flows of a viscous fluid. I. Theory*; Proc. Roy. Soc. Lond., volume [**A359**], pp1-26 (1978)
4. Benjamin, T. B.: *Bifurcation Phenomena in steady flows of a viscous fluid. I. Experiments*; Proc. Roy. Soc. Lond., volume [**A359**], pp27-43(1978)
5. Blohm, C.: *Bifurcation Phenomena in Taylor–Couette flow with asymmetric boundary conditions*, diploma thesis, ZARM, University of Bremen, (1997)
6. Chossat, P.; Iooss, G.: *The Couette–Taylor Problem.* Applied Math. Sc., vol 102, Springer (1994)
7. Cliffe, K.A. and Mullin, T.: *A numerical and experimental study of the Taylor problem with asymmetric end conditions*, 6th Int. Symp. on Finite Element Method in flow problems, June 16-20, Antibes, France, (1986)
8. Bristeau, M.O.; Glowinski, R.; Periaux, J.: *Numerical methods for the Navier–Stokes equations. Application to the simulation of compressible and incompressible flows.* Computer Physics Report 6, 73–188 (1987)
9. Koschmieder, E.L.: *Bénard Cells and Taylor Vortices*; Cambridge University Press, Cambridge, England (1993)
10. Meyer–Spasche, R.: *Pattern Formation in Viscous Flow*; International Series of Numerical Mathematics, volume [**128**], Birkhäuser Verlag (1999)
11. Raffel, M., Willert C., Kompenhans J.: *Particle Image Velocimetry: A Practical Guide* Springer Verlag (1998)
12. Ruck, B.(Edt.): *Lasermethoden in der Strömungsmeßtechnik*, AT-Fachverlag Stuttgart, 1990
13. Ruelle, D. and Takens, F.: *On the nature of turbulence*; Commun. Math. Phys., volume [**20**], pp167-192 (1971)
14. Rumpf, M. and Schmidt, A. et. al.: *GRAPE, Graphics Programming Environment*; report no. 8, SFB 256 Bonn (1990)
15. Tagg, R.: *The Couette–Taylor Problem*; Nonlinear Science Today, volume[**4**], pp1-25 (1994)
16. Taylor, G.I.: *Stability of a viscous liquid contained between two rotating cylinders*; Phil.Trans., volume [**A223**], pp289-343 (1923)
17. Tenhaeff, M.: *Berechnung inkompressibler rotationssymmetrischer Strömungen elektrisch leitender Flüssigkeiten unter dem Einfluß von rotierenden Magnetfeldern.* Diploma thesis, University of Freiburg (1997)
18. Wulf, P.: *Untersuchungen zum laminar turbulenten Überschlag im konzentrischen Kugelspalt* Fortschrittberichte(VDI), Reihe 7, Nr.333 (1997)

Bifurcation and structure of flow between counter-rotating cylinders

Arne Schulz and Gerd Pfister

Institute of Experimental and Applied Physics,
University of Kiel, 24098 Kiel, Germany

Abstract. The properties of fluid flow in the Taylor–Couette experiment between weakly counter-rotating cylinders are investigated experimentally. Attention has been focused on the first instabilities and the detailed structure of the occurring flow states. Modern measurement techniques like LDV and PIV have been used together with visual observations to examine the flow patterns and the stability thresholds very precisely. Our experimental results had been compared with theoretical investigations.

1 Introduction

Much work has been done on the flow states between two concentric rotating cylinders since Taylors [1] landmark paper on this topic. While the different flow patterns occuring between independently rotating cylinders in the small gap case are examined very well experimentally (e.g. by Andereck, Liu and Swinney in 1986 [2]) and can be treated theoretically in form of a small gap approximation, the wide gap case remains up to now over wide parameter ranges unexplored.

If the two cylinders are rotating in the same direction, then the more complex flow patterns appear only for high values of Reynolds numbers. But if one considers counter-rotating cylinders, complex time-dependent flow states may be seen at relatively low Reynolds numbers.
Our experimental investigations were performed in the parameter range from $-310 < Re_o \leq 0$, the case of weakly counter-rotating cylinders.
This paper deals with the detailed examination of the structure and the dynamic properties of the occuring flow states like Taylor vortex flow, two different kind of spiral vortices, wavy vortex flow and with the transitions between them.

2 Experimental setup

The Taylor–Couette experiment, that we report here, consists of two concentric independently rotating cylinders (Fig. 1). The end boundaries are at rest in the laboratory frame.

The inner cylinder of our apparatus has been machined from stainless steel and has a radius of $r_i = 12.5$ mm. The outer one was machined from Duran-glass and its radius is $r_o = 25.0$ mm. Thus the radius ratio is $\eta = r_i/r_o = 0.5$ - the so-called wide gap case.

C. Egbers and G. Pfister (Eds.): LNP 549, pp. 37–54, 2000.

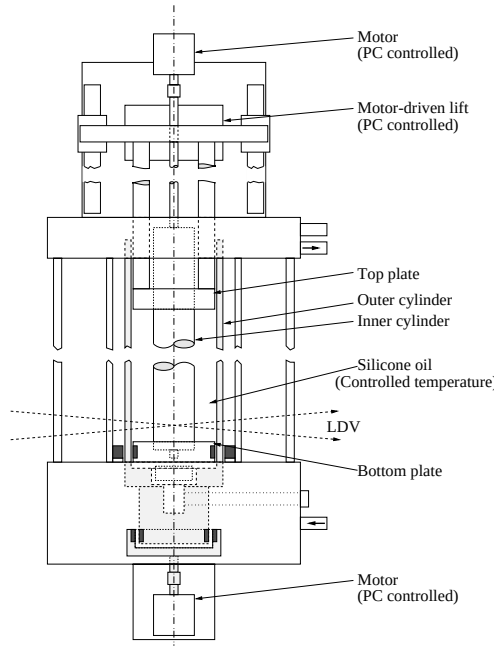

Fig. 1. The Taylor–Couette apparatus.

The dynamic parameters are the inner and outer cylinder Reynolds numbers, which are defined as $Re_{i/o} = (\omega_{i/o} * d * r_{i/o})/\nu$, where ω_i, ω_o are the inner and outer cylinder rotation frequencies, $d = r_o - r_i$ the gap width and ν the kinematic viscosity of the silicone oil in the gap, which is temperature controlled to within $(21 \pm 0.01)°C$. The angular frequency of rotation of the inner and outer cylinder can be adjusted independently with an accuracy better than one part in 10^{-4} per revolution and in direction.

The gap-length to gap-width ratio (aspect ratio) $\Gamma = l/d$ is continuously adjustable between 0.5 and 16.
For the investigations reported here, we fixed l at $l = 150$ mm ($\Gamma = 12$). Gerdts et al. [11] showed for a system with an outer cylinder at rest and $\eta = 0.5$, that there is only a little change in the dynamic properties of the flow for increasing gap-length, if there are six or more vortices in the gap. Just the two- and four-cell systems have a very different behavior due to end effects. So all the resulting flow states are governed by two control parameters: Re_i and Re_o.

We perform high precision Laser-Doppler measurements (LDV) to characterize one component of the velocity field of the flow. Especially for counter-rotating cylinders in the wide gap case the interesting dynamics is located in a region close to the inner cylinder and is not well accessible to visual observations. It

is the rich opportunity of LDV performing experiments with independently rotating cylinder, that the measurement volume of the LDV system can be placed anywhere in the gap, especially at any radial or axial position. The outer cylinder has to be machined at a very high precision for this type of measurement technique, otherwise the quality of the detected signals runs rapidly down.
In addition to this we carry out visual observations to get an overall view of the appearing flow states. So they can be classified more easier.
Our measurement techniques are completed by the use of a Particle-Image-Velocimetry system (PIV), which fills the gap between the LDV measurements and the visual observations. We will show first results here.

3 Stability diagram

The case with an outer cylinder at rest and $\eta = 0.5$ has been treated since many years and is still an actual field of research (e.g. see J. Abshagen and G. Pfister [3]). Many different flow states and interesting dynamics have been uncovered, showing the reach variety of the wide gap Taylor–Couette system (e.g. [4], [5] and papers cited therein).

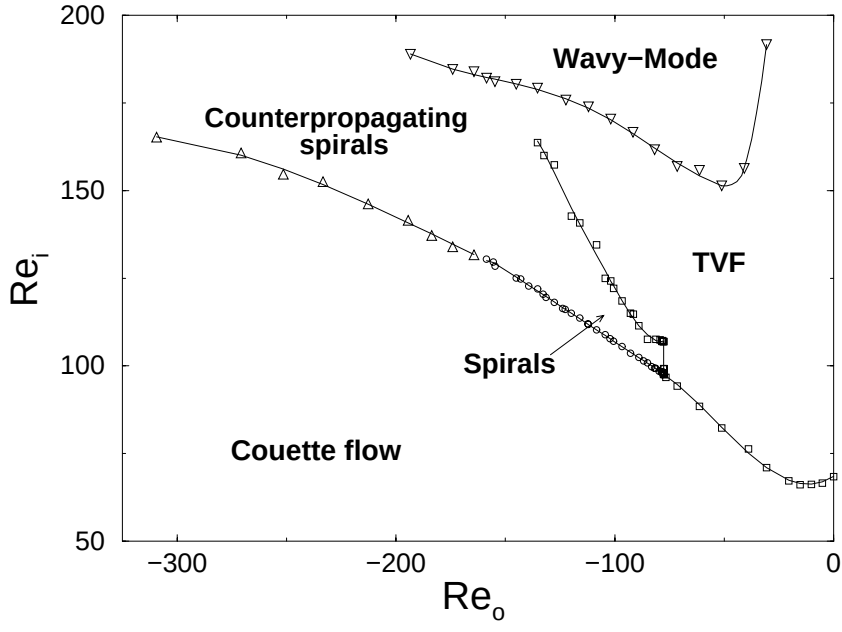

Fig. 2. Stability diagram for counter-rotating cylinders with $\eta = 0.5$. Recorded is the inner cylinder Reynolds number Re_i versus Re_o, the outer cylinder one.

In this presentation we show new flow structures occurring in the Taylor–Couette apparatus with a rotating outer cylinder. Fig. 2 shows a diagram of experimentally observed flow states between counter-rotating cylinders for the selected range of Reynolds numbers.

Recorded is the inner cylinder Reynolds number Re_i versus Re_o, the outer cylinder one. The transition boundaries were located by fixing the outer cylinder Reynolds number Re_o first and then slowly increasing Re_i within $0.01 \leq \Delta Re_i \leq 0.1$. The time between two steps is about 15 minutes.

In the selected parameter range the laminar Couette flow becomes unstable for stationary Taylor vortex flow and for stronger counter-rotation rates it gives way directly to time periodic spiral vortices, which are traveling waves in the azimuthal and axial direction.
This transition takes place for rotation rates of the outer cylinder $Re_o \leq -77.54$ and is directly connected to the region, where the Couette flow becomes unstable for Taylor vortices.

So there is a point, at which modes of two different azimuthal wavenumbers are unstable at the same time (this is called a bicritical point). The first one results from a Hopf bifurcation, the other from a steady state bifurcation.

For $Re_o \leq -160$ the spatio-temporal characteristics of the spiral flow changes and we get counter-propagating spirals.

As Re_i is increased, we found a Wavy-Mode (Fig. 2), which consists of modulated waves on the Taylor vortices with an azimuthal wavenumber $m = 2$ for $Re_o \geq -158$, which was predicted theoretically by Jones [6] as the strongly preferred mode there. A lower azimuthal wavenumber ($m = 1$) could be observed for stronger counter-rotation rates ($Re_o < -158$).

There still is a region in the parameter space ($Re_o \leq -200$ and above the stability threshold of the counter-propagating spirals), that has not been explored in detail up to now, but we find interesting phenomena there, which we will discuss later.

4 Primary instabilities

First of all we consider the primary instabilities, that loses the laminar Couette flow stability for: Taylor vortex flow, spiral flow and counter-propagating spiral flow.

4.1 Transition to Taylor vortex flow (TVF)

For low rotation rates $Re_o \geq -77.54$ a transition to Taylor vortices occurs. It is well known, that end effects in a finite Taylor–Couette apparatus are very

important ([7–10]). The transition from Couette flow to TVF is a continuous process and not an instability. The Ekman vortices induce Taylor vortices, that build up gradually from the end plates.
So we put the measurement volume of the LDV system in the midplane of the cylinder. Then we increase the inner cylinder Reynolds number Re_i and record the amplitude of the detected signal. Finally we fit a square root function,that gives the transition point to TVF.

With this scenario we could find the transition point for an outer cylinder at rest ($Re_o = 0$) as $Re_i = 68.4$. This value agrees well with those obtained experimentally and theoretically (see e.g. [10] and papers cited therein).

A rotation of the outer cylinder is seen here to be at first weakly destabilizing, but soon becomes stabilizing. The minimal value of the transition point is for an outer cylinder Reynolds number $Re_o = -15.26$ and could be determined to $Re_i = 66.05$.
For an outer cylinder at rest, the Taylor vortices fill the whole gap between the outer and inner cylinder. This changes if one considers the counter-rotating case:

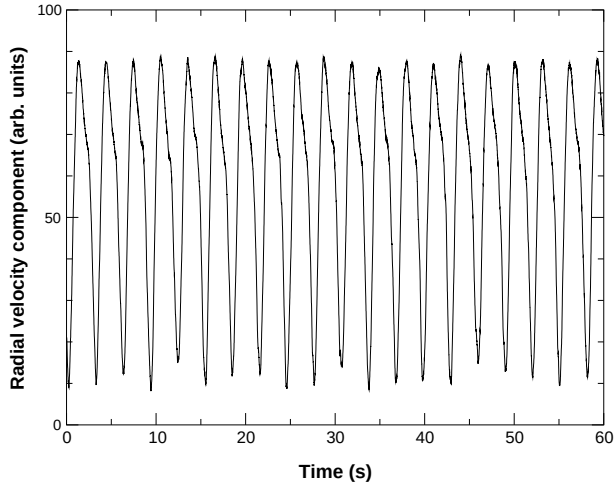

Fig. 3. A typical time series of spiral vortex flow measured with a LDV system at $Re_o = -94.71$ and $Re_i = 111.01$.

The size of the vortices shrinks for stronger counter-rotation. The vortices themselves appear only near the inner cylinder, while there is a weak circulation of the fluid in the area near the outer cylinder in the opposite direction. G.I. Taylor himself [1] was the first one who did experimental and theoretical work on this phenomena, concerning the size of individual vortices at the onset of

instability as a function of the angular speed ratio. Although he worked in the small gap case, his results agree qualitatively with the ones reported here.

Due to the fixed aspect ratio we observed that the number of Taylor vortices N, that develop when the laminar Couette flow becomes unstable, increases from $N = 12$ at $Re_o = 0$ to $N = 14$ at $Re_o \approx -30$.

4.2 Transition to time–dependent flow states

For stronger counter-rotating rates ($Re_o \leq -77.54$) the laminar Couette flow gives way to time-periodic spiral vortex flow.
In the selected parameter range from $-310 < Re_o \leq -77.54$ we found two kinds of spirals: The first one we call just *Spirals* which are either up- or downwards traveling waves, located in the center of the cylinder. This flow state is taken over from the other one, which we call *Counter-propagating Spirals*. They start from the top and the bottom of the cylinder and travel towards the midplane.

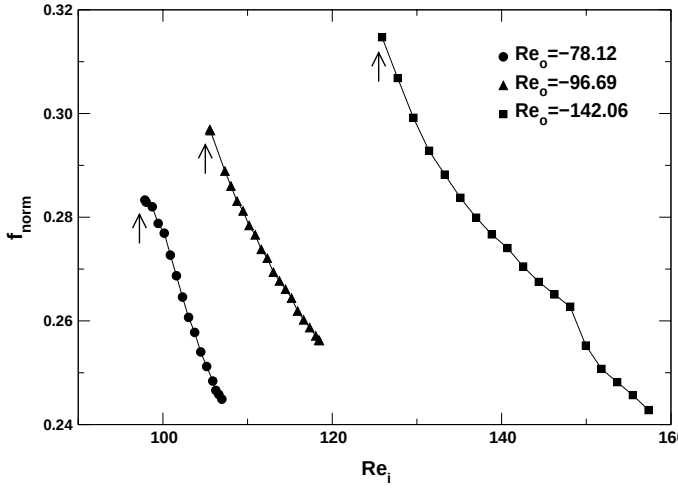

Fig. 4. Normalized frequencies of the spirals for increasing Re_i above its critical values. The onset of the spirals is marked by an arrow.

Spirals:

Figure 3 shows a typical time series of the Spirals at $Re_o = -94.71$ and $Re_i = 111.01$ obtained by Laser-Doppler velocimetry. The spirals are time-periodic and appear as an oscillation of the radial velocity component. The measurement volume of the LDV system is placed in the midplane at a distance

of 4.5 mm from the inner cylinder. The azimuthal wavenumber of the spirals is $m = 1$. This could be specified by visual observations and with two LDV systems placed on both sides of the inner cylinder.

Figure 4 presents the frequency of the spirals normalized to the frequency of the rotation rate of the inner cylinder f_{norm} versus the inner cylinder Reynolds number Re_i. It shows the development of the normalized frequencies from their onset (marked by an arrow) for three different outer cylinder Reynolds numbers $Re_o = -78.12$, $Re_o = -96.69$ and $Re_o = -142.06$. The frequencies decrease for increasing Re_i monotonously until suddenly a transition to stationary Taylor vortex flow occurs (see Fig. 2).
The axial wavenumber $k = 2\pi/\lambda^*$, with the dimensionless wavelength $\lambda^* = \lambda/d$, increases for stronger counter-rotating rates. So we determined experimentally the values of k to $k = 3.57$ at ($Re_o = -94.71$, $Re_i = 111.01$) and $k = 4.16$ at ($Re_o = -142.06$, $Re_i = 125.88$). A more detailed study is in progress.

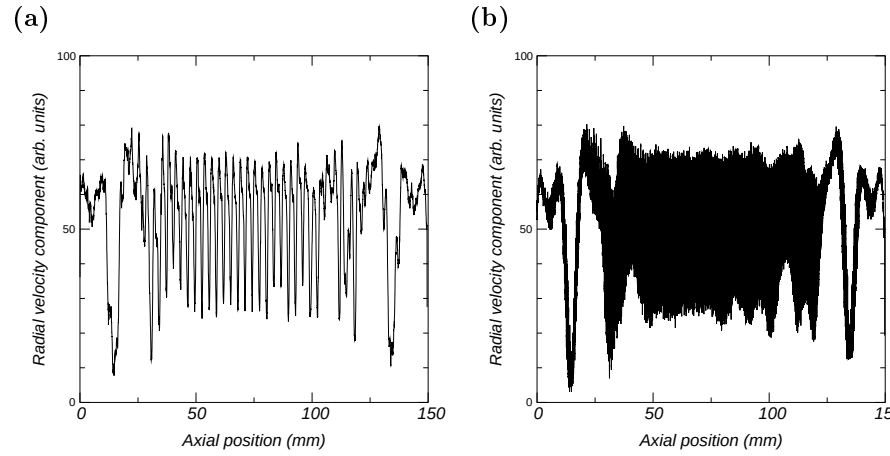

Fig. 5. Radial velocity profiles of the spiral vortex flow at $Re_o = -112$ and $Re_i = 115$, while scanning from bottom to top with (a) 1 mm/s and (b) 0.1 mm/s. Recorded is the radial velocity component versus the axial position within the cylinder (0 mm is the bottom plate, 150 mm the top plate).

The interesting dynamics in the wide gap case for counter-rotating cylinders takes place near the inner cylinder. The LDV system enables us to examine it very well all over the gap.
To get informations about the spatio-temporal characteristics of the flow states we recorded velocity profiles. Fig. 5*a* and 5*b* show profiles of the radial velocity component versus the axial position within the cylinder. We got these profiles by setting the measurement volume of the LDV system at the bottom plate of the

cylinder and move it towards the the top plate at a fixed distance to the inner cylinder and with a given recording velocity v_{rec}. So the measurement volume moves through the whole cylinder and we can imagine which flow state is spread out.

The recording velocity in Fig. 5*a* is $v_{rec} = 1$ mm/s. The axial position $z = 0$ mm is the bottom plate and $z = 150$ mm the top plate. The spiral waves appear in the velocity profile as an oscillation of the radial velocity component (see Fig. 3) and are spread out in the center from $z \approx 30$ mm to $z \approx 120$ mm. At the end boundaries we find stationary Ekman vortices with a strong outflow, that appears as large peaks at $z \approx 15$ mm and $z \approx 135$ mm.

If one moves the measurement volume more slowly ($v_{rec} = 0.1$ mm/s), as shown in Fig. 5*b*, the scan through the entire length of the apparatus takes 25 minutes. In this time more spiral waves move through the volume and the region, where the spirals exist, appears as black area. The Ekman vortices are shown even clearer here.
These spirals move in one direction, either up- or downwards as seen by visual observations.

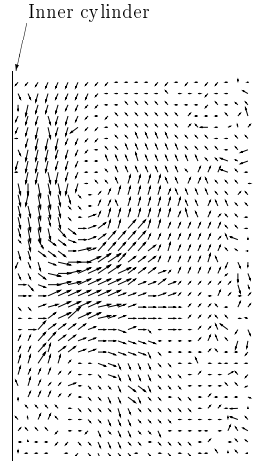

Fig. 6. The velocity field of the spiral vortex flow measured with a PIV system at $Re_o = -100$ and $Re_i = 115$.

Figure 6 shows a snapshot of the velocity field of the spiral flow obtained by PIV measurements at $Re_o = -100$ and $Re_i = 115$. The left-hand edge is at the inner, the right-hand edge at the outer cylinder. This spiral moves from the top to the bottom plate. Obvious there is a steep outward flow. This is in a good agreement with numerical calculations (see Fig. 3b in [18]).

Counter-propagating spirals:

For stronger counter-rotation ($Re_o \leq -160$) a transition from Couette flow to counter-propagating spirals occurs.
This flow state consists of two different spiral waves, one starts at the bottom plate, the other at the top plate. These spiral vortices have the same frequency (same propagation velocity) and travel towards the midplane.

Figure 7 shows profiles of the radial velocity component and demonstrates the growth of counter-propagating spirals at an outer cylinder Reynolds number of $Re_o = -309$ for increasing Re_i.
For values less than the critical Reynolds number $Re_{i,crit}$ for the first instability the laminar Couette flow is present. This can be seen in Fig. 7a at $Re_i = 164.56$. There just appears an Ekman vortex at the top and bottom plate in each case. If one increases the inner cylinder Reynolds number (Fig. 7b to 7e) the counter-propagating spirals spread out into the upper and lower thirds of the cylinder. The two spirals approach to each other step by step and finally meet in the midplane at $Re_i = 171.72$ (Fig. 7f), forming a complex flow state. So it is a weak onset analogous to the one of Taylor vortex flow, but it is yet not understood in detail.

These velocity profiles were recorded while moving the measurement volume of the LDV system from the bottom to the top. One travels in the same direction as one spiral and against the other. So one oscillation appears widened, the other shrunk. When the spirals have met another (Fig. 7f), the wavelength of the spiral vortices in the midplane shrinks, while the frequency has to be the same. It is obvious, that these counter-propagating spirals have another spatio-temporal characteristic than the spirals.
While the codimension-2-point, that separates the Taylor vortex flow from the spirals is sharp and could be determined as $Re_o = -77.54$, we could not find an exact point at which the transition takes place from Couette flow to either spirals or counter-propagating spirals. It is rather a region in the parameter space of about 20 Reynolds numbers of the outer cylinder, where the two flow states coexist.
No hysteresis occurs in traversing the line, that separates the Couette flow from the spirals or the counter-propagating spirals, in any direction.

5 Transition from Spirals to TVF

For outer cylinder Reynolds numbers $Re_o \geq -150$ the spirals become directly unstable to stationary Taylor vortices (Fig. 2), that appear over the entire length of the apparatus.
This transition is a more complex one, e.g. we found hysteresis in traversing the stability threshold. We still work on it and won't discuss it in this paper any further.

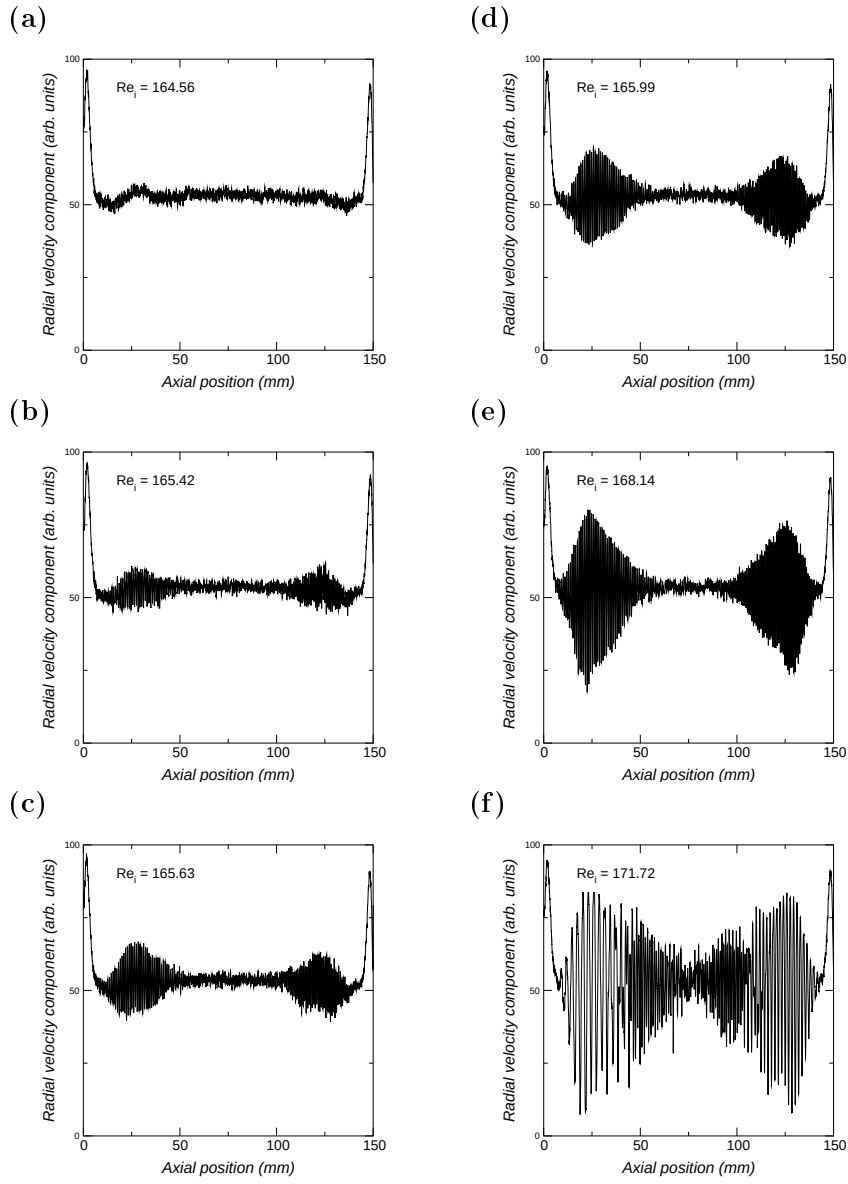

Fig. 7. Counter-propagating spirals at $Re_o = -309$. Recorded is the radial velocity component versus the axial position within the cylinder. Re_i increases from $Re_i = 164.56$ (a) to $Re_i = 171.72$ (f) showing the formation of the flow state.

6 Wavy–vortex flow

With an outer cylinder at rest and radius ratio $\eta = 0.5$, several different flow states occur, that loses Taylor vortex flow stability for: the so-called Small-jet

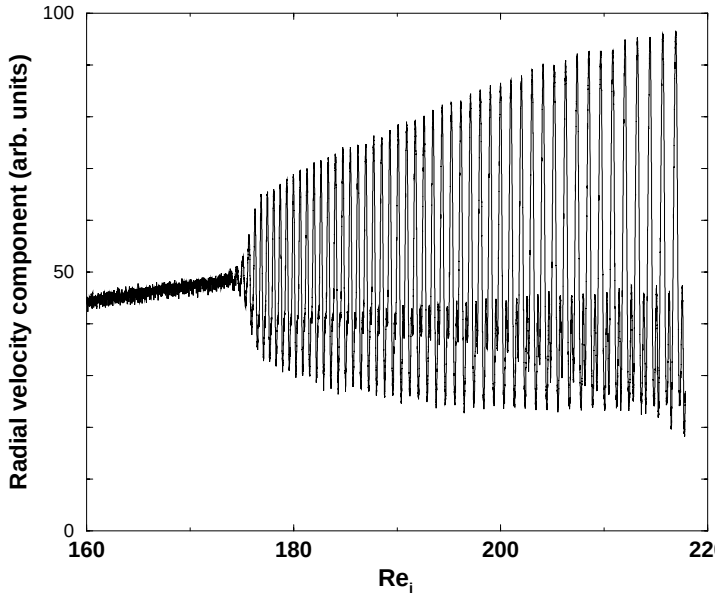

Fig. 8. Bifurcation diagram for the wavy mode at $Re_o = -112$. The Reynolds number is scanned quasistatically from $Re_i = 160$ to $Re_i = 218$ with $\Delta Re_i/\Delta t = 0.09\, s^{-1}$.

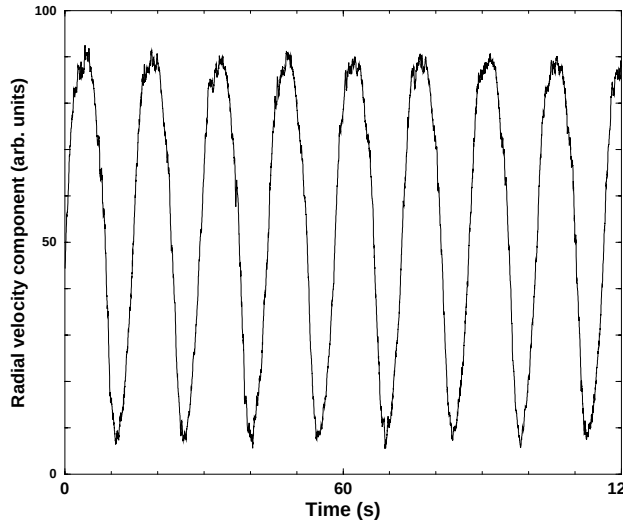

Fig. 9. A typical time series of the wavy flow measured with a LDV system at $Re_o = -100$ and $Re_i = 262.6$.

mode, which is an oscillation of the outward flow while the inward flow remains almost stationary, the antijet mode, which has its strongest oscillation in the inward flow, the core mode, oscillations of the vortex core and a wavy mode, an oscillation of the entire vortex. Gerdts et al. [11] explored the stability diagram for the onset of time dependence for the normal four- to 16-vortex flow. They normalized the aspect ratio Γ by the number of Taylor cells N in the cylinder. $\Gamma/N \approx 1$ is for Taylor vortices having a wavelength twice the gap width d - so the vortices fill the whole gap. This normalisation has been done for reason of classifications of the different time dependent flows.

The wavy mode can be found as the first time periodic instability in a system with extended wavelengths ($1.1 \leq \Gamma/N \leq 1.7$). Different from the classic narrow-gap wavy mode (e.g. [12–14]) the wavy mode one finds in the wide gap Taylor–Couette system with only the inner cylinder rotating has an azimuthal wavenumber $m = 1$ and is characterized by a relatively small amplitude of the oscillation.

In the case of counter-rotating cylinders a new type of wavy mode occurs over a wide parameter range (Fig. 2). Its appearance via a Hopf bifurcation is similar to a wavy mode in the small gap case, with the exception of the lower azimuthal wave number that we find here.
This wavy mode was described for the first time by Snyder [15], who did his experiments in a Taylor–Couette apparatus with $\eta = 0.5$ and an upper free surface. He found that a variation of the wavelength λ with Re_i and Re_o held constant, which he performed by increasing or decreasing the level of the fluid, has a large effect on the drift velocity of the wave form.

Starting from the Taylor vortices the flow undergoes a Hopf bifurcation at higher Reynolds numbers. A typical bifurcation diagram is shown in Fig. 8. Recorded is the radial velocity component versus the Reynolds number of the inner cylinder, with is scanned quasistatically from $Re_i = 160$ to $Re_i = 218$ with $\Delta Re_i/\Delta t = 0.09\ s^{-1}$. Here the outer cylinder Reynolds number is equal to $Re_o = -112$. The wavy mode has an azimuthal wavenumber of $m = 2$ for $Re_o \geq -158$ as shown by visual observations and with two LDV systems, and a lower one ($m = 1$) for $Re_o < -158$. The amplitude of oscillation is small at its onset and grows in the selected parameter range continously for increasing Re_i. The lowest value at which the wavy-mode with $m = 2$ appears is $Re_i = 151.3$.

The time series of the wavy mode obtained by Laser Doppler velocimetry shows a time-periodic oscillation with a relatively low frequency (Fig. 9). The characteristics of the time series depends strongly on the position of the measurement volume of the LDV system. This can be realized from Fig. 10, which results from particle image velocimetry measurements.

The velocity-vector plots (Fig. 10) show one half the cycle of the wave-form at $Re_o = -100$. Starting from a state, where both vortices of a pair have nearly

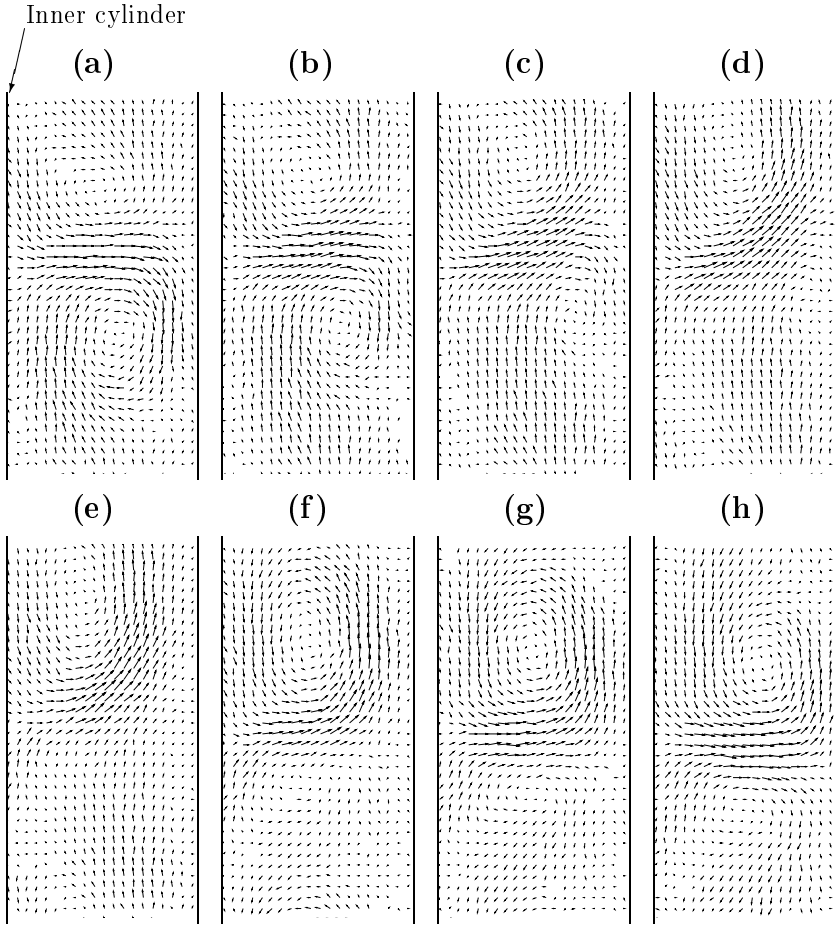

Fig. 10. Results of PIV measurements on the $m = 2$ wavy-mode at $Re_o = -100$ and $Re_i = 306$ showing one half of a period.

the same size and their cores have nearly the same distance to the inner cylinder (Fig. 10a), one finds a strong outflow that tends to one side. One vortex spread out into that direction, the other one gets smaller and the core of that vortex moves to the outer cylinder (Fig. 10b, 10c). If the first vortex has extended to his maximum, the other is hardly visible (Fig. 10d). This is a quarter of the period. In the next quarter the sequence reverses. A small vortex appears near the inner cylinder and begins to grow, until both vortices have the same size (Fig. 10e - 10h). The scenario, that is described up to now, starts in the opposite direction, forming so a complete period of the flow state. All vortices in the

gap are unstable against the wavy mode, even the Ekman vortices.

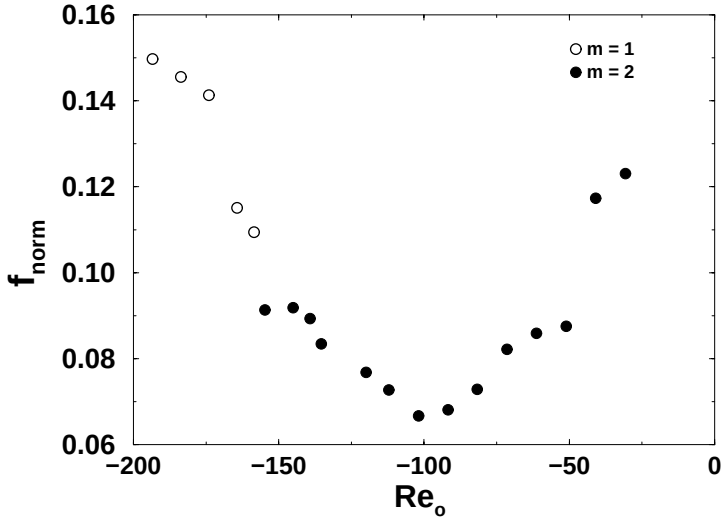

Fig. 11. Frequencies of the wavy mode (normalized to the rotation rate of the inner cylinder) as function of the outer cylinder Reynolds number Re_o. Re_i is for all cases just above its critical value.

The frequencies of the wavy mode, normalized by the rotation rate of the inner cylinder and measured at their onset, is recorded versus Re_o, the outer cylinder Reynolds number (Fig. 11). One finds clearly a minimum of the normalized frequencies at $Re_o \approx -100$, while the wavy mode appears first at an outer cylinder Reynolds number of $Re_o = 51$ (see Fig. 2). There is no connection between these two minima.

For $Re_o \geq -45$ a second $m = 2$-mode has been found. The amplitude is much smaller than in the case of stronger counter-rotation rates. Its properties are close to the wavy-mode with $Re_o = 0$.

Above the onset of the wavy-mode the frequency decreases for increasing Re_i, reaches a minimum and increases again. Finally a transition to modulated wavy vortex flow occurs. This scenario is similar to the one reported by King [16] in the case of an outer cylinder at rest.

7 Observation of propagating Taylor vortices

The region in the stability diagram (Fig. 2) above the onset of the counter-propagating spirals and for counter-rotation rates $Re_o \leq -200$ has not been

examined in detail up to now. We just describe the flow states, that we found there, for $Re_o = -210$ exemplarily.
As described in section 3 the laminar Couette flow loses its stability at $Re_i = 145$ and counter-propagating spirals spread out. This flow state is taken over by propagating Taylor vortices with $m = 0$ at $Re_i \approx 160$. These Taylor vortices arise near the top and the bottom plates and travel in pairs towards the midplane, where they are compressed and finally the outward flows of two neighbouring vortex pairs meet each other and only one pair remains. This flow state is time-dependent, but not periodic.
A further increase in Reynolds number leads to a wavy mode at $Re_i \approx 210$. In contrast to the wavy mode found at lower counter-rotating rates, this one has an azimuthal wavenumber $m = 1$. The wavy mode with $m = 2$ can be found as well, but it appears at higher Reynolds numbers ($Re_i \approx 350$), after the $m = 1$ mode became modulated.

8 Comparison to theoretical investigations

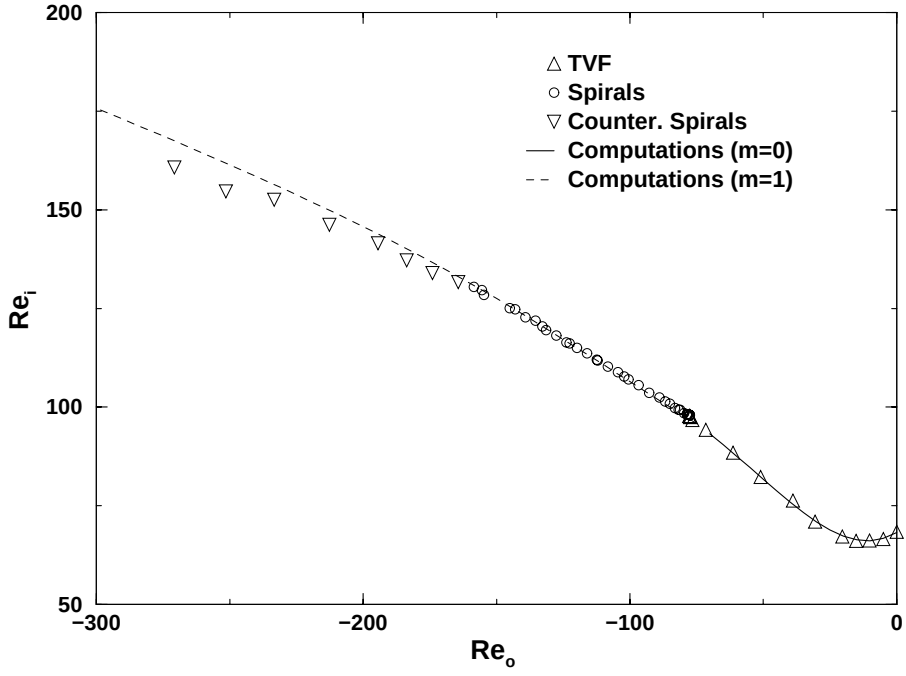

Fig. 12. Critical values of Re_i as function of Re_o for the onset of the first instability. Experimental values compared with theoretical ones [17], [18].

We compared our experimental results to numerical calculations of W.F. Langford, R. Tagg, E.J. Kostelich, H.L. Swinney, M. Golubitsky [17] and Chr. Hoffmann and M. Lücke [18].

There is a good agreement concerning the onset of the first instability. This is shown in Fig. 12 : Recorded is the Reynolds number of the inner cylinder Re_i versus the outer cylinder one Re_o. The symbols are our experimentally determined critical points for TVF, Spirals and Counter-propagating spirals. The solid curve is the calculated stability threshold for $m = 0$ (TVF), the dashed one for $m = 1$ (Spirals). Langford et al. and Hoffmann and Lücke get the same results for the critical values of Re_i as function of Re_o for the onset of the first instability in the selected parameter space ($-300 \leq Re_o \leq 0$).
Although the counter-propagating spirals are not considered in the theoretical analysis, there is a good qualitative agreement. Theoretical and experimental results differ only within a few percent.

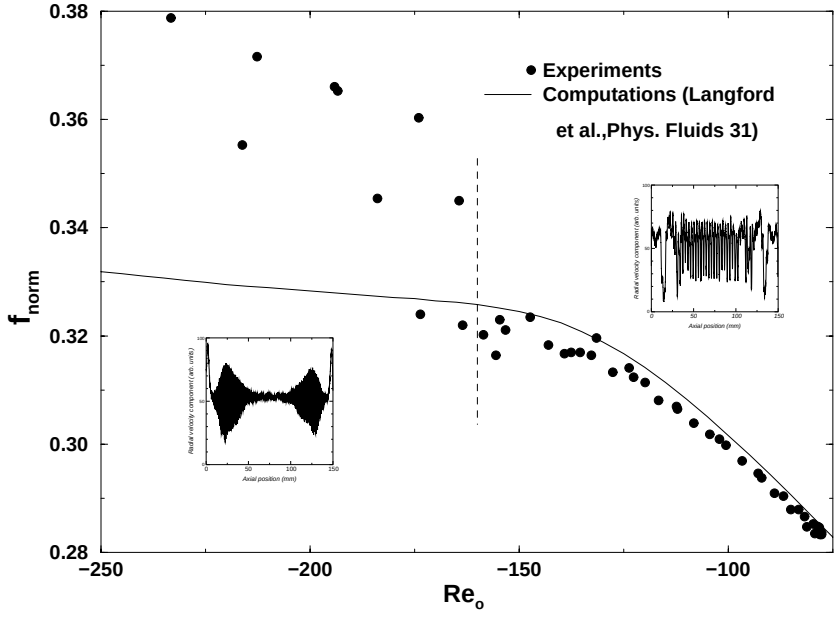

Fig. 13. Normalized frequencies of the spiral flow versus the outer cylinder Reynolds number. As long as there are spirals there is a good agreement between theory (solid line) and experiment (symbols).

The experimentally observed frequencies of the spiral vortices normalized to the rotation rate of the inner cylinder are in good agreement with the theory for outer cylinder Reynolds numbers $Re_0 \leq -160$ (Fig. 13). These values were obtained by Langford et al. [17].

For stronger counter-rotating rates they differ from the computations. Langford et al. considered the spirals up to $Re_o = -300$ in their calculations, while we found the counter-propagating spirals for $Re_o \leq -160$ as indicated by the small pictures inside Fig. 13. At the onset of the counter-propagating spirals the experimentally obtained frequencies differ from theory.

9 Conclusion

We investigated bifurcations and structure of flow between weakly counter-rotating cylinders with $\eta = 0.5$. We could determine the stability thresholds for the occuring flow states Taylor vortex flow, spirals, counter-propagating spirals and wavy mode. Laser-Doppler velocimetry and particle image velocimetry as two modern measurement techniques were used to get precise insight to the flow structure. This becomes necessary especially because with counter-rotating cylinders in the wide gap case the interesting dynamics takes place near the inner cylinder.

We were able to carry out the spatio-temporal characteristics of the two different kinds of spiral flows by use of velocity profiles obtained by LDV. The measurement volume of the LDV system can be placed anywhere in the gap. So the precise properties of the flow become accessible for the first time.

We explored the development of frequencies for the different time-periodic flow states and moreover, we found new interesting flow states like propagating Taylor vortices with $m = 0$, that start at the top and bottom plate and travel towards the midplane, where they collaps. We still work on this phenomena.
Our experimental results concerning critical points and azimuthal wave speed values were compared to theoretical investigations of Langford et al. [17] and Hoffmann and Lücke [18]. They show good agreement over a wide parameter range.

Acknowledgments

We are grateful towards Chr. Hoffmann and M. Lücke for providing the theoretical critical values for the first instability, co-operation and helpful discussions and thank J. Langenberg for help with the PIV measurements.

References

1. G.I. Taylor: Phil. Trans. Roy. Soc. London A **223** (1923)
2. C.D. Andereck, S.S. Liu, H.L. Swinney: J. Fluid Mech. **164** (1986)
3. J. Abshagen, G. Pfister: this book (2000)
4. J. Abshagen, A. Schulz, G. Pfister: 'The Couette-Taylor flow: A paradigmatic system for instabilities, pattern formation and routes to chaos'. In: *Nonlinear physics of complex systems - Current status and future trends*, ed. by J. Parisi, S.C. Müller, W. Zimmermann (Springer, Heidelberg 1996) pp. 63 – 72

5. F.H. Busse, G. Pfister, D. Schwabe: 'Formation of dynamical structures in axisymmetric fluid systems'. In: *Evolution of spontaneous structures in dissipative continuous systems*, ed. by F.H. Busse, S.C. Müller (Springer, Berlin 1998) pp. 86 – 126
6. C.A. Jones: J. Fluid Mech. **120** (1982)
7. D. Coles: J. Fluid Mech. **75** (1976)
8. T.B. Benjamin: Proc. R. Soc. (London) **359** (1978)
9. D.G. Schaeffer: Math. Proc. Camb. Phil. Soc. **87** (1980)
10. G. Pfister, I. Rehberg: Phys. Lett. A **83** (1981)
11. U. Gerdts, J. von Stamm, T. Buzug, G. Pfister: Phys. Rev. E **49** (1994)
12. D. Coles: J. Fluid Mech. **21** (1965)
13. M. Gorman, H.L. Swinney: J. Fluid Mech. **117** (1982)
14. T. Mullin: Physical Review A **31** (1985)
15. H.A. Snyder: J. Fluid Mech. **35** (1968)
16. G.P. King, Y. Li, W. Lee, H.L. Swinney, P.S. Marcus: J. Fluid Mech. **141** (1984)
17. W.F. Langford, R. Tagg, E.J. Kostelich, H.L. Swinney, M. Golubitsky: Phys. Fluids **31** (1988)
18. Chr. Hoffmann, M. Lücke: this book (2000)

Spiral vortices and Taylor vortices in the annulus between counter-rotating cylinders

Christian Hoffmann and Manfred Lücke

Institut für Theoretische Physik,
Universität des Saarlandes, D-66041 Saarbrücken, Germany

Abstract. Vortices in the Taylor-Couette system with counter-rotating cylinders are investigated numerically in a set up with radius ratio $\eta = 0.5$. The full, time dependent Navier-Stokes equations are solved with a combination of a finite difference and a Galerkin method. Structure, dynamics, and bifurcation behavior of Taylor vortices and of spiral vortex solutions are elucidated. Some of their properties obtained for axially periodic boundary conditions are compared with recent experimental results.

1 Introduction

Vortex flow in the Taylor-Couette system with counter-rotating cylinders has attracted an ever increasing research interest since in 1966 Krueger et al. [1] predicted primary transitions to nonaxisymmetric rotating-wave flow which then were observed in experiments by Snyder [2] who had presented experimental evidence for different types of stable helical flow (referred to as 'spirals') a few years earlier. In 1985, an experimental survey was published by Andereck et al. [3] which classified a large variety of different flow states, including some spiral types like linear, modulated, interpenetrating, and wavy spirals etc. An extensive numerical linear stability analysis was then performed for a wide range of radius ratios by Langford et al. [4]. At this time, Tagg et al. [5] experimentally observed a transition from the basic circular Couette flow (CCF) to axially standing and azimuthally traveling waves (ribbons) and found numerically calculated wave speeds to be in accord with experimental results. Edwards [6] studied the transition from CCF to traveling waves. A literature survey has been compiled by Tagg [7] and a review of the bifurcation theory can be found in ref. [8].

Recently, Antonijoan et al. [9] presented an extensive numerical analysis of spiral flow in a system with a relatively narrow gap subject to axially periodic boundary conditions. They used a pseudospectral discretization of the Navier-Stokes equations (NSE) in a co-rotating frame of reference with helical coordinates which were adapted to the expected spiral pattern. In this contribution, we present numerical results obtained with a finite differences algorithm combined with a Galerkin spectral code. The focus of our study is on comparing the spatio temporal structure and the bifurcation behavior of Taylor Vortex Flow (TVF) and Spiral Vortex Flow (SPI), being competing primary vortex patterns that bifurcate out of the CCF basic state.

C. Egbers and G. Pfister (Eds.): LNP 549, pp. 55–66, 2000.

2 System

We report results obtained numerically for a Taylor-Couette system with counter-rotating cylinders. The ratio $\eta = r_1/r_2$ of the radii r_1 and r_2 of the inner and outer cylinders was fixed at the value $\eta = 0.5$ for which also experiments have been performed recently [10]. We consider the fluid in the annulus between the cylinders to be isothermal and incompressible with kinematic viscosity ν. The gap width $d = r_2 - r_1$ is used as the unit of length and the momentum diffusion time d^2/ν radially across the gap as the time unit so that velocities are reduced by ν/d. To characterize the driving of the system, we use the Reynolds numbers

$$R_1 = r_1\Omega_1 d/\nu \; ; R_2 = r_2\Omega_2 d/\nu \, . \tag{1}$$

They are just the reduced azimuthal velocities of the fluid at the inner and outer cylinder, respectively, where Ω_1 and Ω_2 are the respective angular velocities. Within this scaling, the Navier-Stokes equations (NSE) take the form

$$\partial_t \mathbf{u} = \boldsymbol{\nabla}^2 \mathbf{u} - (\mathbf{u} \cdot \boldsymbol{\nabla})\mathbf{u} - \boldsymbol{\nabla} p \tag{2}$$

with p denoting the pressure field that is reduced by $\rho\nu^2/d^2$ where ρ is the mass density of the fluid. Using cylindrical coordinates, the velocity field

$$\mathbf{u} = u\,\mathbf{e}_r + v\,\mathbf{e}_\varphi + w\,\mathbf{e}_z \tag{3}$$

is decomposed into a radial component u, an azimuthal one v, and an axial one w. We have solved the resulting equations subject to no slip conditions at the cylinders. Axially, we imposed periodic boundary conditions at $z = 0$ and $z = \Gamma$ where Γ is the reduced periodicity length. In this work, we mostly considered $\Gamma = 1.6$. Then, the wave number of the TVF and the SPI was $k = 2\pi/\Gamma = 3.927$.

For the numerical calculations, we use a combination of a finite differences formulation in the $r - z$ plane with a spectral decomposition in φ. Since we are studying also finite length cylinders with rigid lids closing the annulus vertically, we do not use a code with an axial Fourier decomposition which for axially periodic systems would be an interesting alternative. The discretization (a FTCS - Forward Time, Centered Space algorithm) has been done on staggered grids in the $r - z$ plane, following the procedure of ref. [11]. In this way, one obtains simple expressions for derivatives in r and z — especially when the derivative, e.g., ∂_r of a field, e.g., u, has to be calculated in the balance equation of another field, e.g. v. Furthermore, since u, v, and w lie on different grids, we never have to impose boundary conditions for more than one velocity field component at the same position. Moreover, the pressure field does not require additional boundary conditions (cf. below). Mostly we used homogeneous grids with discretization lengths $\Delta r = \Delta z = 0.05$ and time steps $\Delta t < 1/3600$.

To allow also nonaxisymmetric flow structures in our code, we expand all fields in azimuthal Fourier modes $e^{im\varphi}$, e.g.,

$$\mathbf{u}(r, \varphi, z, t) = \sum_{m=-m_{max}}^{m_{max}} \hat{\mathbf{u}}_m(r, z, t)\, e^{im\varphi}. \tag{4}$$

The pressure is expanded similarly. For the flows investigated here a truncation of the mode expansion at $m_{max} = 8$ was sufficient to properly resolve the anharmonicities in the fields. Inserting these expansions into the NSE and projecting onto the respective normal modes $e^{im\varphi}$, we obtain a system of coupled equations for the mode amplitudes $\hat{\mathbf{u}}_m(r, z, t)$ that is solved with the FTCS algorithm. To that end, all modes $-m_{max} \leq m \leq m_{max}$ have to be evaluated at time t before any mode can be calculated at the next timestep $t + \Delta t$. Having stepped up the velocity field with the FTCS algorithm, the pressure p is determined with the method of 'artificial compressibility' [12]

$$dp^{(n)} = -\beta \boldsymbol{\nabla} \cdot \mathbf{u}^{(n)} \qquad (0 < \beta < 1) \tag{5}$$

$$p^{(n+1)} = p^{(n)} + dp^{(n)} \tag{6}$$

$$\mathbf{u}^{(n+1)} = \mathbf{u}^{(n)} - \Delta t \, \boldsymbol{\nabla}(dp^{(n)}) \, . \tag{7}$$

With this relaxation method, pressure and velocity fields are iteratively adjusted to each other. The pressure correction $dp^{(n)}$ in the n-th iteration step is proportional to the divergence of $\mathbf{u}$ which should be zero in the relaxed case, satisfying the continuity equation. The corrected pressure is then used to adapt the velocity field. The iteration loop (5-7) is executed for each azimuthal Fourier mode separately. It is iterated until $\boldsymbol{\nabla} \cdot \mathbf{u}$ has become sufficiently small for each m mode considered. After that the next FTCS time step is executed.

3 Linear stability analysis of CCF

We have also performed a linear stability analysis of the basic CCF state using a shooting algorithm with a fourth order Runge-Kutta integration method. Fig. 1 shows for $R_2 = -100$, as a representative example, the marginal stability thresholds $R_{1,stab}$ of the CCF state against perturbations with axial wave number k and azimuthal wave number $M = 0, 1, 2$, respectively. Note that these curves in the $k - R_1$ plane of Fig. 1 are bifurcation thresholds for rotationally symmetric TVF ($M = 0$) and SPI ($M = 1, 2$) solutions, respectively. The linear analysis shows that for wave numbers $k > 5.1$ the $M = 0$ instability to TVF occurs first when increasing R_1. For $k < 5.1$, however, a spiral solution with azimuthal wave number $M = 1$ bifurcates out of the CCF state, first, when increasing R_1, while $M = 0$ perturbations can grow only at larger R_1. The marginal stability thresholds for perturbations with $M \geq 2$ lie substantially above those for $M = 0$ and $M = 1$ perturbations.

Note that the wave number $k = 2\pi/1.6 = 3.927$ for which we have explored nonlinear TVF and SPI states is close to the critical ones for $M = 0$ and $M = 1$ perturbations. This does not hold only for $R_2 = -100$ but also for the wide range of R_2-values covered in Fig. 2: the marginal stability thresholds $R_{1,stab}$ plotted in Fig. 2a versus R_2 are very similar to the correponding critical ones, $R_{1,c}$, shown in Fig. 2b. For completeness, we show in Fig. 2c the critical axial wave numbers for $M = 0, 1, 2$ perturbations and in Fig. 2d the critical frequencies ω_c/M for $M = 1, 2$.

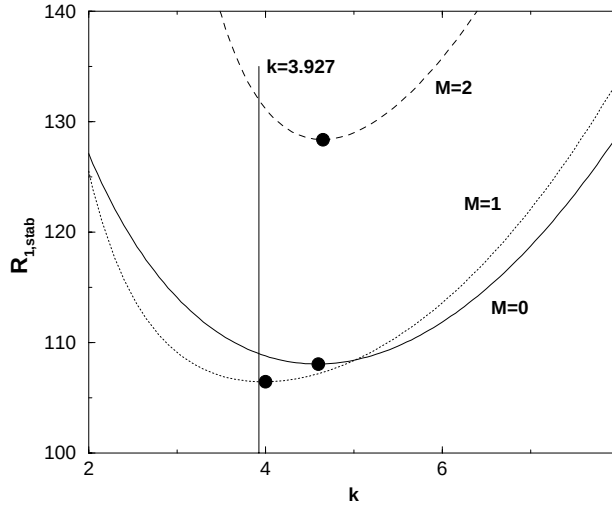

Fig. 1. Stability thresholds of the CCF basic state against perturbations with different azimuthal wave numbers M as indicated. Marginal stability curves $R_{1,stab}$ are shown versus axial wave number k. Points denote the critical values. Parameters are $\eta = 0.5$, $R_2 = -100$.

4 Bifurcation properties of Taylor vortex and spiral flow

Here we present results concerning the bifurcation behavior of the $M = 0$ TVF and of SPI solutions with azimuthal wave number $M = 1$ as functions of the inner cylinder's Reynolds number R_1. We have not tried to locate and investigate the $M = 2$ SPI solution. Parameters are fixed in this section at $\eta = 0.5, R_2 = -100$, and the axial periodicity length is $\Gamma = 1.6$. In order to display the structural differences between TVF and SPI flow, we show in Fig. 3a, for both patterns, the velocity field in the $r - z$ plane and in Fig. 3b the velocity field in the cylindrical $\varphi - z$ plane at mid gap, $r_1 + 0.5$.

Figure 4a shows the bifurcation diagrams of maximal radial flow velocity versus R_1 for $M = 1$ SPI (lozenges) and for TVF (circles). Both flow states bifurcate supercritically out of the basic CCF state. The numerical bifurcation thresholds lie slightly below the respective ones, $R_{1,stab}(M = 1) = 106.4551$ and $R_{1,stab}(M = 0) = 108.9988$, obtained in Sec. 3 within the linear stability analysis due to the discretization errors of the FTCS numerical code. The SPI solution is stable throughout the driving range shown in Fig. 4. Beyond it, the SPI state loses stability to a more complicated time dependent pattern that we shall not discuss here. TVF, on the other hand, is unstable (open circles) close to onset, becomes stable between $R_1 = 120$ and $R_1 = 125$, and finally

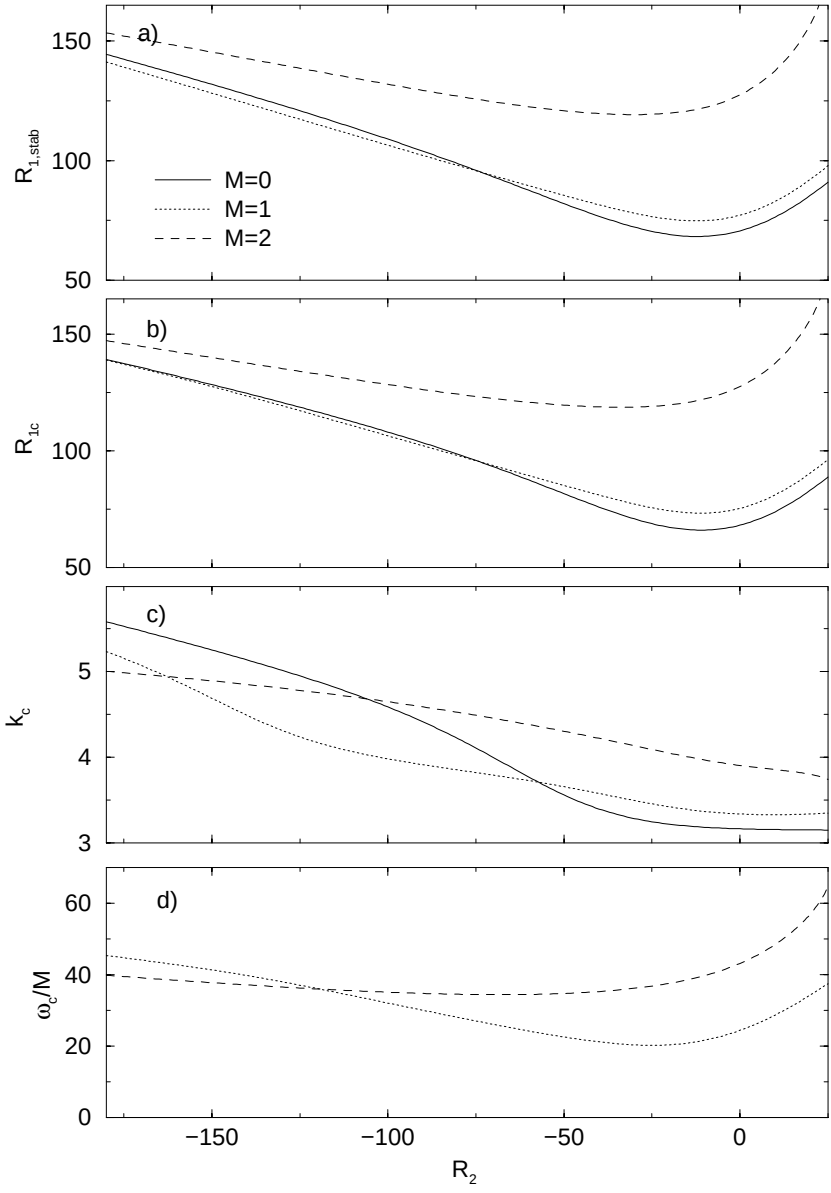

Fig. 2. Results of a linear stability analysis of the CCF basic state for $\eta = 0.5$ as functions of R_2 for perturbations with different azimuthal wave numbers M as indicated: (a) stability threshold $R_{1,stab}$ for axial wave number $k = 3.927$, (b) critical Reynolds number $R_{1,c}$, (c) critical axial wave number k_c, (d) critical frequency ω_c/M.

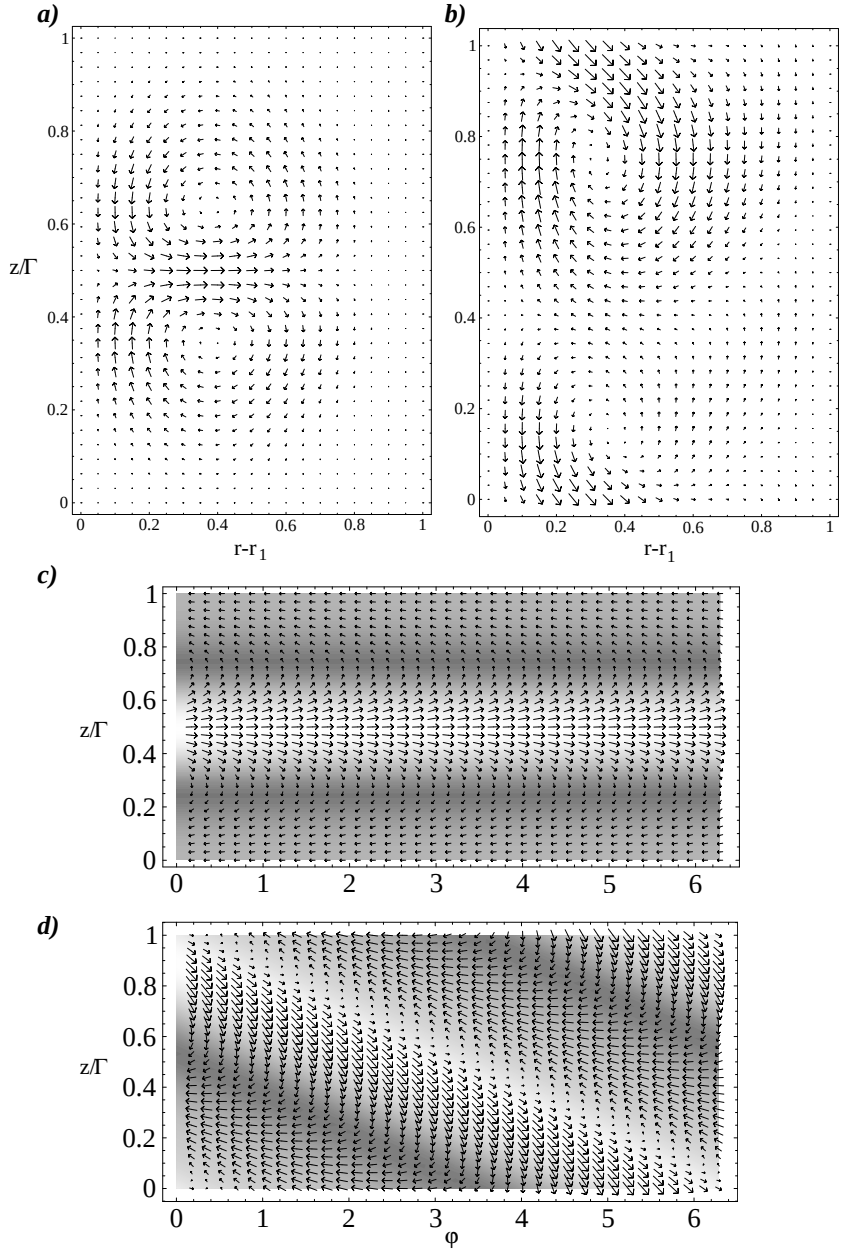

Fig. 3. Structure of TVF and of a left handed SPI state with axial wave number $M = 1$. Snapshots of the velocity field $u\mathbf{e}_r + w\mathbf{e}_z$ in the $r - z$ plane are shown in (a) for TVF and in (b) for SPI. The field $v\mathbf{e}_\varphi + w\mathbf{e}_z$ in the cylindrical $\varphi - z$ plane at mid gap, $r_1 + 0.5$, is shown in (c) for TVF and in (d) for SPI together with a grey scale plot of u with dark grey denoting maximal radial inflow and light grey denoting maximal radial outflow, respectively. See Fig. 6 for axial profiles of u and section 5 for a discussion of the fact that Taylor vortices appear more compressed than spiral vortices. Parameters are $\eta = 0.5$, $\Gamma = 1.6$, $k = 3.927$, $R_1 = 140$, and $R_2 = -100$.

loses stability around $R_1 \simeq 150$. Here, stability of the rotationally symmetric TVF solution refers to the situation covered by our code that allows the development of $M \neq 0$ perturbations which break the rotational symmetry of TVF. The unstable TVF solution (open circles) close to onset was obtained by discarding any azimuthal mode with $m \neq 0$, thus enforcing rotational symmetry. The TVF solution, marked by open circles, is stable against $M = 0$ but unstable against $M \neq 0$ perturbations with the prescribed axial periodicity of $\Gamma = 1.6$. Beyond the last filled circle at $R_1 \simeq 150$ in Fig. 4, the TVF state loses stability even in the $M = 0$ subspace against a time dependent state that we shall not discuss here further. We have not determined the TVF solution that is unstable in the $M = 0$ subspace beyond $R_1 \simeq 150$ since this requires a different procedure. Therefore our TVF solution branch ends in Fig. 4 at $R_1 \simeq 150$.

So, in the driving range $125 \leq R_1 \leq 150$, we found in our axially periodic system bistability between TVF and SPI. At the low driving end, $R_1 \lesssim 125$, of the stability range of TVF the system undergoes a transition to a stable $M = 1$ SPI flow. On the other hand, when increasing R_1 beyond the high driving stability boundary of TVF at $R_1 \gtrsim 150$, the Taylor vortices typically develop an oscillatory time dependence.

It is instructive to compare our numerically obtained bifurcation behavior of TVF and SPI with recent experiments for $\eta = 0.5$ despite the fact that they were done in a relative short system of length $\Gamma = 12$ with rigid, stationary end plates closing the annulus [10]. For $R_2 = -96.69$ being close to our value of $R_2 = -100$, the authors observed $M = 1$ SPI flow in the center part of the systen with axial wave number $k = 3.57$ which differs somewhat from our $k = 3.927$. However, this SPI flow was seen only in the driving range $106 \lesssim R_1 \lesssim 118$. Beyond $R_1 \simeq 118$ the SPI flow underwent a transition into stable TVF. This TVF state lost its stability to wavy vortex flow at a driving value of $R_1 \simeq 168$ that lies above the upper stability boundary for TVF, $R_1 \gtrsim 150$, in our axially periodic system. The significant downwards (upwards) shift in the *upper* stability boundary of experimental SPI (TVF) compared to the axially periodic numerical result is presumably related to the fact that the rigid end plates with adjacent stationary, rotationally symmetric Ekman vortices suppressing axial phase propagation tend to destabilize SPI and stabilize TVF. This stabilizing effect on TVF is presumably also responsible for the downwards extension of experimental TVF down to $R_1 \simeq 118$, i.e., below the *lower* stability boundary of TVF under axially periodic bondary conditions at $R_1 \lesssim 125$.

In Fig. 5a, we show the bifurcation diagrams of the axial mean flow $\langle w \rangle$ of our spiral states shown in Fig. 4. And Fig. 5b displays the axial phase velocities w_{ph} of the spirals versus R_1. The open lozenges therein refer to the experimental results for the phase velocity [10]. For our SPI states the axial mean flow (i.e. w integrated over the annular cross section at a fixed z) is independent of z and t since all spiral fields

$$f_{\mathrm{SPI}}(r, \varphi, z, t) = F_{\mathrm{SPI}}(r, \phi)$$

depend only via the phase variable $\phi = kz + M\varphi - \omega t$ on φ, z and t.

While for our periodic boundary conditions, Reynolds stresses of the SPI velocity field generate a finite $\langle w \rangle$ the rigid end plates of the experimental set up suppress any axial net flow $\langle w \rangle$. However, it should be noted that the difference between experimental and numerical axial phase velocities cannot be explained by $w_{ph} - \langle w \rangle$. For the spirals discussed here $\langle w \rangle$ is directed opposite to the axial phase velocity, w_{ph}.

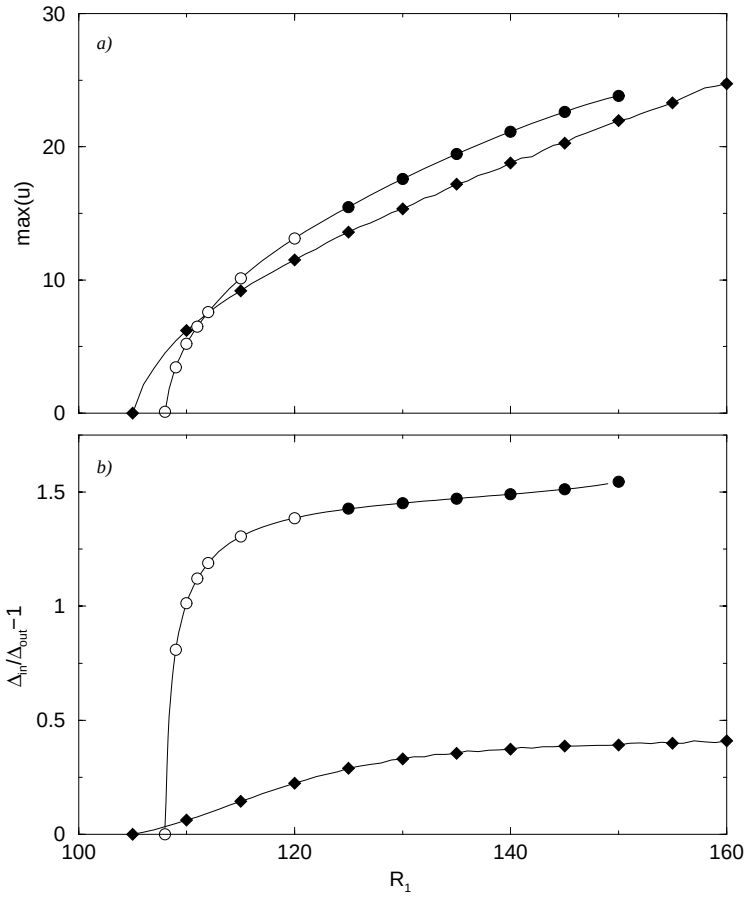

Fig. 4. Bifurcation diagrams of $M = 1$ SPI (lozenges) and TVF (circles) order parameters versus R_1. Filled (open) symbols refer to stable (unstable) solutions; see text for further explanations. (a) maximal radial flow velocity, (b) inflow/outflow asymmetry measured by the ratio of axial ranges Δ_{in} (Δ_{out}) of radial inflow (outflow) in the middle of the gap. Parameters are $\eta = 0.5, k = 3.927, R_2 = -100$.

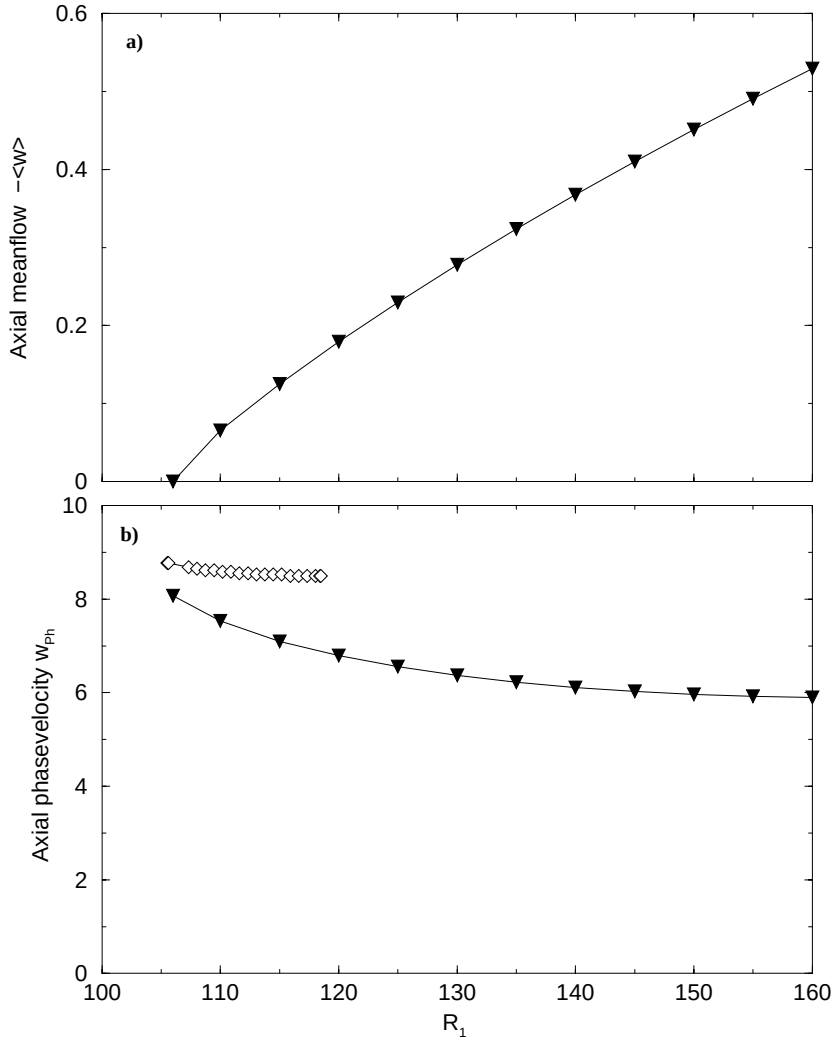

Fig. 5. Axial mean flow (a) and phase velocity (b) of left handed SPI states with azimuthal wave number $M = 1$ versus R_1. Filled triangles show results from our simulations with axially periodic boundary conditions. Open lozenges are experimental results [10]; see text for further explanations. Simulation parameters were $\eta = 0.5$, $k = 3.927$, and $R_2 = -100$.

5 Structure of Taylor vortex and spiral flow

Spirals bifurcate out of the CCF state in a Hopf bifurcation. They break the rotational symmetry, the axial mirror symmetry, the axial translational invariance, and the time translational invariance of the NSE. Their spatio temporal structure in φ, z, t, depending only on the combined phase $\phi = kz + M\varphi - \omega t$, is effectively one dimensional.

All spirals reported here rotate in positive φ direction. Depending on initial conditions, the flow either evolved into a right handed spiral (R-SPI) or into a left handed (L-SPI) being the mirror image of an R-SPI under the operation $z \to -z$ of axial inversion. The rotation in positive φ direction implies for the R-SPI (L-SPI) an axial translation of the phase with negative (positive) phase velocity w_{ph}. At onset, w_{ph} agrees within the numerical accuracy of our code with the phase velocity ω/k resulting from the linear stability analysis.

Finally we want to discuss the axial structure of TVF and of spiral flow. To that end we show in Fig. 6 how the axial profile of the radial velocity u at mid gap position evolves with R_1. Here, positive (negative) u implies radial outflow (inflow). First, one observes that the mirror symmetry of the TVF profiles in Fig. 6a around the position, $z = 0.5$, of maximal radial outflow is broken in the spiral waves that are propagating in Fig. 6b to the right. The axial wave profiles of these travelling SPI states become more and more anharmonic as R_1 increases such that the waves become steeper before (flatter behind) the crests. Measuring the axial anharmonicity of the vortex structures by the difference of the axial ranges of radial inflow and outflow, Δ_{in} and Δ_{out}, respectively, one sees that TVF is much more anharmonic than SPI flow. This is also corroborated by a direct axial Fourier analysis of u. The bifurcation behavior of $\Delta_{in}/\Delta_{out} - 1$ is shown in Fig. 4b. This quantity measures the anharmonicity of u via the asymmetry in the inflow/outflow ranges and also – because of the continuity constraint – the asymmetry of the respective radial flow amplitudes. Thus, Taylor vortices appear to be smaller in size than spiral vortices that seem to fill almost the whole gap in Fig. 3.

6 Summary

For a counter-rotating system with radius ratio $\eta = 0.5$, we have numerically determined the spatio temporal properties and the bifurcation behavior of TVF and of $M = 1$ SPI states that bifurcate with increasing R_1 supercritically out of the basic CCF. We investigated in particular outer cylinder Reynolds numbers R_2 where the bifurcation to stable SPI occurs first and the bifurcation to initially unstable TVF is located at a higher value of the inner cylinder Reynolds number R_1. For axially periodic boundary conditions, SPI remained stable for a wide range of R_1 while the TVF solution becomes stable slightly above onset. Thus, there is a substantial range of R_1 with bistable coexistence and competition of TVF and of the two mirror symmetry degenerated L-SPI and R-SPI states with left handed and right handed spiral vortices, respectively. In the parameter

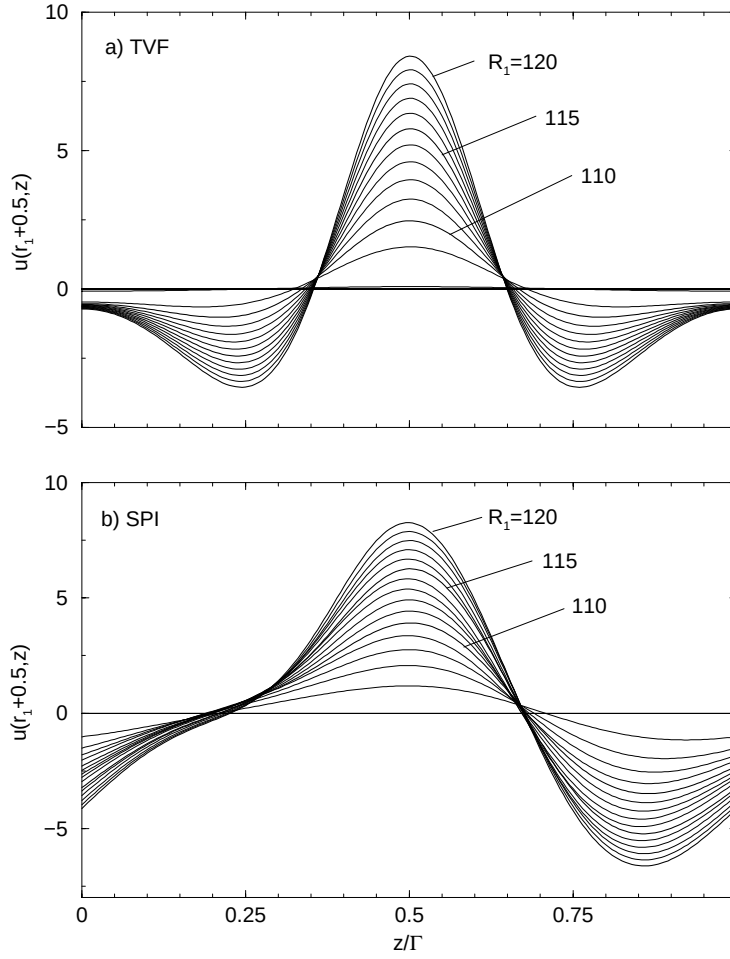

Fig. 6. Axial profiles of the radial velocity field at mid gap location for TVF (a) and L-SPI (b) with azimuthal wave number $M = 1$. The phase velocities in (b) are positive. Parameters are $\eta = 0.5$, $k = 3.927$, $R_2 = -100$, and R_1 as indicated.

range investigated here the two latter rotate both in positive φ direction so that the axial phase velocity w_{ph} of the L-SPI (R-SPI) wave is positive (negative). The axial mean flow generated by the SPI wave is directed opposite to w_{ph}. Typically spiral vortices are for our $\eta = 0.5$ less anharmonic than Taylor vortices. A comparison with recent experimental results suggests that rigid endplates tend to reduce (enlarge) the stability range of SPI (TVF).

Acknowledgments

We thank A. Schulz for communicating the experimental data referred to in this paper.

References

1. E. R. Krueger, A. Gross, and R. C. DiPrima: *On the relative importance of Taylor-vortex and nonaxisymmetric modes in flow between rotating cylinders*, J. Fluid Mech. **24**, 521 (1966).
2. H. A. Snyder: *Stability of rotating Couette flow. I. Asymmetric waveforms*, Phys. Fluids **11**, 728 (1968).
3. C. D. Andereck, S. S. Liu, and H. L. Swinney: *Flow regimes in a circular Couette system with independently rotating cylinders*, J. Fluid Mech. **164**, 155 (1986).
4. W. F. Langford, R. Tagg, E. Kostelich, H. L. Swinney, and M. Golubitsky: *Primary instabilites and bicriticality in flow between counter-rotating cylinders*, Phys. Fluids, **31**, 776 (1988).
5. R. Tagg, W. S. Edwards, H. L. Swinney, and P. S. Marcus: *Nonlinear standing waves in Couette-Taylor flow*, Phys. Rev. A **39**, 3734 (1988).
6. W. S. Edwards: Linear Spirals in the finite Couette-Taylor problem, in *Instability and Transition, Vol. II*, edited by M. Y. Hussaini, (Springer-Verlag, Berlin, 1990), p. 408.
7. R. Tagg: A Guide to literature related to the Taylor-Couette problem, in *Ordered and Turbulent Patterns in Taylor-Couette Flow*, edited by C. D. Andereck and F. Hayot (Plenum, New York, 1992).
8. P. Chossat and G. Iooss: *The Couette-Taylor Problem*, (Springer-Verlag, Berlin, 1994).
9. J. Antonijoan, F. Marquès, and J. Sánchez: *Non-linear spirals in the Taylor-Couette problem*, Phys. Fluids **10** 4, 829 (1998).
10. A. Schulz and G. Pfister: contribution to this volume.
11. C. W. Hirt, B. D. Nichols, and N. C. Romero: *SOLA — A Numerical Solution Algorithm for Transient Fluid Flow*, (Los Alamos Scientific Laboratory of the University of California, LA-5852, 1975)
12. R. Peyret and T. D. Taylor: *Computational Methods in Fluid Flow*, (Springer-Verlag, Berlin, 1983).

Stability of time-periodic flows in a Taylor–Couette geometry

Christiane Normand

C.E.A/Saclay, Service de Physique Théorique,
F-91191 Gif-sur-Yvette Cedex, France.

Abstract. The flows generated by the time-periodic forcing of one or both cylinders of the Taylor-Couette system are of two types: either modulated or pulsed flows whether or not there exists a mean rotation. Their linear stability is analysed within the frame of Floquet theory which predicts synchronous or subharmonic instability modes, a phenomenon known as parametric resonance. The non linear dynamics of time-periodic Taylor vortex flow has been examined both by numerical simulations and through model equations. We shall report on the results of two analytical approaches. The first one due to Hall [18] is based on an amplitude equation which was then modified by Barenghi and Jones [5] to account for imperfections in the system. The second one is a Lorenz model derived by Kuhlmann *et al.* [22].

1 Introduction

Since the discovery of the transition between steady circular Couette flow and axisymmetrical Taylor vortices [1] various aspects of Taylor-Couette flow have been considered, including the effect of time-periodic forcing of the cylinders rotation rates. The stability of time-dependent circular Couette flows is representative of a larger class of problems that originated in the nineteenth century with the discovery of Faraday instability [15]. The appearance of a regular pattern of standing waves on the surface of water in a vertically vibrating vessel, the waves having half the frequency of the periodic forcing, is often quoted to illustrate parametric instability [12]. This phenomenon also known as parametric resonance is encountered in various hydrodynamic systems when one of the parameters of the equilibrium state is subject to periodic modulation. This situation occurs in convective systems when the equilibrium temperature or acceleration of gravity is modulated in time. The effect of parameter modulation on convective instability has been reviewed in the book by Gershuni and Zhukhovitskii [16], showing in particular that the instability may be in the synchronous or subharmonic mode. More recently, Ahlers *et al.* [1] investigated the non linear dynamics of modulated convection above threshold.

In his enlarged review of the stability of periodic states, Davis [10] also discussed the case of plane parallel shear flows. Examples include Stokes layers induced by the oscillations of a flat plate bounded by a semi-infinite fluid medium that is stable to small disturbance [19], [31]. For plane Poiseuille flow driven by a sinusoidal pressure gradient Hall [17] found that rapid modulation slightly destabilizes the flow. Plane Couette flow that is stable according to linear theory cannot be made unstable through modulation of the wall speeds. Davis also

C. Egbers and G. Pfister (Eds.): LNP 549, pp. 67–83, 2000.

reported on the pioneering investigations of centrifugal instability under parameter modulation but since then the problem has received increasing attention and recent contributions have led to a much better understanding into the effect of time-periodic forcing in the Taylor-Couette problem. The aim of the present contribution is to provide an up-to-date review of the subject.

The stability of the flow between concentric circular cylinders when the outer cylinder is at rest and the inner has angular velocity $\Omega(1 + \varepsilon \cos \omega t)$ has been first investigated experimentally by Donnelly [11] who concluded that temporal modulation of the inner cylinder angular velocity stabilizes circular Couette flow at low frequency and for small modulation amplitudes ($\varepsilon < 0.25$). Later on, Thompson [30] reported contradictory data with modulation superimposed on the steady rotation of the inner cylinder being destabilizing. Concomitantly there were theoretical attempts to deal with the experimental configurations of Donnelly and Thompson but the first conclusive results came from the linear stability analyses due respectively to Hall [18] and Riley and Laurence [25] both performed in the narrow-gap approximation.

Hall [18] used asymptotic methods and considered two limits. In the limit in which the amplitude ε and the frequency ω of the modulation tend to zero, he found that the critical Taylor number at which instability first occurs is decreased by an amount of order ε^2 from its unmodulated value. Considering then the limit in which ω tends to infinity with ε arbitrary, Hall found in this case that the critical Taylor number is decreased by an amount of order $\varepsilon^2 \omega^{-3}$ from its unmodulated value. Investigating the non linear behavior of perturbations under supercritical conditions, Hall [18] found that small but finite amplitude perturbations can exist in both the high and low frequency limits.

Riley and Laurence [25] used a different approach in which the governing equations for the disturbances are solved by a Galerkin expansion with time-dependent coefficients, and the stability of the motion determined by Floquet theory. They found that modulation in general destabilizes the flow which is consistent with Hall's results. Riley and Laurence [25] also considered modulation of the inner cylinder about zero mean. As the frequency increases the flow becomes confined to a thin boundary layer of the Stokes type close to the inner cylinder. Thus, the critical parameters become independent of the gap width and tend to the values found by Seminara and Hall [26] for the instability of the flow induced by a circular cylinder oscillating in an infinite viscous fluid.

An extensive study of more complex configurations in which the angular velocities of the inner and outer cylinder are respectively $\Omega_1 + \varepsilon_1 \cos \omega t$ and $\Omega_2 + \varepsilon_2 \cos \omega t$ was conducted by Carmi and Tustaniwskyj [8]. They considered four cases of modulated Couette flow about a zero mean ($\Omega_1 = \Omega_2 = 0$) that correspond to modulation of the inner cylinder only ($\varepsilon_1 \neq 0, \varepsilon_2 = 0$) or the outer cylinder only ($\varepsilon_1 = 0, \varepsilon_2 \neq 0$), modulation of both cylinders with equal amplitude in the same direction ($\varepsilon_1/\varepsilon_2 = 1$) or in the opposite direction ($\varepsilon_1/\varepsilon_2 = -1$). When addressing the non-zero mean modulation problem they focused on the case where the steady component of the flow has the inner cylinder rotating, while the outer is at rest ($\Omega_1 \neq 0, \Omega_2 = 0$). Two values of the amplitude ratio

$\varepsilon_1/\Omega_1 = 5.0$ and 0.5 were considered and the smaller one was associated to the cases $\varepsilon_2 = 0$ or $\varepsilon_1/\varepsilon_2 = \pm 1$. Carmi and Tustaniwskyj [8] argued that the small-gap approximation used in previous theoretical studies [18], [25] is not justified for unsteady flows since terms are neglected which are not small for all time. Thus, they considered gaps of finite length and derived a closed-form analytic solution for the unsteady part of the basic flow in terms of modified Bessel functions. Their study was restricted to two values of the non-dimensional gap size $\delta = 0.0444$ and 0.444. For modulation of the inner cylinder about a zero mean their results are in good agreement with the experimental findings of Thompson [30] while their stability boundary lies below that of Riley and Laurence [25]. For non-zero-mean modulation of the inner cylinder they found that at high frequency the critical Taylor number asymptotically approaches the limit for steady mean flow and that low-frequency modulation produces a destabilizing effect larger compared to the results of Riley and Laurence [25] and Hall [18]. Tustaniwskyj and Carmi [29] also used energy method to obtain a condition for stability. They found that the difference between the energy and the linear limits are more pronounced in the case of zero mean modulation. For the three cases $\varepsilon_1/\varepsilon_2 = \pm 1$ and $\varepsilon_1 = 0$ the neutral curves are flatter than the corresponding linear boundaries and for $\varepsilon_2 = 0$ the stability boundary in the high frequency limit does not increase as rapidly as the linear curve.

For modulation of the inner cylinder, subsequent experimental results by Walsh and Donnelly [32] were in support of a large negative shift of the threshold for instability which did not end up the controversy for a long time since the non linear investigation of Kuhlmann *et al.* [22] yielded the result that modulation weakly destabilizes the flow at low frequency. By analogy with the Lorenz model for Rayleigh-Bénard convection they used a truncation of the Navier-Stokes equation that led to a four-mode model thus improving the previous severely truncated models by Battacharjee *et al.* [6] and Kuhlmann [21]. In addition, as a check for their model, they did finite-difference numerical simulations of the full axisymmetric Navier-Stokes equations. The smallness of the downwards threshold shift was explained as the result of two counteracting effects. They suggested that symmetry-breaking experimental imperfections might account for the differences between the theoretical threshold for onset of Taylor vortex flow and experiments. Parallel to this assertion a similar idea was developped by Barenghi and Jones [5] who discussed imperfections in the modulated Taylor-Couette flow by means of an amplitude equation, modified by including a constant term. They identified transient vortices as being the source of the large destabilization seen in some experiments. They also performed numerical calculations with an initial-value code using a spectral method with collocation. As they failed to reproduce the large negative threshold shifts of Carmi and Tustaniwskyj [8] they suspected the source of disagreement to be numerical and performed several tests. They first investigated the effects of severe mode truncation on their collocation scheme but their results remain consistent with high-resolution runs until the truncation was reduced to a very small number of modes. Finally they discovered that varying the time step in the numerical

code has a critical effect on the stability boundary especially at low modulation frequency where they showed that 500 steps per cycle are needed while Carmi and Tustaniwskyj [8] used a time step $2\pi/30$ which was not sufficient to ensure convergence at all values of the frequency. They concluded that having too large a time step produces a similar effect to physical imperfections.

Barenghi and Jones [5] considered a second configuration in which the inner cylinder is rotated at a constant angular velocity ($\Omega_1 \neq 0, \varepsilon_1 = 0$) and the outer cylinder is oscillating about a zero mean rotation ($\Omega_2 = 0, \varepsilon_2 \neq 0$). For this case, Walsh and Donnelly [33] conducted experiments in the parameter range, $0.3 \leq \varepsilon_2/\Omega_1 \leq 2.0$, and found that modulation of the outer cylinder delays the onset of secondary flow beyond the critical Reynolds number for a steady outer cylinder in contrast to the prediction of Carmi and Tustaniwskyj [8]. The calculations of Barenghi and Jones [5] for $\varepsilon_2/\Omega_1 = 0.5$, confirmed Walsh and Donnelly observations [33]. Moreover, they noted that the result of stabilization in the case of oscillation of the outer cylinder is in accord with the stability curve for the steady problem as demonstrated by Taylor [1]: as Ω_2 is varied at fixed Ω_1 the flow becomes more stable whether Ω_2 is positive or negative. This argument was also given by Wu and Swift [34] who calculated the onset conditions for small amplitudes. The first theoretical results for modulation amplitudes of the outer cylinder as large as $\varepsilon_2/\Omega_1 = 1.5$, were obtained by Murray *et al.* [24] using two distinct implementations of Floquet theory. In the first approach, the time-periodic part of the disturbance was represented by a truncated Fourier series in time following a procedure introduced by Seminara and Hall [26]. The second approach consisted of approximating the spatial behavior of the disturbance solutions by an expansion in terms of Chebyshev polynomials. For small modulation amplitude ($\varepsilon = 0.5$) their stability curves have a shape similar to that of Wu and Swift [34] and are in agreement with the maximum stabilization predicted by the calculations of Barenghi and Jones [5] at low values of the frequency while a slight discrepancy with their results occurs at larger frequency values. For large modulation amplitude ($\varepsilon = 1.5$) they found that the stability curve consists of two distinct branches. The low frequency branch corresponds to a subharmonic response while the high frequency branch is for the synchronous mode. Murray *et al.* [24] performed calculations for two values of the radius ratio η, 0.719 and 0.88, and found that the larger is the gap the better is the agreement between theory and experiment.

In the past several years two of the configurations initially considered by Carmi and Tustaniwskyj [8] from a theoretical point of view were revisited and for the first time experiments were achieved. They correspond to the case of no mean rotation ($\Omega_1 = \Omega_2 = 0$) with the two cylinders oscillating at the same frequency with equal amplitude either in phase ($\varepsilon_1 = \varepsilon_2$) or out of phase ($\varepsilon_1 = -\varepsilon_2$). Introducing $\varepsilon = \varepsilon_1/\varepsilon_2$, the case $\varepsilon = 1$, was first re-examined by Aouidef *et al.* [2]. The results of their experimental investigation are in good agreement with their linear stability analysis and both showed that the stability curve lies above that predicted by Carmi and Tustaniwskyj [8]. For the case $\varepsilon = -1$, considered by Tennakoon *et al.* [28] the agreement between theory

and experiment was less satisfactory in the low-frequency range. In particular as $\omega \to 0$, the experimental threshold approaches a value which is higher than the critical value for two steady counter-rotating cylinders whereas the stability analysis in the narrow gap approximation as well as the wide-gap analysis of Carmi and Tustaniwskyj [8] predict a stronger stabilization. The discrepancy was resolved by taking into account the finite length of the gap [4] which confirms that the too large stabilization found in the wide gap calculations of Carmi and Tustaniwskyj [8] are likely due to insufficient temporal resolution.

Only recently was considered the effect of an overall mean rotation ($\Omega_1 = \Omega_2 = \Omega_m$) when otherwise the two cylinders are oscillating in phase ($\varepsilon = 1$). In the frame rotating at the angular velocity Ω_m the competition between Coriolis and centrifugal effects induced by temporal modulation has an influence on the stability boundary of the system. Both flow visualization [13], [14] and Floquet stability analysis [4] showed that increasing the mean rotation first destabilizes and then stabilizes the flow.

To make an exhaustive review we ought to mention the study by Braun *et al.* [7] of modulated Taylor-Couette system when the inner cylinder consists of a crystalline solid-liquid interface. For materials with moderately large Prandtl number, the two-phase system under pure torsional oscillation about the cylindrical axis is found to be less stable than the analogous rigid-walled system. In the limit of large Prandtl number simplification occurs in the stability problem that allows for an asymptotic expansion of the solution yielding at leading order a time-independent system.

In the three following sections we shall first review the different types of modulated flows so far encountered in the literature. Then, the different approaches for investigating their linear stability will be presented. Finally, the non linear dynamics of modulated Taylor vortex flow will be discussed within the frame of appropriate model equations.

2 Modulated base flow

Consider an incompressible fluid of density ρ and kinematic viscosity ν between two infinitely long concentric cylinders of radii R_1 and $R_2 = R_1 + d$, gap width d, radius ratio $\eta = R_1/R_2$. The basic flow is generated by the rotation of the inner and outer cylinders about their common axis with respective angular velocity $\Omega_1 + \varepsilon_1 \cos \omega t$ and $\Omega_2 + \varepsilon_2 \cos \omega t$. Dimensionless variables are used, the scales for length, time and velocity being respectively $d, d^2/\nu$ and ν/d. Two distinct time scales are present in the system, the viscous diffusion time $t_\nu = d^2/\nu$ and the period of the modulation $T = 2\pi/\omega$. Their relative importance is measured by the frequency parameter $\sigma = \omega d^2/\nu$ which is proportional to the ratio t_ν/T. In cylindrical polar coordinates, the velocity vector in the basic state has a non-zero azimuthal component $V(r,t)$ solution of

$$\frac{\partial V}{\partial t} = \frac{\partial^2 V}{\partial r^2} + \frac{1}{r}\frac{\partial V}{\partial r} - \frac{V}{r^2}\,, \tag{1}$$

The boundary conditions at the inner and outer cylinders, $r_1 = \eta/(1-\eta)$ and $r_2 = 1/(1-\eta)$ respectively, are one of the following sets

- outer cylinder at rest

$$V(r_1,t) = Re(1+\varepsilon\cos\sigma t) \quad \text{and} \quad V(r_2,t) = 0 \tag{2a}$$

$$Re = \Omega_1 R_1 d/\nu \quad \text{and} \quad \varepsilon = \varepsilon_1/\Omega_1 \tag{2b}$$

- steady rotation of the inner cylinder and pure torsional oscillation of the outer cylinder

$$V(r_1,t) = Re \quad \text{and} \quad V(r_2,t) = [\varepsilon Re/\eta]\cos\sigma t \tag{3a}$$

$$Re = \Omega_1 R_1 d/\nu \quad \text{and} \quad \varepsilon = \varepsilon_2/\Omega_1 \tag{3b}$$

- when there is no mean rotation

$$V(r_1,t) = Re\cos\sigma t \quad \text{and} \quad V(r_2,t) = [\varepsilon Re/\eta]\cos\sigma t \tag{4a}$$

$$Re = \varepsilon_1 R_1 d/\nu \quad \text{and} \quad \varepsilon = \varepsilon_2/\varepsilon_1\ . \tag{4b}$$

In the last case the Reynolds number Re is defined in terms of the modulation amplitude ε_1 of the inner cylinder instead of Ω_1 in the two previous cases. The velocity field is decomposed into steady and periodic parts

$$V(r,t) = V_s(r) + V_p(r,t)\ .$$

For the first two sets of boundary conditions (2a) and (3a) the steady part is

$$V_s(r) = \frac{Re\eta}{(1-\eta^2)}\left(\frac{r_2}{r} - \frac{r}{r_2}\right)\ . \tag{5}$$

The time periodic part has one of the following expressions according to the choice of boundary conditions (2a), (3a) or (4a)

$$V_p(r,t) = \frac{Re\exp i\sigma t}{\Delta(r_1,r_2)} \times \begin{cases} \varepsilon\Delta(r,r_2) \\ (\varepsilon/\eta)\,\Delta(r_1,r) \\ [\Delta(r,r_2) + (\varepsilon/\eta)\Delta(r_1,r)] \end{cases} + c.c. \tag{6}$$

where c.c. denotes the complex conjugate expression and

$$\Delta(r_i,r_j) = I_1(\kappa r_i)K_1(\kappa r_j) - I_1(\kappa r_j)K_1(\kappa r_i)\ ,$$

is a notation introduced by Carmi and Tustaniwskyj [8] in which I_1 and K_1 are modified Bessel functions and $\kappa = \sqrt{i\sigma} = \gamma(1+i)$. The parameter $\gamma = (\sigma/2)^{1/2}$ is the ratio of two lengths, the gap width d and the thickness of the Stokes layer $(2\nu/\omega)^{1/2}$. When γ is large the time-periodic part of the flow is confined in boundary layers near the cylinders and asymptotic methods can be used to solve the stability problem [18].

2.1 Narrow gap approximation

Experiments have been conducted for values of the radius ratio η ranging from 0.719 [33] to 0.9623 [11]. When $\eta \to 1$, the narrow gap approximation can be used and simplified expressions of steady and periodic parts of the base flow velocity are obtained. In this case the following change of variable is made

$$r = r_1 + x \quad \text{with} \quad r_1 = \frac{R_1}{d} = \frac{1}{\delta} \, .$$

As $\delta \to 0$, the steady part of the velocity (5) becomes $V_s(x) = Re(1-x)$. When terms of order δ are neglected in (1) the solution for the time-periodic part of the base flow expresses as

$$V_p(x,t) = Re\left[V_1(x)\cos(\sigma t) + V_2(x)\sin(\sigma t)\right] \, .$$

When there is no mean rotation and for $\varepsilon = \pm 1$ the expressions for $V_1(x)$ and $V_2(x)$ are given by

$$V_i(x,\varepsilon) = \left[f_i(x) + \varepsilon f_i(1-x)\right]/W(\varepsilon) \, , \quad i = 1,2 \tag{7}$$

with

$$f_1(x) = \cos(\gamma x)\cosh\gamma(1-x) \, , \quad f_2(x) = \sin(\gamma x)\sinh\gamma(1-x) \, , \tag{8a}$$

$$W(\varepsilon) = f_1(0) + \varepsilon f_1(1) \, . \tag{8b}$$

The corresponding expressions for $V_i(x)$ when $\varepsilon = 0$ are deduced from the previous ones by

$$V_i(x,\varepsilon=0) = \frac{1}{2}\left[V_i(x,\varepsilon=1) + V_i(x,\varepsilon=-1)\right] \, .$$

When the set of boundary conditions (2a) is used the above expression, once multiplied by ε_1/Ω_1 describes the periodic part of the basic flow [25]. Considering the evolution of the velocity profile with the frequency parameter σ (or equivalently γ), the limiting cases of respectively low and high frequency will be examined. In the low frequency limit (σ or $\gamma \to 0$) the time periodic part of the velocity is given by an expansion in ascending powers of σ [3], [18], with the two first terms given below in the case of no mean rotation and for $\varepsilon = \pm 1$ or $\varepsilon = 0$

$$V_p(x,t) = Re\left[\chi_1(x)\cos(\sigma t) + \sigma\chi_2(x)\sin(\sigma t) + \mathcal{O}(\sigma^2)\right] \, , \tag{9a}$$

$$\chi_1(x) = 1 - (1-\varepsilon)x \, , \quad \chi_2(x) = \frac{1}{6}x(1-x)\left[3 - (1-\varepsilon)(1+x)\right] \, . \tag{9b}$$

The leading order term is in-phase with the periodic forcing, its x-dependence is that of a steady Couette flow. In the high frequency limit, the behavior $f_1(x) \sim f_2(x) \sim \exp(-\gamma x)$ shows that the time-periodic part of the base flow decays to zero when $x \sim \gamma^{-1}$ and $(1-x) \sim \gamma^{-1}$ defining respectively the inner and outer Stokes layers.

3 Stability problem

Almost all stability analyses were restricted to axisymmetric perturbations except the analysis by Carmi and Tustaniwskyj [8] who considered the first nonaxisymmetric mode. In general it is argued that for the unmodulated problem the instability thresholds for axi- and nonaxisymmetric disturbances are close and this is expected to remain true for time-periodic flows. On the experimental side, nonaxisymmetric flow patterns were observed when the two cylinders are oscillating in opposite directions with no mean rotation. In this configuration, Tennakoon *et al.* [28] reported on spiral-like patterns occurring at high oscillation frequencies.

In the perturbed state assumed to be axisymmetric, the velocity and pressure fields are written as the sum of the base state $(0, V = ReV_B, 0, P)$ and a perturbation field

$$(\boldsymbol{u}, p) = [u(r,t), v(r,t), w(r,t), p(r,t)] \exp(ikz) \ ,$$

where k is the wave number in the axial direction. The evolution equations for the amplitudes of the velocity components u, v, w and the pressure p are the dimensionless Navier-Stokes equations linearized around the basic state:

$$\frac{\partial u}{\partial t} - 2Re\frac{V_B}{r}v + Dp = DD_*u - k^2u \ , \tag{10a}$$

$$\frac{\partial v}{\partial t} + ReD_*V_Bu = DD_*v - k^2v \ , \tag{10b}$$

$$\frac{\partial w}{\partial t} + ikp = D_*Dw - k^2w \ , \tag{10c}$$

$$D_*u + ikw = 0 \ , \tag{10d}$$

with $D = \partial/\partial r$ and $D_* = D + 1/r$. The boundary conditions are $u = v = w = 0$ at $r_1 = \eta/(1-\eta)$ and $r_2 = 1/(1-\eta)$.

The set of partial differential equations with time periodic coefficients is solved by applying Floquet theory which has been implemented in two distinct ways. In the first approach, [2] [4], [24], [26], a perturbed quantity $\chi(r,t)$ is written as the product of an exponential factor and a periodic function in time

$$\chi(r,t) = \exp(\mu t)\hat{\chi}(r,t) \ ,$$

in which $\hat{\chi}(r,t)$ is a periodic function in the time variable with the same period $2\pi/\sigma$ as $V_B(r,t)$ and μ the Floquet exponent is complex equal to $\mu_r + i\mu_i$, μ_r is the growth rate and μ_i is a second frequency associated with quasi-periodic motion of the system. For the condition of neutral stability ($\mu_r = 0$) and when the time-periodic part of the solution is represented by a truncated Fourier series in time, the perturbed quantities are sought as

$$\{u, v, w, p\} = \exp(i\mu_i t) \sum_{n=-N}^{n=N} \{u_n(r), v_n(r), w_n(r), p_n(r)\} \exp in\sigma t \ . \tag{11}$$

Since a solution of (10a)-(10d) expresses always in real form this imposes restriction on the value of μ_i which is either $\mu_i = 0$ (synchronous solutions) or $\mu_i = 1/2$ (subharmonic solutions). In this approach the set of partial differential equations becomes a set of coupled ordinary differential equations for the complex quantities $u_n(r), v_n(r)$, and $w_n(r)$ which is recasted in the form of a first order system for $12(N+1)$ real quantities. It is solved by superposition of numerically integrated solutions satisfying the boundary conditions at $r = r_1$. The requirement that a combination of independent solutions satisfies the boundary conditions at $r = r_2$ leads to an homogeneous algebraic system which has non trivial solution if the associated determinant vanishes. The neutral curves are obtained by locating the zeros of the determinant as a function of Re, all the other parameters being fixed.

The second approach includes Galerkin as well as pseudo-spectral methods [8], [24], [25]. It is advantageous in this case to eliminate w and p from the set of equations (10a)-(10d) to obtain a reduced set in terms of u and v alone which are expanded in truncated series

$$u(r,t) = \sum_{n=1}^{N} A_n(t)\phi_n(s) \ , \quad v(r,t) = \sum_{n=1}^{N} B_n(t)\hat{\phi}_n(s) \ , \tag{12}$$

where the new radial variable $s = 2(r - r_1) - 1$ varies in the range $[-1, 1]$. The functions $\phi_n(s)$ and $\hat{\phi}_n(s)$ are orthogonal eigenfunctions of elementary operators, for instance $(DD_*)^2$ and DD_* respectively [13]. The Galerkin procedure gives rise to a system of $2N$ ordinary differential equations for the coefficients $A_n(t)$ and $B_n(t)$ which is written

$$\dot{X}_i = G_{ij}X_j \quad \text{with} \quad X_i = \begin{cases} A_i & \text{if} \quad 1 \le i \le N \\ B_i & \text{if} \quad N+1 \le i \le 2N \end{cases}$$

where the dot denotes time differentiation and the G_{ij} are the elements of a $2N \times 2N$ matrix $\mathbf{G}$(t) which is $2\pi/\sigma$ periodic. A set of $2N$ linearly independent solutions $X_i^{(m)}$ is built by numerical integration over one period, starting with the initial conditions $X_i^{(m)}(0) = \delta_{im}$. The values $X_i^{(m)}(2\pi/\sigma)$ are the elements of a $2N \times 2N$ matrix $\mathbf{P}$. The eigenvalues $\lambda_1, ...\lambda_{2N}$ of $\mathbf{P}$ are the Floquet multipliers which are related to the Floquet exponents μ_m by $\lambda_m = \exp(2\pi\mu_m/\sigma)$. Ordering the Floquet exponents such that $\Re(\mu_n) < \Re(\mu_{n+1})$ where $\Re$ denotes the real part, the stability of the system is controlled by the sign of $\Re(\mu_1)$. The critical parameters are determined by finding $\Re\{\mu_1(k_c, Re_c)\} = 0$. When pseudo-spectral methods are used the main change in the method described above concerns the functions $\phi_n(s)$ and $\hat{\phi}_n(s)$ which are replaced by Chebyshev polynomials $T_n(s)$ with the requirement that the governing equations are satisfied at specific collocation points s_i.

3.1 Perturbative analysis

In the narrow gap approximation the perturbation equations (10a)-(10d) can be put in the form

$$\sigma\partial_\tau \mathcal{N}\boldsymbol{\Psi} - \mathcal{L}\boldsymbol{\Psi} + Ta\mathcal{M}\boldsymbol{\Psi} = 0 \,, \tag{13}$$

with $\tau = \sigma t$, $Ta = Re\delta^{1/2}$ and $\boldsymbol{\Psi} = \{u, v\}$. The differential operators $\mathcal{N}$, $\mathcal{L}$ and the time-periodic operator $\mathcal{M}$ are 2×2 matrices

$$\mathcal{N} = \begin{vmatrix} \mathcal{D} & 0 \\ 0 & 1 \end{vmatrix} \,, \quad \mathcal{L} = \begin{vmatrix} \mathcal{D}^2 & 0 \\ 0 & \mathcal{D} \end{vmatrix} \,, \quad \mathcal{M} = \begin{vmatrix} 0 & 2k^2 V_B \\ DV_B & 0 \end{vmatrix} \,, \tag{14}$$

with $\mathcal{D} = \partial_x^2 - k^2$. In the low frequency limit, the base flow velocity admits the following expansion in powers of σ

$$V_B = \chi_0(x) + \varepsilon\chi_1(x)\cos\tau + \varepsilon\sigma\chi_2(x)\sin\tau + \dots \,. \tag{15}$$

For modulation of the inner cylinder $\chi_0(x) = \chi_1(x) = (1-x)$. Hall [18] considered the limit of small amplitude of modulation, $\varepsilon \to 0$, together with $\sigma = \alpha\varepsilon$. As a consequence, $\mathcal{M}$ admits an expansion as:

$$\mathcal{M} = \mathcal{M}_0 + \varepsilon\cos\tau\mathcal{M}_1 + \varepsilon^2\sin\tau\mathcal{M}_2 + \dots \,, \tag{16}$$

where the $\mathcal{M}_i$'s depend only on the x-variable. Following the perturbative approach of Hall [18] (13) is solved by expanding the unknown quantities $\boldsymbol{\Psi}$ and Ta in powers of ε

$$\boldsymbol{\Psi} = \boldsymbol{\Psi}_0 + \varepsilon\boldsymbol{\Psi}_1 + \varepsilon^2\boldsymbol{\Psi}_2 + \dots \,, \tag{17a}$$

$$Ta = T_0 + \varepsilon T_1 + \varepsilon^2 T_2 + \dots \,. \tag{17b}$$

At the lower order, one obtains an homogeneous differential equation

$$\mathcal{L}\boldsymbol{\Psi}_0 - T_0\mathcal{M}_0\boldsymbol{\Psi}_0 = 0 \,, \tag{18}$$

whose solution is sought in the form

$$\boldsymbol{\Psi}_0 = B_0(\tau)\boldsymbol{\Phi}_0(x) \,,$$

where $\boldsymbol{\Phi}_0(x)$ is the eigenvector of the steady Taylor-Couette problem associated to the eigenvalue T_0. At the next order, one obtains an inhomogeneous equation

$$\mathcal{L}\boldsymbol{\Psi}_1 - T_0\mathcal{M}_0\boldsymbol{\Psi}_1 = \alpha\partial_\tau B_0\mathcal{N}\boldsymbol{\Phi}_0 + T_1 B_0\mathcal{M}_0\boldsymbol{\Phi}_0 + T_0 B_0\cos\tau\mathcal{M}_1\boldsymbol{\Phi}_0 \,. \tag{19}$$

The integrability condition requires that the right-hand-side of (19) be orthogonal to the solution $\boldsymbol{\Phi}_0^*$ of the adjoint problem

$$\alpha\partial_\tau B_0\langle\boldsymbol{\Phi}_0^*\mathcal{N}\boldsymbol{\Phi}_0\rangle + T_1 B_0\langle\boldsymbol{\Phi}_0^*\mathcal{M}_0\boldsymbol{\Phi}_0\rangle + T_0 B_0\cos\tau\langle\boldsymbol{\Phi}_0^*\mathcal{M}_1\boldsymbol{\Phi}_0\rangle = 0 \,. \tag{20}$$

The bracket notation denotes here integration over the x-variable. The ordinary differential equation (20) has a periodic solution if $T_1 = 0$. The function $B_0(\tau)$ is given by

$$B_0(\tau) = A \exp(-\Gamma \sin \tau/\alpha) \ ,$$

where

$$\Gamma = T_0 \langle \boldsymbol{\Phi}_0^* \mathcal{M}_1 \boldsymbol{\Phi}_0 \rangle / \langle \boldsymbol{\Phi}_0^* \mathcal{N} \boldsymbol{\Phi}_0 \rangle \ ,$$

and the amplitude A is a constant which can only be determined by a non linear analysis. The solution of (19) is

$$\boldsymbol{\Psi}_1 = B_0(\tau) \cos \tau \boldsymbol{\Phi}_1(x) + B_1(\tau) \boldsymbol{\Phi}_0(x) \ ,$$

where $\boldsymbol{\Phi}_1(x)$ satisfies an equation not reproduced here which has to be solved numerically. At the order ε^2

$$\mathcal{L}\boldsymbol{\Psi}_2 - T_0 \mathcal{M}_0 \boldsymbol{\Psi}_2 = \alpha \partial_\tau \mathcal{N} \boldsymbol{\Psi}_1 + T_2 \mathcal{M}_0 \boldsymbol{\Psi}_0 + T_0 \cos \tau \mathcal{M}_1 \boldsymbol{\Psi}_1 + T_0 \sin \tau \mathcal{M}_2 \boldsymbol{\Psi}_0 \ . \tag{21}$$

The integrability condition gives an ordinary differential equation for $B_1(\tau)$. The condition that the solution is periodic in τ gives the value of T_2

$$T_2 = \frac{1}{2} \frac{[T_0 \langle \boldsymbol{\Phi}_0^* \mathcal{M}_1 \boldsymbol{\Phi}_1 \rangle - \Gamma \langle \boldsymbol{\Phi}_0^* \mathcal{N} \boldsymbol{\Phi}_1 \rangle]}{\langle \boldsymbol{\Phi}_0^* \mathcal{M}_0 \boldsymbol{\Phi}_0 \rangle} \ . \tag{22}$$

For modulation of the inner cylinder, the value of T_2 has been calculated by Hall [18] who found a negative value. For steady rotation of the inner cylinder and oscillation of the outer cylinder about zero-mean Wu and Swift [34] performed the calculation of T_2 for a finite value of the gap, without the small frequency assumption, and they found in this case a positive value.

4 Nonlinear models

4.1 Amplitude equations

In the limit in which the amplitude and frequency of the modulation tend to zero ($\varepsilon \to 0, \sigma \to 0$) with σ/ε held fixed, Hall [18] has derived an amplitude equation for modulated Taylor-Couette flow of the form

$$\frac{dA}{dt} = \{\mu + \varepsilon sin(\sigma t)\} A - A^3 \ , \tag{23}$$

where μ is the distance from the threshold of instability for the modulated flow. The general solution is

$$\left[A^{-2} \phi(x)\right]_{t_i}^{t} = 2 \int_{t_i}^{t} \phi(x) dx \ , \tag{24}$$

where t_i is an initial value and

$$\phi(x) = \exp\left\{2\mu x - \frac{2\varepsilon}{\sigma}\cos(\sigma x)\right\} .$$

If $\mu < 0$, A^2 behaves like $\phi(t)$ and any initial disturbance decays exponentially as $t \to \infty$. When $\mu > 0$ but small the behavior of A as $t \to \infty$ is given by

$$A(t) \sim \frac{\mu^{\frac{1}{2}} \exp\{-\varepsilon/\sigma \cos(\sigma t)\}}{[I_0(2\varepsilon/\sigma)]^{\frac{1}{2}}} ,$$

where I_0 is the modified Bessel function of order zero. Hall [20] and later Barenghi and Jones [5] pointed out that when ε/σ is large, the amplitude takes the form of pulses and is exponentially small over part of the cycle. They also noticed that in practice this is unrealistic since weak imperfections always present in the system will drive low-amplitude motion. There are two ways to remedy this situation. On one way, considering $\sigma << \varepsilon$, Hall [20] has shown that the quasi-steady solution of (23) fails in the vicinity of any instant t^* where the flow is locally neutrally stable $\mu + \varepsilon sin(\sigma t^*) = 0$. In a short time interval of length $\mathcal{O}\left[(\sigma/\varepsilon)^{1/2}\right]$ around t^* it is a non periodic solution which prevails. Hall used this solution to show that the amplitude of the Taylor vortices varies linearly with Ω as for the subcritical transient vortices observed by Donnelly [11]. On the other way, Barenghi and Jones [5] considered a modified amplitude equation which takes into account the effect of imperfections by the addition of a constant term in the right-hand-side of (23)

$$\frac{dA}{dt} = \{\mu + \varepsilon sin(\sigma t)\} A - A^3 + c . \tag{25}$$

This equation was used by Barenghi and Jones [5] to explain why in experiments transient vortices have been observed when the maximum Reynolds number $Re(1 + \varepsilon)$ exceeds the critical value Re_{c0} for the steady problem. This is in contradiction with the perfect bifurcation theory for which the threshold value $\mu = 0$ corresponds to a critical Reynolds number Re_c which differs from Re_{c0} by an amount of order ε^2 [18]. Considering equation (25) for $\mu < 0$ Barenghi and Jones [5] have shown that under certain conditions amplified solutions can exist. Since the two cases $\mu + \varepsilon < 0$ and $\mu - \varepsilon > 0$ correspond respectively to damped and amplified solutions over the whole cycle, the case of interest is when $\mu + \varepsilon > 0$ and $\mu - \varepsilon < 0$. The solution is obtained by asymptotic matching between two regions which differ by the order of magnitude of A. The first region corresponds to $A \sim O(1)$ and it follows the phase of growth characterized by a positive instantaneous growth rate $\mu + \varepsilon sin(\sigma t) > 0$ for $t \in [t_1, t_3]$. In this region the solution is given by (24) where t_i is taken equal to t_1 the time at which the growth rate changes its sign from negative to positive, leading to

$$\frac{1}{A^2} = \frac{1}{\phi(t)}\left[K_1\phi(t_3) + \int_{t_1}^{t} \phi(x)dx\right] . \tag{26}$$

The constant term in (25) has been written as $K_1\phi(t_3)$ where K_1 is a constant to be determined by matching. Owing to the periodicity the solution has to repeat at time $t+T$ where expression (26) still holds provided t_1 and t_3 are replaced by t_1+T and t_3+T respectively. Between this two regions there is a region where A is small and neglecting the term A^3 in the governing equation (25), the solution is given by

$$A = \exp\left\{\mu t - \frac{\varepsilon}{\sigma}\cos(\sigma t)\right\}\left[K_2 + c\int_{t_3}^{t}\exp\left\{-\mu x + \frac{\varepsilon}{\sigma}\cos(\sigma x)\right\}dx\right] ,$$

where K_2 is an unknown constant which is determined with K_1 by the matching conditions. The matching equation obtained by Barenghi and Jones [5] gives a criterion for the occurrence of $\mathcal{O}(1)$ transient vortices which will be seen only if $c \approx c_-$ or larger, with $c_- = \sigma^{1/2}K^{-1}\exp(-\Delta/\sigma)$, where K and Δ are numbers of order unity calculated in [5].

4.2 Lorenz model

The Lorenz model was first introduced as an approximation to the Boussinesq equations for Rayleigh-Bénard convection under a steady driving [23]. Then, it has been generalized to the case of an external modulation [1]. Parallel to modulated convection, the same approach was used to described the non linear dynamics of modulated Taylor vortex flow. The two-mode model of Battacharjee *et al.* [6] provided an approximation for the critical parameters at the instability threshold. At least three modes are needed to allow for non linear effects above threshold [21]. Using the narrow-gap approximation and mixed boundary conditions Kuhlmann [21] derived a three-mode model which was then improved by the four-mode model of Kuhlmann *et al.* [22] we shall give here a brief account. In the derivation of their model the Navier-Stokes equations for the perturbations are written using the streamfunction $\psi(r,z,t)$ such that $u = \partial_z\psi$ and $w = -D_*\psi$. According to Galerkin method the following expansions are introduced

$$\psi(r,z,t) = \sum_n\sum_m \hat{\psi}_{nm}(t)\psi_n(r)\cos mkz \ , \tag{27a}$$

$$v(r,z,t) = \sum_n\sum_m \hat{v}_{nm}(t)v_n(r)\sin mkz \ , \tag{27b}$$

where $\psi_n(r)$ and $v_n(r)$ belong to two distinct sets of orthogonal functions [13]. From linear stability analyses of the unmodulated problem it is known that the critical modes can be approximated with a good accuracy by taking $n = m = 1$. Non linear interactions between these modes occurs via modes with $m = 0, 2$. Since modes with $m = 2$ are linearly damped only modes with $m = 0$ are kept in the expansion. Finally a four-mode truncation was proposed by Kuhlmann *et al.* [22] with one mode for the streamfunction with amplitude $\hat{\psi}_{11}$ and three modes for the v-component of the velocity with respective amplitudes $\hat{v}_{11}, \hat{v}_{20}$ and $\hat{v}_{10}$. The standard projection operation leads to the system of first-order ordinary

differential equations for the temporal evolution of the amplitudes

$$\frac{\tau}{\sigma}\dot{X} = -X + \frac{\hat{t}}{s}Y\left[p(t) + \rho_1 W + \rho_2 Z\right] , \tag{28a}$$

$$\tau\dot{Y} = -Y + X\left[q(t) + \rho_3 W - Z\right] , \tag{28b}$$

$$\tau\dot{Z} = -b_2 Z + XY , \tag{28c}$$

$$\tau\dot{W} = -b_1 W + XY , \tag{28d}$$

where $X(t), Y(t), Z(t)$, and $W(t)$ are rescaled amplitudes of $\hat{\psi}_{11}, \hat{v}_{11}, \hat{v}_{20}$ and $\hat{v}_{10}$. Here $\hat{t} = T/T_c(\varepsilon = 0)$ is the Taylor number defined as $T = Re^2\delta$ reduced by the critical one for onset of instability under stationary driving. The coefficients $p(t)$ and $q(t$

For small ε the stability boundary is given by

$$\alpha_c(\varepsilon, \omega \to 0) = \varepsilon^2 \frac{\beta^2}{2m\Gamma^2} + O(\varepsilon^4) \tag{30}$$

Expansion of $\hat{t}_c$ up to second order in ε gives

$$\hat{t}_c = 1 - \frac{\varepsilon^2}{2} + \varepsilon^2 \frac{2}{m\Gamma^2} \ .$$

The threshold shift consists of two opposite contributions of the same order of magnitude. Kuhlmann *et al.* have shown that the destabilizing effect is slightly larger than the stabilizing one thus yielding as a net effect a small destabilization. A comparison with the modulated Rayleigh-Bénard system has been made since (29) with the condition (30) still hold but now the quantities α and β express in terms of the reduced Rayleigh number $\hat{r}$ with $\alpha = \hat{r} - 1$ and $\beta = \hat{r}$. Thus it is straightforward to conclude that in convective systems only the stabilizing effect of modulation is present.

5 Conclusions

In the past decade, important progress has been made in the understanding of time-periodic Taylor vortex flow. It was due both to constructive interactions between theory and experiments and to an enhanced efficiency of numerical schemes.

Given the first impulse by Donnelly [11] who considered modulation of the inner cylinder when the outer cylinder is at rest, most of the contributions have been concerned with the onset of Taylor vortex flow and how the threshold parameter departed from its unmodulated value. The controversy about the order of magnitude of the threshold shift in the low frequency limit has been resolved by considering non linear theories. The perfect bifurcation theory [18] predicted a negative threshold shift of order ε^2 while it was known that transient vortices appeared as soon as the maximum instantaneous Reynolds number $Re(1 + \varepsilon)$ exceeds its unmodulated value. Using the amplitude equation he had previously derived Hall [20] found that near the instant at which the instantaneous growth rate vanishes non-periodic solutions exist which are connected to the transient vortices seen by Donnelly. Considering a modified amplitude equation where a constant term has been added to account for imperfections, Barenghi and Jones [5] have shown that a criterion for the existence of transient vortices is that the constant term exceeds a certain minimum value which depends on the frequency. By analogy with the Lorenz model for convection, a four-mode model was introduced by Kuhlmann *et al.* [22] which describes the non linear dynamics of modulated Taylor vortex flow above threshold. Its numerical integration gives a valuable insight in the complex behavior of the flow when the forcing is not supercritical over all the period of modulation.

A second configuration corresponding to steady rotation of the inner cylinder and pure oscillation of the outer cylinder was then investigated both experimentally [33] and theoretically [5], [24], [34]. It was found that modulation of the

outer cylinder has a stabilizing effect and that for large amplitude of modulation and low frequencies the response is subharmonic.

The case of zero-mean rotation, often referred as pulsed flows is more difficult to handle analytically because perturbative theories cannot be implemented. Oscillation of the inner cylinder alone [25] and out-of-phase oscillation of the two cylinders [4], [28] are known to bear some analogy. In particular in the low frequency limit the critical Taylor number tends to a finite value which is somehow higher than its value for a steady rotation of the cylinders. The difference is not yet completely understood and there is some evidence that the result is sensitive to the value of the gap size [4]. When the two cylinders are oscillating in phase the maximum of instability is found for a value of the frequency for which the thickness of the Stokes layer is half the gap width.

The behavior of time-periodic Taylor vortex flow (TVF) near instability threshold is now well understood for a variety of configurations. In the future, one can expect that more works will considered the development of TVF at values of the Taylor number significantly beyond its critical value. For in-phase oscillations of the cylinders, experiments [2] have shown that a turbulent regime develops very quickly for a Taylor number which is one-third higher than its critical value. It will be interesting to know how time-periodic TVF loses stability to more complicated types of flow and to identify the scenario for the onset of turbulence.

References

1. G. Ahlers, P. Hohenberg, M. Lücke: Phys. Rev A **32**, 3493 (1985)
2. A. Aouidef, C. Normand, A. Stegner and J. E. Wesfreid: Phys. Fluids **11**, 3665 (1994)
3. A. Aouidef and C. Normand: C. R. Acad. Sci. Paris, Serie II b, **322**, 545 (1996)
4. A. Aouidef and C. Normand: to be published in Eur. J. Mech. B/Fluids
5. C. F. Barenghi and C. A. Jones: J. Fluid Mech. **208**, 127 (1989)
6. J. K. Battacharjee, K. Banerjee and K. Kumar: J. Phys. A **L19**, 835 (1986)
7. R. J. Braun, G. B. McFadden, B. T. Murray, S. R. Coriell, M. E. Glicksman, M. E. Selleck: Phys. Fluids A **5**, 1891 (1993)
8. S. Carmi and J. I. Tustaniwskyj: J. Fluid Mech. **108**, 19 (1981)
9. S. Chandrasekhar, *Hydrodynamic and Hydromagnetic Stability* (Oxford University Press, London, 1961).
10. S. H. Davis: Ann. Rev. Fluid Mech. **8**, 57 (1976)
11. R. J. Donnelly: Proc. Roy. Soc. London A **281**, 130 (1964)
12. P. G. Drazin and W. H. Reid: *Hydrodynamics Stability* (Cambridge University Press, 1981)
13. P. Ern: Instabilités d'écoulements périodiques en temps avec effets de courbure et de rotation, Thèse de doctorat, Université Paris VI (1997)
14. P. Ern and J. E. Wesfreid: J. Fluid Mech. **397**, 73 (1999).
15. M. Faraday: Phil. Trans. R. Soc. London **52**, 319 (1831)
16. G. Z. Gershuni, E. M. Zhukhovitskii: *Convective Stability of Incompressible Fluids* (Keter Publishing House, Jerusalem 1976)
17. P. Hall: Proc. Roy. Soc. London A **344**, 453 (1975)

18. P. Hall: J. Fluid Mech. **67**, 29 (1975)
19. P. Hall: Proc. Roy. Soc. London A **359**, 151 (1978)
20. P. Hall: J. Fluid Mech. **126**, 357 (1983)
21. H. Kuhlmann: Phys. Rev. A **32**, 1703 (1985)
22. H. Kuhlmann, D. Roth, M. Lücke: Phys. Rev. A **39**, 745 (1989)
23. E. N. Lorenz, J. Atmos. Sci. **20**, 130 (1963)
24. B. T. Murray, G. B. McFadden and S. R. Coriell: Phys. Fluids A**2**, 2147 (1990)
25. P. J. Riley and R. L. Laurence: J. Fluid Mech. **75**, 625 (1976)
26. G. Seminara, P. Hall: Proc. R. Soc. London A **350**, 299 (1976)
27. G. I. Taylor: Philos. Trans. R. Soc. London A **223**, 289 (1923)
28. S. G. K. Tennakoon, C. D. Andereck, A. Aouidef, C. Normand: Eur. J. Mech. B/Fluids **16**, 227 (1997)
29. J. I. Tustaniwskyj and S. Carmi: Phys. Fluids **23**, 1732 (1980)
30. R. Thompson: Instabilities of some time-dependent flows. Ph.D. Thesis, Massachussetts Institute of Technology (1968)
31. C. von Kerczek and S. H. Davis: J. Fluid Mech. **62**, 753 (1974)
32. T. J. Walsh, R. J. Donnelly: Phys. Rev. Lett. **58**, 2543 (1988)
33. T. J. Walsh, R. J. Donnelly: Phys. Rev. Lett. **60**, 700 (1988)
34. X. Wu, J. B. Swift: Phys. Rev. A **40**, 7197 (1989)

Low-dimensional dynamics of axisymmetric modes in wavy Taylor vortex flow

Jan Abshagen and Gerd Pfister

Institute of Experimental and Applied Physics,
University of Kiel, 24098 Kiel, Germany

Abstract. The dynamics of the 'very-low-frequency' (VLF) mode in moderate aspect ratio flow is experimentally investigated. The VLF mode is an axisymmetric, time-dependent mode that occurs in wavy Taylor vortex flow at $\eta = 0.5$ [25]. For normalised aspect ratios $\Gamma/N < 0.89$ a 'universal' sequence of states from stationary Taylor vortex flow to chaotic VLF mode has recently been discovered for the 10- to 50-vortex flow [26]. We show that a qualitatively different transition to chaos occurs in the 12-vortex flow compared with flow states having 14 and more vortices. A symmetry-breaking bifurcation that appears within this 'universal' sequence of states is found to be crucial for this new scenario. The onset of chaos via an intermittency route is accompanied with the restoring of the original Z_2-symmetry of the system leading to a 'symmetric' chaotic attractor for a wide range of aspect ratio. The formation of Shil'nikov-type attractor associated with the unstable symmetric fixed point could be found as well. Further investigations show that a new type of VLF mode appears in the Small-jet regime via a Hopf-bifurcation for slightly larger aspect ratio. We present additionally an examination of the VLF mode in a modulated wavy Taylor vortex flow consisting of Small-jet and axially localised Large-jet mode. The transition to chaos in these two VLF regimes is briefly discussed.

1 Introduction

Despite of its ubiquitous appearance in fluid flows and its importance for technical processes are the mechanisms for the onset of turbulence still only poorly understood. A huge amount of work has been done to analyse the successive stages of complexity that arise in fluid flow confined in well-defined experimental configurations driven by external forces (see e.g. [1]). Taylor–Couette flow is one of the classical hydrodynamic systems for the study of instabilities and the transition to turbulence [2–5]. In contrast to the difficulties concerning turbulent Taylor vortex flow is the transition to chaotic or 'weakly turbulent' flow in some situations better understood. Though low-dimensional chaos in a flow is of much less complexity than the intrinsic spatio-temporal dynamics of fully developed turbulence it provides a mechanism for the onset of irregularity governed by deterministic laws.

Chaos had been first observed in Taylor–Couette flow by Gollub and Swinney [8] and Fenstermacher, Swinney and Gollub [9]. They showed that turbulence is not due to a multiperiodic motion with many incommensurate frequency according to Landaus hypothesis but irregular flow appears after a few time-dependent instabilities. Strange attractor behaviour in Taylor–Couette flow was first found

C. Egbers and G. Pfister (Eds.): LNP 549, pp. 84–101, 2000.

by Brandstäter et al. [10] and Brandstäter and Swinney [11] in a chaotic flow resulting from a breakup of a T^2-torus of modulated Wavy vortex flow according to the Ruelle-Takens scenario. Their experiments where performed in an apparatus with a radius ratio $\eta = \frac{r_i}{r_o} = 0.875$ and an aspect ratio, which is the ratio of cylinder length L to gap width d, of $\Gamma = \frac{L}{d} = 20$. The chaotic behaviour was proved with means of nonlinear time-series analysis.

Studying low-dimensional dynamics in a large aspect ratio system may become very intricate because of the high multiplicity of states especially at higher Reynolds number. To overcome these difficulties Pfister et al. [12] investigated the flow in a very small aspect ratio system in order to reduce the multiplicity of steady solutions. The time-dependent behaviour, however, is found to be quite complex as well. They observed e.g. a period doubling cascade in a restabilised 2-vortex flow [13,14] and homoclinicity in a 1-vortex flow [15].

A close connection to Navier-Stokes equation in order to identify a mechanism for the onset of chaos was done by Mullin [19]. The location of steady bifurcation due to cell number changes were examined experimentally as well as numerically [6,7]. Mullin, Cliffe and Pfister [16] found that time-dependent flow can result from the interaction of a fold point originating from a cell number change process and a symmetry-breaking bifurcation. Chaos was investigated by Mullin and Price [17,18] in a modified Taylor–Couette system with rotating inner cylinder. It was found to be organised by the interaction of the time-dependent bifurcation and the symmetry-breaking bifurcation giving rise to Shil'nikov chaos [17]. Additionally they observed a new type of intermittency [18]. Their work stresses the importance of the reflection symmetry for the onset of chaos in Taylor–Couette flow.

Recently, a new transition to chaos that occurs in a wavy Taylor vortex flow ($\eta = 0.5$) at large aspect ratios could be observed [26]. For this radius ratio different time-dependent instabilities can occur in stationary Taylor vortex flow depending on the aspect ratio [25]. Therefore we call the regime of time-periodic flow in the wide gap case 'wavy Taylor vortex flow' in contrast to the classical Wavy vortex flow which is associated with a certain type of time-dependent instability occuring especially in a small-gap Taylor vortex flow. In order to compare the different time-dependent instabilities at $\eta = 0.5$ of flow states having different numbers of vortices it is found useful to normalise the aspect ratio Γ with the vortex number N giving a normalised aspect ratio $\Gamma/N = \frac{L}{Nd}$. The transition reported in [26] was observed in a 10- to 50-vortex flow for $\Gamma/N \leq 0.89$. The sequence of states from stationary Taylor vortex flow to chaotic flow is found to be 'universal'. Taylor vortex flow becomes time-dependent with the onset of the Small-jet mode which is a rotating wave with an azimuthal wave number $m = 1$ and an oscillation frequency of nearly half of the inner cylinder [25]. Oscillations in adjacent vortex pairs are out of phase. Accompanied with the onset of time-dependence the system undergoes a symmetry-breaking bifurcation leading to two asymmetric time-dependent states. A second time-dependent instability occurs at higher Reynolds number on each asymmetric branch leading to a time evolution on a T^2-torus. The very-low-frequency (VLF) mode is a very

slow, axisymmetric ($m = 0$) time-periodic mode. It has been observed in Taylor vortex flow for nearly all aspect ratios as a second or higher time-dependent instability. The oscillation frequencies range for $2 * 10^{-2}$ to $3 * 10^{-5}$ times the inner cylinder's angular velocity. For $\Gamma/N \leq 0.89$ the VLF mode appears via a homoclinic bifurcation on each asymmetric branch. For higher Reynolds number each doubly periodic asymmetric state becomes chaotic via a period-doubling cascade on a torus.

In this work the influence of the symmetry-breaking bifurcation on the transition to chaos in the VLF regime is analysed. Therefore we have investigated again in great detail the transition to chaotic VLF mode for moderate aspect ratios. While for the 14-vortex flow our observations are in accordance with the previous results a new scenario could be found for the 12-vortex flow. The experimental results concerning this scenario will be presented in section 3 after a brief description of the experimental setup in the next section (2). Additionally, we report on a new observation of VLF mode occuring in a flow consisting of Small-jet and axially localised Large-jet mode. The results will be presented in section 4. A discussion is given in the last section (5).

2 Experimental setup

The Taylor–Couette experiment we used consists of two high-precision concentric cylinders. The inner one is machined from stainless steel having a radius of $r_i = 12.5mm$. The stationary outer cylinder is made of optical polished glass with a radius of $r_o = 25mm$. The accuracy is better than $0.01mm$ over the entire length of $640mm$. The top and bottom plates are at rest. In axial direction we are able to vary the position of the top plate continously with a stepper motor having an accuracy of $0.01mm$. As a working fluid we used silicon oil with different viscosities. The temperature of the oil is thermostatically controlled within $0.01K$ by circulation through a surrounding square box. A phase-locked-loop (PLL) circuit controls the speed of the inner cylinder. The accuracy is better than on part in 10^{-4} per revolution and one part in 10^{-7} in the long term average. The local velocity is measured by a real-fringe laser-Doppler velocimeter (LDV) and recorded by a PLL analog tracker. The signal is filtered by an analog Bessel filter of fourth order and then converted with a resolution of 14-bit. The position of the measurement volume can be varied continously. Details can be found e.g. in [26].

3 An intermittency route to chaos

In [26] it has been shown that the symmetry-breaking which occurs together with the onset of the Small-jet mode influences both the distribution of the vortex size and the amplitude distribution of the Small-jet and VLF mode. For larger systems an amplitude distribution of the VLF mode that is nearly localised in either half of the cylinder was found. In these systems the transition to chaos occurs separately on each asymmetric branch and no interaction between the

two branches has been observed. For decreasing number of vortices the degree of asymmetry is reduced while the sequence of states remains unchanged.

3.1 Onset of 'symmetric' chaos

This is true for systems having 14 vortices or more. The transition to chaos in the 12-vortex state is qualitatively different. Instead of period doubling, that appears for larger system, we found a transition to chaos via intermittency. Fig. 1 shows a typical time series of a chaotic VLF mode very close after its onset. It was recorded in the 12-vortex state at $\Gamma/N = 0.84$ and $Re = 412$. The time series is low-pass filtered with a cut-off frequency of $f_c = 0.1Hz$ to filter out the 'fast' Small-jet oscillations. Though the interaction between the

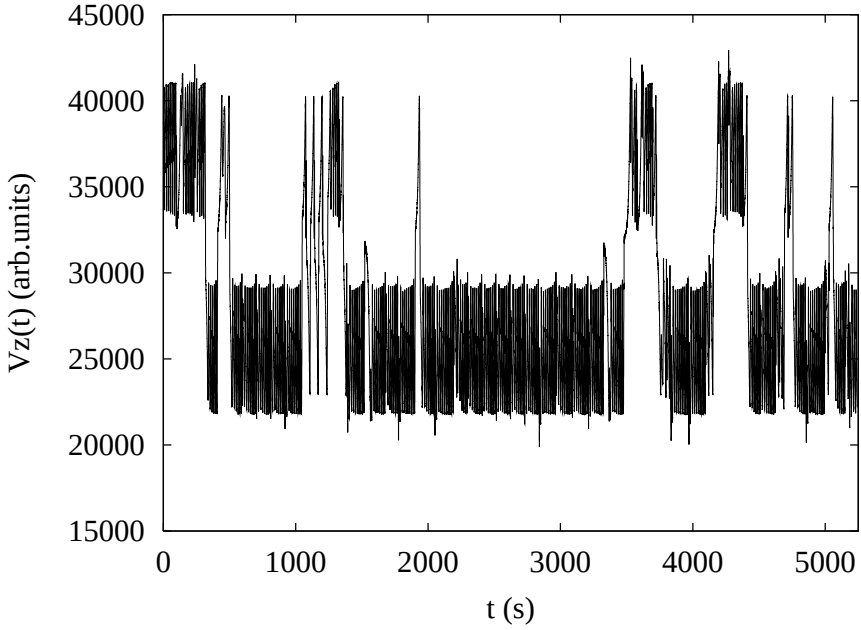

Fig. 1. Chaotic VLF mode at $\Gamma/N = 0.84$ slightly after onset of chaos in a 12-vortex state ($Re = 412$) measured at $L/2$. The 'fast' Small-jet oscillation is filtered out. An intermittent behaviour and a connection between the two asymmetric branches can be recognised.

non-axisymmetric 'fast' Small-jet mode and the axisymmetric 'slow' VLF mode is not completely understood there is strong evidence that they interact on the 'slow' time scale of the VLF. Previous measurement have shown that in the VLF regime the oscillation frequency of the underlying time periodic mode is

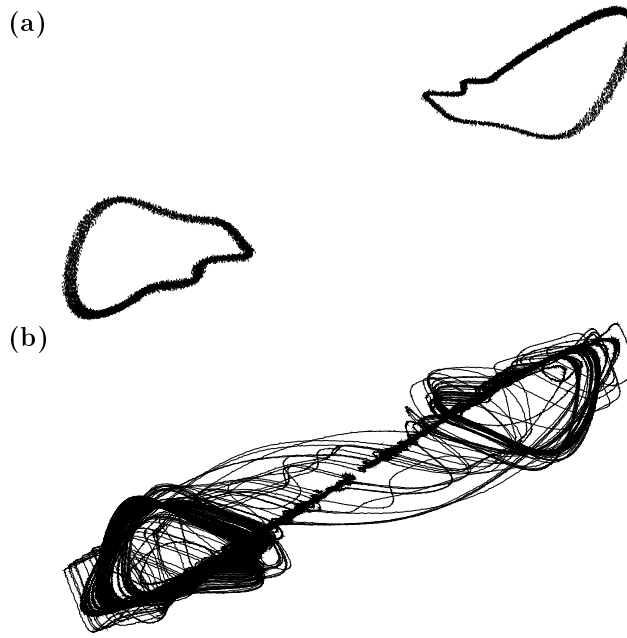

Fig. 2. Delay-embedding reconstruction of (a) periodic ($Re = 411$) and (b) chaotic ($Re = 412$) attractor of VLF mode recorded at $\Gamma/N = 0.84$. The chaotic attractor corresponds to the time series depicted in Fig. 1. The two periodic orbits correspond to oscillatory VLF mode on the asymmetric branches

not influenced but the phases of the oscillation located in adjacent vortex pairs. The evolution of the phase takes place on the same time scale of the VLF mode but it has not been clarified whether the a change in phase is caused by the VLF mode or the phase change causes this mode [25,26]. This implies that the relevant information is gained by measuring the slow evolution. The 'carrier' frequency of the Small-jet mode does not contain any additional information and is therefore omitted in all time series shown in this paper. It should be kept in mind, however, that the dynamics of the original flow is doubly periodic leading to a evolution on a T^2-torus. To ensure a correct detection of the VLF oscillation the measurement volume of the LDV is always positioned in the middle of the cylinder ($L/2$) at a distance of $3mm$ from the inner cylinder. We measure the axial component v_z of the flow velocity. Because for a 12-vortex flow an inward flow boundary is located at $L/2$ if the flow is symmetric the axial velocity v_z is proportional to the axial displacement Δz (for small Δz). From the time series in Fig. 1 the two characteristic properties of the chaotic VLF mode in the 12-vortex state can be seen. The first point is that 'laminar' phases of VLF oscillation can clearly be recognised giving rise to an intermittency route to chaos. Secondly, the time series is symmetric at least at average [32,33]. The unstable symmetric state is located between the two branches in the time series

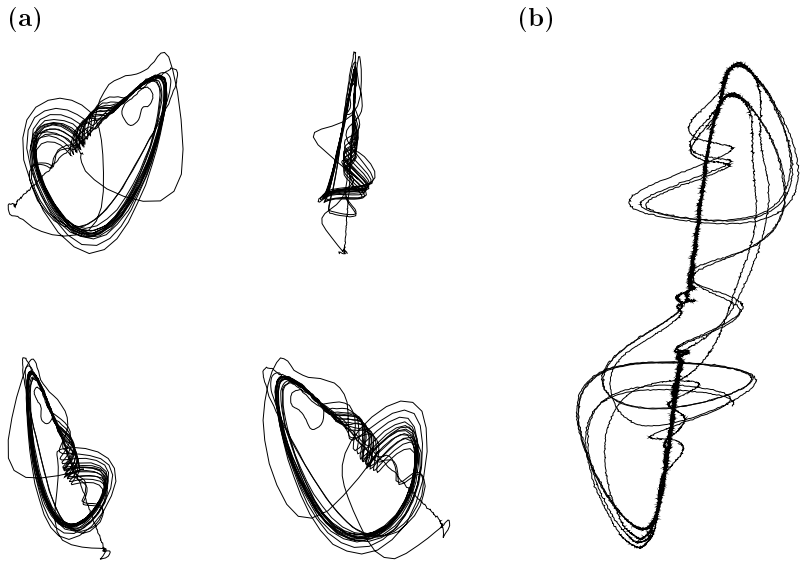

Fig. 3. Reconstruction of parts of chaotic attractor shown in Fig. 2: a) four different views of attractor corresponding to a 'laminar' phase in the time series (Fig. 1). This part of the attractor is located close to the original periodic orbit of the VLF mode in phase space. b) 'symmetric' attractor

shown in Fig. 1. This means that accompanied with the onset of chaos the original Z_2-symmetry of the Taylor–Couette system that is broken at symmetry-breaking bifurcation point at lower Reynolds number is restored. In order to illustrate this behaviour a reconstructed attractor in phase space is shown in Fig. 2. We use time-delay embedding with optimal reconstruction parameters [20–22]. In Fig. 2 (a) two separated periodic orbits corresponding to the VLF oscillation on the two asymmetric branches at $Re = 411$ and $\Gamma/N = 0.84$ are depicted. The chaotic attractor shown below in Fig. 2 (b) correspond to the chaotic time series of Fig. 1. The region in phase space where the two stable periodic orbits are located at $Re = 411$ can be recognised. To illustrate the two different 'phases' of chaotic behaviour Fig. 3 shows reconstructions of small parts of the time series depicted in Fig. 1 corresponding to a 'laminar' phase (Fig. 3, a) and jumping between the two asymmetric branches (Fig. 3, b). The merging of the two separated attractor basins of these periodic orbits at $Re = 411$ leading to an increase of symmetry at the transition to chaos is clearly visible. It should be stressed that no hysteresis has been found within the experimental accuracy of $\Delta Re = 0.2$ though the duration of chaotic transients increases up to 48 hours. To ensure 'asymptotic' stability of the chaotic state in the vicinity of the critical point we waited up to 96 hours before the data were recorded. The scenario found at $\Gamma/N = 0.84$ could be identified as well at different aspect ratios in the 12-vortex flow. For smaller aspect ratios we followed the transition point down to $\Gamma/N = 0.76$. For larger

aspect ratios we observed the attractor crisis occuring up to $\Gamma/N = 0.868$. For $\Gamma/N \geq 0.87$ the two attractor basins remains separated at the onset of chaos. It should be stressed that the appearance of a 'symmetric' attractor is found to depend only on the cylinder length and not on the Reynolds number. We found no attractor-merging-crisis within the chaotic regime for increasing Reynolds number at fixed aspect ratio. Therefore it might be useful in this context to speak of a 'critical' aspect ratio Γ_c. A slightly irregular, slow modulation of the periodic VLF mode could be observed in the vicinity of Γ_c close to the onset of chaos. It should be mentioned that the experimental scenario described here has some similarities with chaos found in low-dimensional dynamical systems, e.g. in the Lorenz system [31], though a complete description is not available at the moment. In order to gain more insight in the dynamics of the chaotic VLF mode we have examined the properties of intermittency.

3.2 Type of intermittency

The different kinds of intermittent behaviour in the Pomeau-Manneville route to chaos are usually characterised by the way the periodic orbit becomes unstable [34–36]. This leads to three different main types depending on whether the Flouquet mutiplier crosses the unit circle at 1 (Type I), at -1 (Type III), or a complex conjugated pair crosses the unit circle (Type II). Additionally, two new types of intermittency have been observed which are both related to a cyclic fold bifurcation. Mullin and Price found a hysteretic type of intermittency which they called Type X [18]. The different behaviour compared with Type I intermittency is caused by a different reinjection mechanism. Another type of intermittency called Type V [40] occurs due to a discontinuous point in the return map. To determine the type of intermittency occuring in the VLF regime we have constructed a return map of laminar phases. Fig. 4 shows (a) long laminar phases of the intermittent VLF mode observed at $\Gamma/N = 0.84$

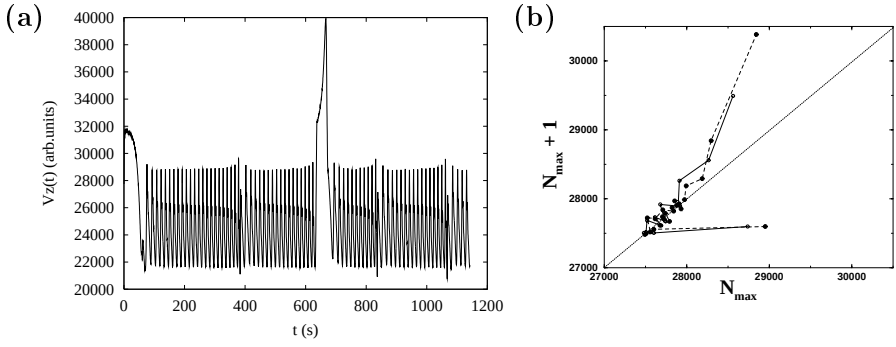

Fig. 4. (a) Long laminar phases of intermittent VLF mode measured at $Re = 411.6$ and $\Gamma/N = 0.84$. (b) Experimental return map of the first (•) and second (○) laminar phase of time series (a). The $N + 1$ maxima is plotted vs. the N maxima.

and $Re = 411.6$ and (b) an experimental return map plotting the subsequent maxima $N_{max} + 1$ vs. N_{max} of the first two laminar phases taken from (a). The lower branch of the cusp shaped curve in the return map represents the injection into the laminar phase. The system remains for some time in the vicinity of the original fixed point before a 'burst' occurs indicated by the upper branch. A cusp shape return map has been observed before in an intermittency scenario in Rayleigh-Bénard convection by [37]. This kind of behaviour was explained with the existence of a stable direction where the reinjection takes place. A comparison between the two scenarios shows a resemblance both in the shape of the laminar phases and of the return map. The scenario described in [37] is viewed as a prototype of Type I intermittency where the limit cycle disappears via a saddle-node bifurcation. The characteristic properties of a time series associated with Type II and Type III intermittency leading to the onset of an unstable oscillation or an unstable subharmonic, respectively, is not present in the time series depicted in Fig. 4. It should be noticed that the resemblance of the time series to Type III intermittency originates from a strong second harmonic that is present in the periodic regime as well. However, the disappearance of the limit

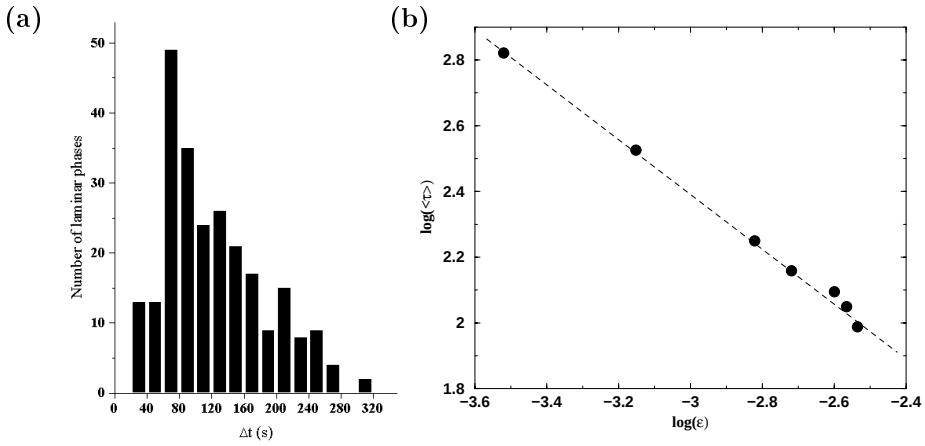

Fig. 5. (a) Distribution of laminar phases of intermittent VLF mode in 12-vortex state slightly after onset of chaos ($Re = 594$, $\Gamma/N = 0.87$). The number of phases is plotted vs. the duration Δt (s) of the phases. (b) log-log plot of average length of laminar phases $< \tau >$ obtained at $\Gamma/N = 0.84$. The dashed line is plotted to guide the eyes.

cycle in Type I intermittency in contrast to the appearance of an unstable limit cycle in Type II and Type III intermittency influences the scaling behaviour of the average length and the distribution of the laminar phases (see e.g.[36]). Fig. 5 (a) depicts an experimentally obtained distribution of laminar phases of the intermittent VLF mode at $\Gamma/N = 0.87$ and $Re = 594$. The smooth decay

from the maximum to longer laminar phases is clearly visible. This is characteristic for an intermittency type related to an unstable limit cycle, like Type II or Type III. In these types a reinjection very close to this cycle is responsible for very long laminar phases. Type I intermittency is characterised in contrast by a sharp low-frequency cut-off representing the longest time a 'walk' through the channel can take. This is because the fixed point has disappeared in the saddle-node and only the 'ghost' of this fixed pont is still present. Fig. 5 (b) shows a log-log plot of the average duration of laminar phases $< \tau >$ versus the relative distance from the critical point $\varepsilon = \frac{Re - Re_{crit}}{Re_{crit}}$. It is related to a scenario recorded at $\Gamma/N = 0.84$. The slope in this case is -0.81. To get a more profound result we investigated on the one hand the influence of the uncertainty in the measurement of the critical point on the scaling and on the other hand two other scenarios were recorded. One is measured at the same aspect ratio, the other at $\Gamma/N = 0.82$. We found a scaling of $< \tau >= \varepsilon^{-(0.74 \pm 0.05)}$. This is in contradiction to the behaviour of the standard type of intermittency where $< \tau >= \varepsilon^{-0.5}$ is found for Type I and $< \tau >= \varepsilon^{-1}$ for Type II and Type III. Recent work on the dependence of the exponent on the reinjection probability shows that a behaviour of $< \tau >= \varepsilon^{-0.75}$ may occur in Type II and Type III intermittency for a different reinjection probability [39]. Such a scaling behaviour cannot be associated with Type I intermittency [38].

The intermittency route to chaos that occurs in the VLF regime of the 12-vortex state cannot obviously be related to neither the three types of the Pomeau-Manneville scenarios nor to the two new types. Though the distribution and the average length of the laminar phases corresponds the existence of an unstable periodic orbit after the onset of chaos, no clear hind on the type of bifurcation is given from the time series and the return map.

3.3 Observation of Shil'nikov attractor

With intermittency it is usually meant that the dynamics consists of two distinct parts. The first one concerns the behaviour close to the original limit cycle which is determined by the type of the local bifurcation. The chaotic 'bursts' between the laminar phases together with the reinjection mechanism depends on the whole phase space structure. Therefore the transition to chaos via intermittency is a global phenomena which is not completely understood by the local behaviour in the vicinity of the limit cycle. It can be seen from the time series depicted in Fig. 1 and the related chaotic attractor (Fig. 2) that two different kinds of 'bursting' are possible at the end of a laminar phase. Either the trajectory remains close to the original limit cycle leading to a very fast and regular reinjection or the trajectory moves away for the region in phase space where the laminar phases are located. Then it may come close to the unstable symmetric fixed point and possibly jump to the other branch. We have analysed this behaviour in detail for different aspect ratios. We found that especially close to the 'critical' aspect ratio and for normalised aspect ratios $\Gamma/N \approx 0.8$ a second type of regular phase related to a second type of oscillation can be observed. In Fig. 6 (a) a chaotic VLF mode recorded in the 12-vortex state at

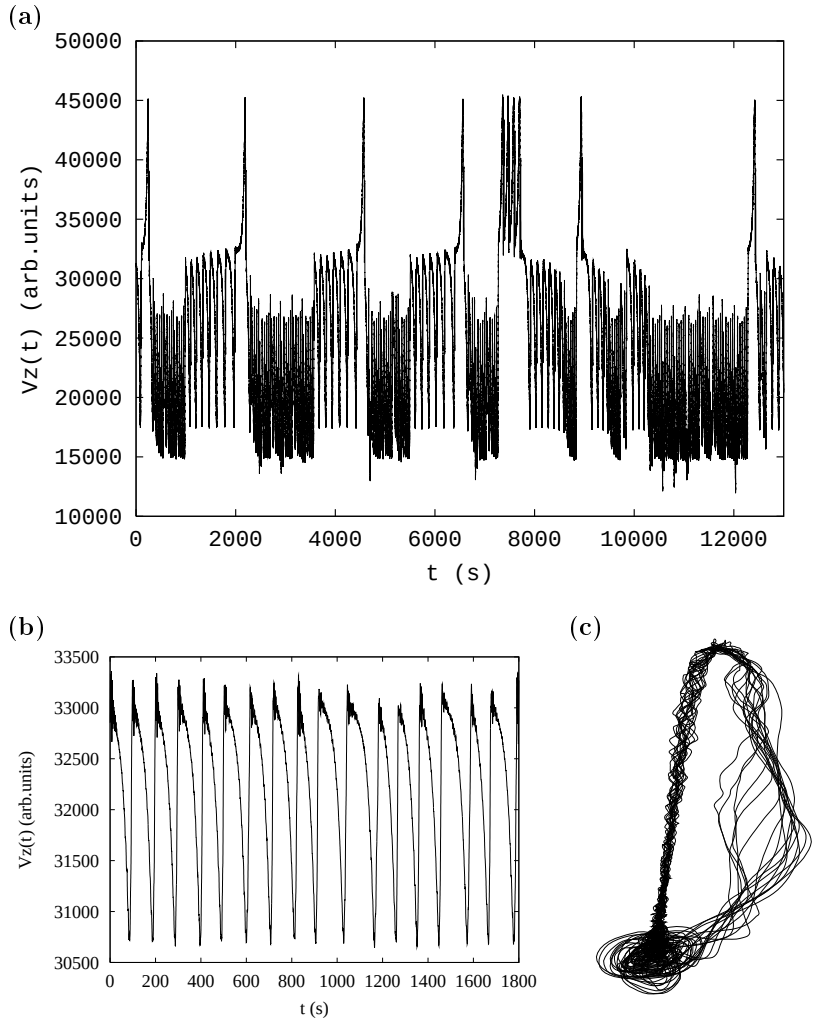

Fig. 6. (a) VLF mode at $\Gamma/N = 0.8$ slightly after onset of chaos in a 12-vortex state recorded at $Re = 366$. Intermittent VLF and 'spiking' oscillations are visible. (b) 'spiking' part of time series recorded at larger aspect ratio $\Gamma/N = 0.87$ due to the stronger oscillatory behaviour close to the unstable symmetric fixed point.(c) Shil'nikov-type attractor reconstructed from time series (b)

$Re = 366$ and $\Gamma/N = 0.8$ is depicted. The original intermittent state is interrupted by long-lasting periods of 'spiking' oscillations. It can be seen that these oscillations results from a direct reinjection from the unstable manifold of the symmetric fixed point in the vicinity of this point. To illustrate this kind of behaviour Fig. 6 (b) shows a single phase of 'spiking' oscillation. They were measured at a normalised aspect ratio $\Gamma/N = 0.87$ and $Re = 594$ where the at-

tractor basins remains separated. A reconstructed attractor is depicted in Fig. 6 (c). It can be seen that the trajectory leaving the unstable symmetric fixed point is directly reinjected in the vicinity of the fixed point having an inward spiraling dynamics in the stable direction. For illustration we have taken a time series from a flow recorded at a larger aspect ratio because the spiraling behaviour is found to become stronger with increasing aspect ratio. The attractor of Fig. 6 (c) is very similar to a homoclinic orbit of Shil'nikov-type. We observed that while approaching the Γ_c an decrease of the frequency of the spiking oscillation though they occur irregular. However, no clear scenario could be identified. It has to been clarified whether or not the transition to chaos in the VLF regime is related to the appearance of a Shilnikov-type attractor. It is well-known that close to a Shil'nikov homoclinic orbit chaotic dynamics can appear [28–30].

3.4 Transition to Hopf regime

We have shown in the last section that the scenario observed in VLF regime of the 12-vortex state is qualitatively the same for a wide range of aspect ratio. It can be observed, however, that the shape a of periodic VLF oscillation changes for normalised aspect ratios slightly below $\Gamma/N \leq 0.907$. Fig. 7 shows three different time series and reconstructed attractors of periodic VLF oscillations measured at (1) $\Gamma/N = 0.9$ and (2, 3) $\Gamma/N = 0.907$. A second type of oscillatory mode becomes visible leading to an inward spiraling behaviour. The attractor has again some similarities with a Shil'nikov-type attractor though the periodic orbit is located on the asymmetric branch away from the unstable symmetric fixed point. For normalised aspect ratios $\Gamma/N > 0.907$ the large VLF oscillation that is dominant at smaller aspect ratios disappears and another type of VLF mode becomes supercritical. This second type occurs via a Hopf bifurcation in contrast to the homoclinic bifurcation that leads to the onset of VLF mode at smaller aspect ratios. It should be stressed that this new type of VLF mode is not due to a change in the type of the underlying 'fast' time-dependent mode, but the Small-jet mode is still present.

Figure 8 (1a) shows a typical time series of the new type of VLF mode recorded at $\Gamma/N = 0.913$ and $Re = 804.4$ in the 12-vortex flow. The 'fast' Small-jet oscillation are filtered out again. This type is of smaller amplitude having an oscillation frequency about a magnitude larger than the type of VLF mode that appears via a homoclinic bifurcation at smaller aspect ratios. The typical square-root behaviour of the amplitude in case of a Hopf bifurcation could be proofed, as shown in Fig. 8 (1b). The oscillation frequency is found to be finite at onset. Our observations give rise to the conjecture that the Hopf-type onset of the VLF mode observed in flows having a larger number of vortices [26] correspond to this type of VLF mode.

We found no aspect ratio where the Hopf and the homoclinic stability line meets. Within the small interval between $0.907 < \Gamma/N < 0.913$ no time-dependent axisymmetric mode occurs until the flow is restabilised by a different modulated wavy Taylor vortex flow. The onset of the Large-jet mode is described in section 4. The appearance of the second type of VLF mode at $\Gamma/N \approx 0.9$

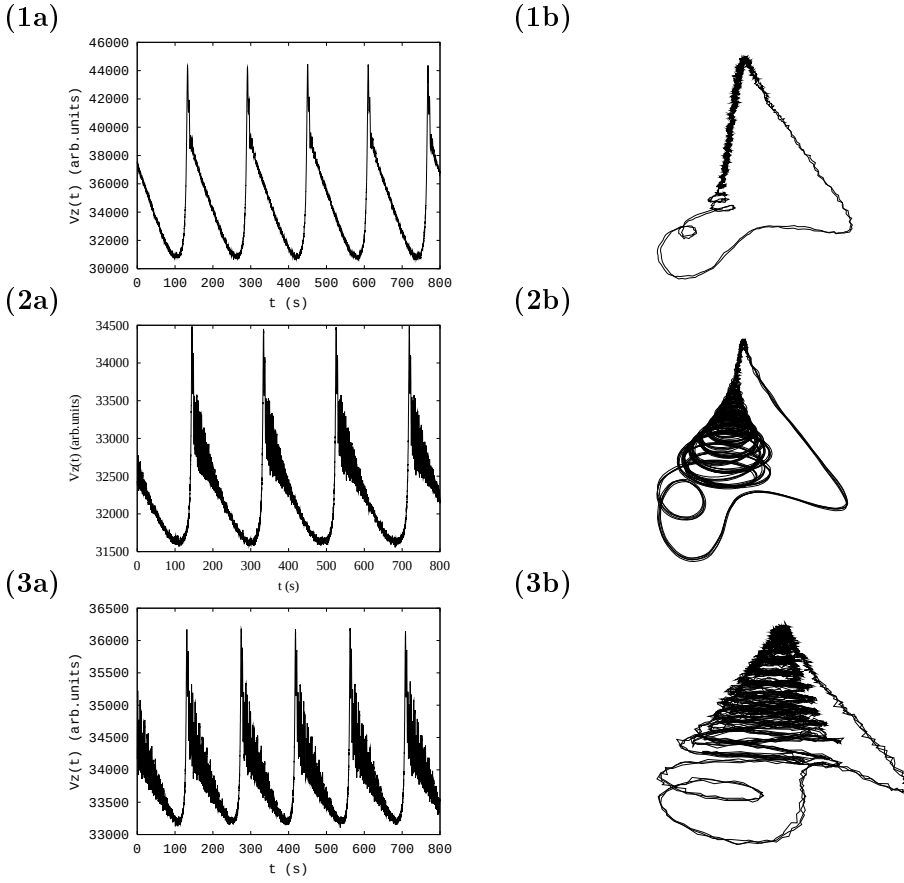

Fig. 7. Three (a) time series and (b) reconstructed attractors of periodic VLF mode measured in the 12-vortex state: Typical VLF mode oscillation (1) recorded in the 'homoclinic' regime at $Re = 660$ and $\Gamma/N = 0.9$. Two time series recorded very close to the Hopf regime at $\Gamma/N = 0.907$ and (2) $Re = 784$ and (3) $Re = 817$. A noise reduction algorithm has been applied to the reconstructed attractor (2,b) [23].

destroys the clear intermittency scenario observed for smaller cylinders in the homoclinic regime. In the Hopf regime which occurs for the 12-vortex flow at $\Gamma/N \geq 0.913$ a completely different transition to chaos has been observed. To illustrate the chaotic VLF mode in the Hopf regime a typical time series is shown in Fig. 8 (2a). This time series was recorded in a Hopf regime of the 10-vortex flow at $\Gamma/N = 0.88$ and $Re = 675$. The reconstructed attractor of time series (Fig. 8, 2a) is depicted in Fig. 8 (2b). The transition is found to be related to intermittency as well, but the complete bifurcation sequence is more complicated. A detailed description is given in [27].

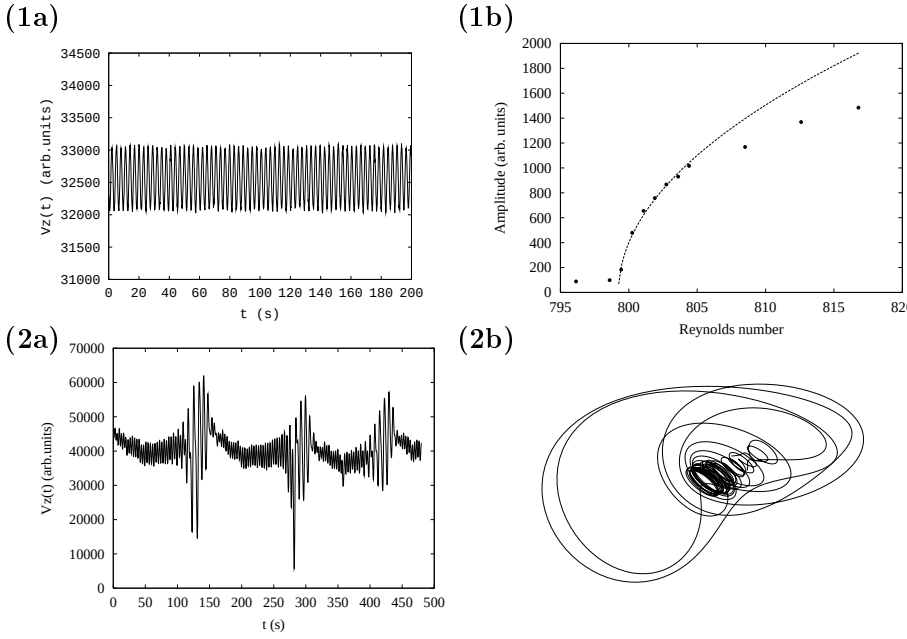

Fig. 8. Periodic and chaotic VLF mode in the Hopf regime: (1) a: Time series obtained in the 12-vortex state at $Re = 804.4$ and $\Gamma/N = 0.913$, b: Amplitude vs. Reynolds number at $\Gamma/N = 0.913$, (2) Chaotic time series obtained in the Hopf regime of the 10-vortex state at $Re = 742$ and $\Gamma/N = 0.888$ close to onset of chaos, b: Reconstructed attractor of time series 2a).

4 A T^3-torus in spatial inhomogeneous flow

In the last section we have reported on a scenario that occurs in wavy Taylor vortex flow. The single time-periodic ($m = 1$) flow becomes doubly periodic by the onset of a axisymmetric ($m = 0$), time-dependent mode. Here, we will describe a scenario where a modulated wavy Taylor vortex flow that consists of two non-axisymmetric ($m = 1$) modes becomes triply periodic by the onset of an axisymmetric time-dependent mode.

4.1 Axially localised Large-jet mode

The modulated wavy Taylor vortex flow considered here consists of the Small-jet mode and the Large-jet mode. The Large-jet mode is an oscillation of the outward flow having an azimuthal wave number $m = 1$ like the Small-jet mode. It differs from the latter by a slightly higher oscillation frequency, a larger amplitude, and the fact that the oscillation in adjacent vortex pairs are in phase in contrast to the out-of-phase oscillations of the Small-jet mode. The interaction between Small-jet mode and Large-jet mode has been described in [24]. They

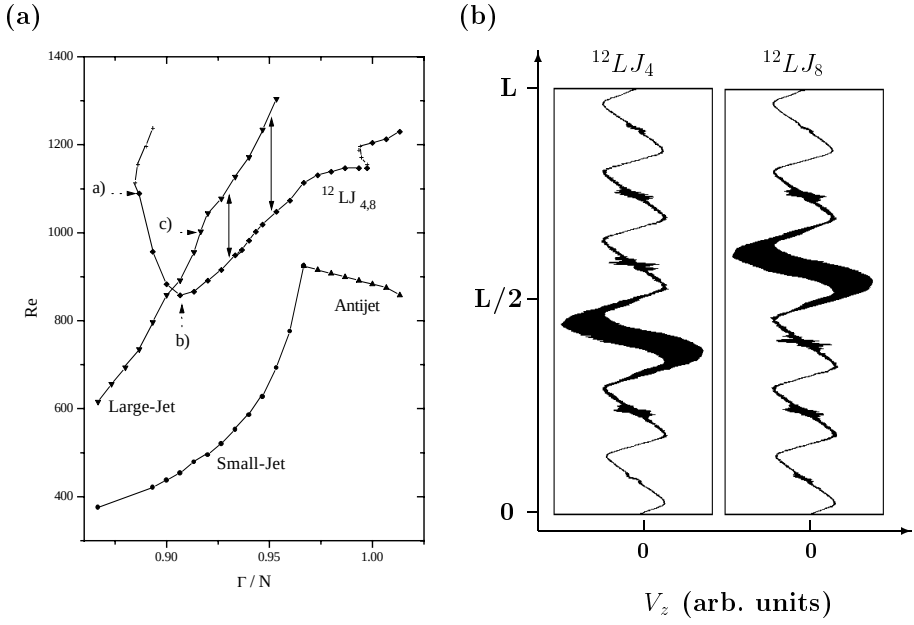

Fig. 9. (a): Stability diagram of non-axisymmetric time dependent instabilities of the 12-vortex state. The onset of Small-jet, Antijet, Large-Jet (below c)), and localised Large-jet ($^{12}LJ_{4,8}$) mode (above c)) as well as the lower stability boundary of $^{12}LJ_{4,8}$ is depicted. The arrows indicate hysteresis. (b): Flow profiles of localised Large-jet mode $^{12}LJ_4$ and $^{12}LJ_8$. The localised Large-jet oscillation in the middle of the cylinder is clearly visible.

found for example frequency locking between the two modes. We will focus on flow states where the Large-jet mode appears not in every vortex pair but only axially localised in some. Pfister [41] was the first who described the appearance of the axially localised Large-jet mode in the Small-jet regime. Other axially localised wavy and modulated wavy Taylor vortex flows has been observed for a radius ratio $\eta = 0.5$. A detailed description of the different types of axially localised modes and their properties is given in [43]. In the case of independently rotating cylinders the formation of dynamical domains was first described by Baxter and Andereck [42]. The stability diagram of the two non-axisymmetric time-periodic modes is shown in Fig. 9. The different axisymmetric instabilities in the Small jet regime are omitted for clarity. Fig. 9 shows the onset of the the Small-jet and the Antijet mode as the first time-dependent instabilities of stationary Taylor vortex flow depicted for the 12-vortex flow. The Antijet mode corresponds to an oscillation of the inward flow and is considered in [25]. The onset of the Large-jet mode which is depicted as well leads to a doubly periodic flow that consists of two non-axisymmetric modes. The axisymmetric time-dependent modes have disappeared. Below $\Gamma/N = 0.89$ the Large-jet mode appears in every vortex pair except of the end vortex pairs. The flow is symmetric with respect

to reflections on the midplane. However, for $\Gamma/N > 0.89$ the Large-jet mode does not occur in every vortex pair, but axially localised only in some. This corresponds to a symmetry-breaking leading to two asymmetric branches. We always observed both states with axially localised oscillations which are symmetric to each other. The flow states considered in this work appear for $\Gamma/N \geq 0.92$ which correspond to point c) in Fig. 9. The flow profiles are shown in Fig. 9 (b). They are obtained by a quasistatically shift of the measurement volume of the LDV through the cylinder while recording the axial velocity component at a fixed distance from the inner cylinder. The position of the localised Large-jet oscillation in the middle of the cylinder is clearly visible. We use a binary code for describing the different states with axially localised oscillations. ${}^{12}LJ_4$ means e.g. that in the 12-vortex state the Large-jet mode oscillates in third vortex pair counted from the bottom (${}^{12}LJ_{000100}$). This approach is very useful especially for larger systems where many different states having localised oscillations could been observed [43]. The lower stability boundary of the two states ${}^{12}LJ_{4,8}$ can be found in Fig. 9 (a). The arrows indicate a hysteresis and above point a) a transition to the 10-vortex state occurs. Point b) in Fig. 9 indicates the region where a VLF mode have been observed which was only in the small interval $0.9 \leq \Gamma/N \leq 0.91$.

4.2 Onset of VLF mode and transition to chaos

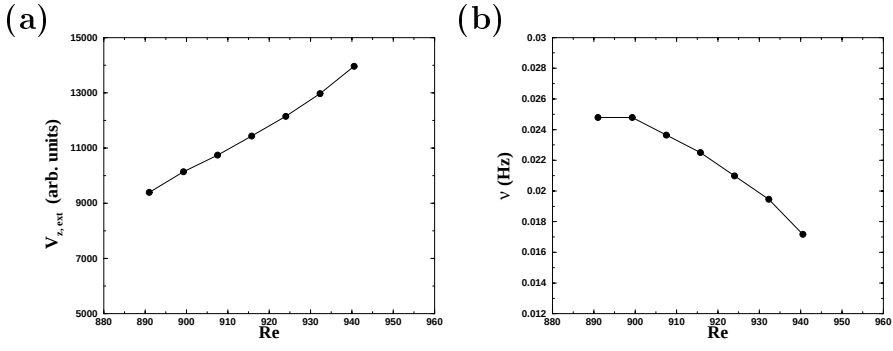

Fig. 10. (a) Amplitude of the VLF oscillation vs. Reynolds number measured in ${}^{12}LJ_4$ at $\Gamma/N = 0.9$. The VLF mode appears at $Re = 940.5$ while reducing Re with a large amplitude. (b): Oscillation frequency of VLF mode vs. Reynolds number

The VLF mode appears in ${}^{12}LJ_{4,8}$ while reducing the Reynolds number within this interval. Fig. 10 shows the amplitude and oscillation frequency ω of the VLF mode measured in ${}^{12}LJ_4$ at $\Gamma/N = 0.9$. The VLF oscillation appears with a large amplitude and a very low frequency that increases if the distance to the critical point increases. We observed no hysteresis. This indicates an inverse

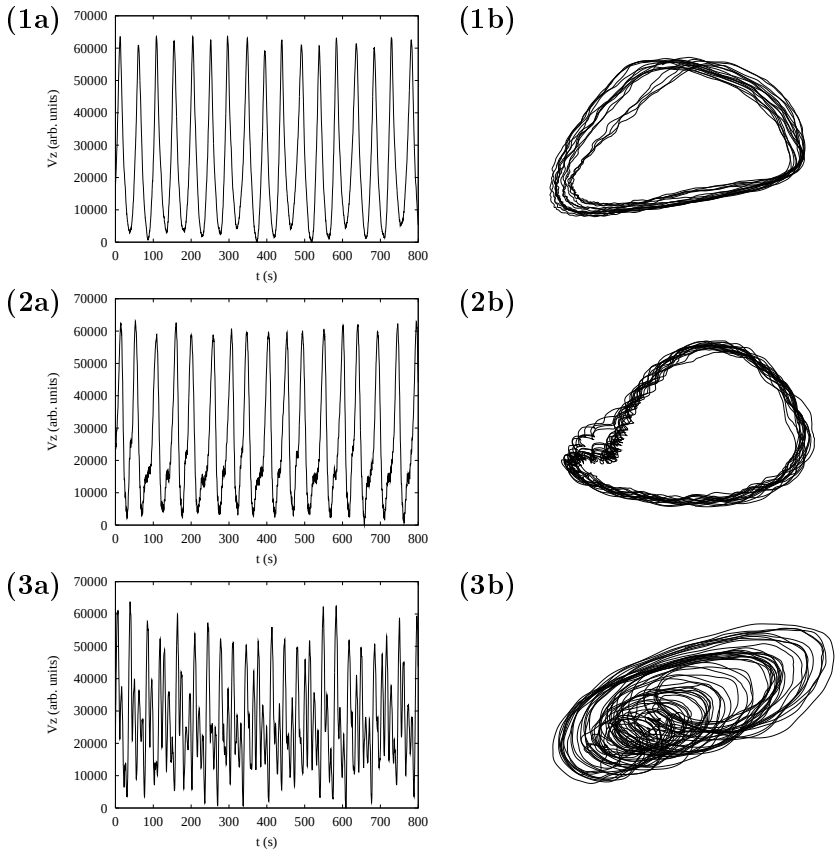

Fig. 11. Transition to chaos in VLF regime of ${}^{12}LJ_4$ in the 12-vortex state at $\Gamma/N = 0.9$. (a) Time series and (b) reconstructed attractors of (1, $Re = 924$) periodic, (2, $Re = 866.2$) slightly irregular, and (3, $Re = 849.8$) chaotic VLF mode are depicted.

homoclinic bifurcation like the onset of the VLF mode in the Small-jet regime though the indication are not so striking. The dynamics evolves in the VLF regime of ${}^{12}LJ_4$ on a T^3-torus of Small-jet, Large-jet, and VLF mode. Fig. 11 shows a scenario for the break-up of the T^3-torus while approaching the lower stability boundary of ${}^{12}LJ_4$ at $\Gamma/N = 0.9$. Again only the 'slow' VLF mode is shown and the 'fast' Small-jet and Large-jet oscillations are filtered out. The periodic times series (1a) is recorded at $Re = 924$. The small irregularities found in the time series are probably not due to any dynamical effect but caused by experimental inaccuracies. It should be kept in mind that the amplitude of the VLF mode is much smaller then the amplitude of Small-jet and Large-Jet oscillations. The dynamics at $Re = 866.2$ (Fig. 11.2a,b) corresponds still to the same periodic regime but the dynamics is more irregular. The periodic orbit seems to approach a fixed point (Fig. 11, 2b). At $Re = 849.8$ we observed a chaotic

dynamics of the VLF mode that is shown in Fig. 11 (3a,b). The transition from the periodic to the chaotic state correspond to a break-up of a stable T^3-torus. A further decrease of Reynolds number leads to a transition to flow state with a different axial distribution of Large-jet mode oscillations.

5 Discussion

We reported on an experimental investigation of the dynamics of the 'very-low-frequency' mode in the Small-jet regime of Taylor vortex flow for $\eta = 0.5$. The 'universal' sequence of states recently observed in this regime [26] is found to be modified if the number of vortices is reduced. For a flow having twelve vortices the symmetry-breaking occuring at lower Reynolds number is found to be crucial for the onset of chaos in the VLF regime. The two asymmetric branches merge at the onset of chaos leading to a 'symmetric' chaotic attractor that restores the original Z_2-symmetry of the system for a wide range of aspect ratio. The transition to chaos is accompanied with an intermittent behaviour in contrast to the period-doubling cascade found in system having 14 or more vortices. Though the intermittency scenario could not be related to one of the known types there is strong evidence that it caused by a local bifurcation of the VLF mode rather than a global event associated with the complete phase space of Taylor–Couette flow. However, we found evidences that global events occur in the reduced phase space related to the axisymmetric behaviour of the wavy Taylor vortex flow which we have dealt with exclusively in this work. We observed a Shil'nikov-type attractor associated with the unstable symmetric fixed point. Though a complete description of the scenario is not available it has become apparent that ideas from low-dimensional dynamical system are helpful and applicable to describe the behaviour of a fluid flow for large aspect ratio and higher Reynolds number. The observations of the two new VLF regimes stresses the crucial role of the VLF mode for the dynamical organisation of wavy and modulated wavy Taylor vortex flow at $\eta = 0.5$.

References

1. M.C.Cross, P.C.Hohenberg: Rev.Mod.Phys. **65**, 851 (1993)
2. E.L.Koschmieder: Bénard Cells and Taylor Vortices, Cambridge UP (1993)
3. R.Tagg: Non.Sci.Today **4**, 1 (1994)
4. J.Abshagen, A.Schulz, G.Pfister: in J.Parisi, S.C.Müller, W.Zimmermann (Eds.): Nonlinear Physics of Complex Systems, Lec.Notes Phys. **476**, Springer (1996)
5. F.H.Busse, G.Pfister, D.Schwabe: in F.H.Busse,S.C.Müller (Eds.): Evolution of Spontaneous Structures in Dissipative Continuous Systems, Lec.Notes Phys., **m55**, Springer (1998)
6. T.B. Benjamin: Proc. R. Soc. (London) **359** (1978)
7. T.Mullin: J.Fluid Mech. **121**, 207 (1982)
8. J.P.Gollub, H.L.Swinney: Phys.Rev.Lett **35**, 927 (1975)
9. P.R.Fenstermacher, H.L.Swinney, J.P.Gollub: J.Fluid Mech.**94**, 103 (1979)

10. A. Brandstäter, J.Swift, H.L.Swinney, A.Wolf, J.D.Farmer, E.Jen, P.C.Crutchfield: Phys.Rev.Lett **51**, 1442 (1983)
11. A. Brandstäter, H.L.Swinney: Phys.Rev A **35**, 2207 (1987)
12. G.Pfister, H.Schmidt, K.A.Cliffe, T.Mullin: J. Fluid Mech. **191**, 1 (1988)
13. G.Pfister: in G.E.A.Meier, F.Obermeier (Eds.): Flow of Real Fluids, Lec.Notes Phys. **235**, Springer (1985)
14. Th.Buzug, J.von Stamm, G.Pfister: Phys.Rev.E **47**, 1054 (1993)
15. G.Pfister, A.Schulz, B.Lensch: Eur.J.Mech. B/Fluids **10**,247 (1991)
16. T.Mullin, K.A.Cliffe, G.Pfister: Phys.Rev.Lett. **58**, 2212 (1987)
17. T.Mullin, T.J.Price: Nature **54**, 294(1989)
18. T.J.Price, T.Mullin: Physica D **48** (1991) 29-52
19. T.Mullin, J.J.Kobine: in P.T.Aston (Ed.): Nonlinear Mathematics and its applications, Cambridge UP (1996)
20. Th.Buzug, T.Reimers, G.Pfister: Europhys. Lett. **13**, 605 (1990)
21. Th.Buzug, G.Pfister: Phys.Rev.A **45**, 7073 (1992)
22. Th Buzug, G.Pfister: Physica D **58**, 127 (1992)
23. N.Enge, Th.Buzug, G.Pfister: Phys.Lett.A **175**, 178 (1994)
24. J.von Stamm, Th.Buzug, G.Pfister: Phys.Lett.A **194**, 173 (1994)
25. U.Gerdts, J.von Stamm, Th.Buzug, G.Pfister: Phys.Rev.E **49**, 4019(1994)
26. J.von Stamm, U.Gerdts, Th.Buzug, G.Pfister: Phys.Rev.E **54**, 4938(1996)
27. J.Abshagen, G.Pfister: in preparation
28. A.Arneodo, P.Coullet, C.Tresser: J.Stat.Phys. **27**, 171 (1982)
29. P.Glendinning, C.Sparrow: J.Stat.Phys. **35**, 645 (1984)
30. P.Gaspard, R.Kapral, G.Nicolis: J.Stat.Phys. **35**, 697 (1984)
31. C.Sparrow: "The Lorenz equation", AMS **41**
32. P.Chossat, M.Golubitsky: Physica D **32**, 423 (1988)
33. M.Dellnitz, M.Golubitsky, I.Melbourne: in E.Allgower, K.Böhmer, M.Golubitsky (Eds.): Bifurcation and Symmetry, Birkhäuser (1992)
34. Y.Pomeau, P.Manneville: Com.Math.Phys. **74**, 189 (1980)
35. J.E.Hirsch, B.A.Huberman, D.J.Scalapino: Phys.Rev.A **25**, 319 (1982)
36. P.Bergé, Y.Pomeau, C.Vidal: Order within chaos, Wiley (1984)
37. P.Bergé, M.Dubois, P.Manneville, Y.Pomeau: J.Physique-Lett. **41**, L341 (1980)
38. Chil-Min Kim, O.J.Kwon, Eok-Kyun Lee, Hoyun Lee: Phys.Rev.Lett **73**, 525 (1994)
39. M.O.Kim, Hoyun Lee, Chil-Min Kim, Hoyun-Soo Pang, Eok-Kyun Lee, O.J.Kwon: Int.J.Bif.Chaos **7**, 831 (1997)
40. M.Bauer, S.Habib, D.R.He, W.Martienssen: Phy.Rev.Lett **68**, 1625 (1992)
41. Pfister: in Proc. 4th Int. Conf. on Photon Correlation Techniques in Fluid Mech., Stanford CA (1980)
42. G.W.Baxter, C.D.Andereck: Phys.Rev.Lett. **57**, 3046 (1986)
43. J.Abshagen, A.Schulz, J.von Stamm, U.Gries, G.Pfister: in preparation

Spatiotemporal intermittency in Taylor–Dean and Couette–Taylor systems

Innocent Mutabazi[1], Afshin Goharzadeh[1] and Patrice Laure[2]

[1] Laboratoire de Mécanique, Université du Havre,
25, rue Philippe Lebon, B.P. 540, 76058 Le Havre Cedex, France
[2] Institut-Non Linéaire de Nice, UMR 129 CNRS-Université de Nice,
1361, route des Lucioles, 06560 Valbonne, France

Abstract. Spatiotemporal intermittency manifests itself by the coexistence of laminar and turbulent domains for the same value of the control parameter. In the Taylor-Dean system, the distributions of laminar domains size after algebraic and exponential regimes allow for a determination of critical properties in an analogy with directed percolation. In the Couette-Taylor system, only algebraic distribution of laminar domains size has been evidenced. A turbulent spiral coexists with laminar spiral destroying the occurrence of exponential regime.

1 Introduction

The spatiotemporal intermittency (STI) represents a special scenario of transition to turbulence in extended systems: it is characterized by the coexistence of laminar (ordered) and turbulent (disordered) domains that occur randomly in different places of the system for the same values of the control parameters [1]. The intermittency occurs in many hydrodynamic systems: it has been observed in boundary layer flows [2], in plane Poiseuille flow [3], in plane Couette flow [4–6], in pipe flow [7], in counter-rotating Couette flow [8,9], in the Taylor-Dean system [10]. In one-dimensional extended systems, spatiotemporal intermittency has been observed in rectangular and annular Rayleigh-Bénard cells at large values of the Rayleigh number [11,12], in the electromagnetically induced line vortices [13] and in the film flow between eccentric cylinders (so called *printer instability* experiment) [14]. The spatiotemporal intermittency has also been evidenced in numerical simulations of discrete systems such as coupled map lattices [15] or probabilistic cellular automata [16] and of nonlinear partial differential equations such as damped Kuramoto-Sivashinsky equation [17] or Ginzburg-Landau equation [18–20]. The spatiotemporal intermittency occurs via a subcritical bifurcation from purely laminar state and the coexistence of two different stable states can be described phenomenologically using an amplitude equation derived from a Lyapunov functional [21]. The large interest of the spatiotemporal intermittency was risen by Pomeau's conjecture [21] which states the existence of a striking analogy of STI with the directed percolation: turbulent bursts correspond to active or contaminating phase and laminar zone to passive or absorbing phase. This analogy suggests the existence of a second-order phase transition from laminar to turbulent regime with well defined critical

C. Egbers and G. Pfister (Eds.): LNP 549, pp. 102–117, 2000.

properties: in particular, there must exist a net threshold below which turbulent patches decay in time and above which they invade the laminar domains. Recent experimental and numerical studies have reported the main features of the spatiotemporal intermittency, such as the spontaneous nucleation of the turbulent bursts when the number of laminar domains of a given size decay algebraically and the contamination phase in which the number of laminar domains of a given size decay exponentially. However, contrary to the direct percolation which has universal critical properties, the spatiotemporal intermittency does not bear a universal character in the sense that the critical exponents differ from an experiment to another[1,22]. The non universality of STI is related to differences between laminar phases in the different systems [22].

In this paper, after a brief review of the Pomeau model of STI, we will illustrate the properties of spatiotemporal intermittency, and in particulary its non universality character, with help of experimental systems in which centrifugal instability induces the primary roll pattern. In the Taylor-Dean system, we will show that the analogy with directed percolation works quite well, while in the Couette-Taylor system, there is no similarity with the directed percolation. In fact, the spatiotemporal intermittency observed in the Couette-Taylor system reveals special features : for small values of the control parameter, turbulent bursts (Fig.1-a) occur erratically in time and space in the laminar phase of interpenetrating spiral, while for a finite range of large values of the control parameter, turbulent spiral (Fig.1-b) coexists with a spiral of laminar base flow [8,9]. The transition to turbulent bursts from interpenetrating spiral pattern has been investigated numerically by Coughlin and Marcus [23] and experimentally by Colovas and Andereck [24] who have measured their turbulent fraction and the statistical properties of laminar domains as function of the control parameter. The latter noticed the lack of a region of exponential decay of laminar domains length which would correspond to the supercritical transition analogous to the contamination phase of the directed percolation. In fact, above a given value of the control parameter, the turbulent bursts connect each other to form a turbulent spiral. The resulting flow state called *spiral turbulence* is characterized by coexistence of stable turbulent and laminar spirals for finite range of the control parameter. Hegseth et *al.* [25] have investigated experimentally the kinematics of a turbulent spiral and explained some of its properties (pitch and azimuthal velocity) using a phase dynamics equation. Later on, Hayot and Pomeau [26] explained the stabilization of turbulent spiral together with a laminar one using the quintic Ginzburg-Landau equation in which they included a nonlocal term that serves to prevent the expansion of the turbulent domain.

2 Pomeau model of spatiotemporal intermittency

The spatiotemporal intermittency is a special form of the manifestation of weak turbulence in extended systems: it consists of a space-time fluctuating mixture of coherent laminar domains and disordered turbulent bursts in the flow for the

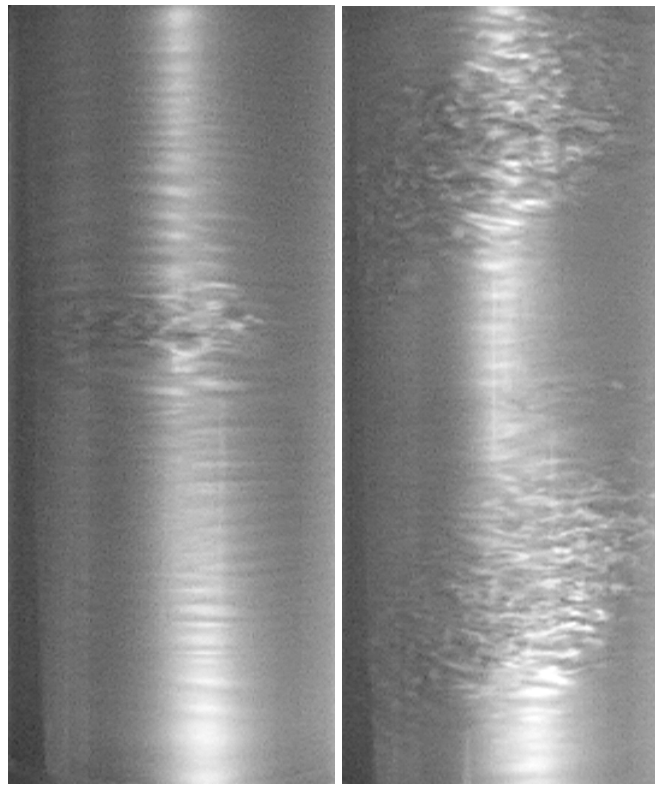

a) b)

Fig. 1. Pictures of intermittent states in the Couette-Taylor system: a) Turbulent burst spontaneously nucleated in the interpenetrating spiral ($R_o = -1420$, $R_i = 550$), b) Spiral turbulence ($R_o = -1482$, $R_i = 650$)

same values of the control parameters. Pomeau, in his seminal paper [21], conjectured the analogy of spatiotemporal intermittency with directed percolation, giving this way to STI a more strict sense [1]. Spatiotemporal intermittency in the strict sense, implies a strong asymmetry between two local states in extended systems: disordered turbulent state can spontaneously decay to regular laminar state because of intrinsic fluctuations, while laminar state cannot decay spontaneously, it can only be triggered by neighboring turbulent domains.

2.1 Analogy with the directed percolation

The directed percolation can be realized in probabilistic cellular automaton which models various contamination processes [16]: it iterates synchronously at discrete time steps, the sites of a lattice according to transition probabilities which depend on the configuration of the sites neighborhood. Each site is on one of two possible states: an active state or an absorbing state. In case of directed

bond percolation in one space dimension, the control parameter is the probability p for a bond to be open. The density d of active sites in directed percolation is given by

$$d \begin{cases} = 0 & \text{if } p < p_c \\ \sim (p - p_c)^{\beta} & \text{if } p > p_c \end{cases} \tag{1}$$

where p_c is the threshold and $\beta = 0.277$ is the critical exponent of the directed percolation in one dimension [1]. The absorbing state corresponds to the laminar part of the flow and the active state to the disordered turbulent bursts. The transition from the regular laminar domains to turbulent patches might have the same critical behaviour as the directed percolation. The turbulent fraction that is the analog of the probability for an open bond must vanish continuously when approaching the threshold of spatiotemporal intermittency as does the density d of active sites in directed bond percolation. The transition to spatiotemporal intermittency should then be a second-order phase transition: below a critical value of the control parameter, turbulent bursts are transient and decay in the laminar phase and above the critical value, the turbulent domains become active and contaminate the flow.

In order to achieve such a comparison, it is necessary to make a binary reduction of the space-time diagrams with an artificial cutoff [4,10]: turbulent domains are represented by black pixel and laminar domains by white pixel. One defines the turbulent fraction f as the ratio of the total area of turbulent patches to the total area of the space-time diagram. The temporal turbulent fraction called also *intermittency factor* is defined as the ratio of the mean duration of turbulent patches to the total measurement time.

¿From binarized space-time diagrams, one can also compute the histograms of distribution of laminar domains with their size $N(l)$ or with their duration $N(t)$. If the $N(l) \sim l^{-\gamma}$ or $N(t) \sim t^{-\gamma'}$, we have algebraic decay of laminar domains, if $N(l) \sim e^{-l/\lambda}$ or $N(t) \sim e^{-l/\tau}$, we have exponential decay of laminar domains. In the latter case, it is possible to define a coherence length λ or a coherence time τ. These quantities can be obtained also from the correlation function $C(x)$ or $C(t)$ of the space-time signal I(t,x):

$$C(x) = \frac{< I(t, x' + x) I(t, x') >}{< I(t, x')^2 >} \quad or \quad C(t) = \frac{< I(t' + t) I(t', x') >}{< I(t', x')^2 >}$$

The correlation length λ and correlation time τ are obtained from the best fit of these correlation functions to exponential functions as follows: $C(x) \sim e^{-x/\lambda}$ or $C(t) \sim e^{-t/\tau}$. The transition between algebraic and exponential regimes of laminar size histograms occurs at a critical value μ_c of the control parameter, this value is taken as the threshold of spatiotemporal intermittency in the strict sense [1]. Since the scales of laminar domains become small and those of turbulent domains increases, the coherence length of the laminar domains might have critical behavior near the onset of the spatiotemporal intermittency, i.e. $\lambda \sim |\mu_c - \mu|^{-\alpha}$, where α is a critical exponent.

2.2 Ginzburg–Landau amplitude equation

Spatiotemporal intermittency can be considered as the hydrodynamic (no thermal fluctuations) partner of the first-order transitions in thermodynamics with a two-phase state existing for the same value of the temperature (for example a liquid-gas transition in Van der Waals fluids). In fact, one of two phases of the STI is metastable while the other is stable, the stability depends on the control parameter μ, the analog of the temperature in equilibrium thermodynamic systems. The main properties of spatiotemporal intermittency can be retrieved from a fifth order real Ginzburg-Landau equation [26]:

$$\frac{\partial A}{\partial t} = \mu A + \beta |A|^2 A - \delta |A|^4 A + \xi_0^2 \frac{\partial^2 A}{\partial x^2} = -\frac{\delta V}{\delta A^*} + \xi_0^2 \frac{\partial^2 A}{\partial x^2} \tag{2}$$

where A is the amplitude of the perturbations and A^* its complex conjugate, μ is the distance from the onset of the turbulence (i.e. $\mu < 0$ in the laminar regime and $\mu > 0$ in the completely turbulent state), ξ_0^2 is a characteristic coherence length of the perturbations, the Landau nonlinear constants β and δ are positive in order to ensure nonlinear saturation of the amplitude at the fifth order of expansion. To evidence the analogy with thermodynamics, the equation (2) is represented in variational form: the quantity $V[A, A^*]$ called *Lyapunov functional* is the analog of a thermodynamic potential such as the free energy. In order to describe the spatiotemporal intermittency, the "potential" V may have two minima corresponding to stable and metastable states in a given range of the control parameter. From the above amplitude equation, $V[A, A^*]$ is obtained by straightforward integration and reads:

$$V[A, A^*] = \frac{\delta}{6}|A|^6 - \frac{\beta}{4}|A|^4 - \frac{\mu}{2}|A|^2 \tag{3}$$

This potential has two minima corresponding to stationary states in the range: $\mu_0 = -\beta^2/4\delta < \mu < 0$. The laminar phase is given by $A = 0$ and the turbulent phase corresponds to a finite amplitude perturbation $A \neq 0$. The two minima acquire the same value for $\mu_c = -3\beta^2/16\delta = 3\mu_0/4$. For this value of the control parameter, turbulent and laminar phases have the same stability and can coexist in the flow system for the same value of the control parameter. When the two minima are different, one phase called *active* or *stable* phase invades the other one which is *metastable*: for $\mu_0 \preceq \mu < \mu_c$, the laminar phase $A = 0$ is stable and the turbulent bursts are metastable, they decay after a transient time. For $\mu_c \preceq \mu < 0$, the laminar phase is metastable and decay into the turbulent stable phase. The critical value μ_c of the control parameter separates therefore two different domains of stability and can be considered as the onset of spatiotemporal intermittency similar to the onset of directed percolation (p_c). Stationary amplitudes corresponding to the minima of the potential are given by:

$$A_s = \begin{cases} 0, & \text{for laminar phase} \\ \frac{\beta + \sqrt{\beta^2 + 4\mu\delta}}{2\delta} & \text{for turbulent phase} \end{cases} \tag{4}$$

The complex counterpart of the equation (3) was investigated in detail by Hakim-Pomeau who have shown that fifth order complex Ginzburg-Landau equation possess stable solutions describing stable localized states in extended systems [27].

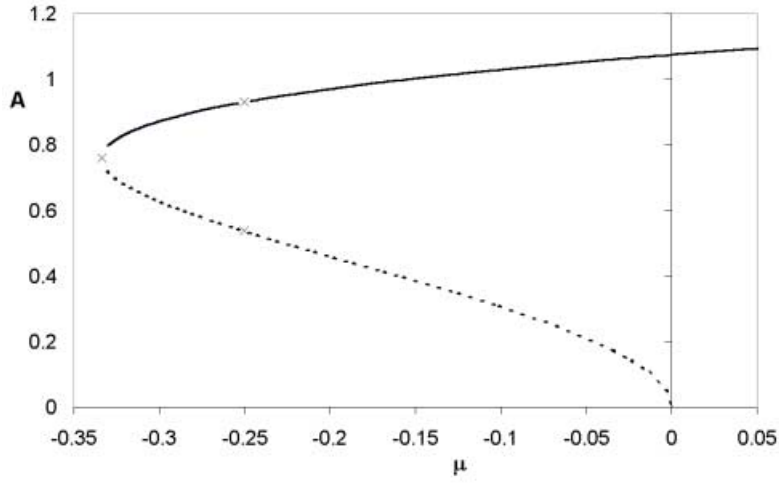

Fig. 2. The stationary amplitude as a function of the control parameter μ for $\beta = 1.15$ and $\delta = 1$. Solid lines represent the stable and metastable states, dashed line represents unstable state. The laminar state ($A = 0$) and the turbulent state ($A \neq 0$) coexist for $-0.33 < \mu < 0$. The threshold of STI in the strict sense occurs at $\mu_c = -0.24$

3 STI in the Taylor–Dean system

We illustrate the main ingredients of Pomeau model with results obtained in the Taylor-Dean system. The latter consists of two coaxial horizontal cylinders in differential rotation, with a partially filled gap [28]. Spatiotemporal intermittency has been observed in this system when the inner cylinder is fixed and only the outer cylinder is rotating [10]. The control parameter is the outer cylinder Reynolds number defined as follows: $R_o = \Omega_o bd/\nu$, where Ω_0 is the rotation angular velocity, $b = 5.08\,cm$ is the outer cylinder radius, $d = 0.590\,cm$ is the gap between the cylinders and ν is the kinematic viscosity.

3.1 Main results on critical properties

We summarize the main results obtained in this system since they reproduce the main properties of STI developed above. The laminar state consists of a roll pattern oscillating with 2 frequencies. This pattern exhibits a continuous nucleation of spatiotemporal defects which reduce its correlation length and

induce locally a chaotic behavior that generate transient turbulent bursts. The STI was observed in the range of the control parameter $R_o \in]649, 769[$. The increase of the control parameter R_o leads to the coexistence of spatially ordered oscillating roll pattern with turbulent bursts which appear irregularly in time at different positions of the flow (Fig. 3-a, b). The turbulent fraction increases with the control parameter R_o following the law $f(R_o) \sim \varepsilon^{\beta}, \beta = 1.30 \pm 0.26$ where $\epsilon = (R_o - R_o^*)/R_o^*$ where $R_o^* = 649$ is the onset of turbulent bursts. Statistical analysis was made on data files consisting of 5000 frames of total duration of 12 minutes. Analyzing the distribution of laminar domains with their length, we have distinguished two different regimes: for $R_o < R_{o,c} = 675$, the number N of domains having a length l is given by $N(l) \sim l^{-\gamma}$ with $\gamma = 1.7 \pm 0.1$(Fig. 4-a) , this regime is called *algebraic regime*; for $R_o > R_{o,c} = 675$, the number of laminar domains of size l is given by $N(l) \sim e^{-l/\lambda}$ (Fig.4-b) where the characteristic length of laminar domains λ decreases with the control parameter as follows: $\lambda(R_o) \sim (R_o - R_{o,c})^{-\alpha}$ with $\alpha = 0.64$. Therefore, this value $R_{o,c}$ of the control parameter which separates algebraic and exponential regimes of the distribution of laminar domains versus their length, is considered as the threshold of a second-order type transition [10]. Hence, the spatiotemporal intermittency in the Taylor-Dean system is defined in the strict sense i.e. in the analogy with the directed percolation. Below $R_{o,c}$, turbulent bursts decay in the laminar pattern and above $R_{o,c}$, turbulent bursts contaminate the laminar pattern. It corresponds to the value $\mu_c \simeq 0.122$ in the Pomeau model, while the onset of turbulent bursts $R_o = 649$ corresponds to $\mu_0 \simeq -0.156$.

3.2 STI in other extended systems

There are different experimental extended systems in which the two different regimes of spatiotemporal intermittency have been observed and well characterized, for example: the Rayleigh-Bénard convection in rectangular and annular cells [11,12], the linear vortices induced by electromagnetic field [13] and the printer instability experiment [14]. All these systems enter into the framework of the Pomeau model although measured critical exponents are different from an experiment to another. The existence of different critical exponents in hydrodynamic experiments (Table 1) illustrates the non universality of the spatiotemporal intermittency.

Table 1. Critical exponents measured from few experiments

Experimental System	β	γ	α
Convection in chanel [12]	0.30±0.05	1.6±0.2	0.50
Printer instability [14]	0.45±0.05	0.63±0.02	0.50
Taylor-Dean system [10]	1.30±0.26	1.67±0.14	0.64
Line of Vortices [13]	0.50	1.7	0.5

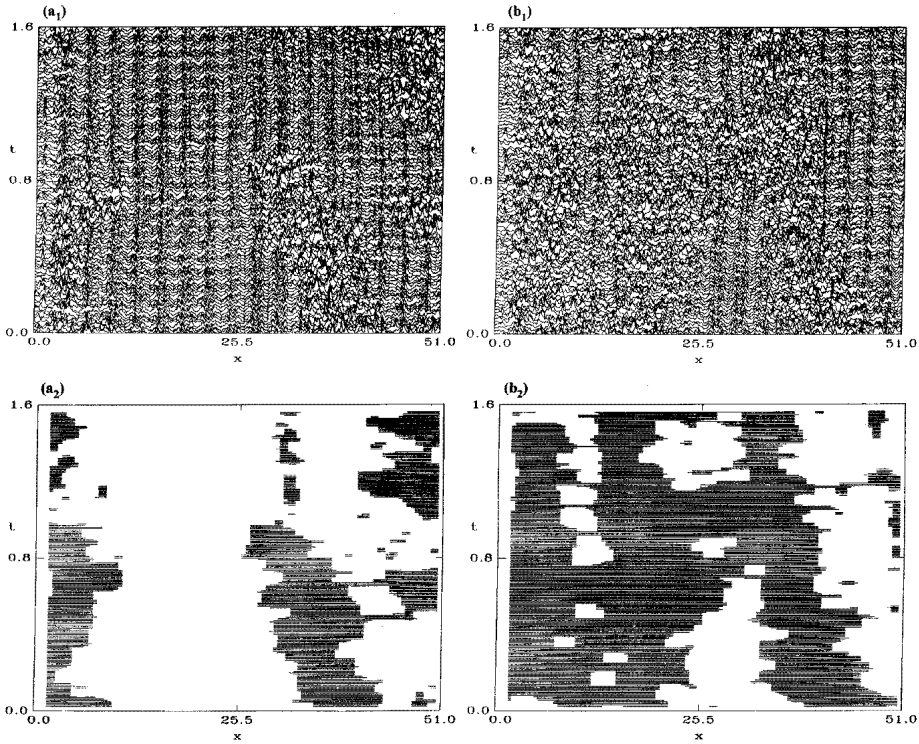

Fig. 3. Space-time diagrams of the pattern observed in the Taylor-Dean system and binarized versions: a) $R_o = 669$: turbulent bursts are metastable in the laminar phase, b) $R_o = 683$: turbulent bursts are active in a metastable laminar phase.

4 STI in the Couette–Taylor system

The intermittent states in the Couette-Taylor were observed by D. Coles [8] and C.D. Andereck et *al.* [9] who mapped them into a phase diagram (R_o, R_i). The spatiotemporal intermittency in the Couette-Taylor system is of particular interest since it does not enter into the Pomeau model described above. In fact, as shown by Colovas and Andereck [24] from analysis of histograms distribution of laminar domain size, STI in the Couette-Taylor system has no exponential regime. This is due to the existence of the spiral turbulence regime in which a stable turbulent spiral coexists with a laminar one. We describe in this section some of properties of STI obtained in the counter-rotating Couette-Taylor system.

4.1 Experimental setup

The Couette-Taylor system consists of two coaxial horizontal counter-rotating cylinders in the gap of which flows a newtonian liquid. The inner cylinder is

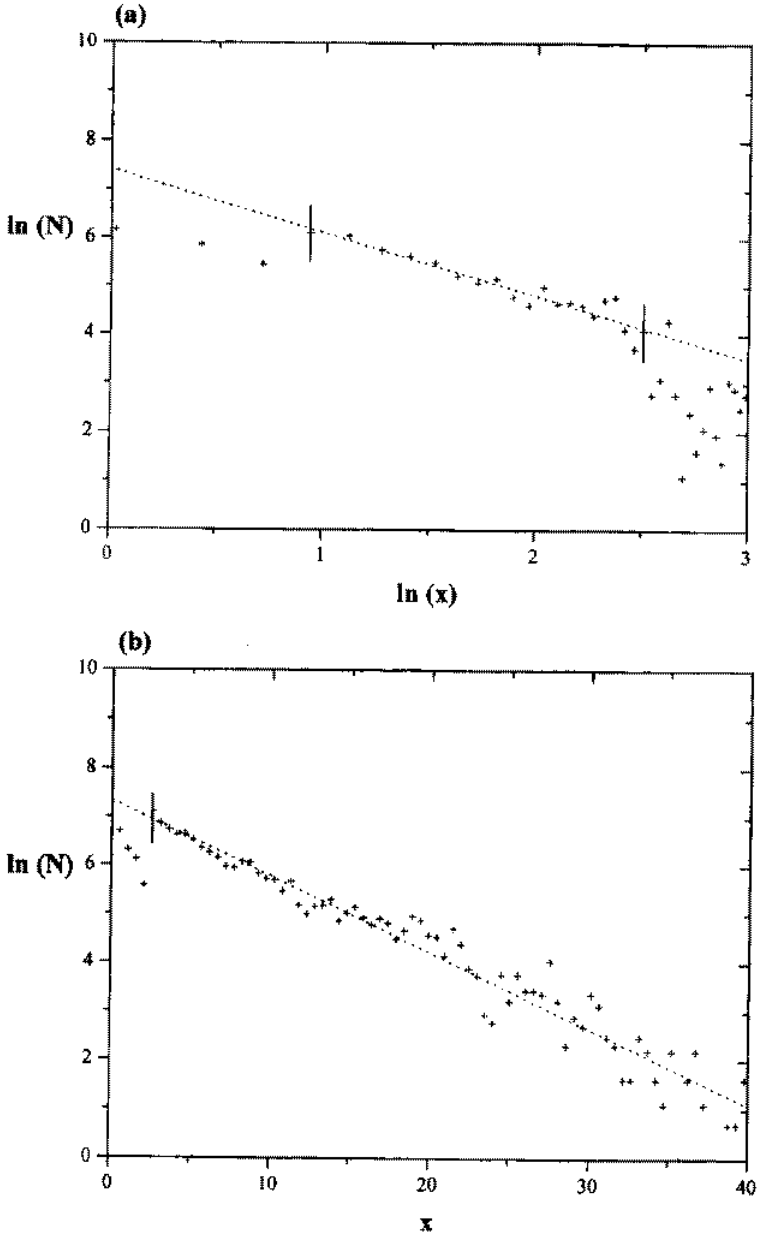

Fig. 4. Distribution of the laminar domains with their size: a) algebraic decay ($R_o = 664$), b) exponential decay ($R_o = 675$).

made of black Delrin with a radius $a = 4.459\,\text{cm}$. The outer cylinder is made of transparent plexiglass with a radius $b = 5.050\,\text{cm}$. The gap between the cylinders is $d = b - a = 0.591\,\text{cm}$ over a length $L = 27.5\,\text{cm}$. Hence the system has a radius ratio $\eta = a/b = 0.88$, and an aspect ratio $\Gamma = L/d = 46$. The both cylinders are driven independently in opposite direction by two DC servomotor. Thus the control parameters of the Couette-Taylor system are the Reynolds numbers defined for the inner and outer cylinders respectively: $R_i = \Omega_i ad/\nu$ and $R_o = \Omega_o bd/\nu$, where Ω_i and Ω_o are angular frequencies of inner and outer cylinder respectively and ν the kinematic viscosity of the fluid. We have used distilled water ($\nu = 10^{-2}\text{cm}^2/\text{s}$ at $T = 21^0\text{C}$) with 2% Kalliroscope AQ1000 for visualization. With a light from a fluorescent tube, the flow was visualized on the front side. To obtain spatial information about the flow dynamics, a linear 1024-pixel charge coupled device (CCD) array records the intensity distribution I(x) of the light reflected by Kalliroscope flakes from a line along the axis at the middle of the cylinders. The recorded length is from 20 to 25 cm in the central part of the system, corresponding to a spatial resolution of 41 to 51 pixels /cm.

4.2 Results

We describe the weak turbulent states observed for outer cylinder rotation fixed at $R_o = -1375$ and increasing the inner cylinder rotation (Fig.5 a-d). The turbulent bursts occur as a result of subcritical bifurcation of the interpenetrating spirals to finite amplitude perturbations. They appear irregularly in time at different positions of the pattern. In the wake of a turbulent burst, there is no periodic structure of interpenetrating spirals. This disappearance of roll pattern in the wake of a burst is a consequence of a strong energy dissipation by the bursts. The generation of burst occurs, not in the wake of previous one, but either at the left or the right of this wake where the energy is less dissipated. A similar structureless wake has been observed in the turbulent spots occurring in boundary-layers [2].

The average number per unity time, the lifetime and the size of turbulent bursts increase with R_i. As R_i increases, the turbulent bursts acquire an axial velocity component, smaller than the azimuthal velocity component, and hence they are inclined with respect to the cylinder axis. When the length of a turbulent burst becomes comparable with the half circumference of the cylinder, the bursts connect to form a turbulent spiral (Fig. 5-c). The pattern is then composed of alternating turbulent and laminar spirals (Fig. 5-d). The laminar spiral has no periodic structure, it does not contain any interpenetrating spirals. The turbulent spiral and the laminar spiral coexist in the flow for a long time without cancelling each other. For very large values of R_i, the turbulent spiral spreads in width while the laminar spiral decays giving rise to completely turbulent flow.

The mean turbulent fraction of bursts increases with R_i (Fig.6) and is sensitive to the value of R_o in agreement with results obtained previously [24]. With an increase of R_i, the turbulent bursts occur more frequently and grow in size until they connect each other and form a turbulent spiral. The fraction of the

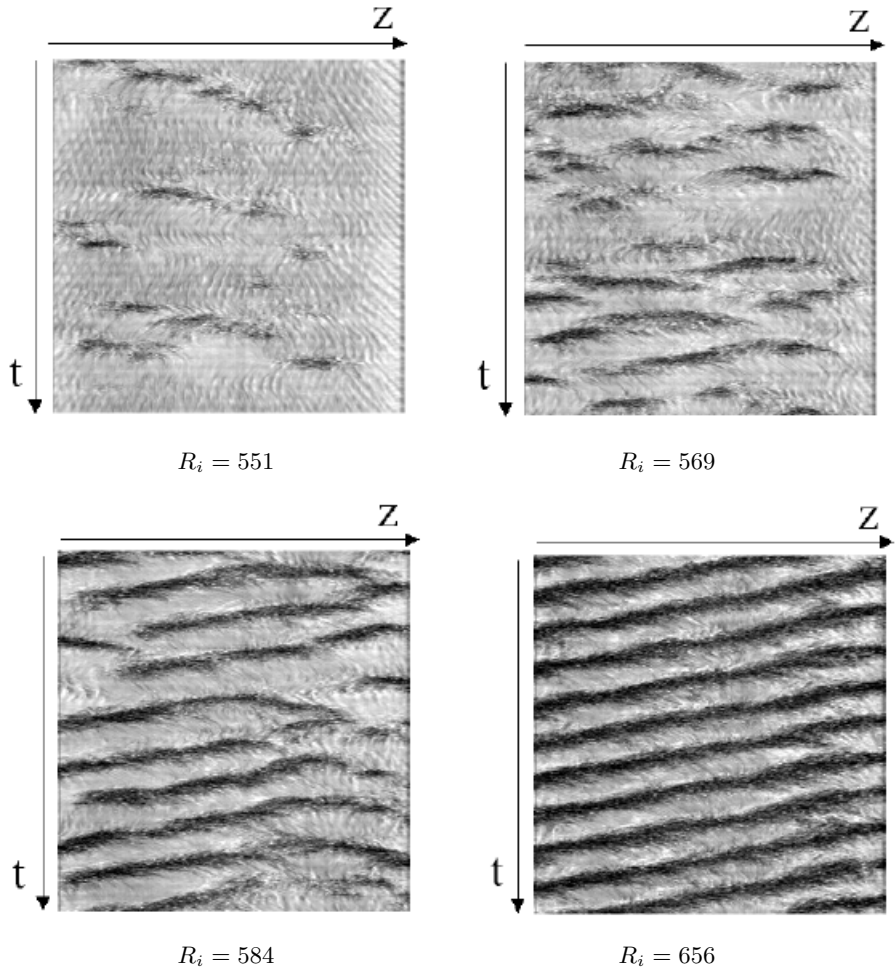

Fig. 5. Spatio-temporal diagram of representative states observed for $R_o = -1375$: a) Spontaneous nucleation of turbulent bursts in the laminar phase, b)Turbulent bursts occur frequently in the flow, c) Turbulent bursts are connecting to form a turbulent spiral, d) Laminar-turbulent spiral.

turbulent spiral is a linear function of R_i and is not sensitive to the variation of R_o.

4.3 Physical origin of turbulent bursts

The strong dependence of turbulent fraction on R_i suggests that the inner cylinder is more responsible than the outer cylinder for the energy transfer to the fluctuation that will dissipate it in the turbulent regime. This is due to the fact that the centrifugally unstable region is close to the inner cylinder. According to

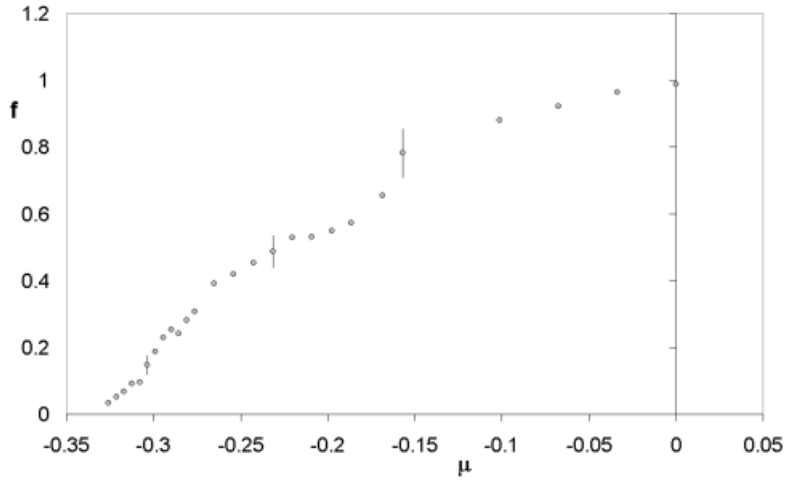

Fig. 6. Turbulent fraction in the Couette-Taylor system as a function of $\mu = (R_i - R_{i,c})/R_{i,c}$ for $R_o = -1375$.

numerical simulations of Coughlin and Marcus [23], the bursting phenomenon is governed by space distribution of energy transferred from the rotating cylinders to the pattern of interpenetrating spirals, i.e. to the laminar phase. The interpenetrating spirals (coherent structures) are destabilized by an azimuthal traveling wave (induced by a secondary instability). This azimuthal wave perturbs drastically the inner region which is dominated by the centrifugal instability and induces an explosive occurrence of turbulence that collapses after a short time. The nonlinear stability analysis of the interpenetrating spirals [29] shows that azimuthal and axial mean field velocities possess inflexion points. According to Rayleigh criterion for parallel flows [30], such a flow is unstable to time-dependent perturbations which may lead to the occurrence of transverse waves. The azimuthal waves, reported in the numerical simulations of Coughlin and Marcus might originate from the axial mean flow velocity and play important role in the generation of turbulent bursts. The inflexion point is located in the inner region whose extent depends on the inner rotation speed and that is the reason for a strong dependence of turbulent fraction upon R_i.

4.4 Kinematics of turbulent spiral

The lifetime of turbulent bursts increases with R_i, while the period of turbulent spirals does not depend on R_i. For a fixed R_o, the axial velocity of turbulent spiral does not vary significantly with R_i. The frequency of turbulent spirals increases with R_o while their lifetime decreases. The axial velocity of turbulent spiral increases with R_o (Fig. 7). The azimuthal velocity which is the same order as the axial velocity (Fig. 8) was deduced from measurement of the inclination angle of turbulent spiral also called *pitch angle* which was found to vary from

21° to 40°. The azimuthal velocity of the turbulent spiral is a linear function of R_o and does not depend on R_i in agreement with previous results [9].

,

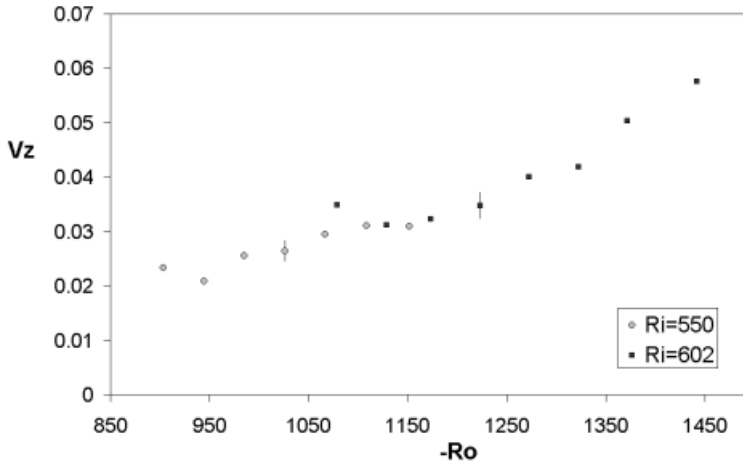

Fig. 7. Axial velocity of turbulent spirals in units of the diffusion velocity ν/d as a function of R_o.

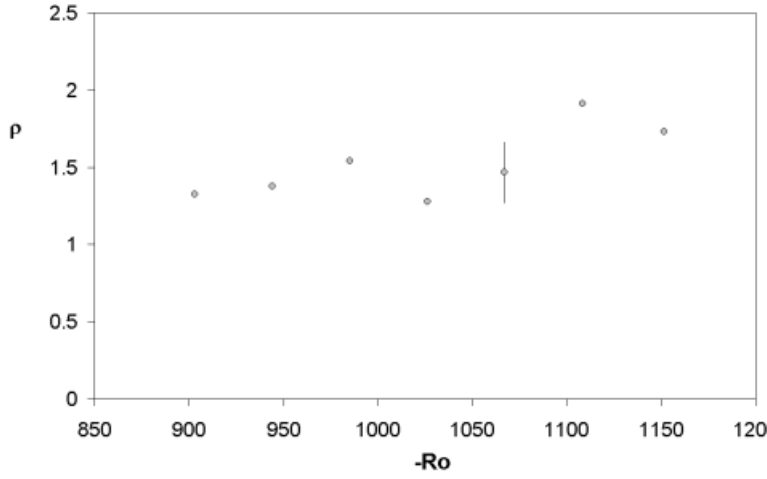

Fig. 8. Ratio ρ of the azimuthal velocity to the axial velocity of the turbulent spiral in the Couette-Taylor system.

We found that the axial velocity of turbulent spiral is a linear function of R_o but does not depend on R_i. This behavior may be explained if one considers that the turbulent and laminar spirals form a pattern with a selected wavelength and drifting at the same velocity. The period of the turbulent spiral increases with R_i while that of laminar spiral decreases keeping constant the mean period of the turbulent-laminar front. Therefore, the fraction of turbulent spirals increases with R_i but their axial velocity remains constant. For fixed R_i, the period of turbulent-laminar spirals increases and since its average size is constant, the axial velocity of spirals increases with R_o.

4.5 Hayot–Pomeau model for spiral turbulence

After Hayot and Pomeau [26], the existence of a mean azimuthal Poiseuille flow in the counter-rotating Couette-Taylor system [29,31] is the main key of the existence of stable turbulent spirals. In fact, this mean azimuthal velocity component is responsible for a regulatory mechanism of the turbulent and laminar domains size. In order to describe quantitatively this regulatory mechanism, Hayot and Pomeau introduced a nonlocal term due to this mean azimuthal velocity into the real fifth order Ginzburg-Landau (3) that then reads:

$$\frac{\partial A}{\partial t} = \mu A + \xi_0^2 \frac{\partial^2 A}{\partial x^2} + \beta(|A|^2 - I)A - \delta|A|^4 A \tag{5}$$

where the new term $I \sim \frac{1}{L}\int_0^L |A|^2 dx$ is the mean energy of the perturbation in the system where L is the length of the circumference [26]. In the experiments, the quantity I is related to the mean turbulent fraction. When the turbulent fraction increases, the perturbation amplitude decreases due to larger friction and the expansion of the turbulent domain is reduced. For $\mu_0 < \mu < \mu_c$, turbulent bursts are metastable and decay in the absorbing laminar phase, the turbulent fraction is very small and so is the nonlocal term I. The increase of the rotation rate of the inner cylinder is accompanied by a large transfer of energy to the flow, therefore it gives large contribution of the nonlocal term I. For $\mu \geq \mu_c$, the contribution to I reduces the value of the nonlinear coefficient β, and then μ_c decreases until the value of μ_0, reducing the local expansion of the burst. In numerical simulations of the equation (5), Hayot and Pomeau [26] have shown that for $\mu \geq \mu_c$, the expansion of turbulent domains saturates in time and in size leading to a stable turbulent spiral that coexists with a laminar spiral. A similar model using a pressure gradient of mean flow was developed by Stassinopoulos in order to describe periodic states of intermittency observed in pipe flows [32].

In order to describe the kinematics of the turbulent spiral observed in a system with an aspect ratio $\Gamma = 73$, Hegseth et *al.* [25] suggested a phase equation compatible with the symmetries of the problem:

$$\frac{\partial \phi}{\partial t} + v\frac{\partial \phi}{\partial x} = D\frac{\partial^2 \phi}{\partial x^2} \tag{6}$$

where ϕ is a phase describing the mean azimuthal position of the spiral at the height x and time t, D is a phase diffusion coefficient, v is the axial velocity of

spiral in the laboratory frame of reference. The phase ϕ is related to the pitch angle by $\partial\phi/\partial x$. The solution of this phase equation reads [25]

$$\phi(t,x) = A(x - vt) + Be^{vx/D}, A = Bv/D - \alpha, B = \frac{D}{v}\frac{\alpha - \beta}{1 - exp(vL/D)} \qquad (7)$$

where α and β are the pitch angle at the bottom and the top of the system. For asymmetric boundary conditions at the ends ($\alpha \neq \beta$), the pitch angle varies continuously between α and β. These boundary conditions are realized in most experiments with finite aspect ratio ([25,33]) and therefore the behavior of spiral turbulence is much influenced by the boundary conditions. In the case of symmetric boundary conditions at the ends ($\alpha = \beta$), then $B = 0$ and the phase equation is invariant under reflection symmetry and therefore can possess in particularly stable solutions of turbulent spirals of opposite helicity (i.e. propagating in opposite directions along the cylinder axis). Such symmetric boundary conditions at the ends can be achieved only in infinite aspect ratio system like that one has been built recently in CEA at Saclay ($\Gamma = 400$), in fact, in this case the ends effects are confined inside a layer of characteristic length D/v.

5 Conclusion

The spatiotemporal intermittency observed in most extended hydrodynamic systems exhibits critical properties analog to those of the directed percolation although no universality cannot be established because of differences in the laminar phase. We have illustrated these properties with the Taylor-Dean system in which it was possible to define the spatiotemporal intermittency in the strict sense. In the counter-rotating Couette-Taylor system, the mean azimuthal Poiseuille flow induces a stabilization of turbulent-laminar front and inhibits the exponential decay of laminar domains size. Therefore, in the Couette-Taylor system, the spatiotemporal intermittency has no analogy with directed percolation.

6 Acknowledgments

One of us (I.M.) would like to thank Ch. Normand and O. Dauchot for fruitful discussions on this subject during his visit in CEA at Saclay. A. Goharzadeh benefits from a MENRT scholarship.

References

1. P. Manneville, *Structures Dissipatives et turbulence*, ed. Alea-CEA Saclay (1991). See also H. Chaté and P. Manneville: 'Spatiotemporal intermittency', In: *Turbulence: a tentative dictionary*, ed. by P. Tabeling and O. Carodos, Plenum Press, N.Y. (1995), **341**, 111-116.
2. D.J. Tritton, *Physical Fluid Dynamics*, Oxford University press, Oxford (1989). see also G.B. Schubauer and P.S. Klebanoff, NACA TN-3489 (1955).

3. I.J. Wygnanski and F. Champagne, *J. Fluid Mech.* **59**, 281 (1973).
4. F. Daviaud, J.J. Hegseth, P. Bergé, *Phys.Rev. Lett.* **69**, 2511(1992).
5. O. Dauchot and F. Daviaud, Phys. Fluids **7**, 335 (1995). See also O. Dauchot and F. Daviaud, *Phys. Fluids* **7**, 901 (1995).
6. S. Bottin, O. Dauchot and F. Daviaud, *Phys. Rev. Lett.***79**, 4377(1997).
7. D. R. Carlson, S. E. Widnall and M.F. Peters, *J. Fluid Mech.***121**, 487 (1982). See also M. Nishioka and M. Asai, *J. Fluid Mech.* **150**, 441 (1985).
8. D Coles, *J. Fluid Mech.* **21**, 385 (1965). See also C. Van Atta, J. Fluid Mech **25**, 495 (1966).
9. C.D. Andereck, S.S. Liu and H.L. Swinney, *J. Fluid Mech.* **164**, 155 (1986).
10. M. Degen, I. Mutabazi and C.D. Andereck, *Phys. Rev. E* **53**, 3495 (1996).
11. S. Ciliberto and P. Bigazzi, *Phys. Rev. Lett.* **60**, 286 (1988).
12. F. Daviaud, M. Bonetti and M. Dubois, Phys. Rev. A **42**, 3388 (1990).
13. H. Willaime, O. Cardoso and P. Tabeling, *Phys. Rev. E* **48**, 288 (1993).
14. M. Rabaud, S. Michalland and Y. Couder, *Phys. Rev. Lett.* **64**, 184 (1990).
15. K. Kaneko, *Prog. Theo. Phys.* **74**, 1033 (1985).
16. H. Chate and P. Manneville, *Europhys. Lett.* **6**, 591 (1988). See also H. Chate and P. Manneville, *J. Stat. Phys.* **56**, 357 (1989).
17. H. Chate et P. Manneville, *Phys. Rev Lett.* **58**, 112 (1987).
18. F. Daviaud, J. Lega, P. Bergé, P. Coullet and M. Dubois, *Physica D* **55**, 287 (1992).
19. R.J. Deissler, *J. Stat. Phys.* **40**, 371 (1985).
20. H. Chate, *Nonlinearity* **7**, 185 (1994).
21. Y. Pomeau, *Physica D* **23**, 3 (1986).
22. P. Grassberger and T. Schreiber, *Physica D* **50**, 177 (1991).
23. K. Coughlin and P.S. Marcus, *Phys. Rev. Lett.* **77**, 2214 (1996).
24. P.W. Colovas et C.D. Andereck, *Phys. Rev. E* **55**, 2736 (1997).
25. J.J. Hegseth, C.D. Andereck, F. Hayot and Y. Pomeau, *Phys. Rev. Lett.* **62**, 257 (1989).
26. F. Hayot and Y. Pomeau, *Phys. Rev. E* **50**, 2019 (1994).
27. V. Hakim and Y. Pomeau, *Eur.J. Mech.B.***10** *Suppl.*, 131 (1991).
28. I. Mutabazi,J.J. Hegseth, C.D. Andereck and J. Wesfreid, *Phys. Rev. Lett.* **64**, 1729 (1990).
29. Y. Demay, G. Iooss and P. Laure, *Eur. J. Mech. B***11**, 621 (1992).
30. P.G. Drazin and W.H. Reid, *Hydrodynamic Stability*, Cambridge University Press, N.Y. (1981).
31. P. Chossat and G. Iooss, *The Couette-Taylor problem*, Springer-Verlag, N.Y. (1994).
32. D. Stassinopoulos, J. Zhang, P. Alström and M.T. Levinsen, *Phys. Rev. E* **50**, 1189 (1994).
33. H. Litschke and K.G. Roesner, *Exp. Fluids* **24** , 201 (1998).

Axial effects in the Taylor–Couette problem: Spiral–Couette and Spiral–Poiseuille flows

Álvaro Meseguer[1] and Francesc Marquès[2]

[1] Oxford University Computing Laboratory (Numerical Analysis Group), Wolfson Building, Parks Road, Oxford OX1 3QD, United Kingdom
[2] Universitat Politècnica de Catalunya (Departament de Física Aplicada), Jordi Girona Salgado s/n, Mòdul B4 Campus Nord, 08034 Barcelona, Spain

Abstract. A comprehensive study of the linear stability of the Taylor–Couette problem with imposed axial effects is examined. The study will be focused on two different flows: Spiral Couette (SCF) and Spiral Poiseuille (SPF) flows. In SCF flow, the axial effect is introduced by an inertial axial sliding mechanism between the cylinders. In the SPF, the axial effect is introduced via an imposed axial pressure gradient. For both problems, a wide range of parameters has been explored. In both systems, zeroth order discontinuities are found in the critical stability surface; they are explained as a result of the competition between the centrifugal and shear instability mechanisms, which appears only in the co–rotating case, close to the rigid body rotation region. In both problems, good agreement with the experimental results has been obtained.

1 Introduction

We consider an incompressible viscous fluid which is contained in the gap between two concentric cylinders that rotate independently about a common axis at constant angular velocities. An axial motion is induced by an inertial sliding of the cylinders relative to one another along the pipe axis in the SCF, and by an imposed axial pressure gradient in the SPF case. The basic motions whose linear stability will be studied are, therefore, a superposition of the Couette flow in the azimuthal direction and the axial velocity field induced by the relative sliding, in the former case or by the axial pressure gradient in the second, [13].

The SCF problem was first studied in [15] and [14], where an inviscid stability criteria in the narrow gap case was obtained. The experiments carried out in [14] are, as far as we know, the only experiments made in this problem until now. The general problem was studied in [22] and in [12] with special emphasis in energy methods; an excellent review can be found in [13], chapter VI. In a recent work, [2], a linear stability analysis of the Spiral Couette flow was carried out, in the stationary outer cylinder case, in the so called enclosed geometry, which includes end effects. The more general problem of oscillatory sliding has been recently considered in [11] and [17], whose numerical simulations are in good agreement with the experimental results reported in [28].

The first approaches to the study of the stability of the SPF were carried out in [6] and in [10]. In a more recent study, reported in [25], both numerical and experimental, it was demonstrated that the axial effects may stabilize or

C. Egbers and G. Pfister (Eds.): LNP 549, pp. 118–136, 2000.

destabilize the basic flow depending on the sign of the speed rotation ratio of the cylinders. Our study provides the first comprehensive numerical exploration of the linear stability of the SPF flow, covering a wide range of angular velocities, being focused on the co-rotation situations because of the presence of new phenomena not observed before. The numerical computations reported here were carried out for the same experimental parameters used in [25].

We have found that SCF and SPF exhibit zeroth order discontinuities in their critical surface, a result recently reported by the authors in [20] for the SCF. In both cases, this pathology is due to a common fact; the competition between centrifugal and shear instability mechanisms. Mathematically, the spectra of the linear stability operators exhibit radical changes in the space of physical parameters. In other words, the spectra may be, in both problems, split up in two independent subsets, associated to the two instability mechanisms. The behaviour of both subsets is independent of each other, swapping radically their dominance in the transition in different parts of the space of physical parameters.

An understanding of the stability of these flows could have applications in some industrial processes like the purification of industrial waste water, the production of wire and cables and the optical fibre fabrication techniques, see [23], [26] and [4]. In all of them, axial sliding and axial pressure gradients in a cylindrical annulus takes place, and the rotation of one or both cylinders may change the stability and properties of the flow.

The work is structured as follows. Section 2 is devoted to the SCF. In Sec. 2.1 the linear stability in the standard normal mode analysis is formulated. In Sec. 2.2 the difficulties encountered when computing the neutral stability curves, and the algorithms we have used, are described. The linear stability analysis for $\eta = 0.5$ is explained in detail in Sec. 2.3. The mechanism of competition between centrifugal and shear instability mechanisms is explained mathematically as an abnormal behaviour of the topological structure of the neutral stability curves. Comparisons with experimental results for $\eta = 0.8$ are reported in Sec. 2.4. Section 3 is devoted to the linear stability analysis of the SPF. In Sec. 3.1, the stability analysis for $\eta = 0.5$ is reported and comparisons with previous numerical and experimental works are provided.

2 Spiral–Couette flow

Spiral-Couette flow is the term used to describe fluid motion between two concentric rotating cylinders, whose radius and angular velocities are r_{i}^*, r_{o}^* and Ω_i, Ω_o respectively. The annular gap between the cylinders is $d = r_{\mathrm{o}} - r_{\mathrm{i}}$. In addition, the inner cylinder is moving parallel to the common axis with a constant velocity U_c (see Fig. 1). The independent nondimensional parameters appearing in this problem are: the radius ratio $\eta = r_{\mathrm{i}}^*/r_{\mathrm{o}}^*$, which fixes the geometry of the annulus; the Couette flow Reynolds numbers $R_i = dr_{\mathrm{i}}\Omega_i/\nu$ and $R_o = dr_{\mathrm{o}}\Omega_o/\nu$ of the rotating cylinders and the axial Reynolds number $R_z = dU_c/\nu$ measuring the translational velocity of the inner cylinder. Henceforth, all variables will be rendered dimensionless using d, d^2/ν, ν^2/d^2 as units for space, time and the

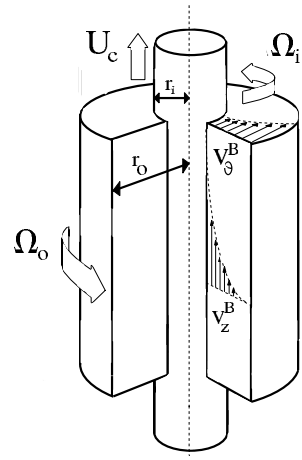

Fig. 1. Physical description of the Spiral-Couette problem. The basic axial-azimuthal flow has also been depicted

reduced pressure (p^*/ϱ^*). The Navier–Stokes equation and the incompressibility condition for this scaling become

$$\partial_t \boldsymbol{v} + (\boldsymbol{v}\cdot\nabla)\boldsymbol{v} = -\nabla p + \Delta\boldsymbol{v}, \quad \nabla\cdot\boldsymbol{v} = 0\,. \tag{1}$$

Let (u, v, w) the physical components of the velocity $\boldsymbol{v}$ in cylindrical coordinates (r, θ, z). The boundary conditions for the flow described above are:

$$u(r_{\rm i}) = u(r_{\rm o}) = 0\,, \tag{2}$$

$$v(r_{\rm i}) = R_i, \quad v(r_{\rm o}) = R_o\,, \tag{3}$$

$$w(r_{\rm i}, t) = R_z, \quad w(r_{\rm o}) = 0\,, \tag{4}$$

where $r_{\rm i} = \eta/(1-\eta)$, $r_{\rm o} = 1/(1-\eta)$.

In order to compare with experiments and also with previous works, we are going to consider the usually termed *open flow* case. The only experiments of the Taylor–Couette flow with axial sliding of the inner cylinder known to us are those of [14] which were carried out in an annulus with open endwalls. The steady velocity field $\boldsymbol{v}_B$, independent on the axial and azimuthal variables, satisfying (1), (2), (3) and , (4) is

$$u_B = 0,\ v_B = Ar + B/r\ ,\ w_B = C\ln(r/r_{\rm o})\ , \tag{5}$$

as can be seen in [13]. The constants A, B, C are given by

$$A = \frac{R_o - \eta R_i}{1+\eta}\ ,\ B = \frac{\eta(R_i - \eta R_o)}{(1-\eta)(1-\eta^2)}\ ,\ C = \frac{R_z}{\ln\eta}\ . \tag{6}$$

2.1 Linear stability of the SCF

In the preceding section the basic flow was obtained. We now perturb this basic state by a small disturbance which is assumed to vary periodically in the azimuthal and axial directions:

$$\boldsymbol{v}(r,\theta,z,t) = \boldsymbol{v}_B(r) + \boldsymbol{u}(r)\mathrm{e}^{\mathrm{i}(n\theta+kz)+\lambda t} , \tag{7}$$

$$p(r,\theta,z,t) = p_B(r,z) + p'(r)\mathrm{e}^{\mathrm{i}(n\theta+kz)+\lambda t} , \tag{8}$$

where $\boldsymbol{v}_B = (0, v_B, w_B)$ is given by (5), $n \in \mathbb{N}$, $k \in \mathbb{R}$, $\lambda \in \mathbb{C}$ and the boundary conditions for $\boldsymbol{u}$ are homogeneous, $\boldsymbol{u}(r_\mathrm{i}) = \boldsymbol{u}(r_\mathrm{o}) = \boldsymbol{0}$. Linearizing the Navier–Stokes equations about the basic solution, we obtain the eigenvalue problem

$$\lambda\boldsymbol{u} = -\nabla p' + \Delta\boldsymbol{u} - \boldsymbol{v}_B \cdot \nabla\boldsymbol{u} - \boldsymbol{u} \cdot \nabla\boldsymbol{v}_B . \tag{9}$$

In order to solve (9) numerically, a spatial discretization of the problem is accomplished by a solenoidal Petrov-Galerkin scheme [19]. A comprehensive analysis of the method can be found in [21] or [3]. The discretization scheme leads to a generalized eigenvalue problem of the form

$$\lambda G\boldsymbol{x} = H\boldsymbol{x} , \tag{10}$$

where matrices G and H explicitly depend on the physical parameters of the problem (see [20], for details).

Let us consider the symmetries of our problem. The Navier–Stokes equations are invariant with respect to the specular reflections $\{z \to -z,\ w \to -w\}$ and $\{\theta \to -\theta,\ v \to -v\}$. They are also invariant with respect to rotations around the axis, axial translations and time translations. The boundary conditions break some of these symmetries. R_i or R_o different from zero breaks the specular reflection $\theta \to -\theta$, and $R_z \neq 0$ breaks the specular reflection $z \to -z$. In order to keep the invariance we must change the sign of these Reynolds numbers, and of the corresponding wavenumbers n and k in the solutions of the linearized system (10). Therefore the symmetries allow us to restrict the computations to the cases $R_z > 0$ and $R_i > 0$. Furthermore, since the Navier–Stokes equations are real, the complex conjugate of a perturbation (7, 8) is also a solution, and we can change simultaneously the sign of n, k and the imaginary part of λ. Then we can restrict the computations to the case $k \geq 0$.

When n and k are nonzero, the eigenvector of the linear problem has the form of a spiral pattern (see Fig. 9, showing an experimentally observed spiral flow). The wavenumbers n and k fix the shape of the spiral. The angle α of the spiral with a z–constant plane is given by $\tan\alpha = -n/(r_\mathrm{o}k) = -(1-\eta)n/k$.

If $R_z = 0$, the symmetry $z \to -z$ is not broken, and at the bifurcation point, in the $n \neq 0$ case, we get two pairs of purely imaginary eigenvalues bifurcating at the same time, representing spirals with opposite slope –or angle– [5]. These spirals have opposite values of n. For $R_z \neq 0$, the corresponding eigenvalues split apart, and one of the two spirals $\pm n$ becomes dominant. Therefore we expect mode competition and switching between $+n$ and $-n$ for R_z close to zero.

2.2 Computation of the neutral stability curves

It has long been known that whenever two or more control parameters representing different physical mechanisms for instability compete, one can observe stability turning points, islands of stability, multiple minima, and large changes in the critical azimuthal wavenumber. Examples include the competition between buoyancy–induced shear and rotation in radially Couette–flow [1], between rotation and axial sliding in modulated Taylor–Couette flow [17]. In the present problem, the competition between wall–driven shear and centrifugal instability mechanisms will lead to possible hysteresis experimental phenomena.

Let σ be the real part of the first eigenvalue of the linear system (10) which crosses the imaginary axis. The stability of the basic flow is determined by the sign of σ. For negative values of σ, the basic flow is stable under infinitesimal perturbations. When σ is zero or slightly positive, the steady flow becomes unstable and bifurcated secondary flows may appear. It should be remarked that $\sigma(n, k, \eta, R_i, R_o, R_z)$ is a function of the physical parameters which play an essential role in the dynamics of the system. For fixed η, R_o, R_z, and given n, k the inner Reynolds number $R_{i,c}(n, k)$ such that $\sigma = 0$ is computed. The critical inner Reynolds number is given by $R_{i,crit} = \min_{n,k} R_{i,c}(n, k)$, and the corresponding values of n, k are the critical azimuthal and axial wavenumbers n_{crit}, k_{crit} which will dictate the geometrical shape of the critical eigenfunction, which may be a spiral flow or travelling Taylor vortices.

The curves in the (k, R_i) plane given by $\sigma(k, R_i) = 0$ are commonly termed Neutral Stability Curves (NSC). The main goal at this stage is to compute the absolute minimum of the NSC, which will give the critical parameters $(k_{\text{crit}}, R_{i,crit})$ – in fact, the absolute minimum of the set of the NSC corresponding to integer values of n will be found. As it will be seen later, the NSC curves for this problem may have multiple extrema (maxima and minima), exhibit disconnected parts and sharp geometrical forms. Furthermore, these curves may exhibit multivalued branches as functions of k, and these features can change abruptly in some parameter ranges (see Fig. 2). Standard methods applied to a regular grid in the plane (k, R_i) require exorbitantly high accuracy computations. Consequently, an alternative 2-dimensional Newton-Raphson method has been used; see [19] for details.

2.3 Stability analysis for $\eta = 0.5$

The computation of $R_{i,c}(R_z, R_o)$ for the wide gap $\eta = 0.5$, gives as a first striking result the presence of a zeroth–order discontinuity in $R_{i,c}$, in the co–rotating case $(R_o > 0)$. Although this behavior has been considered possible by some authors, [7], specific examples showing this kind of discontinuity are very unusual in the fluid mechanics literature.

For $R_o = 200$ the discontinuity appears for $R_z = 82.63$. We have shown in Fig. 2a the critical R_i as a function of k. For $R_z = 80$ the dominant mode is $n = -1$, giving $R_{i,c} = 373.43$ and $k_c = 1.68$; but for $R_z = 82.63$ the marginal stability curve of the $n = -4$ mode develops an island of instability for a much

lower $R_{i,c} = 119.13$, introducing a discontinuity in $R_{i,c}$. Notice too that the change in n_{crit} is not ± 1 as usual, but it changes in three units. The island of instability is very small (Fig. 2a, $R_z = 84$), becoming larger when we move away of the discontinuity. All these features make the numerical computation of the critical parameters very difficult from the algorithmic point of view. For these reasons we have developed specific numerical methods, outlined in [20], in order to detect the islands as soon as they appear. Similar islands of instability have been found in [17]. Before crossing the $R_{i,c}$ discontinuity, the marginal stability curve for $n = -4$ has a single extremum, a minimum (Fig. 2a, $R_z = 80$), giving the critical parameter values $(R_{i,c}, k_c)$. After crossing, and due to the appearance of the island, we have three extrema, two minima and a maximum, and the marginal stability curve has two disconnected branches. If we move to higher R_z values, the island grows until it merges with the other branch (Fig. 2a, $R_z = 120, 122$); the marginal curve has now a single minimum. Plotting the position of all the extrema as a function of R_z, we get an S-shaped curve, displayed in Fig. 2b; the solid curve gives the absolute minimum, and the dashed curve corresponds to the other extrema. The critical Reynolds number $R_{i,c}$ becomes discontinuous (zeroth order discontinuity) as soon as the island of instability appears for $R_z = 82.64$; experiments made by increasing R_i and R_z held fixed would report the solid curve in Fig. 2b. The whole critical surface is multivalued and continuous, but is folded in such a way that a cusp develops; Fig. 3a shows a perspective view of the critical surface. Fig. 3b shows the same critical surface with the curves corresponding to a change in the critical azimuthal wavenumber n, where the surface is not smooth (the tangent plane is discontinuous along these curves). The projection of the curves corresponding to a change in the azimuthal wavenumber n are plotted in Fig. 4. The edges of the cusp region are plotted as thick lines in both Figs. 3b and 4. These discontinuities and fold structure may have important consequences which could be detected experimentally, like hysteresis phenomena, as well as the discontinuity in $R_{i,c}$.

Figure 5 shows $R_{i,c}$ and α as a function of R_o for different values of R_z. The critical Reynolds number $R_{i,c}$ (Fig. 5a) is almost independent of R_z in the counter–rotating region $R_o < 0$. But in the co–rotating region, where the cusp develops, we have two well–separated kinds of behavior. This figure is a front view of the cusp structure (Fig. 3) along the R_z axis. For small axial sliding R_z, before the discontinuity, $R_{i,c}$ is very close to the values without sliding (Taylor–Couette flow). For higher axial sliding, after the discontinuity, $R_{i,c}$ falls to much lower values. The axial sliding is destabilizing, except in the small region where the axisymmetric mode ($n = 0$) is dominant. The destabilizing effect becomes significant only in the co–rotating case, after the discontinuity. The centrifugal instability seems to be the dominant mechanism (as in Taylor–Couette, $R_z = 0$) except after the discontinuity, where a shear instability due to the axial sliding becomes dominant; the cuspidal zone can be thought as the transition region between both mechanisms. This qualitative change can also be noticed in the angle of the spiral pattern α (Fig. 5c), which jumps from values less than 0.2 radians (10^o) to values close to 1.2 radians (70^o). We also notice that the shear–

(**a**)

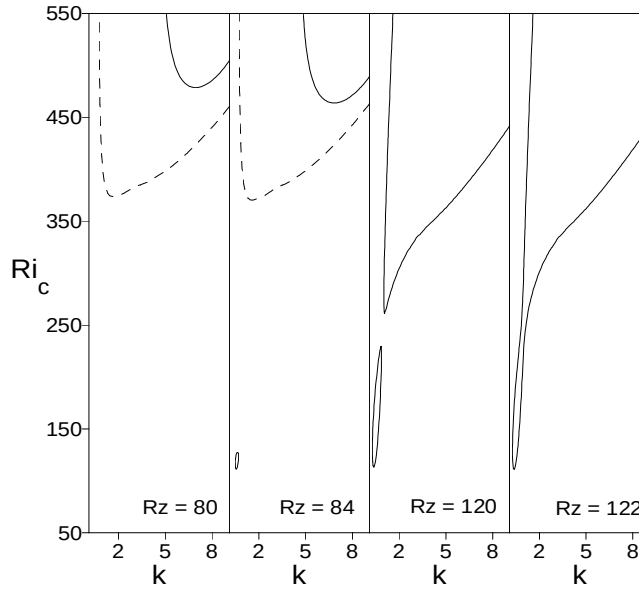

(**b**)

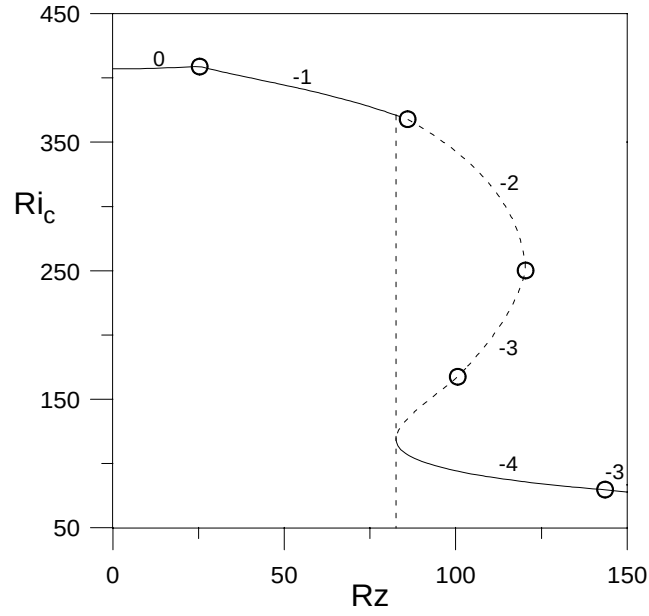

Fig. 2. (**a**) Formation and evolution of an island of instability for $\eta = 0.5$ and the dashed one to $n = -1$. (**b**) The corresponding critical inner Reynolds number $R_{i,c}$ as a function of R_z (solid line); the dashed line is a section ($R_o = 200$) of the critical surface (Fig. 5). The labels refer to the dominant azimuthal mode number n; the hollow circles are the transitions between different n. $R_{i,c}$ is discontinuous for $R_z = 82.64$

(**a**)

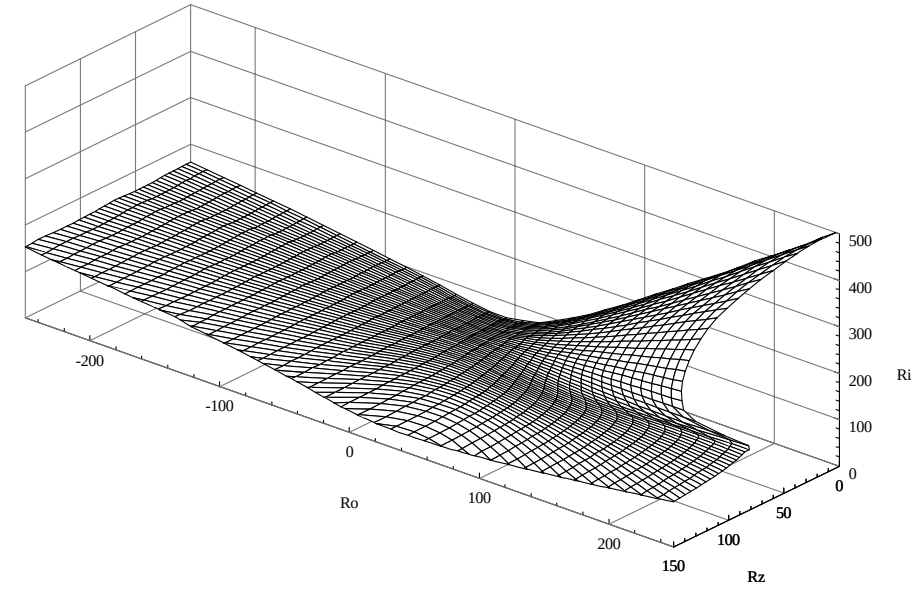

(**b**)

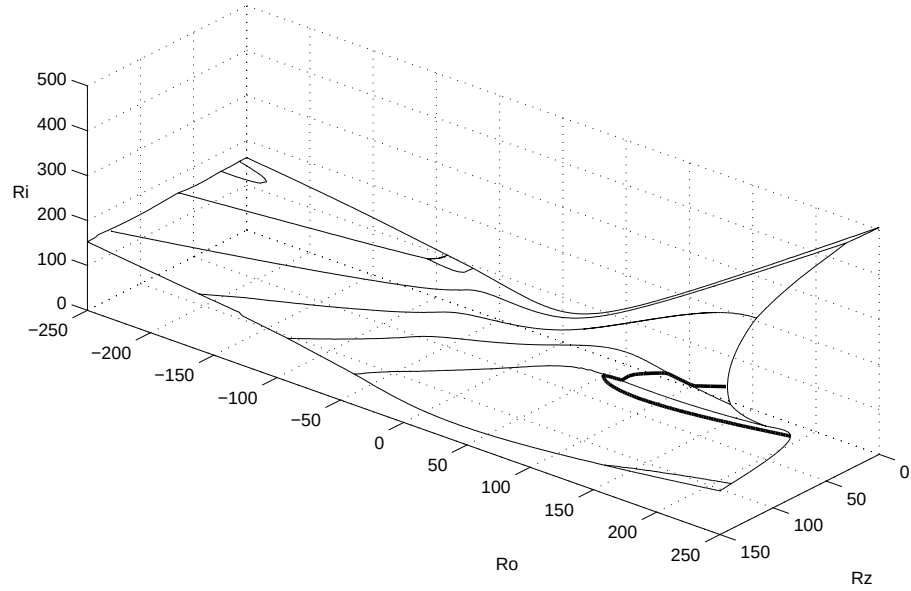

Fig. 3. (**a**) Perspective view of the critical surface $R_{i,c}(R_o, R_z)$ for $\eta = 0.5$ (**b**) Same view, explicitly showing the changes in the dominant azimuthal mode n at criticality. The edges of the cusp region are also plotted as thick lines

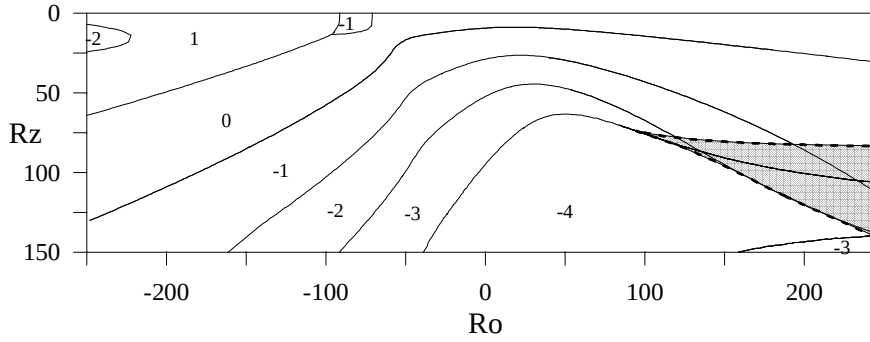

Fig. 4. Dominant azimuthal mode n at criticality, as a function of R_o, R_z; $\eta = 0.5$. The shaded region corresponds to the fold, whose edges are plotted as thick dashed lines

instability dominated branch is very close to the solid body rotation line (see Fig. 5a), where the centrifugal instability does not play a significant role; see [16]. Figure 6 shows $R_{i,c}$ and α as a function of R_z for different values of R_o

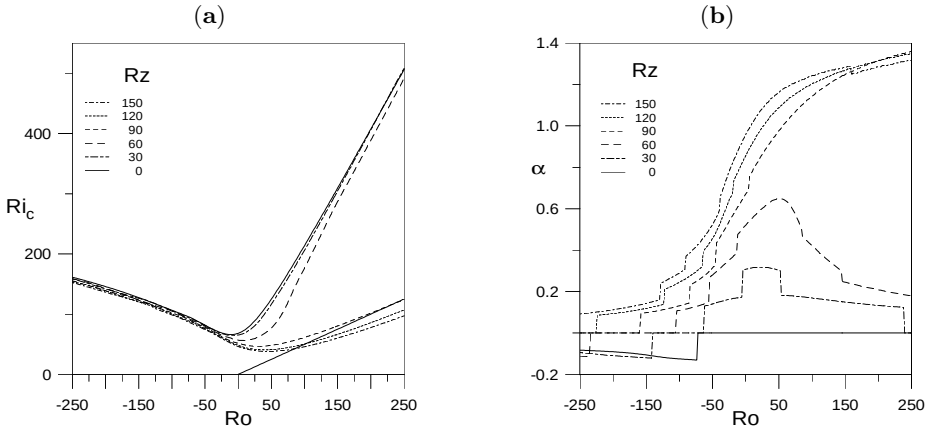

Fig. 5. Critical parameters for $\eta = 0.5$, as functions of the outer Reynolds number R_o. (**a**) Critical inner Reynolds number $R_{i,c}$; the solid straight line is the rigid rotation line $R_i = \eta R_o$. (**b**) Angle of the spiral pattern α in radians

in the co–rotating case. In Fig. 6a sections of the cusp region are displayed; the critical $R_{i,c}$ is in fact the minimum of the values in the multivalued region, so we have a discontinuity which grows when increasing R_o. The discontinuity has been displayed in Fig. 6b.

The bicritical points where the azimuthal wavenumber n changes and two eigenvalues bifurcates simultaneously are distinguished with a vertical bar. The effect of the sliding on these axisymmetric modes is slightly stabilizing, in con-

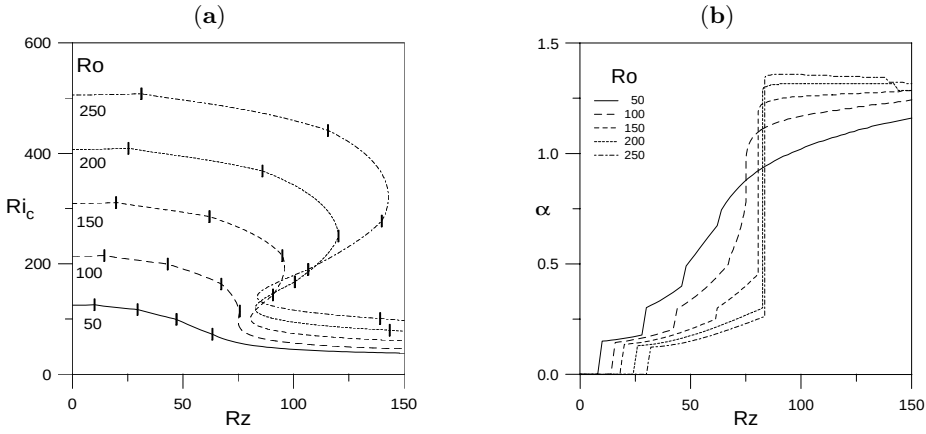

Fig. 6. Critical parameters for $\eta = 0.5$, as functions of the axial Reynolds number R_z in the co–rotating case $R_o > 0$. (**a**) Critical inner Reynolds number $R_{i,c}$. ‘ (**b**) Angle of the spiral pattern α in radians

trast to their destabilizing effect on the non-axisymmetric modes, mainly in the co–rotating region, an effect also reported by Ali et al. [2].

2.4 Comparison with experimental results ($\eta = 0.8$)

Some previous experimental studies have been reported on the stability of the spiral Couette flow. In fact, in an excellent study done in [14], both theoretical and experimental, a stability analysis has been devoted to an specific zone on the parameter space, inside the cusp region. The experimental apparatus has a gap $\eta = 0.8$, with open ends, corresponding to our open flow case. The rotational speed of the external cylinder is held fixed at $R_o \approx 750$. Ludwieg's experimental device needed high external rotation speeds in order to avoid pre–turbulent stages induced by transients. The unique design of the experimental apparatus enforced a linear dependence between axial velocity and azimuthal rotation speed of the inner cylinder moving relative to an outer stationary cylinder (without axial velocity but rotating). As a result, the experimental paths in the parameter space (R_i, R_z) were straight lines, as can be seen both in Figs. 7, 8. Ludwieg's experimental results (Fig. 7) are given in terms of two nondimensional parameters $\tilde{c}_\phi$ and $\tilde{c}_z$ which describe the motion of the fluid. As in [12], we have used the values of $\tilde{c}_\phi$, $\tilde{c}_z$ to compare with Ludwieg's results. A more detailed discussion about the parameters used by different authors is given in [20]. The dependence between $\tilde{c}_\phi$, $\tilde{c}_z$ and our variables R_i, R_o, R_z are given by the following equations (for $\eta = 0.8$):

$$\tilde{c}_\phi = \frac{1+\eta}{1-\eta}\frac{R_o - R_i}{R_o + R_i}, \quad \tilde{c}_z = \frac{1+\eta}{1-\eta}\frac{R_z}{R_o + R_i}. \tag{11}$$

For the $\eta = 0.8$ case the narrow gap approximation is not clearly justified. This can be a source of error in the experimental values given by [14]. It would be

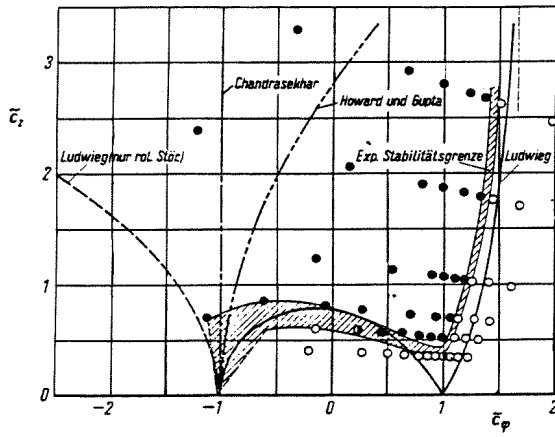

Fig. 7. Ludwieg experiments. Experimental results, from [14]; $\eta = 0.8$, $R_o = 750$

necessary to know the original experimental results in terms of the Reynolds numbers in order to work with the *true* control parameters R_z and R_i.

The experimental results of Ludwieg are summarized in Fig. 7. The shaded area is the error bandwidth experimentally obtained. These errors are very large in the fold region of the critical surface, and the reasons will be analyzed shortly thereafter. Figure 7 also shows several stability criteria. Three of them, labelled *Ludwieg (nur rot. Stöc)*, *Chandrasekhar* and *Howard und Gupta*, were obtained assuming axisymmetric perturbations, and using physical considerations as in the Rayleigh's criterion (labelled *Chandrasekhar* in Fig. 7). All of them are in very poor agreement with the experimental data. Instead, Ludwieg's stability criterion, obtained by exactly solving the linearized Euler equations in the narrow gap limit, is reasonably close to the experimental data.

A linear stability analysis of the Spiral Couette problem was reported by Hung, Joseph & Munson (1972) (referred from now on as HJM), where only particular regions in parameter space where considered. Their results are in good agreement with some of Ludwieg's results, although there where some unexplored zones that the present work has studied in detail. We have computed the critical curve for $R_o = 750$, which is single–valued considering $R_z(R_i)$, but it is well within the cusp region. The joint results of the three analyses have been sketched in Fig. 8, which corresponds to the section $R_o = 750$ of the critical surface. Our results are fully coincident with the previous computations of HJM, except for two points on the left of the minimum of our critical curve in Fig. 8, where the results of HJM clearly diverge from the experimental results. It is apparent that the results of HJM are confined to the intermediate branch of the critical surface fold, where the changes in $R_{z,c}$ are small. The other branches shows

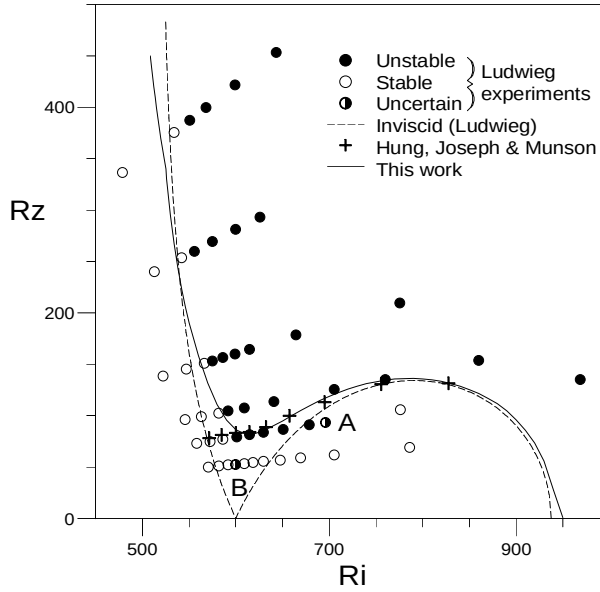

Fig. 8. Comparison between the experimental and theoretical results of Ludwieg (1964), Hung, Joseph & Munson (1972) and the present work. Parameters: $\eta = 0.8$, $R_o = 750$

very high slopes of $R_{z,c}(R_i)$; furthermore, the change in the critical azimuthal wavenumber n is of more than 15 units in this range. This is an indication of the difficulties HJM encountered outside the intermediate branch, which explains the discrepancy of their two computed points in the high slope region of the stability curve. The experimental results of Ludwieg show remarkable agreement with our

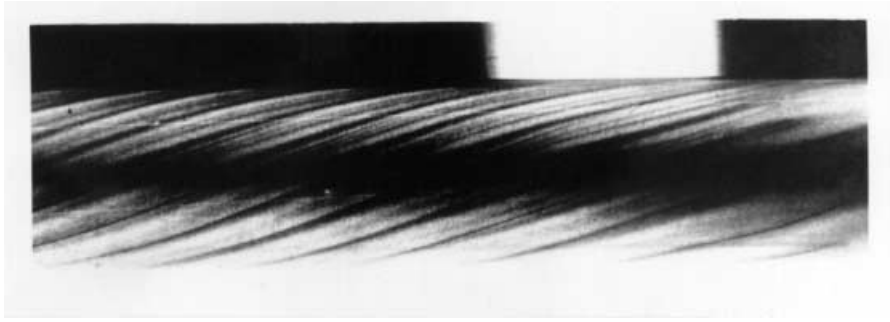

Fig. 9. Ludwieg experiments. Picture of the spirals, from [27]

numerical results. The best experimentally defined bifurcation points correspond

to the vertical branch (where shear is the dominant instability mechanism), and on this curve the discrepancies with our results are less than 4%; we must mention that this is the first time the vertical branch has been computed numerically. In the region close to the minimum of the critical curve, the onset of instability is in very good agreement with the experiments, but some points on the right side of the minimum clearly deviate from the numerical predictions. Notice that the points A and B, marked with a black and white circle, where Ludwieg could not decide about their stability, are very close to the hysteresis region, strongly suggesting that the bifurcation could be subcritical in this region of parameter space. Ludwieg acknowledged the experimental uncertainties in this parameter region; Fig. 7b shows the estimated uncertainty as a dashed area. For a detailed explanation of Ludwieg's experimental procedure, see [14] or [20] .

3 Spiral–Poiseuille flow

The first study of the stability of the spiral Poiseuille problem against three-dimensional perturbations, was carried out in [6] and in [10]. In [6], a monotonical dependence between the critical parameters was assumed for axisymmetric and non-axisymmetric perturbations. In a more recent study, reported by Takeuchi & Jankowski in 1981, [25], both numerical and experimental, it was demonstrated that the axial effects may stabilize or destabilize the basic flow depending on the sign of the speed rotation ratio of the cylinders. Takeuchi & Jankowski (TJ) experiments, are, as far as we know, the most recent ones and they were carried out for the wide gap $\eta = 0.5$ case and for three different azimuthal angular speed ratios of the cylinders ($\mu = \Omega_o/\Omega_i = 0, 0.2, -0.5$).

A comprehensive numerical exploration of the linear stability of the spiral Poiseuille flow is presented, covering a wide range of angular velocities, and being focused on the co-rotation situations because of the presence of new phenomena not observed before experimentally. The numerical computations were carried out for the same wide gap case ($\eta = 0.5$) studied in [25] in order to compare our numerical results with the experimental ones.

The independent nondimensional parameters appearing in this problem are the same described SCF, where the axial sliding effect R_z is no longer present, but replaced by the *Poiseuille* number, $P = (\partial_z P^*)(r_\mathrm{o} - r_\mathrm{i})^3/\varrho\nu^2$, measuring the imposed axial pressure gradient. A physical description of the problem can be found in Fig. 10. As in the SCF, the azimuthal component of the basic vector field is dictated by the Couette flow. The axial basic flow, represented in Fig. 10, is now a superposition of logarithmic and parabolic profiles. The explicit expressions for the basic flow can be obtained under the same symmetry assumptions that in SCF; see [13]:

$$u_B = 0, \quad v_B = Ar + \frac{B}{r}, \quad w_B = C\ln(\frac{r}{r_\mathrm{o}}) + \frac{P}{4}(r^2 - r_\mathrm{o}^2), \tag{12}$$

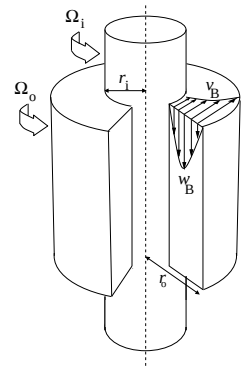

Fig. 10. Physical description of the Spiral-Poiseuille problem. The basic axial-azimuthal flow has also been depicted

where the constants A, B and C are

$$A = \frac{R_o - \eta R_i}{1+\eta},\ B = \frac{\eta(R_i - \eta R_o)}{(1-\eta)(1-\eta^2)},\ C = \frac{1}{\ln \eta}\frac{P(1+\eta)}{4(1-\eta)}. \tag{13}$$

3.1 Linear stability results ($\eta = 0.5$)

As before, the basic spiral Poiseuille flow $\boldsymbol{v}_B = (0, v_B, w_B)$ is perturbed by a small disturbance which is assumed to be periodic in the azimuthal and axial variables. The linear stability analysis is carried out by the same solenoidal Petrov-Galerkin scheme, [19], already used in the analysis of the sliding case, SCF, Sec. 2. The linear stability of the SPF has been explored in the range of values $R_o \in [0, 450]$, $P \in [0, 1500]$ and $R_i \in [0, 900]$. The numerical algorithm used to compute the neutral stability curves and their minima is the same that was used in [20]. For each pair of values (P, R_o), the critical inner Reynolds number $R_{i,c}$ and the critical axial wavenumber k_c are computed for different values of the azimuthal wave-number n. The selection of the minimum R_i value leads to a functional dependence $R_{i,c} = f(P, R_o)$. Geometrically, the function f defines a surface in the parameter space which is usually termed *marginal* or *critical* surface. This surface is not regular, being not differentiable in the points were the change of azimuthal dominance take place. This is a common feature in hydrodynamic stability. In Fig. 11, R_o-constant sections of the critical surface have been depicted for low outer rotations. It can be observed that the axial pressure gradient has a stabilization effect over the axisymmetric and non-axisymmetric perturbations with low azimuthal wave number ($|n| \leq 3$). Nevertheless, for higher values of R_o, the transition curves exhibit multiplicity with respect to the variable P and zeroth-discontinuities due to the competition between centrifugal and shear instability mechanisms. Mathematically, this phenomenon has the same explanation as in the SCF.

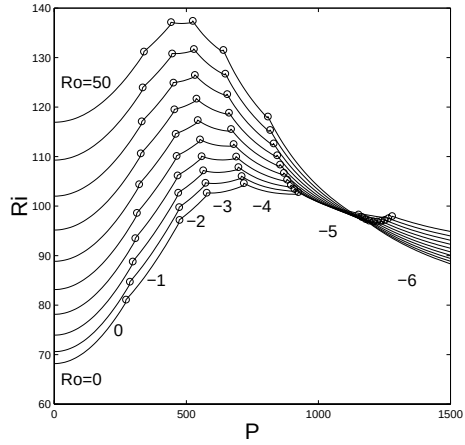

Fig. 11. R_o–constant sections of the critical surface for low outer rotations. The curves correspond to the values $R_o = 5, 10, \ldots, 50$. The circles have been plotted in the transitions of azimuthal dominance $n = 0, -1, -2, \ldots$. The first curve $R_o = 0$ agrees with [25] (case $\mu = 0$)

Figures 12**a-d** show the formation of an island of instability as long as the Poiseuille number is increased, for a fixed outer rotation Reynolds number ($R_o = 450$). Initially, for $P = 1000$, the dominant azimuthal mode is $n = -3$, see Fig. 12**a**. For $P = 1100$, an island of instability appears. This island is associated to another azimuthal mode ($n = -6$), being dominant and lowering radically the critical R_i value in a factor of four approximately, see Fig. 12**b**. As long as P is increased, the island grows in size, and eventually merges with the upper branch of the $n = -6$ mode, as shown in Fig. 12**c** and Fig. 12**d**. Altogether, this mechanism leads to the presence of a folding in the critical surface, in the same way as it appeared in the SCF. As it can be observed in Fig. 13, the critical curves exhibits a folding as long as the outer rotation R_o parameter is increased. Figure 13 is a cross section of the critical surface plotted in Fig. 14 for different values of R_o. For $R_o > 250$, the critical curves exhibit a multivalued branch which can not be computed as a function of P. Therefore, R_i is the fixed parameter in those branches, being $P_{crit.}$ the sought value for instability. The whole phenomena can be observed globally in Fig. 14. This anomalous behaviour has been already reported numerically in [20] and experimentally in [14] for the spiral Couette flow. Apparently, this anomaly was not detected in TJ experiments because they worked in restricted planes $R_o = \mu\eta R_i$. In Fig. 14, we have indicated two curves, named TJ1 and TJ2, which correspond to the numerical and experimental exploration made by Takeuchi & Jankowski for their cases $\mu = 0$ and $\mu = 0.2$, respectively. As depicted in Fig. 14, TJ numerical and experimental exploration range is far away from the cuspidal zone where the folding appears. The projection of the transition curves between different azimuthal wavenumbers n has been plotted in Fig. 15. The projection of the

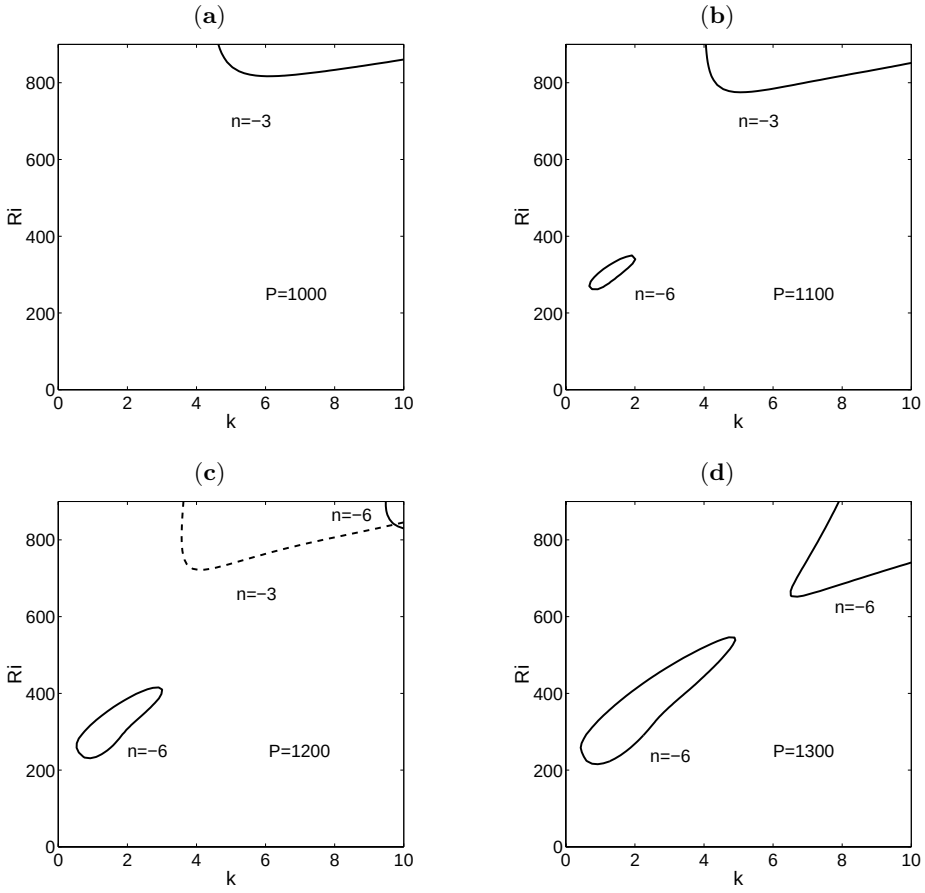

Fig. 12. Formation of an island of instability in the SPF for $R_o = 450$

curves of maxima (M) and minima (m) of Fig. 14, which are the boundary of the cuspidal zone, and where hysteresis phenomena may appear, are also included in Fig. 15. Similar computations, not reported here, were done in the *counter-rotation* ($R_i\, R_o < 0$) situations. Due to the dominance of the centrifugal instability mechanism in this region, the critical surface exhibits a quite regular behaviour, as in the SCF.

4 Conclusions

A comprehensive exploration of the linear stability of the Taylor–Couette flow with imposed axial effects has been done. The study has been focused in two particular problems, the Spiral Couette and Spiral Poiseuille flows. In both problems, complex critical behaviour has been detected for co-rotation situations. The critical surfaces $R_{i,c} = f(R_z, R_o)$ and $R_{i,c} = f(P, R_o)$ exhibit zeroth order

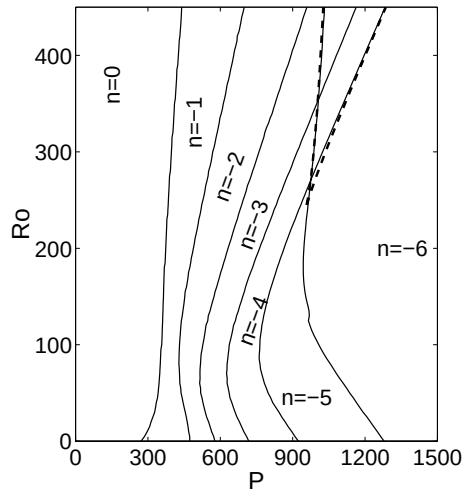

Fig. 15. Projection of the transition curves between different dominant azimuthal modes n. The dashed lines correspond to the projection of the curves M and m from Fig. 14

discontinuities which can only be detected making use of a specifically tailored, efficient and robust numerical scheme for the computation of the neutral stability curves. This unusual phenomena in hydrodynamical stability problems has been explained in terms of competition between two independent instability mechanisms: in the current problems the centrifugal instability, dominant in the counter–rotating regime and also for small axial effect, competes with the shear instability induced by the axial motion. For the Spiral Couette flow, experimental evidences confirm this anomalous behaviour. For this problem, our numerical computations are in complete agreement with the experimental results and with previous numerical approaches. For the Spiral Poiseuille flow, additional experiments would be required to confirm the presented computations. Overall, both problems would require suitable experimental procedures (i.e. independence between axial and azimuthal speeds) in order to properly detect the first instability of the basic spiral flow, and explore the competition between the different instability mechanisms in the fold region.

References

1. M.E. Ali, P.D. Weidman: J. Fluid Mech., **220** 53-84 (1990)
2. M.E. Ali, P.D. Weidman: Phys. Fluids A **5** 1188-1200 (1993)
3. C. Canuto, M.Y. Hussaini, A. Quarteroni, T.A. Zang: *Spectral Methods in Fluid Dynamics.* (Springer Series in Computational Physics, 1988) ‘
4. K. Chida, S. Sakaguchi, M. Wagatsuma, T. Kimura: Electronic Letters, *18*, 713–715 (1982)

5. P. Chossat, G. Iooss: *The Couette-Taylor Problem.* Applied Mathematical Sciences, *102*, Springer-Verlag, New York (1994)
6. K. C. Chung & K. N. Astill: J. Fluid Mech. **81** 641-655 (1977)
7. S.H. Davis & S. Rosenblat: Studies App. Math., **57**, 59–76 (1977)
8. W.S. Edwards, R.P. Tagg, B.C. Dornblaser, H.L. Swinney: Eur. J. Mech. B Fluids, **10**, 205–210 (1991)
9. J.E. Hart: J. Fluid Mech., **47**, 547–576 (1971)
10. M. A. Hasoon and B. W. Martin: Proc. R. Soc. Lond. A, **352**, 351–380 (1977)
11. H.C. Hu, R.E. Kelly: Phys. Rev. E, **51**, 3242–3251 (1995)
12. W.L. Hung, D.D. Joseph, B.R. Munson: J. Fluid Mech., **51**, 593–612 (1972)
13. D. D. Joseph: *Stability of Fluid Motions* vol. I and II (Springer-Verlag, Berlin 1976)
14. H. Ludwieg: Z. Flugwiss, 12, 304–309 (1964)
15. I. Kiessling: Deutsche Versuchsanstalt für Luft- und Raumfahrt—Bericht 290 (1963)
16. P.A. Mackrodt: J. Fluid Mech., **73**, 153-164 (1976)
17. F. Marques and J. M. Lopez: J. Fluid Mech., **348**, 153-175 (1997)
18. G.B. McFadden, S.R. Coriell, B.T. Murray, M.E. Glicksman and M.E. Selleck: Phys. Fluids A**2**, 700-705 (1990)
19. A. Meseguer: Bifurcations in Fluid Systems: Petrov-Galerkin Schemes. Thesis, Universitat Politècnica de Catalunya, Barcelona (1998)
20. A. Meseguer, F. Marques: J. Fluid Mech., **402**, 33-56 (2000)
21. R.D. Moser, P. Moin, A. Leonard: J. Comput. Phys. **52**, 524-544 (1983)
22. J.E. Mott, D.D. Joseph: Phys. Fluids **11**, 2065-2073 (1968)
23. D.F. Ollis, E. Pelizzetti, N. Serpone: Environ. Sci. Technol., **25**, 1523–1529 (1991)
24. J. Sanchez, D. Crespo & F. Marques: App. Sci. Res., **51**, 55–59 (1993)
25. D. I. Takeuchi & D. F. Jankowski: J. Fluid Mech. **102**, 101-126 (1981)
26. Z. Tadmor, R.B. Bird: Polymer Eng. and Sci., **14**, 124–136 (1974)
27. E. Wedemeyer: AVA–Bericht 67, A34 (1967)
28. A.Y. Weisberg, A. Smits & I. Kevrekidis: J. Fluid Mech., **348**, 141–151 (1997)

Stability and experimental velocity field in Taylor–Couette flow with axial and radial flow

Richard M. Lueptow

Northwestern University, Evanston, IL 60208, USA

Abstract. The imposition of a radial or axial flow on cylindrical Couette flow alters the stability of the system and modifies the velocity field. An axial flow stabilizes cylindrical Couette flow. The supercritical flow includes a rich variety of vortical structures including helical and wavy vortices. An axial flow also results in translation of the vortices with the axial flow. A radial flow through porous cylinders stabilizes cylindrical Couette flow, whether the radial flow is inward or outward. An exception is that a small radial outward flow destabilizes the flow slightly. The radial flow results in displacing vortex centers toward the cylinder from which fluid exits the annulus. For combined axial and radial flow, the axial flow stabilizes the cylindrical Couette flow regardless of the radial flow. In addition, the radial flow stabilizes the flow compared to the situation with no radial flow. Above the supercritical transition a wide variety of flow regimes occur in the case where the inner cylinder is porous and the outer cylinder is nonporous. The velocity field for cylindrical Couette flow with axial flow and a radial inflow at the inner cylinder is altered very little for small radial flows. However, the vortices shrink in size as they translate in the annulus as fluid is lost through the inner cylinder.

1 Introduction

The stability of Taylor vortex flow is altered when an additional flow is superimposed on the cylindrical Couette flow. In particular, the superposition of axial flow in the annulus or radial flow through a porous wall of the cylinders as shown in Fig. 1 can modify the conditions at which supercritical transition occurs and can modify the nature of the supercritical vortex structure. The effect of axial flow, radial flow, and combined axial and radial flow on the stability of the flow, the nature of the vortex structure, and the resulting velocity field are discussed in this chapter. We restrict this discussion to the cases where the inner cylinder rotates within a fixed outer cylinder in the presence of an axial flow, a radial flow through both cylinders, combined axial flow and radial flow through both cylinders, or combined axial flow with radial sink flow through the inner cylinder.

Pressure-driven axial flow in an annulus between a rotating inner cylinder and a fixed outer cylinder has several important engineering applications including journal bearings, biological separation devices, and rotating machinery. Two potential instabilities are present when an axial flow is imposed on cylindrical Couette flow with the inner cylinder rotating and the outer cylinder fixed. First, a centrifugal instability related to the curved streamlines of the flow results in vortices in the annulus. Upon reaching a critical speed of the inner cylinder, the

C. Egbers and G. Pfister (Eds.): LNP 549, pp. 137–155, 2000.

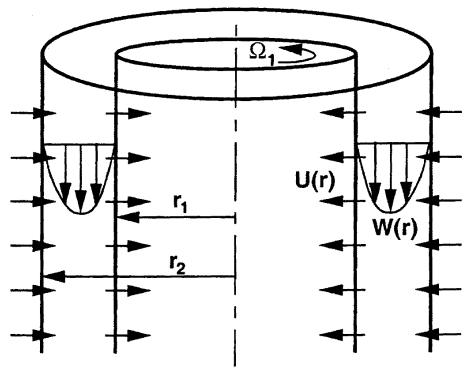

Fig. 1. Sketch of the flow configuration. The radial flow can be inward as shown or outward [1]. (Reprinted with permission of AIP)

vortices that appear are toroidal, but higher order vortical flows including wavy and turbulent vortices can appear at rotational speeds above the critical speed for vortices to appear. The second instability that can occur is a shear instability related to Poiseuille channel flow as the fluid flows axially in the annulus. This instability appears as turbulence. Of course, the two instabilities interact with one another so that the flow that appears depends on both the rotational speed of the inner cylinder and the axial flow velocity.

Radial flow in the annulus between differentially rotating porous cylinders occurs during dynamic filtration using a rotating filter. In these filtration devices, a suspension is contained between a rotating porous inner cylinder and a stationary nonporous outer cylinder. Filtrate passes radially through the porous wall of the rotating inner cylinder, while the concentrate is retained in the annulus. It is thought that the supercritical vortices wash particles off of the filter surface preventing the plugging of pores of the filter medium with particles. The imposition of a radial flow in addition to cylindrical Couette flow can alter the nature of the unstable flow regimes that appear. However, the situation is different from that for an imposed axial flow. For a radial flow, the only instability that is present is the centrifugal instability. However, the imposed radial flow can alter the nature of this instability substantially.

Of course, both axial and radial flow in the annulus of a cylindrical Couette flow cell can be imposed simultaneously, as shown in Fig. 1. In this case, both the centrifugal instability and the shear instability can occur. But both can be altered by the presence of a radial flow.

Before proceeding, it is helpful to define three dimensionless parameters related to the flow. The cylindrical Couette flow is characterized by a Taylor number. Although the Taylor number, which relates the centrifugal forces to the viscous forces, has several different forms, we use $Ta = r_\mathrm{i}\omega d/\nu$, where r_i is the radius of the inner cylinder, ω is the rotational speed of the inner cylinder, d

is the width of the annular gap, and ν is the kinematic viscosity. This form of the Taylor number, often called a rotating or inner Reynolds number, is used because it is simple and consistent with the form used in several recent studies [2], [3], [4], [5], [6]. The axial flow is characterized by the axial Reynolds number, which is defined as $Re_a = wd/\nu$, where w is the average axial velocity based on the axial volume flow rate. The radial flow is described by the radial Reynolds number, $\alpha = ud/\nu$, where u is the radial velocity at the inner cylinder based on the radial volume flow rate divided by the surface area of the inner cylinder. A single geometric parameter, the radius ratio, $\eta = r_i/r_o$, where r_o is the radius of the outer cylinder, is also necessary to fully specify the flow.

2 Cylindrical Couette flow with an imposed axial flow

2.1 Stability

The linear stability of circular Couette flow in the annulus between a rotating inner cylinder and a concentric, fixed outer cylinder has been studied from both theoretical and experimental standpoints. The instability appears as pairs of counter-rotating, toroidal vortices stacked in the annulus. Taylor [7] conducted a simple flow visualization experiment to confirm his analytic prediction for the onset of the instability. At higher rotational speeds of the inner cylinder the vortices become wavy and, eventually, turbulent. Chandrasekhar [8], DiPrima and Swinney [9], Kataoka [10], and Koschmieder [11] provide extensive summaries of the abundant research on this topic since Taylor's pioneering work.

Taylor's analysis of the stability of cylindrical Couette flow can be extended to include an axial flow in the annulus for the transition from stable Couette-Poiseuille flow to axial flow with Taylor vortices. The first such analyses were for the case of axisymmetric disturbances in a narrow annular gap [12], [13]. The analysis was later extended to arbitrarily wide annular gaps [14], [15]. In all cases the analysis was the standard linear stability analysis: The velocity and pressure are expressed as the sum of the stable flow plus a small perturbation. Upon substitution into the unsteady, incompressible, axisymmetric Navier–Stokes equations, the higher order terms are discarded and the equations for the stable motion subtracted leaving equations in terms of the perturbations. The perturbations are expressed as normal modes in terms of a radially-dependent amplitude function, an axial wavenumber, and an amplification factor. Upon appropriate manipulation of the equations, a sixth order ordinary differential equation for one of the amplitude functions results. The resulting eigenvalue problem is solved with the ultimate goal being the determination of the minimum Taylor number and associated wavenumber and amplification factor that satisfy the ordinary differential equation for specified axial Reynolds number Re_a and geometry η. The amplification factor is directly related to the axial velocity of the vortices in the annulus. Several methods have been used to solve the eigenvalue problem.

The results of the axisymmetric stability analysis indicates that an axial flow in the annulus stabilizes the circular Couette flow, so that the transition to

supercritical Taylor vortex flow occurs at a higher Taylor number. These results have been experimentally confirmed [16], [17]. In addition, the theory predicts that the vortices translate axially in the annulus in the same direction as the bulk axial flow. More recent analyses have indicated that the vortices travel axially at about 1.17 times the average axial velocity of the imposed axial flow [2], [15], [18] [19], [20].

The axisymmetric analysis described above fails to properly predict the flow for $Re_a > O(10)$. Above this axial Reynolds number, non-axisymmetric modes dominate [2], [5], [17], [18], [21], [22]. The non-axisymmetric modes are in the form of a pair of helical vortices. The helix angle of the vortices corresponds to that of the vortex being shifted by one vortex pair for each revolution of the vortex [6]. Experimental results show that the inclination of the vortices is opposite that of the flow and that the spiral vortices translate axially with the flow [6]. Chung and Astill [2] contend that this inclination is logical based on the nature of the asymmetric perturbation. Takeuchi and Jankowski [21] indicate that there is no theoretical basis upon which to select the sign of the helical vortex angle.

Recently, cylindrical Couette flow with an axial flow has been used as a model for the study of the distinction between absolutely unstable flow and convectively unstable flow. Early experiments did not differentiate between these flow regimes. But at low axial Reynolds number and Taylor numbers very near the transition to vortical flow, the spatio-temporal behavior of the flow can be classified absolutely stable, convectively unstable, and absolutely unstable. A stability diagram is shown in Fig. 2 [20]. The flow regimes can be described as follows:

1. In the absolutely stable flow regime, any perturbation to the flow decays, and the flow vortices do not form. The boundary of absolute stability is computed using the standard linear stability analysis described earlier in this section. When there is no axial flow, the flow is absolutely stable below the critical Taylor number and absolutely unstable above it.
2. In the convectively unstable flow regime, a localized perturbation cannot propagate upstream, but it will grow as it is advected downstream. Eventually the perturbation is carried downstream out of the system. Without a permanent source of perturbations, the system returns to the basic, stable state everywhere. Convectively unstable flow is evident experimentally in two forms [19], [23], [24]. In the first form, a localized perturbation is introduced experimentally by rotating both cylinders back and forth once through a small angle or by moving the inlet boundary forward and back one time. The resulting pulse consists of two or three vortex pairs that appear near the upstream end of the test cell where no vortices are otherwise present. The vortex pairs propagate axially with the axial flow growing in amplitude and number as they proceed downstream. In the second form, the perturbation is noise inherent in the system. In this case, no vortices appear near the inlet, but far enough downstream axially propagating vortices appear. At a given Reynolds number, the distance downstream from the inlet

that the propagating vortices appear increases with decreasing Taylor number. Although experiments are necessarily restricted to a finite aspect ratio, it is likely that far enough downstream the noise-sustained propagating vortices will always appear, as long as the system is above the limit for absolute stability in the convectively unstable flow regime [19]. The convectively unstable flow regime occurs at larger driving conditions (higher Taylor number) and smaller through-flow conditions (lower axial Reynolds number) than the absolutely stable flow regime.

3. In the absolutely unstable flow regime, a localized perturbation grows and propagates both upstream and downstream. This flow regime occurs at larger driving conditions and smaller through-flow conditions than convectively unstable flow. The flow itself appears similar to that for noise-sustained propagating vortices in the convectively unstable regime [19], [24]. Near the inlet vortices are not evident, because the flow enters the system with negligible azimuthal velocity. Farther downstream propagating vortices occur. However, there are several differences with convectively unstable regime [24]. First, the boundary between the nonvortical flow and the propagating vortices is stationary for absolutely unstable flow, but is time dependent for convectively unstable flow. Second, the distance from the inlet to the boundary between nonvortical and vortical flow scales differently in the two flow regimes. Third, the power spectrum of the propagating vortices velocity is much noisier for the convectively unstable regime than for the absolutely unstable regime.

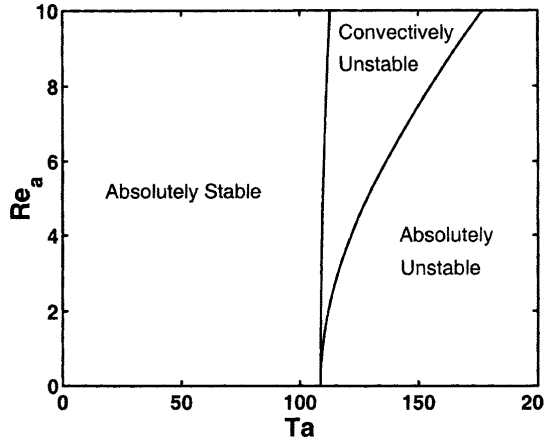

Fig. 2. Bounds for convective and absolute instability at $\eta = 0.85$ based on [20].

All of the studies mentioned to this point were concerned with the first instability transition from stable Couette-Poiseuille flow to translating toroidal vortex

flow or helical vortex flow at relatively low Re and Ta near the critical values. For instance, the stability map shown in Fig. 2 is only valid at relatively low Re. At higher Re nonaxisymmetric spiral modes grow [19]. In fact, a rich variety of flow regimes occur at higher Taylor and Reynolds numbers. The earliest study of higher order instability transitions was undertaken by Kaye and Elgar [16] and extended by others [25], [26]. Kaye and Elgar varied the flow over a wide range of Taylor numbers and axial Reynolds numbers and found two flow regimes in addition to stable Couette-Poiseuille flow and translating Taylor vortex flow. At high Taylor numbers they found a flow regime consisting of turbulent Taylor vortices. At high axial Reynolds numbers they found fully turbulent channel flow with no vortices. Their results indicate that the transition from nonvortical flow to vortex flow is stabilized by the axial flow, while the transition from stable flow to turbulent flow is destabilized by the cylindrical Couette flow.

In the absence of axial flow, several other unstable flow regimes consisting of toroidal vortices have been experimentally observed as the Taylor number is increased. These flow regimes include wavy vortex flow, modulated wavy vortex flow, and turbulent vortex flow [3], [4]. However, as a result of the experimental techniques that they used, the Kaye and Elgar study and its extensions did not differentiate between these different flow regimes. Nevertheless, Schwartz et al. [27] identified the appearance of wavy vortex flow for non-zero axial flow. They found that, like the first instability, the transition from Taylor vortex flow to wavy vortex flow is delayed to a higher Taylor number when an axial flow is imposed. Other studies have mentioned higher-order transitions. Kataoka et al. [28] presented a map of flow regimes in the Taylor number-Reynolds number plane, although they offered minimal explanation of their experimental methodology or their results. Bühler and Polifke [5] also presented a map of flow regimes for a limited range of Taylor and Reynolds numbers. Since their emphasis was on helical vortex flow at low Taylor numbers, they did not differentiate between nonwavy and wavy vortex flow or other higher order instabilities.

Lueptow et al. [6] used visual and optical detection to map the vortical flow regimes over a wide range of Tayor numbers and axial Reynolds numbers. They identified eleven flow vortical flow regimes, depending on Taylor number and Reynolds number, seven of which are shown in Fig. 3. Several types of nonwavy and wavy vortices that appeared (LV, WV) are similar to those that exist for no axial flow, except that the vortices are carried downstream with the axial flow. Translating helical vortices appear at low Taylor number and high Reynolds number. At the lowest Taylor number the helical vortices are nonwavy (HV). But at higher Taylor number the helical vortices become wavy (HWV). At still higher Taylor numbers the vortices are helical and wavy but quite random and disordered in character (RWV). An odd helical flow resulted in a very narrow range of conditions in which the vortices were stationary and had an inclination angle opposite that of all other helical vortex flows (SHV). No explanation could be found for this flow regime, although others have found similar anomalous helical flow regimes [5]. At high Taylor number, the vortices are no longer helical. Interestingly, the number of waves for the wavy vortex regimes decreases

with increasing axial Reynolds number and Taylor number. More recent studies indicate a wide range of translation velocities for the vortices ranging from nearly zero for "stationary vortices" to over two times the average axial velocity [29]. Furthermore, there seems to be no overall trend in the vortex translation velocity with respect to axial Reynolds number or Taylor number. Nevertheless, there seems to be a very strong linear relation between the frequency of axial vortex passage past a point and the frequency of the inner cylinder for helical vortices. The axial vortex passage frequency is exactly two times the rotational frequency of the inner cylinder. There seems to be no theoretical explanation for this result.

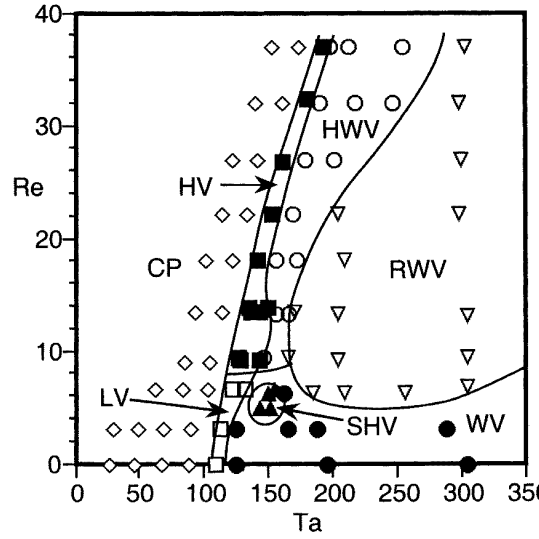

Fig. 3. Flow regimes for cylindrical Couette flow with an imposed axial flow for $\eta = 0.85$ [6]. Symbols represent measurement points: CP=stable Couette Poiseuille flow; LV=laminar vortices; HV=helical vortices; HWV=helical wavy vortices; SHV=stationary helical vortices; WV=wavy vortices; RWV=random wavy vortices. (Reprinted with permission of AIP)

2.2 Velocity field

Although the stability of the flow and the variety of flow regimes for cylindrical Couette flow with an imposed axial flow have been studied in depth, the velocity field has not been studied in detail until recently. Very limited hot-wire and laser Doppler velocimetry (LDV) measurements of the time-averaged axial and azimuthal velocities have been performed [30], [31], [32]. Recently extensive measurements of the instantaneous axial and radial velocity fields have been measured using Particle Image Velocimetry (PIV) [29].

The hot-wire measurements, which were performed at high axial Reynolds numbers ($Re_a > 100$) using air as the working fluid, indicate that the average axial velocity profile is generally parabolic when vortices are present in the annulus [30], [31]. These measurements were made prior to the understanding that a variety of vortical flows could occur, as indicated in Fig. 3. However, more recent Particle Image Velocimetry (PIV) measurements confirm that the axial velocity profile is nearly parabolic, at least at lower axial Reynolds numbers ($Re_a = 23$) regardless of the nature of the vortical state. The normalized time- and space-averaged axial velocity profile is shown in Fig. 4 for five different vortical flow states along with the theoretical axial velocity profile for stable, laminar annular Poiseuille flow. The averaged velocity profiles for unstable flow are remarkably similar to the stable theoretical velocity profile. The only difference seems to be the slightly fuller velocity profile near the inner cylinder resulting from a slight shift of the velocity profile toward the inner cylinder, apparently due to vortical transport of axial momentum toward the inner cylinder. This result is consistent with previous hot-wire studies. Also noteworthy is that the velocity profiles for the five different vortical flow states are quite similar to one another. Together these two results indicate that the vortical flow has only a very small effect on the axial velocity profile and that the effect is largely independent of the details of the vortical flow state.

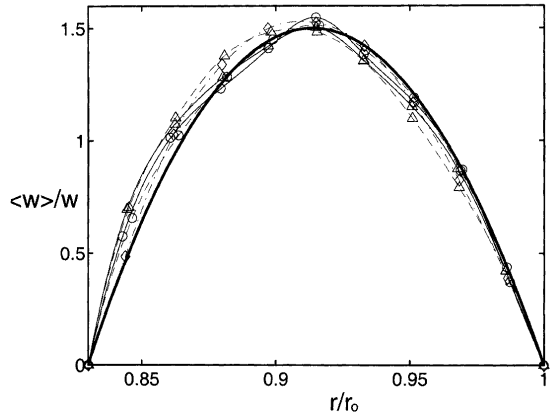

Fig. 4. The normalized average axial velocity profile [29]. Circles: nonwavy vortex flow, Ta=123, $Re_a = 5.3$, $\eta = 0.83$; wavy vortex flow, Ta=139, $Re_a = 5.0$; Triangles: nonwavy helical vortex flow, Ta=129, $Re_a = 14.2$; wavy helical vortex flow, Ta=167, $Re_a = 14.2$; Diamonds: random wavy vortex flow, Ta=215, $Re_a = 23.2$; Heavy solid curve is the theoretical velocity profile for stable, laminar Poiseuille flow. (Reprinted with permission of AIP)

The averaged azimuthal velocity profile is similar to that for Taylor–Couette flow with no axial flow [33]. An example is shown in Fig. 5. Rather than a

linearly varying azimuthal velocity that occurs for nonvortical flow, the velocity profile has steep gradients near both walls of the annulus and a relatively uniform velocity across the middle third of the annular gap. This is a result of the transport of high momentum fluid from near the inner cylinder and low momentum fluid from near the outer cylinder toward the center of the annulus. The net effect is a region near the center of the annulus with a nearly flat azimuthal velocity profile with steep gradients in azimuthal velocity near the walls to achieve the necessary no-slip boundary condition at the walls. Hot-wire measurements of the azimuthal velocity profile at higher axial Reynolds numbers are consistent with this result [30], [31].

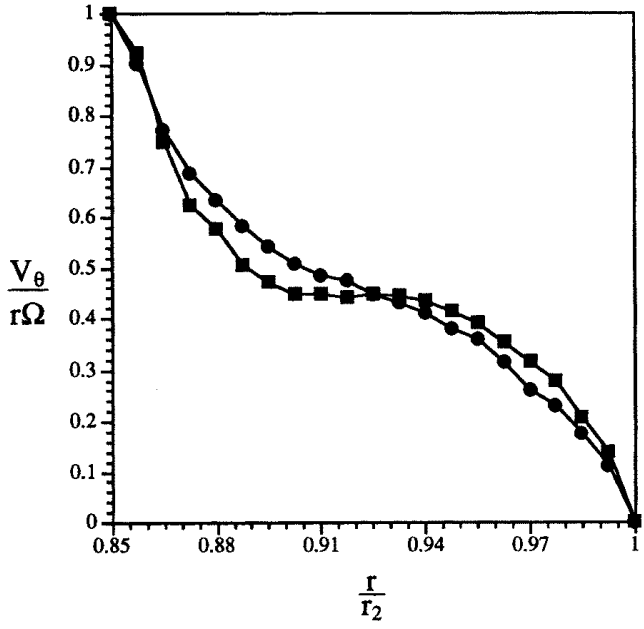

Fig. 5. Average azimuthal velocity profile at Ta=140 and $\eta = 0.85$. Squares: $Re_a = 5.3$; Circles: $Re_a = 16.6$ [32].

Perhaps more interesting are the PIV measurements of the velocity in a meridional plane [29]. Fig. 6 shows the azimuthal velocity contours superposed on the velocity vector field for the non-wavy, non-helical vortices. Fig. 6(a) shows the axial-radial velocity vectors as measured in the frame of reference attached to the apparatus. The left-to-right axial flow is evident as a strong stream of fluid winding around vortices that do not fill the annular gap and appear alternately displaced toward the inner and outer cylinders. This has been called a "winding" flow [34], [35]. However, removing the axial velocity profile, shown in Fig. 6(b), results in vortices that fill the gap, are centered in it, and have stronger outflow

regions than inflow regions. In fact, these vortices appear nearly the same as they would with no axial flow imposed. As indicated in Fig. 4, the spatially averaged axial velocity profile that has been removed in going from Fig. 6(a) to Fig. 6(b) is nearly identical to the velocity profile for stable laminar Poiseuille flow in an annulus. Thus, it appears that winding flow is nearly a linear superposition of annular Poiseuille flow and non-wavy Taylor vortex flow.

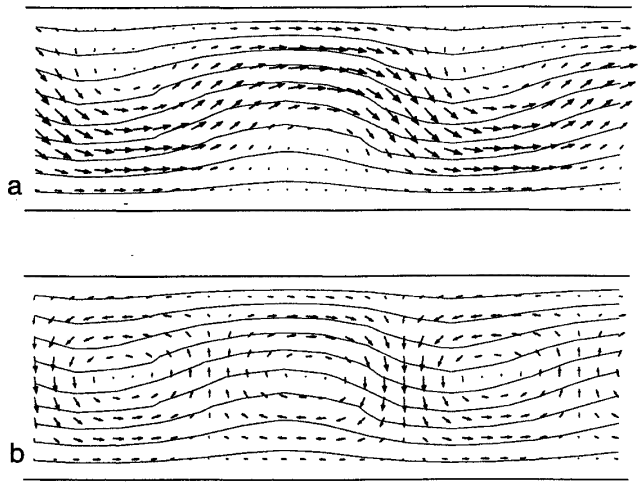

Fig. 6. Radial and axial velocity vectors with azimuthal velocity contours for nonwavy vortical flow at Ta=123, $Re_a = 5.3$, $\eta = 0.83$ [29]. The upper line in each frame is the rotating inner cylinder; the lower line is the stationary outer cylinder. (a) Velocity field including the axial velocity profile. (b) Velocity field with the axial velocity profile removed. (Reprinted with permission of AIP)

The azimuthal velocity component for non-wavy flow can be calculated numerically from the radial and axial velocity components using the azimuthal momentum equation and noting the axisymmetry of the flow [36]. The resulting azimuthal velocity contours in Fig. 6 are distorted from the straight horizontal contours that would appear if no vortices were present. The cause of the distortion is the advection of high azimuthal momentum fluid from near the inner cylinder outward and low azimuthal momentum fluid from near the outer cylinder inward. When an axial flow is present, the extrema are somewhat downstream of the inflow or outflow regions. This result is different from that for non-wavy Taylor vortex flow with no axial flow [36] where the extrema in the bulges of the contours are exactly aligned with the inflow or outflow regions between vortices. The imposed axial flow transports azimuthal momentum downstream at the same time that it is being carried radially, shifting the extrema in the azimuthal velocity contours downstream from the radial outflow regions.

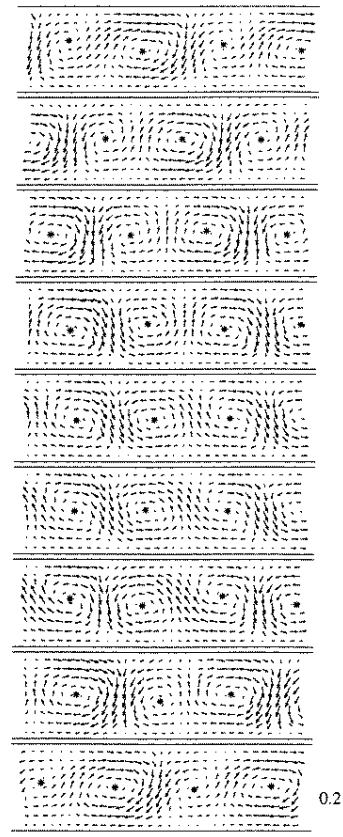

Fig. 7. Radial and axial velocity vectors for wavy vortical flow at Ta=139, $Re_a = 5.0$, and $\eta = 0.83$ [29]. Frames are shown for nine time steps (from top to bottom) spanning the period of one traveling wave, with the first and last frames representing the same phase in the wave. The upper line in each frame is the rotating inner cylinder; the lower line is the stationary outer cylinder. The axial velocity profile has been removed. (Reprinted with permission of AIP)

The situation for vortices that are wavy is much more complicated as shown in Fig. 7 [29]. The velocity field with the axial velocity profile removed is shown at 9 time instants progressing from top to bottom. Eight time instants correspond to the period of one azimuthal wave of the wavy vortex, so that the first and ninth frames depict the same phase of the azimuthal wave. Comparison of the first and last (ninth) frames illustrates the axial translation of the vortices over the period of one azimuthal wave, but the vortices do not translate at a uniform speed. For instance, the counter-clockwise vortex on the left side of the first frame moves downstream (right) in frames 1-4, but then moves upstream in frames 5 and 6, before continuing downstream in frames 7-9. The retrograde motion is related to

the azimuthal waviness. The axial oscillations related to the azimuthal traveling wave add to the axial translation of the vortex due to the axial flow. Thus, the vortices oscillate axially due to the passage of the azimuthal waviness of the wavy vortex, while continually making progress in the same direction as the net axial flow. A fundamental difference between wavy vortex flow and toroidal vortex flow, each with no imposed axial flow, is that a significant portion of fluid is transferred from one vortex to another for wavy vortices [36], [37] whereas toroidal vortices are essentially closed cells. The cyclic transfer of fluid between vortices is also apparent when an axial flow is imposed.

3 Cylindrical Couette flow with an imposed radial flow

Taylor's analysis of the stability of cylindrical Couette flow can also be extended to include a radial through flow in which it is assumed that the walls of the concentric cylinders are porous. Both radial inflow (toward the axis of rotation) and radial outflow (away from the axis of rotation) can be considered. Again the analysis is the standard linear stability analysis. However in this case, the amplification factor is set to zero at the onset of the instability, as is done with the linear stability analysis of Taylor–Couette flow with no axial or radial flow. The resulting eigenvalue problem is solved with the ultimate goal being the determination of the minimum Taylor number and associated wavenumber that satisfy the sixth order ordinary differential equation for specified radial Reynolds number α and radius ratio η.

Chang and Sartory [38], [39] first considered the hydromagnetic stability of an electrically conducting fluid between porous concentric cylinders with a wide gap between the cylinders. Although they were primarily concerned with the asymptotic behavior of the flow at large radial Reynolds numbers, they predicted that radially inward flow through the porous cylinders should stabilize the flow. Radially outward flow should destabilize the flow for weak radial flows but stabilize the flow for strong radial flows. Bahl [40] considered the linear hydrodynamic stability for the case where the gap between the cylinders is small compared to the radius of the cylinders and the axial wavenumber is fixed, rather than being a result of the analysis. His stability analysis indicated that an inward radial velocity stabilizes the flow, while an outward radial velocity destabilizes the flow. Bühler [41], found a similar result in the narrow gap approximation. Reddy and Reddy [42], and Reddy et al. [43] extended Bahl's linear stability analysis to non-Newtonian fluids. In contrast to other results, they concluded that for Newtonian fluids radial inflow destabilizes the flow, and radial outflow stabilizes the flow. But several ambiguities in their analysis hint that their results may be unreliable.

The most recent and thorough analyses of the stability problem are presented by Min and Lueptow [44] and Kolyshkin and Vaillancourt [45]. In both cases, the narrow gap restriction was not imposed. Min and Lueptow considered only axisymmetric perturbations, while Kolyshkin and Vaillancourt considered both axisymmetric and non-axisymmetric perturbations. Non-axisymmetric pertur-

bations are the most unstable ones only for the situation where the cylinders are rotating in opposite directions. For the situation of the outer cylinder fixed, which is of interest here, the axisymmetric perturbations are most unstable.

Figure 8 shows the dependence of the critical Taylor number for the onset of vortical flow on the radial Reynolds number. Radial inflow, corresponding to negative radial Reynolds numbers, increases the critical Taylor number for the four radius ratios considered, ranging from 0.5 to 0.95. Min and Lueptow [32], [44] attributed the stabilizing effect of radial inflow to the location of the appearance of the incipient Taylor vortex. The incipient motion leading to a vortex for cylindrical Couette flow with no imposed radial flow appears first near the inner cylinder and progresses radially outward as the Taylor number increases [14], [46]. The imposition of a radial inflow at the inner cylinder washes the incipient vortex into the porous inner cylinder and out of the annulus delaying the onset of vortical flow. It is also evident from Fig. 8 that a radial outflow (positive radial Reynolds number) also stabilizes the flow. However, expanding the vertical scale of Fig. 8 at small positive radial Reynolds numbers indicates that a small radial outflow destabilizes the flow slightly so that transition to vortical flow occurs at a value a few percent less than the critical Taylor number with no radial flow. Again Min and Lueptow [44], [45] attribute this to the location of the incipient vortical motion near the inner cylinder. A weak radially outward flow carries the incipient vortical motion from near the inner cylinder outward across the annulus, resulting in the supercritical transition at a lower Taylor number. If the outflow is stronger, it overwhelms the incipient vortical motion delaying the onset of supercritical vortical motion to higher Taylor numbers. The axial wavenumber increases with either inflow or outflow [44], [45] resulting in vortices with a longer axial length than radial width.

The radial flow has a significant impact on the position of vortices in the annulus in supercritical flow. Based on the mode shapes of the perturbations in their linear stability analysis, Min and Lueptow [44] were able to create velocity vector plots of the vortices at the point of supercritical transition. For no radial flow, the vortices are centered in the annulus. A radial inflow shifts the vortex centers inward, and a radial outflow shifts the vortex centers outward. This results in a larger axial velocity in the vortex on the side of the vortex that is compressed against the wall.

There appear to be no experimental studies of either the stability or velocity field for cylindrical Couette flow with an imposed radial flow between two porous cylinders. This is probably a consequence of the difficulty of making such measurements. The requirement that both cylinders be porous, and consequently opaque, makes many traditional visual and optical methods of detecting the transition to supercritical flow quite difficult. In addition, devising a flow cell to provide a uniform radial flow at both the inner and outer cylinders is challenging.

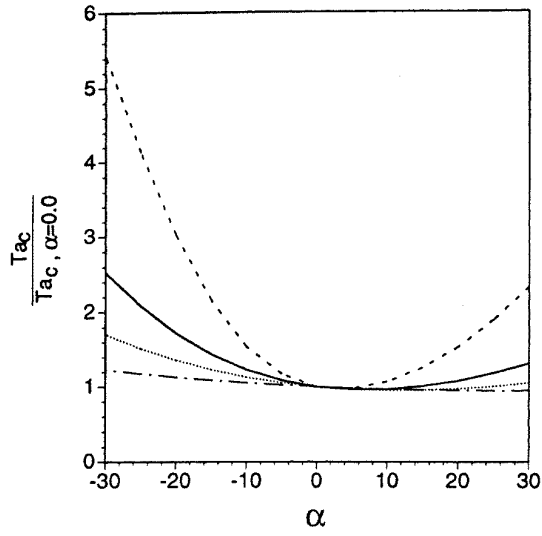

Fig. 8. The effect of radial Reynolds number α on the critical Taylor number Ta_c normalized by the critical Taylor number for no radial flow [44]. Curves are for η=0.5, 0.75, 0.85, 0.95 from top to bottom. (Reprinted with permission of AIP)

4 Combined radial and axial flow

The linear stability analysis of cylindrical Couette flow with an imposed axial and radial flow is substantially more difficult than the analysis for either axial or radial flow alone. The analysis follows generally the same approach as that for axial or radial flow individually, but their appearance simultaneously complicates the analysis. The first attempt at the linear stability analysis for this case was performed by Bahl and Kapur [47]. They considered the narrow gap case for co-rotating porous cylinders with an axial flow, but they made several problematic simplifying assumptions in their analysis by prescribing a simplistic axial velocity profile and fixed values for the axial wave number and amplification factor.

Kolyshkin and Vaillancourt [45] and Johnson and Lueptow [1] simultaneously improved the analysis of the absolute stability limit for cylindrical Couette flow with both an axial and a radial flow. Kolyshkin and Vaillancourt considered both axisymmetric and nonaxisymmetric perturbations at a radius ratio of 0.5 and 0.85. Johnson and Lueptow considered only axisymmetric perturbation at radius ratios of 0.65, 0.75, and 0.85. Both studies conclude that both radial inflow and radial outflow stabilize the flow resulting in transition to vortical flow at a higher Taylor number than with no radial flow as shown in Fig. 9. Johnson and Lueptow noted that a weak radial outflow destabilizes the flow. Both studies concluded that as the radial Reynolds number increases, the critical Taylor number is nearly independent of the axial Reynolds number, as is evidenced by the negligible difference in the curves at different axial Reynolds numbers

in Fig. 9. At small radial Reynolds numbers, Kolyshkin and Vaillancourt found that the nonaxisymmetric modes can be important. Both studies indicate that the wavenumber increases with radial Reynolds number.

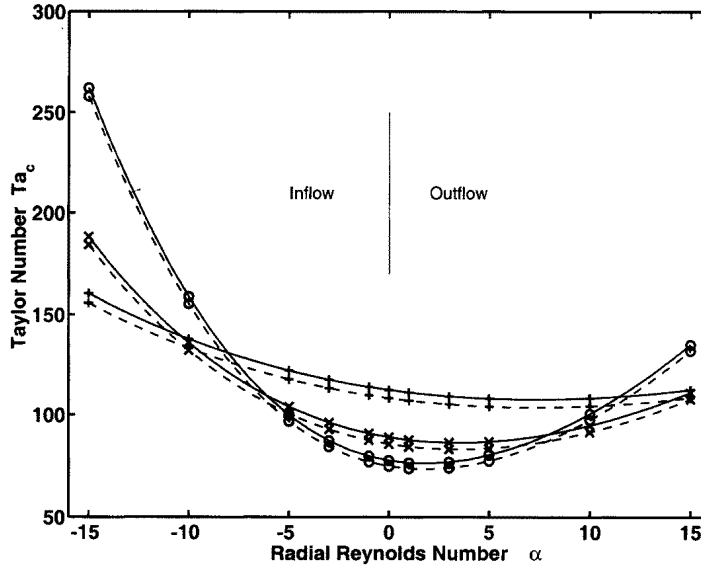

Fig. 9. The effect of radial Reynolds number α on the critical Taylor number Ta_c [1]. Curves are for η=0.65, 0.75, 0.85 from top to bottom. Dashed curves are for $Re_a = 0$; Solid curves are for $Re_a = 10$. (Reprinted with permission of AIP)

An interesting effect of the radial flow is that it increases the velocity at which the vortices translate for radial inflow and strong radial outflow [1]. The vortex translation velocity decreases slightly for a weak radial outflow.

Of course the stability analysis is only valid for the first transition from nonvortical to vortical flow. No measurements have been made for the case of radial flow between two porous cylinders with an imposed axial flow. However, the case of a single rotating inner porous cylinder has been studied in some detail [32]. In this case, the source for the fluid exiting the annulus radially at the inner cylinder is the axial flow. Consequently, the axial flow decreases along the length of the annulus as fluid is removed through the porous inner cylinder.

Like the case of pure axial flow, higher order transitions occur in the case of a rotating porous inner cylinder with axial flow as shown in Fig. 10. The stability map is quite different from that for no radial flow (shown in Fig. 3). Although helical vortices are the most stable state for the initial transition from stable flow to vortical flow at $Re_a > O(10)$ for axial flow only, the radial flow seems to prevent the appearance of this helical vortex structure. Apparently the radial inflow alters the stability such that toroidal vortices are stable even at high axial

flow rates. Since the mechanism for the appearance of helical vortices is unclear, it is difficult to speculate on why a radial flow should prevent helical vortices. Nevertheless, this result is consistent with the nonsymmetric linear stability analysis of Kolyshkin and Vaillancourt [45] indicating that the axisymmetric (toroidal) mode is most stable for radial inflow. They also find a satisfactory comparison between their stability analysis and the experimental results of Min and Lueptow [32], in spite of the differences between the radial through-flow condition of the analysis and the non-porous outer cylinder condition for the experiments.

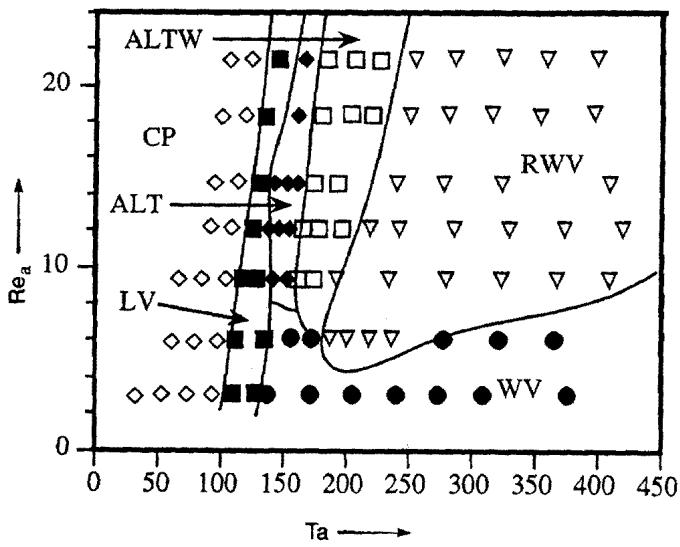

Fig. 10. Flow regimes for cylindrical Couette flow with an imposed axial and radial flow ($\alpha = 0.05$), $\eta = 0.85$) [32]. Symbols represent measurement points: CP=stable Couette Poiseuille flow; LV=laminar vortices; ALT=alternating helical vortices; ALTW=alternating helical wavy vortices; WV=wavy vortices; RWV=random wavy vortices.

Helical vortices appear at higher Taylor numbers, denoted as ALT in Fig. 10. In this case, there is not a single pair of helical vortices as occurs for the case with no radial flow. Instead, groups of helical vortices appear with an alternating sign for the helix angle. Typically, vortices of both signs appear in the annulus simultaneously, each in different axial portions of the annulus. Each helix group consists of five or six vortex pairs. The dislocation between the helix groups translates in the same direction as the axial velocity. New dislocations appear at the inlet to the annulus maintaining the system of alternating helical vortex

groups. At higher Taylor number the vortices of the helical vortex groups become wavy (ALTW).

The wavelength of a vortex decreases as it travels axially in the annulus. In the case studied by Min and Lueptow [32], the vortex wavelength decreased from 2.0d to 1.4d for laminar vortices (LV). The most likely explanation for this is the removal of fluid from an individual vortex due to the radial flow into the inner cylinder. If the vortices translate without intermixing, the removal of fluid necessarily reduces the vortex size. It is unclear what would happen to the vortex structure if the annulus were longer and fluid is continued to be removed from the vortices as they translate axially.

The stability of flow with an inner porous cylinder and an outer non-porous cylinder with an axial flow has not been studied analytically because of the difficulty in obtaining a stable solution for the flow. However, Marques, Sanchez, and Weidman [48] have recently made substantial progress toward a solution based on a generalized similarity formulation. Unfortunately, they point out that determining the stability with respect to three-dimensional perturbations is still quite difficult.

The velocity field in cylindrical Couette flow with an axial and radial through-flow has not been measured, again due to the difficulty in measurements with porous inner and outer cylinders. However, LDV measurements of the azimuthal velocity for the case of a nonporous outer cylinder have been made [32]. For small radial Reynolds numbers, the effect of the radial flow on the azimuthal velocity profile is virtually unmeasureable. The measurement of the velocity field is, however, important to the understanding of the flow field in rotating filter separators.

5 Summary

While stability of Taylor–Couette flow has been studied in great detail, little research has been performed on the effect of relatively small axial and radial flow. The transition from stable to toroidal or helical flow has been studied for the case of an imposed axial flow. But there appears to be no clear explanation for the physics of the origin of helical vortices, although nonaxisymmetric linear stability analysis predicts that nonsymmetric vortices are the most stable configuration under certain conditions. Higher order transitions for an imposed axial flow have not been considered at all except for a handful of experimental studies. Likewise, measurements of the velocity field in Taylor–Couette flow with an imposed axial flow are quite limited. Clearly, much work is necessary to fully understand the stability and velocity field for conditions of high Taylor and axial Reynolds numbers.

The effect of radial flow on cylindrical Couette flow has been studied even less than the effect of axial flow. This is probably a result of the difficulty in making observations or measurements of the flow through porous cylinders. Consequently, the only research on the effect of radial flow has been been linear stability theory. The theory predicts that radial inflow and strong radial out-

flow stabilize the flow, while a weak radial outflow destabilizes the flow slightly. Although a mechanism based on washing out the incipient vortical structure has been proposed to explain this result, it has not been shown that this is the case either analytically or experimentally. In fact, experiments have not been performed to confirm the theoretical prediction that a radial flow enhances stability. Likewise, no measurements or computational results have been published on the velocity field for cylindrical Couette flow with an imposed radial flow.

The combination of axial and radial flow stabilizes Taylor–Couette flow based on linear stability theory. This has not been confirmed by experiments because of the difficulty with observation through porous outer cylinder. However, a few measurements have been made for the case of a porous inner cylinder rotating within a nonporous outer cylinder. In this case, measurements indicate that the stabilizing effect predicted from linear stability theory occurs. Above the critical Taylor number a wide variety of vortical flows occur including helical and helical wavy vortices with dislocations between group of helical vortices of opposite signs. The only velocity measurements that have been made were at a very low radial Reynolds number. These results indicate that the velocity field is nearly the same as that without radial flow.

Much room is available for further work on cylindrical Couette flow with a radial or axial flow. While a practical motivation for such research is the application of rotating filtration, a wide variety of other important issues arise. These include explaining the physical basis for the stabilizing effect of either axial or radial flow, predicting higher order transitions to wavy or helical flow, explaining the wide range of velocities at which vortices translate in axial flow, making measurements of stability and velocity for the case of radial flow through two porous cylinders, determining the effect of suspended particles on the stability and velocity field, and determining the degree of chaotic advection in cylindrical Couette flow with an axial or radial flow. Finally, Taylor–Couette flow with an axial or radial flow offers a unique system in which the stable base flow is easily described analytically, but for which the instability of the flow greatly complicates the character of the system.

References

1. E.C. Johnson, R.M. Lueptow: Phys. Fluids **9**, 3687 (1997)
2. K.C. Chung, K.N. Astill: J. Fluid Mech. **81**, 641 (1977)
3. P.R. Fenstermacher, H.L. Swinney, J.P. Gollub: J. Fluid Mech. **94**, 103 (1979)
4. C.D. Andereck, S.S. Liu, H.L. Swinney: J. Fluid Mech. **164**, 155 (1986)
5. K. Bühler, N. Polifke: 'Dynamical behavior of Taylor vortices with superimposed axial flow'. In: *Nonlinear Evolution of Spatio-Temporal Structures in Dissipative Continuous Systems* ed. by F. H. Busse, L. Kramer (Plenum Press, New York 1990), vol. Series B:Physics Vol. 225, pp. 21
6. R.M. Lueptow, A. Docter, K. Min: Phys. Fluids A **4**, 2446 (1992)
7. G.I. Taylor: Phil. Trans. A **223**, 289 (1923)
8. S. Chandrasekhar: *Hydrodynamic and Hydromagnetic Stability*, (Oxford University Press, 1961)

9. R.C. DiPrima, H.L. Swinney: 'Instabilities and transition in flow between concentric rotating cylinders'. In: *Topics in Applied Physics, Hydrodynamic Instabilities and the Transition to Turbulence*, ed. by H. L. Swinney, J. P. Gollub (Springer-Verlag, Berlin, 1985) pp. 139-180
10. K. Kataoka: 'Taylor vortices and instabilities in circular Couette flows'. In *Encyclopedia of Fluid Mechanics*, ed. by N. P. Cheremisinoff (Gulf Publishing Company, 1986), vol. 1, pp. 237-273
11. E.L. Koschmieder: *Benard Cells and Taylor Vortices* (Cambridge University Press, 1993)
12. S. Chandrasekhar: Proc. Natl. Acad. Sci. **46**, 141 (1960)
13. R.C. DiPrima: J. Fluid Mech. **9**, 621 (1960)
14. M.A. Hasoon, B.W. Martin: Proc. R. Soc. Lond. A **352**, 351 (1977)
15. R.C. DiPrima, A. Pridor: Proc. R. Soc. Lond. A **366**, 555 (1979)
16. J. Kaye, E.C. Elgar: Trans ASME **80**, 753 (1958)
17. H.A. Snyder: Proc. R. Soc. Lond. A **265**, 198 (1962)
18. B.S. Ng, E.R. Turner: Proc. R. Soc. Lond. A **382**, 83 (1982)
19. K.L. Babcock, G. Ahlers, D.S. Cannell: Physical Review Letters **67**, 3388 (1991)
20. A. Recktenwald, M. Lücke, H.W. Müller: Physical Review E **48**, 4444 (1993)
21. D.I. Takeuchi, D.F. Jankowski: J. Fluid Mech. **102**, 101 (1981)
22. K. Bühler: ZAMM **64**, T180 (1984)
23. A. Tsameret, V. Steinberg: Physical Review Letters **67**, 3392 (1991)
24. A. Tsameret, V. Steinberg: Physical Review E **49**, 1291 (1994)
25. K.M. Becker, J. Kaye: J. Heat Transfer **84**, 97 (1962)
26. K. Beranek, I. Streda, J. Sestak: Acta Technica CSA V **24**, 665 (1979)
27. K.W. Schwarz, B.E. Springett, R.J. Donnelly: J. Fluid Mech. **20**, 281 (1964)
28. K. Kataoka, H. Doi, T. Komai: Int. J. Heat Mass Transfer **20**, 57 (1977)
29. S.T. Wereley, R.M. Lueptow: Phys. Fluids **11**, 3637 (1999)
30. K.N. Astill: J. of Heat Transfer **86**, 383 (1964)
31. D.A. Simmers, J.E.R. Coney: Int. J. Heat Fluid Flow **1**, 177 (1979)
32. K. Min, R.M. Lueptow: Exp. Fluids **17**, 190 (1994)
33. S.T. Wereley, R.M. Lueptow: Exp. Fluids **18**, 1 (1994)
34. R.M. Lueptow, A. Hajiloo: Am. Soc. Artif. Int. Organs J. **41**, 182 (1995)
35. M. Stöckert, R.M. Lueptow: 'Velocity field in Couette–Taylor flow with axial flow'. In *10th International Couette–Taylor Workshop*, ed. by C. Normand, J. E. Wesfreid (Paris, 1997) pp. 147-148.
36. S.T. Wereley, R.M. Lueptow: J. Fluid Mech. **364**, 59 (1998)
37. P.S. Marcus: J. Fluid Mech. **146**, 65 (1984)
38. T.S. Chang, W.K. Sartory: J. Fluid Mech. **27**, 65 (1967)
39. T.S. Chang, W.K. Sartory: J. Fluid Mech. **36**, 193 (1969)
40. S.K. Bahl: Def. Sci. J. **20**, 89 (1970)
41. K. Bühler, 'Taylor vortex flow with superimposed radial mass flux'. In: *Ordered and Turbulent Patterns in Taylor–Couette Flow*, ed. by E. D. Andereck, F. Hayot (Plenum Press, New York, 1992) pp. 197-203.
42. P.G. Reddy, Y.B. Reddy: Def. Sci. J. **26**, 47 (1976)
43. P.G. Reddy, Y.B. Reddy, A.G.S. Reddy: Def. Sci. J. **28**, 145 (1978)
44. K. Min, R.M. Lueptow: Phys. Fluids **6**, 144 (1994)
45. A. Kolyshkin, R. Vaillancourt: Phys. Fluids **9**, 910 (1997)
46. N. Gravas, B.W. Martin: J. Fluid Mech. **86**, 385 (1978)
47. S.K. Bahl, K.M. Kapur: Def. Sci. J. **25**, 139 (1975)
48. F. Marques, J. Sanchez, P.D. Weidman: J. Fluid Mech. **347**, 221 (1997)

Transport phenomena in magnetic fluids in cylindrical geometry

Stefan Odenbach

ZARM, University of Bremen, Am Fallturm, 28359 Bremen, Germany

1 Introduction

Flow and properties of suspensions of magnetic nanoparticles - commonly called magnetic fluids or ferrofluids - can significantly be controlled and influenced by the action of weak magnetic fields with a strength below 100 mT. This makes them an interesting medium for various investigations in hydrodynamic research. In particular transport phenomena like the transport of heat, momentum or matter will depend qualitatively as well as quantitatively on the strength and direction of magnetic fields applied to the magnetic fluids under investigation. Due to the usual technique for generation of variable magnetic fields by means of solenoids - providing a homogeneous axial magnetic field - or straight current leading wires - generating an azimuthal field with radial gradient - such investigations are preferably carried out in cylindrical geometry (see Fig. 1), matching the geometry of the magnetic fields applied.

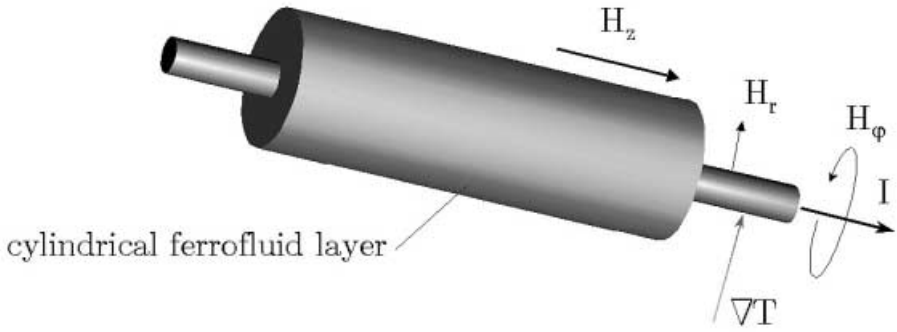

Fig. 1. General sketch of a cylindrical magnetic fluid layer with the magnetic field directions corresponding to the systems symmetries.

In principle coupled experiments, combining rotation of one of the fluid layer boundaries with temperature gradients are possible and will be discussed later on. Following the main topic of this issue we will now focus on the transport of momentum - i.e. on the magnetic field effects in Taylor rotation in magnetic fluids. Beside this we will also shortly discuss the mentioned coupled situation of a magnetic fluid between rotating cylinders subjected to a radial temperature gradient since interesting phenomena have been predicted therefor. This

C. Egbers and G. Pfister (Eds.): LNP 549, pp. 156–170, 2000.

will be discussed in the last chapter of this review. Nevertheless, before starting the description of the mentioned transport phenomena an introduction concerning magnetic fluids and their properties as far as they concern the transport phenomena will be given.

1.1 Magnetic fluids

In the early 60ies a lot of effort has been spend to the development of a liquid material which can strongly be influenced by moderate magnetic fields. Such a material, enabling the control of it's flow and physical properties over a wide range by means of a controllable magnetic force, was expected to give rise to numerous new applications. All known ferromagnetic materials have a Curie point well below their melting temperature. Thus, they loose their ferromagnetic properties before getting liquid. The only exception, undercooled melts of Co-Pd alloys, found to show a magnetic phase transition in 1996 [19,20], is of no technical importance concerning magnetic field controlled flows and related applications. Paramagnetic salt solutions exhibit force densities in the order of 50 $\mathrm{N/m^3}$ in magnetic fields of about 40 kA/m with gradients around 10^6 $\mathrm{A/m^2}$. These values for the field strength and it's gradient are typical for controllable magnetic fields produced with coils. The mentioned force density on paramagnetic salt solutions is about three orders of magnitude smaller than the gravitational force density. Thus they are also not applicable for technical use. Therefore a completely new class of materials had to be developed to meet the necessities of the prospected use of a magnetic fluid. The final breakthrough was made by S. Pappell's success in producing stable suspensions of magnetic nanoparticles in appropriate carrier liquids [13]. These suspensions show liquid behavior coupled with superparamagnetic properties. That means that moderate magnetic fields can exhibit magnetic forces to the liquid, which are comparable to gravitational forces.

Intense efforts undertaken shortly after the discovery of a method of preparation of ferrofluids - as these suspensions are commonly called - forced the development of fluids exhibiting longtime colloidal stability and reproducible properties. Parallel to further development and improvement of the liquids themselves, applications have been published, some of them gaining high commercial importance.

Commercially available ferrofluids contain magnetic nanoparticles with a mean diameter of about 10 nm. To ensure colloidal stability of the liquid, the thermal motion of the magnetic particles has to avoid their sedimentation in the gravitational field and in magnetic field gradients, as well as agglomeration due to magnetic interaction. For particles with a diameter of about 10 nm one can easily calculate that the thermal energy of the particles kT (k denoting Boltzmann's constant and T the absolute temperature) is sufficient to ensure these stability requirements. Nevertheless, colloidal stability of bare magnetic particles of this size in a carrier liquid can not be guaranteed, since agglomeration due to van der Waals attraction will occur as soon as particles come into contact. To avoid irreversible agglomeration of the particles, they have to be protected from coming into contact. This is usually done by means of a surfactant layer

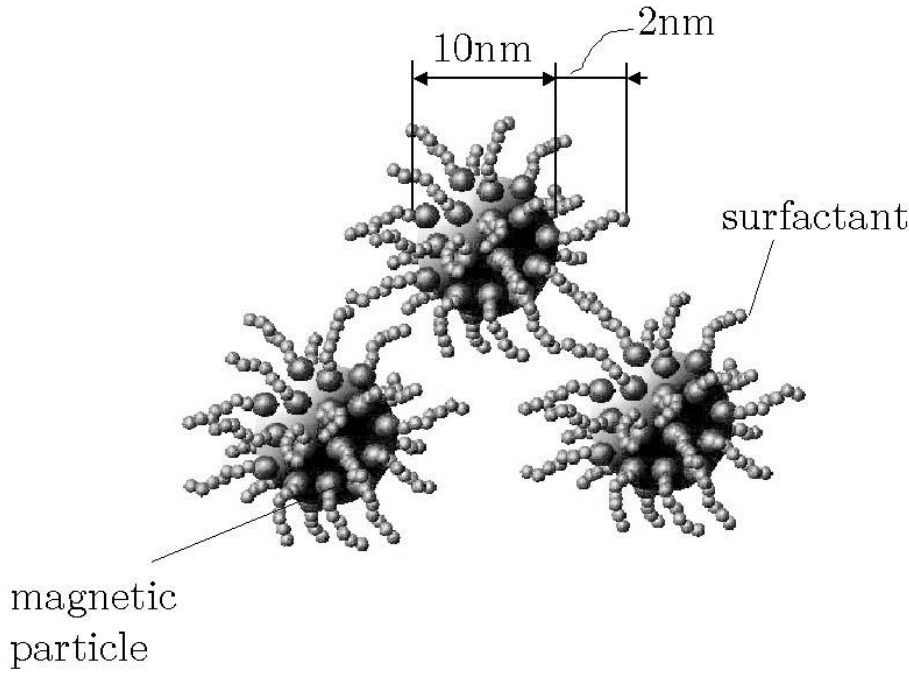

Fig. 2. Schematic sketch of ferrofluid particles with surfactant (for reasons of clearness, particles and surfactant molecules are not shown in scale)

consisting of long chain molecules with a polar head and an unpolar tail (see Fig. 2). The head is attached to the particle, while the tail reaches into the carrier liquid. The molecules have to be chosen in a way, that the dielectric properties of the tails match those of the carrier liquid. Modern ferrofluids contain usually magnetite (Fe_3O_4) as magnetic component. Carrier liquids can be different oils, water, kerosene, heptane or some esters. The surfactant is always chosen to match the dielectric properties of the carrier liquid. As an example acidic acid can be used for magnetite in water, but in general the composition of surfactants in commercial ferrofluids is a secret of the producers. The volume concentration of the magnetic component is usually in the order of 5 vol.% - 15 vol.%.

1.2 Magnetic properties of ferrofluids

The most important feature of magnetic fluids is the combination of normal liquid behavior with superparamagnetic properties. The magnetic particles, having a mean diameter of about 10 nm, can be assumed to be magnetic single domain particles [4]. Thus, their alignment with an external magnetic field will be determined by a counteraction of thermal energy with the magnetic energy of the particle - which can be described as a dipole - in the field. Therefore the mag-

netization M of a ferrofluid follows the well known Langevin law

$$M = M_s(\coth(\alpha) - 1/\alpha) \qquad (1)$$
$$\alpha = \frac{\mu_o m H}{kT}$$

where M_s denotes the saturation magnetization of the fluid, m the magnetic moment of a single particle, H the applied magnetic field, k Boltzmann's constant, T the absolute temperature and μ_o the vacuum permeability. For small values of α, i.e. for weak magnetic fields, one can approximate the expression for M in (1) by

$$M \approx M_s \frac{1}{3}\frac{\mu_o m H}{kT} = \frac{M_s}{3}\frac{\mu_o \pi \bar{d}^3 M_o}{6kT} H = \chi H \qquad (2)$$

with $\bar{d}$ the mean diameter of the particles, the spontaneous magnetization of the magnetic material M_o and the initial susceptibility χ of the fluid. This approximation is valid up to $H \approx$15 kA/m in a fluid with a saturation magnetization of about M_s =32 kA/m containing particles with mean diameter $\bar{d} = 10$ nm.

Using equations (1) and (2) one can obtain important information on the composition of a ferrofluid from a measured magnetization curve like that shown in Fig. 3. First of all one can determine the saturation magnetization of the fluid by extrapolation to $H \to \infty$. Using $M_s = \phi M_o$ one can deduce the volume concentration ϕ if the spontaneous magnetization of the particles magnetic material is known. For magnetite the spontaneous magnetization equals $M_o = 4.5 \cdot 10^5$ A/m [4]. In addition, using the information on saturation magnetization, the initial susceptibility provides the information on the mean size of the particles using equation (2).

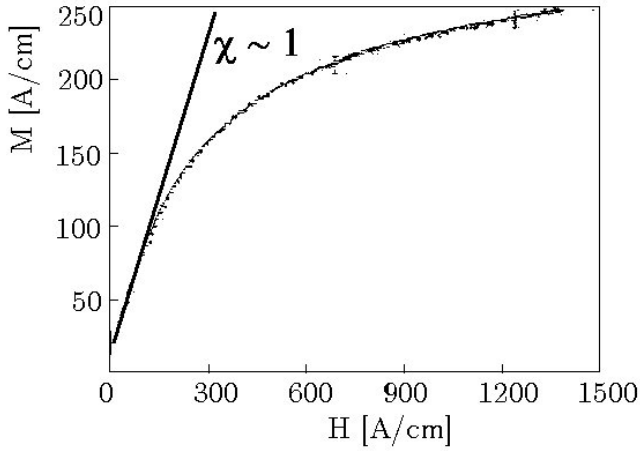

Fig. 3. Typical magnetization curve of a ferrofluid containing approximately 7 vol.% of magnetite particles with a mean diameter of about 10 nm.

The relaxation of magnetization in a ferrofluid is determined by two different processes. On the one hand the magnetization can relax by Brownian motion of the particles in the fluid, on the other hand the magnetic moment can relax inside the particle without a movement of the particle itself - the so called Néel relaxation process [2]. The Brownian relaxation time is given by

$$\tau_B = \frac{3\tilde{V}\eta}{kT} \tag{3}$$

where $\tilde{V}$ denotes the volume of the particles including the surfactant layer and η the dynamic viscosity of the liquid. For the Néel relaxation time it holds

$$\tau_N = f_o^{-1} \exp\left(\frac{K_1 V}{kT}\right) \tag{4}$$

with the crystal anisotropy constant of the magnetic material K_1 and a relaxation frequency f_o that is given by the Larmor frequency of the magnetization vector in the anisotropy field of the particle. For the standard ferrofluid described in the appendix, the Brownian relaxation time will be about $\tau_B = 1.1 \cdot 10^{-5}$ s, while the Néel relaxation will take place in $\tau_N = 2.8 \cdot 10^{-10}$ s (for 10 nm particles). One can easily see, that the Néel process will dominate for small particles, while the relaxation will be due to Brownian particle motion for large ones. Particles relaxing by the latter process are called magnetically hard. For magnetite the transition size between both processes is about 20 nm.

The possibility to exert strong forces on ferrofluids is due to the high initial susceptibility which is in the order of $\chi \approx 1$ compared to $\chi \approx 10^{-4}$ for paramagnetic salt solutions. That means, that the magnetization of the fluid is about three orders of magnitude higher at weak magnetic fields, than it is known from usual paramagnetic liquids. Thus one can easily calculate, that the magnetic force density

$$|F_{mag}| = \mu_o M \nabla H \tag{5}$$

is comparable to the gravitational force for a standard ferrofluid in moderate magnetic field gradients. For example a magnetic field of about $H = 20$ kA/m with a gradient of about $\nabla H = 7 \cdot 10^5$ A/m^2 as it is typically present some 5 cm from a pole of an electromagnet (see Fig. 4) will exert a force density of about 14 kN/m^3 to the standard fluid, while the gravitational force density on the same fluid is approximately 13 kN/m^3.

Thus the magnetic field is able to produce a force strong enough to lift the fluid out of the pool towards the pole of the magnet as shown in the photograph in Fig. 4. This magnetic force enables the control of the flow of magnetic fluids. In addition it gives rise to significant changes in their physical properties.

1.3 Viscous properties of ferrofluids

The most famous field induced property of magnetic fluids is the change of their viscosity. Assuming, that the fluid is subjected to a shear flow with vorticity $\boldsymbol{\Omega}$,

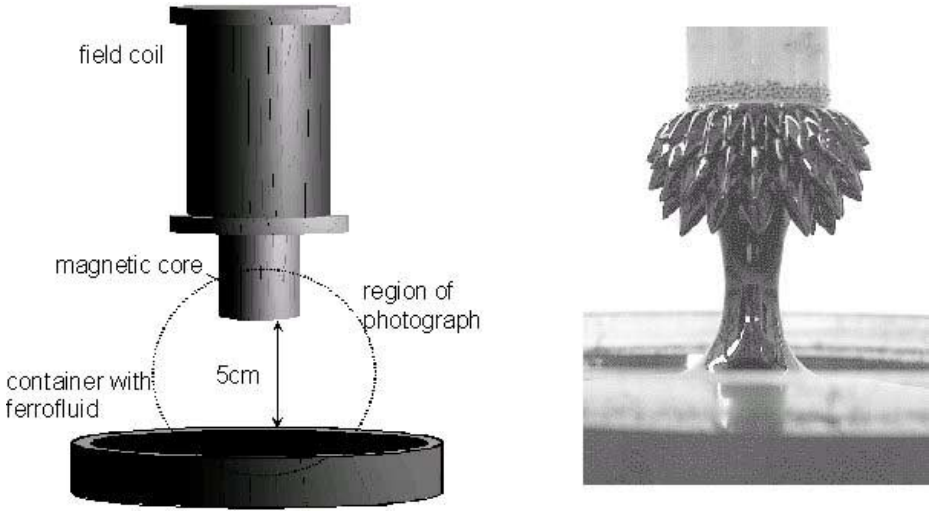

Fig. 4. The attraction of a ferrofluid towards the pole of an electromagnet. The typical spike structure is determined by the strength of the magnetic field, it's gradient, the surface tension of the fluid and earth's gravitational acceleration.

a mechanical torque will be exerted to the particles due to viscous friction at the solid liquid interface. This torque will cause the particle to rotate (see Fig. 5).

It is assumed in the following, that the magnetic moment is fixed in the particle, i.e. the Brownian process determines the relaxation of magnetization in the fluid. If, in this case, a magnetic field is applied to the fluid under shear, it's interaction with the magnetic moment of the particles will give rise to a magnetic torque trying to align the moment - and thus the particle - with the magnetic field direction. If the magnetic field is parallel to the vorticity of the flow, no hindrance of the rotation of the particle will occur (see Fig. 5). In the opposite case, i.e. for $\boldsymbol{H} \perp \boldsymbol{\Omega}$, the viscous flow will twist the particles magnetic moment out of the field direction. This will create a magnetic torque counterdirected to the mechanical torque (see Fig. 5). This magnetic torque hinders the free rotation of the particles, and produces an increase of the fluid's viscosity. This increase is anisotropic, since it depends on the mutual orientation of vorticity and magnetic field. The phenomenon, called rotational viscosity, was theoretically investigated by M. Shliomis [15] in 1972. He found, that for non interacting particles of spherical shape, the viscosity increase $\eta_r = \eta_{(H)} - \eta_{(H=0)}$ can be written in the form

$$\eta_r = \frac{1}{2}\phi'\eta_{(H=0)} < \sin^2(\beta) > \frac{\alpha - \tanh(\alpha)}{\alpha + \tanh(\alpha)} \tag{6}$$

where ϕ' denotes the volume concentration of the magnetic particles including their surfactant and β the mean angle between vorticity $\boldsymbol{\Omega} = \frac{1}{2}\mathrm{rot}\,\boldsymbol{v}$ and mag-

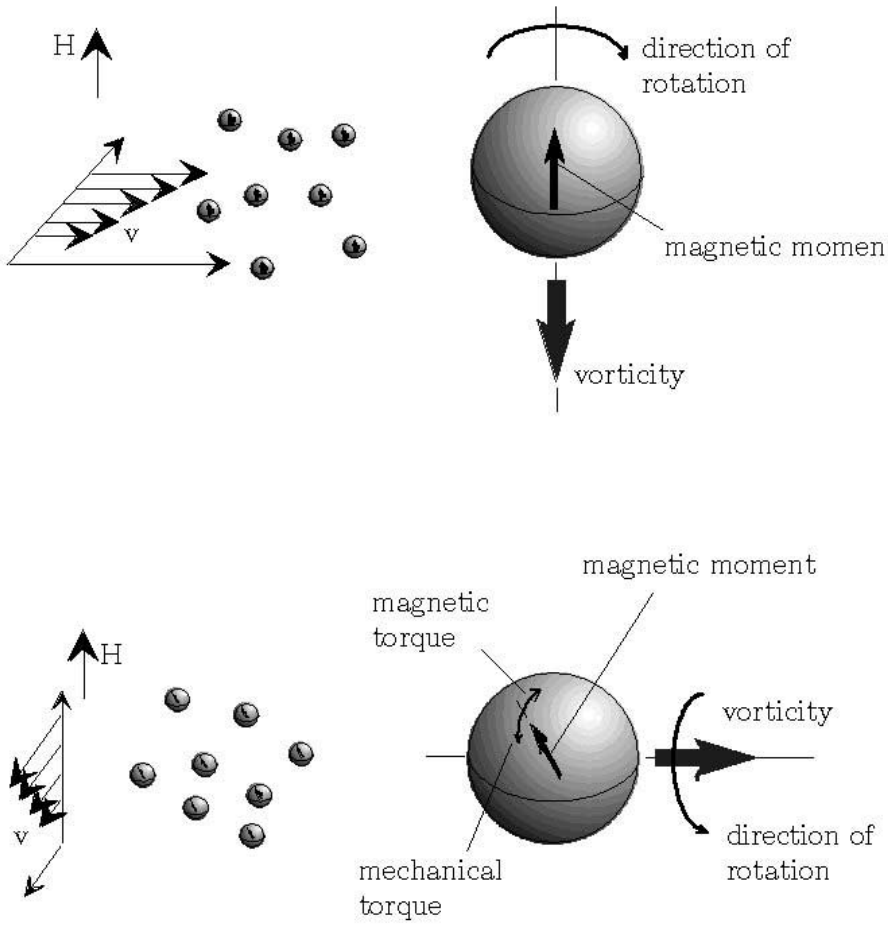

Fig. 5. On the origin of rotational viscosity in a magnetic fluid under magnetic field influence. Explanation see text.

netic field direction. The effect of rotational viscosity has first been observed in highly diluted magnetic suspensions by McTague [6].

In this case good agreement has been found with respect to the theoretical model. Later on experiments have been performed using commercial, concentrated ferrofluids [3,1,10]. In this case strong quantitative differences between experiment and theoretical prediction (6) have been observed (see Fig. 6). These discrepancies can be related to the formation of agglomerates of magnetic particles in the fluid, which first of all would explain the strong rotational viscosity and which would be magnetically hard. This second point overcomes the problem, that single magnetite particles of 10 nm diameter would relax by the Néel relaxation process, and a fluid containing such particles should therefore not

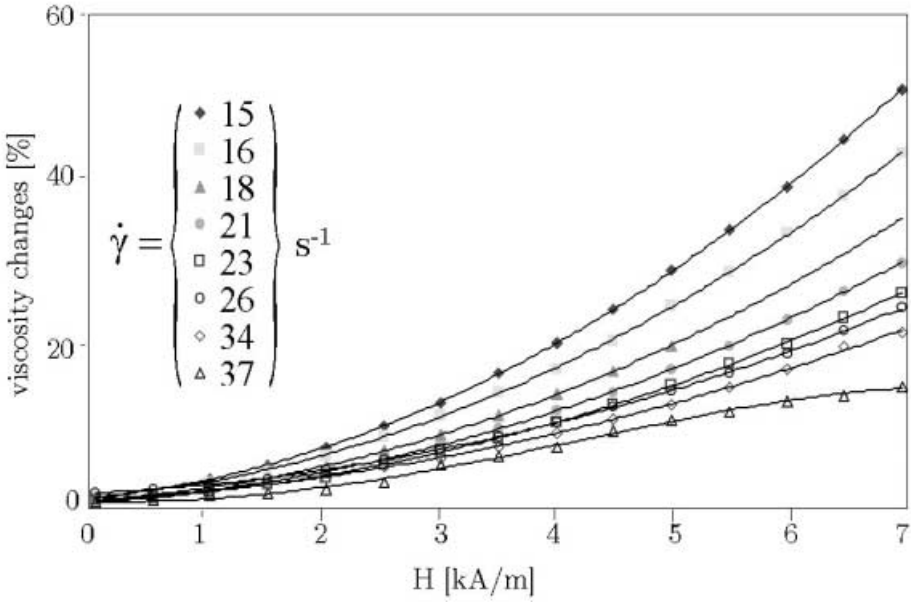

Fig. 6. Magnetoviscous effect in a ferrofluid at low shear rate.

show any rotational viscosity. Such agglomerates are usually formed during the preparation process [12]. In any way Fig. 6 shows clearly, that the magnetoviscous effect in a fluid of reasonable concentration of magnetic particles is strong enough to be necessarily considered in investigations, and in the design of applications of magnetic fluids.

2 Taylor vortex flow in magnetic fluids

2.1 Taylor vortex flow as a tool for magnetic fluid characterization

We will now discuss the problem of an isothermal magnetic fluid contained between two concentric cylinders with the inner cylinder rotating. As it was mentioned before, magnetic fields may change the viscosity of a magnetic fluid due to hindrance of the free rotation of the particles in a shear flow. Thus the flow between concentric cylinders might be used as tool for the determination of rotational viscosity in magnetic fluids.

In principal there are two different approaches to realize viscosity measurement on this basis. On the one hand a typical rheometer setup with a Couette cell could be used. In this case the vorticity of the flow points in axial direction and thus would be parallel to an axial magnetic field. Therefore only radial or azimuthal magnetic fields would be sufficient to induce a change of viscosity in such a measuring set up (see Fig. 7). Azimuthal and radial magnetic fields are - due to the techniques that have to be used for their generation - usually of significantly

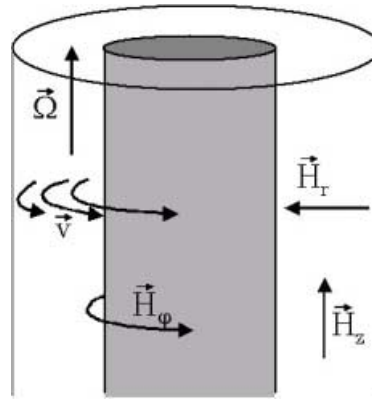

Fig. 7. Vorticity and field direction in Couette flow.

lower field strength than axial fields that may be generated by long solenoids [1]. Thus they are obviously not preferable for the investigation of field induced changes of magnetic fluid viscosity over a wide range of magnetic field strength. Furthermore a prove of the above mentioned theory by Shliomis would require a comparison of results on rotational viscosity obtained for various mutual directions of magnetic field and vorticity. Thus a flow restricting to distinguished field directions decreases the possibility for a check of the $< \sin^2 \beta >$-law.

The second possible way is the observation of the transition from Couette to Taylor vortex flow. It is obvious, that for given temperature, geometry of the fluid layer and rotation frequency f of the inner cylinder, the Reynolds number of the system

$$Re = \frac{2\pi f R_i a}{\nu} \tag{7}$$

(with a: thickness of the fluid layer, R_i: Radius of inner cylinder and ν the viscosity of the fluid) will change with direction and strength of an applied magnetic field since the viscosity is field dependent. Since the critical Reynolds number for the transition from Couette to Taylor vortex flow is constant for fixed geometry of the cylindrical cell, the change of viscosity will cause a change in the critical frequency at which the transition occurs. Thus a determination of the change of the transition frequency will provide a direct measure of the viscosity changes by

$$\frac{\nu(H)}{\nu_o} = \frac{f^*(H)}{f_o^*} \tag{8}$$

where $\nu(H)$ denotes the viscosity in a magnetic field, ν_o the viscosity without field and $f^*(H)$ and f_o^* the respective transition frequencies.

Independent from the direction of the magnetic field this will cause an increase of the critical frequency for the transition from Couette to Taylor vortex flow. This can immediately be understood, if one remembers, that the vorticity

of Taylor vortex flow varies spatially in a way that it's angle to each of the three field directions discussed before differs from $\pi/2$ in most positions, thus the factor $< \sin^2 \beta >$ is larger than zero for each of the field directions. It's actual value can be computed from numerical flow profiles for Taylor vortex flow [5] and one finds for an axial magnetic field $< \sin^2 \beta >= 0.68$, for a radial field 0.69 and for the azimuthal case 0.63.

Since magnetic fluids are optically opaque, the transition from Couette to Taylor vortex flow (TVF) can not be observed by the usual optical means as e.g. direct flow visualization with tracers or LDA. The alternate measuring technique used with magnetic fluids is the determination of the torque forcing the rotation of the inner cylinder as a function of it's rotation frequency. The linear relation that holds for the dependence of the torque on frequency as well for the Couette as for the TVF region has different slopes in both regions. If the viscosity of the fluid changes due to the action of a magnetic field, the critical frequency, and thus position of the slope change will vary too (see Fig. 8).

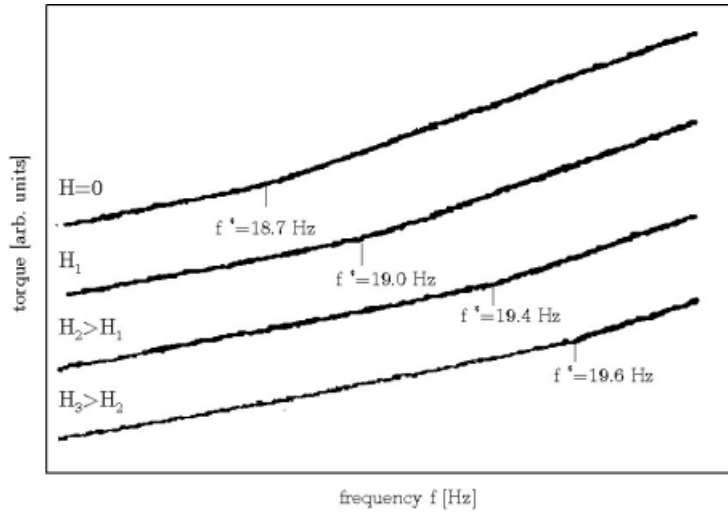

Fig. 8. The change of critical frequency in Taylor Couette flow due to the increase of viscosity in a magnetic fluid caused by the action of a magnetic field.

It is obvious that the determination of the frequency where the slope of the torque-frequency relation changes provides immediately the critical frequency for the onset of TVF. An experimental realization of this concept, providing the possibility to apply magnetic fields in all three mentioned field directions requires a double gap system as it was used in [1]. Such a system ensures that no additional friction due to sealing between the rotating cylinder and e.g. current feedthroughs in the inner cylinder for production of the azimuthal field will occur. This reduction of friction is necessary to ensure proper determination of the critical frequency and it's field induced shift from the torque curves.

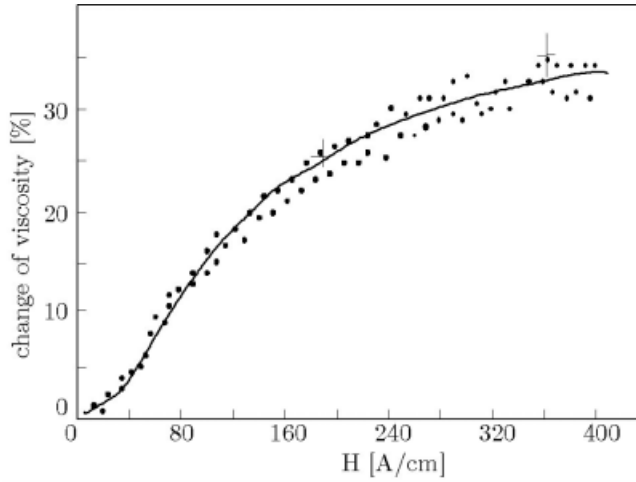

Fig. 9. Viscosity increase in an axial magnetic field measured by means of the shift of critical frequency in TVF [1].

Using this technique, the increase of viscosity in a magnetic fluid has been determined for all three field directions [1,10]. Fig. 9 shows the increase of viscosity measured this way for the case of an axial field. The absolute value of the increase is significantly lower than in the situation shown for the rheometer measurement (Fig. 6). This is due to the fact, that the results shown here were obtained with a much higher shear rate of about 500 s^{-1}. The increase of shear rate causes a break of magnetically induced structures in the fluid and thus leads to a reduction of the magnetoviscous effects. The advantage of this break of structures and thus of measurements at high shear rates is given by the fact, that the theory by Shliomis deals with independent particles and not with structures. Therefore higher shear rates provide data more sufficient for a comparison with the theoretical predictions. In particular the possibility to apply magnetic fields in three different directions allows a proof of the $< \sin^2 \beta >$-law in equation (6).

The definition of a reduced rotational viscosity, given by

$$S^*(H) = \frac{\eta_r(H)}{\eta_o < \sin^2 \beta >} \tag{9}$$

makes the results independent from the relative orientation of field and vorticity and thus allows a direct comparison of the results for different field geometries. Due to the fact that radial and azimuthal magnetic fields can only be generated with relatively low field strength, Fig. 10 shows this comparison for the three mentioned field directions in the region of weak magnetic fields. Obviously all three curves coincide within the margin of error, giving a good proof for Shliomis' theory.

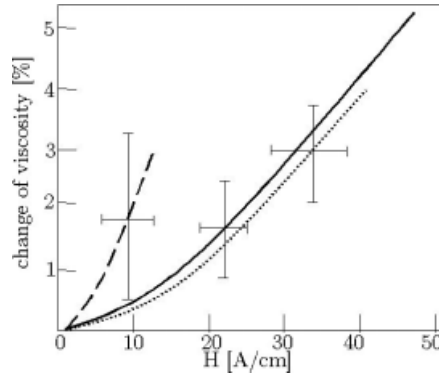

Fig. 10. Viscosity changes for various mutual directions of field and vorticity. Full line: axial field, dashed line: azimuthal field, dotted line: radial field. All curves are given with representative error bars.

2.2 Changes of the flow profile in magnetic fields

As it was shown, the appearance of rotational viscosity forces a shift of the critical frequency of Taylor–Couette flow. Beside this the change of the viscous properties of ferrofluids under influence of magnetic fields causes changes in the flow profile of TVF. As it was already mentioned, the viscosity changes have strongly anisotropic character, varying with the angle between vorticity of the flow and magnetic field direction. In a complex flow like TVF with spatially varying vorticity this will force a preference of those flow directions causing a contribution to vorticity which is as parallel to the magnetic field direction as possible.

For a simplified discussion of the influence of magnetic fields on the structure of TVF we divide the flow into an azimuthal contribution and a superimposed circular contribution in the $z - r$-plane (z: direction along the cylinder axis, r: radial direction). The azimuthal component of the flow will cause a contribution to the total vorticity which is vertical to the field for radial and azimuthal fields and parallel to an axial field. For azimuthal magnetic fields the vorticity of the superimposed circular flow is parallel to the field direction and thus no deformation of the profile will appear. If a radial field is applied, the vorticity for the azimuthal base flow and the superimposed flow are both perpendicular to the field and the combination of the effects results finally in a reduction of wavelength. Contrary to this an axial magnetic field will cause an increase of wavelength since only the circular flow is influenced by the field.

These changes of the flow profile have been independently predicted by Niklas [7] and Vislovich et al. [8]. To observe them experimentally a measuring technique for the determination of isothermal flow profiles in opaque fluids is needed. A technique enabling such kind of investigations is the use of pulsed ultrasound Doppler velocimetry (PUDV) providing position dependent velocity information from a liquid containing tracers scattering the ultrasound waves. This technique has been introduced by Takeda [17] for use with liquid metals. As it was shown,

even weak scatterers like impurities in liquid mercury provide sufficient scattered ultrasound intensity to allow a reliable velocity determination. In the case of ferrofluids, the suspended particles themselves can be used as appropriate scatterers [9]. Using Takeda's ultrasound equipment, we've carried out a test experiment to check the use of PUDV for the determination of field induced wave-length changes in magnetic fluid TVF. Therefore the ultrasound transducer was mounted on the bottom of the fluid gap with the ultrasound beam parallel to the cylinder axis (see Fig. 11).

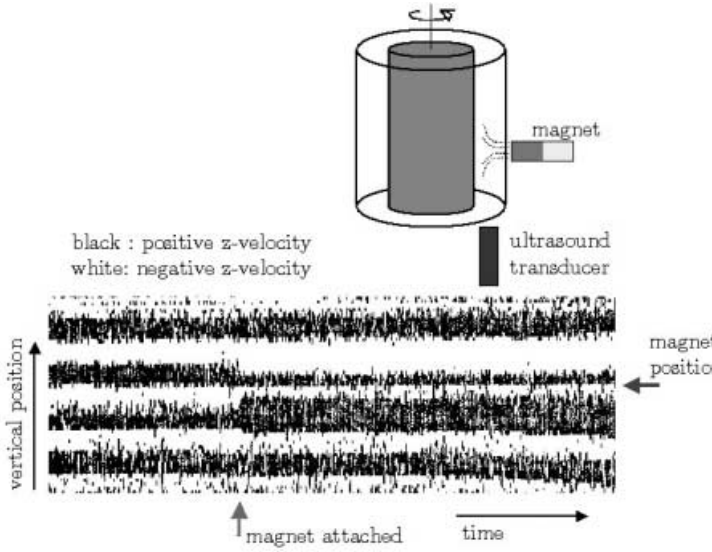

Fig. 11. Test experiment for the determination of the influence of a magnetic field on the flow profile of magnetic fluid TVF and of the suitability of PUDV for the detection of velocities in ferrofluids.

The velocity was taken as a function of time at 128 vertical positions in the fluid gap and plotted as a time series using white for velocities towards the transducer and black for velocities in the opposite direction, i.e. in positive z-direction. As it is seen from Fig. 11., a periodic pattern is observed, indicating normal undisturbed TVF. At a certain instant of time a permanent magnet was attached to the wall of the outer cylinder, providing a radial magnetic field in a small region of the flow. As it can be observed in Fig. 11., the application of this radial field forces the flow profile to change and induces a smaller wavelength in the region of the magnetic field as it was predicted in [7,8]. Even this rough test shows, that the PUDV is suitable for the investigation of magnetic fluid TVF and that interesting effects of magnetic fields on this flow phenomenon have to be expected.

3 Taylor vortex flow in magnetic fluids with radial heat gradient

In various experiments it has been shown, that not only TVF of ferrofluids can be influenced by magnetic fields. In particular a lot of effort has been spend to investigate the changes of heat transfer processes in ferrofluids due to magnetic field action, and various new effects like the appearance of thermomagnetic convection [11] and it's influence on thermal convection [14] were discovered. Until now a combination of both effects, i.e. TVF in a ferrofluid under influence of magnetic fields and a radial temperature gradient has only theoretically been discussed [16]. Assuming a radial magnetized commercial ferrofluid with a pyromagnetic coefficient (variation of magnetization with temperature) in the order of 50 A/Km in a small gap one has in general to distinguished two different cases. For the situation of a weak magnetic field in the order of several 10 mT the critical Reynolds number is practically independent from the radial temperature gradient for temperature differences of several Kelvin over a 1 mm gap. This corresponds well to the weak dependence of stability of Couette flow against radial temperature gradients, that has been found for nonmagnetic fluids earlier [18]. In contrary a strong magnetic field will significantly influence the stability of Couette flow subjected to a radial temperature gradient. It was shown in [16], that increasing temperature difference will reduce the critical Reynolds number to zero, i.e. the fluid layer will be destabilized by thermomagnetic convection only. Up to now no predictions concerning the flow profile of TVF and it's dependence on superimposed thermomagnetic convection have been made for the interesting intermediate range where thermomagnetic convection and TVF are coupled.

4 Conclusion and outlook

As it was discussed above transport phenomena in magnetic fluids may strongly be influenced by the action of magnetic fields. For the special case of TVF in ferrofluids the characteristics of the changes are not yet experimentally proved due to the difficulties in the determination of the flow profile in a magnetic fluid. Nevertheless this field provides a variety of new and interesting effects that could be investigated. Especially the work of Niklas [7] provides numerous calculations concerning asymmetries of the flow profile, changes in the velocity of wave propagation after sudden changes of Reynolds number and time dependent changes of the flow profile. Beside this the calculations of Stiles show that further interesting problems appear as soon as the coupling between different transport mechanisms is considered [16]. Thus, the use of magnetic fluids in TVF opens the possibility to investigate various new effects which can directly be controlled by means of strength and direction of the applied magnetic fields. Beside the basic interest in this question, such investigations have high importance for the optimization of applications of magnetic fluids since numerous applications - like e.g. the often used sealing of rotating shafts with a ferrofluid - have comparable

geometries to TVF and subject the fluid to external influences due to magnetic fields and temperature differences similar to those discussed above.

References

1. O. Ambacher, S. Odenbach, K. Stierstadt: *Rotational viscosity in ferrofluids.* Z. Phys. B-Condensed Matter **86** 29 (1992)
2. P. Fannin, B. K. P. Scaife, S. W. Charles: *Relaxation and resonance in ferrofluids.* J. Magn. Magn. Mat. **122** 159 (1993)
3. M. Holderied, L. Schwab, K. Stierstadt Z. Phys. B-Condensed Matter **(**70) 257 (1988)
4. E. Kneller: *Ferromagnetismus.* 1st edition, (Springer-Verlag, Berlin 1962).
5. M. Lücke priv. comm.
6. J. P. McTague: *Magnetoviscosity of magnetic colloids.* J. Chem. Phys. **51**, 1 133 (1969)
7. M. Niklas: *Taylor-Wirbel Strömung von Ferrofluiden im Spalt zwischen konzentrischen rotierenden Zylindern im Magnetfeld.* Ber. KFA Jülich **Jül-2246** (1988)
8. A. N. Vislovich, V. A. Novikov, A. K. Sinitsyn J. Appl. Mech. Tech. Phys. **27**, 1 72 (1986)
9. S. Odenbach: *Taylor Rotation in magnetischen Flüssigkeiten Diplom Thesis,* University of Munich (1989)
10. S. Odenbach, H. Gilly: *Taylor vortex flow of magnetic fluids under the influence of an azimuthal magnetic field.* J. Magn. Magn. Mat. **152** 123 (1996)
11. S. Odenbach: *Microgravity experiments on thermomagnetic convection in magnetic fluids.* J. Magn. Magn. Mat. **(**149) 155 (1995)
12. K. O'Grady, H. K. Stewardson, R. W. Chantrell, D. Fletcher, D. Unwin, M. R. Padur. IEEE Trans. Magn. **22**, 5 1134 (1986)
13. S. S. Papell U.S. Patent No.3,215,572 (1965)
14. L. Schwab: *Konvektion in Ferrofluiden Doctoral Thesis,* University of Munich (1990)
15. M. Shliomis: *Effective viscosity of magnetic fluids.* Sov. Phys. JETP **34**, 6 1291 (1972)
16. P. J. Stiles, P. J. Blennerhassett: *Stability of cylindrical Couette flow of a radially magnetized ferrofluid in a radial temperature gradient,* J. Magn. Magn. Mat. **122** 207 (1993)
17. Y. Takeda: *Measurement of velocity profile of mercury flow by ultrasound Doppler shift method.* Nuclear Technology **79** 120 (1987)
18. J. Walowit, S. Tsao, R.C. DiPrima: Trans. AME: J. Appl. Mech. **31** 585 (1964)
19. G. Wilde, G. P. Gorler, R. Willnecker: *Specific heat capacity of undercooled magnetic melts.* Appl. Phys. Lett. **68**, 21 2953 (1996)
20. G. Wilde, G. P. Gorler, R. Willnecker: *The specific heat of highly undercooled (Co, Ni, Fe)-Pd melts.* J. Non-Cryst. Solids **205-207**, 1 317 (1996)

Secondary bifurcations of stationary flows

Rita Meyer-Spasche[1], John H. Bolstad[2], and Frank Pohl[1]

[1] MPI für Plasmaphysik, EURATOM-Association, D-85748 Garching, Germany
[2] Laurence Livermore National Laboratory, L-23, U of California, POB 808, Livermore, CA 94550, USA

Abstract. Numerical investigations of stationary Taylor vortex flows with periodic boundary conditions led Meyer-Spasche/Wagner [13] to speculate that there is a curve of loci of secondary bifurcations in the (period, Reynolds number)-plane which connects two *double points*, i.e. two intersection points of neutral curves of flows with different numbers of vortices (n-vortex flows, $n = 2, 4$, and a double vortex flow). Lortz et al. [12] proved analytically the existence of such a curve for a model problem derived from the equations of the Boussinesq approximation, and also the existence of a second such curve.

It remained unclear then if the results carry over to the full Boussinesq system and thus to the narrow-gap approximation, and how the results generalize to flows with other numbers of vortices. These questions were treated in [14]. In the present contribution we continue these investigations and present computations that justify speculations in [14] about the structure of other secondary interactions. We also present a curve of Hopf bifurcation points which was found in the course of computations discussed here, as a by-product.

1 Stationary Taylor-vortex flows

Consider steady axisymmetric flows in a wide gap between long concentric cylinders, neglecting end effects (periodic boundary conditions). With both cylinders rotating, there are four parameters in the problem: The Reynolds number Re, the axial period λ, the radius ratio η, and the rotation rate μ. The code TAYPERIO solves the Navier–Stokes equations for such flows with $\mu = 0$ numerically, using the very reliable methods described in [13,14]. The code allows systematic variation of Re and λ (method of continuation with Gauss-Newton iterations).

Numerical investigations of stationary Taylor vortex flows with this code led the authors of [13] to speculate that there is a curve of loci of secondary bifurcations in the (λ, Re)-plane which connects two *double points*. One of them is the intersection point of the neutral curve of the basic 2-vortex flow with its periodic repetition (4-vortex flow), called 'the (2,4)-double point'. The other one is the intersection point of the neutral curve of the 4-vortex flow with that of the double-vortex flow (2 vortices in radial direction), called 'the (d,4)-double point'.

Lortz et al. [12] proved analytically the existence of such a curve for a model problem: a system of 7 ordinary differential equations derived from the equations of the Boussinesq approximation for infinitely large Prandtl number. They also showed the existence of a second, unbounded, curve starting in the analog of the (2,4)-double point.

C. Egbers and G. Pfister (Eds.): LNP 549, pp. 171–193, 2000.

A comparison of the model system of [12] with the 3rd order approximation of the Boussinesq equations used by Knobloch et al. [10] showed mainly the following differences [14]:

- The bifurcation analysis of [10] is done locally, in a neighborhood of the $(2k, 2k+2)$-double point, $k = 1, 2, \ldots$, with a system of 9 equations. The analysis of [12] applies globally, i.e. for varying wave number and Rayleigh number, in a region of the (wave number, Rayleigh number)-plane which covers several intersection points of neutral curves, not only the $(2, 4)$-double point.
- In the case $k = 1$, the systems of equations used in [10] and [12] are the same except that two modes are neglected in [12] which must be kept in a 3rd order perturbation approach.

Though the system treated in [12] has its own interest as a model problem (it is a generalized Lorenz system in the sense of Curry [7]), it was desirable to know if the results obtained carry over to the full Boussinesq system with rigid boundary and thus to the narrow-gap approximation. This question is approached here in two steps:

First we review analytical and numerical investigations of the model problems with 7 and 9 equations. We report that a detailed comparison showed that both systems essentially yield the same results, i.e. the numbers computed are different, but the maximum absolute errors caused by neglecting those two equations are small enough to be neglected. This simplifies the analysis of interactions caused by other double points and thus led to predictions of which two double points are connected by curves of secondary bifurcations. Details of these investigations are given in ([14], p.160ff).

Then we report in detail on investigations of those curves of secondary bifurcations for the full Boussinesq system with rigid boundaries on top and bottom. In particular we show that one of the predictions of [14] could be verified. The Rayleigh–Bénard code used for these investigations was constructed from the Taylor–Couette code developed by Bolstad [1] for steady, axisymmetric, incompressible flow. This code performs one-parameter continuation for computing solutions (flows) and two-parameter continuation for computing paths of critical points (pitchfork bifurcation points, transcritical bifurcation points or fold points).

2 Convection rolls with stress-free boundaries

Consider steady convection rolls between infinitely extended horizontal planes, the lower one heated. Let x denote the horizontal and z the vertical direction. The temperature deviation from the conduction solution is denoted by θ, and the velocity by v. We introduce the stream function ψ satisfying $v_x = -\partial_z \psi$, $v_z = \partial_x \psi$, and get from the Boussinesq approximation in dimensionless form [6]

$$(\partial_z \psi \partial_x - \partial_x \psi \partial_z) \Delta \psi = -\mathrm{Pr}\ Ra\ \partial_x \theta - \mathrm{Pr}\ \Delta^2 \psi, \tag{1}$$

$$(\partial_z \psi \partial_x - \partial_x \psi \partial_z) \theta \quad = -\partial_x \psi - \Delta \theta. \tag{2}$$

Here Ra is the Rayleigh number and Pr the Prandtl number. We first consider the perfect problem, i.e. the problem with stress-free boundary conditions (no tangential stresses) on top and bottom and periodic boundary conditions in the horizontal direction. With the period $2\pi/\alpha$ the boundary conditions then read

$$\begin{aligned}
\partial_{zz}\psi(x,0) &= \partial_{zz}\psi(x,1) = 0, \\
\psi(x,0) &= \psi(x,1) = 0, \qquad 0 \le x \le \frac{2\pi}{\alpha}, \\
\theta(x,0) &= \theta(x,1) = 0, \\
\partial_z\psi(0,z) &= \partial_z\psi(\frac{2\pi}{\alpha},z), \\
\partial_x\psi(0,z) &= \partial_x\psi(\frac{2\pi}{\alpha},z), \qquad 0 \le z \le 1, \\
\theta(0,z) &= \theta(\frac{2\pi}{\alpha},z).
\end{aligned} \tag{3}$$

The configuration and the equations allow a reflection symmetry with respect to the mid-plane $z \equiv 1/2$ which we can formulate as [5]

$$\partial_x\psi(x, z-\frac{1}{2}) = -\partial_x\psi(\frac{\pi}{\alpha} - x, -z+\frac{1}{2}). \tag{4}$$

The usual Fourier expansion of the stream function ψ and the temperature deviation θ in both spatial directions [7,10,12,14]

$$\psi(x,z) = \sum_{i=1}^{M}\sum_{j=1}^{N} \psi_{ij}\sin(i\alpha x)\sin(j\pi z), \tag{5}$$

$$\theta(x,z) = \sum_{k=0}^{M}\sum_{l=1}^{N} \theta_{kl}\cos(k\alpha x)\sin(l\pi z), \tag{6}$$

produces a system

$$G(Ra, \mathrm{Pr}, \psi_{ij}, \theta_{ij}, a_{ij}, b_{ij}, c_i; M, N) = 0 \tag{7}$$

of infinitely many equations for the Fourier coefficients if $N = M = \infty$. For finite M and N we obtain a system of $MN + (M+1)N = N(2M+1)$ equations. For sufficiently large M and N this is a satisfactory Galerkin approximation to eqs. (1) – (3). Here we used the abbreviations

$$a_{ij} := i^2\alpha^2 + j^2\pi^2, \qquad b_{ij} := \frac{i\alpha j\pi}{4}, \qquad c_i := i\alpha. \tag{8}$$

Detailed forms of system (7) are given in ([14],eqs. (4.74)– (4.76) for general N, M and eqs. (4.78)–(4.91) for $N = 2, M = 3$).

It should be noted, however, that this ansatz restricts the solution manifold to solutions which are skew-symmetric with respect to $x \equiv 0$. According to Busse and Or [5], we are actually losing solutions that way. In the present contribution

we are interested in curves similar to the curve of secondary bifurcations shown in ([14], Fig. 3.24). The related solutions are skew-symmetric in the horizontal direction. This justifies the approach (5). As is seen from eq. (2), ψ and θ are phase-shifted by $\pi/2$ in the x-direction, and this explains the ansatz (6). With the ansatz (5), (6), the boundary conditions (3) are identically satisfied.

2.1 Critical curves of the primary solution

System (7) depends on three parameters: Rayleigh number Ra, Prandtl number Pr and the wave number α, which is hidden in the coefficients defined in (8). For the following, let N and M be large. For small values of Ra the system is uniquely solvable by the *conduction solution* $\psi_{ij} = 0, \theta_{ij} = 0$ for all values of Pr and α. For larger Ra, this conduction solution is unstable, and convection occurs. To compute the critical values for the bifurcation of the convection solutions from the conduction solution, we linearize system (7) at the conduction solution and require that the determinant vanishes. We obtain a linear system which depends only on Ra and α, but not on Pr. The system is reducible with respect to the unknowns ψ_{ij} and θ_{ij}. The quantities ψ_{11} and θ_{11} occur only in two equations. We thus get the critical values $Ra^{11}_{cr}(\alpha)$ for the lowest modes ψ_{11}, θ_{11} from a 2x2 determinant. The critical curve reads

$$R^{11}_{cr}(\alpha) := \frac{a^3_{11}}{c^2_1} = \frac{(\alpha^2 + \pi^2)^3}{\alpha^2}. \tag{9}$$

It gives the loci in the (α, Ra)-plane where the 2-roll convection solutions bifurcate from the conduction solution ([6], p. 35).

Along the same lines we get the critical curves for the other modes ψ_{pq}, θ_{pq} since these formulas reproduce the periodicity of the boundary conditions and are independent of the truncation parameters N and M, as long as $p < M,\ q < N$. Thus the determinant reads in general

$$\begin{vmatrix} a^2_{pq} & -c_p Ra \\ c_p & -a_{pq} \end{vmatrix} \tag{10}$$

and leads to

$$R^{pq}_{cr}(\alpha) = \frac{a^3_{pq}}{c^2_p} = \frac{(p^2\alpha^2 + q^2\pi^2)^3}{(p\alpha)^2} \tag{11}$$

for the p, q^{th} critical curve. At this curve convection solutions of eq. (7) with p pairs of rolls in the horizontal direction and q rolls in the vertical direction bifurcate from the basic conduction solution, $p < M,\ q < N$. All these bifurcations are of the pitchfork type (Z_2-symmetry preserving). The first six curves ($p \le 3,\ q \le 2$) are shown in Fig. 1.

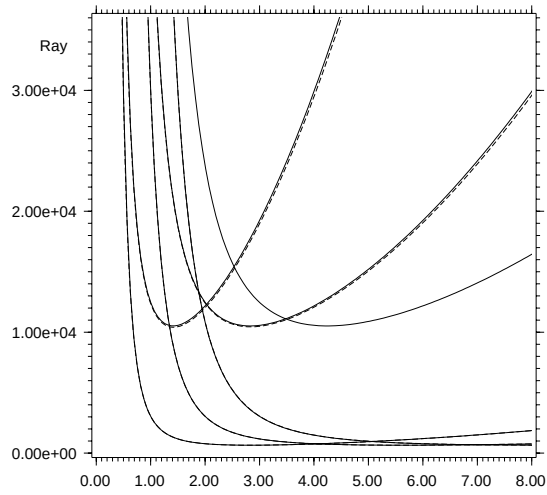

Fig. 1. *The six critical curves* $R_{cr}^{pq}(\alpha)$, $(p \le 3,\ q \le 2)$, *in the* $(2\pi/\alpha, Ra)$*-plane for the case of stress-free boundary conditions.* The solid curves were obtained from formulas (11), the dashed curves (in this scale visible only in the cases $p = 1, 2,\ q = 2$) were obtained numerically using the two-parameter continuation algorithm described in section 4.1

Several of these curves intersect. Some α-values of intersection points are

$$\alpha_{21}^{11} = \pi \left(\frac{4^{1/3} - 1}{4 - 4^{1/3}} \right)^{1/2}; \qquad \alpha_{21}^{12} = \pi \left(\frac{4 \cdot 4^{1/3} - 1}{4 - 4^{1/3}} \right)^{1/2};$$

$$\alpha_{22}^{12} = \pi \left(\frac{4 \cdot 4^{1/3} - 4}{4 - 4^{1/3}} \right)^{1/2} = 2\alpha_{21}^{11}; \qquad (12)$$

$$\alpha_{31}^{11} = \pi \left(\frac{9^{1/3} - 1}{9 - 9^{1/3}} \right)^{1/2}; \qquad \alpha_{31}^{22} = \pi \left(\frac{4 \cdot 9^{1/3} - 4^{1/3}}{9 \cdot 4^{1/3} - 4 \cdot 9^{1/3}} \right)^{1/2}.$$

In general, we get from $R_{cr}^{ij}(\alpha) = R_{cr}^{mn}(\alpha)$ the expression

$$\alpha_{mn}^{ij} = \pi \left(\frac{i^{2/3} \cdot n^2 - j^2 \cdot m^{2/3}}{m^{2/3} \cdot i^2 - m^2 \cdot i^{2/3}} \right)^{1/2}, \qquad i \ne m. \qquad (13)$$

For $i = m,\ j \ne n$ the curves do not intersect. Also, they do not intersect if (13) produces non-real complex numbers, as for instance $\alpha_{22}^{11} = \pi\sqrt{-1}$.

2.2 Pure-mode solutions

To find pure-mode 2-roll solutions of system (7), we first assume that the coefficients of all modes vanish, except ψ_{11} and θ_{11}. To obtain a nontrivial solution, θ_{02}

has to be non-zero as well. Under these assumptions, we obtain the pure-mode solution

$$\begin{aligned}
\psi_{11}^2(\alpha, Ra) &= \frac{8}{a_{11}^2(\alpha)}\ (Ra - R_{cr}^{11}(\alpha)) = \frac{a_{02}c_1^2}{4b_{11}b_{12}a_{11}^2}\ (Ra - R_{cr}^{11}),\\
\theta_{11}^2(\alpha, Ra) &= \frac{8a_{11}^2(\alpha)}{\alpha^2}\ \frac{Ra - R_{cr}^{11}(\alpha)}{Ra^2} = \frac{a_{02}a_{11}^2}{4b_{11}b_{12}}\ \frac{Ra - R_{cr}^{11}}{Ra^2},\\
\theta_{02}(\alpha, Ra) &= -\frac{Ra - R_{cr}^{11}(\alpha)}{\pi\ Ra} = -\frac{c_1}{2b_{12}}\ \frac{Ra - R_{cr}^{11}}{Ra}.
\end{aligned} \tag{14}$$

Similarly we assume $\psi_{21}, \theta_{21}, \theta_{02} \neq 0$ and compute the Fourier coefficients of the 4-roll solutions:

$$\begin{aligned}
\psi_{21}^2(\alpha, Ra) &= \frac{8}{a_{21}^2(\alpha)}\ (Ra - R_{cr}^{21}(\alpha)) = \frac{a_{02}c_2^2}{4b_{21}b_{22}a_{21}^2}\ (Ra - R_{cr}^{21})\\
\theta_{21}^2(\alpha, Ra) &= \frac{2a_{21}^2(\alpha)}{\alpha^2}\ \frac{Ra - R_{cr}^{21}(\alpha)}{Ra^2} = \frac{a_{02}a_{21}^2}{4b_{21}b_{22}}\ \frac{Ra - R_{cr}^{21}}{Ra^2},\\
\theta_{02}(\alpha, Ra) &= -\frac{Ra - R_{cr}^{21}(\alpha)}{\pi Ra} = -\frac{c_2}{2b_{22}}\ \frac{Ra - R_{cr}^{21}}{Ra}\ .
\end{aligned} \tag{15}$$

Assuming that only $\psi_{p1}, \theta_{p1}, \theta_{02} \neq 0$ we get similarly

$$\begin{aligned}
\psi_{p1}^2 &= \frac{a_{02}c_p^2}{4b_{p1}b_{p2}a_{p1}^2}\ (Ra - R_{cr}^{p1})\\
\theta_{p1}^2 &= \frac{a_{02}a_{p1}^2}{4b_{p1}b_{p2}}\ \frac{Ra - R_{cr}^{p1}}{Ra^2},\\
\theta_{02} &= -\frac{c_p}{2b_{p2}}\ \frac{Ra - R_{cr}^{p1}}{Ra}.
\end{aligned} \tag{16}$$

The solutions ψ_{11} and ψ_{21} are shown in ([14], Fig. 4.5) as functions of α^{-1} for fixed Ra values. The solution (14) is known as steady state of the Lorenz equations [11]. Also solution (15) was computed earlier for a truncated system of 7 equations [12]. Solution (16) was found under the assumption that only $\psi_{p1}, \theta_{p1}, \theta_{02} \neq 0$ for $M > p \geq 1$ fixed, but without truncating the system otherwise. The periodicity of the solutions of the full system is preserved by the solutions given in (14) – (16): $\psi_{21}(\alpha^{-1}) = \psi_{11}(2\alpha^{-1})$, and $\psi_{p1}(\alpha^{-1}) = \psi_{11}(p\alpha^{-1})$ in general, for $p < M$. This follows from definitions (8) of the coefficients and from the periodicity behavior of the critical curves (11).

If we now try to find similarly pure-mode solutions bifurcating at the critical curves $Ra_{cr}^{p2}(\alpha)$ from the trivial solution, we do not succeed: As shown in ([14], pp. 168f), the assumption that ψ_{12} and θ_{12} do not vanish forces θ_{01}, ψ_{11}, θ_{11} and θ_{02} to be non-zero for a non-trivial solution, and this forces $\psi_{21} \neq 0$, and so on. We thus do not obtain a small closed subset of the full equations because the equations for ψ_{p2} and θ_{p2} involve a different mix of indices than the equations for ψ_{p1} and θ_{p1}.

3 Secondary bifurcations on pure mode solutions

System (7) is too complicated to be solved explicitly for the loci of secondary bifurcation points on solutions (16) in the same way as for the primary bifurcation points. We are now going to discuss alternative methods.

To investigate the hypothesis that the nonlinear interaction of pure-mode solutions of different numbers of rolls generates curves of secondary bifurcations connecting intersection points of critical curves, the first question is: is there *any* system with such a curve of secondary bifurcations? This question was studied analytically by Lortz et al. [12] for the interaction of the pure-mode 2-roll solution with the pure-mode 4-roll solution in a 7x7 *model problem.* Matern and Meyer-Spasche re-did these calculations and then investigated similarly the interaction of the pure-mode 2-roll solution with the pure-mode 6-roll solution in a different 7x7 model problem. The 2-roll,4-roll interaction was found to behave as expected from the results for Taylor-vortex flows. We review here those findings and further investigations. Details are given in ([14], pp. 160ff).

3.1 The 2-roll,4-roll interaction in a model problem

Truncating system (7) by a Galerkin approach with $N = M = 2$ gives a 10x10 system. This system was further reduced using perturbation arguments. With these simplifications, the following 7x7 system was obtained:

$$\begin{aligned}
&(b_{11} - b_{22})(a_{21} - a_{12})\psi_{12}\psi_{21} - \mathrm{Pr}\ Ra\ c_1\theta_{11} + \mathrm{Pr}\ a_{11}^2\psi_{11} &&= 0,\\
&(b_{11} + b_{12})(a_{11} - a_{12})\psi_{11}\psi_{12} - \mathrm{Pr}\ Ra\ c_2\theta_{21} + \mathrm{Pr}\ a_{21}^2\psi_{21} &&= 0,\\
&(b_{11} + b_{21})(a_{21} - a_{11})\psi_{11}\psi_{21} - \mathrm{Pr}\ Ra\ c_1\theta_{12} + \mathrm{Pr}\ a_{12}^2\psi_{12} &&= 0,\\
&-2b_{12}\psi_{11}\theta_{02} + (b_{11} - b_{22})(\psi_{21}\theta_{12} + \psi_{12}\theta_{21}) - c_1\psi_{11} + a_{11}\theta_{11} &&= 0,\\
&-2b_{22}\psi_{21}\theta_{02} - (b_{11} + b_{12})(\psi_{11}\theta_{12} - \psi_{12}\theta_{11}) - c_2\psi_{21} + a_{21}\theta_{21} &&= 0,\\
&(b_{11} + b_{21})(\psi_{21}\theta_{11} + \psi_{11}\theta_{21}) - c_1\psi_{12} + a_{12}\theta_{12} &&= 0,\\
&2b_{11}\psi_{11}\theta_{11} + 2b_{21}\psi_{21}\theta_{21} + a_{02}\theta_{02} &&= 0.
\end{aligned} \tag{17}$$

A necessary condition for secondary bifurcation is that the determinant of the Jacobian of this system vanishes on the solution branch under consideration.

Calculation of secondary bifurcation points on the 2-roll solutions: We first consider bifurcation from the 2-roll solution (14). In this case elementary changes of rows and columns allow us to reduce the 7x7 determinant of the Jacobian to a 6x6 determinant

$$\begin{vmatrix} A & 0 \\ 0 & B \end{vmatrix}, \tag{18}$$

where A is a 2x2 matrix which is computed to be non-singular for all $Ra \geq R_{cr}^{11}(\alpha)$, i.e. in the domain of existence of solution (14). Thus those parameter values have to be found for which B turns singular. Expansion of det(B) is a

bit cumbersome, but allows us to find a formula relating the parameters Pr, α and *Ra*. It is given in ([14], eq. (4.118)). With respect to Pr and *Ra* it is a polynomial of second order, a rational function with respect to α. For each given α and Pr the formula thus gives the *Ra* value $R_{pr}^{11}(\alpha)$ for which there is a secondary bifurcation on the 2-roll solution. These are the bifurcation points of the mixed-mode solutions described by Busse and Or [5] and discussed earlier. The resulting curve is shown in Fig. 2 for $\mathrm{Pr} = 1$. It was obtained through eigenvalue computation as explained in the section 3.2.

For the limiting cases $\mathrm{Pr} \to 0$ and $\mathrm{Pr} \to \infty$ the formula simplifies considerably: For $\mathrm{Pr} = 0$ we obtain $R_0^{11}(\alpha) = R_{cr}^{11}(\alpha)$ for all appropriate α, i.e. the curve of secondary bifurcations coincides with the neutral curve. The expression for $\mathrm{Pr} \to \infty$ is obtained by neglecting all terms that do not contain a factor Pr^2. With the abbreviations

$$\gamma_1 := \frac{(b_{12}+b_{11})^2 a_{02} c_1}{4 b_{11} b_{12}} (a_{12}^2 - a_{11}^2)(c_2 + c_1 \frac{a_{21}^2}{a_{11}^2}) \tag{19}$$
$$\delta_1 := c_1^2 c_2^2 (R_{cr}^{11} - R_{cr}^{21})$$

we obtain

$$R_\infty^{11}(\alpha) = \frac{\gamma_1(\alpha) + \delta_1(\alpha) R_{cr}^{12}(\alpha)/R_{cr}^{11}(\alpha)}{\gamma_1(\alpha) + \delta_1(\alpha)} R_{cr}^{11}(\alpha). \tag{20}$$

If we evaluate eq. (20) at $\alpha = \alpha_{21}^{11}$, we find that δ_1 vanishes. We thus can see analytically that $R_\infty^{11}(\alpha_{21}^{11}) = R_{cr}^{11}(\alpha_{21}^{11}) = R_{cr}^{21}(\alpha_{21}^{11})$, i.e. that the curve $R_\infty^{11}(\alpha)$ emanates from the intersection of R_{cr}^{11} with R_{cr}^{21}. In the present approach, we cannot make any statement, however, about "where this curve goes" for large *Ra* (note that R_{cr}^{11} and R_{cr}^{12} do not intersect).

Calculation of secondary bifurcation points on the 4-roll solutions: Starting from system (17) again, we evaluate the Jacobian now on the 4-roll solution involving ψ_{21}, θ_{21} and θ_{02}. Again, relatively simple elementary changes of rows and columns allow us to obtain a 6x6 determinant with the structure shown in (18). This time matrix A contains expressions in ψ_{21}, θ_{21} and θ_{02}, and its determinant can be shown to be non-zero for all *Ra* and α for which solution (15) exists. Thus we are left with a 4 x 4 matrix, which is nearly full and thus produces a lengthy expression which can be found in ([14], eq. (4.121)). Again, it is a polynomial of second order in Pr and *Ra*, and a rational function with respect to α. Figure 2 shows the curve R_{pr}^{21} versus α^{-1} for $\mathrm{Pr} = 1$, obtained through computation of eigenvalues, see paragraph 3.2.

The limiting cases $\mathrm{Pr} \to 0$ and $\mathrm{Pr} \to \infty$ can be obtained analytically again. We find again that the curve coincides with the neutral curve for $\mathrm{Pr} = 0$ and the appropriate α-values, and that the expression for $\mathrm{Pr} \to \infty$ is obtained by neglecting all terms that do not contain a factor Pr^2. With the abbreviations

$$\gamma_2 := \frac{(b_{11}+b_{21})(b_{22}-b_{11}) a_{02}}{4 b_{21} b_{22}} \left(c_1 c_2 (a_{12}^2 + a_{11}^2) + c_1^2 a_{21}^2 + c_2^2 \frac{a_{11}^2 a_{12}^2}{a_{21}^2} \right) \tag{21}$$
$$\delta_2 := c_1^4 (R_{cr}^{21} - R_{cr}^{11})$$

we obtain

$$R_{\infty}^{21}(\alpha) = \frac{\gamma_2(\alpha) + \delta_2(\alpha) R_{cr}^{12}(\alpha)/R_{cr}^{21}(\alpha)}{\gamma_2(\alpha) + \delta_2(\alpha)} R_{cr}^{21}(\alpha). \tag{22}$$

$R_{\infty}^{21}(\alpha)$ is the locus of secondary bifurcation points on the 4-roll solution for $\mathrm{Pr} = \infty$. If we evaluate eq. (22) at $\alpha = \alpha_{21}^{11}$, we find that δ_2 vanishes. We thus can see analytically that $R_{\infty}^{21}(\alpha_{21}^{11}) = R_{cr}^{21}(\alpha_{21}^{11}) = R_{cr}^{11}(\alpha_{21}^{11})$, i.e. that the curve $R_{\infty}^{21}(\alpha)$ emanates from the intersection of R_{cr}^{11} with R_{cr}^{21}.
If we evaluate eq. (22) at $\alpha = \alpha_{12}^{21}$, we find that $R_{\infty}^{21}(\alpha_{12}^{21}) = R_{cr}^{21}(\alpha_{12}^{21}) = R_{cr}^{12}(\alpha_{12}^{21})$, i.e. that the curve $R_{\infty}^{21}(\alpha)$ emanates also from the intersection of R_{cr}^{21} with R_{cr}^{12}. The curve $R_{\infty}^{21}(\alpha)$ thus connects the intersection point of $R_{cr}^{11}(\alpha)$ and $R_{cr}^{21}(\alpha)$ with the intersection point of $R_{cr}^{21}(\alpha)$ and $R_{cr}^{12}(\alpha)$, as was speculated in the case of the Taylor problem [13].

3.2 The perturbation approach

If the full system (7) is reduced for local investigations of mode interactions by a perturbation approach to third order in $(\lambda - \lambda_o)^{1/2}$ and $(Ra - Ra_o)^{1/2}$, $\lambda = 2\pi/\alpha$, the resulting system involves the 7 modes and equations used in the model problem (17), plus two more: the modes ψ_{32} and θ_{32} and their equations. Interactions of the kth and the $(k+1)$st mode were investigated by Knobloch and Guckenheimer [10] in a neighborhood of the intersection point $P_{k1}^{(k+1)1} := (\alpha_{k1}^{(k+1)1}, Ra_{k1}^{(k+1)1})$. In the case $k = 1$, the system of equations they used ([10], eqs. (15), (16)) is identical with the 9x9 system we get from system (17) by including ψ_{32} and θ_{32}. Note, however, that the coefficients of the system vary with α in the approach discussed here, but not with time t.

Knobloch and Guckenheimer did not calculate loci of secondary bifurcation points. Indeed, we doubt that the 9x9 system could be treated the way the 7x7 system was treated: not even when using such a device as Mathematica. Both first calculations of the 7x7 determinants did contain minor errors which were eliminated in [14]. In [14] the methods to be discussed next were used to reproduce the results on the 7x7 model problem, and then it was checked how much the results change when the two additional modes and equations are included.

The methods employed avoid the computation of determinants: for given wave number and Rayleigh number, all eigenvalues of the Jacobians were computed with standard software (RG of Eispack). The critical values were found by iteration for a zero eigenvalue (bisection or Newton iterations), using continuation in α and Ra. The curves of critical points were then obtained by linear interpolation between the computed points.

For both curves of secondary bifurcation points emanating from the double point P_{11}^{21} it was found that the two curves corresponding to the 7x7 model and to its 9x9 companion do differ, but that the deviations are so small that they cannot be seen in the scale of Fig. 2. A change of Prandtl number, however, is clearly visible. For several points in the parameter plane all eigenvalues of corresponding

matrices were compared in detail, both for Pr = 1 and for Pr = 1000 ([14], p. 175–178). This confirmed that neglecting the modes ψ_{32}, θ_{32} does not change the eigenvalues *noticeably*. This is probably due to the fact that the influence of matrix entries on the eigenvalues very much depends on the position of the entry in the matrix [16].

3.3 A Hopf curve

When computing all 7 or 9 eigenvalues of these Jacobians for many parameter values, i.e.when producing the dashed curves in Fig. 2, we happened to notice a pair of conjugate complex eigenvalues moving through the imaginary axis. This is the condition for Hopf bifurcation. Systematically searching for those parameter values at which the real part of a conjugate pair of eigenvalues changes sign we found the Hopf curve shown dotted in Fig. 2. At each point on this curve the real part of a pair of eigenvalues vanishes.

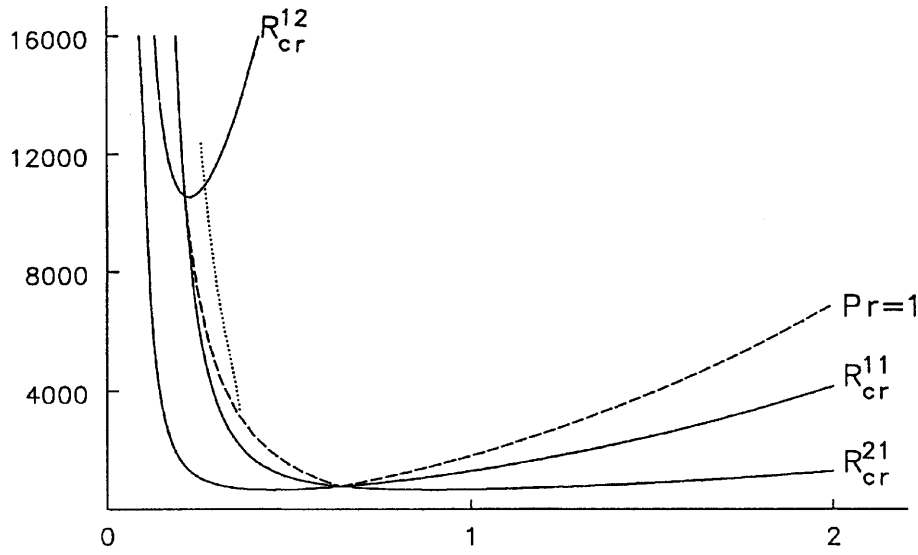

Fig. 2. *Curve of bifurcation points* in the stress-free case in the (α^{-1}, Ra)-plane for Pr = 1. Solid: neutral curves R_{cr}^{11}, R_{cr}^{21} and R_{cr}^{12}; Dashed: curves of secondary bifurcations emanating from the double point P_{11}^{21}, obtained through eigenvalue computation; Dotted: Hopf curve

When producing this curve we expected that it would end in some double point, as the other curves do and as Hopf curves do under certain circumstances [8]. We were surprised to see that the curve does end on one of the curves of secondary bifurcations with three vanishing eigenvalues, but 'in the middle of nowhere' on this curve. Why at $(1/\alpha_e, Ra_e) \approx (0.36708, 3024.87)$ in the 9x9 case and not at some other values? To make sure that the curve actually ends there

we performed further computations on three sides of a rectangle surrounding the end point found, both for the 7x7 case and for the 9x9 case. No continuation of the curve was found.

3.4 The 2-roll, 6-roll interaction in a model problem

To investigate the interaction of the 2- and 6-roll solutions, there are now the same two ways for obtaining a simplified model problem as in the 2-roll,4-roll case:

- make a perturbation approach as just discussed for the 2-roll,4-roll case. A 3^{rd} order perturbation analysis of the interaction of the (k,1)-mode with the (m,1)-mode shows that the modes (k,1), (m,1), (k+m,2), (m-k,2), (0,2) should be taken into account [15,10]. For $k = 1,\ m = 3$ this leads to a model with the modes

$$\psi_{11}, \psi_{22}, \psi_{31}, \theta_{02}, \theta_{11}, \theta_{22}, \theta_{31}, \psi_{42}, \theta_{42}.$$

- truncate system (7) at $N = 2,\quad M = 3$ and use perturbation arguments to further simplify this system.

This second approach leads to the following model:

$$\begin{aligned}
&(b_{21} - b_{32})(a_{31} - a_{22})\psi_{22}\psi_{31} - \mathrm{Pr}\ Ra\ c_1\theta_{11} + \mathrm{Pr}\ a_{11}^2\psi_{11} &&= 0,\\
&(b_{12} + b_{21})(a_{11} - a_{22})\psi_{11}\psi_{22} - \mathrm{Pr}\ Ra\ c_3\theta_{31} + \mathrm{Pr}\ a_{31}^2\psi_{31} &&= 0,\\
&(b_{11} + b_{31})(a_{31} - a_{11})\psi_{11}\psi_{31} - \mathrm{Pr}\ Ra\ c_2\theta_{22} + \mathrm{Pr}\ a_{22}^2\psi_{22} &&= 0,\\
&-2b_{12}\psi_{11}\theta_{02} + (b_{21} - b_{32})(\psi_{31}\theta_{22} + \psi_{22}\theta_{31}) - c_1\psi_{11} + a_{11}\theta_{11} &&= 0,\\
&-2b_{32}\psi_{31}\theta_{02} + (b_{12} + b_{21})(\psi_{22}\theta_{11} - \psi_{11}\theta_{22}) - c_3\psi_{31} + a_{31}\theta_{31} &&= 0,\\
&(b_{11} + b_{31})(\psi_{31}\theta_{11} + \psi_{11}\theta_{31}) - c_2\psi_{22} + a_{22}\theta_{22} &&= 0,\\
&2b_{11}\psi_{11}\theta_{11} + 2b_{31}\psi_{31}\theta_{31} + a_{02}\theta_{02} &&= 0.
\end{aligned} \tag{23}$$

The situation is very similar to the 2-roll,4-roll case, and we expect that the more accurate results obtained with the 9x9 model will differ only slightly from the results obtained with the 7x7 model, which we will discuss next.

Calculation of secondary bifurcation points on the 2-roll solutions: A necessary condition for secondary bifurcation on a branch of solutions of (23) is that the determinant of the Jacobian vanishes. As in the 2-roll,4-roll interaction, this determinant simplifies considerably on both solution branches under consideration, leads again to a 6x6 determinant of the form (18) and to a 4x4 determinant which actually has to be computed. In the case of the 2-roll solution, obtained is thus a quadratic polynomial in Ra and in Pr and a rational function in α, with a structure very similar to the one in the 2-roll,4-roll case. Figure 4.9 of [14] shows curves for 6 different values of Pr which were obtained by numerically evaluating this formula with a root-finding algorithm. Again, there

are simple expressions for the limiting cases: for $\mathrm{Pr} = 0$, the curve coincides with R_{cr}^{11}, and for $\mathrm{Pr} \to \infty$ we get

$$R_{31}^{11}(\alpha; \mathrm{Pr} \to \infty) = \frac{\gamma_3 + \delta_3 R_{cr}^{22}/R_{cr}^{11}}{\gamma_3 + \delta_3} R_{cr}^{11} \tag{24}$$

with

$$\begin{aligned} \gamma_3 &:= \frac{(b_{12} + b_{21})(b_{11} + b_{31})a_{02}}{4b_{11}b_{12}}(c_1 a_{22}^2 - c_2 a_{11}^2)(c_3 + c_1 \frac{a_{31}^2}{a_{11}^2}) \\ \delta_3 &:= c_2^2 c_3^2 (R_{cr}^{11} - R_{cr}^{31}). \end{aligned} \tag{25}$$

Note that δ_3 vanishes at $\alpha = \alpha_{31}^{11}$, i.e. the curve $R_{31}^{11}(\alpha; \mathrm{Pr} \to \infty)$ emanates from the double point $(\alpha_{31}^{11}, Ra_{31}^{11})$, as was to be expected. R_{cr}^{22} plays a prominent role in formula (24), but $R_{cr}^{22}(\alpha)$ and $R_{cr}^{11}(\alpha)$ do not intersect. As in the case of the 2-roll,4-roll interaction, we cannot say anything about 'where this curve goes'. Maybe it continues to infinity, maybe it ends in some other singular point which has been neglected in this simplified model.

Calculation of secondary bifurcation points on the 6-roll solutions: To find the secondary bifurcation points on the 6-roll solutions, we start from the determinant of the Jacobian of system (23) again. Quite a number of terms turn into zero when solution (16), $p = 3$, is inserted. The resulting pattern of zeros is inconvenient, but very similar to the pattern in the 4-roll case. Interchanges of columns and rows, elimination of an entry and one expansion produce again a 6x6 determinant of form (18), and the 2x2 matrix A can be shown to be nonsingular in the (α, Ra) domain of existence of the 6-roll solutions. Thus a 4x4 determinant has to be computed again and leads to a formula very similar to the one in the 2-roll,4-roll case. The curves for $\mathrm{Pr} = 1$ and for $\mathrm{Pr} \to \infty$ are shown in ([14], Fig. 4.10). Again, the curve for $\mathrm{Pr} = 1$ had to be obtained numerically, while there are simple expressions for the limiting cases: for $\mathrm{Pr} = 0$ the curve coincides with R_{cr}^{31}, and for $\mathrm{Pr} \to \infty$ it becomes

$$R_{11}^{31}(\alpha; \mathrm{Pr} \to \infty) = \frac{\gamma_4 + \delta_4 R_{cr}^{22}/R_{cr}^{31}}{\gamma_4 + \delta_4} R_{cr}^{31} \tag{26}$$

with

$$\begin{aligned} \gamma_4 &:= \frac{(b_{32} - b_{21})(b_{11} + b_{31})a_{02}}{4b_{31}b_{32}} \left(c_2 c_3 a_{11}^2 + c_1 c_3 a_{22}^2 + c_1 c_2 a_{31}^2 + c_3^2 \frac{a_{22}^2 a_{11}^2}{a_{31}^2} \right) \\ \delta_4 &:= c_1^2 c_2^2 (R_{cr}^{31} - R_{cr}^{11}). \end{aligned}$$

The curve given in (26) connects the two double points $P_{31}^{11} = (\alpha_{31}^{11}, Ra_{31}^{11})$ and $P_{31}^{22} = (\alpha_{31}^{22}, Ra_{31}^{22})$.

3.5 Other interactions

As we have seen, the modes $(k,1),\ (m,1),\ (k+m,2),\ (m-k,2),\ (0,2)$ have to be taken into account in a perturbation approach to 3^{rd} order to investigate the interaction of the $(k,1)$-mode with the $(m,1)$-mode. Comparison of the 7x7 and 9x9 models approximating the full Rayleigh–Bénard problem showed that modes $(k+m,2)$ did not change results qualitatively. For finding the basic pattern, it thus seems to be sufficient to investigate systems of 7 equations composed by the modes $(k,1),\ (m,1),\ (m-k,2),\ (0,2)$. The structures of the resulting determinants were found to be very similar for the 2-roll,4-roll and the 2-roll,6-roll cases, because the underlying equations (7) have the same structure with respect to the different modes.

So we think that the general case $(1,1)$ with $(m,1)$ will follow the pattern found here. We expect that there are two curves emanating from each of the double points $P_{m1}^{11} = (\alpha_{m1}^{11}, Ra_{m1}^{11}),\ m > 1$. One of the curves connects P_{m1}^{11} with $P_{m1}^{m-1,2}$ the other curve either goes to infinity, or interacts with a double point excluded by the simplified analysis using only 9 or 7 equations.

Other interactions can be investigated in a very similar way if it turns out that the computed curves of secondary bifurcations stay close to the critical curves, as they do in the cases investigated here: remember that they merge with the critical curves for $\mathrm{Pr} \to 0$. So we expect from the foregoing analysis that there will be two curves emanating from P_{m1}^{k1}, $m > k$, and that they will be found to go to the double point $P_{m1}^{m-k,2}$ and to infinity, respectively. This means that one of the two curves emanating from P_{31}^{21} will go to the double point P_{31}^{12}. This was confirmed for a numerical model of the full Rayleigh–Bénard problem with rigid boundary conditions. These results will be reported in the next section, see especially Figs. 5 and 9.

As we have seen, the curves of secondary bifurcation points are generated by intersections of neutral curves, i.e. by intersections of curves of bifurcation points. The question thus arises if these curves of secondary bifurcation points intersect with other curves of bifurcation points and thus generate additional curves of (tertiary) bifurcation points. Many intersection points in the figures presented here are due to projection. Some intersection points in the parameter plane, however, correspond to actual intersections: this is so if the projected curves lie on the same solution surface. The curves given in eqs. (20) and (24) both lie on the surface of the 2-roll solutions. As was reported in [14] near Fig. 4.11, these curves intersect, and not only for $\mathrm{Pr} \to \infty$, but for all Prandtl numbers. Generalizing we find that from all double points $P_{p1}^{11}, p \geq 2$ presumably emanates a curve of secondary bifurcation points lying on the surface of the 2-roll solutions. We cannot exclude that all these curves intersect each other, producing further curves of bifurcation points.

There are also intersections in the other families of secondary bifurcation curves. An example are the curve connecting P_{31}^{11} with P_{31}^{22} and the curve connecting P_{31}^{21} with P_{31}^{12}. Both curves lie on the surface of the 6-roll solutions. As we can see from Fig. 1, both thus can reach their destination only by intersecting the other curve. The analysis presented in the next section shows that these

curves do not only intersect for the small model problems with 9 or 7 modes, but also for the numerical approximation of the full system with no-slip boundary conditions on top and bottom, see Figs. 5 – 8.

If the calculations presented in this section are further generalized, the question if neglecting the $(k+m,2)$-modes is appropriate has to be newly investigated. It should be kept in mind that this strict truncation to systems of 7 or 9 equations was done to find basic patterns. There probably are higher order interactions which got excluded in the simplified models studied here. But even when restricting the analysis to these basic patterns, coalescence of three and more points of secondary bifurcation has to be expected, and this will give rise to new patterns of solutions. A glimpse into the zoo to be expected for Taylor vortex flows is given by Fig. 10 and by some of the figures in ([14], Chapter 3).

4 Numerical investigations

4.1 The Rayleigh–Bénard code used

Now we briefly describe the Rayleigh–Bénard code used for the numerical investigations. As before, let v_x and v_z be the velocity components in the x and z directions, respectively, ψ the stream function satisfying $v_x = -\partial_z\psi$, $v_z = \partial_x\psi$, and θ the temperature deviation. Ra is the Rayleigh number, and Pr the Prandtl number. In addition we introduce the (negative of the) vorticity $\omega = \Delta\psi$. Then we obtain the coupled set of three second-order differential equations

$$\begin{aligned} \partial_z\psi\,\partial_x\omega - \partial_x\psi\,\partial_z\omega + \mathrm{Pr}Ra\,\partial_x\theta + \mathrm{Pr}\,\Delta\omega &= 0, \\ \partial_z\psi\,\partial_x\theta - \partial_x\psi\,\partial_z\theta + \partial_x\psi + \Delta\theta &= 0, \\ \omega - \Delta\psi &= 0. \end{aligned} \tag{27}$$

We solve them on the region

$$0 \le x \le \frac{2\pi}{\alpha}, \qquad 0 \le z \le 1. \tag{28}$$

The boundary conditions on the sides are

$$\begin{aligned} \psi(0,z) &= \psi(2\pi/\alpha,z) = 0, \\ \partial_x\psi(0,z) &= \partial_x\psi(2\pi/\alpha,z), \qquad 0 \le z \le 1, \\ \theta(0,z) &= \theta(2\pi/\alpha,z). \end{aligned} \tag{29}$$

The boundary conditions on the top and bottom are, for $0 \le x \le 2\pi/\alpha$,

$$\begin{aligned} \psi(x,0) = \psi(x,1) &= 0, \\ \theta(x,0) = \theta(x,1) &= 0, \end{aligned} \tag{30}$$

and

$$\partial_z\psi(x,0) = \partial_z\psi(x,1) = 0 \tag{31}$$

for rigid boundaries; or

$$\partial_{zz}\psi(x,0) = \partial_{zz}\psi(x,1) = 0 \tag{32}$$

for stress-free boundaries.

Discretization: A uniform mesh in the coordinate directions is introduced; the boundaries of region (28) coincide with grid lines. The equations (27) are discretized in the interior of this region using centered second order finite differences. The boundary conditions are implemented in the following way:
Stress-free case: from eq. (30) we see that $\partial_{xx}\psi(x,z) = 0$ for $z = 0, 1$ and all x. Thus eq. (32) yields that $\omega(x,z) = 0$ for $z = 0, 1$ and all x. In the code, ψ and ω are set to zero on top and bottom of the computational region (28).
Rigid case: again, the only nontrivial boundary conditions are those for ω. We now discuss how to use eq. (31) at the bottom; the top is treated similarly, and also conditions (29) are treated similarly.

Let h_x and h_z be the grid sizes in the x and z directions, let (i,j) denote a grid point near or at the bottom, $i \geq 0$, $0 \leq j \leq 2$, and let $\psi_{i,j}$ be an approximation to the exact value $\psi(ih_x, jh_z)$. We extrapolate from interior values of the stream function in the following way: we approximate ψ with a cubic polynomial in the three intervals normal to the boundary, say $\psi(ih_x, jh_z) = A + Bh_z + Ch_z^2 + Dh_z^3$, $j = 0, 1, 2$ (A, B, C, D depend on i). Using (30) and (31) gives $A = B = 0$. Applying this formula for $i = 1$ and $i = 2$, one finds C in terms of $\psi_{i,1}$ and $\psi_{i,2}$ and then uses $\partial_{zz}\psi(ih_x, 0) = 2C$. This leads to

$$\omega(ih_x, 0) = \partial_{zz}\psi(ih_x, 0) \approx \frac{4\psi_{i,1} - \psi_{i,2}/2}{h_z^2}. \tag{33}$$

This is called Jensen's, Wilkes', or Pearson's method.

Numerical model: We thus obtain a block-tridiagonal system of equations, $G(u) = 0$. Here u is a vector consisting of the unknown values of ψ, θ, ω at the interior grid points. Before we report on how the system $G(u) = 0$ is solved, we compare the equations for the stress-free case treated here with equations (1)–(3) treated above. Both deviations between the two systems are theoretically unimportant and were introduced for purely numerical reasons.

The introduction of the vorticity in eqs. (27) avoids direct discretization of derivatives of 4^{th} order. For a fixed number of grid points, the number of equations and of unknowns is increased by 50% by the introduction of ω, but all three differential equations in (27) are second order now. This allows us to use 5-point stencils in the interior throughout. It thus yields a system with block tridiagonal instead of (quite complicated) block pentadiagonal structure, and also it makes the boundary treatment much simpler. Moreover, away from singular points, the Jacobian matrix G_u has better numerical properties: its condition number is reduced from $\mathcal{O}(h_x^{-2}h_z^{-2})$ to $\mathcal{O}(h_x^{-1}h_z^{-1})$. (Previous versions

of this (Taylor) code used one fourth order equation and one of second order [1].)

Differentiation of $\psi(x_0, z) = 0,\ 0 \le z \le 1$ with respect to z leads to $\partial_z \psi(x_0, z) = 0,\ 0 \le z \le 1$. The fourth equation in (3) thus follows from the first equation in (29). Solutions of system (1)– (3) which are excluded by the first equation in (29) are also excluded by our Fourier expansion (5). Note that all solutions satisfying the ansatz (5) satisfy also $\psi(0, z) = \psi(2\pi/\alpha, z) = 0$, $0 \le z \le 1$. The Dirichlet boundary conditions in (29) are easier to implement than the periodic Neumann boundary conditions in (3).

Taylor–Couette code: This Rayleigh–Bénard code was constructed from a Taylor–Couette code for steady, axisymmetric, incompressible flow. This code performs one-parameter continuation for computing solutions (flows) and two-parameter continuation for computing paths of critical points (pitchfork bifurcation points, transcritical bifurcation points or fold points). The details of the algorithms and of their implementations are explained in [1–4].

The Taylor–Couette code is conceptually divided into two parts: the *discretized system of equations,* together with first and second derivatives with respect to the unknowns and with respect to the parameters, computed either analytically or with finite differences; and the *continuation apparatus* itself, which involves Newton's method, repeated solutions of systems of linear algebraic equations, and combinations of the above derivatives. Only the first part changes in converting from the Taylor–Couette system to the Rayleigh–Bénard system. Since the two systems are intimately related to each other and have very similar structure ([14], Sect. 4.2.3), it was relatively easy to replace the Taylor–Couette system by the Rayleigh–Bénard system. The Taylor–Couette system contains repeated references to the radial coordinate, however, but the Rayleigh–Bénard system is autonomous.

Continuation in one parameter is implemented using the techniques in [9,14]. Branches of solutions are parameterized by *pseudo-arclength*, a numerical approximation to the intrinsic parameter arclength. This allows us to compute tangents to solution branches and thus to follow such branches around fold points with respect to control parameters. Also, it is possible to detect bifurcation points and to compute the tangent direction of the other bifurcating branch. If the Jacobian G_u is of size n by n, one repeatedly solves 'inflated' $(n+1)$ by $(n+1)$ systems. The 'bordering algorithm' nevertheless allows us to take advantage of the block-tridiagonal structure of the Jacobian. Once a fold point or bifurcation point is located, we can follow a (two-parameter) fold or bifurcation path in any two of the parameters Ra, Pr, or aspect ratio $2\pi/\alpha$. One repeatedly solves inflated systems of $(2n+3)$ equations in $(2n+2)$ unknowns. Orthogonal projections reduce this to a consistent system, and the bordering algorithm is repeatedly used at each step to reduce this system to one involving a linear system with matrix G_u or its transpose [1–4].

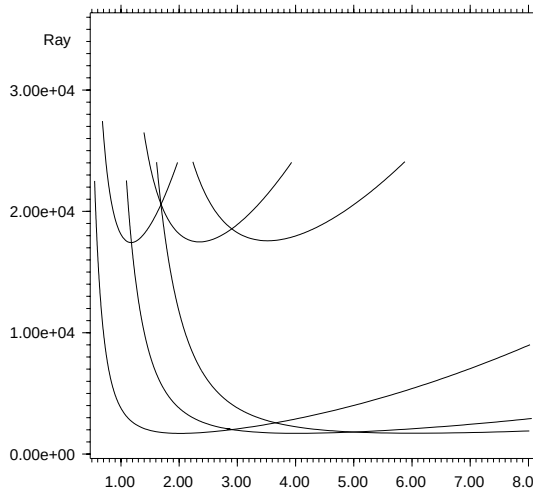

Fig. 3. *The six critical curves* $R_{cr}^{pq}(\alpha)$*,* $(p \leq 3,\ q \leq 2)$*, in the* $(2\pi/\alpha, Ra)$*-plane for the case of rigid boundary conditions (29)–(31).* The curves were obtained numerically

Numerical tests: For debugging of the new Rayleigh–Bénard code and for finding adequate mesh sizes we first compared computed results for system (27) with stress-free boundaries to analytical results. Figure 1 shows such a comparison. Four pairs of curves overlay each other to graphical accuracy; there is a slight discrepancy in the other two pairs of curves. This is a measure of the discretization error of our approximation, and was found to be small enough.

Numerical results for the rigid boundary version of the code were compared to the results given in [6]. Satisfactory agreement was found between the bifurcation curves computed by Chandrasekhar/Elbert and those computed with our code. During these runs we produced Figs. 3 and 4.

Figure 4 shows a comparison of the critical curves with rigid and stress-free boundary conditions in the $(2\pi/\alpha, Ra)$-plane. Same curves as in Figs. 3 and 1. The minimum of the R_{cr}^{11}-curve for rigid-boundary is located at $(\alpha, Ra) = (3.117, 1707.762)$ and for stress-free it is located at $(\alpha, Ra) = (\pi/\sqrt{2}, 657.5)$, ([6], pp. 36 and 38). Here, the rigid-boundary curve is shown in its proper scale. For the stress-free boundary curves, the true Rayleigh numbers have been divided by 0.3850, and the true aspect ratios $2\pi/\alpha$ have been divided by 1.39.

4.2 Convection rolls with rigid boundaries on top and bottom

We now investigate the curves of secondary bifurcations for rigid boundaries at top and bottom, i.e. with boundary conditions (29)–(31) and for $\mathrm{Pr} = 1$. This analysis was done numerically, using the code just described.

Figure 5 shows the loci of the secondary bifurcations in the $(2\pi/\alpha, \sqrt{Ra/R_c})$-plane, $R_c = 1708$, $\mathrm{Pr} = 1$. The curve connecting the double point $P_{11}^{21} =$

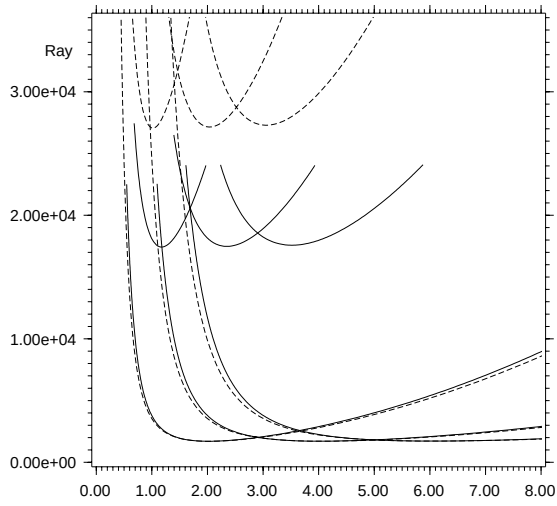

Fig. 4. *Comparison of critical curves with rigid (——) and stress-free (- - -) boundary conditions in the* $(2\pi/\alpha, Ra)$*-plane.* The curves for rigid boundaries are shown in their proper scale. The scales for the stress-free curves are changed such that the minima of the two R_{cr}^{11}-curves coincide

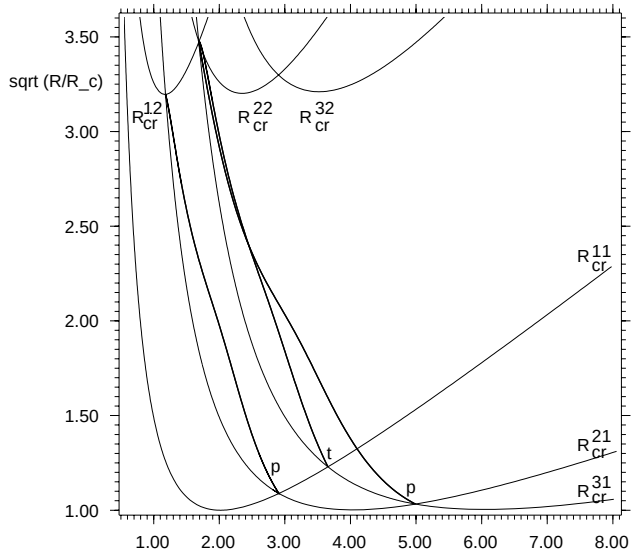

Fig. 5. *Loci of secondary bifurcation points in the* $(2\pi/\alpha, \sqrt{Ra/R_c})$*-plane,* $R_c = 1708$, $\mathrm{Pr} = 1$, rigid boundary conditions (29)–(31). The curves marked with 'p' are projections of paths of pitchfork bifurcation points; those with 't' are projections of paths of transcritical bifurcation points

$(2\pi/\alpha_{11}^{21}, R_{11}^{21})$ with the double point $P_{12}^{21} = (2\pi/\alpha_{12}^{21}, R_{12}^{21})$ consists of pitchfork bifurcation points. The curve connecting the double point P_{11}^{31} with the double point P_{22}^{31} consists of transcritical bifurcation points. The curve connecting the double point P_{21}^{31} with the double point P_{12}^{31} consists of pitchfork bifurcation points. These curves were computed using the two-parameter continuation algorithm described earlier.

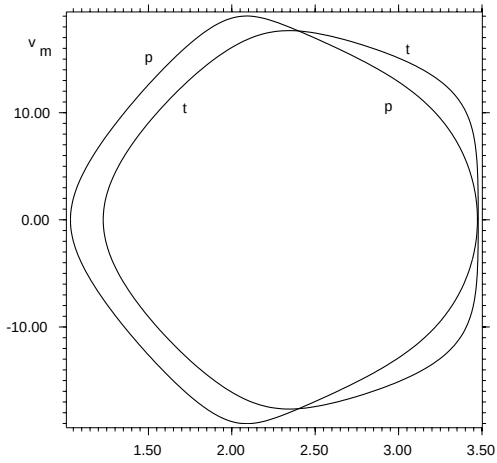

Fig. 6. *Vertical velocity at midpoint, v_m, versus $\sqrt{Ra/R_c}$ for the rightmost two secondary bifurcation curves shown in Fig. 5*

Let v_m be the value of the vertical component of the velocity at the midpoint of the computational domain, i.e. $v_m := v_z(\pi/\alpha, 1/2)$. Figure 6 shows v_m versus $\sqrt{Ra/R_c}$ for the two secondary bifurcation curves of Fig. 5 generated in the double points P_{11}^{31} and P_{21}^{31}, respectively. The curve generated in the double point P_{11}^{31} is identified by its existence at lower values of $\sqrt{Ra/R_c}$. Two points symmetric with respect to the line $v_m \equiv 0$ in Fig. 6 correspond to the same point in Fig. 5. That is, each secondary bifurcation curve in Fig. 5 is a projection of two paths. Following [14] we call such flows **twins**. Both curves of Fig. 5 also shown in Fig. 6 lie on the surface of the 6-roll solutions. Figure 6 shows that the two curves do not coincide as much as suggested by Fig. 5. They are different from each other, but there are two possible intersection points. As we are going to show next, the intersection just to the left of $\sqrt{Ra/R_c} = 2.5$ is a proper intersection point and thus a secondary double point, while the other intersection at $\sqrt{Ra/R_c} \approx 3.5$ is due to the projection used. We now consider a different projection of the same two curves.

Figure 7 shows a projection of these curves for v_m versus $2\pi/\alpha$. Again, the two twin flows can both be seen. In this figure we identify the curve originating at the double point P_{21}^{31} by noticing that it exists at larger aspect ratios $2\pi/\alpha$ than the other curve does. Again, we find two possible intersection points of the

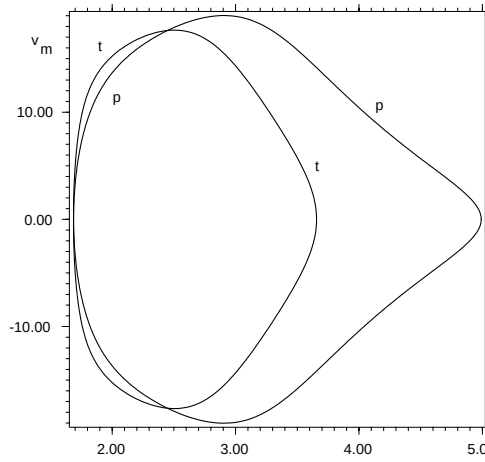

Fig. 7. *Vertical velocity at midpoint, v_m, versus $2\pi/\alpha$ for the rightmost two secondary bifurcation curves shown in Fig. 5*

two curves, not counting twins. The one for $2\pi/\alpha \approx 2.5$ was identified as a proper intersection point. A projection of its neighborhood onto the $(2\pi/\alpha, \sqrt{Ra/R_c})$-plane is shown in Fig. 8. The possible intersection at minimum aspect ratio in Fig. 7 corresponds to the possible intersection at maximum Rain Fig. 6. A closeup of a neighborhood of the intersection points of the three curves R_{cr}^{22}, R_{cr}^{31} and R_{cr}^{12} clearly shows that the two curves of secondary bifurcations do not intersect again.

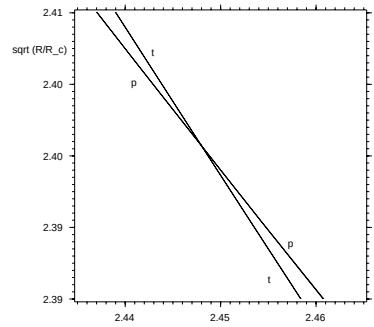

Fig. 8. *Enlargement of Fig. 5* for $2\pi/\alpha \in [2.435, 2.465]$, $\sqrt{Ra/R_c} \in [2.39, 2.41]$, $R_c = 1708$, showing the intersection point of the two secondary bifurcation curves

Summarizing, we thus see that the curve of secondary bifurcations starting at P_{21}^{31} (see Fig. 5) crosses the curve starting at P_{11}^{31} (see Fig. 8) and ends at the

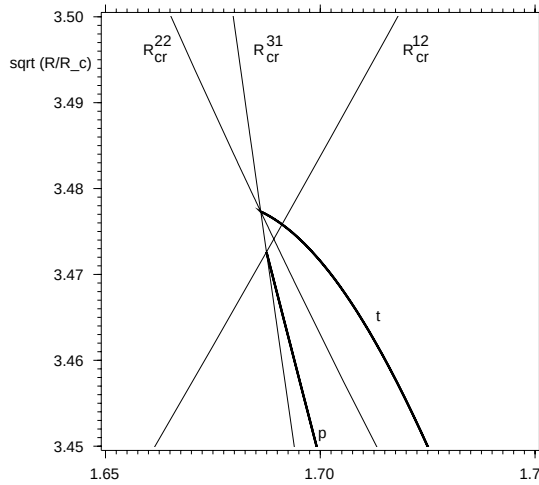

Fig. 9. *Enlargements of Fig. 5* for $2\pi/\alpha \in [1.65, 1.75]$, $\sqrt{Ra/R_c} \in [3.45, 3.50]$, a neighborhood of the intersections of the R^{31}_{cr}, R^{12}_{cr}, and R^{22}_{cr} critical curves

double point P^{31}_{12} while the curve starting in P^{31}_{11} goes to P^{31}_{22}. This is a special case of the general rule formulated speculatively in section 3.5.

4.3 Secondary bifurcations in the Taylor problem revisited

These investigations should be complemented by a short report on computations of Taylor vortex flows. Using the Taylor-version of the code described in section 4.1, the loci of secondary bifurcations and folds were computed for several η-values. In Fig. 10 we show computations for the 2-vortex, 4-vortex interaction for $\eta = 0.727$, $\mu = 0$. Similar computations for $\eta = 0.615$ are shown in ([2], Fig. 2) ($\mathrm{Re} \leq 340$) and ([3], Fig. 2) ($\mathrm{Re} \leq 1100$), $\mathrm{Re} := \Omega_1 R_1 (R_2 - R_1)/\nu$. Here R_1 and Ω_1 are the radius and the angular velocity of the inner cylinder, R_2 and Ω_2 of the outer, $\eta = R_1/R_2$, $\mu = \Omega_2/\Omega_1$, and ν is the kinematic viscosity.

The curve marked by **(6)** in Fig. 10 is a curve of fold points. It corresponds to the curve of secondary bifurcation points emanating from the double point P^{11}_{21} and going to infinity in Fig. 2 [14]. The curves marked **(4)** and **(5)** in Fig. 10 correspond to the two $\lambda/2$-shifted twins of the secondary bifurcation curve connecting the double points P^{11}_{21} and P^{12}_{21} (see Figs. 2 and 5). As explained in ([14], p. 110ff), they got shifted to different parameter values by breaking of the midline symmetry (4). We thus expected that these curves would meet at the point $(\mathrm{Re}_{d4}, \lambda_{d4})$ corresponding to the point P^{12}_{21}. In Fig. 10 we see that they actually do so. A detailed analysis showed that the curves are connected smoothly, both at $(\mathrm{Re}_{d4}, \lambda_{d4})$ and at the point $(\mathrm{Re}_{24}, \lambda_{24})$ corresponding to P^{11}_{21}. The intersection of the curves is due to the projection. Unexpected is the detour of curve **(4)** to the regime of flows with three vortices in the radial direction

corresponding to flows bifurcating from R_{cr}^{p3} in the Rayleigh–Bénard case. We do not know which other double point causes it. Also, we did not investigate and thus cannot explain the fold emanating from curve **(4)** near its relative minimum.

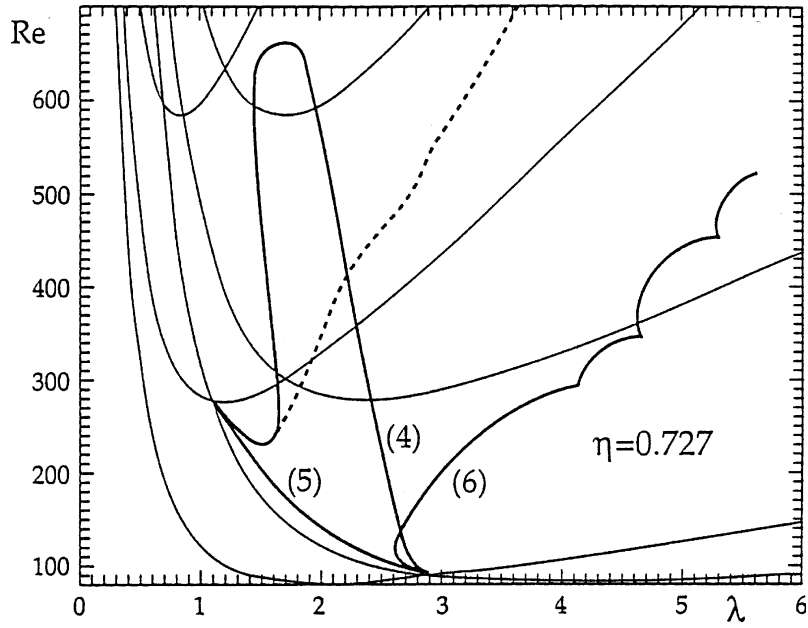

Fig. 10. *The 2-vortex, 4-vortex interaction for* $\eta = 0.727,\ \mu = 0$*:* projections of paths of bifurcation points and of fold points in the (λ, Re)-plane, $\mathrm{Re} = \Omega_1 R_1 (R_2 - R_1)/\nu$. Computations with the Taylor-version of the code described in section 4.1

The curves for $\eta = 0.615$ shown in ([3], Fig. 2) look quite similar to the ones for $\eta = 0.727$ up to Re-values corresponding to P_{21}^{12}. But then curve **(4)** takes several other detours, meets the double points corresponding to P_{21}^{13} and P_{21}^{14}, respectively, and disappears to higher Re-values. This was found to be due to a bifurcation between **(4)** and another secondary curve for $\eta \approx 0.707,\ \mu = 0$.

Secondary curves generated by the 2-vortex, 6-vortex and the 4-vortex, 6-vortex interactions for $\eta = 0.615,\ \mu = 0$ are shown in ([4], Figs. 1,3,4). These computations do not confirm our results on these interactions. But they also do not contradict them: as we have just seen, the perturbation of the Rayleigh–Bénard problem is too massive for these parameter values to draw any conclusions for the Rayleigh–Bénard problem.

References

1. J.H. Bolstad, H.B. Keller: 'Computation of anomalous modes in the Taylor experiment'. J. Comp. Phys. **69**, 230–251 (1987)
2. J.H. Bolstad: Following paths of symmetry-breaking bifurcation points. LLNL Tech. Rep. UCRL-99530, 1988; Int. J. Bif. Chaos **3** (1992) 559-576
3. J.H. Bolstad: Following paths of pitchfork bifurcation points. LLNL Tech. Rep. UCRL-JC-110570, 1992;
4. J.H. Bolstad: Following paths of transcritical bifurcation points. LLNL Tech. Rep. UCRL-JC-113312, March, 1993.
5. F.H. Busse, A.C. Or: Subharmonic and asymmetric convection rolls. ZAMP **37**, 608–623 (1986)
6. S. Chandrasekhar: *Hydrodynamic and Hydromagnetic Stability.* (Oxford University Press, London 1961)
7. J.H. Curry: A generalized Lorenz system. Commun. math. Phys. **60**, 193–204 (1978)
8. K. Gatermann, B. Werner: 'Secondary Hopf bifurcation caused by steady-state steady-state mode interaction'. In: *Pattern Formation: Symmetry Methods and Applications* ed. by J. Chadam et al., Fields Institute Comm. **5**, 1996
9. H.B. Keller: Numerical solution of bifurcation and nonlinear eigenvalue problems. 359 – 384 in *Applications of Bifurcation Theory.* P. Rabinowitz, ed., (Academic Press, New York 1977)
10. E. Knobloch, J. Guckenheimer: Convective transitions induced by a varying aspect ratio. Phys. Rev. A **27**, 408–417 (1983)
11. E.N. Lorenz: Deterministic nonperiodic flow'. J. Atmospheric Sci. **20**, 130–141 (1963)
12. D. Lortz, R. Meyer-Spasche, P. Petroff: A global analysis of secondary bifurcations in the Bénard problem and the relationship between the Bénard and Taylor problems. Methoden und Verfahren der mathematischen Physik **37** (Verlag Peter Lang, Frankfurt a.M., 1991) pp. 121–142
13. R. Meyer-Spasche, M. Wagner: The basic (n, 2n)-fold of steady axisymmetric Taylor vortex flows. In: *The Physics of Structure Formation*, ed. by W. Güttinger, G. Dangelmayr (Springer, Berlin, New York 1987) pp. 166–178
14. R. Meyer-Spasche: *Pattern Formation in Viscous Flows*, ISNM vol. **128**, (Birkhäuser, Basel, Boston 1999)
15. L. A. Segel: The non-linear interaction of two disturbances in the thermal convection problem. J. Fluid Mech. **14**, 97 – 114 (1962)
16. J.H. Wilkinson: Rounding Errors in Algebraic Processes, Her Magesty's Stationery Office, 1963, Springer Verlag 1969, Dover Reprint 1994

Taylor vortices at different geometries

Manfred Wimmer[1]

Fachgebiet Strömungsmaschinen, Universität (TH) Karlsruhe,
Kaiserstr. 12, D-76128 Karlsruhe, Germany

Abstract. Flow fields between differently shaped bodies of revolution are studied. These bodies are rotating cones with different apex angles, cylinder-cone combinations, disks as well as oblate and prolate ellipsoids. The basic flows are fully three-dimensional and influence the occurring instabilities. The dependence of the occurrence and the development of Taylor vortices, Görtler vortices and cross-flow instabilities on the described geometries are discussed. By separating the influence of the dynamics and the geometry on the vortices the effect of both parameters can be studied separately. Due to the simultaneous existence of sub- and supercritical flows the development at the threshold can be studied very clearly. Furthermore, the rich variety of occuring flow patterns - often existing side by side - offers new insides in unstable flows. A possible transition from counter-rotating Taylor vortices to unidirectional-rotating cross-flow instabilities is described. The influence of the governing parameters, like acceleration, gap width etc. are discussed.

1 Introduction

The existence of Taylor vortices is not confined to the flow between straight rotating circular cylinders. They may also occur for other geometries, different from the classical Taylor [1] arrangement. Taylor vortices can be detected for instance between rotating spheres, as described by Wimmer [2] and in this book by Bühler, and as it is displayed in Fig. 1. An extensive study of the behaviour of various vortical instabilities near differently shaped rotating bodies may be found in Wimmer [3]. The occurrence of Taylor vortices between rotating conical cylinders and between rotating ellipsoids will be discussed in the following. The flow between conical cylinders represents only a slight geometrical variation with respect to the classical Couette–Taylor experiment. Between cones we have, however, already a three-dimensional basic flow field, influencing the vortices to be generated. We can also investigate combinations of circular and conical cylinders. In the gap between these combinations a rich variety of flow patterns can be obtained. By changing the apex angle of the cones consequently from $\Phi = 0°$ (cylinder) to $\Phi = 180°$ (disk) the change from counter-rotating Taylor vortices to unidirectional-rotating cross-flow vortices can be demonstrated. Finally the flow between oblate and prolate ellipsoids represents the transition from the flow between disks to the flow between spheres or that one from the flow between spheres to the flow between cylinders, respectively.

C. Egbers and G. Pfister (Eds.): LNP 549, pp. 194–212, 2000.

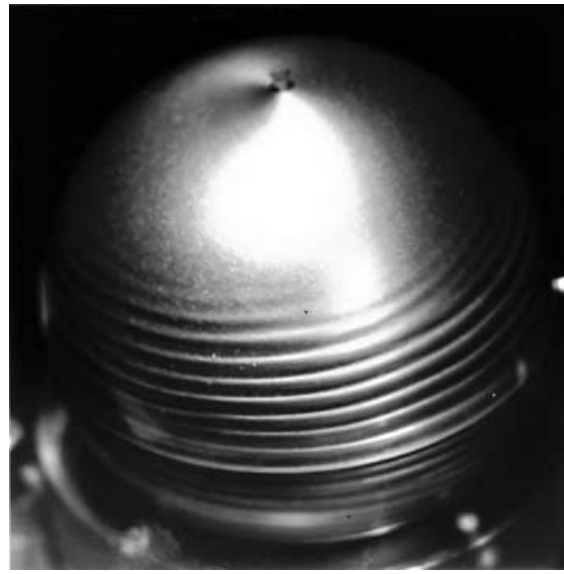

Fig. 1. Taylor vortices between spheres

2 Flow between cones with a constant width of the gap

2.1 Experimental set-up

The test arrangement consists of an inner rotating cone and an outer one at rest, as previously described by Wimmer [4]. Both cones have the same apex angle of $\Phi = 16.03°$, resulting in a constant width of the gap between the two coaxial cones. For all experiments silicone oils as working fluids are used with some aluminium flakes acting as tracers. The flows are characterized by the following parameters: the Reynolds number $Re = R_{1max}^2 \omega/\nu$ and the Taylor number $T = R_{1max} s^3 \omega^2/\nu^2$, where R_{1max} is the largest radius of the inner rotating body, s the width of the gap and ω and ν denote the angular velocity and the kinematic viscosity, respectively.

2.2 Flow field and Taylor vortices

Since the radius changes now linearly with the length of the cylinder, we obtain a linear distribution of the centrifugal forces in the gap. The imbalance of the centrifugal forces causes the three-dimensional flow field even in the subcritical state. The fluid is centrifuged at the largest radius, moves in spirals towards the smaller radius in the vicinity of the stationary cone and flows back to the larger radius near the rotating cone, still in spirals. They join and form a closed flow, as it is illustrated in Fig. 2.

The three-dimensional basic flow and especially the meridional component of the flow has a crucial influence on the Taylor vortices.

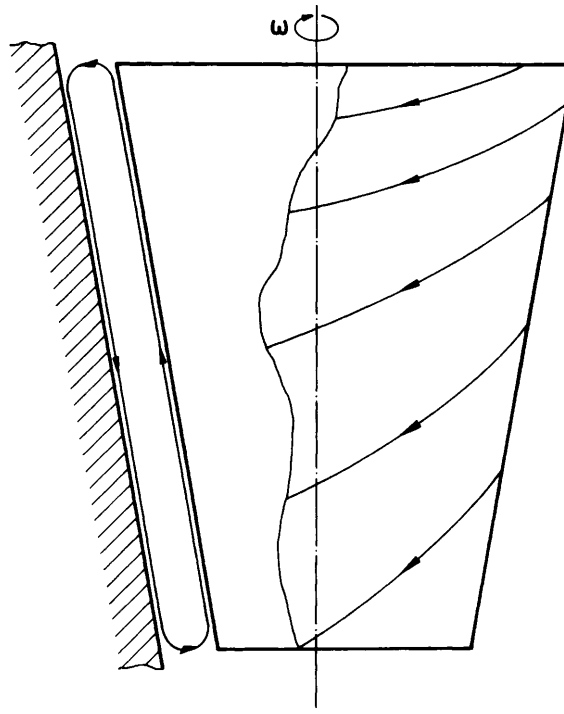

Fig. 2. Three dimensional basic flow

Taylor vortices appear first at the largest radius - in the upper part - whilst in the lower part - at the smaller radius - the undisturbed basic flow is still preserved. Hence, we obtain regions with sub- and supercritical flows in the gap, similar to the situation between rotating spheres (cf. Wimmer [2]). The still weak vortices at the beginning are most influenced by the three-dimensional flow and are floating upwards with the meridional flow. Such a situation is displayed in Fig. 3.

The occurrence of travelling closed toroidal vortex cells is astonishing, since we have here a closed system. The travelling can only happen, if the upper cells are compressed to such an extent that one of them vanishes, while the two neighbouring vortices join together, forming one large cell. The adjacent vortex pair follows up. At the same time, in the lower part a new pair is generated and the periodic process starts again. For more details see Wimmer [4]. The velocity of the floating vortices depends on the ratio of the strength of the meridional flow and the rotation of the vortices. The strength of the meridional flow and hence the velocity of the travelling vortices depends upon i) the apex angle ϕ, ii) the angular velocity ω, iii) the width of the gap s and iv) the axial location z.

As Fig. 4 shows, the travel velocity diminishes linearly with growing Reynolds number until a steady state is reached. The stationary vortices, too, are still

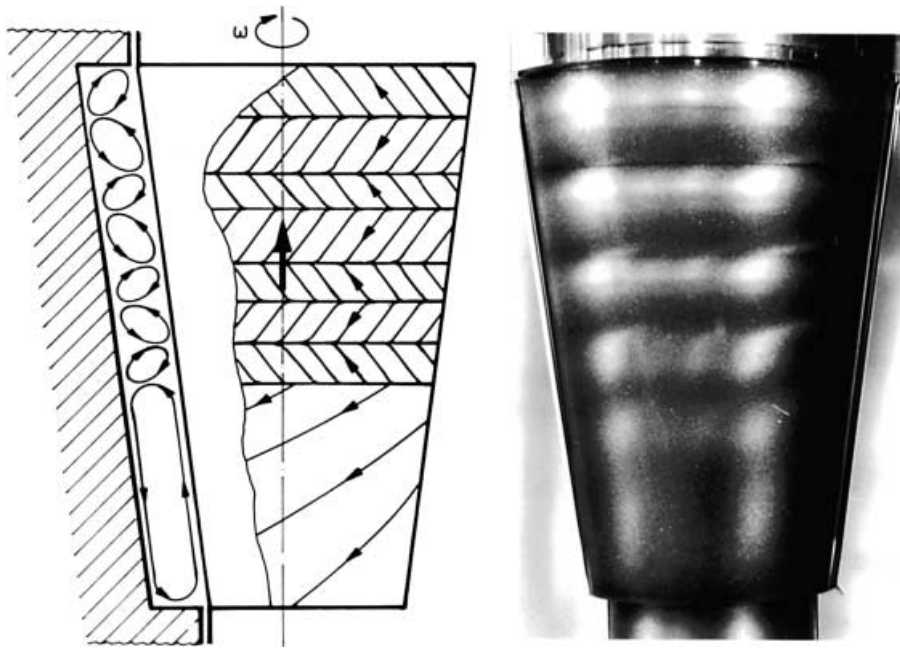

Fig. 3. Sketch and photo of sub- and supercritical regions. Toroidal vortices travel upwards.

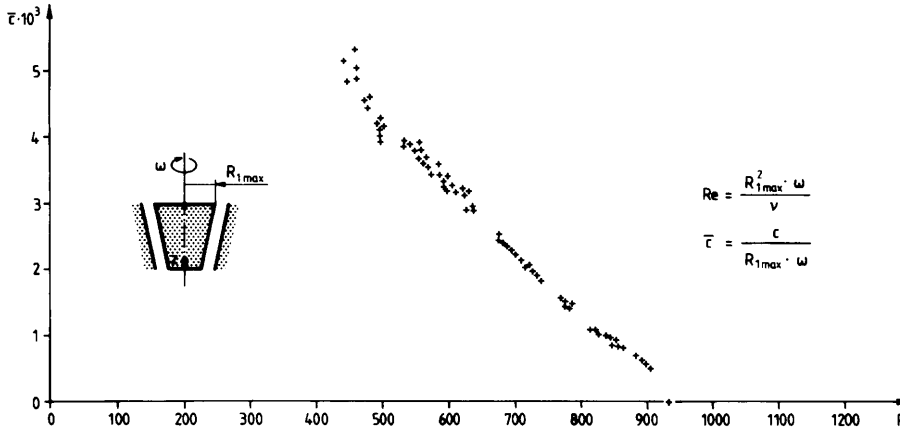

Fig. 4. Travel velocity of toroidal vortices.

influenced by the meridional flow, resulting in a deformation of single vortex cells. Vortices rotating *in* the direction of the meridional flow become stronger and are stretched, those rotating *opposite* to it are compressed. Since Taylor

vortices appear as pairs of counter-rotating cells, we obtain alternately big and small vortex cells in the gap between conical cylinders, as displayed in Fig. 5.

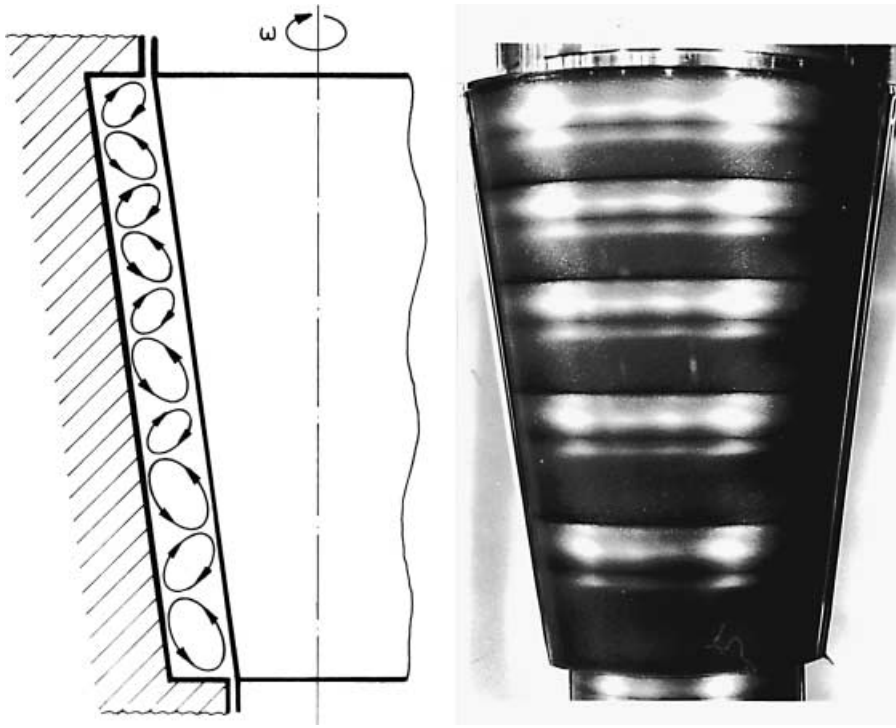

Fig. 5. Sketch and photo of the steady state with five vortex pairs.

Furthermore, because of the interaction of the locally different strength of the meridional flow and the vortices we observe, that a "large" cell at the bottom has a greater axial extension than a "large" one at the top, also demonstrated by Fig. 5. Measurements of the wavelength, described by Wimmer [4], give a difference of more than 100%.

2.3 Influence of initial and boundary conditions

For different initial conditions, e. g. in the experiment different rates of acceleration of the inner cone to supercritical flows, different final steady states can be obtained, showing the non-uniqueness of the process. A quasi-steady acceleration generates five pairs of vortices (see Fig. 5), while higher acceleration rates produce six or even seven pairs of vortices in the same gap at the same Reynolds numbers.
By applying another rate of acceleration an unsteady state with helical vortices

appear in the gap with a stationary outer cone. The helix winds around the inner rotating cone like a coil, as illustrated in Fig. 6a.

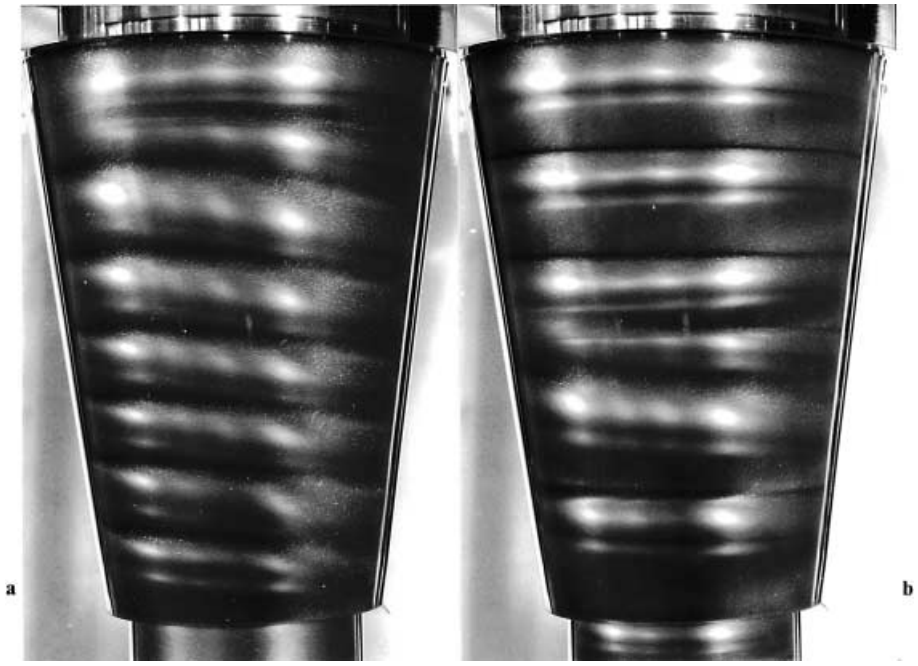

Fig. 6. Taylor vortices between coaxial cones. a) Propagating helical vortices (left), b) combination of toroidal and helical vortices (right).

For a clockwise rotation of the inner cone, the present helix with a right-hand orientation moves downwards to the smaller radius. For again another acceleration rate a combination of steady toroidal and unsteady helical vortices can be observed. Fig. 6b shows, that downwards moving helical vortices are e.g. confined between steady toroidal ones. Thus, we have the rare effect, that unstable steady and unstable unsteady flows exist side by side.

Different boundary conditions influence the occurrence of Taylor vortices as well. Different end plates, which limit the annulus, affect and modify the flow either by their geometry or by their dynamic effects. End plates may bridge the gap either completely or only partially, being either rotating or stationary. Combinations of stationary and rotating end plates generate asymmetric conditions in the gap, which results normally in an odd number of vortex cells. Another interesting boundary condition is impressed by an upper free surface and the filling rate of the fluid column. A detailed description of the various occurring flow configurations caused by the free surface effect can be found in Noui-Mehidi and Wimmer [5].

The size of the gap between the cones is another important parameter. For all

gap sizes, the first Taylor vortices appear at the largest radius. The critical Taylor number is smaller for smaller gap widths and the toroidal vortices start later to travel upwards. The regime of existence, i.e. the Taylor numbers where toroidal vortices appear or disappear, is shifted to smaller characteristic numbers with growing gap widths. Furthermore, the different axial extension of anti- and co-rotating vortex cells is the more pronounced the larger the gap width. A detailed study of the effect of different end plates and gap sizes on the vortices has been published by Denne and Wimmer [6].

3 Combinations of circular and conical cylinders

In the foregoing the width of the gap has been kept constant. It has also been demonstrated, that the geometry crucially affects the flow and the occurring vortices. By a combination of circular and conical cylinders the geometric effect can be studied very clearly.
Fig. 7 illustrates the idea and shows the possible combinations of cylinders and cones.

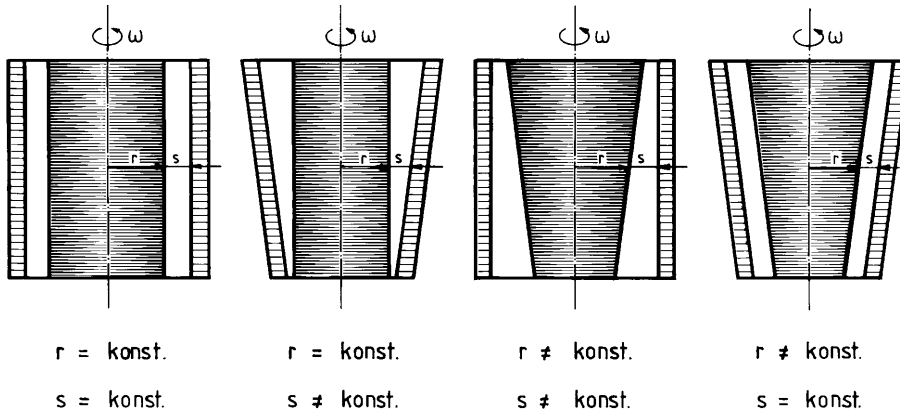

Fig. 7. Possible combinations of cylinders and cones.

If a cylinder rotates in a conical shell or a cone in a cylindrical container, the width of the gap is no longer constant. Since the Taylor number $T = Rs^3\omega^2/\nu^2$ contains the influence of dynamics and geometry, the effect of the geometric particularity on the flow can be separated. If we ensure for all cases, that the dynamic part ω^2/ν^2 is constant -which is easily practicable by controlling the angular velocity and the fluid's temperature- then the Taylor number depends only on the geometric parameters of the radius R and gap size s. The alteration of these geometric quantities is specified for each case in Fig. 7. Considering that the Taylor number depends linearly on the radius R and to the third power on the gap size s, it is apparent that the alteration must have an influence on the behaviour of the vortices.

3.1 Rotating cylinder in a cone

For the combination of a rotating cylinder in a stationary cone, we obtain, in spite of a constant radius, a three-dimensional flow, caused by the non-constant gap width. In this case, first vortices appear, according to $T \sim s^3$, at the location of the largest gap size. Thus, as for coaxial cones, regions with and without vortices may be observed within the gap. Finally, for higher Taylor numbers, the whole annulus is filled with vortices. Due to the meridional flow and the non-constant gap width the Taylor vortices are deformed, having larger differences in their axial extension. Measurements, previously described by Wimmer [7], clearly show the linear increase of the vortex extension with increasing gap width. This behaviour was also confirmed by Abboud's [8] numerical calculations.

3.2 Rotating cone in a cylinder

If a cone rotates in a stationary cylindrical container, the situation is more complicated because now neither the radius R nor the gap size s remain constant. Naturally, the basic flow is again three-dimensional. The meridional flow, which considerably influences the vortices, is not uniform, because of the different gap cross-sections.
For the present configuration first vortices are observed at middle axial positions with medium seized gap widths, according to $T \sim Rs^3$. A simple calculation for the local Taylor number is presented in Wimmer [7] and [9]. At the threshold the vortices are very weak and move therefore upwards along with the meridional flow. Thus, they come into regions where locally the critical conditions are not yet fulfilled, because of the smaller gap size. They decay. Only by increasing the angular velocity, vortices can be generated also here and adjacent vortices below become stronger. The whole system travels, however, upwards as for the coaxial cones, until a steady state is reached. The velocity of the travelling toroidal vortices again decreases linearly with increasing Reynolds numbers. The steady state is again not unique, but depends on different parameters, as for instance, on the end plates, the apex angle of the cone, the rate of acceleration and the Reynolds number.

For a constant apex angle of e.g. $\Phi = 16.03°$ we obtain for different acceleration rates, four steady states with two, three, four and five toroidal vortices in the upper part and the swirl of the remaining secondary flow in the lower part. The different modes of flow can be obtained either by different initial accelerations directly out of the basic flow or by a change from one mode into the other. Consequently, the different modes can only exist in a limited Reynolds number range - their regimes of existence.

Figure 8 illustrates the different Reynolds number regimes and the way in which one mode changes into another. The mode with three vortices, which is generated by a quasi-steady acceleration, is the most stable one. It appears first and exists longest, even for very high Reynolds numbers after all other modes have merged into it. For different widths of the gap and for different apex angles

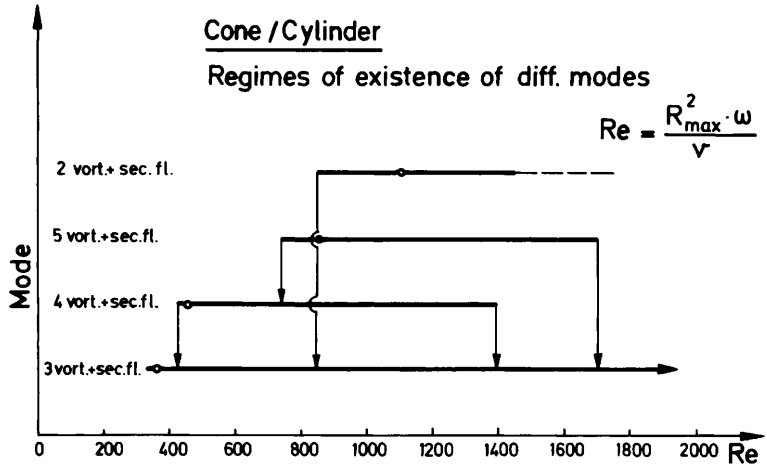

Fig. 8. Regimes of existence of different modes and possible transitions.

of the cone, we obtain other Reynolds numbers for the regimes of existence. In general, the smaller the apex angle, i.e. the more the cone resembles a cylinder, the smaller the number of modes.

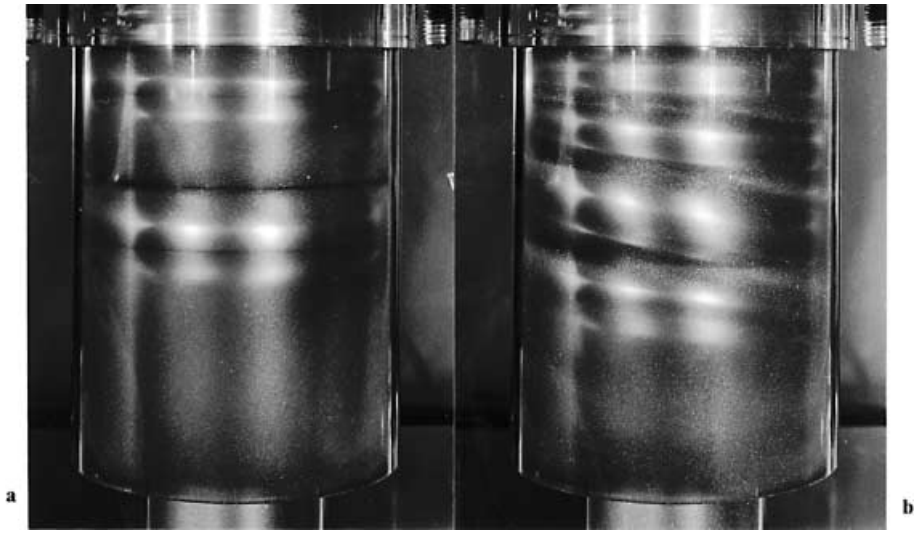

Fig. 9. Taylor vortices between a rotating cone in a cylinder. a) Steady state with three Taylor vortices and the remaining secondary flow (left), b) helical vortices in a non-constant gap and stationary outer cylinder (right).

As an example for the different modes of flow, Fig. 9a shows the most stable configuration with three toroidal vortices and remaining secondary flow in the lower part. The different axial extension of the Taylor vortices is apparent.
Also for the non-constant gap between a cone and a cylinder, a configuration with helical vortices exists, displayed in Fig. 9b. The mode is again unsteady for all Reynolds numbers and the helical vortices propagate downwards from the larger to the smaller radius. This is the first evidence of the existence of helical vortices in a non-constant gap and a stationary outer shell.

The flow between cone-cylinder combinations is also of interest to the process of wave-number selection, which is accomplished by a spatial variation of the Taylor number. For this purpose Dominguez-Lerma et al. [10] used conical ramps to combine the subcritical part of the gap with the supercritical one. The combining conical part can either be established in the outer stationary shell - called ramps - or at the inner rotating body - called tapered cylinder. Hence, we have exactly the same geometric combination as described above. As soon as Taylor vortices are generated in the section of the conical ramps, they influence - together with the meridional flow in this section - the just occurring vortices in the so far subcritical part of the smaller gap width. In order to learn something about the influence during the generation of these vortices, it is necessary to study the conditions within the conical ramps.

4 Flow between cones with different apex angles

Now we consider again flows between cones with a constant width of the gap; but the apex angle of the cones is permanently enlarged. As a result, the meridional flow becomes stronger and stronger with all consequences for the occurring vortices.
For all instabilities, described above, we always obtain vortex systems of the Taylor-Görtler type with pairs of alternately counter-rotating vortices. They occur either as closed toroidal cells or as propagating helical vortices. There exists, however, another widespread form of unstable flow: the cross-flow instabilities. They exist only in the presence of a three-dimensional basic flow. Cross-flow instabilities produce vortices rotating all in the same direction and in rotating systems having axes in form of spirals.

With the following set of six cones with different apex angles, already used by Wimmer and Zierep [11], it can be demonstrated, that one vortex system may be transformed in another one. For this purpose we imagine, that the unidirectional-rotating cross-flow instabilities may be generated by a superimposed cross-flow acting on the equidistant, counter-rotating Taylor vortices.

Figure 10 elucidates and explains the idea. All Taylor vortex cells, rotating *in* the direction of the cross-flow are strengthened and enlarged and those rotating *opposite* to it are weakened and compressed. Now it depends only on the ratio of the strength of the cross-flow and the vortex rotation how far this effect is

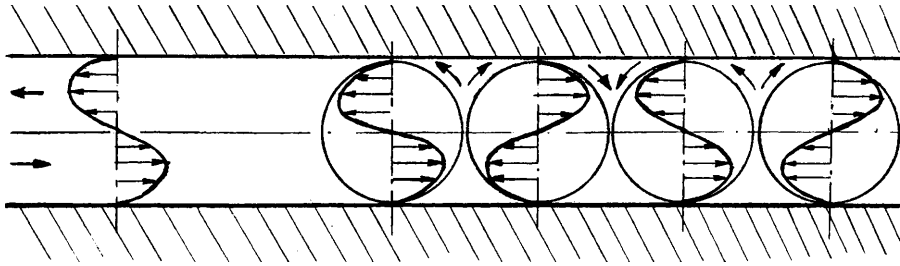

Fig. 10. Superposition of a cross-flow and Taylor vortices.

pronounced. It may result in only a small deformation of the Taylor cells or in enlarged co-rotating cells while anti-rotating cells are extinct. Thus, every second cell is compressed to such an extent that it vanishes and a system of vortices rotating all in the same direction remains. Such a development can be verified experimentally by changing the geometry of the cones, as it is demonstrated in Fig. 11.

If the inclination of the cylindrical walls is increased step by step, the configuration changes from the coaxial circular cylinder to finally a rotating disk in a housing - with passing intermediate stages of conical geometries. The change from counter-rotating to unidirectional-rotating vortices is only possible since the variation of the cone's apex angle allows the variation of the strength of the cross-flow. Between rotating cylinders we have no cross-flow and hence regular Taylor vortices of the same size appear, as it is displayed in Fig. 13a. The meridional flow between the cones represents the cross-flow for the Taylor vortices. With increasing apex angle it grows stronger and stronger until at $\Phi = 180°$ the meridional flow between cones becomes the radial flow between a rotating disk in a housing. For moderate apex angles of $\Phi = 16°$ and $32°$, the toroidal Taylor vortices appear with different axial extensions of the cells as described in section 2 and shown in Fig. 13b.

For larger apex angles between $\Phi = 32°$ and $60°$ the propagating helical vortices are the preferred states with more or less large differences for co- and anti-rotating vortex cells as is evident by the photos of Fig. 13c and 13d. In Fig. 13d it is manifested that only two helical vortex pairs remain. For an apex angle of $\Phi = 60°$ the difference between adjacent vortices is so big, that for high Reynolds numbers only one pair of helical, deformed Taylor vortices is left, as it is shown in Fig. 12.

Looking from above we see in the plainview the spiral form of the vortex system. For cones with an apex angle larger than $\Phi = 60°$ no Taylor vortices could be detected. Finally at $\Phi = 180°$ we have the configuration of a rotating disk in a housing. Here the well-known cross-flow instabilities appear, as shown in Fig. 13f, with unidirectional-rotating vortices. The axes of the vortices form logarithmic spirals with an angle of $14°$ with respect to the circumferential direction, as it was already mentioned by Gregory, Stuart and Walker [12].

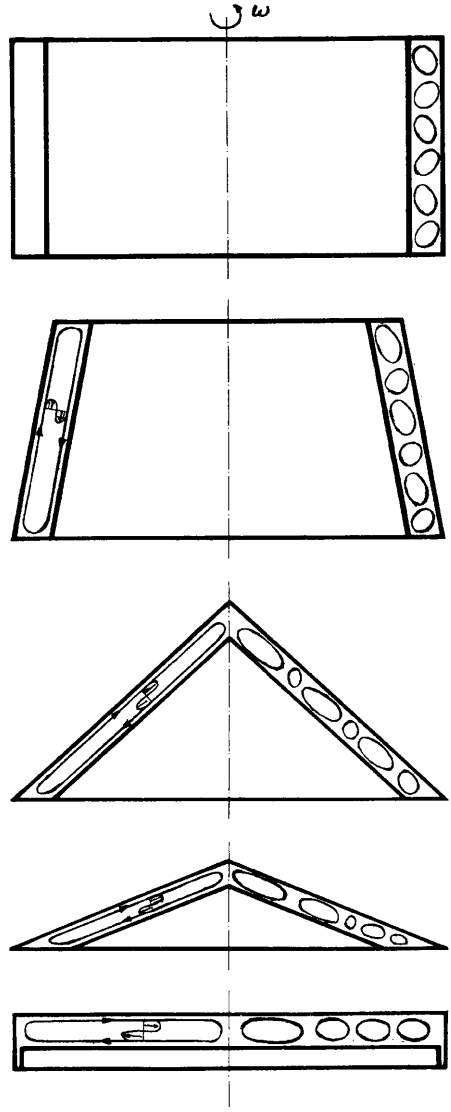

Fig. 11. Transition from cylinder to disk with growing apex angle Φ.

More details about intermediate stages of flow patterns between the cones for various apex angles and Reynolds numbers can be found in Wimmer and Zierep [11]. It should be pointed out that the method of a transition from Taylor vortices to cross-flow instabilities is only practicable as long as helical Taylor vortices exist. In the present investigation this is the case up to an apex angle of $\Phi = 60°$. This fact is also in accordance with resent calculations of Hoffmann and Busse [13].

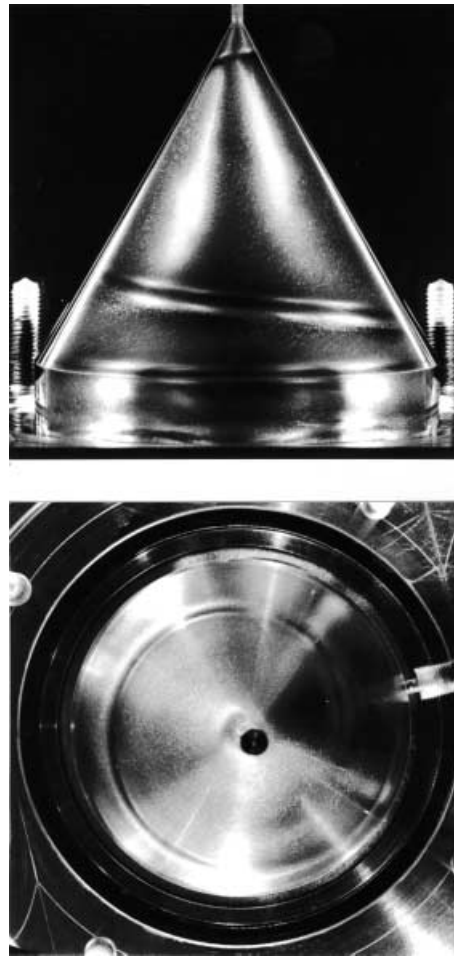

Fig. 12. One pair of helical vortices for $\Phi = 60°$. Front- and plainview.

5 Flow between rotating ellipsoids

Another variation of the geometry is represented by rotating coaxial ellipsoids. During the last years it could repeatedly be demonstrated (e.g. Wimmer [2]), that in the neighbourhood of the equator between concentric spheres the flow conditions are similar like those between coaxial cylinders and in the vicinity of the poles like those between rotating disks. There was, however, the unanswered question, up to which latitude of the spheres the similarity to the cylinders is guaranteed and how far the analogy to the rotating disks is valid. In order to clarify these regimes of validity, we investigate rotating bodies with a shape between cylinder and sphere or between sphere and disk, respectively, as it was suggested by Wimmer [14].

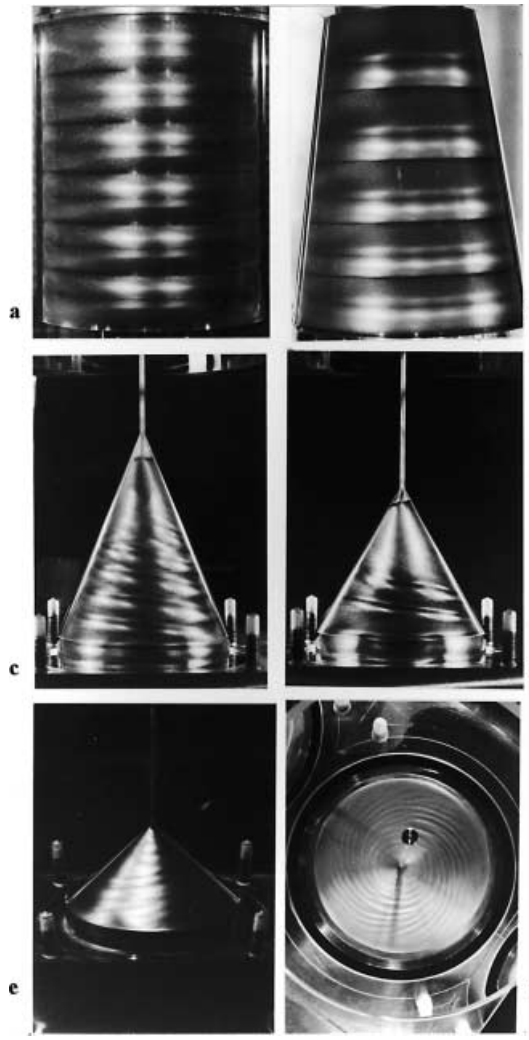

Fig. 13. Transition from counter-rotating cylinder Taylor vortices to unidirectional-rotating cross-flow instabilities. From left to right and top to bottom: a) Taylor vortices between cylinders; b) toroidal Taylor vortices between cones, $\Phi = 16°$; c) helical travelling Taylor vortices, $\Phi = 45°$; d) different size of helical travelling vortices, $\Phi = 60°$; e) spiral instability, $\Phi = 90°$; f) cross-flow instability between disks, $\Phi = 180°$.

These bodies are, as Fig. 14 shows, ellipsoids rotating about their shorter or longer axes to give oblate or prolate rotating ellipsoids, respectively. A theoretical treatment of the elliptical geometry has already been published by Hocking [15].

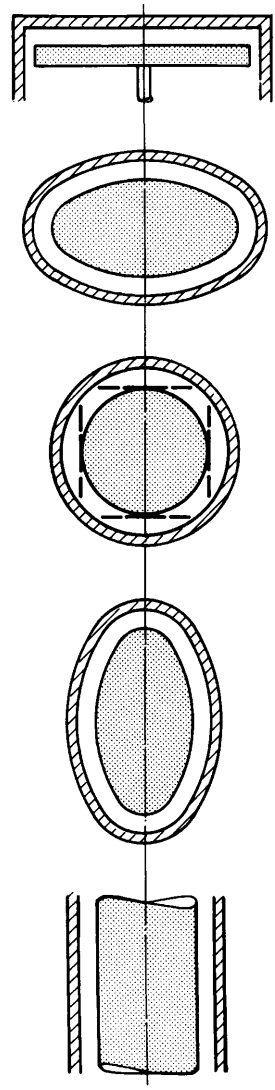

Fig. 14. Ellipsoids between disk, sphere and cylinder.

So far we have studied ellipsoids with an axis ratio of $A : B = 2 : 1$ for the outer, stationary oblate ellipsoid and axis ratios between $a : b = 2.0519 : 1$ and $2.1149 : 1$ for the inner, rotating oblate ellipsoid, to give constant gap widths between $s = 2.0$ mm and 4.175 mm. For the prolate ellipsoids the axis ratio of the outer ellipsoid is $A : B = 1 : 2$ and for the inner, rotating one $a : b$ is between $1 : 2.0158$ and $1 : 2.1441$, resulting in gap sizes between $s = 1.24$ and $s = 10.075$ mm. Here A and a denote the horizontal axes of the ellipsoids. The adaptation of the axis ratios of the inner ellipsoids for different gap widths is necessary to

produce same gap sizes at the equator and the poles. The basic flow field between rotating ellipsoids is again fully three-dimensional. It is however more complex than that between concentric rotating spheres because of the different curvature of the ellipsoids in circumferential and meridional direction. This effect will have an influence on the vortices to be generated.

5.1 Oblate rotating ellipsoids

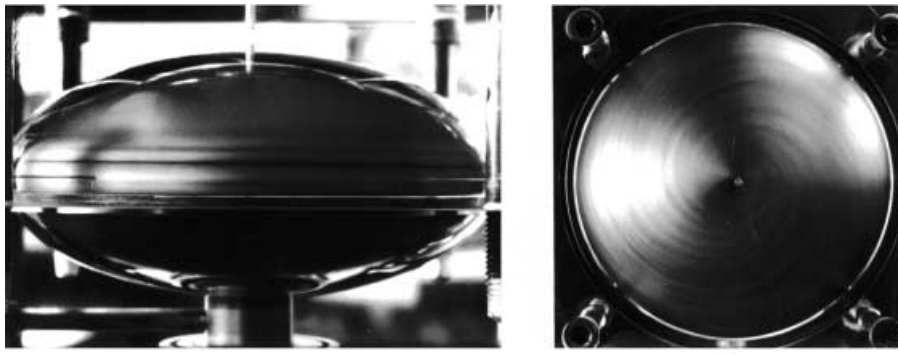

Fig. 15. Oblate ellipsoid with $A : B = 2 : 1$.a) Two Taylor vortices on each hemisphere (top), b) spiral instability around the pole (bottom).

The oblate ellipsoids illustrate the transition of geometric and fluid mechanical conditions from a sphere to a disk. At the equator of oblate ellipsoids with an axes ratio of $A : B = 2 : 1$, there is only a very small region that resembles the cylindrical geometry; and hence we expect only a small number of Taylor vortices, if at all. For the smallest investigated gap size of $s = 2.0$ mm one obtains - at the maximum - four Taylor vortices on each side of the equator, by applying the adequate initial acceleration. For a gap size of $s = 4.175$ mm only one regular Taylor vortex is generated on each hemisphere. Here we observe again a radial inward jet at the equator, as in the spherical case for medium sized gap widths (cf. Wimmer [2]).

Figure 15a shows a situation with two straight Taylor vortices on each side of the equator for a gap width of 2.0 mm. The number of Taylor vortices depends on the gap size and initial accelerations. It can be stated, that the smaller the gap width and the higher the rate of acceleration, the higher the number of generated Taylor vortices. For higher Reynolds numbers the Taylor vortices become disturbed and take a wavy form and often some vortex fragments are hurled off to the poles. For gap sizes larger than 6.0 mm no regular Taylor vortices can be detected. Thus, Taylor vortices exist in the present case only in a small region in the equator's vicinity.

Since the oblate ellipsoid resembles more the configuration of a disk, the flow conditions are alike. The largest part of the elliptical surface is therefore occupied by a spiral cross-flow instability. Fig. 15b shows these spirals at moderate Reynolds numbers. The arms of the spirals may already influence eventually existing Taylor vortices in the equator region. For higher Reynolds numbers the spirals become stronger, reaching entirely down to the equator and leaving no chance for the generation of Taylor vortices.

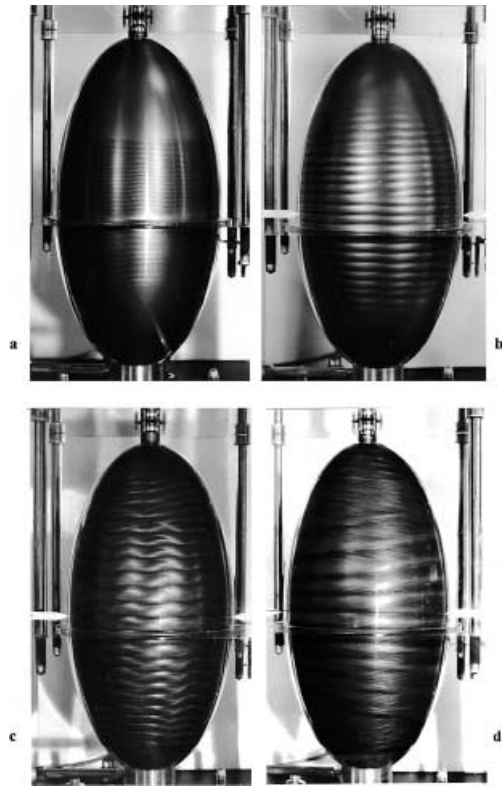

Fig. 16. Vortex configuration between prolate ellipsoids, $A : B = 1 : 2$. Inner one rotates, outer one at rest. From left to right and top to bottom: a) Taylor vortices for narrow gap sizes, $s = 1.24$mm, $T = 2075$; b) broader Taylor vortices for broader gap sizes, $s = 4.90$mm, $T = 6000$; c) wavy Taylor vortices, $s = 4.90$mm, $T = 26500$; d) Taylor vortices near the equator and spirals around the poles; inbetween both systems overlap each other, $s = 6.35$mm, $T = 1311000$.

5.2 Prolate rotating ellipsoids

The prolate ellipsoids represent the transition from the spheres to the cylinders. We obtain, therefore, a situation as if the section around the equator between

the spheres is stretched; and hence we expect vortex configurations looking more like those between coaxial cylinders. For very small gap sizes between the prolate ellipsoids the analogy to the coaxial cylinders matches nearly ideally. For a gap width of $s = 1.24$ mm on obtains for example a broad band of small Taylor vortices beneath and above the equator, as it is displayed in Fig. 16a.

By increasing the angular velocity, more vortices are added in the direction of the poles, because also here the centrifugal forces are a function of the latitude. The pole regions remain always free of Taylor vortices. For the small gap sizes the Taylor vortices in the neighbourhood of the equator are only slightly inclined. The inclination grows with growing distance from the equator and growing gap widths. For larger gap sizes the wavelength of the vortices becomes larger, too, as it is shown in Fig. 16b. The angle of inclination of the axes of the vortices also grows with the gap size, and the occurrence of the Taylor vortices resembles more those between spheres rather than those between cylinders. When the Reynolds number is increased, the vortices become wavy as for the spheres and cylinders. Fig. 16c shows such a regular, aesthetic pattern, caused by a secondary instability in circumferential direction. For even larger gap widths the number of vortices diminishes and they are limited to a region near the equator. For these gap sizes and high Reynolds numbers a spiral instability around the poles appears, like for the rotating spheres. The arms of the spirals grow towards the equator with increasing angular velocity and reduce the Taylor vortices in this region. Fig. 16d shows a situation, where the remaining Taylor vortices near the equator are influenced by the spiral cross-flow instability. Both systems overlap each other, forming in this region another system with a new, not clearly defined structure.

6 Conclusions

By a variation of the geometry one can study the influence of geometric parameters very clearly by separating the geometric and the dynamic part of the Taylor number. The effect of the three-dimensional basic flow on the instabilities depends on the ratio of the strength between the basic flow and the vortices. The varying centrifugal forces in the gap produce sub- and supercritical regions existing side by side. This fact allows to study the gradual spatial transition from sub- to supercritical flows. It has been demonstrated that a non-constant gap width - together with the three-dimensional basic flow - crucially influences the onset and the shape of the vortices. Most recently, Rafique [16] contributed to this problem by rotating a sinusoidally shaped inner rotating cylinder in a straight stationary outer one. For certain geometries it is possible to have simultaneously two different types of instability in the gap, e.g. counter-rotating Taylor vortices and unidirectional-rotating cross-flow vortices. They are either separated or they influence and overlap each other, forming this way own, not clearly defined flow patterns. It has also been demonstrated that a change from one instability system into another is possible by gradually changing the geometry. By varying the geometry one can learn a lot about the onset and the further development of vortex configurations and pattern forming systems.

References

1. Taylor, G. I. : Stability of a viscous liquid contained between two rotating cylinders. Phil.Trans. Roy. Sci. A **223**, 289 - 343 (1923).
2. Wimmer, M.: Experiments on a viscous fluid flow between concentric rotating spheres. J. Fluid Mech. **78**, 317 - 335 (1976).
3. Wimmer, M.:Viscous flows and instabilities near rotating bodies. Prog. Aerospace Sci. **25**, 43- 103 (1988).
4. Wimmer, M.: An experimental investigation of Taylor vortex flow between conical cylinders. J. Fluid Mech. **292**, 205 - 227 (1995).
5. Noui-Mehidi, M. N. , Wimmer, M. : Free surface effects on the flow between conical cylinders. Acta Mech. **135**, 13 - 25 (1999).
6. Denne, B. , Wimmer, M. : Travelling Taylor vortices in closed systems. Acta Mech. **133**, 69 - 85 (1999).
7. Wimmer, M. : Wirbelbehaftete Strömungen im Spalt zwischen Zylinder-Kegel-Kombinationen. Strömungsmechanik und Strömungsmaschinen, Universität Karlsruhe, **44**, 59 - 83 (1992).
8. Abboud, M. : Ein Beitrag zur theoretischen Untersuchung von Taylor-Wirbeln im Spalt zwischen Zylinder/Kegel-Konfigurationen. ZAMM **68**, 275 - 277 (1988).
9. Wimmer, M.: 'Vortex patterns between cones and cylinders'. In: *Ordered and turbulent patterns in Taylor–Couette flow.* Eds.: C. D. Andereck, F. Hayot. NATO ASI Series B. Physics 297, Plenum Press N. Y. 205 - 211 (1992).
10. Dominguez-Lerma, M. A. , Cannel, D. S. , Ahlers, G. : Eckhaus boundary and wave-number selection in rotating Couette–Taylor flow. Phys. Rev. A **34**:6, 4956 - 4970 (1986).
11. Wimmer, M., Zierep, J. : Transition from Taylor vortices to cross-flow instabilities. Acta Mech. (to appear : 2000).
12. Gregory, N. , Stuart, J. T. , Walker, W. S. : On the stability of three-dimensional boundary layers with application to the flow due to a rotating disk. Phil. Trans. Roy. Sci. A **248**, 155 - 199 (1956).
13. Hoffmann, N. , Busse, F, H. : Instabilities of shear flows between two coaxial differentially rotating cones. Phys. of Fluids **11**:6, 1676 - 1678 (1999).
14. Wimmer, M. : Strömungen zwischen rotierenden Ellipsen. ZAMM **69**, 616 - 619 (1989).
15. Hocking, L. M.: The instability of flow in the narrow gap between two prolate spheroids. Q. J. Mech. Appl. Math. **34**, 475 - 488 (1981).
16. Rafique, M. : Contribution a lécoulement entre deux cylindres coaxiaux a entrefer constant et a entrefer ondule par la surface du cylindre interieur tournant. Ph. D. Thesis, INPL, Nancy (1999)

Isothermal spherical Couette flow

Markus Junk and Christoph Egbers

Centre of Applied Space Technology and Microgravity (ZARM), University of Bremen, 28359 Bremen, Germany

Abstract. We summarise different types of instabilities and flow patterns in isothermal spherical Couette flows as a function of the aspect ratio. The flow of a viscous incompressible fluid in the gap between two concentric spheres was investigated for the case, that only the inner sphere rotates and the outer one is stationary. Flow visualisation studies were carried out for a wide range of Reynolds numbers and aspect ratios to determine the instabilities during the laminar-turbulent transition and the corresponding critical Reynolds numbers as a function of the aspect ratio. It was found, that the laminar basic flow loses its stability at the stability threshold in different ways. The instabilities occurring depend strongly on the aspect ratio and the initial conditions. For small and medium aspect ratios ($\beta \leq 0.25$), experiments were carried out as a function of Reynolds number to determine the regions of existence for basic flow, Taylor vortex flow, supercritical basic flow. For wide gaps, however, Taylor vortices could not be detected by quasistationary increase of the Reynolds number. The first instability manifests itself as a break of the spatial symmetry and non-axisymmetric secondary waves with spiral arms appear depending on the Reynolds number. For $\beta = 0.33$, spiral waves with an azimuthal wave number $m = 6$, 5 and 4 were found, while in the gap with an aspect ratio of $\beta = 0.5$ spiral waves with $m = 5$, 4 and 3 spiral arms exist. For $\beta = 1.0$, we could detect spiral waves with $m = 4$, 3 and 2 arms. We compare the experimental results for the critical Reynolds numbers and wave numbers with those obtained by numerical calculations. The flow modes occurring at the poles look very similar to those found in the flow between two rotating disks. Effects of non-uniqueness and hysteresis are observed in this regime.

1 Introduction

The subject of hydrodynamic instabilities and the transition to turbulence is of importance for the understanding of nonlinear dynamic systems. Progress in understanding instabilities, bifurcations and routes into chaos has been made primarily by focusing attention on a small number of relatively simple hydrodynamic systems like Rayleigh-Bénard convection and the flow between two concentric rotating cylinders (Taylor-Couette flow). Furthermore, a considerable progress in understanding the first instability in the form of Taylor vortices of a viscous incompressible fluid flow between two concentric rotating spheres for small and medium gap widths has been achieved over the last decades. The three examples just reviewed are examples of transition to turbulence through a repeated finite number of symmetry-breaking bifurcations. Especially the study of instabilities and turbulence in spherical Couette flow is of basic importance for the understanding of global astrophysical and geophysical motions. Much of

C. Egbers and G. Pfister (Eds.): LNP 549, pp. 215–233, 2000.

the universe is filled with fluids in turbulent motion, and instabilities are quite common in planetary atmospheres. But the study of spherical Couette flow is also important for general theory of hydrodynamic stability since this flow is a natural combination of circular Couette flow at the equator and the flow between rotating disks at the poles. Another important feature of the spherical geometry is that the basic flow involves two types of symmetry, the reflection symmetry with respect to the equator and the translational symmetry with respect to the axis of rotation. Depending on the aspect ratio, both types of symmetry-breaking bifurcations can exist in the spherical Couette flow.

In this work, we consider the flow between two concentric spheres with the inner sphere rotating and the outer one at rest as illustrated in Fig.1. This flow can be characterised by the following control parameters: The aspect ratio $\beta = (R_2 - R_1)/R_1$ and the Reynolds number $Re = (R_1^2 \Omega)/\nu$, where R_1 and R_2 are the inner and outer radii, Ω is the angular velocity of the inner sphere and ν is the kinematic viscosity. Another important control-parameter coming into account is the acceleration rate, because the occurring flow pattern during the transition to turbulence are also determined by the history of the flow, i.e. it depends on whether the Reynolds number is increased or decreased, quasistationary or fast.

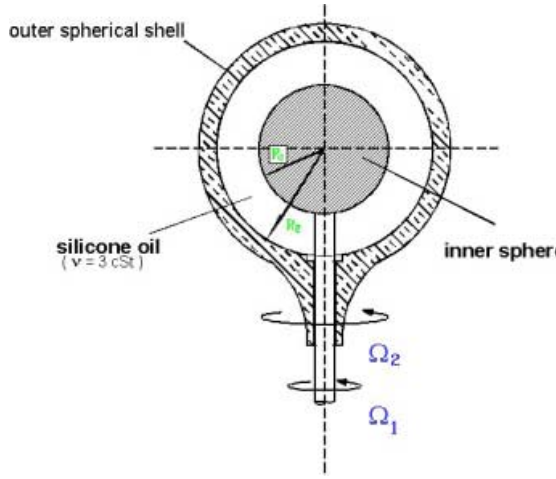

Fig. 1. Principle sketch of the spherical Couette flow model

The problem of the flow between concentric rotating spheres is similar to the flow between coaxial cylinders, but nevertheless, there are some important differences: In the cylindrical case, there are often unwanted effects because the necessary end plates lead to boundary conditions with discontinuities, while there are no boundary effects in the spherical Couette flow. The basic flow in the spherical case is three-dimensional and consists of an azimuthal motion superposed by a meridional flow which forms a large vortex in the meridional plane.

This meridional flow is caused by the so-called Ekman pumping due to the centrifugal forces at the pole. It leads to the formation of an outward-flow region at the equator. Its strength increases with the Reynolds number and the gap width: for low Reynolds numbers, it is rather weak and in the limit $Re \to 0$, the basic flow is the purely azimuthal Stokes flow. A principal sketch of a meridional section of the basic flow and of some typical supercritical flow structures can be seen in Fig. 2. Another decisive difference between cylindrical and spherical Couette flow is the meridional dependence of the centrifugal force in the spherical geometry which can lead to the spatial coexistence of different flow states in the sphere at a fixed Reynolds number. Two limiting cases allow comparisons with other flow geometries: The equatorial region resembles a region between two cylinders, while in the pole regions, there are some similarities to the flow induced by a rotating disk.

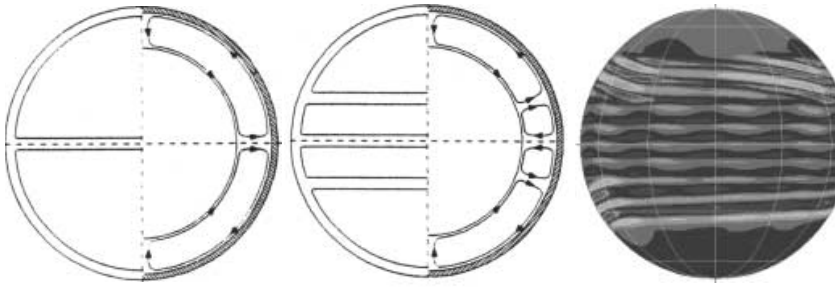

Fig. 2. Illustration of typical flow structures in the isothermal spherical Couette flow: basic state, Taylor vortex flow and spiral vortex flow (higher instability)

Most of previous experimental investigations on spherical Couette flow were restricted to small and medium gap widths, where the first instability of the basic flow leads to the formation of Taylor vortices in the equatorial region, as reported e.g. by Khlebutin (1968), Sawatzki & Zierep [34], Munson & Menguturk [29], Wimmer [39,40] , Yavorskaya et al.[48], Bühler [12], Bühler & Zierep [14,15]. Although spherical Couette flow is more relevant to astrophysical and geophysical applications, in comparison with the Taylor-Couette flow system, the dynamic behaviour during the laminar-turbulent transition of the flow between two concentric spheres has been studied less (e.g. Belyaev et al. [9], Nakabayashi & Tsuchida [31], Egbers [19]).

Some different aspects of the dynamic behaviour of the spherical Couette flow during the transition to turbulence for a wide range of Reynolds numbers and for the case of a wide gap width are presented in this article. The instabilities arising are in contrast to Taylor instabilities. They occur in the form of non-axisymmetric secondary waves with spiral arms, which break the spatial symmetry behaviour of the basic flow. With increasing Reynolds number, the number of secondary waves with spiral arms decreases, before the flow loses its stability. The flow seems to become chaotic with increasing the Reynolds number

(Egbers & Rath [20]). In early studies of the flow in wide gaps, this transition was thought to be a direct transition into turbulence without the existence of pattern-forming instabilities (Munson & Menguturk [29]); the first observations of the mentioned supercritical spiral waves in wide gaps are reported by Yavorskaya, Belyaev et al. [47,7].

With the means of time series analysis of the LDV measurements some additional quantitative estimates for the existence of a transition region from laminar basic flow to chaotic motion and for the onset of turbulence in the wide gap width were given. Experimental results connected with the problems of stability, bifurcation, non-axisymmetry, periodicity, quasi-periodicity, chaotic and turbulent motions in the spherical Couette flow are discussed in a paper by Wulf et al. [41]

2 Summary of previous investigations

In this chapter, we summarise previous results on the spherical Couette flow and present a stability diagrams showing the critical Reynolds numbers of the flow as a function of the aspect ratios for smaller and medium gaps as well as for wide gaps (Fig. 3), making use of data available in the literature and from own investigations. Frequent experimental investigations on spherical Couette flow with the inner sphere rotating and the outer sphere at rest were carried out in the region of small and medium aspect ratios, where Taylor vortices exist like in circular Couette flow [37]. The existence of Taylor vortices in spherical gaps was first discovered experimentally by Khlebutin [24]. For aspect ratios $\beta \leq 0.19$, he calculated a good fit of the critical Reynolds number for the onset of Taylor instability to give $Re_c = 49\beta^{-3/2}$; later, this power law was improved to $Re_c = 41.3(1+\beta)\beta^{-3/2}$. He carried out flow visualisation experiments and torque measurements in the range of $0.037 \leq \beta \leq 1.515$, but for $\beta > 0.44$, he did not find Taylor vortices in his experiments. Further investigations of Taylor instability in spherical Couette flow were carried out by Sawatzki & Zierep [34], Yakushin [42], Munson & Menguturk [29], Wimmer [39], Yavorskaya et al. [48] and Nakabayashi [30]. Bühler & Zierep [14] found new secondary instabilities for higher Reynolds numbers and medium sized gap widths. A survey of the work so far on Taylor vortex flow in small and medium sized gap widths is enclosed in the work of Bühler [12]. For the case of large aspect ratios, however, only a few experimental investigations were carried out: Sorokin [36] experimentally tested the validity of Bratukhins [11] linear stability analysis for the case of a large gap ($\beta = 1.0$) and they found a continuous change with Reynolds number, but not a sudden transition. Munson & Menguturk [29] and Waked & Munson [38] reported that the laminar basic flow becomes unstable by transforming directly into turbulent flow and not by Taylor instability, while Yavorskaya et al. [47] could detect a transition region for $\beta = 0.54$, where secondary waves exist before the flow becomes turbulent. Similar phenomena could later be observed in other wide gaps. However, their description of the behaviour of these secondary waves was not very detailed. Only a few investigations on spherical Couette flow were extended to the case that both spheres can rotate independently. Experiments

on the stability of co- and counter- rotating spheres were carried out by Wimmer [40], Yavorskaya et al. [48] and Monakhov [28] for small aspect ratios, and by Waked & Munson [38] for wide gaps. Furthermore, the flow between eccentric rotating spheres was investigated experimentally and numerically both for co- and counter-rotating spheres by Bar-Yoseph et al. [5,6].

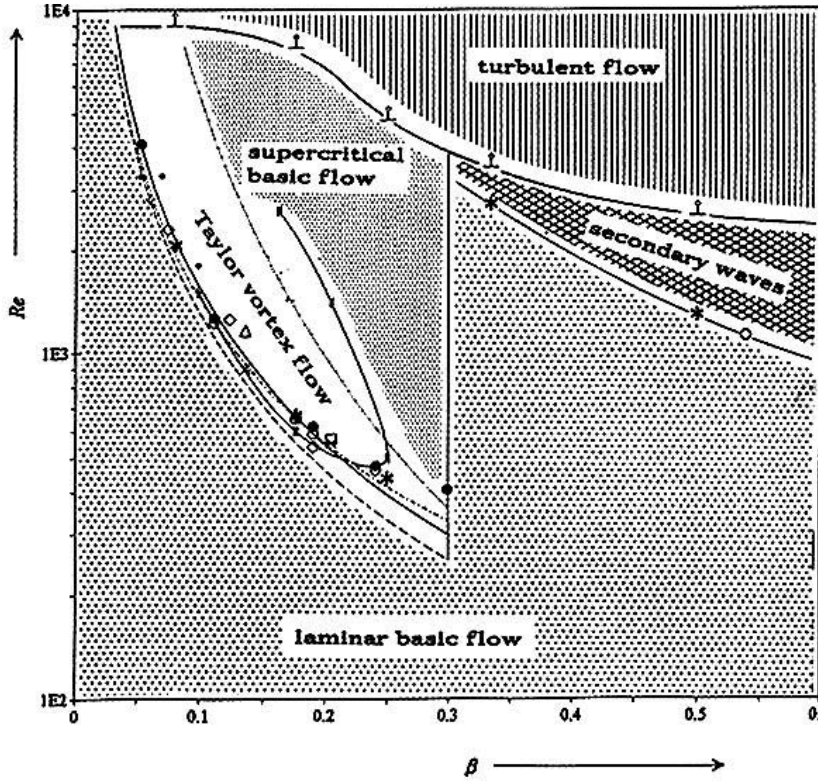

Fig. 3. Stability diagram: Overview of observed critical Reynolds numbers as a function of the aspect ratio

Numerical investigations of the supercritical spherical Couette flow in wide gap widths are rare, as well as simulations of higher instabilities in small gaps, because of the difficulties arising to simulate non-axisymmetric flows. On the other hand, for small and medium sized gap widths, especially for $\beta = 0.18$, several steady axisymmetric flows with 1 or 2 Taylor vortices in each hemisphere were calculated by Bonnet & Alziary de Roquefort [10], Bartels [10], Dennis & Quartapelle [16] and Marcus & Tuckerman [27], who also examined the transitions between the different flow modes and the bifurcations. Bühler [13] discovered an 1-vortex mode asymmetric with respect to the equator. The bifurcation behaviour of this asymmetric mode was investigated by Mamun &

Tuckerman [26]. Yang [46] applied in his simulations of the axisymmetric flow fictitious symmetric boundary conditions to find all possible flow modes.

Three-dimensional simulations of flow states in the spherical Couette system were for the first time reported by Dumas & Leonard [18] who successfully calculated spiral Taylor vortices as observed by Nakabayashi [30] in his experiments. This flow mode was also calculated by Zikanov [49] with co-rotating and counter-rotating spheres as well. Sha et al. [32] studied thoroughly the structure, evolution process and formation mechanism of this flow.

Dumas [17] also performed calculations for the wide gap case. For several gap widths, he presented slightly supercritical flow modes and determined critical Reynolds numbers for the wide gap transition from his calculations; furthermore, he proposed a mechanism for this instability.

Schrauf [35] investigated the influence of β on the first appearance of a pair of Taylor vortices in the spherical Couette flow by calculating steady, but not necessarily stable axisymmetric solutions with a continuation method. He concluded that Taylor vortices can exist up to $\beta = 0.45 - 0.48$, but they can not be generated in the usual way (only inner sphere rotation) for $\beta > 0.24$, where no bifurcation point was found and the basic state remains stable until the three-dimensional wide gap instability occurs. Experimentally, Taylor vortices could be generated in this gap width regime by Belyaev et al. [8] for $\beta = 0.3038$ and by Liu et al. [25] for $\beta = 0.33$; in the latter work, the authors also could generate Taylor vortices numerically up to $\beta = 0.483$. Motivated by this work, a detailed numerical study of the Taylor vortices for $\beta = 0.336$ was presented by Hollerbach [22].

Recently, Yamaguchi et al. [43–45] published a series of papers (experiments and numerics, inner and outer sphere rotation) extending the investigations of the flow in the spherical Couette system to viscoelastic fluids.

3 Experimental methods

3.1 Spherical Couette flow apparatus

Two different experimental setups for spherical Couette flow were constructed, consisting of an inner sphere rotating concentrically inside another rotating outer spherical shell. In the former experimental apparatus, the outer sphere ($R_2 = 40.00 \pm 0.02$mm) is composed of two transparent acrylic plastic hemispheres. The upper hemisphere has a spherical outer surface of about $0° < \Theta < 110°$ to investigate whether the occurring flow patterns are symmetric with respect to the equatorial plane or not. The inner sphere is made out of aluminium having the five various radii R_1, to vary the aspect ratio β from 0.08, 0.18, 0.25, 0.33 to 0.5.

Another experimental setup was constructed to investigate the different types of instabilities for larger aspect ratios of $\beta = 1.0$ and $\beta = 2.0$. The outer sphere of the second apparatus is much larger than the first one ($R_2 = 120.00 \pm 0.05$mm) and is composed of two transparent acrylic plastic hemispheres, too. Two different inner spheres exist with radii of ($R_1 = 60.00 \pm 0.05$mm and $R_1 = 40.00 \pm$

0.05mm), to vary the aspect ratio β from 1.0 to 2.0. Photographs of this laboratory experimental setup are shown in Fig. 4. To cool the outer shell, the whole sphere can be enclosed by a rectangular box filled with cooling fluid.

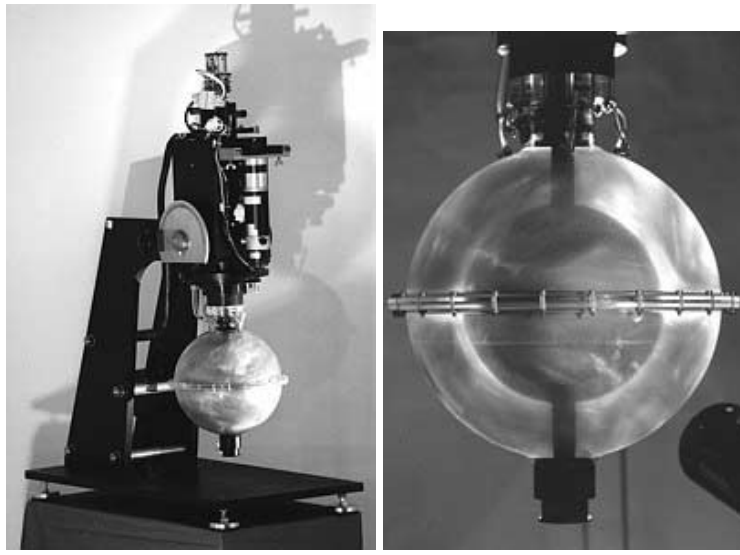

Fig. 4. Laboratory experimental setup spherical gap flow

Generally, both spheres can be rotated independently by means of two belt-drives. The eccentricity between outer and inner sphere could be minimised to $\pm$0.015mm using high precision bearings and shafts. Two different synchronous motor drives were adapted, which provide a uniform and stable rate of rotation up to n=850 rev/min with fluctuations of less than 1.5%. They vary the Reynolds numbers of the inner and outer sphere respectively in a range from $Re = 0$ to $Re = 10^6$. The revolutions were calibrated using an optical tracking system (optical coupling). Most of our experiments were carried out by increasing the Reynolds number quasistationary from zero. However, because the occurring flow structures depend also on initial conditions, the acceleration rate for both spheres could be varied. Experiments with the spherical Couette flow system were carried out in a laboratory condition, where the temperature could be kept uniformly up to $\pm 0.3°C$. Since the viscosity of the silicone oils, which were used as working fluids, vary by approximately $2\%/°C$, the temperature must be precisely controlled and measured in order to have a well-defined Reynolds number. A temperature accuracy of $\pm 0.15°C$ was achieved for all six temperature sensors (PT 1000) used in the experiments: For measuring the fluid temperature, three temperature sensors are installed just below the outer surface of the inner spheres. These temperature data are transferred from the rotating sphere to the stationary part by a slip-ring system. For investigations with only the inner sphere rotating three other temperature sensors are installed at the inner surface

of the outer sphere. Our measurements were carried out with the silicone oil M3 at a constant temperature of $25°C$. As tracer particles small aluminium flakes or polystyrene spheres were used. The concentration by weight was 0.05%. An effect of the tracer particles on the viscosity of the fluid was not detected.

3.2 LDV measuring system and visualisation methods

Because the investigated flow structures appearing in the spherical Couette flow during the laminar-turbulent transition are non-axisymmetric, it was necessary to use an observation-technique, which provides a simultaneously flow visualisation of both the azimuthal and the meridional flow. Therefore, a combination of the following two visualisation methods was used: To investigate the flow structures occurring in the meridional cross-section of the spherical annulus, a slit illumination technique is employed. In addition, a system with a fibre-optic is applied to visualise the polar region with the azimuthal waves. In this way, the cellular structure of the occurring vortices in the meridional plane as well as the azimuthal and polar behaviour of the arising flow pattern can be obtained. Photographs or prints from video records were taken.

For the application of laser-Doppler-velocimetry (LDV) on the spherical Couette flow experiment, a special traversing system has been constructed to mount the LDV optic probe on the spherical Couette flow experiment, while the laser is mounted apart from the experiment on a mounting bench. The traversing system consists of a high-precision bow with a traversing sledge and a traversing table. The traversing sledge is capable of moving the optic probe in meridional direction ($0° < \Theta < 110°$) and the traversing table is capable of moving in radial direction over a range of 60 mm in order to determine the meridional dependence of the velocity and to obtain velocity profiles. The laser-Doppler-velocimeter system used in our experiments, consists of a 20 mW He-Ne laser and a 1-D fibre flow optic probe (DANTEC Electronics, Denmark). A frequency shift is added by the Bragg cell to one of the beam pair to allow for measurements of reversing flows. The optic probe with a fibre optic cable is connected to the transmitter via manipulators. The backscattered light is focused on a photomultiplier tube. As tracer particles for the LDV measurements we use polystyrene spheres with a diameter of 1.6 μm. The concentration of tracers in the working fluid was 0.01 Vol.%. The application of the LDV technique on the spherical Couette flow experiment requires an optical correction for the accurate determinations of the probe volume locations and for the interference fringe spacing due to refraction effects of the spherical outer surface. Because the probe is adjusted in radial direction, the optical axis of the front lense of the probe passes perpendicular through the spherical outer surface. Thus, the correction for the two laser beams, which are in the same plane, could be calculated for a cylindrical surface. However, the fact, that a small probing volume is needed to produce sufficient spatial resolution, which could be obtained only by a large intersection angle, the small-angle approximation cannot be used in this case. The correction method used in this work for the case of large intersection angles was derived in our previous work [21].

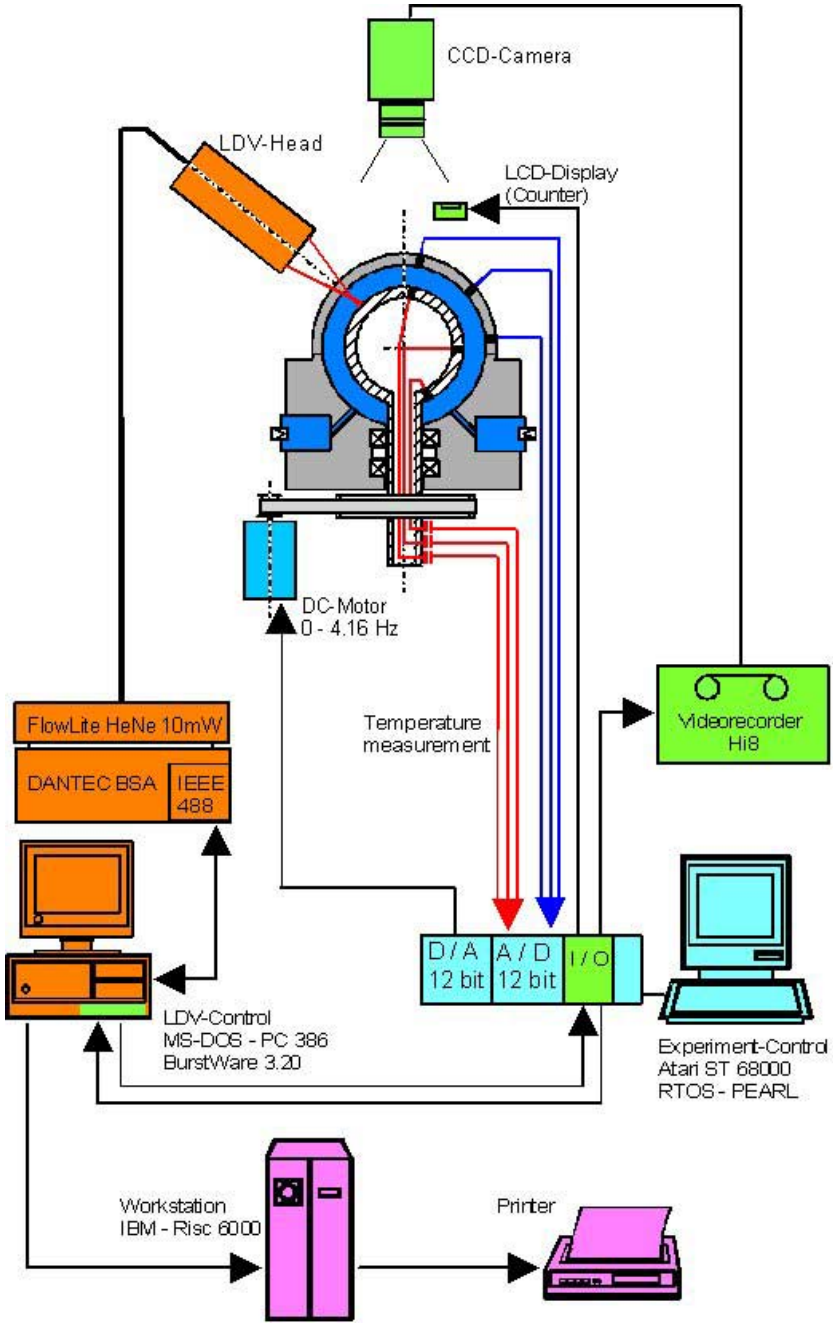

Fig. 5. Principle sketch of the experimental apparatus with the applied LDV measuring technique and the observation technique with CCD-camera

4 Transitions

4.1 Small and medium gap instabilities

The flow in the gap between two rotating spheres, where only the inner sphere rotates and the outer one is at rest, is not only a function of Reynolds number and aspect ratio β, but it also depends on the initial or boundary conditions. The different types of instabilities can be described as follows: Below a critical Reynolds number, the laminar basic flow is a steady axisymmetric and equatorially symmetric three-dimensional flow. Above a critical Reynolds number, however, the occurring flow structure depends strongly on the aspect ratio β. For small aspect ratios, the flow conditions near the equator are similar to the flow between concentric rotating cylinders. Hence, the first instability occurs in the form of a pair of Taylor vortices on each hemisphere for small β.
For $\beta = 0.25$, the initial and/or boundary conditions become most important: The resulting different flow modes are illustrated in Fig. 6 as a function of the Reynolds number. If the rotation rate of the inner sphere is increased quasistationary, the basic state is stable up to very large Reynolds numbers ($Re \approx 3800$), before spiral waves occur as the first instability, which are typical for wide gaps. But small disturbances, which are realized in the experiment by short-time counterrotating of the outer sphere, can lead to instabilities of the Taylor vortex type. In this way, one Taylor vortex on each side of the equator as depicted in Fig. 7 can be produced by exceeding the Reynolds number $Re_c = 420$. Up to $Re \approx 4200$ this mode is very stable, before it becomes wavy up to $Re \approx 4350$. The wavy mode only exists up to $Re \approx 4700$ where the flow becomes turbulent. In the same way (short-time counterrotating of the outer sphere), a pair of two Taylor vortices could be produced in the region of about $900 \leq Re \leq 1000$, while with further increase of Reynolds number spiral Taylor vortices occur ($Re \approx 2000$).

For $\beta = 0.33$, a comparable dependence on the boundary conditions can be observed (see Fig. 8): The laminar basic state is stable up to very large Reynolds numbers ($Re = 2860$), before spiral waves occur, if the Reynolds number is increased quasistationary. But one pair of Taylor vortices (symmetric and asymmetric with respect to the equator) can be produced by short-time counterrotating the outer sphere. This Taylor vortex pair coexists in the range of about $470 \leq Re \leq 1850$ before the flow merges into supercritical basic flow with further increasing the Reynolds number (see the paper of Liu et al. [25] for a detailed description).

For the aspect ratio $\beta = 0.18$, however, Taylor vortices form at the onset of instability. States with one or two toroidal Taylor vortex pairs are possible, which can also exist as instationary modes [34]. A detailed study of the flow in this gap width can be found in a paper by Wimmer [39] who classified the observed modes. With decreasing aspect ratio, the number of possible Taylor vortices increases with increasing Reynolds number as illustrated in Fig. 9 for the case of $\beta = 0.08$. As can be seen there, the flow with slightly inclined vortices is replaced by additional spiral vortices with increasing Reynolds number. This flow loses its stability to a time-periodic flow beginning at the equator and then

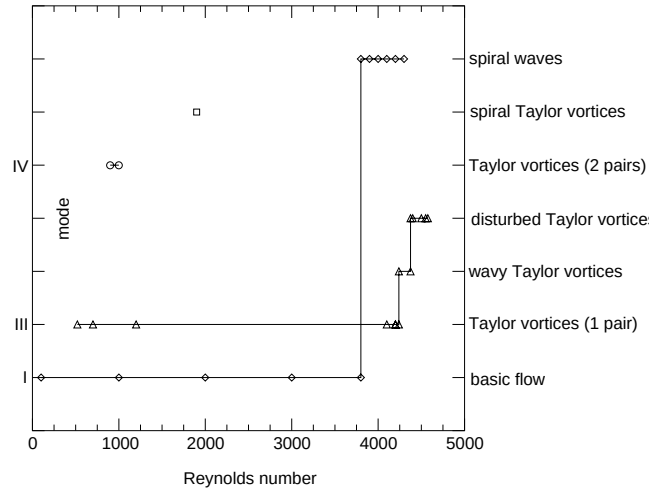

Fig. 6. Observed flow modes in the aspect ratio $\beta = 0.25$

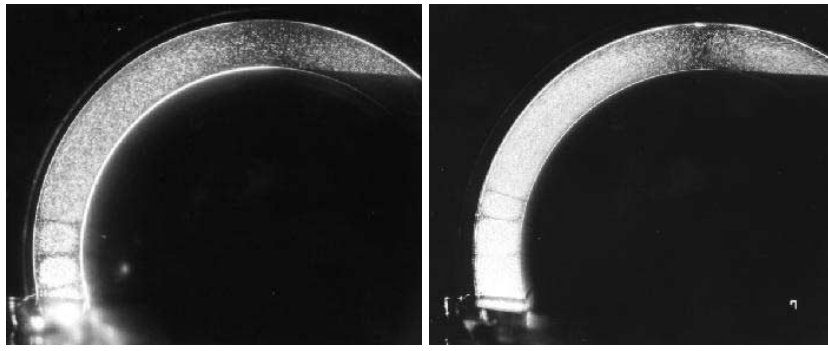

Fig. 7. Taylor vortices in a gap with $\beta = 0.25$ generated by counterrotation of the outer sphere: one-vortex state at $Re = 520$, two-vortex state at $Re = 900$

to a wavy vortex flow. By increasing the Reynolds number, this flow changes into a turbulent one.

The critical Reynolds number Re_c is a function of the aspect ratio β. In the range of very small aspect ratios ($\beta < 0.08$), the stability curve is in a good agreement with the cylindrical theory of Taylor [37]. For the region of aspect ratios $0.08 \leq \beta \leq 0.25$ Yavorskaya et al. [48] found empirically, that Re_c for spherical Couette flow is larger than in the cylindrical and can be approximated as $Re_c = 41.3(1 + \beta)\beta^{-3/2}$, which is in a good agreement with our and other experimental results for $\beta < 0.25$. Experiments with increasing the Reynolds number were also carried out to determine the maximum possible number of Taylor vortices as a function of the aspect ratio. The best fit for the maximum number i of Taylor vortex pairs could be obtained by $i = 0.21\beta^{-4/3}$.

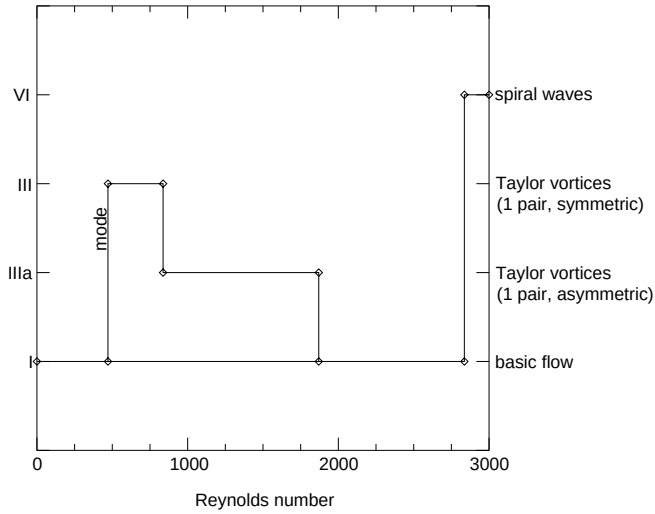

Fig. 8. Flow modes in the aspect ratio $\beta = 0.33$

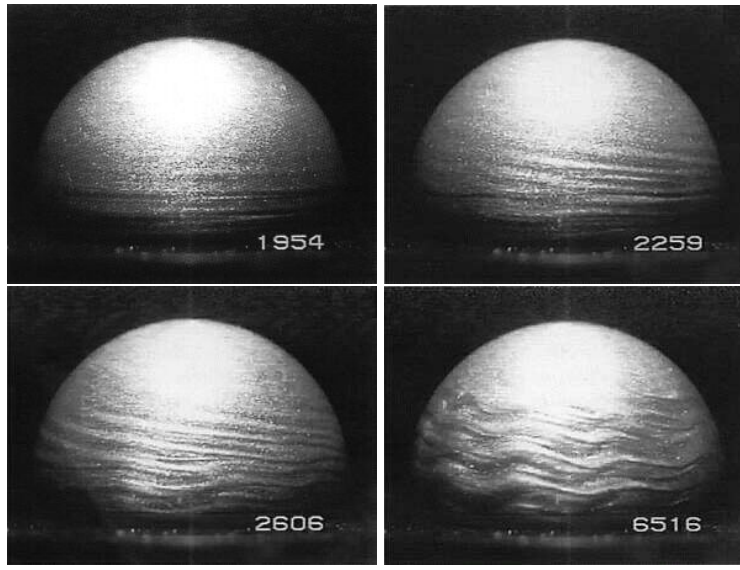

Fig. 9. Visualisation of flow states in a small gap $\beta = 0.08$: slightly inclined vortex at $Re = 1954$, spiral vortex flow at Re=2259, time-periodic vortex flow at $Re = 2606$, wavy vortex flow at $Re = 6516$

4.2 Bifurcation behaviour

Several studies, experimental and numerical as well, concentrated on $\beta = 0.18$. Especially the experiments of Wimmer [39] and the numerical work by Marcus & Tuckerman [27] and Schrauf [35] led to a deeper understanding of the bifurcation phenomena of the axisymmetric flow states in this gap width regime. Before any transition to a supercritical flow state occurs, a so-called pinching of the meridional vortex of the basic flow is observed, that is the formation of a stagnation point in each hemisphere located about one gap width from the equator; between the stagnation points and the outflow regime at the equator there are closed streamlines (which are no Taylor vortices) with circulation in the same direction as in the adjacent meridional basic vortex.
Two axisymmetric (and reflection-symmetric with respect to the equator) Taylor vortex states exist which both can be generated from the basic state: a 1-vortex state with just one Taylor vortex in each hemisphere next to the equator, and a 2-vortex state. Among the possible transitions between the three axisymmetric states, the transitions to the 1-vortex state (from the base flow and from the 2-vortex state) break the equatorial symmetry, with the final 1-vortex equilibrium state showing this symmetry again.
The 2-vortex state can be generated by fast acceleration of the inner sphere from the basic state to a sufficiently high supercritical Reynolds number. It is shown in the numerical studies that these two solutions lie on the same equilibrium curve, and with increasing Reynolds number the flow develops steadily from the pinched basic state to the 2-vortex state.
If the acceleration is sufficiently slow, above a critical Reynolds number ($Re \approx 651$ for $\beta = 0.18$) a transition from the basic state to a 1-vortex state occurs. The basic flow is unstable to antisymmetric eigenmodes, hence during the temporal evolution of the transition, the flow is not reflection-symmetric. This transition exhibits a slight hysteresis, however small enough that it could not be resolved in all experiments.
The observed phenomena can be understood from the calculated bifurcation diagram: the equilibrium curve of the 0-2-vortex flow is linearly unstable to non-equatorial-symmetric perturbations over a certain range of Reynolds numbers ($651 < Re < 775$ in case of $\beta = 0.18$). If the perturbations can grow, finally the 1-vortex state develops. On the other hand, when the acceleration is fast enough that the flow can follow the 0-2-equilibrium curve up to the stable regime of this curve but the perturbations do not have the time to grow, the 2-vortex state is observed. The unstable range of the 0-2-solution is limited by two pitchfork bifurcations (subcritical at the lower limit and supercritical at the upper limit respectively) with bifurcating unstable solutions which are asymmetric with respect to the equator. The 1-vortex state originates from a saddle-node-bifurcation [33] at a Reynolds number ($Re = 645$ for $\beta = 0.18$) slightly below the critical Reynolds number of the basic state. This explains the slight hysteresis in the transition which is even smaller for smaller gaps.

Schrauf extended his studies of the bifurcation behaviour in the (Re, β)-plane and predicted that the basic state does not become unstable (to axisymmetric

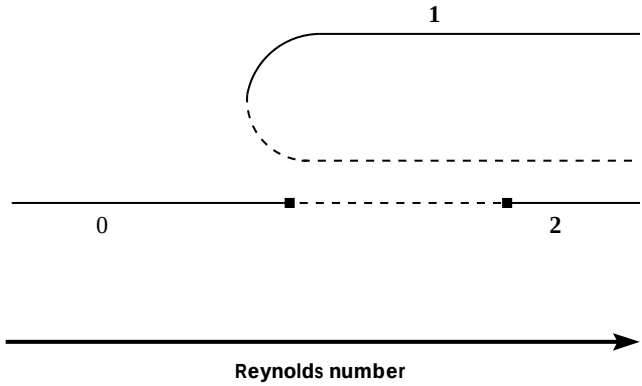

Fig. 10. Schematic graph of the bifurcation behaviour in the gap $\beta = 0.18$ (after [27]) as desribed in the text. Solid lines represent stable solutions, dashed lines unstable branches. The numbers denote the number of Taylor vortices per hemisphere in this flow state.

perturbations) for $\beta > 0.24$ (Yavorskaya et al. [48] could detect in their experiments a transition to 1-vortex flow up to $\beta = 0.2413$). Above this limit gap width, the basic Couette flow remains stable to axisymmetric perturbations and the flow with one Taylor vortex exists as an isolated solution, which can only be produced by special initial conditions (as successfully done by Belyaev et al. [8] and Liu et al. [25]). Above a limit gap, where the Taylor vortex solution is unstable to three-dimensional perturbations for all Re, no Taylor vortices can be observed; the estimate of Schrauf for this limit gap width is $\beta \approx 0.45 - 0.48$.

4.3 Wide gap instabilities

In comparison to the rather large number of studies dealing with the instabilities in small and medium spherical gaps, there are considerably less investigations of the flow in wide gaps. In this case, the basic flow is stable to axisymmetric perturbations, and no Taylor vortices arise. Experimental descriptions of the supercritical flow are given by Yavorskaya and Belyaev for $\beta = 0.398, 0.54, 1.0, 1.33$ [47,7,9] and by Egbers [20] and Wulf [41] for $\beta = 0.33$ and $\beta = 0.5$. Additionally, there are investigations by Munson and Menguturk [29] of the flow in large gaps with $\beta = 1.27$ and $\beta = 2.29$; however, as it was pointed out by Yavorskaya and Belyaev, these latter results need some interpretation, because Munson and Menguturk did not observe visually any supercritical flow. Instead, they reported some break-points in the torque-Re relation without pattern formation, and finally they assumed a transition to turbulent flow. In fact, this transition is the transition to the typical supercritical wave flow, as described below, not the transition to turbulence.
In these experiments, the following common features of the transition and the supercritical flow could be found: The basic flow is linearly unstable to three-dimensional perturbations. The supercritical flow consists of a number m equally

spaced secondary waves which spread from the pole to the equatorial region. The number of these waves depends on the gap width. In the gap widths, which we realized experimentally, there are $m = 6$ for $\beta = 0.33$, $m = 5$ for $\beta = 0.5$ and $m = 4$ for $\beta = 1.0$. The equatorial region is sinusoidally perturbed. The whole pattern propagates with an angular velocity which decreases slightly with the Reynolds number. The patterns exist in both hemispheres, but they are shifted to each other; thus, the azimuthal symmetry and the equatorial symmetry as well are broken in this transition. When the Reynolds number is increased further, higher order transitions are observed, which show a clear hysteresis. In the sequence of these transitions, similar flow states with a lower number of spiral waves (e.g. $m = 4$ and $m = 3$ for $\beta = 0.5$) are observed, before the flow becomes turbulent at sufficiently high Reynolds number.
A somewhat different transition behaviour was described by Wulf et al. [41]. In this paper, he investigated the dynamical behaviour with chaos analysing techniques applied on time series from LDV measurements; furthermore, he gave an extensive description of all flow modes up to the transition to turbulence. While he observed the same flow as first instability for $\beta = 0.5$, he found for $\beta = 0.33$ a corotating spiral vortex and a ring vortex as first supercritical flow structures, before at higher Reynolds numbers, the spiral wave pattern ($m = 6$) forms.
Flow visualisation pictures of some supercritical wide gap flows are shown in Fig. 11; the character of the spiral wave flow and the different number of vortices is clearly visible.

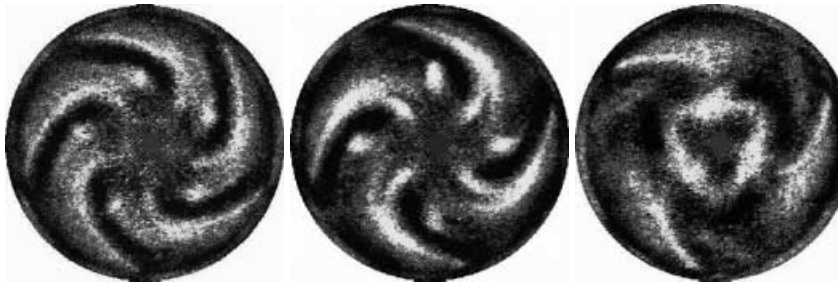

Fig. 11. Flow visualisation of the wide gap flow structures for $\beta = 0.5$ (view on the polar region): spiral wave flow with $m = 5$ ($Re = 1320$), $m = 4$ ($Re = 1575$) and $m = 3$ ($Re = 1680$)

Only a few numerical studies of these phenomena exist, mainly because of the complex three-dimensional nature of the occurring flows. The first work was published by Dumas [17], who successfully calculated by numerical simulation with a pseudo-spectral code some critical Reynolds numbers. The flow structures, which he calculated for $\beta = 1.27$ for slightly supercritical values of Re, show the described characteristic properties. He assumed that the transition results from a jet instability of the radial outflow region near the equator, which is rather distinct in wide gaps. With a model based on this assumption, he could qualitatively predict some of the properties of the supercritical flow. Hollerbach

[23] calculated the spiral wave flow structures and critical Reynolds numbers for the gap widths $\beta = 0.33$ and $\beta = 0.5$ which were used by Egbers. For the latter gap width, Araki [2] performed a numerical stability analysis. The results of both works are in perfect agreement with the experimental data. Critical Reynolds numbers for some wide gaps were also calculated by Astafyeva [3]. See Tab. 1 for a survey of all determined critical values for the first transition.

With the numerical code of Hollerbach, we calculated the critical Reynolds numbers for a wide range of gap widths. The code uses a spectral method; it was originally developed for the calculation of magneto-convective phenomena in spherical geometry (see the contribution of Hollerbach in this book) and is described in [23]. For the calculation of the critical Reynolds numbers, the linearised equations for a perturbation (with a given azimuthal wave number m) to a precalculated axisymmetric basic equilibrium state are numerically treated. From the growth rates of the perturbation for different Reynolds numbers and azimuthal modes, the critical Reynolds number and critical wave number can be determined. The results in cases where other data are available for comparison are listed in the table below. A complete description will be given in a future paper.

β	0.33	0.398	0.5	0.54	1.0	1.27	1.33	2.0	2.29
Belyaev		1900 (5)		1120 (5)	463 (4)		406 (3)		
Munson						407			425
Egbers	2628 (6)		1244 (5)						
Wulf	2395		1190 (5)						
Dumas				1122 (5)	489 (4)	406 (3)			
Araki			1245 (5)						
Astafyeva			1150 (6)		493 (4)			457 (3)	
Hollerbach	2684 (6)		1244 (5)						
our study		1937 (5)	1245 (5)	1115 (5)	489 (4)	405 (3)	395 (3)	383 (3)	

Table 1. Comparison of available values (upper part: experimental, lower part: numerical) for the critical Reynolds numbers and wave numbers (in parenthesis) in the wide gap regime

5 Conclusion

In this overview, we reported several flow states in the spherical Couette system which is investigated experimentally and numerically. The kind of instability of the basic flow depends strongly on the gap width: for small gaps, Taylor vortices in the equatorial region are found, while in wide gaps, we observe time-dependent spiral vortices.

Present investigations concentrate on this wide gap regime. Experimentally, the transitions are analysed by means of time series analysis of velocity data from LDV measurements. Thus, the critical values and the route to chaos are determined. Numerically, we could calculate critical Reynolds numbers for a wide range of gap widths in good agreement with the experimental observations. Now we focus on comparison between experiments and numerical simulation of the supercritical spiral wave flow.

Acknowledgements. The financial support of Deutsche Forschungsgemeinschaft (DFG) is gratefully acknowledged.

References

1. C.D. Andereck,S.S. Liu, H.L. Swinney: *Flow regimes in a circular Couette system with independently rotating cylinders.* J. Fluid Mech. **164**, 155-183 (1986)
2. K. Araki, J. Mizushima, S. Yanase: *The nonaxisymmetric instability of the wide-gap spherical Couette flow.* Phys. Fluids **9**, 1197-1199 (1997)
3. N.M. Astafyeva: *Nonlinear shear flow in rotating spherical layers and global atmosphere motion modelling* (in Russian). Izv. Vusov PND **5**, 3-30 (1997)
4. F. Bartels: *Taylor vortices between two concentric rotating spheres.* J. Fluid Mech. **119**, 1-25 (1982)
5. P. Bar-Yoseph, A. Solan, R. Hillen, K.G. Roesner: *Taylor vortex flow between eccentric coaxial rotating spheres.* Phys. Fluids A **2**, 1564-1573 (1990)
6. P. Bar-Yoseph, K.G. Roesner, A. Solan: *Vortex breakdown in the polar region between rotating spheres.* Phys. Fluids A **4**, 1677-1686 (1992)
7. Yu.N. Belyaev, A.A. Monakhov, I.M. Yavorskaya: *Stability of spherical Couette flow in thick layers when the inner sphere revolves.* Fluid Dyn. **13**, 162-163 (1978)
8. Yu.N. Belyaev, A.A. Monakhov, G.N. Khlebutin, I.M. Yavorskaya: *Investigation of stability and nonuniqueness of the flow between rotating spheres* (in Russian). Rep. No. 567, Space Research Institute of the Academy of Sciences, Moscow, USSR (1980)
9. Yu.N. Belyaev, A.A. Monakhov, S.A. Scherbakov, I.M. Yavorskaya: *Some routes to turbulence in spherical Couette Flow.* in: V.V. Kozlov (ed.): Laminar-Turbulent Transition. IUTAM-Symp. Novosibirsk/USSR, Springer (1984)
10. J.P. Bonnet, T. Alziary de Roquefort: *Ecoulement entre deux spheres concentriques en rotation.* J. Mec. **13**, 373 (1976)
11. Yu.K. Bratukhin: *On the evaluation of the critical Reynolds number for the flow of fluid between two rotating spherical surfaces.* PMM **25**, 858-866 (1990)
12. K. Bühler: *Strömungsmechanische Instabilitäten zäher Medien im Kugelspalt.* VDI-Berichte, Reihe7: Strömungstechnik Nr.96 (1985)

13. K. Bühler: *Symmetric and asymmetric Taylor vortex flow in spherical gaps.* Acta Mechanica **81**, 3-38 (1990)
14. K. Bühler, J. Zierep: *New secondary instabilities for high Re-number flow between two rotating spheres.* in: Kozlov,V.V. (ed.): Laminar-Turbulent Transition. IUTAM-Symp. Novosibirsk/USSR, Springer (1984)
15. K. Bühler, J. Zierep: *Dynamical instabilities and transition to turbulence in spherical gap flows.* in: G. Comte-Bellot, J. Mathieu: Advances in turbulence. Proc. 1st Europ. Turb. Conf., Lyon, France, Springer (1986)
16. S.C.R. Dennis, L. Quartapelle: *Finite difference solution to the flow between two rotating spheres.* Comp. Fluids. **12**, 77-92 (1984)
17. G. Dumas: *The spherical Couette flow and its large-gap stability by spectral simulations.* Proceedings of CFD 94, Canadian Society of CFD, Toronto, Canada, 67-75 (1994)
18. G. Dumas, A. Leonard: *A divergence-free spectral expansions method for three-dimensional flows in spherical-gap geometries.* J. Comput. Phys. **111**, 205-219 (1994)
19. C. Egbers: *Zur Stabilität der Strömung im konzentrischen Kugelspalt.* Dissertation, Universität Bremen (1994)
20. C. Egbers, H.J. Rath: *The existence of Taylor vortices and wide-gap instabilities in spherical Couette flow.* Acta Mech. **111**, 125-140 (1995)
21. C. Egbers, H.J. Rath: *LDV-measurements on wide-gap instabilities in spherical Couette flow.* Developments in Laser Techniques and Applications to Fluid Mechanics (Eds.: R.J. Adrian, D.F.G. Durao, F. Durst, M.V. Heitor, M. Maeda, J.H. Whitelaw), Springer, 45-66 (1996)
22. R. Hollerbach: *Time-dependent Taylor vortices in wide-gap spherical Couette flow.* Phys. Rev. Lett. **81**, 3132-3135 (1998)
23. R. Hollerbach: *A spectral solution of the magnetoconvection equations in spherical geometry.* Int. J. Num. Meth. Fluids **32**, 773-797 (2000)
24. G.N. Khlebutin: *Stability of fluid motion between a rotating and a stationary concentric sphere.* Fluid Dyn. **3**, 31-32 (1968)
25. M. Liu, C. Blohm, C. Egbers, P. Wulf, H.J. Rath: *Taylor vortices in wide spherical shells.* Phys. Rev. Lett. **77**, 286-289 (1996)
26. C.K. Mamun, L. Tuckerman: *Asymmetry and Hopf bifurcation in spherical Couette flow.* Phys. Fluids **2**, 1564-1573 (1995)
27. P. Marcus, L. Tuckerman: *Simulation of the flow between concentric rotating spheres.* J. Fluid Mech. **185**, 1-65 (1987)
28. A.A. Monakhov: *Limit of main flow stability in spherical layers.* Fluid Dynamics **31**, 535-538 (1996)
29. B.R. Munson, M. Menguturk: *Viscous incompressible flow between concentric rotating spheres. Part 3: Linear stability and experiments.* J. Fluid Mech. **69**, 705-719 (1975)
30. K. Nakabayashi: *Transition of Taylor-Görtler vortex flow in spherical Couette flow.* J. Fluid Mech. **132**, 209-230 (1983)
31. K. Nakabayashi, Y. Tsuchida: *Spectral study of the laminar-turbulent transition in spherical Couette flow.* J. Fluid Mech., **194**, 101-132 (1988)
32. K. Nakabayashi, W. Sha: *Vortical structures and velocity fluctuations of spiral and wavy vortices in the spherical Couette flow.* this book (2000)
33. G. Nicolis: *Introduction to nonlinear science.* Cambridge University Press (1995)
34. O. Sawatzki, J. Zierep: *Das Stromfeld im Spalt zwischen zwei konzentrischen Kugelflächen, von denen die innere rotiert.* Acta Mech. **9**, 13-35 (1970)

35. G. Schrauf: *The first instability in spherical Taylor-Couette flow.* J. Fluid Mech. **166**, 287-303 (1986)
36. M.P. Sorokin, G.N. Khlebutin, G.F. Shaidurov: *Study of the motion of a liquid between two rotating spherical surfaces.* J. Appl. Mech. Tech. Phys. **6**, 73-74 (1966)
37. G.I. Taylor: *Stability of a viscous liquid contained between two rotating cylinders.* Phil.Trans. A **223**, 289-293 (1923)
38. A.M. Waked, B.R. Munson: *Laminar turbulent flow in spherical annulus.* J. Fluids Eng. **100**, 281-286 (1978)
39. M. Wimmer: *Experiments on a viscous fluid between concentric rotating spheres.* J. Fluid Mech. **78**, 317-335 (1981)
40. M. Wimmer: *Experiments on the stability of viscous flow between two concentric rotating spheres.* J. Fluid Mech. **103**, 117-131 (1981)
41. P. Wulf, C. Egbers. H.J. Rath: *Routes to chaos in wide-gap spherical Couette flow.* Phys. Fluids **11**, 1359-1372 (1999)
42. V.I. Yakushin: *Instability of the motion of a liquid between two rotating spherical surfaces.* Fluid Dyn. **5**, 660-661 (1970)
43. H. Yamaguchi, J. Fujiyoshi, H. Matsui: *Spherical Couette flow of a viscoelastic fluid. Part 1: Experimental study of the inner sphere rotation.* J. Non-Newtonian Fluid Mech.**69**, 29-46 (1997)
44. H. Yamaguchi, H. Matsui: *Spherical Couette flow of a viscoelastic fluid. Part 2: Numerical study for the inner sphere rotation.* J. Non-Newtonian Fluid Mech.**69**, 47-70 (1997)
45. H. Yamaguchi, B. Nishiguchi: *Spherical Couette flow of a viscoelastic fluid. Part 3: A study of outer sphere rotation.* J. Non-Newtonian Fluid Mech.**69**, 47-70 (1997)
46. R.-J. Yang: *A numerical procedure for predicting multiple solutions of a spherical Taylor-Couette flow.* Int. J. Numer. Methods Fluids **22**, 1135-1147 (1996)
47. I.M. Yavorskaya, Yu.N. Belyaev, A.A. Monakhov: *Experimental study of a spherical Couette flow.* Sov. Phys. Dokl. **20**, 256-258 (1975)
48. I.M. Yavorskaya, Yu.N. Belyaev, A.A. Monakhov, N.M. Astaf'eva, S.A. Scherbakov, N.D. Vvedenskaya: *Stability, non-uniqueness and transition to turbulence in the flow between two rotating spheres.* IUTAM-Symposium, Toronto, Canada (1980)
49. O.Yu. Zikanov: *Symmetry breaking bifurcations in spherical Couette flow.* J. Fluid Mech. **310**, 293-324 (1996)

Vortical structures and velocity fluctuations of spiral and wavy vortices in the spherical Couette Flow

Koichi Nakabayashi[1] and Weiming Sha[2]

[1] Department of Mechanical Engineering, Nagoya Institute of Technology
Gokiso-Cho, Showa-Ku, Nagoya ,466-8555, Japan
[2] Geophysical Institute, Graduate School of Science, Tohoku University
Aoba-Ku, Sendai, 980-8578, Japan

1 Introduction

Due to the spherical geometry and rotating effect in the spherical Couette flow(SCF) situation, understanding the dynamics of the fluid motion (vortices and waves) within such a spherical shell is relevant to both global astrophysical and geophysical processes and engineering applications. Most of previous experimental investigations on the spherical Couette flow were restricted to the cases of small and medium gap widths in which the first instability occurred as Taylor vortices at the equator (e.g., Munson & Menguturk [13]; Wimmer [22],[23]; Yavorskaya et al. [25]; Nakabayashi [14]; Bühler [4]; Bar-Yoseph et al. [2]; Egbers & Rath [6]). Some experimental and theoretical studies were also conducted recently on the case of wide gap widths in which the first instability appeared in a form of non-axisymmetric spiral waves (Egbers & Rath [6]; Araki et al. [1]; Wulf et al. [24]). When the outer sphere is held stationary, the spherical Couette flow between two spheres with the inner sphere rotating can be characterized by three control parameters. There are the Reynolds number, clearance ratio and rotative acceleration rate. Usually, the spherical Couette flow between two concentric rotating spheres shows dynamical behaviors analogous to the classical circular Couette flow between two concentric rotating cylinders in the equatorial regions, and the flow between two plane rotating disks in the polar regions, respectively. A series of our experimental work have been carried out on the spherical Couette flow between two concentric spheres for a range of the clearance ratio where the Taylor instability occurs in the equatorial region (Nakabayashi [14]; Nakabayashi & Tsuchida [15],[16]), and our previous experimental investigations on the spherical Couette flow showed a similar laminar-turbulent transition to that in the circular Couette flow(CCF).

In this lecture note, we give a review on the laminar-turbulent transition phenomena for the cases of various gap widths in SCF, among which we mainly focus on the vortical structures and velocity fluctuations of spiral and wavy vortices occurred in the transition processes. In next Sect. 2, the onset Reynolds numbers of different kinds of disturbances for various clearance ratios are presented first. The results on the spiral TG vortex flow are presented in Sect. 3, in which the vortical structure and formation mechanism of the spiral TG vortices

C. Egbers and G. Pfister (Eds.): LNP 549, pp. 234–255, 2000.

are discussed from the experimental work and numerical simulation. Section 4 gives the results on fluid motion of the wavy vortices, and the velocity fluctuations of the spiral and wavy vortices are analyzed systematically in Sect. 5. In Sect. 6, a particular relaminarization phenomenon observed in intermediate clearance ratio cases is represented and discussed in detail, and a explanation for this particular phenomenon is also made. Concluding remarks are given in Sect. 7.

2 Onset Reynolds numbers of various disturbances

In Fig. 1, results of the present and previous investigations on the relationship between clearance ratio β and onset Reynolds numbers Re_t of SCF disturbances for $\beta < 0.6$ are illustrated in the form of a stability diagram. The clearance ratio β is defined as $(R_2 - R_1)/R_1$, where R_1, R_2 are the radii of the inner and outer spheres, respectively. The critical Reynolds number of Taylor instability for SCF is given by $Re_c = 41.3(1+\beta)^{-3/2}$ for $\beta < 0.3$ (Nakabayashi [14]). Its tendency is similar to that of CCF for $\beta < 0.3$. Concerning the rotating cylinder-type disturbances, Re_t of the spiral TG vortex decreases in close relation to the Taylor instability curve with increasing β for $\beta < 0.3$. The Re_t curve of traveling waves also decreases almost parallel to the Re_c curve with increasing β , but suddenly increases above $\beta < 0.13$. According to Bühler [4], traveling waves occur for $\beta = 0.154$, but not for $\beta = 0.178$, so we can conjecture that an upper limit of β, i.e., β_{c2}, for the occurrence of traveling waves exists between 0.154 and 0.178 in SCF.

With respect to rotating disk-type disturbances, Yavorskaya et al. [25], Bühler and Zierep [3], and Nakabashi & Tsuchida [15] reported the occurrence of shear waves for $\beta = 0.14$ and 0.177, but not at $\beta = 0.11$. Egbers & Rath [6] reported non-axisymmetric secondary waves due to cross-flow instability at $\beta = 0.5$. The lower limit values of Re_t of shear waves, Stuart vortex and ring vortex are located on the curve of cross-flow instability. No disk-type disturbance can be observed for $\beta < 0.11$, because the Re_t for the occurrence of turbulence is lower than that of rotating disk-type disturbances for $\beta < 0.14$. Accordingly, there exists a lower limit of β (i.e., β_{c1}), where the disk-type disturbances are observable. Here, β_{c1} is given by a value between 0.11 and 0.14. The relaminarization reported previously by Nakabashi & Tsuchida [15] exists in the range of $\beta_{c1} < \beta < \beta_{c2}$. The occurrence of relaminarization can obviously be linked to the disappearance of traveling waves due to the occurrence of rotating disk-type disturbances.

From the foregoing discussion, the following conclusions can be made. For $\beta < 0.3$ there are two critical values of β : β_{c1} and β_{c2} . For $0 < \beta < \beta_{c1}$, only cylinder-type disturbances (spiral TG vortices and travelling waves) can occur, and their onset Reynolds numbers decrease with increasing β . In the region of $\beta_{c1} < \beta < \beta_{c2}$, both cylinder-type and disk-type disturbances occur, so the two types of disturbance interact, and the relaminarization phenomenon may emerge.

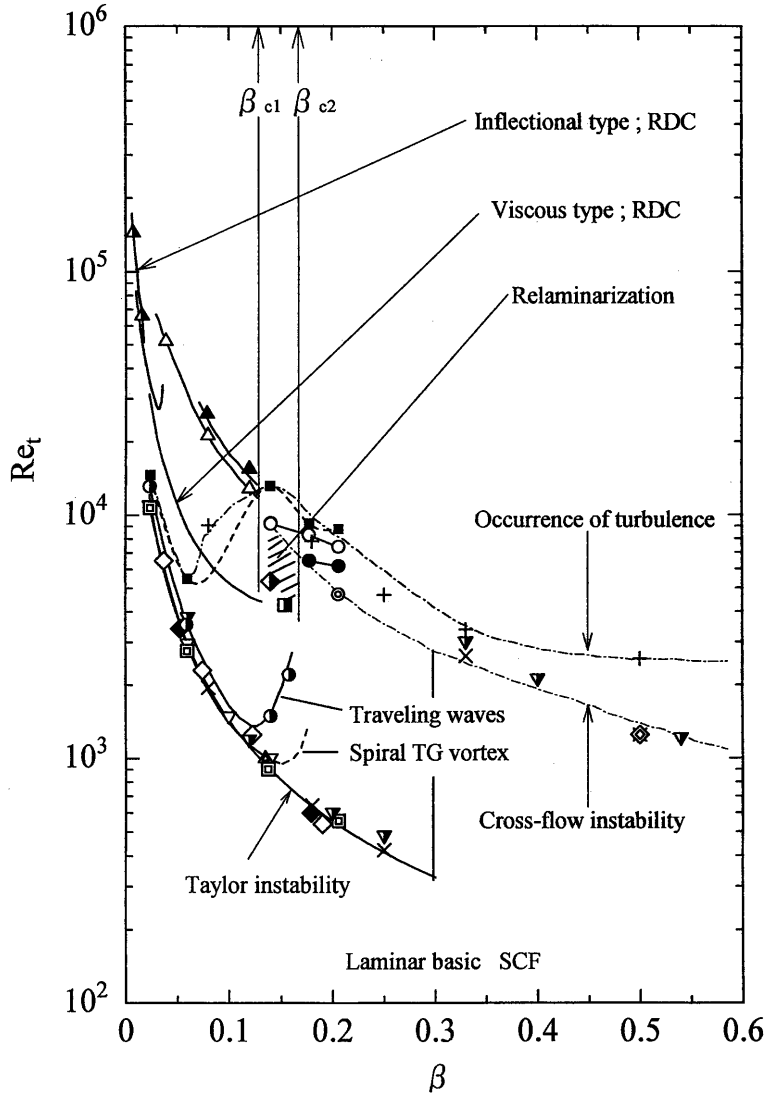

Fig. 1. Clearance ratio dependence of the onset Reynolds number of various disturbances. The onset Reynolds number for shear waves, Stuart vortex, spiral TG vortex, ring vortex, relaminarization, traveling waves and turbulence are indicated by the data obtained from the present experiment and previous work of Sawatzki & Zierep [20]; Munson & Menguturk [13]; Yavorskaya [25]; Nakabayashi [14]; Khlebutin [10]; Itoh [9]; Bühler [4]; Egbers & Rath [6]; Araki et al.[1].

3 Structure and formation of the spiral TG vortices

As described in last section, a fascinating vortex formation in the spherical Couette flow was observed at a higher Reynolds number, and the induced vortices

were called spiral Taylor-Görtler (TG) vortices by Nakabayashi [14]. Then a direct numerical simulation, which can provide a feasible source of information, is considered as a suitable tool for a more detailed investigation of the spiral TG vortices. With a spectral method Dumas & Leonard [5] have been successful in numerical simulation of the spiral TG vortices in the spherical Couette flow between two concentric spheres with the inner sphere rotating, and their simulated spiral TG vortex flow was in very good agreement with our previous experimental flow in a narrow gap case (Nakabayashi [14]). Later Zikanov [26] was able to compute the spiral TG vortices in the co-rotating and counter-rotating cases by using a pseudospectral method, and his numerical results provided a detailed description of the three dimensional flows and the pattern of transitions among various regimes. Recently, we considered a numerical algorithm designed for three-dimensional, time-dependent incompressible Navier–Stokes fluids, and the numerical method, which is second-order accurate in time and space based on the finite-difference scheme, was used to compute the spherical Couette flow between two spheres with the inner sphere rotating, and we successfully simulated the subcritical and critical flows, i.e., 0-vortex flow, 0-vortex flow with pinch and 1-vortex flow (Marcus & Tuckerman, [11], [12]), and the supercritical flows (spiral TG vortex flow) (Sha et al. [18]). For comparison with our previous experiments, a moderate gap case with clearance ratio $\beta = 0.14$ was chosen in the numerical study. With adequate initial and boundary conditions, we have successfully simulated the supercritical spiral TG vortex flow in this spherical Couette flow system.

Figure 2 shows the plots of the velocity vectors on the (θ, ϕ) spherical cross-section at mid-gap viewed from $\phi = 310°$. The pattern rotates in the same direction as that of the inner sphere (counterclockwise). The contour of the zero radial velocity in the section is also drawn with two types of thin and thick solid lines, which are the boundaries between existing inflow and outflow regions. Thin solid lines indicate the center positions of the two toroidal TG vortices. The thick ones, which are counted by every two thick lines from each side of the equator, correspond to the center lines of the TG spiral vortices. The lines of the center positions of the toroidal TG vortices are nearly parallel to the equator while the center lines of the spiral TG vortices are inclined with respect to the azimuthal direction. The flow fields, portrayed in mid-latitude regions, appear to wrap the spherical cross-section with three converging/diverging zones in each hemisphere. The features of the spiral TG vortex flow are of the rotational and equatorial asymmetries.

In order to gain more insight in the three-dimensional structure of the spiral TG vortices, visualizations of the azimuthal vorticity are shown in Fig. 3. Here, grey colors represent the azimuthal vorticity iso-surfaces: the dark color denotes positive and the light color is for negative. In the spiral TG vortex flow there exists one toroidal TG vortex, one toroidal vortex cell and three spiral TG vortices in each hemisphere. This spiral flow in each hemisphere is identical except for a change sign of the vorticity. So in the following text we mainly focus our discussion in the northern hemisphere only. In Fig. 3 (d), the toroidal TG vortex, the

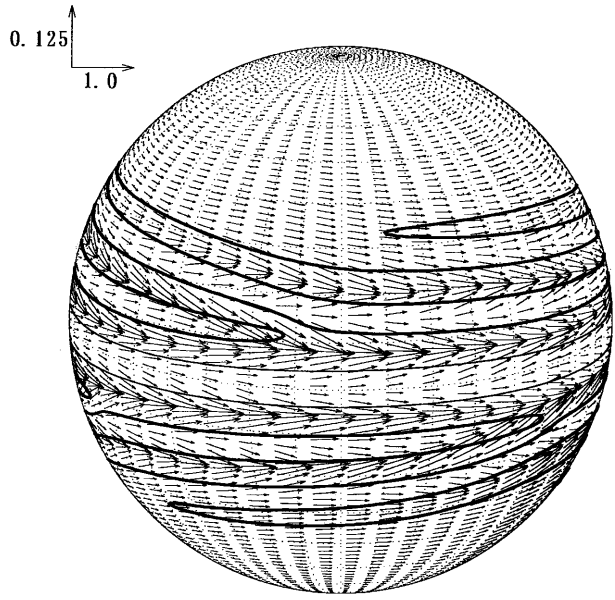

Fig. 2. Plots of the velocity vectors of the spiral TG vortex flow in the spherical cross-section at the radial position $r = 1 + d/2$ (the mid-gap radius) viewed from $\phi = 310°$. The Reynolds number is $Re_s = 1100$ in the numerical simulation. The contour of the zero radial velocity ($u_r = 0$) on the section is also drawn with two types of thin and thick solid lines. The thin solid lines indicate the center positions of the two toroidal TG vortex. The thick ones, which are counted by every two thick lines from each side of the equator, correspond to the center lines of the spiral TG vortices.

toroidal vortex cell A, the two spiral vortices B and C, the fore portion D of the same class as C and the thin vorticity layer E adjacent to the outer sphere are indicated in the northern hemisphere. There is a toroidal vortex cell A on one side of the toroidal TG vortex. The toroidal vortex cell A is essentially different from the toroidal TG vortex. They have the opposite sign of circulation to each other in the north hemisphere, and the toroidal vortex cell A is connected with the spiral vortex C. Furthermore, the toroidal TG vortex near the equator is caused by the Taylor-type first instability while the toroidal vortex cell A is a strengthened axisymmetric azimuthal vorticity cell in the secondary flow circulation. Next, two spiral vortices B and C are observed to coexist. The spiral vortex C is found to be connected to the toroidal vortex cell A. The part at which the spiral vortex C splits from the toroidal vortex cell A is the vortex-branch reported by Dumas & Leonard [5]. The vortex D represents the fore portion of the same class as the spiral vortex C at higher latitude. The spiral vortex B between the toroidal vortex cell A and the spiral vortex C is a counter-rotating pairing vortex to the spiral vortex C. The spatial helical pairing of the spiral vortex B and the spiral vortex C forms the spiral TG vortices which were defined in our previous experimental study (Nakabayashi [14]). It is found that the spiral TG

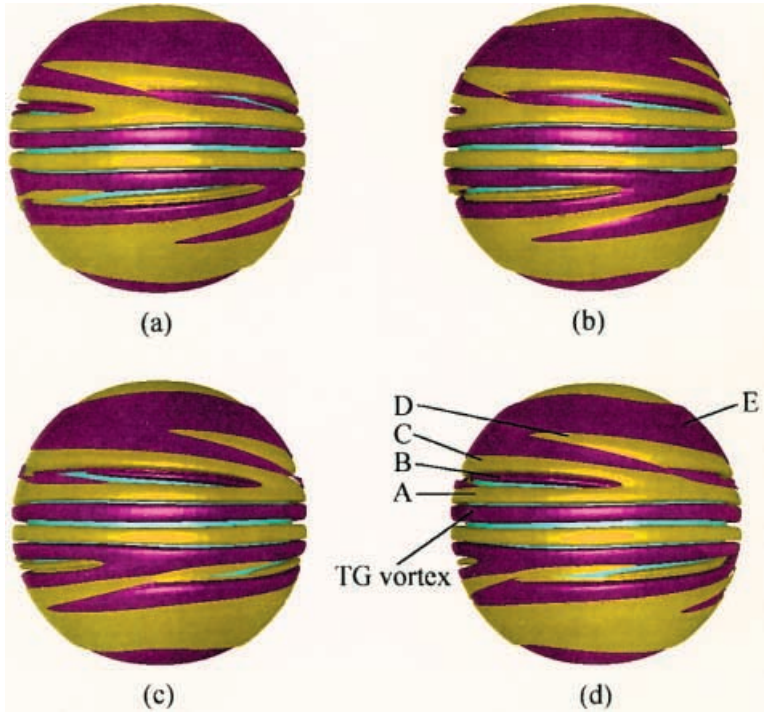

Fig. 3. Iso-surfaces of positive and negative azimuthal vorticity components of levels 0.9 for the spiral TG vortex flow at $Re_s = 1110$. Dark implies the positive value and light implies the negative one. They are viewed from (a) $\phi = 310°$; (b) $\phi = 220°$; (c) $\phi = 130°$; (d) $\phi = 40°$. 'A' denotes the toroidal vortex cell in the neighborhood of the toroidal TG vortex. 'C' is the spiral vortex being connected with the toroidal vortex cell A. 'B' between A and C is an accompanying spiral vortex of C, and has an opposite sign to the vorticity of the toroidal vortex cell A and spiral vortex C. 'D' indicates a fore portion of another spiral vortex. 'E' represents a thin vorticity layer adjacent to the outer spherical boundary.

vortices are a pair of two counter-rotating helical vortices. Actually, there are three pairs of these spiral vortices in each hemisphere. For each pair, a stronger, larger helical vortex (spiral vortex C) is accompanied by its counterpart of a relatively weaker, small helical vortex (spiral vortex B). The spiral TG vortices are rotational and equatorial asymmetric and travel in the azimuthal direction as the same as the inner rotating sphere. It is estimated that the spiral TG vortices incline to the azimuthal direction approximately by an angle of 4°. It can be also estimated from the simulation results that the phase speed of the spiral TG vortices is about half of the inner sphere rotation speed. The thin vorticity layer E is caused by the rapid variation of the meridional velocity near the outer spherical surface.

Table 1. Summary of some characteristics for the spiral Taylor-Görtler(TG) vortices in the spherical Couette flow between two spheres with the inner sphere rotating and the outer sphere fixed. The clearance ratio is 0.14 in laboratory experiments and in this numerical study.

	Dynamical Characteristics	Geometrical Characteristics
Previous Experiments (Nakabayashi [14]; Nakabayashi & Tsuchida [15])	$R^* = 1.13$ ($Re_s = 1017$) Move in direction of rotation Phase speed about half of the inner sphere rotation speed	Three pairs of spiral vortices in the northern hemisphere Rotational asymmetry Inclination angle 3°
Present Numerical Study	$R^* = 1.18$ ($Re_s = 1110$) Move in rotating direction Phase speed about half of the inner sphere rotating speed	Three pairs of spiral vortices in each hemisphere Rotational and equatorial asymmetries Inclination angle 4°

In Tab. 1, we summarize the characteristics of the spiral TG vortices obtained from the previous experiments (Nakabayashi [14]; Nakabayashi & Tsuchida [15]) and the present numerical study. Obviously, the present numerical simulation on the spherical spiral TG vortex flow gives good agreement with the previous experiments. Finally, an illustration of the three-dimensional structure of the spiral TG vortex flow in the northern hemisphere is given in Fig. 4.

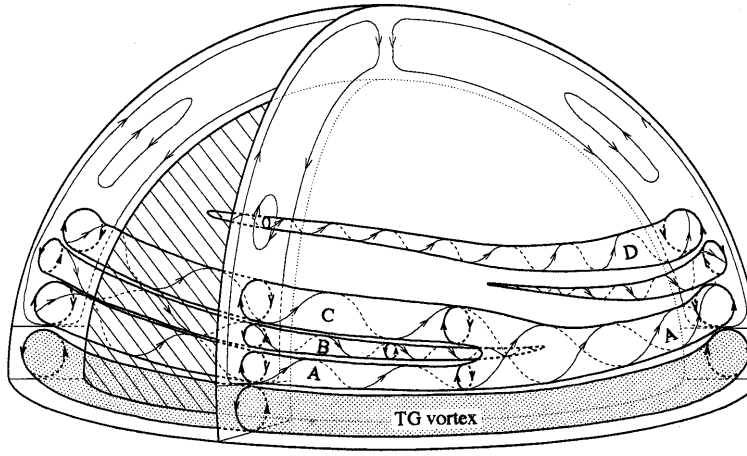

Fig. 4. An illustration of the three-dimensional structure of the spiral Taylor-Görtler(TG) vortex flow in the spherical Couette flow. The sketch is drawn for the north hemisphere. The outer sphere is held stationary and the inner sphere is constrained to rotate about the vertical axis. The clearance ratio is 0.14 for a moderate gap case, and the Reynolds number Re is quasi-statically increased to obtain this supercritical vortex flow at $Re_s = 1100$. The labels A, B, C and D have the same indications as those in Fig. 3.

To investigate the formation mechanism of the spiral TG vortex flow, we consider the vorticity production by analyzing the physical quantities in the vorticity equation (Sha & Nakabayashi, [19]). It was shown that the important vorticity tilting and stretching terms play different roles in the formation process of these two counter-rotating spiral vortices. The effect of the vorticity tilting term is responsible for generating both of the spiral vortices. The vorticity stretching term acts to stretch one of the spiral vortices from the inner sphere to the outer sphere while suppressing the stretching of the other spiral vortex in the azimuthal direction. The different formation mechanisms with respect to these two counter-rotating spiral vortices lead to the structure of the spiral TG vortices.

4 Motion of the azimuthally travelling waves

After the occurrence of spiral TG vortices, travelling waves appear on the spiral and toroidal TG vortices, with increasing Re. For the wavy vortices, modal analysis of unmodulated and modulated travelling waves on the toroidal TG vortices were investigated experimentally and theoretically for $\beta = 0.138$ by Nakabayashi & Tsuchida [16]. When Re increases quasi-statically, no modulation occurs on the travelling waves. However, when Re is increased from zero to a particular value with a specific acceleration of the inner sphere, modulation occurs on the wavy toroidal TG vortices. The necessary condition for the occurrence of modulation is the prevention of spiral TG vortices. The travelling wave corresponds to the motion of the inflow or outflow boundary, which can be measured by the oscillation of source and/or sink on the outer and inner spheres, respectively. Figure 5 shows the schematic representation of the sources and sinks labelled $j = a_2 \sim a_{2s}$ and $i_2 \sim i_{2s}$ on the outer and inner spheres at the meridian cross-section of the spherical annulus, respectively, for four toroidal vortex cells N=4. Here N stands for the number of TG vortex cells.

Firstly, let us see the unmodulated travelling waves. $j = a_1$ and a_{1s} which are sources on the outer sphere barely show any oscillation, but sinks on the outer sphere and both sources and sinks on the inner sphere show entirely sinusoidal oscillations with same frequency f_1, as shown in Fig. 6. Here f_1 stands for the fundamental frequency of the travelling wave. Figure 6 shows the schematic representation of colatitude $\theta_j(\phi') = \theta_j - \theta_j(\phi')$, for each j except for a_1 and a_{1s} in the rotating frame, which rotates with angular speed $2\pi f_1/m$. m stands for wave number of the travelling waves. θ_j is the average meridian angle, and ϕ' and ϕ'_j are the reference azimuthal angle and the azimuthal angle for each j, respectively, which are measured with respect to the rotating frame and increase in the direction of the inner sphere rotation. And $\Delta\phi'_j = \phi' - \phi'_j$ is the azimuthal phase difference between ϕ' and ϕ'_j. Let $\theta_j(\phi')$ be assumed to the form $\theta_j(\phi') = A_j \sin(m\phi'_j)$, where A_j is the constant amplitude. Since the relation between the azimuthal angles ϕ' in the rotating frame and ϕ in the laboratory

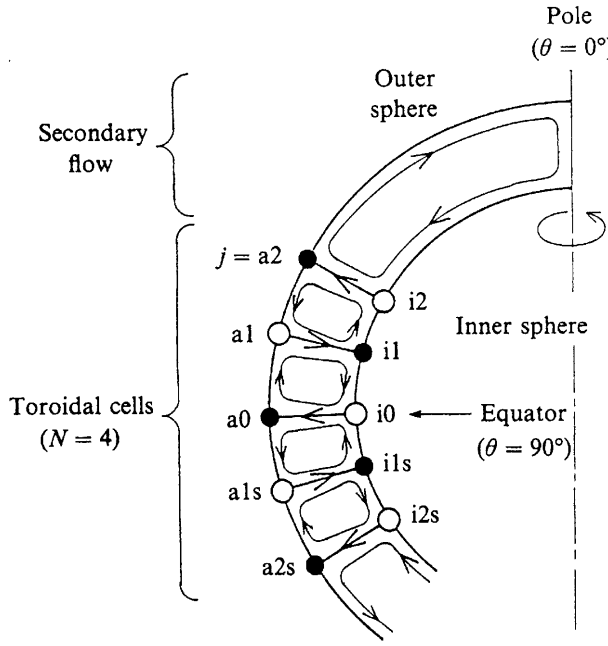

Fig. 5. Schematic representation of streamlines, sources and sinks labelled $j = a_2 - a_{2s}$ and $i_2 - i_{2s}$ on the outer and inner spheres at the meridian cross-section, respectively, for the toroidal vortex flow state with four cells (N=4);○, source; ●, sink. (Nakabayashi & Tsuchida, [17])

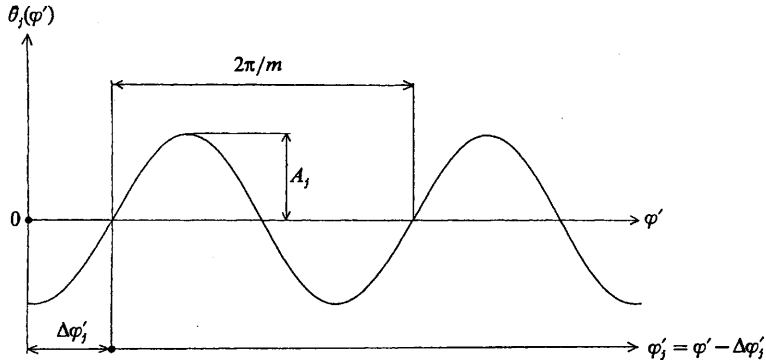

Fig. 6. Schematic representation of the fluctuating colatitude $\theta_j(\phi')$ given by Eq. 1 (Nakabayashi & Tsuchida, [17]).

frame is given by $\phi' = \phi - 2\pi f_1 t/m$:

$$\theta_j(\phi') = A_j \sin[m(\phi' - \Delta\phi'_j)] \tag{1}$$

$$\theta_j(t,\phi) = \theta_j - \theta_j(t,\phi) = A_j \sin[m(\phi - 2\pi f_i(t - \Delta t_j)/m)], \tag{2}$$

where $\Delta\phi'_j = -2\pi f_1 \Delta t_j$, and Δt_j is the temporal phase difference. The above equation gives the wave motion of the wavy toroidal TG vortices in the laboratory frame. Reynolds number dependence of the amplitude A_{a_0} (at $j = a_0$) and the rotation frequency of the travelling azimuthal waves f_1/m are shown in Fig. 6 (Nakabayashi & Tsuchida, [16]), respectively. Generally speaking about the case for the clearance ratio around $\beta = 0.14$, the amplitude decreases with increasing $R^* = Re/Re_c$, where Re_c stands for critical Reynolds number of Taylor instability. And the travelling waves disappear for $R^* > 7$. This tendency is due to the relaminarization described later. The wave speed also decreases with increasing R^* for β =0.138.

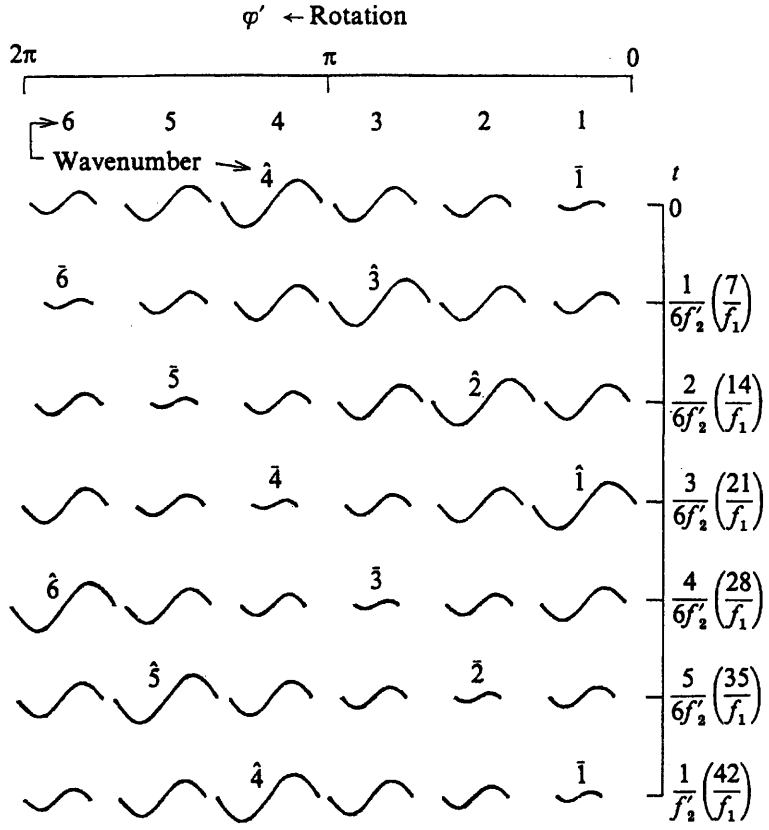

Fig. 7. Schematic representation of the evolution in time of the modulation in a reference frame rotating with the waves (Nakabayashi & Tsuchida, [17]).

For the modulation of the travelling waves, Fig. 7 shows a schematic diagram showing the temporal evolution of modulation patterns in a reference frame rotating with the speed of the travelling azimuthal waves $2\pi f_1/m$. t increases downward and the azimuthal angle ϕ' increases leftward. This diagram

was obtained by analyzing successive photographs of the whole spherical surfaces taken at the time interval $1/f_2 = 7/f_1$. The waves with the bar and hat over the number are the flattened and S-shaped waves, respectively. Both amplitude and frequency modulations occur simultaneously for SCF similar to CCF. The modulation frequency f_2' for both of them in the rotating frame is given by $f_2' = f_1/42$ (at $R^* = 2.2$). So that $f_2' = 0.065$ is obtained, because $f_1 = 2.73$ at $R^* = 2.2$.

Table 2. Comparison of characteristics of the modulated wavy-vortex flow state with $m = 6$ and $k = -1$ for the same β between SCF (Nakabayashi & Tsuchida, [17]) and CCF (Gorman & Swinney, [8])

	SCF	CCF
β	0.138	0.133
m	6	6
k	-1	-1
R^*	$1.77 \sim 2.64$	10.5(onset)
f_1	2.730 ± 0.066	2.03
f_1/m	0.445 ± 0.011	0.34
f_2	0.387 ± 0.009	0.21
f_2'	0.066 ± 0.018	0.55
Relation	$f_2' = -f_2 - kf_1/m$	$f_2' = f_2 - kf_1/m$

Table 2 shows comparison of the characteristics of the wavy toroidal vortex with $m = 6$ and $k = -1$ for SCF with those for CCF. Here k stands for a modulation parameter of the superposed modulation just as for CCF (Swift et. al, [21]). R^* range of the occurrence of the modulation for SCF is very different from that for CCF. Although the values of the wave speed f_1/m and the modulation frequency in the laboratory f_2 for SCF are approximately similar to those of CCF, the values f_2' differ very much, because the relations among f_2', f_2 and f_1 are different.

5 Spectral analysis of velocity fluctuations

Hot-wire measurements of azimuthal velocity components were done at $\theta = 80°$ and 90° by Nakabayashi & Tsuchida [15] for $\beta = 0.14$. Non-dimensional profiles of the mean azimuthal velocity component measured in the clearance at $\theta = 90°$ show great dependence on R^*. Especially the non-dimensional profiles in the center region of the clearance go up and down with increasing R^* for the supercritical flow region, although a non-dimensional profile for the laminar basic flow agrees well with the theoretical one. Such a Reynolds number dependence is corresponding to the exchange of outflow-and inflow-boundaries near the equator, which is caused by the movement of the toroidal TG vortex with increasing R^*. When R^* is increased to 57.3, the profile approaches that of a turbulent Couette flow.

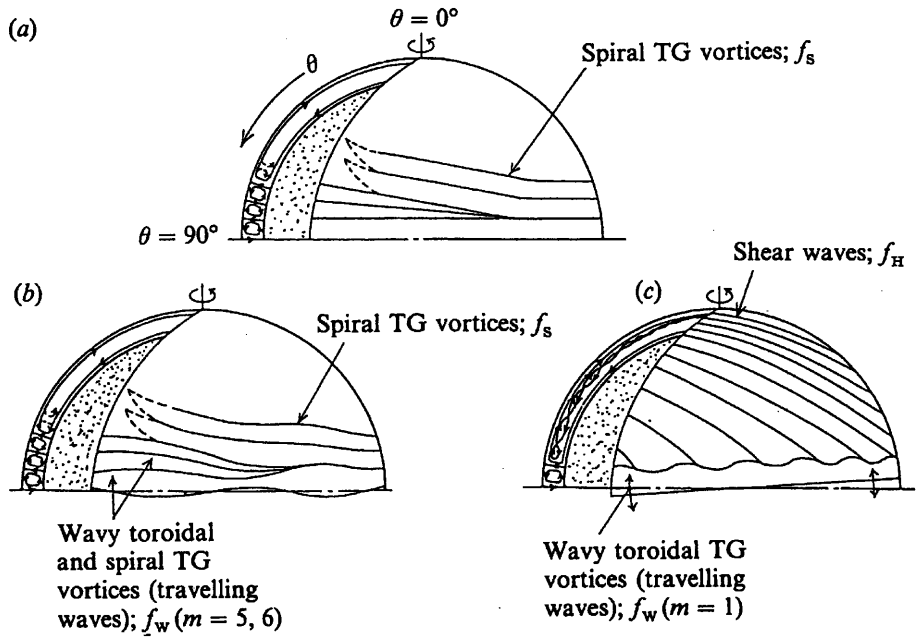

Fig. 8. Schematics of the flows in typical flow regimes and the three fundamental frequency components f_S, f_W and f_H (Nakabayashi & Tsuchida, [15])

Velocity fluctuations are observed simultaneously with the occurrence of the spiral TG vortices. In the quasi-static laminar-turbulent transition, three typical vortical flow patterns (flow regimes) were observed. The quasi-static transition means the condition that the Reynolds number is increased stepwise by a quasi-static increase of the rotation of the inner sphere from zero, since the flow mode depends on the rate of increase of the Reynolds number (Nakabayashi & Tsuchida, [17]). Figure 8 shows schematics of these vortex structures and the three fundamental frequency components f_S, f_W and f_H for the flow regimes: II TS or III TS with f_S (toroidal and spiral TG vortices), the flow regime III WTS with f_S and f_W (wavy toroidal and spiral TG vortices)and the flow regime IV WTS_H with f_W and f_H (wavy toroidal TG vortex and shear waves). The number of toroidal TG vortex cells N, that of spiral TG vortex pairs S_P, the wave number of the travelling azimuthal waves on the toroidal TG vortex m and the wave number of shear waves S_H were measured from the flow visualization and the simultaneous spectral measurements by the scattered laser-light intensity. The fundamental frequency components for the spiral TG vortex f_S, the travelling azimuthal waves f_W and the shear waves f_H found as peaks in the power spectra obtained by the hot-wire measurements were also identified by the simultaneous spectral measurements, respectively.

Figure 9 shows Reynolds number dependence of the fundamental frequencies of the spiral TG vortices, the travelling azimuthal waves and the shear waves,

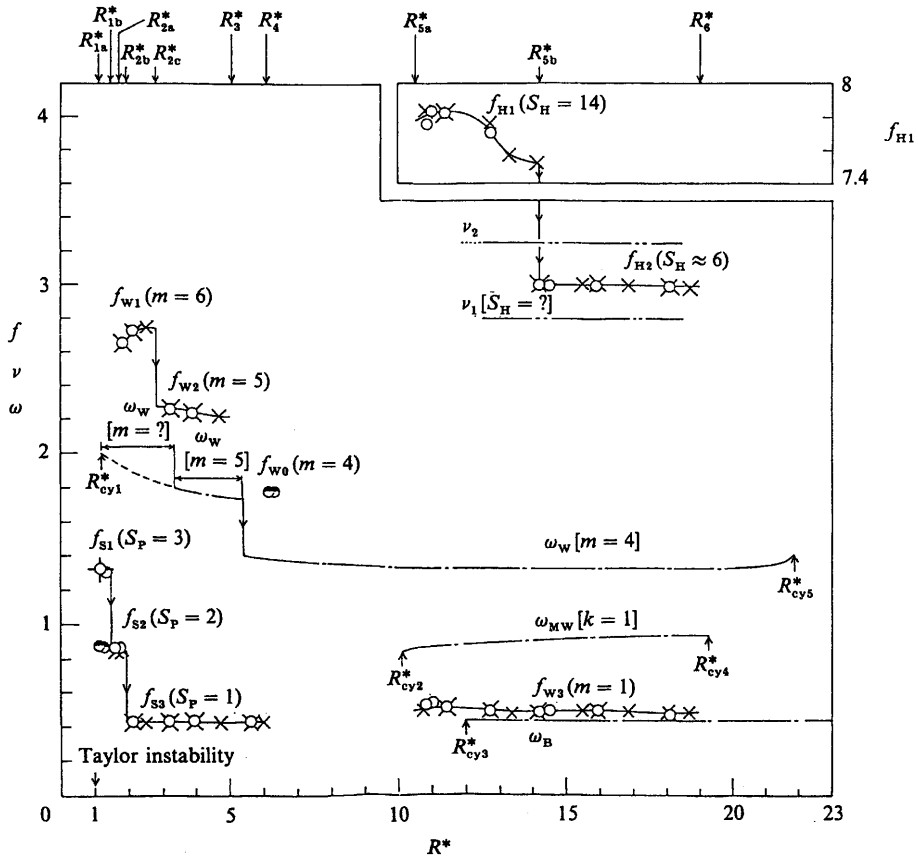

Fig. 9. Reynolds number dependence of the fundamental frequency components of the velocity fluctuations. $\circ, \times, +$ etc. indicate the data obtained from the power spectra by Nakabayashi & Tsuchida [15]. ν_1 and ν_2 indicate the data obtained by Bühler & Zierep [3]. ω_W, ω_{MW} and ω_B , data, and $R^*_{cy1} - R^*_{cy5}$, transition Reynolds numbers for the regime transition, respectively, obtained in the circular Couette flow for $\beta = 0.14$ and $\Gamma = 20.0$ by Fenstermacher et al. [7]

compared with those of the travelling waves in CCF. The fundamental frequency decreases stepwise with the decrease of the number of S_P, m and S_H with increasing R^*. In the range of $R^* = 6 \sim 10$, there are no fundamental frequencies, because the velocity fluctuation becomes zero, where we can observe the disappearance of both spiral TG vortex and travelling wave. We shall discuss later about this phenomenon which is called as the relaminarization. Rotation frequencies i.e. wave speeds f_S/S_P, f_W/m and f_H/S_H are nearly constant with increasing R^* and differ slightly from one another. The value of the wave speed for the travelling azimuthal waves decreases with an increase of the clearance ratio. This tendency is similar to that in CCF. At the case of same clearance

ratio, however, the wave speed in SCF is higher than that in CCF, although the toroidal TG vortex structure observed near the equator in SCF is same as Taylor vortex in CCF. The ranges of R^* where the travelling azimuthal waves occur are also very different from those in CCF. These differences are caused by the Ekman boundary-layer effect on the toroidal TG vortex .

The occurrence of the disturbances or vortices are spatially restricted. The meridian ranges of θ where the fundamental frequency components of the disturbances could be measured by the power spectra of the scattered laser-light intensity extend over the meridian ranges where the corresponding disturbances were clearly observed. The values of the frequency components are constant independently of colatitude θ and the distance from the walls, although the powers at the fundamental frequency components of the disturbances depend on the distance from the walls.

6 Relaminarization

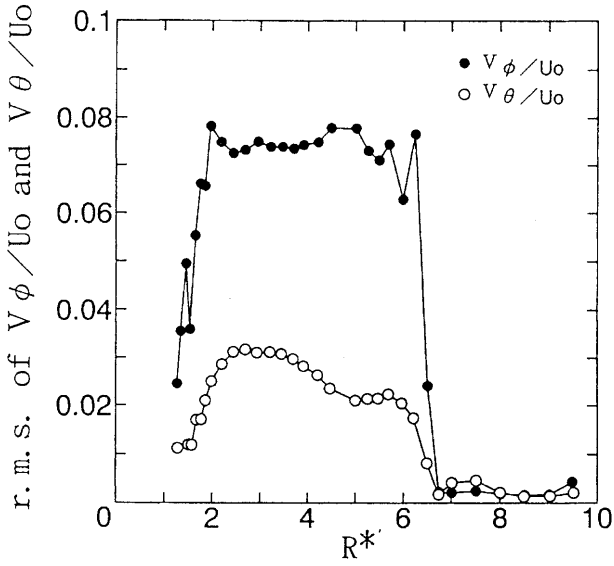

Fig. 10. Evolution of RMS values of V_ϕ/Uo and V_θ/Uo

Table 3 shows the radius of the inner sphere R_1 and the critical Reynolds number of Taylor instability Re_c measured for each clearance ratio β . Figure 10 shows the evolution of non-dimensional RMS (root mean square) values of V_ϕ and V_θ divided by U_0 against R^*. V_ϕ and V_θ stand for fluctuations of azimuthal and meridian velocity components, respectively. U_0 stands for peripheral velocity of rotating inner sphere. Solid and open circles indicate for V_ϕ and V_θ, respectively.

Table 3. Radius of inner sphere and critical Reynolds number for each β

Clearance ratio β	Inner sphere R_1 (mm)	Critical Reynolds number Re_c
0.06	82.55 ± 0.04	2760
0.10	79.74 ± 0.03	1440
0.14	76.88 ± 0.03	900
0.158	75.71 ± 0.03	760
0.206	72.57 ± 0.04	554

The RMS values sharply increase with the occurrence of the spiral TG vortices. With increasing R^*, they keep approximately constant. But beyond around $R^* = 6.5$, they suddenly decrease, because the velocity fluctuations attenuate and become zero. We shall call this phenomena as the relaminarization. Here it is notable that the RMS data for V_ϕ are much greater than for V_θ.

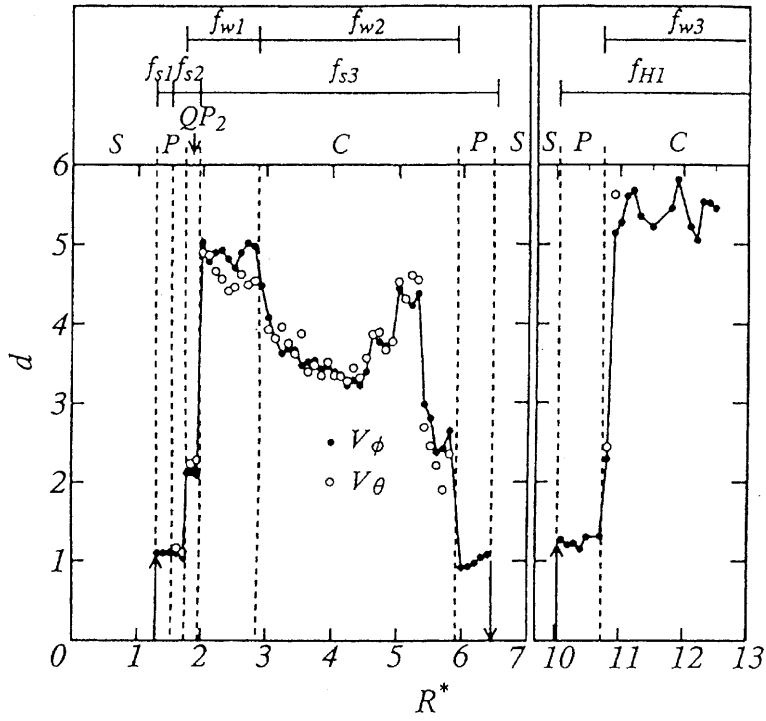

Fig. 11. Evolution of correlation dimension and scenario of the transition.

Figure 11 shows the evolution of correlation dimension d, the non-dimensional fundamental frequencies of disturbances (spiral TG vortex f_S, travelling waves f_W and shear waves f_H; see Fig. 9) and the scenario leading up to the relaminar-

ization against R^*. Open and closed circles indicate the correlation dimensions for V_ϕ and V_θ which were measured in the center of the gap at the equator, respectively. They are in agreement with each other, although their values of intensities are different. The scenario up to the occurrence of the relaminarization is explained on the attractor of the flow as follows. In the region of $1.0 < R^* < 1.20$, the attractor is a fixed point (S, steady state), which corresponds to the toroidal TG vortex. After the first Hopf bifurcation at $R^* = 1.20$ (the occurrence of f_{S1}), the attractor is a limit cycle (P, periodic state) for $1.20 < R^* < 1.74$, while the transition from f_{S1} to f_{S2} occurs at $R^* = 1.60$. At $R^* = 1.74$, the second Hopf bifurcation (the occurrence of f_{W1}) takes place, leading to the appearance of the quasiperiodic regime (QP_2) with two fundamental frequencies f_{S2} and f_{W1}. At the bifurcation near $R^* = 1.95$, the frequency f_{S2} changes to f_{S3} and d increases from 2 to 5. Therefore, the attractor is characteristic of a strange attractor corresponding to low-dimensional chaos (C). The value of d decreases with increasing R^* after the transition from f_{W1} to f_{W2} at $R^* = 2.95$, where the fourth bifurcation occurs. The bifurcation around $R^* = 6.0$ re-transforms the chaotic regime into the periodic regime with f_{S3}, where the attractor has a noisy limit cycle. At $R^* = 6.50$, the value of d becomes zero and the successive attractor is a fixed point (S). Then the relaminarization occurs in the region of $6.50 < R^* < 10.02$. When R^* increases further more after the relaminalization, shear waves f_{H1} occur at $R^* = 10.02$ and the attractor is a noisy limit cycle. At $R^* = 10.79$, travelling wave f_{W3} occurs suddenly up to about 5. For $R^* > 12.8$, the attractor has a strange attractor which has the degree of freedom higher than that in the range of $2.95 < R^* < 6.03$, because the convergence of the correlation dimension regarding the embedding dimension is worse and we could not get exact value of d. Accordingly, the scenario of the transition to the turbulent flow is following. From a fixed point, through a limit cycle, a T2 torus, a chaos, a noisy limit cycle, a fixed point, a noisy limit cycle, to a chaos.

Figure 12 shows the dependence of β on the relationship between d and R^*. The curve of Re_c and the region of relaminarization (shaded region) are shown on the $\beta - Re$ surface. For smaller β cases, i.e. $\beta = 0.06$ and 0.10, and larger β case, i.e. $\beta = 0.206$, the values of d increase sharply with Re after the first Hopf bifurcation, where no relaminarization occur. But for intermediate β cases, i.e. $\beta = 0.14$ and 0.158, the relaminarization occurs.

Figure 13 shows the relation among onset Reynolds number of disturbances, contour lines of d and the region of relaminarization. $d = 1$ and 2 lines agree with the onset Reynolds number Ret of spiral TG vortex and travelling waves, respectively. Around $\beta = 0.135 \sim 0.17$, contour lines turn twice. This is the reason why the relaminarization occurs around the intermediate β range.

Figure 14 shows power spectra of azimuthal velocity fluctuation components for $\beta = 0.06 \sim 0.158$. The evolutions of the power spectra for $\beta = 0.06$ and 0.10 are mimic each other as well as for $\beta = 0.14$ and 0.158. Let us divide the power of the disturbances into two parts, higher and lower frequency regions than $f = 2$. Figure 15 (a), (b) and (c) show the power of disturbances $\left\{\int E(f)df\right\}$ contained in the lower and higher frequency regions against R^* for $\beta = 0.06$,

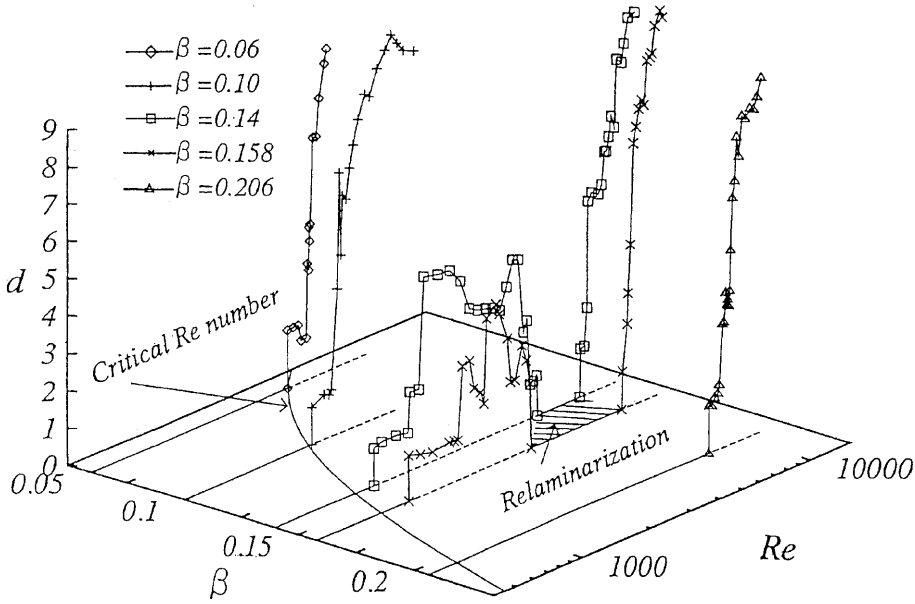

Fig. 12. Re dependence of correlation dimension for each β.

0.14 and 0.158, respectively. For β =0.06 (no relaminarization case), the power of disturbances increases with R^* in the higher frequency region, but decreases with increasing R^* in the lower frequency region. For $\beta = 0.14$ and 0.158 (relaminarization cases), however, the tendency is opposite to the former. The power in the higher frequency region decreases three times preceding the occurrence of relaminarization. Rise of the power in the lower frequency region with increasing R^* is caused by the reappearance of line spectra. Drop of the power in the high frequency region is caused by the attenuation of background noise level. When the relaminarization occurs, the energy of disturbances in the higher frequency region decreases with increasing R^*, but it in the lower frequency region increases with R^*.

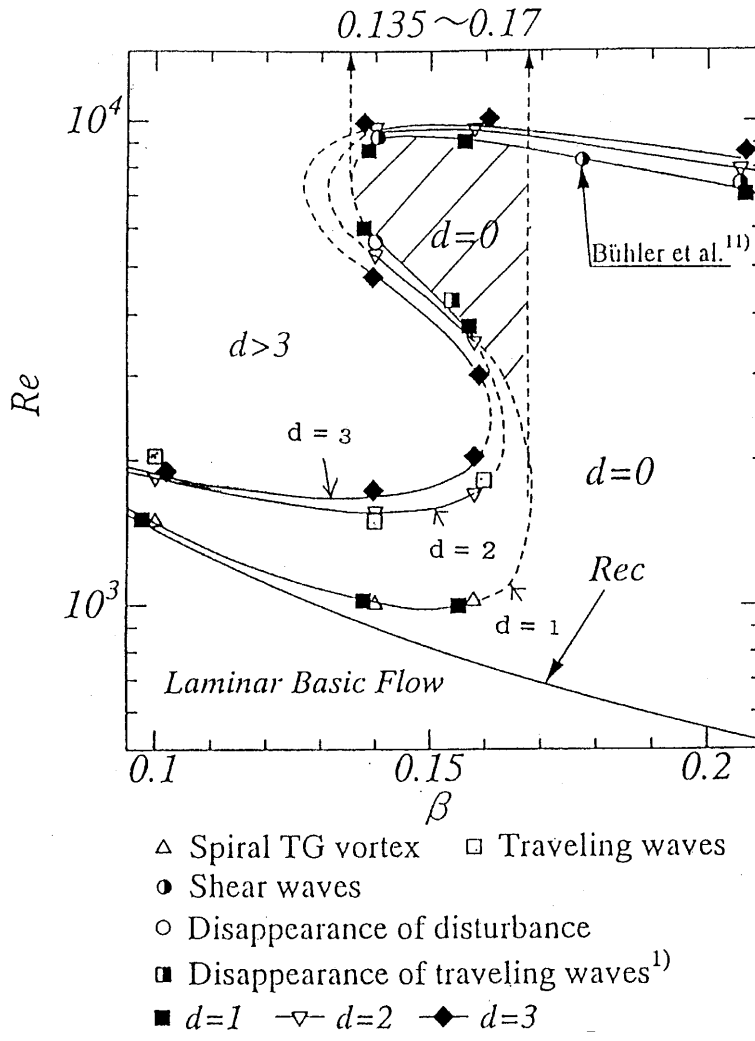

Fig. 13. Region of velocity fluctuation destruction.

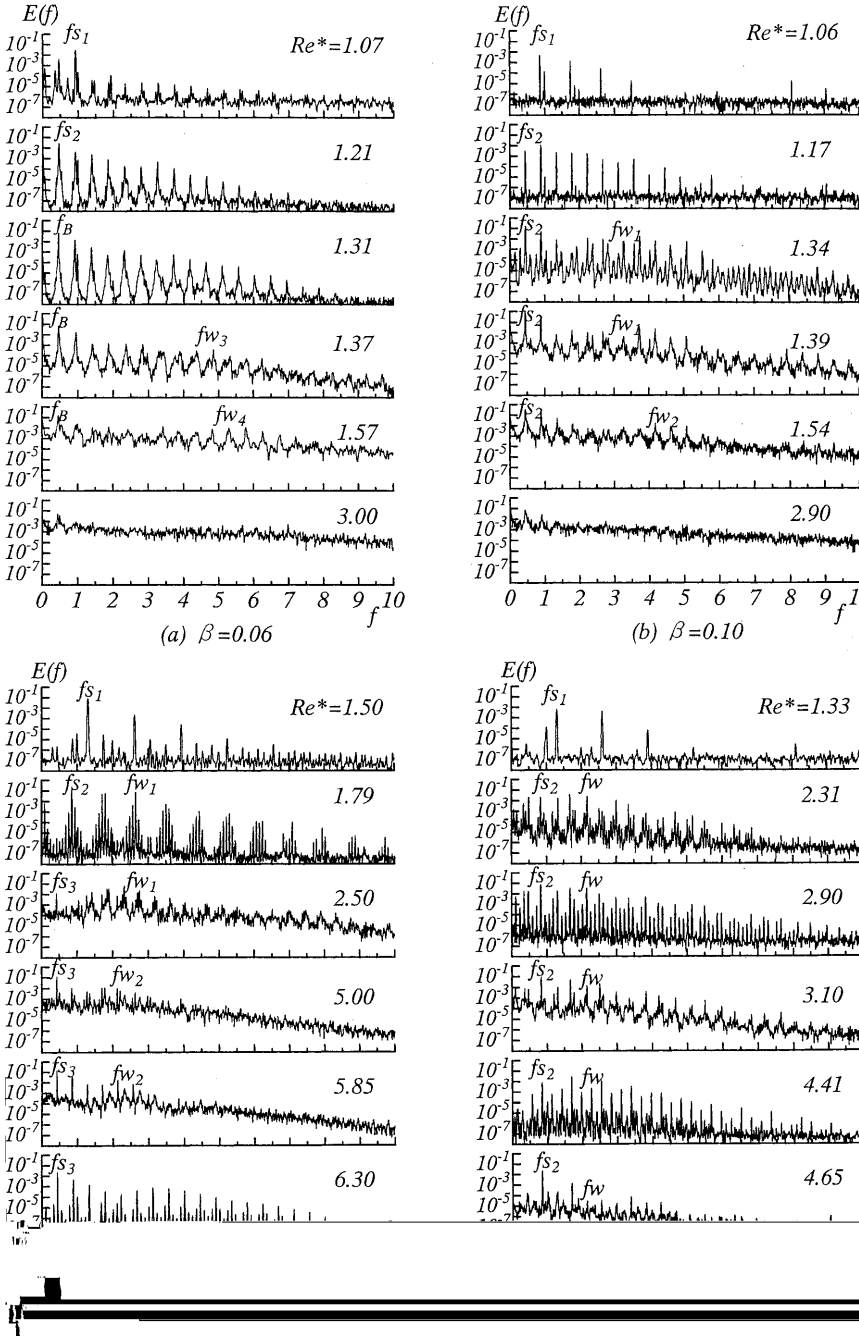

Fig. 14. Power spectra.

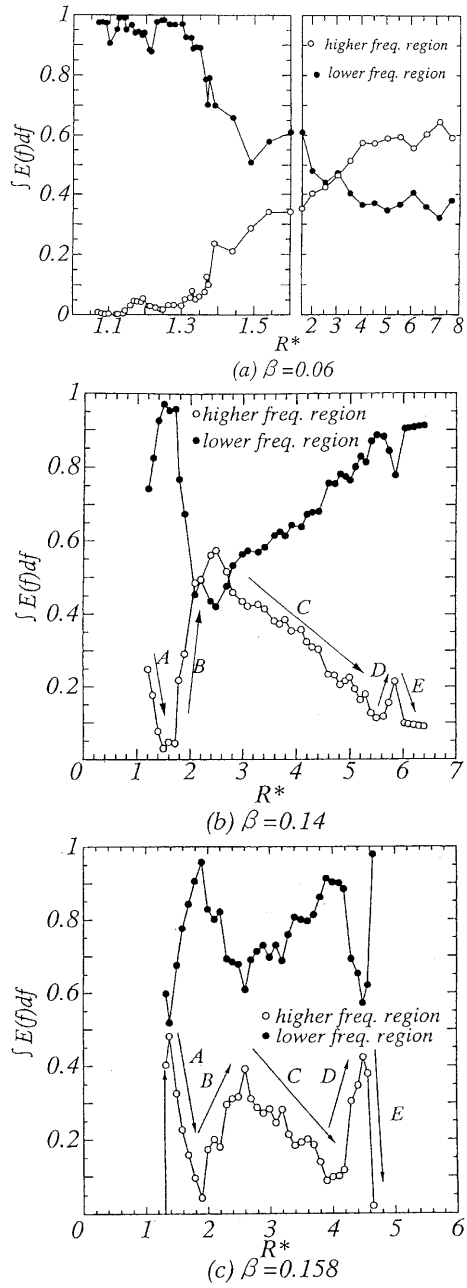

Fig. 15. Powers of disturbances contained in the higher and lower frequency regions. (a)$\beta = 0.006$, (b)$\beta = 0.14$, (c)$\beta = 0.158$.

7 Concluding remarks

The laminar-turbulent transitions for cases of the narrow and medium gap widths in SCF shows quasiperiodic transitions similar to those in CCF. But the transition phenomena for SCF depend on the clearance ratio very much. We have clarified the clearance ratio dependence of the onset Reynolds number of various disturbances, and showed the characteristics of the disturbances depended on the acceleration of Reynolds number, the initial flow mode and the history of Reynolds number increase or decrease.

We have also discussed the vortical structures and velocity fluctuations of the disturbances, i.e., the spiral and wavy vortices observed near the equator for the narrow and medium gap widths. The experimental and numerical results on the vortical structure and formation of the spiral and wavy vortices are presented. It is shown that there are very difference in the vortical structures between these gap widths and the wide gap width. We further divide the narrow and medium gap widths into three cases, i.e., the small, intermediate and large clearance ratios. For the case of intermediate clearance ratio case, the relaminarization phenomenon occurs. Although the formation mechanism has not been clarified yet, a locking of wave motion can be conjectured to be due to, and further experimental, theoretical and numerical studies are needed.

References

1. Araki, K., Mizushima, J. and Yanase, S.; *The nonaxisymmetric instability of the wide-gap spherical Couette flow.* Phys. Fluids **9(4)**, 1197-1199, (1997).
2. Bar-Yoseph, P., Solan, A., Hillen, R. and Roesner, K.G.; *Taylor vortex flow between eccentric coaxial rotating spheres.* Phys. Fluids A**2(9)**, 1564-1573, (1990)
3. Bühler, K., J. Zierep; *New secondary flow instabilities for high Re-number flow between two rotating spheres.* In Laminar-Turbulent Transition ed. by V. V. Kozlov (Springer) pp. 677-685, (1984).
4. Bühler, K.; *Symmetric and asymmetric Taylor vortex flow in spherical gaps.* Acta Mech. **81**, 3-38, (1990).
5. Dumas, G. & Leonard, A.;*A divergence-free spectral expansions method for three-dimensional flows in spherical-gap geometries.* J. Comput. Phys. **111**, 205-219, (1994).
6. Egbers, C. & Rath, H.J.; *The existence of Taylor vortices and wide-gap instabilities in spherical Couette flow.* Acta Mech. **111**, 125-140,(1995).
7. Fenstermacher, P.R., H. L. Swinney, J. P. Gollub; J. Fluid Mech.,**94**, 103, (1979)
8. Gorman, M., H. L. Swinney, 1982; J. Fluid Mech., **117**, 123, (1982).
9. Itoh, M.; *On the stability of flow between parallel rotating conical surfaces (1st report, the case of one stationary conical surface).* Trans. Japan Soc. Mech. Engrs. (Japanese), **55**, 305, (1989).
10. Khlebutin, G.H.; *Stability of fluid motion between a rotating and a stationary concentric sphere*, Fluid Dynamics, **3**, 31, (1968).
11. Marcus, P. S. & Tuckerman, L. S.; *Simulation of flow between concentric rotating spheres.* Paper 1. Steady states. J. Fluid Mech. **185**, 1-30, (1987a).
12. Marcus, P. S. & Tuckerman, L. S.; *Simulation of flow between concentric rotating spheres.* Paper 2. Transition. J. Fluid Mech. **185**, 31-65, (1987b).

13. Munson, B.R. & Menguturk, M.; *Viscous incompressible flow between concentric rotating spheres.* Part 3: Linear stability and experiments. J. Fluid Mech. **69**, 705-719, (1975).
14. Nakabayashi, K.; *Transition of Taylor-Görtler vortex flow in spherical Couette flow.* J. Fluid Mech. **132**, 209-230, (1983).
15. Nakabayashi, K & Tsuchida, Y.; *Spectral study of the laminar-turbulent transition in spherical Couette flow.* J. Fluid Mech. **194**, 101-132, (1988a).
16. Nakabayashi, K & Tsuchida, Y.; *Modulated and unmodulated traveling azimuthal waves on the toroidal vortices in a spherical Couette system.* J. Fluid Mech. **195**, 495-522, (1988b).
17. Nakabayashi, K & Tsuchida, Y.; *Flow-history effect on higher modes in the spherical Couette system.* J. Fluid Mech. **295**, 43-60, (1995).
18. Sha, W., Nakabayashi, K. and Ueda, H.; *An accurate second-order approximation factorization method for time-dependent incompressible Navier–Stokes equations in spherical polar coordinates.* J. Comput. Phys. **142**, 47-66, (1998).
19. Sha, W. and K.Nakabayashi, 1999; *On the structure, evolution processes and formation mechanism of spiral Taylor–Couette vortices in spherical Couette flow.* J. Fluid Mech.; (1999) (revised).
20. Sawatzki, O. & J.Zierep; *Das Stromfeld im Spalt zwischen zwei konzentrischen Kugelflächen, von denen die innere rotiert.* Acta Mechanica, **9**, 13, (1970).
21. Swift, J., M.Gorman, H. L. Swinney; Phys. Lett. **87 A**, 457, (1982).
22. Wimmer, M.; *Experiments on a viscous fluid flow between concentric rotating spheres.* J. Fluid Mech. **78**, 317-335, (1976).
23. Wimmer, M.; *Experiments on the stability of viscous flow between two concentric rotating spheres.* J. Fluid Mech. **103**, 117-131, (1981).
24. Wulf, P., Egbers, C., and Rath, H.J.; *Routes to chaos in wide gap spherical Couette flow.* Phys. Fluids **11(6)**, 1359-1372, (1999).
25. Yavorskaya, I.M., Belyaev, Yu.N., Monakhov, A.A, Astaf'eva, N.M., Scherbakov, S.A. and Vvedenskaya, N.D.; *Stability, non-uniqueness and transition to turbulence in the flow between two rotating spheres.* Proc. XV IUTAM Symposium, Toronto, 431-443, (1980).
26. Zikanov, O. Yu.; *Symmetry-breaking bifurcations in spherical Couette flow.* J. Fluid Mech. **310**, 293-324, (1996).

Spherical Couette flow with superimposed throughflow

Karl Bühler

University of Applied Science
Badstrasse 24, D-77652 Offenburg, Germany

Abstract. This work deals with the generalization of the spherical Couette flow from a closed flow into an open flow system. A superimposed throughflow in meridional direction leads to novel flow structures and stability behaviour. A analytical solution for the superposition of the spherical Couette and the source-sink flow is given for the creeping flow. Numerical simulations for steady and time-dependent rotationally symmetric solutions are presented for a large Reynolds number range. These solutions represents the non-uniqueness of the supercritical spherical Couette flows. Their symmetry with respect to the equator and time-behaviour depends strongly on the throughflow Reynolds number. The experiments show the rich variety of supercritical solutions depending on the rotation and throughflow parameters. Rotationally symmetric vortices and spiral vortices are realized in steady and time-dependent form. For the pure source-sink flow the instabilities are formed like banana shaped structures. The existence regions and transitions between the different modes of flow are presented in maps. For the rotationally symmetric states there is a good agreement between theory and experiments.

1 Introduction

Hydrodynamic instabilities in spherical gap flows are important in nature and technology. The stability, structure development and dynamics of these flows have an direct influence on the momentum and energy transfer. The closed spherical gap is treated in many theoretical and experimental investigations [1–5]. We extend this closed flow into an open flow problem by superimposing a mass flux in meridional direction [6,7].

A principal sketch of the geometry is given in Fig.1. The important non-dimensional parameters are the gap width σ for the geometry, the Reynolds number Re for the rotation of the inner sphere and the throughflow Reynolds number Re_D describing the superimposed mass flux in meridional direction. The mean meridional velocity in the equatorial plane is characteristic for the mass flux.

Analytical solutions can be obtained for low Reynolds numbers. Figure 2 displays some elementary velocity distributions and streamlines. The spherical Couette-flow is realized by a rotation of the inner sphere about the vertical axes, while the outer sphere is at rest. For the limiting case $Re \to 0$ the streamlines are concentric circles. For finite Reynolds numbers the flow has three non vanishing velocity components with a induced secondary flow in meridional plane.

C. Egbers and G. Pfister (Eds.): LNP 549, pp. 256–268, 2000.

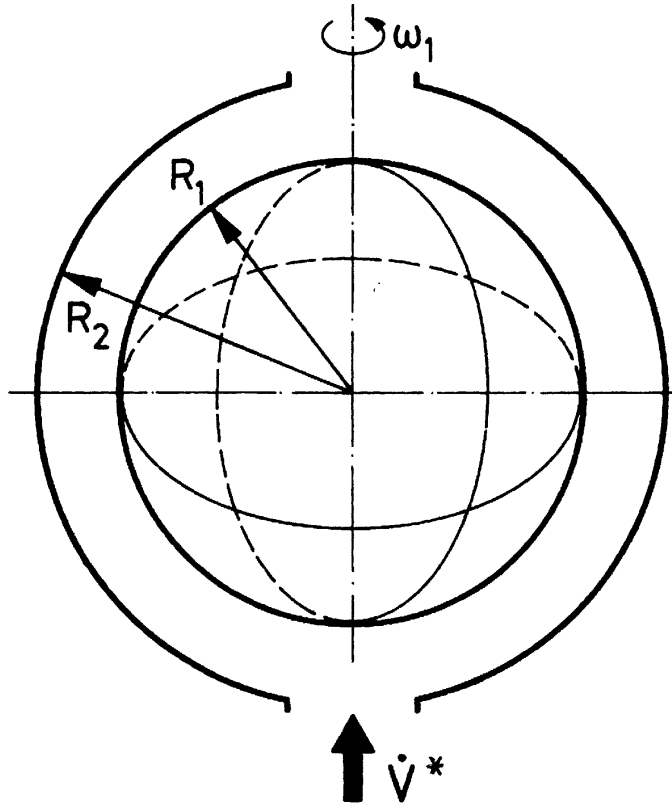

$$\sigma = \frac{R_2 - R_1}{R_1} \qquad Re = \frac{R_1^2 \omega_1}{\nu} \qquad Re_D = \frac{\bar{u}(R_2 - R_1)}{\nu}$$

Fig. 1. Principal sketch of the spherical geometry and definitions of non- dimensional parameters: gap width σ, rotation Reynolds number Re and throughflow Reynolds number Re_D.

A source-sink flow in the spherical gap is realized by superimposing a mass flux in meridional direction from pole to pole as shown in the middle of Fig.2. These flow is decelerated in the lower and accelerated in the upper hemisphere. A superposition of the spherical Couette and the source-sink flow results in spiral streamlines shown in the lower part of Fig.2. The velocity distributions of these basic solutions are shown in Fig.3.

An analytical solution for superposition of rotation and throughflow is developed in [7]. The lines of constant streamfunction in the meridional plane are plotted in Fig.4 for the single solutions and there superposition. A characteristic asymmetry with respect to the equator occurs. These analytical solutions are important as initial flows for the development of the flow structures at higher Reynolds numbers.

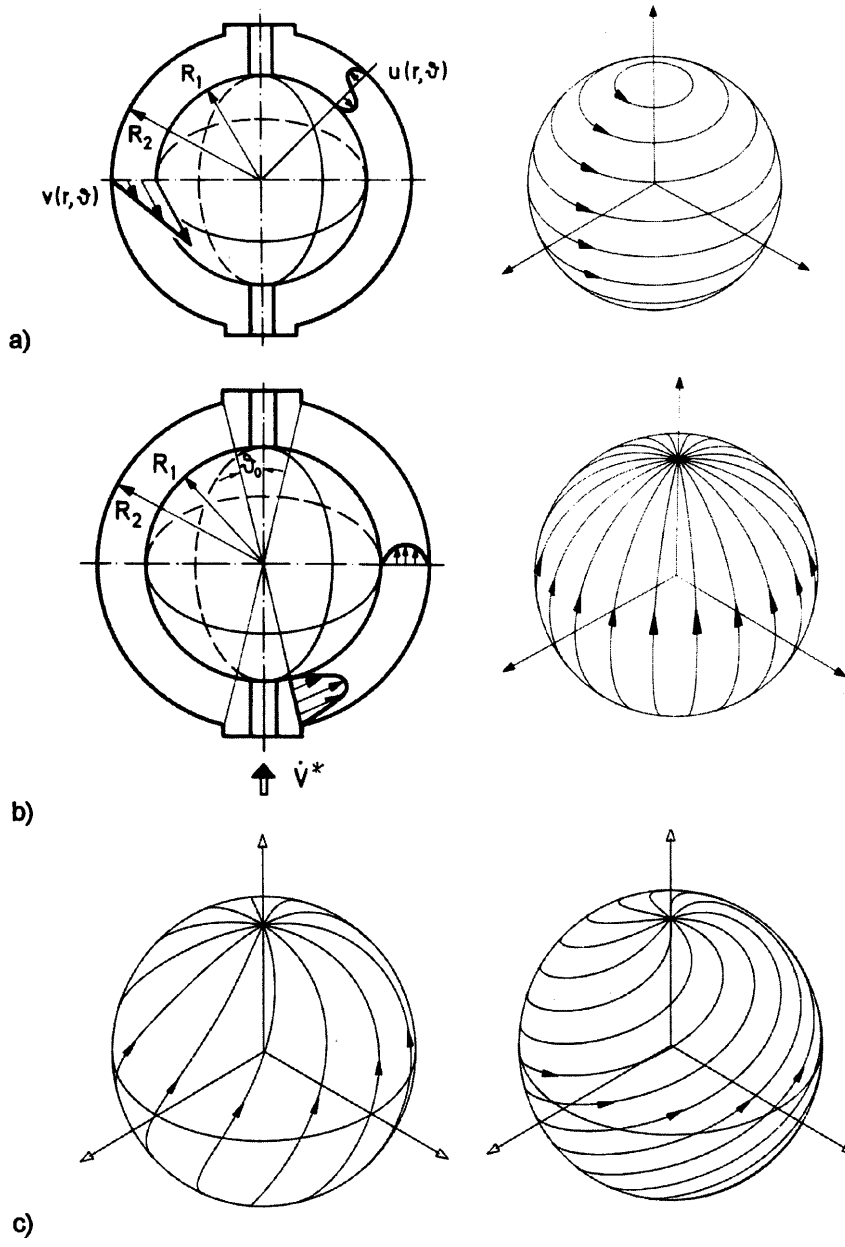

Fig. 2. Streamlines of the basic solutions. From top to bottom: a) spherical Couette flow , b) source-sink flow and, c) superposition of spherical Couette-flow and source-sink flow for different rotation to throughflow rates

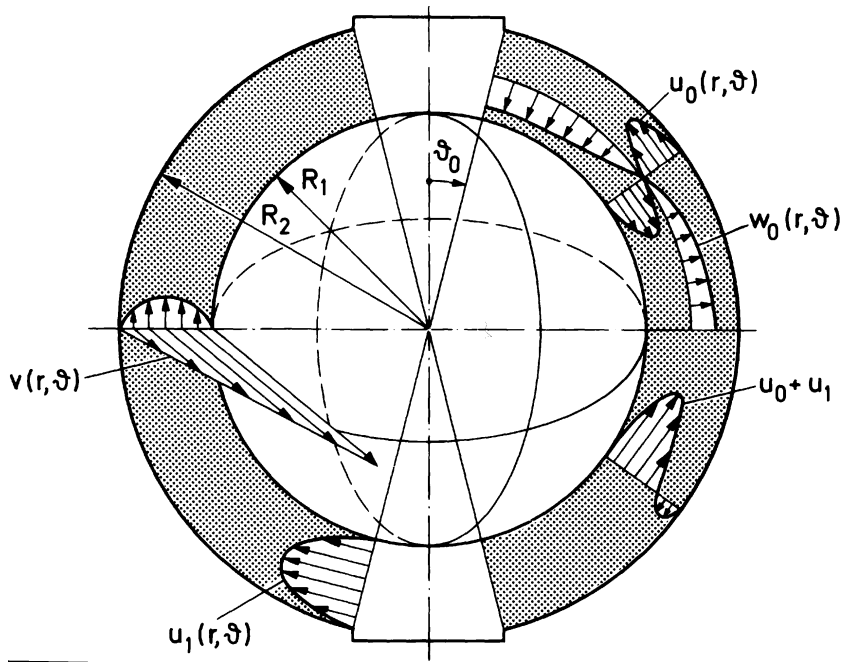

Fig. 3. Velocity distributions of the single and combined basic solutions

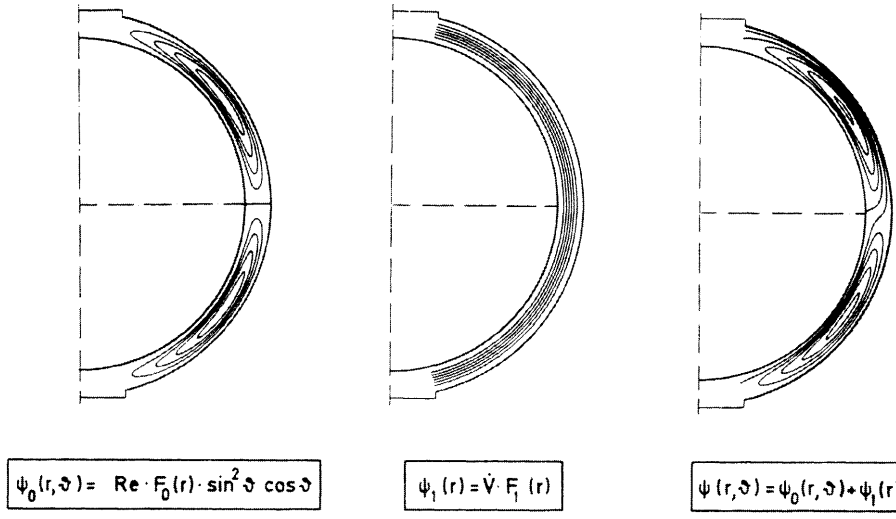

Fig. 4. Analytical solution for the superposition of rotation and throughflow, Lines of constant streamfunction in the meridional plane

2 Numerical simulations

The supercritical spherical gap flow is non-unique with respect to the number of Taylor vortices. These fact was shown experimentally for medium sized gaps by Sawatzki and Zierep [1] and studied in detail by Wimmer [2] and Bühler [7]. Numerical simulations of the supercritical flows are also done by different methods and described in the papers [3–5,7].

An initial value code, based on a finite difference method, is used to obtain rotationally symmetric solutions of the Navier–Stokes equations in terms of the streamfunction-vorticity formulation. The results for the closed spherical gap flows concerning non-uniqueness, symmetric and asymmetric transitions, symmetry behaviour with respect to the equator and existence ranges of the supercritical solutions. A comprehensive description is given in the review article [8].

Numerical solutions with superimposed mass flux are shown in Fig.4. We start with the four-vortex solution, which is symmetric with respect to the equator. Then the flow becomes asymmetric by superimposing a mass flux in meridional direction and the shape of the vortices changes into larger and smaller size, depending on the direction of rotation. A further increase of the throughflow changes the flow into a two vortex state by disappearing of two vortices. If the throughflow is increased further again, the vortices completely disappear and we find the asymmetric supercritical basic flow without any vortices.

A periodic oscillating mode of flow can be realized with other special conditions of the rotation and throughflow parameters. The flow structure during the oscillation is given in Fig.6 and shows the time-dependent variation between the asymmetric two-vortex and four-vortex state. The torque oscillates during the period as shown in Fig.7.The marked positions for the different times t correspond to the flow structures plotted in Fig.6. There is a significant influence of the number of vortices. A more stronger modulation during the oscillation period is shown on the maximum values of the streamfunction plotted in Fig.5. These result depends on the fact, that the vortex development in the lower hemisphere and the disappearance of vortices in the upper hemisphere occurs pairwise.

3 Experiments

The experiments are done to study the stability behaviour of the flow system by different measuring techniques and flow visualization. For closed spherical gap flows experimental results are described in the papers [1,2,9–12].

Figure 9 gives a overview of the flow structures in spherical gap flows with and without superimposed mass flux. Depending on the different initial and time- dependent boundary condition symmetric and asymmetric modes of flow can be realized. Some special flow structures are shown in Fig.9. Starting with the spherical Couette flow the three rotationally symmetric supercritical solutions are realized by different accelerations of the inner sphere from rest to a supercritical Reynolds number. These modes become asymmetric with respect

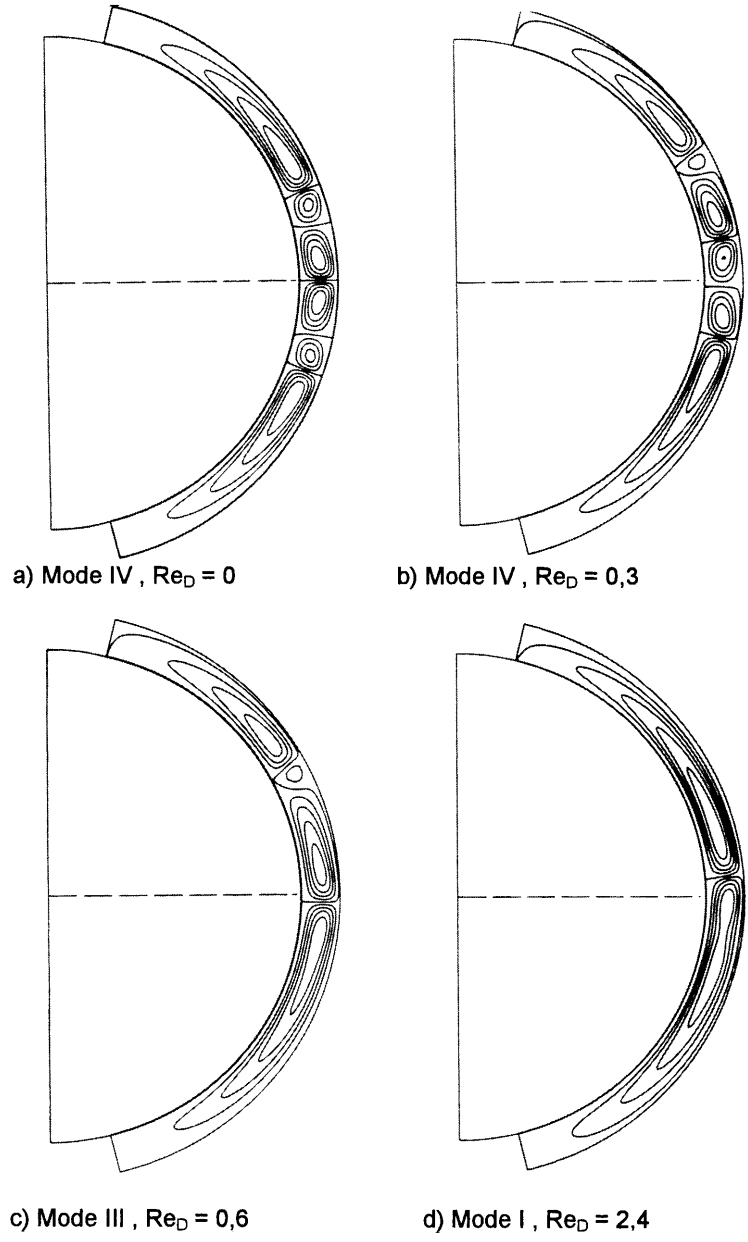

Fig. 5. From symmetric to asymmetric modes of flow by superimposed mass flux, gap width $\sigma = 0,154$, Reynolds number $Re = 2600$. From left to right and top to bottom: a) Mode IV, $Re_D = 0$, b) Mode IV, $Re_D = 0.3$, c) Mode III, $Re_D = 0.6$, d) Mode I, $Re_D = 2.4$

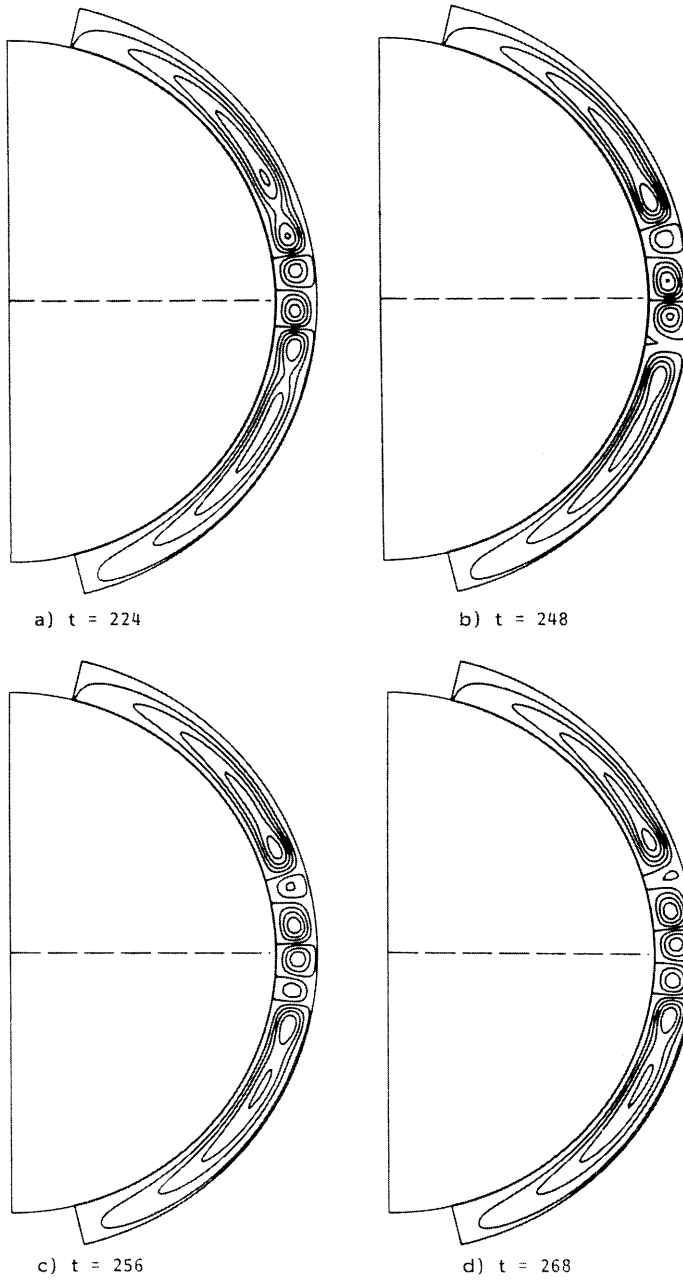

Fig. 6. Flow structure in the meridional plane during the periodic oscillation between the two-vortex and four-vortex mode, $Re = 1000$, $Re_D = 0,7$

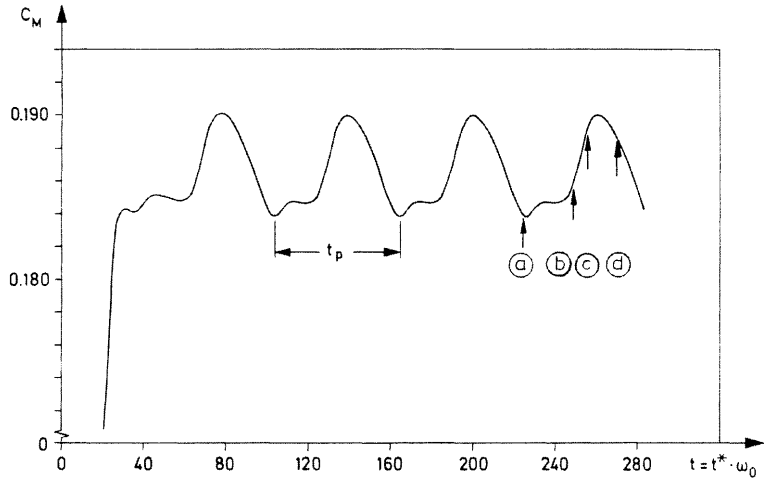

Fig. 7. time-dependent variation of the torque of the periodic solution, $Re = 1000$, time of one period $t_p = 60,8$

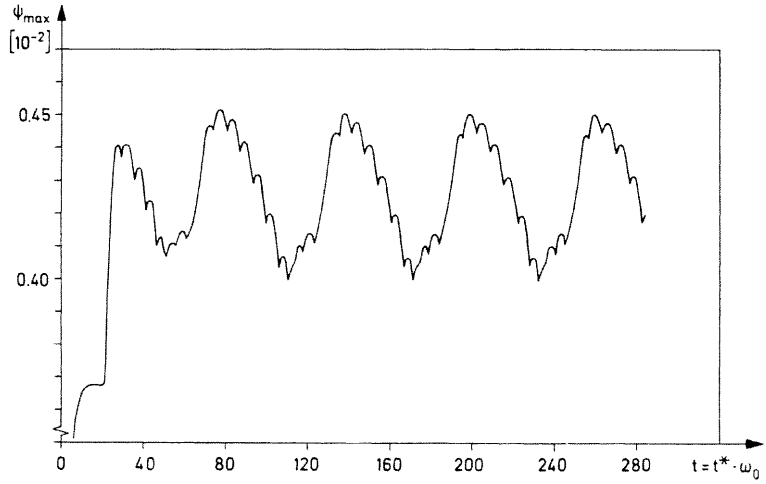

Fig. 8. Time-dependent variation of the maximum value of the streamfunction

to the equator by superimposing a mass flux in meridional direction. Transitions between these modes of flows are also realized.

Interesting steady and time-depending modes of flows occur with a spiral basic flow as initial condition as shown in the middle of Fig.9. A lower throughflow leads to the time-dependent vortices, which are rotationally symmetric with respect to the equator. Spiral vortices with discrete inclination angles occur at higher throughflow in steady or time-dependent form. The time-behaviour strongly depends on the values of the rotation and throughflow. An explanation

of the motion of spiral vortices in the direction of throughflow or in opposite direction is given in [13].

The pure source-sink flow becomes unstable with respect to Görtler vortices in meridional direction as shown in the lower part of Fig.9. The structure of these vortices is like banana-shaped. A superimposed throughflow changes the Görtler vortices significantly in the upper part of the gap in the direction of rotation. The diameter of the vortices changes in meridional direction.

Visualizations of three typical modes of flows are shown in Fig.6 on the left and the principal structure on the right. The Taylor vortices with superimposed mass flux in Fig.6a are shifted into the upper hemisphere in direction of throughflow. The flow structure is then typically asymmetric with respect to the equator.The torque decreases significantly with the asymmetry. With a further increase of the mass flux the vortices disappear and the supercritical basic flow without any vortices is established.

The spiral vortices in Fig.6b are non-axisymmetric and can be realized with different discrete inclination angles depending on the parameters of rotation and throughflow. A special combination of both parameters Re and Re_D leads to a steady state of the spiral vortex system. The neighboring solutions are time-dependent in a way, that the vortex system moves in the direction of throughflow with increasing Re_D and in opposite direction with decreasing Re_D while the rotation Reynolds number is held constant. An explanation for this interesting behaviour is given by Bühler and Polifke [13].

In the lower part of Fig.6 the instabilities of the pure source-sink flow are shown in form of Görtler vortices. The size of the banana-shaped structure of the vortices changes in longitudinal direction. The behaviour of these instability is strongly influenced by the fact, that the meridional flow is decelerated from the south-pole toward the equator in the lower hemisphere and accelerated from the equator toward the north-pole in the upper hemisphere.

The existence regions and transition boundaries are shown in the map of Fig.7 as function of the rotation rate given by the Taylor number and the mass flux described by the throughflow Reynolds number. For low Taylor number and throughflow Reynolds numbers the stable spiral basic flow occurs. In the upper left part of the map in Fig.7 the steady Taylor vortices occur. A superimposed mass flux leads to the transitions into the modes III and I with and without vortices. The ranges of the time-dependent ring vortices and for the steady spiral vortices with different inclination angles δ are also marked in the map of Fig.7. At low rotation rates and high throughflow is the region of the Görtler vortices. The dashed line marks a stability boundary, for which no theoretical results is known.

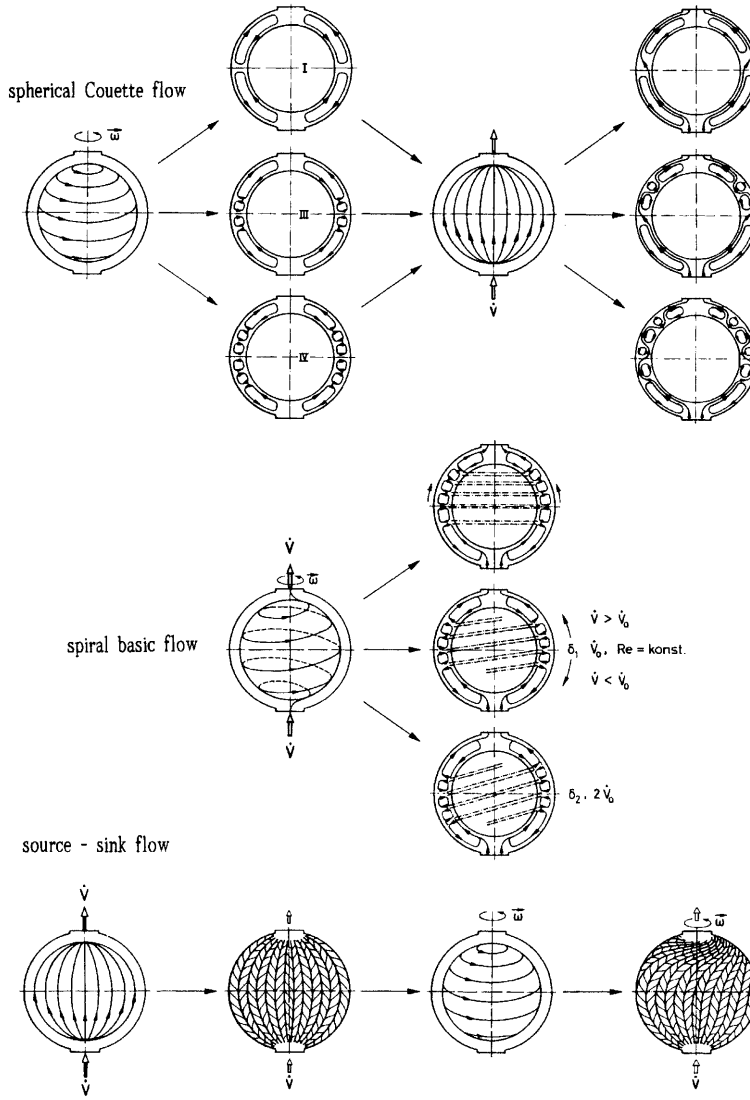

Fig. 9. Overview of possibilities of flow structures in spherical gaps with and without superimposed mass flux

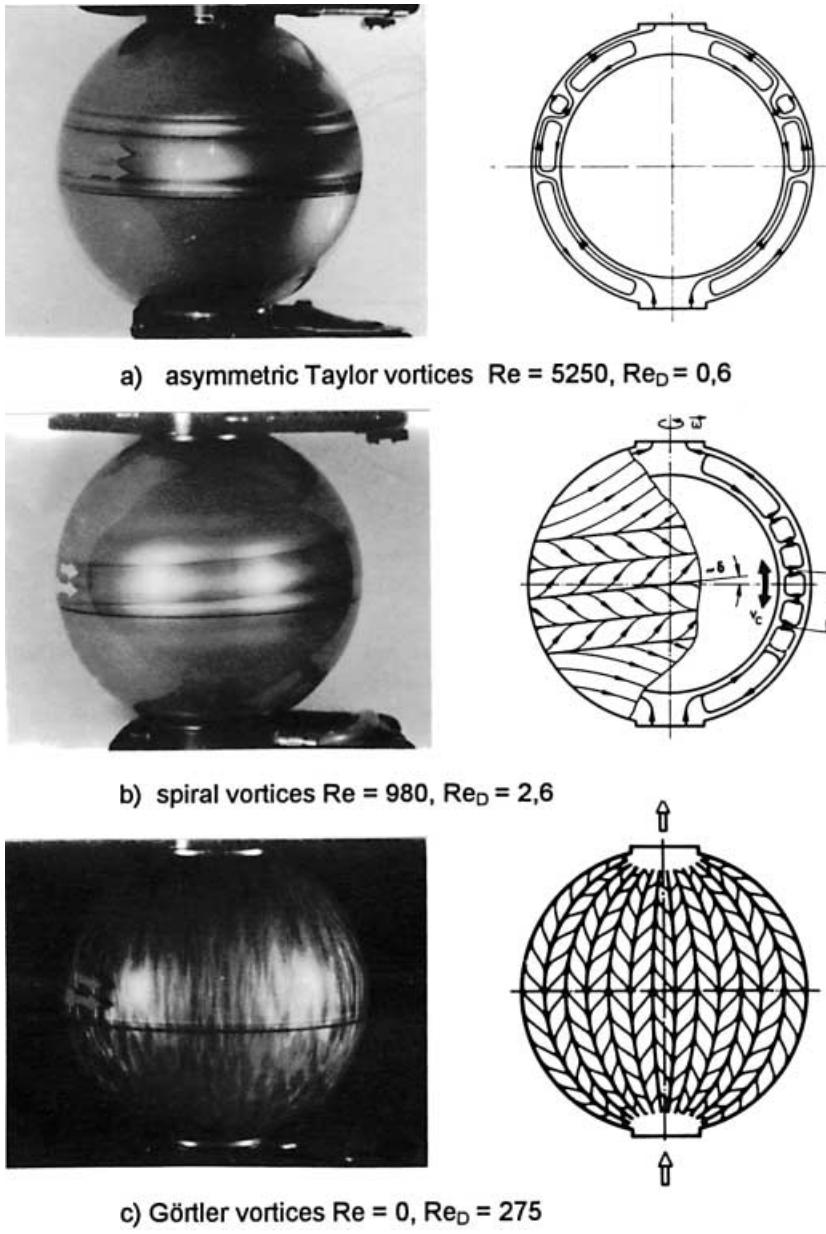

Fig. 10. Experimental realization of different types of vortices, visualized flow structure on the left and principal sketch on the right. From top to bottom: a) asymmetric Taylor vortices $Re = 5250$, $Re_D = 0,6$, b) spiral vortices $Re = 980$, $Re_D = 2,6$ c) Görtler vortices $Re = 0$, $Re_D = 275$

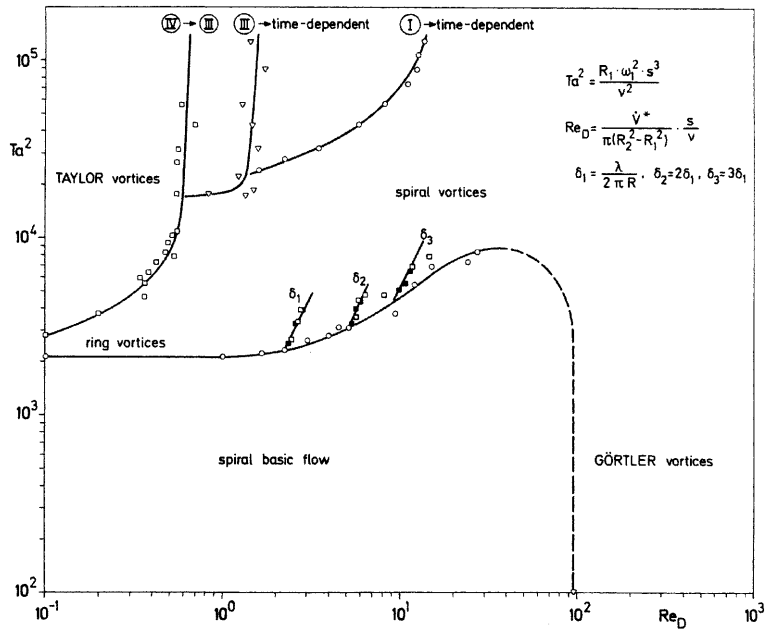

Fig. 11. Existence regions and transitions of supercritical modes of flow

4 Conclusion

The extension of the closed flow between two concentric rotating spheres into an open flow system with superimposed mass flux in meridional direction exhibits a rich number of novel flow structures. The results of the theoretical and experimental investigations show a good agreement within the limits of the used analytical and numerical methods. The results are of interest in practical applications of rotating flow systems.

References

1. O. Sawatzki, J. Zierep: Das Stromfeld im Spalt zwischen zwei konzentrischen Kugelflächen, von denen die innere rotiert. Acta Mechanica 9, pp.13-35 (1970)
2. M. Wimmer: Experiments on a viscous fluid flow between concentric rotating spheres, J. Fluid Mech. 78, pp. 317-335 (1976)
3. I.M. Yavorskaya, N.M. Astav'eva: Numerical analysis of the stability and non-uniqueness of spherical Couette flow. Notes on Num. Fluid Mech. 2, pp.305-315 (1980)
4. F. Bartels: Taylor vortices between two concentric rotating spheres. J.Fluid Mech. 119, pp.287-303 (1982)

5. P.S. Marcus, L. Tuckerman: Simulation of flow between concentric rotating spheres, Part 1 and Part 2, J. Fluid Mech. 185, pp. 1-65 (1987)
6. J. Zierep: Special solutions of the Navier–Stokes equations in the case of spherical geometry. Rev.Roum. Math.,TOME XXVII,3,pp.423-428 (1982)
7. K. Bühler: Strömungsmechanische Instabilitäten zäher Medien im Kugelspalt. Fortschritt-Ber. VDI, Reihe 7 Nr.96 Düsseldorf 1985
8. K. Bühler: Symmetric and asymmetric Taylor vortex flow in spherical gaps. Acta Mechanica 81, pp.3-38 (1990)
9. C. Egbers: Zur Stabilität der Strömung im konzentrischen Kugelspalt. Dissertation Universität Bremen (1994)
10. K. Bühler, J. Zierep: Dynamical instabilities and transition to turbulence in spherical gap flows. Advances in Turbulence,Ed.:G.Comte-Bellot and J.Mathieu,Springer Berlin pp.16-26 (1987)
11. C. Egbers, H.J. Rath: Routes to chaos in rotating fluid flows. Advances in Fluid Mechanics and Turbomachinery, Springer pp.147-168 (1998)
12. K. Nakabayashi: Transition of Taylor-Görtler vortex flow in spherical Couette flow. J. Fluid Mech. 132, pp.209-230 (1983)
13. K. Bühler, N. Polifke: Dynamical behaviour of Taylor vortices with superimposed axial flow. Proc. Nato-Workshop Streitberg, ed. Busse & Kramer,Plenum Press pp. 21-29 (1990)

Three-dimensional natural convection in a narrow spherical shell

Ming Liu and Christoph Egbers

Center of Applied Space Technology and Microgravity (ZARM),
University of Bremen, Am Fallturm, D-28359 Bremen

Abstract. The convective motions in a shallow fluid layer between two concentric spheres in the presence of a constant axial force field have been studied numerically. The aspect ratio of the fluid layer to inner radius is $\beta = 0.08$, the Prandtl number $Pr = 37.5$. A three-dimensional time-dependent numerical code is used to solve the governing equations in primitive variables. Convection in the spherical shell has then a highly three-dimensional nature. Characteristic flow patterns with a large number of banana-type cells, oriented in north-south direction and aligned in the azimuthal direction, are formed on the northern hemisphere, which grow gradually into the equatorial region accompanied by the generation of new cells as the Rayleigh number is increased. Various characteristics of these flows as well as their transient evolution are investigated for Rayleigh numbers up to 20 000.

1 Introduction

In this paper we consider thermal convection in the gap between two concentric spheres under the action of an axial force field downward from the north pole to the south pole, corresponding to experiments under terrestrial conditions. The inner sphere is heated homogeneously, while the outer sphere is maintained at a lower temperature. This problem is of some practical interest in engineering applications such as nuclear reactor design, thermal storage systems, and solar energy collectors.

Previous investigations on thermal convection in spherical shells have concentrated on central force fields due to its geophysical application (e.g. Chandrasekhar [4]; Busse [3]; Hart, Glatzmaier & Toomre [18]; Liu [25]; Schubert [36]). Natural convection in an axially stratified spherical fluid shell has been studied only sparsely. The problem was first investigated experimentally by Bishop, Mack & Scanlan [1] from the point of view of heat transfer with two isothermal concentric spheres of various diameter ratios filled with air. The natural convective heat transfer for other fluids (water and silicone oils) in spherical shells of medium aspect ratio was studied experimentally by Scanlan, Bishop & Powe [35], and a corresponding study of the flow patterns was performed by Yin et al. [40]. The problem was also studied by Powe, Warrington & Scanlan [32] by considering the natural convective flow between a body and its spherical enclosure. Linear stability of natural convection in narrow spherical annuli was analysed by Gardner, Douglass & Trogdon [12] using the basic flow expressed as a truncated power series in gap width. Pattern formation of convective motions

C. Egbers and G. Pfister (Eds.): LNP 549, pp. 269–294, 2000.

in a narrow spherical shell was studied experimentally by Nakagawa et al. [29]. Further experimental investigations on natural convection in different spherical shells have been carried out by Egbers [6].

The majority of theoretical investigations on natural convection in spherical shells under an axial force field has been carried out based on the assumption of axial symmetry of the flow, which is, as known from experiments (Bishop et al. [1]; Yin et al. [40]), valid for not too high Rayleigh numbers in moderate to large aspect ratios. For small Rayleigh numbers, Mack & Hardee [27] obtained analytical solutions by expanding the dependent variables in a power series with respect to the Rayleigh number. Numerical calculations have been performed for steady convection of a Boussinesq fluid enclosed between two concentric rotating spheres by Dallman & Douglass [5], for free-convection in a sphere by Geoola & Cornish [14], Fujii, Honda & Fujii [10] and Fujii, Takamatsu & Fujii [11], and recently by Garg [13] and Chu & Lee [2]. A three-dimensional numerical analysis of natural convection in a wide spherical shell but under non-symmetric thermal boundary conditions was presented by Ozoe et al. [30], in which however only one parameter was considered. For narrow gaps, where the convective flow becomes highly three-dimensional, theoretical investigation has not yet been made.

2 Mathematical formulation

We consider a viscous incompressible fluid in the gap between two concentric spheres. The inner and outer spheres with the radii R_i and R_o (gap width $d = R_o - R_i$) are maintained at different temperatures T_i and T_o ($< T_i$), respectively. A uniform gravitational acceleration is assumed to be present and parallel to the vertical axis $\mathbf{e}_z$ as $\mathbf{g} = -g_0\mathbf{e}_z$. The fluid is assumed to follow the Oberbeck–Boussinesq approximation.

The mathematical formulation of the problem uses spherical coordinates (r, θ, ϕ). The equations governing the three-dimensional unsteady flow and temperature field in the spherical shell are the continuity equation, the Navier–Stokes equations and the energy equation:

$$\nabla \cdot \mathbf{v} = 0, \tag{1}$$

$$\frac{\partial \mathbf{v}}{\partial t} + (\mathbf{v} \cdot \nabla)\,\mathbf{v} = -\nabla p + Ra\,Pr T\,\mathbf{e}_z + Pr\nabla^2\mathbf{v}, \tag{2}$$

$$\frac{\partial T}{\partial t} + (\mathbf{v} \cdot \nabla)\,T = \nabla^2 T, \tag{3}$$

where $\mathbf{e}_z = (\cos\theta\mathbf{e}_r - \sin\theta\mathbf{e}_\theta)$ and $\mathbf{v} = (v_r, v_\theta, v_\phi)$. In these equations, all variables are non-dimensionalised by using scales d for length, d^2/κ for time, κ/d for velocity, $\rho_0\kappa^2/d^2$ for pressure and $\Delta T = T_i - T_o$ for temperature, where ρ_0 is the reference density and κ the thermal diffusivity of the fluid. The natural convection in the spherical shell is then characterised by the following dimensionless

parameters:

$$\text{Rayleigh number:} \qquad Ra = \frac{g_0\,\gamma\,d^3\,\Delta T}{\kappa\nu}, \tag{4}$$

$$\text{Prandtl number:} \qquad Pr = \frac{\nu}{\kappa}, \tag{5}$$

$$\text{aspect ratio:} \qquad \beta = \frac{d}{R_i}, \tag{6}$$

where γ is the thermal expansion coefficient and ν the kinematic viscosity of the fluid.

As initial conditions, a quiescent state with a homogenous temperature field was applied for all calculations presented in this paper, viz.

$$\mathbf{v} = 0, \quad T = 0 \quad \text{at} \quad t = 0. \tag{7}$$

The boundary conditions are no-slip rigid boundaries on both spherical surfaces and free-slip conditions on the vertical axis z. Furthermore, for numerical calculations, the spherical shell is cut at the longitude $\phi = 0$, where periodic boundary conditions are applied. In summary these are

$$\mathbf{v} = 0, \quad T = 1 \qquad \text{at} \quad r = 1/\beta, \tag{8}$$

$$\mathbf{v} = 0, \quad T = 0 \qquad \text{at} \quad r = 1 + 1/\beta, \tag{9}$$

$$\partial\mathbf{v}/\partial\theta = 0, \quad \partial T/\partial\theta = 0 \qquad \text{at} \quad \theta = 0, \pi, \tag{10}$$

$$\mathbf{v}_{(\phi=0)} = \mathbf{v}_{(\phi=2\pi)}, \quad T_{(\phi=0)} = T_{(\phi=2\pi)} \qquad \text{at} \quad \phi = 0, 2\pi. \tag{11}$$

With our numerical calculations, some advanced diagnostic studies have been made. The efficiency of the heat transfer due to convection can be measured by the Nusselt number, which is the ratio of total heat flux in the presence of convection to that in the conductive state. In the pure conductive state the radial distribution of the spherically symmetric temperature field can be found from the energy equation:

$$T(r) = \frac{R_i}{d}\left(\frac{R_o}{r} - 1\right). \tag{12}$$

The Nusselt numbers at the inner and outer spheres are then defined by:

$$Nu_i = \frac{-1}{4\pi\,(1+\beta)} \int_0^{2\pi}\int_0^{\pi} \left(\frac{\partial T}{\partial r}\right)_{r=R_i} \sin\theta\,\mathrm{d}\theta\,\mathrm{d}\phi, \tag{13}$$

$$Nu_o = \frac{-\,(1+\beta)}{4\pi} \int_0^{2\pi}\int_0^{\pi} \left(\frac{\partial T}{\partial r}\right)_{r=R_o} \sin\theta\,\mathrm{d}\theta\,\mathrm{d}\phi. \tag{14}$$

In the steady state, the total heat is conserved and these two Nusselt numbers must be equal. Because of the numerical approximations, this condition is not necessarily fulfilled. A comparison of these values provides a quantitative measure of the accuracy of a solution.

The azimuthally averaged heat fluxes at the inner and outer spheres are

$$H_{i,o} = -\left(\frac{\partial \langle T \rangle_\phi}{\partial r}\right)_{r=R_i,R_o}, \tag{15}$$

where the bracket with the subscript ϕ defines the average over longitude.

The kinetic energy and temperature (entropy) variance are

$$E_v = \frac{1}{2V}\int_0^{2\pi}\int_0^{\pi}\int_{1/\beta}^{1+1/\beta} \mathbf{v}^2\, r^2 \sin\theta \,\mathrm{d}r\,\mathrm{d}\theta\,\mathrm{d}\phi, \tag{16}$$

$$E_T = \frac{1}{2V}\int_0^{2\pi}\int_0^{\pi}\int_{1/\beta}^{1+1/\beta} T^2\, r^2 \sin\theta \,\mathrm{d}r\,\mathrm{d}\theta\,\mathrm{d}\phi, \tag{17}$$

with $V = \frac{4}{3}\pi\left[(1+1/\beta)^3 - (1/\beta)^3\right]$ standing for the volume of the fluid shell.

For some diagnostic studies, the three-dimensional modes obtained numerically are decomposed into an azimuthally averaged (axisymmetric) and a ϕ-dependent (non-axisymmetric) part:

$$\mathbf{v} = \bar{\mathbf{v}} + \tilde{\mathbf{v}}, \tag{18}$$

$$T = \bar{T} + \tilde{T}. \tag{19}$$

In this way, the total kinetic energy and temperature variance can be divided into axisymmetric and non-axisymmetric parts by replacing $\mathbf{v}$ and T in Eqs. (16)-(17) correspondingly. For the non-axisymmetric flow the kinetic energy balance is given by

$$\begin{aligned}\frac{\partial}{\partial t}\tilde{E}_v = {} & RaPr\left\langle \cos\theta\, \tilde{v}_r \tilde{T}\right\rangle - RaPr\left\langle \sin\theta\, \tilde{v}_\theta \tilde{T}\right\rangle \\ & - \left\langle \tilde{v}_r^2 \frac{\partial \bar{v}_r}{\partial r} + \frac{\tilde{v}_\theta^2}{r}\frac{\partial \bar{v}_\theta}{\partial \theta} + \tilde{v}_r\tilde{v}_\theta\left(\frac{1}{r}\frac{\partial \bar{v}_r}{\partial \theta} + \frac{\partial \bar{v}_\theta}{\partial r}\right)\right\rangle - Pr\Phi,\end{aligned} \tag{20}$$

with the angle brackets indicating the average over the spherical fluid shell. On the right hand side, the first two terms are the work done by the radial and latitudinal buoyancy forces, respectively. The third term is the nonlinear transfer of energy from the axisymmetric flow to the non-axisymmetric perturbations. The last term is the viscous dissipation by friction. For later reference, we denote these four terms as $\tilde{E}_r$, $\tilde{E}_\theta$, $\tilde{E}_n$, $\tilde{E}_\nu$, respectively. Further, we define $\tilde{E}^* = \tilde{E}_r + \tilde{E}_\theta + \tilde{E}_n$. Note that the curvature terms appearing in the momentum equations do not contribute to the total kinetic energy.

For solving the partial differential Eqs. (1)–(3) in primitive variables (v_r, v_θ, v_ϕ, p, T) associated with the initial and boundary conditions given above, a numerical code based on finite-difference techniques has been developed. Briefly, the continuity equation at each time step is satisfied through the solution of a Poisson equation for the pressure. The momentum equations are split by using the projection technique and fractional-step procedure, which is also applied to the energy equation. These equations are expressed in finite-difference form on a staggered grid. The scheme used is essentially implicit.

3 Results and discussion

In the numerical investigation to be discussed in the following we used the aspect ratio $\beta = 0.08$, although computations with other aspect ratios ($\beta = 0.18$, 0.25, 0.33, 0.5) have been carried out too. The Prandtl number of the fluid was set at $Pr = 37.5$, corresponding to a silicone oil of medium viscosity. These parameters were chosen in connection with the experiments of Egbers [6]. For all calculations presented here, a uniform staggered grid of $25(r) \times 151(\theta) \times 180(\phi)$ points was used for the whole domain of the spherical shell, and a dimensionless time step of 10^{-5} was chosen. The Rayleigh number ranged from 1500 to 20 000.

3.1 Axisymmetric basic flow

Different from the situation with a central gravity field, the flow in a spherical shell under an axial force field cannot be in equilibrium for non-zero temperature difference between both spheres. By heating the inner sphere, the fluid near the inner sphere becomes lighter and moves upward along the inner sphere. The continuity condition imposes the fluid to move downward along the outer sphere. In this way, an axisymmetric single vortex of crescent shape is formed as the basic flow in spherical shells under an axial force field. Generally speaking, the nonlinear equations must be solved to find a steady solution of the system.

For small Rayleigh numbers, Mack & Hardee [27] analysed the problem by using a perturbation expansion of the dependent variables in terms of power series of the Rayleigh number. The solutions up to the third power of Ra for steady axisymmetric convection were considered. In the first approximation for the creeping-flow, applicable in the limit of infinitesimal Rayleigh number, the conductive isotherms are concentric circles and the vortex centre is at $\theta = 90°$, i.e.the vortex is symmetric to the equatorial plane. The higher order approximation improves the solution for larger Rayleigh numbers with the centre of the crescent-vortex shifted northward. Their reliability analysis showed that steady axisymmetric solutions are valid from about $Ra = 9300$ to 2200 as the aspect ratio increases from $\beta = 0.15$ to 2. No comment was made for smaller gaps. For comparison, we have solved the problem analytically following the way of Mack & Hardee, but with the help of a symbolic solver (Maple V).

From our numerical simulation for $\beta = 0.08$, it has been found that the convective flow remains axisymmetric up to $Ra = 1500$, and becomes slightly three-dimensional at the computed next higher Rayleigh number $Ra = 2000$. The velocity vector field and the temperature field at a meridional cross-section is shown in Fig. 1 for $Ra = 1500$. For comparison, streamlines obtained from the analytical solution have been also included. Good agreement between the numerical and analytical solutions at this Rayleigh number is achieved. The velocity field indicating an elongated crescent-type vortex is essentially symmetric with respect to the equatorial plane. From the maximum values of the three velocity components, the meridional flow is characterised by strong latitudinal motions along both spheres. The radial velocity component is almost two orders smaller than the latitudinal component. The very weak azimuthal component, although

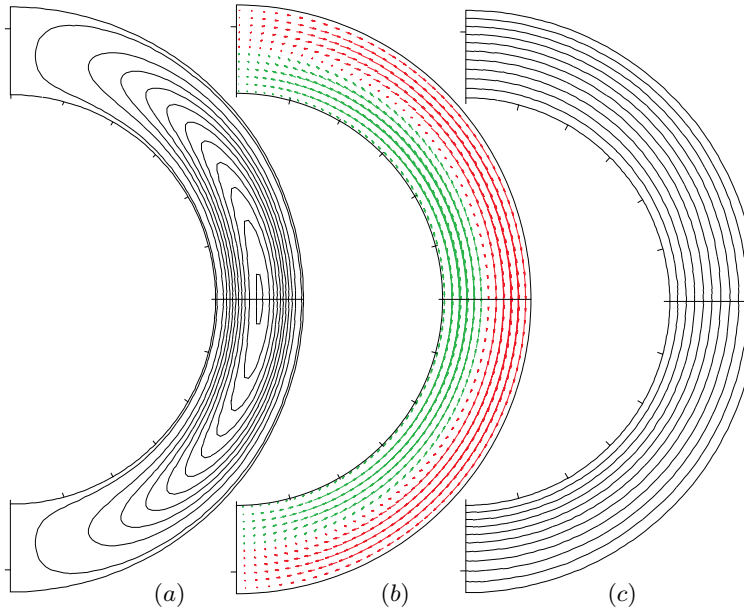

Fig. 1. Axisymmetric basic flow for $\beta = 0.08$, $Ra = 1500$: a) Contour lines of stream function (the maximum stream function is 50.57) from the analytical solution up to third order approximation; b) Meridional velocity field (the maximum values of the velocity components are $v_{r\max} = 0.6107$ and $v_{\theta\max} = 11.64$) and c) isotherms from the numerical solution. For clarity, the velocity vectors are drawn on each second node, and the gaps are exaggerated in the radial direction, the real aspect ratio of $\beta = 0.08$ is indicated by two bars on the left side of vertical axis. This convention will also be used in the following cross-section graphics.

not equal to zero, represents a negligible disturbance. In the temperature field a minor shift of the essentially concentric isotherms in the vicinity of both poles along the meridional flow can be seen.

3.2 Three-dimensional convective motions

For Rayleigh numbers $Ra \geq 2000$ convection in a spherical shell under an axial force field becomes three-dimensional for $\beta = 0.08$. This is consistent with the fact that the onset of the classical Rayleigh-Bénard convection in a horizontal layer heated from below is at $Ra_c \approx 1708$, and for $Ra > Ra_c$ the flow often becomes three-dimensional. In general, the characteristics of the flow patterns are broadly similar with increasing Rayleigh number. The convection concentrates more and more in the northern hemisphere, where new secondary vortices will be generated, while in the southern hemisphere, the axisymmetric basic vortex remains essentially unchanged due to the stable stratification.

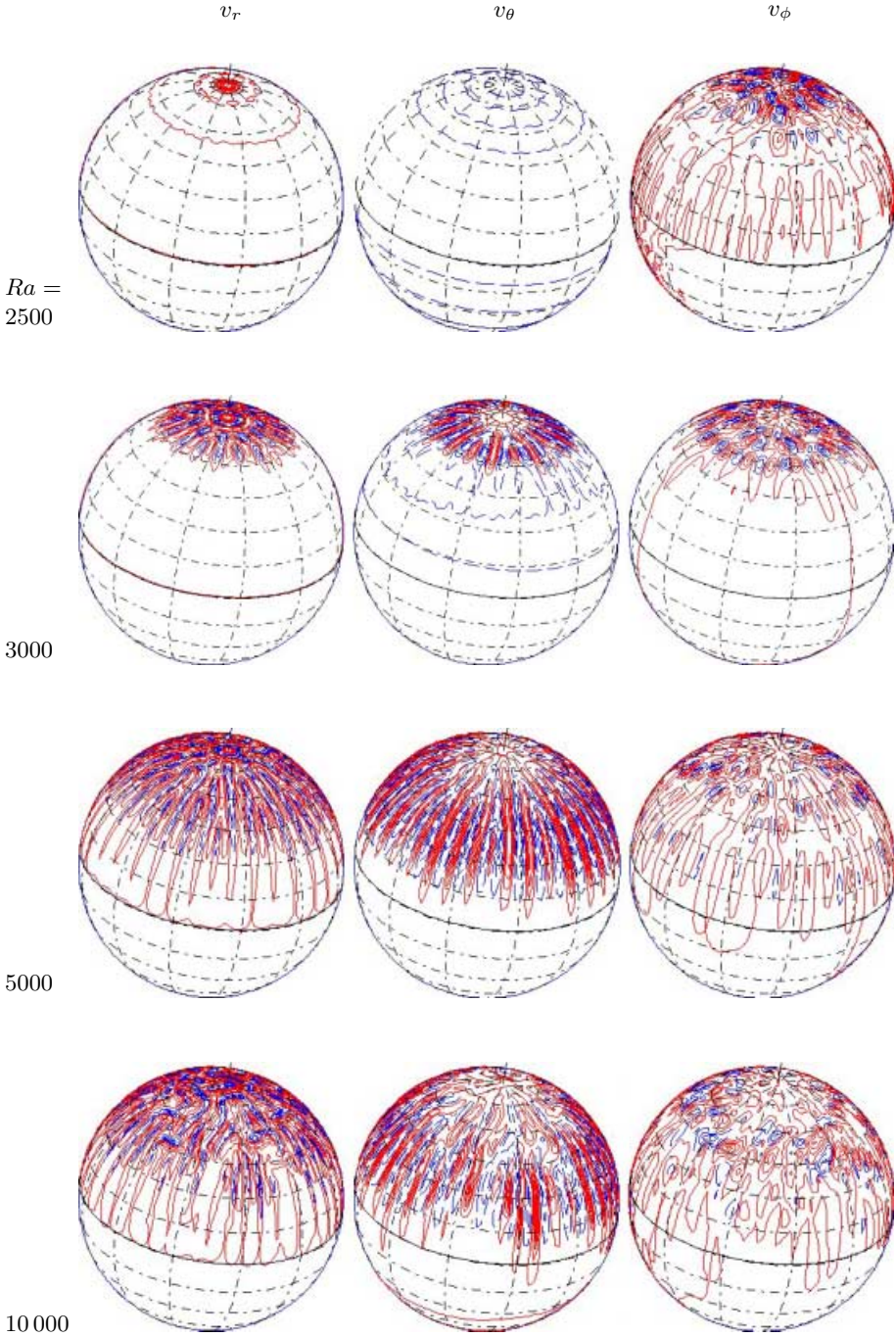

Fig. 2. For caption see next page.

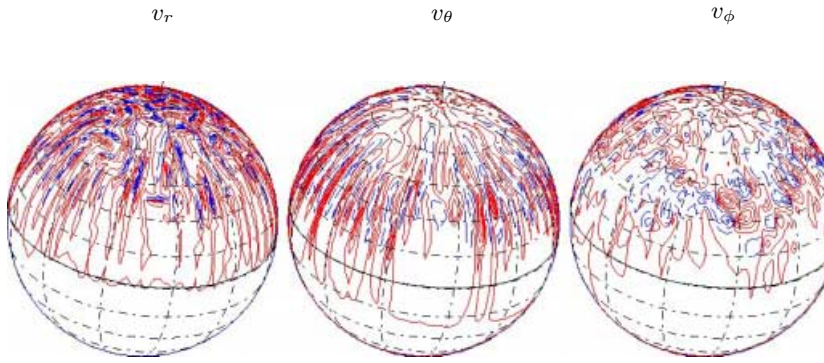

Fig. 2. Three-dimensional perspectives of the flow pattern in the form of contour lines of the radial (v_r), latitudinal (v_θ) and azimuthal (v_ϕ) velocity component on a spherical surface midway through the shell at the different Rayleigh numbers indicated. The contour lines are normalised by the absolute maximum value of the component on the relevant spherical surface (not in the whole spherical shell) given below. The solid lines correspond to positive values and the dotted lines to negative values. The sphere is mapped by dash-dot lines, with 30° interval in longitude and 15° in latitude (the equator is indicated by the solid line). The north pole is additionally depicted by an outward axis.

Patterns of convection Figure 2 shows several typical configurations of such convective cells at different Rayleigh numbers at $t = 1$ (the unit thermal diffusion time from the inner to outer sphere). The contour lines of the three velocity components are drawn on a spherical surface midway through the shell (i.e.$(r - R_i)/d \approx 1/2$). Due to the staggered grid arrangement the actual radial level is displaced by a half grid between the radial velocity component and the other two components. The main feature emerging from these plots is the formation of banana-type cells in the northern hemisphere. It is interesting that at first glance the flow patterns shown by the three velocity components are not well related to each other. The banana-cells are most pronounced in the latitudinal velocity component v_θ. In the radial velocity component v_r the cell structure is additionally characterised by new branches in the direction to the equator. The contour lines of the azimuthal velocity component v_ϕ display a rather irregular three-dimensional structure. However, a close examination reveals that a good correlation between patterns shown by the three velocity components can be recognised. The solid contour lines of the radial velocity component correspond essentially to the dashed lines of the latitudinal velocity (i.e.the radial outflow is accompanied by a latitudinal upward flow) and vice versa, and the small vortices shown in the azimuthal velocity are located in the vicinity of both ends of banana-cells. The temperature field corresponds essentially to the radial velocity, and is therefore not shown here separately.

At $Ra = 2000$, the flow is still essentially axisymmetric, although the azimuthal component, which is two to three orders smaller than the other two

components, already shows small vortices in the northern hemisphere. A weak disturbance can be seen in the radial component at $\theta \approx 35°$, where the contour line becomes wavy. The velocity vector field and the temperature field on the meridional plane are similar to those for $Ra = 1500$ in Fig. 1. At the computed next Rayleigh number $Ra = 2500$, no essential change in the latitudinal and the azimuthal velocity component can be recognised, but the radial component shows a concentration of (axisymmetric) contour lines close to the north pole and a weak disturbance outside develops to a visible grain-like structure. It can be seen from the meridional velocity vectors (not shown here) that a small vortex (pinching) adjacent to the north pole is formed. This axisymmetric secondary vortex will be referred to as the ring vortex. Its formation can be explained as follows. At the north pole the vertical temperature gradient is in a first approximation uniform, with a small latitudinal gradient. According to the standard Rayleigh-Bénard problem, convection should set in at the pole, where $\mathrm{d}T/\mathrm{d}z$ is largest, when the critical temperature gradient is reached. Convection should then be axisymmetric and have the form of circular rolls as shown by Koschmieder [22], see also the discussion in §4.4.

As the Rayleigh number is increased to 3000, a dramatic transformation of the flow pattern to a three-dimensional structure occurs. A pair of ring vortices is formed around the north pole, and outside the rings a flame-like pattern arises in the radial velocity component. The contour lines of the latitudinal velocity, on the other hand, display a pattern with banana-like cells. The cells have different length and are, although accompanied by some defects, well ordered in the azimuthal direction. The azimuthal velocity component grows in strength with increasing Rayleigh number and becomes comparable to the other two components as the banana-cells are formed.

With increasing Rayleigh number, the banana-cells grow in the direction to the equator, and simultaneously, new cells are generated through branches (the branches are displayed by dashed lines in the latitudinal component, which are, in these plots, not so apparent as the solid lines in the radial component). By increasing the Rayleigh number up to 5000, the banana-cells approach quickly the equator. After that the growth rate decreases. This is obviously due to the stable stratification in the lower hemisphere, which stops the further growth of the cells into the southern hemisphere. In fact, the three-dimensional structure of the radial velocity component does not exceed the equatorial plane. The ring vortices around the north pole are gradually disturbed by banana-cells and disappear at $Ra \geq 10^4$. With the disappearance of the ring vortices, the flow pattern in the neighbourhood of the north pole becomes less ordered, the banana-cells in the front region close to the equator are accompanied by increasing defects and the contour lines of the radial velocity component behind the banana-cells ($\theta < 45°$) display some azimuthally oriented structures.

In Tab. 1 the number of cells and their latitudinal position at different Rayleigh numbers are listed (the data are to some extent subjective, as the cells are not always distributed regularly in the azimuthal direction, especially at high Rayleigh numbers). The dependence of the number of banana-cells on the

Table 1. Number of cells and their latitudinal position at different Rayleigh numbers, and ratios of the circumference to the gap width with respect to the inner (σ_i) and outer sphere (σ_o)

Ra	3000	4000	5000	8000	10 000	15 000
Number of cells (n)	32	58	68	80	80	∼80
Lat. expansion of cells (deg.)	10–30	20–65	30–75	40–80	45–85	45–90
Latitudinal angle θ (deg.)	15	30	45	60	75	90
$\sigma_i = 2\pi R_i \sin\theta/d$	20.32	39.26	55.53	68.01	75.86	78.53
$\sigma_o = 2\pi R_o \sin\theta/d$	21.95	42.41	59.97	73.45	81.93	84.82

Rayleigh number can be explained as follows. In the slightly supercritical state, the cells tend to have a unit size in radius and azimuth. When the banana-cells are located near the north pole, the short circumference ($2\pi r \sin\theta$) can therefore contain only small numbers of cells. As the cells grow to the equator with increasing Rayleigh number, more cells have to be branched to fit the larger circumferential length. For comparison, the ratios of the circumference (relating to the inner and outer sphere) to the gap width are also given in Tab. 1 for several latitudinal positions. A good correlation between the cell number and the circumferential length can be found.

In order to reveal features at different radial levels, Fig. 3 shows contour lines at two other radii for $Ra = 5000$, the one near the inner sphere by $(r - R_i)/d = 1/4$ and the other one near the outer sphere by $(r - R_i)/d = 3/4$. Compared to those in Fig. 2 for the mid-plane, most changes of the flow structure with regard to the radial position can be seen from the latitudinal velocity component. Near the inner sphere, the flow is dominated by an upward movement, as shown by dense dotted contour lines, while the dense solid contour lines near the outer sphere indicate the main flow downward along the outer sphere. Furthermore, the contour line of the azimuthal velocity component near both spheres display a more banana-cell like structure, whereas they are rather irregular in the mid-plane. The pattern of the radial velocity component remains essentially unchanged.

In order to see the inner structure of the global three-dimensional flow patterns described above, velocity vector fields of the radial and latitudinal components at six (longitudinally equidistant) meridional cross-sections in the region $0° \leq \theta \leq 20°$ for $Ra = 5000$ are plotted in Fig. 4. As can be seen from the contour plots in Fig. 2, this azimuthal portion involves about 4 banana-cells with different length and is characteristic for the whole spherical shell. It should be realised that for three-dimensional flows one can not draw streamlines on a meridional plane as in the axisymmetric case, and the vector fields show in some cases a very curious fluid motion.

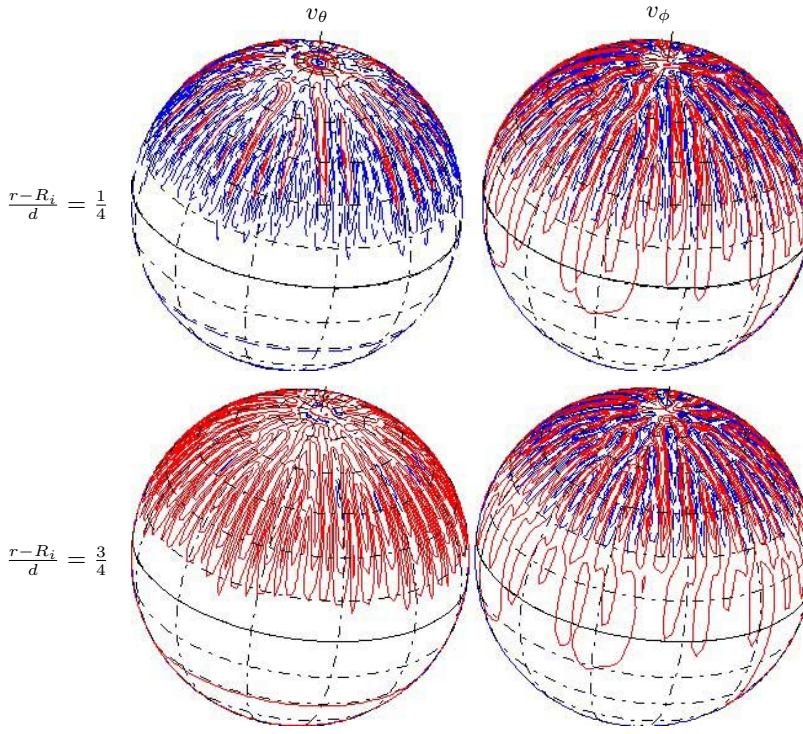

Fig. 3. Flow patterns seen at two different radial levels at $Ra = 5000$. Conventions as in Fig. 2.

It is obvious that the fluid in the northern hemisphere up to about $\theta = 75°$ is convecting in a very vigorous fashion. Near the north pole, two small vortices can be seen in all plots, although they are not axisymmetric. The majority of the gap is filled by the basic vortex extending to the south pole, where the flow remains essentially axisymmetric for $\theta \geq 75°$. In the region of about $10° \leq \theta \leq 30°$ (near the north pole), various vortices are generated. Compared with the contours in Fig. 2, it can be seen that in the region (about $30° \leq \theta \leq 75°$), where most banana-cells are visible, the meridional flow essentially represents an extension of the basic vortex with the fluid moving upward near the inner sphere and downward near the outer sphere. However, the boundary of these two flow streams (as depicted in the vector plots by the light line lying approximately in the middle of the gap at the equator) does not remain at a fixed radius, but changes very quickly from plane to plane.

Another aspect of the flow patterns is shown in Fig. 5, where velocity vector fields of the radial and azimuthal components on the azimuthal cross-section at two latitudinal angles within the northern hemisphere for $Ra = 5000$ are presented. It can be seen that the velocity fields vary also very dramatically in the latitudinal direction. In the banana-cells there also exist azimuthal circulations.

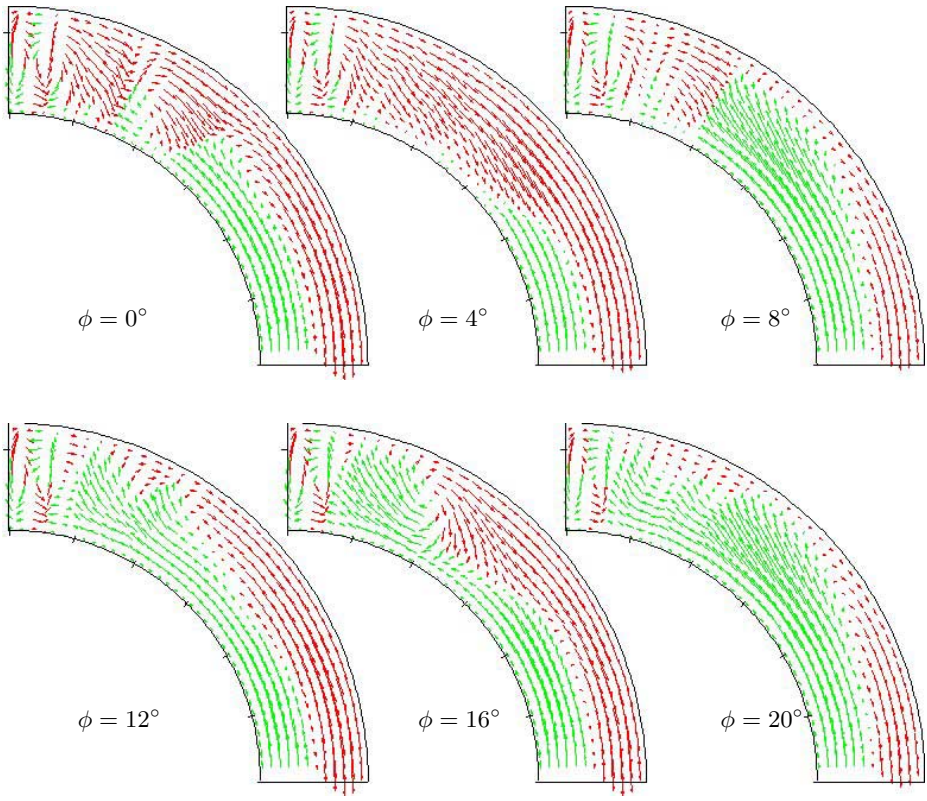

Fig. 4. Velocity vectors on the meridional cross-section (r, θ) at different azimuthal angles (ϕ) for $Ra = 5000$, c.f.Fig. 2. The southern spherical shell is cut off as the flow there is essentially the axisymmetric basic flow as shown in Fig. 1.

Near the north pole at $\theta = 15°$, 10 pairs of vortices are well ordered in the azimuthal direction corresponding to the 10 long banana-cells formed there (see Fig. 2). Note that for this latitudinal position, the circumference is almost equally enlarged as the gap width, and therefore, the vortices appear in a nearly unit size. With increasing latitudinal angle, the enlargement of the circumference decreases, and the vortices are stretched more in the radial direction.

From the above examination, we have learned that, with increasing Rayleigh number, the convective flow in a narrow spherical shell of $\beta = 0.08$ becomes three-dimensional in form of banana-type cells aligned in the direction of the basic vortex flow. The dominant motion in the banana-cells is still of basic character, i.e.upward near the inner sphere and downward near the outer sphere, but the boundary of the two streams changes in the azimuthal direction, which gives the main impression of the banana-cells. Within the banana-cells also radial and azimuthal circulations take place. It is clear that there is no closed

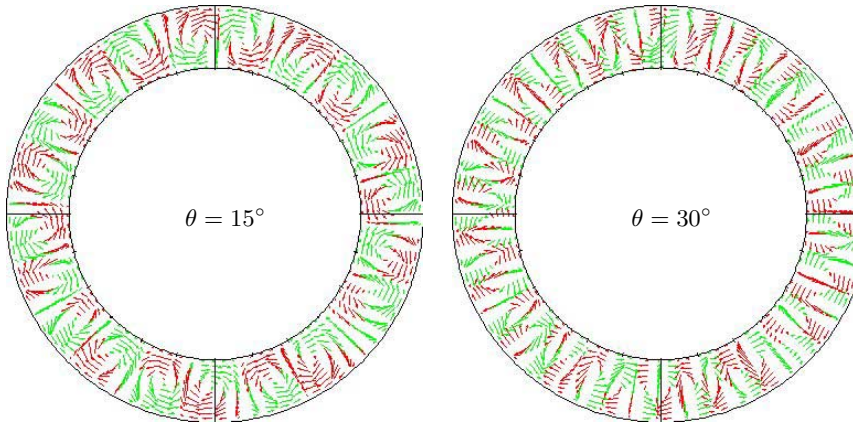

Fig. 5. Velocity vectors on the azimuthal cross-section (r, ϕ) at two latitudinal angles (θ) for $Ra = 5000$, c.f.Fig. 2. Note that the gaps between inner and outer sphere are enlarged uniformly in the radial direction as in Fig. 1, but non-uniformly in the azimuthal direction for different latitudes.

circulation between the north pole and the equator, as it might be derived from the experimental observation of Nakagawa et al. [29].

Heat transport As mentioned before, the isotherms on a spherical surface correspond essentially to the contour lines of the radial velocity component, as shown in Fig. 2. The vertical structure of temperature fields are shown in Fig. 6 where azimuthally-averaged temperature profiles for various Ra at different latitudinal positions (θ) are displayed. The characteristics are wholly different between the northern and southern hemisphere. As the Rayleigh number increases, a large central portion of the shell in the northern hemisphere becomes more stably stratified as the boundary layers narrow. The profile in the southern hemisphere is however continuously shifted downward with increasing Ra. An increasing portion of the fluid near the outer sphere approaches the temperature of the outer sphere and the temperature gradient between both spheres is essentially established within the boundary layer near the inner sphere. The temperature drop there is comparable with that in the northern inner boundary layer. We note that on average the thermal boundary layers are resolved by at least five grid points.

Figure 7 shows azimuthally-averaged heat flux profiles for various Ra on the outer and inner sphere. The curves near the north pole at low Rayleigh numbers (e.g. $Ra = 3000$ and 5000) are characterized by a wavy form indicating an axisymmetric radial flow occurred there (c.f. Fig. 2). This characteristic disappears as the Rayleigh number is increased. On the inner sphere convection contributes

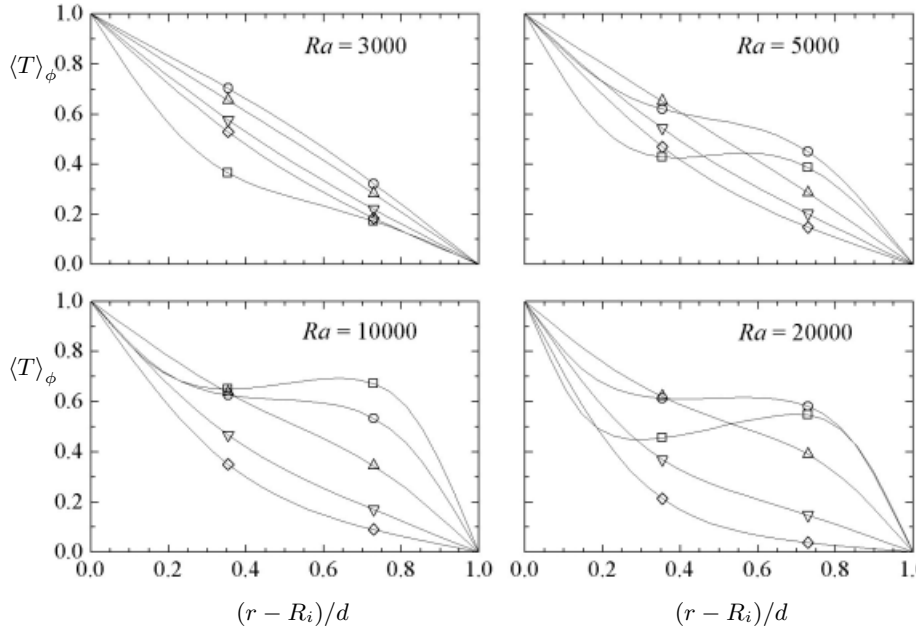

Fig. 6. Azimuthally-averaged radial temperature profiles at different latitudinal positions $\theta = 6^\circ$ (□), 36° (○), 72° (△), 126° (▽), 180° (◇) for $Ra = 3000$, 5000, 10 000 and 20 000.

to an overall increase of the heat flux ($H_i > 1$ everywhere) with the regime around $\theta = 75^\circ$ remaining nearly conductive. On the outer sphere, however, the heat is mainly transferred within the northern hemisphere, while the southern hemisphere is in the conductive state ($H_T < 1$). This is consistent with the characteristics of the radial temperature profile discussed before. It is also reasonable that the heat flux rate on the northern outer hemisphere is higher than that on the inner sphere.

For the global characteristics of the heat flow, the dependence of the averaged Nusselt number $Nu = (Nu_i + Nu_o)/2$, and its deviation between both spheres $\Delta Nu = |Nu_i - Nu_o|/Nu$, upon the Rayleigh number is shown in Fig. 8. The analytical solution for small Rayleigh numbers is also included, which to second-order approximation is given by

$$Nu = 1.0 + 0.21491346 \times 10^{-8} Ra^2. \tag{21}$$

(We note that the third order approximation of the temperature field does not contribute to the total heat transfer). We see that the computed results at small Rayleigh numbers are consistent with the analytical solutions, as long as the flow remains axisymmetric (i.e.$Ra < 2000$). When the flow becomes three-dimensional, however, the curvature of Nu vs. Ra changes from concave to convex. It can be seen that the banana-cells are significantly more efficient

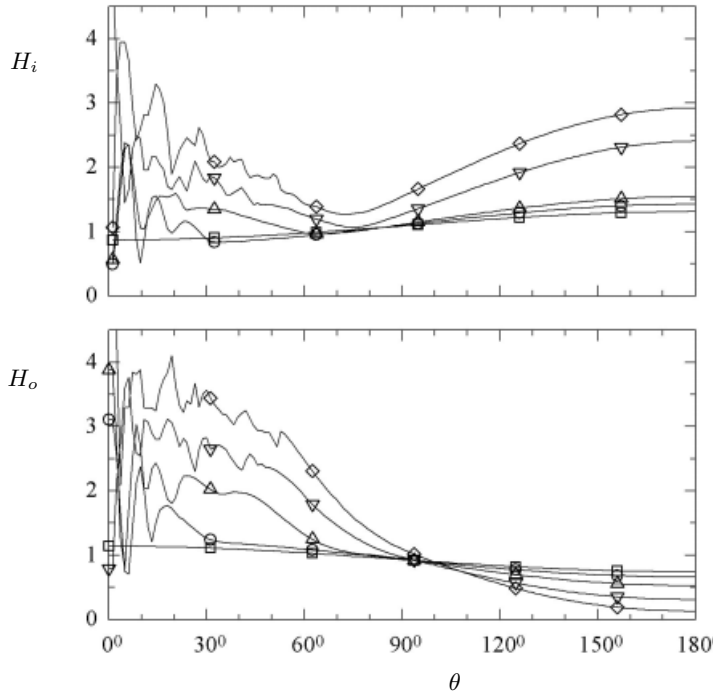

Fig. 7. Azimuthally-averaged heat flux profiles on the inner (H_i) and outer (H_o) surface as a function of the latitudinal angle for $Ra = 2000$ (□), 3000 (○), 5000 (△), 10 000 (▽) and 20 000 (◇).

in enhancing heat transfer than the axisymmetric basic vortex. In the range of $Ra = 3000$–$20\,000$ the curve can be well fitted by

$$Nu = 0.135\, Ra^{0.256}, \tag{22}$$

as indicated in Fig. 8. The exponent in Eq. (22) lies well within the experimental estimates of Bishop et al. [1] and Scanlan et al. [35]. With air in (wide) spherical shells, Bishop et al.established an overall relationship of $Nu \sim Ra^{0.276}$. For various fluids with different Prandtl numbers, an overall relationship of $Nu \sim Ra^{0.226}$ is given by Scanlan et al.(this was said to be valid for $0.09 < \beta < 1.81$).

The deviation of the Nusselt number obtained on both spheres ΔNu increases quickly as the flow becomes three-dimensional. This indicates a growing numerical error. For $Ra = 20\,000$, $\Delta Nu = 0.136$. Therefore, higher resolution is required at large Rayleigh numbers.

Energetics Figure 9 shows different aspects of the kinetic energy versus the Rayleigh number in the Ra range of this study. The total kinetic energy increases monotonously with increasing Rayleigh number, as both the axisymmetric and non-axisymmetric parts do. The non-axisymmetric part increases

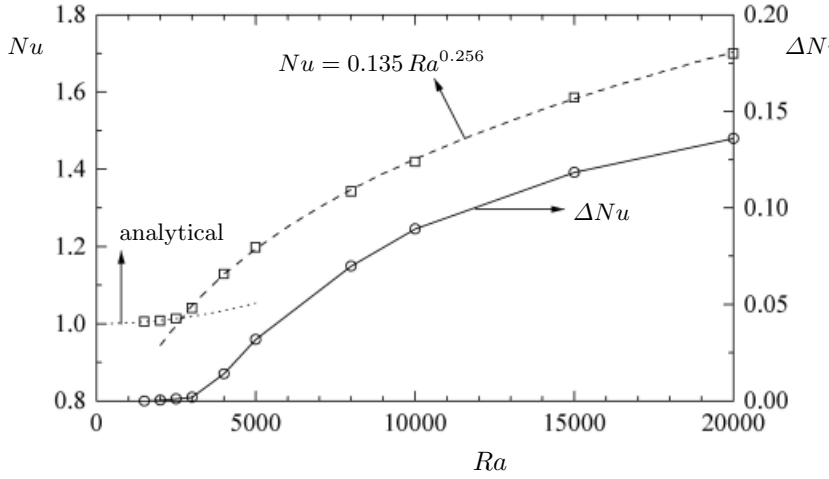

Fig. 8. Averaged Nusselt number Nu (□) and its deviation ΔNu (○) as a function of the Rayleigh number. The dashed line is the least-square fit of the Nu–Ra-relationship for the range of Ra = 3000–20 000. The dotted line is the analytical solution for the axisymmetric basic flow up to the second order approximation.

sharply as the banana-cells are generated from $Ra = 2500$, and then remains from about $Ra = 10\,00$ nearly constant at 32% of the total kinetic energy. Looking at contributions of each velocity component in Fig. 9(b), it can be seen that the largest contribution (over 90%) of the total kinetic energy is made by the latitudinal components (north-south movement), which however decrease with the increasing Rayleigh number. In the range from $Ra = 2500$ to 5000 the radial and the azimuthal components grow sharply at nearly the same rate. After that the azimuthal part increases steadily with the Rayleigh number, while the radial part essentially remains at about 2% of the total kinetic energy. The increase of the azimuthal kinetic energy indicates that the flow becomes more three-dimensional.

Figure 10 shows the temperature variance versus Rayleigh number. The volume-averaged temperature variance is an integral scale of thermal energy of the fluid shell. It is interesting that as the Rayleigh number increases, the total temperature variance first increases slightly and then decreases. The initial increase is due to the temperature increase in the interior of the spherical shell. But then, as the Rayleigh number increases further, the temperature boundary layers on both spheres build up, which leads to a decrease of the volume-averaged temperature variance. A major contribution comes from the portion in the southern hemisphere near the outer sphere where the fluid is of nearly the same temperature of the outer sphere. The axisymmetric part of the temperature variance changes in a similar way as the total variance for the same reason. The non-axisymmetric part of the temperature variance is generally very weak.

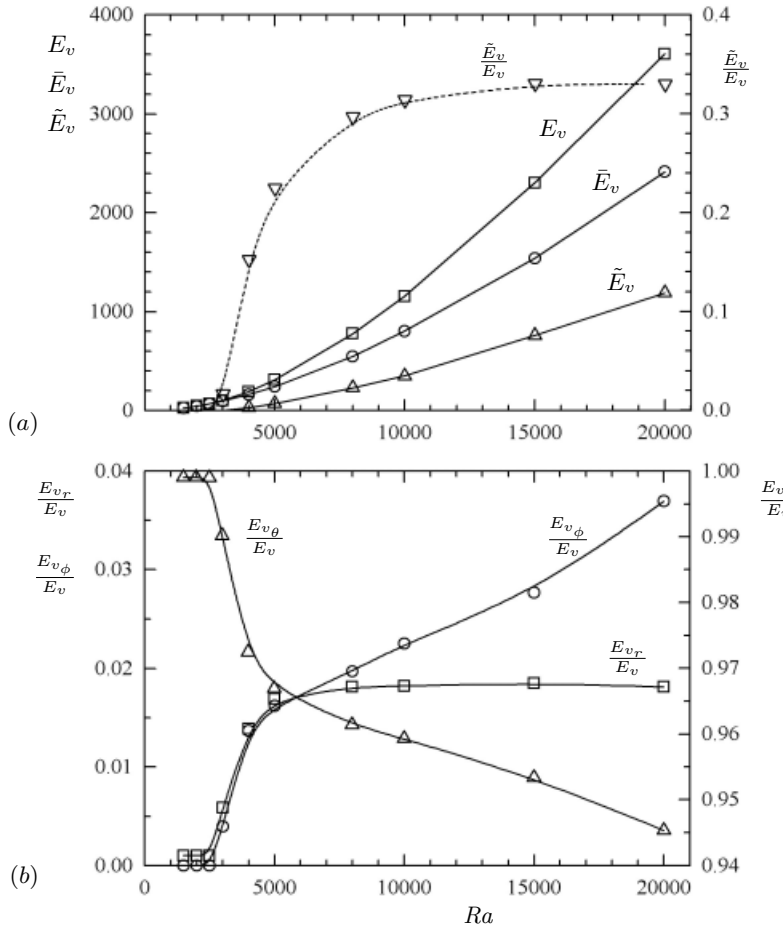

Fig. 9. Kinetic energies as a function of the Rayleigh number: (*a*) The total kinetic energy E_v and its axisymmetric $\bar{E}_v$ and non-axisymmetric $\tilde{E}_v$ parts. (*b*) Relative scales of three components normalized by the total kinetic energy.

It increases sharply as the banana-type cells are generated, and remains nearly constant for $Ra > 10\,000$.

Figure 11 shows the kinetic energy balance of the three-dimensional (non-axisymmetric) perturbations as a function of the Rayleigh number. The first three terms on the right-hand site of Eq. (20) are considered, as the dissipation just balances these three terms. For comparison, each term is also represented in units of their sum by the dashed curve with the same symbol. The scale for the solid curves is given on the left-hand axis, and the scale for the dashed curves is on the right axis.

The absolute values of the three terms increase monotonically with the Rayleigh number. Looking at the dashed curves, at low Rayleigh numbers the

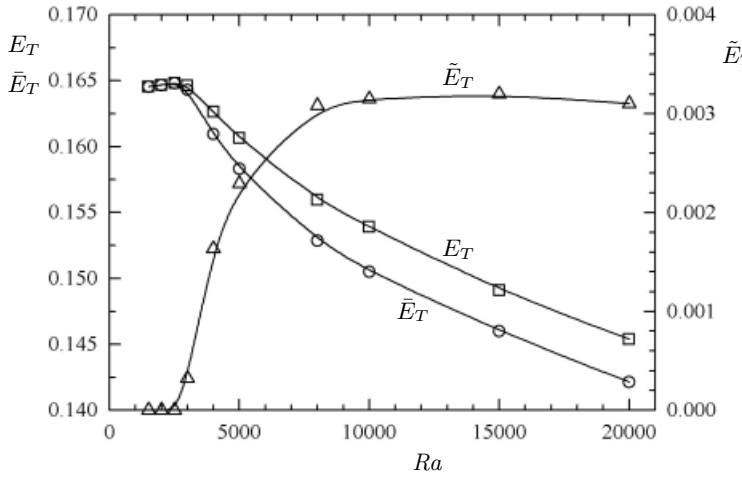

Fig. 10. Temperature variance E_T and its axisymmetric $\bar{E}_T$ and non-axisymmetric $\tilde{E}_T$ part as a function of Rayleigh number.

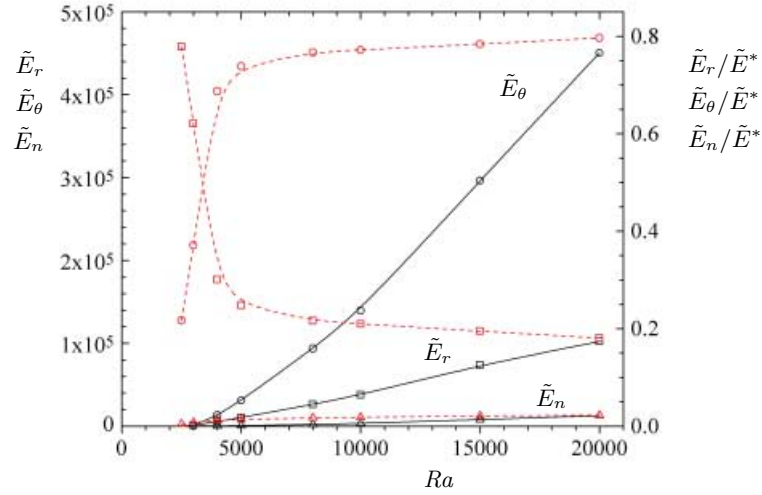

Fig. 11. Kinetic energy balance of the three-dimensional perturbations as a function of the Rayleigh number, see Eq. (20). $\tilde{E}_r$ and $\tilde{E}_\theta$ are the energy driven by the radial and meridional component of the buoyancy, respectively. $\tilde{E}_n$ is the nonlinear transfer rate of energy from the mean axisymmetric to non-axisymmetric part of velocity. The solid curves are to scale with the left-hand axis, and the dashed curves with the right-hand axis. The dashed curves are corresponding quantities normalized by their sum $\tilde{E}^*$.

kinetic energy is mainly generated by the radial buoyancy force. In the transient stage into the banana-type mode up to $Ra \approx 5000$, the radial and latitudinal part of the buoyancy change its role. At high Rayleigh number ($Ra > 5000$), the largest kinetic energy generation ($\sim 80\%$) is through the action of the latitudinal buoyancy force, about 18% of the kinetic energy comes from the radial buoyancy. This change can be understood by the fact that the banana-type mode is generated at low Ra near the north pole where the radial component of the buoyancy is largest. As the banana-cells grow into the equator with increasing Ra, the meridional component of the buoyancy becomes stronger and makes a dominant contribution. Note that in the whole Ra range the energy transferred from the mean axisymmetric flow is no more than 2% and, therefore, plays a negligible role in the process. Therefore, banana-cells result from the buoyancy driven convective instability.

3.3 Transient evolution

The above discussion is related to the (nearly) steady state at the unit thermal diffusion time. As an example at $Ra = 5000$, we want to show how the banana-type patterns develop with time. We recall that the calculation was started from a quiescent initial state at a constant temperature of the outer sphere ($\mathbf{v} = 0$, $T = 0$). For $t > 0$, the inner sphere is now set at a constant higher temperature $T_i = 1$, while the outer sphere is still maintained at $T_o = 0$. Some typical flow configurations up to 1.5 thermal diffusion times are shown in Fig. 12 in grey-scaled contour plots of the radial and latitudinal velocity components, to give a more qualitative impression comparable to experimental observations.

As already observed above in the steady states, each of the three velocity components displays some special characteristics of the three-dimensional convection. At the beginning up to $t \approx 0.2$, the convective flow in the spherical shell is essentially axisymmetric. A small axisymmetric ring vortex is formed around the north pole. The rings around the north pole grow in strength and size with time. At $t = 0.3$, a pair of rings expanding to $\theta \approx 15^\circ$ can be seen from the contour plot of the radial velocity component. Outside of the rings, the flow becomes three-dimensional. The wavy structure is more pronounced in the latitudinal velocity component than in the radial component. At $t = 0.4$, the contour lines of the radial velocity outside of the ring vortices display a nice flame-like pattern, while small banana-cells can be seen from the contour lines of the latitudinal velocity.

In the following time, the growth of the flame-like patterns in the direction to the equator and the formation of banana-type cells dominates the evolution of the flow pattern. On the other hand, the ring vortices around the north pole are disturbed by banana-cells and transform gradually to wavy and finally to entirely three-dimensional cells. As the banana-cells grow into the equator, new cells are generated to fit the increasing circumferential space. In the nearly steady state, 10 pairs of banana-cells are present at $\theta \approx 15^\circ$, 22 pairs at $\theta \approx 30^\circ$, and 34 pairs at $\theta \approx 60^\circ$. After a unit thermal diffusion time (compare with $t = 1$ for $Ra = 5000$ in Fig. 2), most changes can be seen in the contour lines of the radial

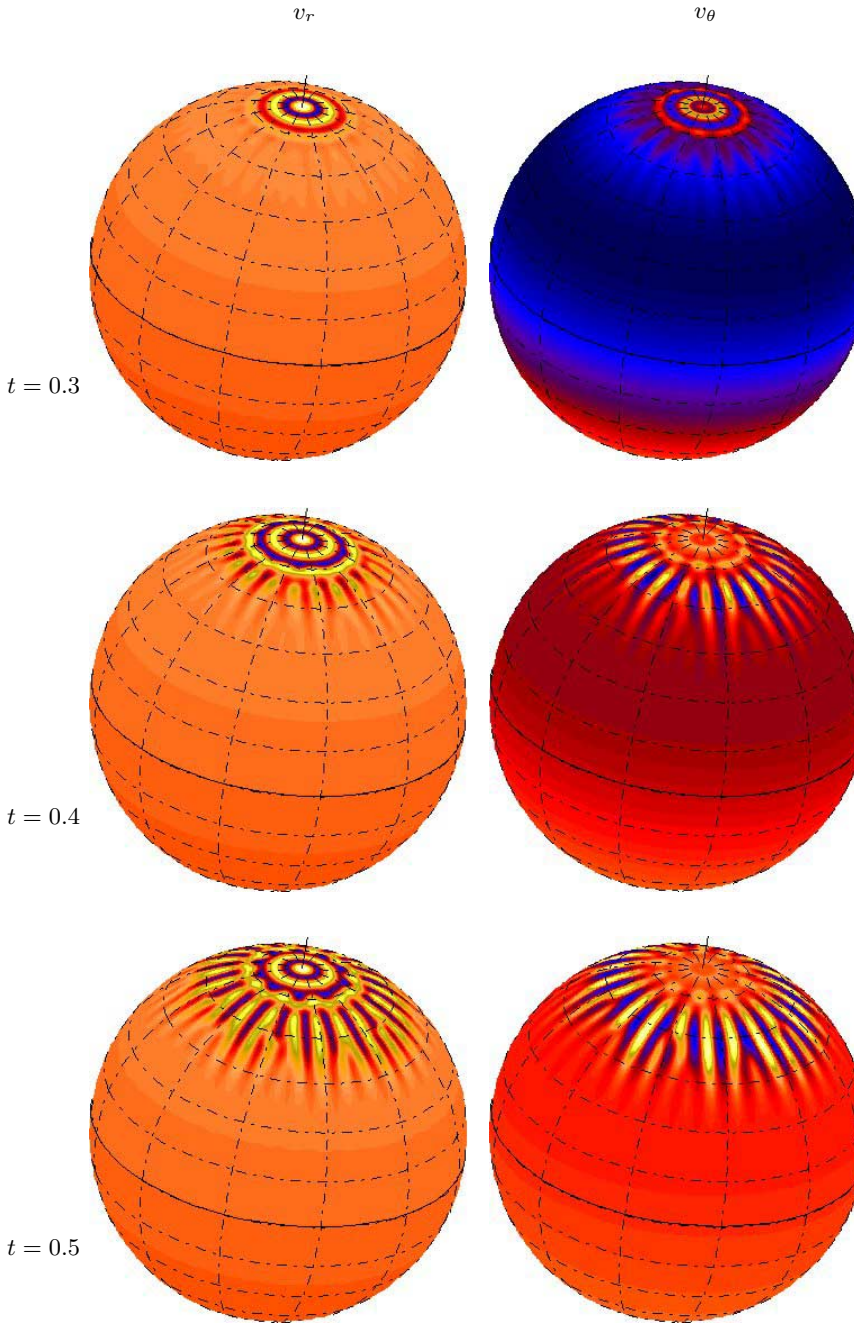

Fig. 12. For caption see next page.

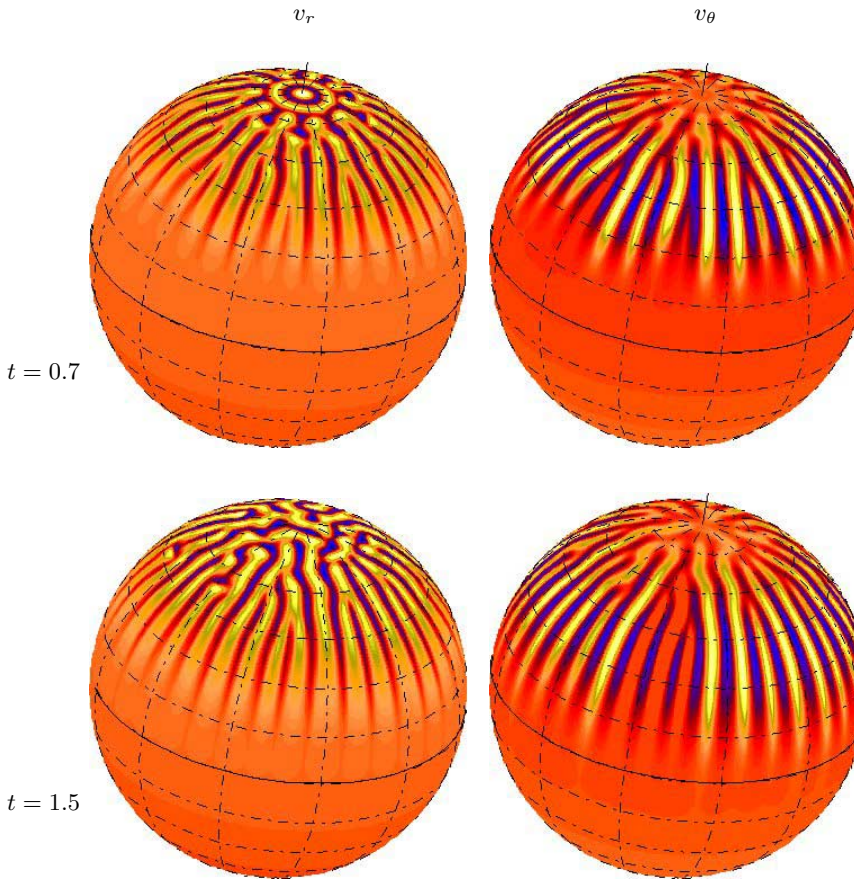

Fig. 12. Contour plots of the radial (v_r) and latitudinal (v_θ) velocity component on the mid-gap surface at different times for $Ra = 5000$ showing some typical stages of the unsteady evolutions of banana-type flow pattern. All components are normalised by the absolute maximal value of the component as given below. The dark area corresponds to negative values, and the light area to positive values.

velocity component near the north pole, while the banana-cell structure near the equator remains essentially steady, and the cells do not grow further with time (a check of the steadiness of the flow structure up to another characteristic thermal diffusion time from equator to pole is desirable but not feasible with the present numerical code).

Comparing Fig. 12 with Fig. 2, we see a close resemblance of the flow patterns with increasing time in Fig. 12 to those with increasing Rayleigh number in Fig. 2. In fact, the time development for other Rayleigh numbers is also similar. For smaller Rayleigh numbers, the onset of the visible structure (rings or banana-cells) begins later and the evolution with time is slower. At higher Rayleigh numbers, the scenario described above is practically compressed into a short

initial phase and a regular banana-type structure is always established, although the flow patterns after some time may become irregular. For example, similar flow structures as shown in Fig. 12 up to $t = 1.5$ for $Ra = 5000$ occur within $t = 0.25$ for $Ra = 20\,000$.

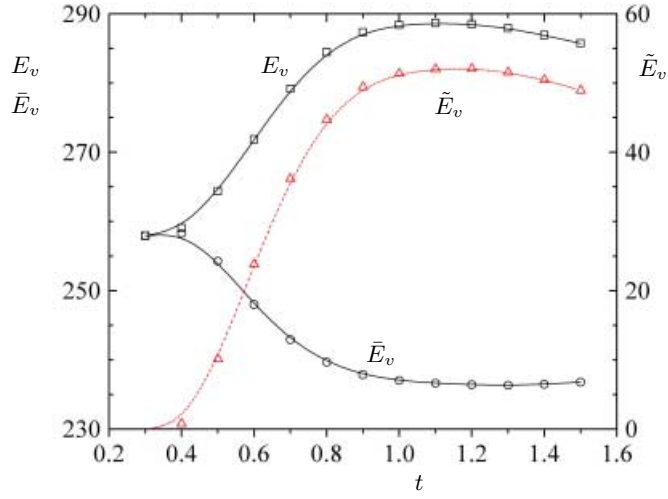

Fig. 13. E_v, total, $\bar{E}_v$, axisymmetric and $\tilde{E}_v$, non-axisymmetric energy as a function of time at $Ra = 5000$.

Figure 13 shows the total energy as well as its axisymmetric and non-axisymmetric part as a function of time at $Ra = 5000$. The scale for the total and axisymmetric energy is given on the left-hand axis, and the scale for the non-axisymmetric energy (which is much smaller than the axisymmetric energy) is on the right-hand axis. The units between tick marks on the both axes are the same, but the origin on the right has been shifted so that the sum of the axisymmetric and non-axisymmetric part just gives the total energy.

At the beginning the flow is axisymmetric, so the total energy is equal to the axisymmetric part. Although the three-dimensional structure becomes clearly visible from $t = 0.3$ in Fig. 12, a sharp increase of the non-axisymmetric energy begins at about $t = 0.4$ first. At the same time, the axisymmetric energy drops down less intensely, so that the total energy still increases. From about $t = 1.0$, all components remains nearly constant.

Up to now, we considered evolution from a quiescent initial state. In order to examine the pure energy flux during the transition towards banana-type modes, a calculation is made for $Ra = 5000$ starting from an initial state which is the azimuthally averaged axisymmetric part of the steady flow at the same Rayleigh number. Figure 14 shows energy balances with time up to 0.25. To this time the steady mode with banana-cells as shown in Fig. 2 is essentially reestablished. We see from Fig. 14 that the same energy profiles as in Fig. 11 at steady state

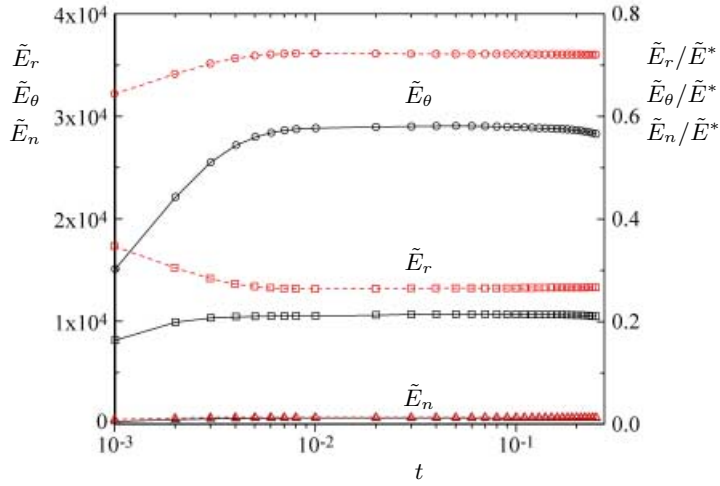

Fig. 14. Kinetic energy balance of the three-dimensional perturbations as a function of the time at $Ra = 5000$ from an (averaged) axisymmetric initial state. The abscissa for the time is scaled logarithmically to emphasise the evolution in the initial period. The symbols are used in the same manner as in Fig. 11.

are reestablished already at about $t = 0.01$. In fact, Fig. 14 just represents a portion of the corresponding graph obtained from a quiescent initial state (not shown here). Therefore, the same dynamics takes place during this transition as from a quiescent initial state.

4 Concluding remarks

In this paper, natural thermal convection in a narrow spherical shell with the aspect ratio $\beta = 0.08$ is studied numerically. Detailed characteristics of the convective motions have been presented and discussed. A novel feature representative for thermal convection in narrow spherical shells is the formation of banana-type cells in the northern hemisphere, as the Rayleigh number exceeds about $Ra = 2000$.

The development of the flow patterns with increasing Rayleigh number is similar to the development with time at a fixed *Ra*. An axisymmetric basic circulation extending through the whole spherical shell, with the fluid moving upward near the inner sphere and downward near the outer sphere, is generated at low Rayleigh numbers. As the Rayleigh number increases or the time elapses, a ring vortex or ring vortices are formed around the north pole. Outside the rings, the flow becomes unstable and transforms to banana-cells, which grow in the direction to the equator. Simultaneously, the ring vortices near the north pole are disturbed and disappear gradually. The banana-cells are, in contrast to ring vortices, still part of the basic circulation extending to the south pole. At

high Rayleigh numbers ($Ra \geq 10^4$), the flow structure becomes less ordered. The banana-cells are the result of an instability of buoyancy driven convection.

The numerical results presented here are in qualitative agreement with the results of previous experiments (Bishop et al. [1]; Nakagawa et al. [29]; Egbers [6]). Compared to laboratory experiments, the main advantage of direct numerical simulations is the possibility to explore various aspects of the flows, which can help us in understanding the dynamics. While experiments can primarily reveal some broad characteristics of these fascinating convective phenomena, the numerical simulation allows us to examine the detailed inner structure of the pattern formations. It was not clear, for example, what exactly happens in the flow when the banana-cells were observed experimentally for the first time. Through this numerical study, various phenomena observed in different experiments (the "falling-vortices" seen in a cross-section by Bishop et al. [1], and the banana-cells seen in the global visualisation by Egbers [6]) are combined to give a complete picture of these very complicated flows.

References

1. E. H. Bishop, L. R. Mack, J. A. Scanlan: *Heat Transfer by natural convection between concentric spheres.* Int. J. Heat Mass Transfer **9**, 649–662, (1966)
2. H. S. Chu, T.-S. Lee: *Transient natural convection heat transfer between concentric spheres.* Int. J. Heat Mass Transfer **36**, 3159–70 (1993)
3. F. H. Busse: *Fundamentals of thermal convection. Mantle convection, plate tectonics and global dynamics* ed. W. R. Peltier. (Gordon and Breach 1989)
4. S. Chandrasekhar: *Hydrodynamic and hydromagnetic stability.* Clarendon (1961)
5. R. J. Dallmann, R. W. Douglass: *Convection in a rotating spherical annulus with a uniform axial gravitational field.* Int. J. Heat Mass Transfer **23**, 1303–1312 (1980)
6. C. Egbers: *Zur Stabilität der Strömung im konzentrischen Kugelspalt.* Dissertation, University of Bremen. (1994)
7. C. Egbers, H. J. Rath: *The existence of Taylor vortices and wide-gap instabilities in spherical Couette flow.* Acta Mechanica **111**, 125–140 (1995)
8. C. Egbers, M. Liu, H. J. Rath: *Simulation of large-scale geophysical motions with the model of a rotating spherical fluid layer.* Microgr. Sci. Technol. **5**, 192–202 (1993)
9. C. A. J. Fletcher: *Computational Techniques for Fluid Dynamics 2: Specific Techniques for Different Flow Categories.* Springer (1991)
10. T. Fujii, T. Honda, M. Fujii *A numerical analysis of laminar free convection around an isothermal sphere: finite-difference solution of the full Navier–Stokes and energy equations between concentric spheres.* **7**, Num. Heat Transfer (1984)
11. M. Fujii, H. Takamatsu, T. Fujii: *A numerical analysis of free convection around an isothermal sphere (effects of space and Prandtl number).* Proc. 1987 ASME–JSME Thermal Eng Joint Conf., vol. **4**, pp. 55–60 (1987)
12. D. R. Gardner, R. W. Douglass, S. A. Trogdon: *Linear stability of natural convection in spherical annuli.* J. Fluid Mech. **221**, 105–129 (1990)
13. V. K. Garg: *Natural convection between concentric spheres.* Int. J. Heat Mass Transfer **35**, 1935–1945 (1992)
14. F. Geoola, A. R. H. Cornish: *Numerical simulation of free convective heat transfer from a sphere.* Int. J. Heat Mass Transfer **25**, 1677–1987 (1982)

15. G. Z. Gershuni, E. M. Zhukhovitskii: *Convective stability of incompressible fluids (translated from Russian)*. Keter Publishing House Jerusalem (1976)
16. K. Goda: *A multistep technique with implicit difference schemes for calculating two- or three-dimensional cavity flows*. J. Comp. Phys. **30**, 76–95 (1979)
17. J. E. Hart: *Stability of the flow in a differentially heated inclined box*. J. Fluid Mech. **47**, 547–576 (1971)
18. J. E. Hart, G. A. Glatzmaier, J. Toomre: *Space-laboratory and numerical simulations of thermal convection in a rotating hemispherical shell with radial gravity*. J. Fluid Mech. **173**, 519–544 (1986)
19. A. P. Ingersoll: *Thermal convection with shear at high Rayleigh number*. J. Fluid Mech. **25**, 209– (1966)
20. J. Kim, P. Moin: *Application of a fractional-step method to incompressible Navier–Stokes equations*. J. Comp. Phys. **59**, 308–323 (1985)
21. K. R. Kirschartz, H. Oertel, jr., J. Zierep: *Time-dependent convection*. Convective Transport and Instability Phenomena (eds. J. Zierep and H. Oertel, jr.), pp. 101–122 Braun Karlsruhe (1982)
22. E. L. Koschmieder: *On Convection on a Nonuniformly Heated Plane*. Beitr. Phys. Atmos. **39**, 208–216 (1966)
23. E. L. Koschmieder: *On Convection on a Uniformly Heated Rotating Plane*. Beitr. Phys. Atmos. **40**, 216–225 (1967)
24. E. L. Koschmieder: *Bénard Cells and Taylor Vortices*. Cambridge University Press (1993)
25. M. Liu: *Numerische Untersuchungen zu rotationssymmetrischen Strömungen im konzentrischen Kugelspalt*. Dissertation, University of Bremen (1993) Fortschrittberichte Reihe 7: Strömungstechnik, Nr. 249, VDI-Verlag
26. M. Liu, C. Egbers, H. J. Rath: *Spiral- und wellenförmige Taylor–Wirbel im Kugelspalt*. Proceedings of DGLR-Jahrestagung Erlangen, Germany, Oct. 1994, vol. **III**.
27. L. R. Mack, H. C. Hardee: *Natural convection between concentric spheres at low Rayleigh numbers*. Int. J. Heat Mass Transfer **11**, 387–396 (1968)
28. M. L. Mansour, A. Hamed: *Implicit solution of the incompressible Navier–Stokes equations on a non-staggered grid*. J. Comp. Phys. **86**, 147–167 (1990)
29. T. Nakagawa, J. Zierep, K. Bühler, M. Wimmer, K. R. Kirchartz: *Thermal convection between two concentric spheres*. Proc. 2nd JSME-KSME thermal engineering conference Oct. 19–21, 1992, 13–18
30. H. Ozoe, K. Fujii, T. Shibata, H. Kuriyama, S. W. Churchill: *Three-dimensional numerical analysis of natural convection in a spherical annulus*. Num. Heat Transfer **8**, 383–406 (1985)
31. R. Peyret, D. T. Taylor: *Computational Methods for Fluid Flow*. Springer (1982)
32. R. E. Powe, R. O. Warrington, J. A. Scanlan: *Natural convective flow between a body and its spherical enclosure*. Int. J. Heat Mass Transfer **23**, 1337–1350 (1980)
33. F. M. Richter, B. Parsons: *On the interaction of two scales of convection in the mantle*. J. Geophys. Res. **17**, 2529–2541 (1975)
34. H. T. Rossby: *A study of Bénard convection with and without rotation*. J. Fluid Mech. **36**, 309–335 (1969)
35. J. A. Scanlan, E. H. Bishop, R. E. Powe *Natural convection heat transfer between concentric spheres*. Int. J. Heat Mass Transfer **13**, 1857-1872 (1970)
36. G. Schubert *Numerical models of mantle convection*. Ann. Rev. Fluid Mech **24**, 359–394 (1992)
37. S. N. Singh, J. Chen *Numerical solution for free convection between concentric spheres at moderate Grashof numbers*. Num. Heat Transfer **3**, 441–459 (1980)

38. G. P. Williams: *Numerical integration of the three-dimensional Navier–Stokes equations for incompressible flow.* J. Fluid Mech. **37**, 727–750 (1969)
39. I. M. Yavorskaya, N. I. Fomina, Y. N. Belyaev: *A Simulation of central-symmetry convection in microgravity conditions.* Acta Astronautica **11**, 179–183 (1984)
40. S. H. Yin, R. E. Powe, J. A. Scanlan, E. H. Bishop: *Natural convection flow patterns in spherical annuli.* Int. J. Heat Mass Transfer **16**, 1785–1795 (1973)

Magnetohydrodynamic flows in spherical shells

Rainer Hollerbach

Department of Mathematics, University of Glasgow, Glasgow, G12 8QW, UK

Abstract. After reviewing the derivation of the equations governing the evolution of magnetic fields in electrically conducting fluids, I consider two largely distinct classes of such phenomena in spherical shells. The first is kinematic dynamo theory, in which a flow is prescribed, and one searches for self-excited magnetic fields. The second is magnetic Couette flow, in which a magnetic field is imposed, and one solves for the flow and the induced field. In both cases existing results are reviewed; in the latter case some new results are also presented.

1 Introduction

Magnetohydrodynamics is the study of the flow of electrically conducting fluids in the presence of magnetic fields. To understand why such flows should be so distinct from ordinary, non-magnetic hydrodynamics as to constitute a separate subject, one must understand the nature of the interaction between the field and the flow. We recall from basic physics that moving a conductor through a magnetic field induces electric currents, which in turn create new magnetic fields. We thus see how the flow will modify the original field. In addition, we again recall from basic physics that the combination of electric currents and magnetic fields leads to forces, which then modify the original flow. It is this mutual interaction between the flow and the field that makes magnetohydrodynamics such a fascinating subject, and gives it an even greater richness than that already found in ordinary hydrodynamics.

In addition to its intrinsic interest, magnetohydrodynamics also has a huge variety of applications, ranging from the industrial control of liquid metals to understanding the origin of planetary and stellar fields. Because these geo- and astrophysical applications typically involve spherical shells of various aspect ratios, I will focus attention on that geometry in this review. Nevertheless, I will endeavour to concentrate more on the abstract and generally applicable aspects, and less on the specific geo- or astrophysical applications. For recent reviews devoted specifically to planetary magnetic fields, readers are referred to any one of [1-3], and for stellar fields, to [4-5]. Finally, with an eye to stimulating greater interaction between experimentalists and theoreticians, I will also discuss a number of interesting configurations that could be set up in a laboratory.

C. Egbers and G. Pfister (Eds.): LNP 549, pp. 295–316, 2000.

2 The induction equation

To go beyond a mere qualitative description of how the fluid flow might be expected to influence the magnetic field, we need to derive the so-called induction equation. To do that we will need first of all Maxwell's equations

$$\nabla \cdot \mathbf{E} = \epsilon^{-1} \rho_c \ , \qquad \nabla \times \mathbf{E} = -\frac{\partial \mathbf{B}}{\partial t} \ , \tag{1a,b}$$

$$\nabla \cdot \mathbf{B} = 0 \ , \qquad \mu^{-1} \nabla \times \mathbf{B} = \mathbf{J} + \epsilon \frac{\partial \mathbf{E}}{\partial t} \ , \tag{1c,d}$$

and later also Ohm's law in a conductor moving with velocity $\mathbf{U}$,

$$\mathbf{J} = \sigma(\mathbf{E} + \mathbf{U} \times \mathbf{B}) \ . \tag{2}$$

Here $\mathbf{E}$ and $\mathbf{B}$ are the electric and magnetic fields, ρ_c and $\mathbf{J}$ are the charge and current densities, ϵ and μ the permittivity and permeability, and finally σ the conductivity.

In their complete form, we know of course that Maxwell's equations support wave solutions travelling at a speed $c = 1/\sqrt{\epsilon\mu}$, which turns out to be the speed of light, and indeed Maxwell's great accomplishment was precisely to demonstrate that light is an electromagnetic wave. However, if one is interested in studying the relatively slow phenomena that we will be considering here, it is extremely inconvenient to have to deal with equations that also support such very fast phenomena. For example, if we are developing a numerical solution, the well-known Courant condition [6] states that the largest timestep one can use must be less than the time it takes for the fastest wave allowed by the equations to travel one spatial gridspace. For comparison, the time it would take light to travel the entire diameter of the Earth's core is a small fraction of a second, and yet its magnetic field evolves over timescales of tens of thousands of years. If we really insisted on including light waves, we would thus have to take an unpleasantly large number of timesteps!

It is thus clear that we must approximate Maxwell's equations in such a way as to filter light waves out again. We do that by neglecting the displacement current $\epsilon\, \partial \mathbf{E}/\partial t$ in (1d) and reverting to the pre-Maxwell Ampere's law

$$\mu^{-1} \nabla \times \mathbf{B} = \mathbf{J} \ . \tag{1d'}$$

Of course, we cannot throw away certain terms simply because it is convenient to do so; we must justify neglecting them. So, we compare typical magnitudes of $\epsilon\, \partial \mathbf{E}/\partial t$ versus $\mu^{-1} \nabla \times \mathbf{B}$,

$$\frac{\epsilon \partial \mathbf{E}/\partial t}{\mu^{-1} \nabla \times \mathbf{B}} \sim \frac{\epsilon E/T}{\mu^{-1} B/L} = \epsilon\mu \, \frac{L}{T} \frac{E}{B} = \epsilon\mu \, U \, \frac{E}{B} \ ,$$

where L and T are typical length and time scales, and U is thus a typical velocity scale. From (1b), we obtain further

$$\frac{E}{L} \sim \frac{B}{T} \ , \qquad \text{so} \qquad \frac{E}{B} \sim \frac{L}{T} = U \ ,$$

and so finally

$$\frac{\epsilon \partial \mathbf{E}/\partial t}{\mu^{-1} \nabla \times \mathbf{B}} \sim \epsilon \mu U^2 = \frac{U^2}{c^2} \ .$$

We thus see that in order to justify the neglect of the displacement current, the typical velocity scale must be very small compared with the speed of light, hardly a very onerous condition. We note in particular that if U ever did become comparable to c, then much of our original motivation for wanting to neglect the displacement current in the first place, namely the disparity between the timescales T and L/c, evaporates completely. The requirement $U \ll c$ is thus quite acceptable.

There is, however, another condition that must also be satisfied for the neglect of the displacement current to be justified. Returning for the moment to Maxwell's equations in their complete form, if we take the divergence of (1d) and use (1a) to replace $\epsilon \nabla \cdot \mathbf{E}$ by ρ_c, we obtain

$$\frac{\partial \rho_c}{\partial t} + \nabla \cdot \mathbf{J} = 0 \ , \tag{3}$$

which we recognize as a statement of conservation of charge. In fact, historically (3) was not derived from (1d) and (1a) as we did here. Quite the reverse: charge conservation was known long before the complete form of Maxwell's equations, and Maxwell added the displacement current to Ampere's law precisely because he recognized that doing so would make it consistent with conservation of charge. That the resulting equations suddenly supported wave solutions whose speed agreed with the experimentally measured speed of light was merely an added bonus.

Well, if we are then proposing to neglect the displacement current again, we will have to consider carefully what implications that might have in terms of charge conservation. If we take the divergence of (1d') now, we obtain simply $\nabla \cdot \mathbf{J} = 0$, and since we still do believe in conservation of charge, that implies $\partial \rho_c / \partial t = 0$. This in turn implies $\rho_c = 0$, since it is simply not plausible that a charge imbalance inside a conductor could maintain itself indefinitely in such a way that $\rho_c \neq 0$ but $\partial \rho_c / \partial t = 0$. We thus see that another condition that must be satisfied for the neglect of the displacement current to be justified is that there can be no separation of positive and negative charges. For the phenomena we will be discussing, this condition is well satisfied, but it is important to realize that there could conceivably be phenomena where $U \ll c$ is satisfied, but one nevertheless cannot neglect the displacement current because $\rho_c \approx 0$ is not satisfied.

Having considered the conditions under which the so-called magnetohydrodynamic approximation of neglecting the displacement current may be justified (see also [7-9] for far more detailed discussions), we use (1b), (2), and (1d') to obtain

$$\frac{\partial \mathbf{B}}{\partial t} = -\nabla \times \mathbf{E}$$

$$= -\nabla \times (\sigma^{-1} \mathbf{J} - \mathbf{U} \times \mathbf{B})$$

$$= -\nabla \times (\sigma^{-1}\mu^{-1}\nabla \times \mathbf{B}) + \nabla \times (\mathbf{U} \times \mathbf{B}) \,,$$

and assuming the magnetic diffusivity $\eta \equiv 1/\sigma\mu$ is constant, we obtain finally

$$\frac{\partial \mathbf{B}}{\partial t} = \eta \nabla^2 \mathbf{B} + \nabla \times (\mathbf{U} \times \mathbf{B}) \,, \tag{4}$$

the magnetic induction equation governing the evolution of the field $\mathbf{B}$ under the action of the flow $\mathbf{U}$.

An important parameter in (4) is then the ratio of the inductive term $\nabla \times (\mathbf{U} \times \mathbf{B})$ to the diffusive term $\eta \nabla^2 \mathbf{B}$. This ratio defines the magnetic Reynolds number

$$Rm \equiv \frac{UL}{\eta} \,,$$

where U and L are again typical velocity and length scales. This magnetic Reynolds number is sufficiently important that we want to get a feel for its typical size in some of the applications we will be dealing with. The diffusivity η of course is a material property of whatever fluid we happen to be dealing with; typical values are around $1\,\mathrm{m}^2/\mathrm{s}$ for most liquid metals, and even for many plasmas. Variations in Rm are thus primarily due to variations in U and L; for example, in the Earth's core one has $L \approx 10^6$ m and $U \approx 10^{-4}$ m/s, so $Rm \approx 10^2$, whereas in a lab one might have $L \approx 0.1\,\mathrm{m}$ and $U \approx 0.1\,\mathrm{m/s}$, so $Rm \approx 10^{-2}$. Rm is thus typically small to moderate in lab configurations, but large to very large in planetary and stellar applications.

In view of these potentially large values of Rm, we want to explore a few properties of the $Rm = \infty$ limit. We begin by noting the extremely close analogy between the perfectly conducting induction equation

$$\frac{\partial \mathbf{B}}{\partial t} = \nabla \times (\mathbf{U} \times \mathbf{B}) \tag{5a}$$

and the inviscid vorticity equation

$$\frac{\partial \Omega}{\partial t} = \nabla \times (\mathbf{U} \times \Omega) \tag{5b}$$

of ordinary hydrodynamics. A familiar result found in any textbook is then that vortex lines evolve as material lines, a result known as Helmholtz's vortex theorem. While (5a) and (5b) are clearly not identical, since $\mathbf{B}$ and $\mathbf{U}$ are independent in (5a) whereas $\Omega = \nabla \times \mathbf{U}$ in (5b), readers are invited to check the proof of Helmholtz's theorem and convince themselves that nowhere does it rely on any particular relationship between Ω and $\mathbf{U}$. We therefore immediately obtain the analogous result that magnetic field lines also evolve as material lines, a result known as Alfvén's frozen flux theorem.

An immediate consequence of Alfvén's theorem is that the flux through any material surface remains constant. When applied to most material surfaces, this result is not very useful, since these surfaces typically become very convoluted very quickly under the action of the flow. There is one material surface, however, which always maintains its original shape, namely the boundary of the domain.

We can thus conclude that the flux through the boundary remains constant. Of course, this result isn't very useful either, since we already know from $\nabla \cdot \mathbf{B} = 0$ that the flux through the boundary is in fact zero, and concluding that zero remains constant is hardly a publishable result. However, by considering separately those parts of the boundary where the flux is positive and those parts where it's negative, one finds that because these separate parts are again material surfaces, these equal and opposite fluxes must also remain constant. Taking absolute values and adding these various parts up again, we can thus conclude that the so-called pole strength

$$\int_{\partial V} |\mathbf{B} \cdot \hat{\mathbf{n}}| \, dS \tag{6}$$

remains constant (again only in the $Rm = \infty$ limit though). And this result was not only publishable [10], it is sufficiently important that it is referred to as the Bondi-Gold theorem. We will see an interesting consequence of it in the next section.

While we're on the subject of $\mathbf{B}$ on the boundary, we should also discuss the appropriate boundary conditions. It is convenient to begin by making the so-called toroidal-poloidal decomposition

$$\mathbf{B} = \nabla \times (g\hat{\mathbf{r}}) + \nabla \times \nabla \times (h\hat{\mathbf{r}}) \, , \tag{7}$$

thereby automatically satisfying $\nabla \cdot \mathbf{B} = 0$. Conversely, any solenoidal field can indeed be decomposed in this way [11]. If g and h are then further expanded in spherical harmonics,

$$g = \sum_{l,m} g_{lm}(r,t) \, P_l^m(\cos\theta) \, e^{im\phi} \, , \qquad h = \sum_{l,m} h_{lm}(r,t) \, P_l^m(\cos\theta) \, e^{im\phi} \, ,$$

the decomposition (7) yields

$$B_r = \sum_{l,m} \frac{l(l+1)}{r^2} \, h_{lm} \, P_l^m(\cos\theta) \, e^{im\phi} \, ,$$

$$B_\theta = \sum_{l,m} \frac{1}{r} \frac{d}{dr} \, h_{lm} \, \frac{d}{d\theta} \, P_l^m(\cos\theta) \, e^{im\phi} + \frac{1}{r} \, g_{lm} \, \frac{im}{\sin\theta} \, P_l^m(\cos\theta) \, e^{im\phi} \, , \tag{8}$$

$$B_\phi = \sum_{l,m} \frac{1}{r} \frac{d}{dr} \, h_{lm} \, \frac{im}{\sin\theta} \, P_l^m(\cos\theta) \, e^{im\phi} - \frac{1}{r} \, g_{lm} \, \frac{d}{d\theta} \, P_l^m(\cos\theta) \, e^{im\phi} \, ,$$

for the individual field components. To obtain then the boundary conditions we should impose on g and h, we must first consider the nature of the exterior region $r > r_o$.

If we take this region to be an insulator, then in terms of the physics the condition we want to impose there is that the current density must vanish. We thus have,

$$\mathbf{J}_{ext} = 0 \quad \Longrightarrow \quad \nabla \times \mathbf{B}_{ext} = 0 \quad \Longrightarrow \quad \mathbf{B}_{ext} = \nabla\psi \, ,$$

for some field potential ψ. We also need to satisfy $\nabla \cdot \mathbf{B}_{ext} = 0$ though, so ψ must satisfy $\nabla^2 \psi = 0$, which has suitably decaying at infinity solutions

$$\psi = \sum_{l,m} C_{lm}\, r^{-(l+1)}\, P_l^m(\cos\theta)\, e^{im\phi} \;,$$

and so

$$B_{ext,r} = \sum_{l,m} -(l+1)\, C_{lm}\, r^{-(l+2)}\, P_l^m(\cos\theta)\, e^{im\phi} \;,$$

$$B_{ext,\theta} = \sum_{l,m} C_{lm}\, r^{-(l+2)}\, \frac{d}{d\theta} P_l^m(\cos\theta)\, e^{im\phi} \;,$$

$$B_{ext,\phi} = \sum_{l,m} C_{lm}\, r^{-(l+2)}\, \frac{im}{\sin\theta} P_l^m(\cos\theta)\, e^{im\phi} \;,$$

are the individual components of this so-called potential field.

Of course, what we really wanted were boundary conditions on the toroidal and poloidal parts of the internal field, so we need to consider which field components must be continuous across the boundary. Well, $\nabla \cdot \mathbf{B} = 0$ implies that the normal component must certainly be continuous, so

$$C_{lm} = -l\, r_o^l\, h_{lm}(r_o) \;, \tag{9}$$

which determines the external field, but doesn't yet give us any conditions on the internal field. So, we turn next to the tangential components. If these were discontinuous, according to $\mathbf{J} = \mu^{-1} \nabla \times \mathbf{B}$ that would imply infinite current densities. Now, in the perfectly conducting limit, such current sheets are acceptable, and so in the $Rm = \infty$ limit there are simply no boundary conditions on the internal field — which is why we didn't need to consider any in our derivation of the Bondi-Gold theorem. In the finitely conducting limit, however, such current sheets are not acceptable, and so, using also (9), we additionally require

$$\frac{1}{r}\frac{d}{dr} h_{lm}\, \frac{d}{d\theta} P_l^m + \frac{1}{r}\, g_{lm}\, \frac{im}{\sin\theta} P_l^m = -\frac{l}{r^2}\, h_{lm}\, \frac{d}{d\theta} P_l^m \bigg|_{r=r_o}$$

$$\frac{1}{r}\frac{d}{dr} h_{lm}\, \frac{im}{\sin\theta} P_l^m - \frac{1}{r}\, g_{lm}\, \frac{d}{d\theta} P_l^m = -\frac{l}{r^2}\, h_{lm}\, \frac{im}{\sin\theta} P_l^m \bigg|_{r=r_o}$$

which finally yield

$$g_{lm} = 0 \;, \qquad \frac{d}{dr} h_{lm} + \frac{l}{r}\, h_{lm} = 0 \;, \tag{10}$$

as the appropriate boundary conditions to impose at $r = r_o$.

One can then obviously go through similar considerations, now using bounded at zero solutions for ψ, and derive similar boundary conditions to impose at $r = r_i$. However, in terms of the physics taking the interior region $r < r_i$ to be an insulator is often not justifiable; in planetary or stellar applications this region is typically also a conductor. In this case, one cannot simply impose boundary conditions at $r = r_i$; one must solve for the field in the interior as well, and apply appropriate matching conditions across the interface. See, for example, [12] for a discussion of these matching conditions and their numerical implementation.

3 Kinematic dynamo action

Having derived the induction equation and the appropriate boundary conditions, we next consider those solutions most relevant in planetary or stellar contexts, namely so-called dynamo solutions, in which the magnetic field is not externally imposed, but is instead spontaneously generated. On an abstract level, this dynamo process is simply an instability, just like Rayleigh-Bénard convection, for example. That is, in convection, $\mathbf{U} \equiv 0$ is always a solution of the governing equations, but once the forcing — as measured by the Rayleigh number — exceeds some critical value, this non-convecting solution becomes unstable, and infinitesimal disturbances begin to grow. Similarly, $\mathbf{B} \equiv 0$ is always a solution of the induction equation, but once the forcing — as measured by the magnetic Reynolds number now — exceeds some critical value, this non-magnetic solution may become unstable, and infinitesimal seed fields may begin to grow.

Ultimately, of course, the field must equilibrate at some finite amplitude, just as convection ultimately equilibrates. We will explore the equilibration mechanism in the next section, but for now we will consider only so-called kinematic dynamo action, in which the flow is prescribed, and no back-reaction from the field is included. The dynamo process then becomes an eigenvalue problem, with the eigenvalue λ being the (generally complex) exponential growth or decay rate. That is, one looks for solutions of the form $\mathbf{B} = e^{\lambda t}\hat{\mathbf{B}}$, where $\hat{\mathbf{B}}$ has the same time-dependence — stationary or periodic — as $\mathbf{U}$ does. (If $\mathbf{U}$ has a more complicated time-dependence, the definition of λ is not so precise.) The question that kinematic dynamo theory then asks is, is it possible to choose $\mathbf{U}$ such that at least one of the eigenmodes is exponentially growing rather than decaying, and if so, what is the lowest Rm for which this occurs?

Unfortunately, all of the early results were negative, beginning with Cowling's theorem [13] stating that no fluid flow, whatever its structure, and however large its amplitude, can amplify a purely axisymmetric field. Quite a number of individuals have subsequently strengthened and extended this result; for example, whereas Cowling's original proof only applies to steady fields, Braginsky's [14] applies to time-dependent fields as well. Similarly, whereas Braginsky's proof (reproduced in [1]) only applies to incompressible flows, Hide & Palmer [15] and also Lortz & Meyer-Spasche [16] independently showed that Cowling's theorem remains valid even if compressibility is allowed, and even if variations in the diffusivity are allowed (note how (4) would have to be modified if η is no longer constant). These last results are particularly important, as the huge pressure variations found in planetary and stellar contexts make variations in the material properties of the fluid potentially far more important than they are in a laboratory context. However, it seems that Cowling's theorem holds true under just about any conceivable generalization (see also [17] for some more of these results), and so we must conclude that — if it is possible at all — dynamo action is an inherently three-dimensional process.

Another early negative result is the so-called toroidal theorem, first suggested by Elsasser [18], and rigorously proved by Bullard & Gellman [11], stating that no purely toroidal flow can act as a dynamo, where the distinction between toroidal

and poloidal flows is just like the distinction (7) between toroidal and poloidal fields. If the flow must therefore be at least partly poloidal, the equivalent of (8) implies it must have all three components non-zero. That is, we previously found that dynamo action must be three-dimensional in the sense that the field must depend on all three coordinates; we now find that it must also be three-dimensional in the sense that the flow must have all three components. The toroidal theorem has also subsequently been extended by Busse [19], who derived a lower bound on the poloidal part of the flow in terms of the ratio between the poloidal and toroidal parts of the field. This in turn suggests that a purely toroidal field should perhaps also be impossible, a result formally proved by Kaiser *et al.* [20]. We thus find that the field must also have all three components.

Yet another necessary, but unfortunately not sufficient, condition for dynamo action is that Rm must exceed certain $O(1)$ – $O(10)$ lower bounds [21-23]. The physical interpretation of all of these bounds is that the advective timescale must be more rapid than the diffusive timescale, that is, the flow must be stretching and thereby amplifying the field more rapidly than diffusion is damping it. As plausible and reasonable as this condition undoubtedly is, it does make it difficult to achieve dynamo action in the lab, where we previously saw how difficult it is to achieve even $Rm = O(1)$ – $O(10)$, let alone the $O(10)$ – $O(100)$ that realistic dynamos turn out to require. In planetary and stellar contexts, however, these lower bounds on Rm should pose no problems.

The first attempt at providing a more positive result was by Bullard & Gellman [11], who prescribed a certain flow consisting of an $m = 0$, $l = 1$ toroidal part and an $m = 2$, $l = 2$ poloidal part, and solved the resulting eigenvalue problem numerically. They claimed that for $Rm \gtrsim 50$ or so, they obtained a growing mode, that is, dynamo action. However, the resolution they used, only including spherical harmonics up to $m = l = 6$, and only including ten finite difference grid points in r, was hardly sufficient to resolve the $O(Rm^{-1/2})$ structures one expects to find in the field [24], and so this claim to have obtained dynamo action was not entirely convincing. And indeed, a subsequent recalculation by Lilley [25] at a higher resolution showed that the Bullard-Gellman flow fails as a dynamo. Lilley then went on to propose a different flow that he claimed did succeed, but another recalculation by Gubbins [26] showed that this flow too fails! One must thus be very careful about claiming dynamo action on the basis of numerical results that are not necessarily fully resolved.

In fact, the first successful proof of dynamo action in a sphere, by Backus [21], did not rely on numerical calculations at all. Instead, Backus chose his flow so cleverly that it was possible to prove dynamo action entirely analytically. The trick turned out to be to take the flow to be time-dependent, with pulses of flow separated by stationary intervals. During these stationary intervals the field simply decays of course, and since the higher harmonics decay more quickly than the lower ones, one can adjust the length of these intervals so that the higher harmonics decay away whereas the lower ones remain. And once one only has a small number of low harmonics to deal with, one can show analytically that

the effect of these periodic flow pulses is to amplify them from one pulse to the next, thereby proving dynamo action.

It is also of interest to note how Gubbins [26] not only showed that the earlier Bullard-Gellman and Lilley numerical solutions were not sufficiently well resolved to be even qualitatively correct, but also provided probably the first convincingly resolved numerical dynamo. In particular, the reason he succeeded where they had failed is not only due to the increased computing power in the intervening years, it is once again largely due to a clever choice of flow: besides the Bullard-Gellman and Lilley flows, Gubbins also considered a purely axisymmetric flow, for which the field conveniently decouples into distinct azimuthal modes. Cowling's theorem of course tells us that the $m = 0$ mode cannot be a dynamo, but it says nothing about the $m \neq 0$ modes. That is, Cowling's theorem only states that the field must depend on all three coordinates, but the flow may still depend on only two, in which case the dependence of the field on the third coordinate is sufficiently trivial that effectively one is still solving only a two-dimensional problem.

In recent years, the available computing power has increased so much further that even genuinely three-dimensional fields can now be fully resolved, and the kinematic dynamo problem continues to attract a surprising amount of attention. For example, Love & Gubbins [27] show that there is no corresponding "poloidal theorem", by presenting an example of a purely poloidal flow that does act as a dynamo. However, given that a poloidal flow already has all three components non-zero, it is perhaps not so surprising that a purely poloidal flow could succeed where a purely toroidal flow necessarily fails. Also of interest is the work of Gubbins *et al.* [28], who show that dynamo action is surprisingly delicate, in that a relatively slight change in the flow can completely destroy its dynamo properties. In the next section we will very briefly mention some of the possible implications of this result. In this context it is also worth mentioning Love & Gubbins [29], who have come up with an ingenious method of systematically adjusting the flow to optimize its dynamo properties, by solving a related inverse problem rather than the direct forward problem.

Having demonstrated that dynamo action in general is possible, we end this section with a brief discussion of the so-called invisible dynamo. That is, is it possible to have a dynamo that is completely contained within the sphere, with no external field at all? The possible existence of such dynamos would obviously have considerable geo- and astrophysical implications, as we can only ever observe the external fields of such bodies. Remembering our matching and boundary conditions (9) and (10), where we found that only the poloidal field extends outside the sphere, whereas the toroidal field always remains inside, we see that the most obvious way to have an invisible dynamo would simply be to have a purely toroidal field. However, remembering also the result [20] that a purely toroidal field dynamo is impossible, we realize that this option is not available. One should be careful not to conclude from this, though, that an invisible dynamo is necessarily also impossible. After all, [20] show that one cannot have a dynamo with the poloidal field zero everywhere, but not that one

cannot have a dynamo with the poloidal field zero everywhere on the boundary, which is all that we require.

Now, at this point one might legitimately object that such a configuration is highly contrived. After all, why should the dynamo just happen to arrange its poloidal field in such a way that the single boundary condition (10b) is effectively replaced by the much more stringent double condition $h_{lm} = dh_{lm}/dr = 0$? Well, it turns out that there is in fact a very good reason why the dynamo might be compelled to tend toward such a configuration, namely the constraint imposed by the Bondi-Gold theorem. We saw earlier that the Bondi-Gold theorem states that the pole strength (6) can only change through diffusion, so if there is a dynamo operating inside the sphere, it can only generate an external field through diffusion. But that means that in the limit of increasingly large Rm, as diffusion becomes weaker and weaker, it becomes increasingly difficult to generate an external field, and so one should expect the field to become increasingly contained within the sphere, that is, to tend to an invisible dynamo. This hypothesis has been verified in a direct numerical simulation by Hollerbach *et al.* [30], who were able to go up to $Rm = 10^5$ by using the same trick as Gubbins [26] did of choosing a purely axisymmetric flow. Furthermore, this same result was also conjectured by Rädler [31], and proved by Rädler & Geppert [32], in the context of so-called mean-field dynamics, in which the flow is assumed to be turbulent, and certain large-scale averages are taken. A discussion of mean-field dynamics is obviously beyond the scope of this review, but readers are referred to [33].

It is certainly gratifying to find that two such radically different approaches both lead to the same conclusion, that in the limit of sufficiently large Rm invisible dynamos are not only possible but almost inevitable, but it does raise the question as to how the Sun, for example, does manage to have an external field? The answer is that the Sun is not operating as a kinematic dynamo, with no influence of the field back on the flow. If one does include this effect, one finds that there are powerful forces, such as magnetic buoyancy [34], that act to bring the field to the surface, where the solar wind can then also help to extend it outward. However, these results about the invisible dynamo do illustrate two points. First, it is not enough to generate a field inside some object; one also has to be able to extend it outward. And second, for many objects, including the Sun, it is still quite likely that the internal field is many times stronger than the external field.

4 The Lorentz force

Turning next to this influence of the field back on the flow, we note that the combination of electric currents and magnetic fields gives rise to the so-called Lorentz force $\mathbf{J} \times \mathbf{B}$, which can also be written as

$$\mathbf{J} \times \mathbf{B} = \mu^{-1}(\nabla \times \mathbf{B}) \times \mathbf{B} = -\mu^{-1}\nabla|\mathbf{B}|^2/2 + \mu^{-1}(\mathbf{B} \cdot \nabla)\,\mathbf{B},$$

using first (1d') and then a standard vector identity. It is in this latter form that this force is particularly amenable to physical interpretation; we recognize

right away that the term $-\mu^{-1}\nabla|\mathbf{B}|^2/2$ amounts to an isotropic magnetic pressure. For the largely incompressible flows in planetary interiors this part of the Lorentz force is relatively unimportant, but for the highly compressible flows in stellar interiors it is enormously important. For example, this magnetic buoyancy alluded to above [34] is caused by the magnetic pressure force: regions of strong field respond to their high magnetic pressure by expanding; the resulting lower density then gives rise to an upward buoyancy force. The physical interpretation of the term $\mu^{-1}(\mathbf{B}\cdot\nabla)\,\mathbf{B}$ is not quite so straightforward, but it can be shown (see for example [7-9]) that it amounts to an anisotropic magnetic tension, in which the magnetic field lines act like elastic bands. This part of the Lorentz force is important in virtually all situations; we will see some interesting effects of it and its highly anisotropic nature in the next section.

This tension in the field lines also allows us another interpretation of dynamo action, which we have previously thought of from a purely kinematic point of view as simply the stretching and hence amplification of field in accordance with Alfvén's frozen flux theorem. We now realize that from a dynamic point of view, stretching the field lines in this way will require us to do work against the magnetic tension, and assuming conservation of energy, this work will presumably reappear as an increase in the magnetic energy, that is, an amplification of the field.

Of course, we shouldn't simply assume conservation of energy; we should be able to derive it from the governing equations, and prove that the work done against the magnetic tension really does reappear as magnetic energy. We can do so easily enough by adding the dot products of the induction equation with $\mu^{-1}\mathbf{B}$ and the momentum equation with $\mathbf{U}$ to obtain

$$\frac{\partial}{\partial t}\left(\frac{1}{2}\,\rho\mathbf{U}^2+\frac{1}{2}\,\mu^{-1}\mathbf{B}^2\right)=\mu^{-1}\big[\mathbf{B}\cdot\nabla\times(\mathbf{U}\times\mathbf{B})+\mathbf{U}\cdot(\nabla\times\mathbf{B})\times\mathbf{B}\big]+\ldots\,,$$

where we're focussing attention only on the two terms coupling $\mathbf{U}$ and $\mathbf{B}$. Again using standard vector identities, one can then show that

$$\mathbf{B}\cdot\nabla\times(\mathbf{U}\times\mathbf{B})+\mathbf{U}\cdot(\nabla\times\mathbf{B})\times\mathbf{B}=\nabla\cdot\big[(\mathbf{U}\times\mathbf{B})\times\mathbf{B}\big].$$

Integrating over the volume and using the divergence theorem, these terms thus contribute

$$\mu^{-1}\int_{\partial V}\big[(\mathbf{U}\times\mathbf{B})\times\mathbf{B}\big]\cdot\hat{\mathbf{n}}\,dS \tag{11}$$

to the global energy balance. So if our boundary conditions are $\mathbf{U}=0$, we obtain the desired result immediately. Of course, the boundary conditions aren't always $\mathbf{U}=0$ — the Couette flows considered in the next section for example are driven entirely by inhomogeneous boundary conditions on $\mathbf{U}$. However, in that case one can show with only a little more effort that (11) corresponds precisely to the external work done against a possible magnetic torque on the boundary, so once again we obtain the desired result.

This magnetic tension also provides the equilibration mechanism that prevents a dynamo field from growing indefinitely; eventually the field must surely

become so great that its tension simply prevents the flow from stretching it any further. In fact, the precise details of this equilibration mechanism are potentially extremely complicated, and are the subject of most current research in dynamo theory. For example, the Lorentz force could simply reduce the amplitude of the flow everywhere until the magnetic Reynolds number is just critical. Alternatively, it could leave the amplitude of the flow largely unchanged, but subtly alter its structure and thereby its dynamo properties to the point where the field stops growing — we recall from our discussion of kinematic dynamo theory that only very slight changes in the flow are needed for this to happen.

Finally, and most dramatically, the Lorentz force could cause the whole system to switch to a completely different state. This possibility is particularly relevant in planetary dynamos, where it is generally believed that the extremely rapid rotation leads to the existence of distinct weak and strong field regimes, characterized by very different amplitudes and structures for both the field and the flow. A detailed discussion of the dynamics leading to these two states is beyond the scope of this review, but see Jones [35], who also estimates just how rapid the rotation must be for these two states to emerge. And as if this wasn't complicated enough, Zhang & Gubbins [36] then speculate — again on the basis of the known fragility of a flow's dynamo properties — that neither of these states will be stable, so that the system might oscillate between the two.

In fact, one need not go to such extreme parameter values to observe a system switching between completely different states in response to the Lorentz force; Fuchs *et al.* [37] provide very nice examples of what they call "self-killing" and "self-creating" dynamos. In the first scenario one starts with a flow that is a dynamo, but the Lorentz force switches it to a flow that is not, and even after the field then decays away, one does not switch back to the original flow. In the second scenario one starts with a flow that is not a dynamo, but if one starts it off with the right finite amplitude field, the Lorentz force switches it to a flow that is a dynamo.

We thus see that although the general principles whereby the Lorentz force must ultimately equilibrate a dynamo field are well understood, the details of how this may come about are surprisingly subtle and varied. There is undoubtedly much still to be learned in this area, not just on specific planetary or stellar applications, but also in terms of more abstract, general principles.

5 Magnetic Couette flow

We end with a discussion of various phenomena that occur when magnetic fields interact with Couette flows. Although this subject dates back to Chandrasekhar [38], it has rather languished since then. However, given that this volume is devoted primarily to Couette flows of various kinds, and given the range of interesting phenomena that can occur in magnetic Couette flow, it seems appropriate to discuss it here, and in the process perhaps arouse further interest in it. We will present two configurations; in the first both spheres are rapidly rotating, with a slight differential rotation between them, in the second only the

inner sphere is rotating. In both cases we will consider the effects that imposing magnetic fields with various orientations and amplitudes has on the previously non-magnetic solutions.

If both spheres are rapidly rotating about the same axis at almost the same rate, the non-magnetic solution consists of the so-called Stewartson layer situated on the tangent cylinder $\mathcal{C}$, the cylinder circumscribing the inner sphere and parallel to the axis of rotation. The reason this particular cylinder is singled out is because of the Taylor-Proudman theorem, stating that in rapidly rotating systems the flow must be independent of the coordinate along the axis of rotation. As a result of this requirement, the tangent cylinder naturally separates the flow into two distinct regions, with the fluid outside $\mathcal{C}$ in solid-body rotation at a rate Ω_o, and the fluid inside $\mathcal{C}$ in almost solid-body rotation at a rate intermediate between Ω_o and Ω_i.

Since there is a slight difference between Ω_o and Ω_i, this implies that there must be a jump in angular velocity across $\mathcal{C}$, proportional to the differential rotation $\Delta\Omega$. The detailed structure of the shear layer that resolves this jump was deduced by Stewartson [39], and consists of three intricately nested layers, an innermost one of thickness $E^{1/3}$, and two outer ones of thicknesses $E^{2/7}$ just inside $\mathcal{C}$, and $E^{1/4}$ just outside $\mathcal{C}$. The Ekman number $E = \nu/\Omega_o L^2$ is an inverse measure of the overall rotation rate. The Stewartson layer has been reproduced numerically by Hollerbach [40] down to $E = 10^{-5}$, and by Dormy *et al.* [41] down to $E = 10^{-8}$, who both obtained results in excellent agreement with the asymptotic scalings.

So, the obvious next question to ask is, what effect might a magnetic field have on this layer? The first to address this question were Ingham [42] and Vempaty & Loper [43], who considered the effect of imposing a uniform field aligned with the axis of rotation. (Actually, they considered a very similar shear layer in cylindrical rather than spherical geometry. However, the non-magnetic layers in the two geometries are virtually identical, the main difference being that what was the $E^{2/7}$ layer in spherical geometry becomes another $E^{1/4}$ layer in cylindrical geometry. Given this similarity, it is then likely that the magnetic adjustments are also similar.) They found that the field has no effect at all until $\Lambda \gtrsim 1$, where the Elsasser number $\Lambda = \sigma B_0^2/\rho\Omega_o$ is a measure of the strength of the imposed field $\mathbf{B}_0$. There is then a transition regime $1 \lesssim \Lambda \lesssim E^{-1/3}$ in which the $E^{1/3}$ layer is unchanged, the $E^{1/4}$ layers become thinner $(E/\Lambda)^{1/4}$ layers, and a new Λ^{-1} layer emerges. All three of these layers merge when $\Lambda \approx E^{-1/3}$, and for $\Lambda \gtrsim E^{-1/3}$ there is a single thinner $(E/\Lambda)^{1/4}$ layer.

We thus find that imposing an axial field has relatively little effect until its strength becomes quite large, and even then it acts to enhance the shear, that is, to reinforce the effect of the rapid overall rotation. On reflection, that is hardly surprising, since the tension in the field lines is acting to couple the same regions that were already coupled by the Taylor-Proudman theorem, namely these nested cylindrical shells each undergoing essentially solid-body rotation. This does suggest, though, that we could achieve very different results if we imposed a different field, one coupling regions not previously coupled. In particular, if

we chose a field with a component perpendicular to the Stewartson layer, the magnetic tension should surely act to suppress the shear.

The first to explore this possibility was Hollerbach [40], who imposed a dipole field, and showed numerically that it does indeed suppress the shear, and at quite small field strengths. The asymptotic scalings of this configuration were subsequently deduced by Kleeorin *et al.* [44], and are in complete agreement with the numerical results. Their main results are: first, the $E^{2/7}$ and $E^{1/4}$ layers become thinner $(E/\Lambda)^{1/2}$ layers once Λ exceeds $E^{3/7}$ for the $E^{2/7}$ layer and $E^{1/2}$ for the $E^{1/4}$ layer. However, even though these layers become thinner, the shear is already starting to be suppressed, because the jump across them decreases even faster. Once $\Lambda \approx E^{1/3}$ then, these layers merge with the $E^{1/3}$ layer, which is thus far unaffected. And finally, once Λ exceeds $E^{1/3}$, there is a single thicker Λ layer.

So we see that imposing different fields does indeed lead to radically different results; in one case a thinner $(E/\Lambda)^{1/4}$ layer once $\Lambda \gtrsim E^{-1/3}$, in the other a thicker Λ layer once $\Lambda \gtrsim E^{1/3}$. But again, both of these results are only to be expected, since in one case the field does not have a component perpendicular to the Stewartson layer, whereas in the other it does; so in one case the tension in the field lines has no tendency to oppose the shear whereas in the other it does.

For the dipole configuration, once $\Lambda = O(1)$, this Λ layer then fills the whole shell, that is, the shear layer is completely suppressed, and the whole fluid is in essentially solid-body rotation, with all of the adjustment to the imposed differential rotation occurring in the Ekman-Hartmann boundary layers. Increasing Λ still further though, it turns out that entirely new shear layers arise once $\Lambda \gtrsim E^{-1/3}$, as Starchenko [45] was the first to realize. He noted first that for any given imposed field there could be some field lines that only connect to the inner sphere, some that only connect to the outer sphere, and some that connect to both. And given that at such large field strengths the magnetic analog of the Taylor-Proudman theorem states that the flow should be constant along field lines — essentially the frozen flux theorem in reverse, with the fluid frozen to the field rather than vice versa — we should expect those field lines that only connect to the inner sphere to co-rotate with it, those that only connect to the outer sphere to co-rotate with it, and those that connect to both to rotate at some intermediate rate. So the location of these new shear layers will be wherever we switch from one type of field line to another. Starchenko went on to show that the thickness of these new layers is once again $(E/\Lambda)^{1/4}$. We thus realize that our previous $(E/\Lambda)^{1/4}$ layer is really nothing more than a special case of these new layers; it just so happens that for an axial field you switch from one type of field line to another in the same place as you previously had the Stewartson layer, so it's not so obvious that it's really a fundamentally different layer.

In fact, if we examine the thickness of these layers in more detail, we find that since

$$\left(\frac{E}{\Lambda}\right)^{1/4} = \left(\frac{\nu/\Omega_o L^2}{\sigma B_0^2/\rho\Omega_o}\right)^{1/4} = \left(\frac{\nu\rho}{\sigma B_0^2 L^2}\right)^{1/4}$$

doesn't actually involve the overall rotation Ω_o at all, it should be possible to obtain the same layers in our second configuration, in which only the inner sphere is rotating. The advantage of this is that we thereby have one parameter less to deal with; that is, instead of having one parameter measuring viscous to Coriolis forces (E), and another measuring Lorentz to Coriolis forces (Λ), we dispense with the Coriolis force entirely, and simply have one parameter measuring Lorentz to viscous forces, the so-called Hartmann number $M^2 = \sigma B_0^2 L^2/\nu\rho$. In terms of this parameter, we then expect these layers to scale as $M^{-1/2}$.

Since we will be considering this configuration in some detail, we note the precise equations we will be solving. In the limit of small Rm, the momentum and inductions equations can be simplified to

$$\frac{\partial \mathbf{U}}{\partial t} + Re\mathbf{U}\cdot\nabla\mathbf{U} = -\nabla p + \nabla^2\mathbf{U} + M^2(\nabla\times\mathbf{b})\times\mathbf{B}_0 \ , \tag{12}$$

$$0 = \nabla^2\mathbf{b} + \nabla\times(\mathbf{U}\times\mathbf{B}_0) \ , \tag{13}$$

where the Hartmann number is as above, and the Reynolds number $Re = \Omega_i L^2/\nu$ is a measure of the inner sphere's rotation rate. The total magnetic field is then

$$\mathbf{B} = \mathbf{B}_0 + Rm\,\mathbf{b} \ ,$$

where $\mathbf{B}_0$ is the externally imposed field, and $Rm\,\mathbf{b}$ the induced field. That is, Rm no longer appears at all in the equations to be solved, only in the meaning we subsequently ascribe to the solution $\mathbf{b}$. This is precisely why we're willing to limit ourselves to small Rm in this way, to effectively eliminate yet another parameter from the problem.

The boundary conditions associated with (12) are of course just the usual spherical Couette flow boundary conditions, namely matching to $\mathbf{U} = r\,\sin\theta\,\hat{\mathbf{e}}_\phi$ at $r = r_i$ and to $\mathbf{U} = 0$ at $r = r_o$, where we will take $r_i = 1$ and $r_o = 2$. The boundary conditions associated with (13) depend on whether we take the regions $r < r_i$ and $r > r_o$ to be insulators or conductors. Since it will turn out that this choice has a surprisingly large effect on the solutions we obtain, we will systematically consider all four possibilities II, CI, IC, and CC, where the first letter denotes the inner boundary and the second the outer. Also, we might just note that in this small Rm limit, where the field adjusts to the flow instantaneously, it is possible to simply impose boundary conditions even at conducting boundaries. See, for example, [46] for a detailed derivation of these simplified equations and boundary conditions.

For our externally imposed field $\mathbf{B}_0$, we will consider in turn axial (A), dipole (D) and quadrupole (Q) fields, normalized so that $|\mathbf{B}_0| = 1$ at $r = r_o$, $\theta = 0$. Figure 1 then shows the angular velocity of the steady-state solutions, at a Hartmann number $M^2 = 10^5$ and a Reynolds number $Re = 0$, corresponding to a very strong field and an infinitesimally weak rotation. From left to right we see the three field configurations A, D and Q, respectively, and from top to bottom the four boundary configurations II, CI, IC, and CC.

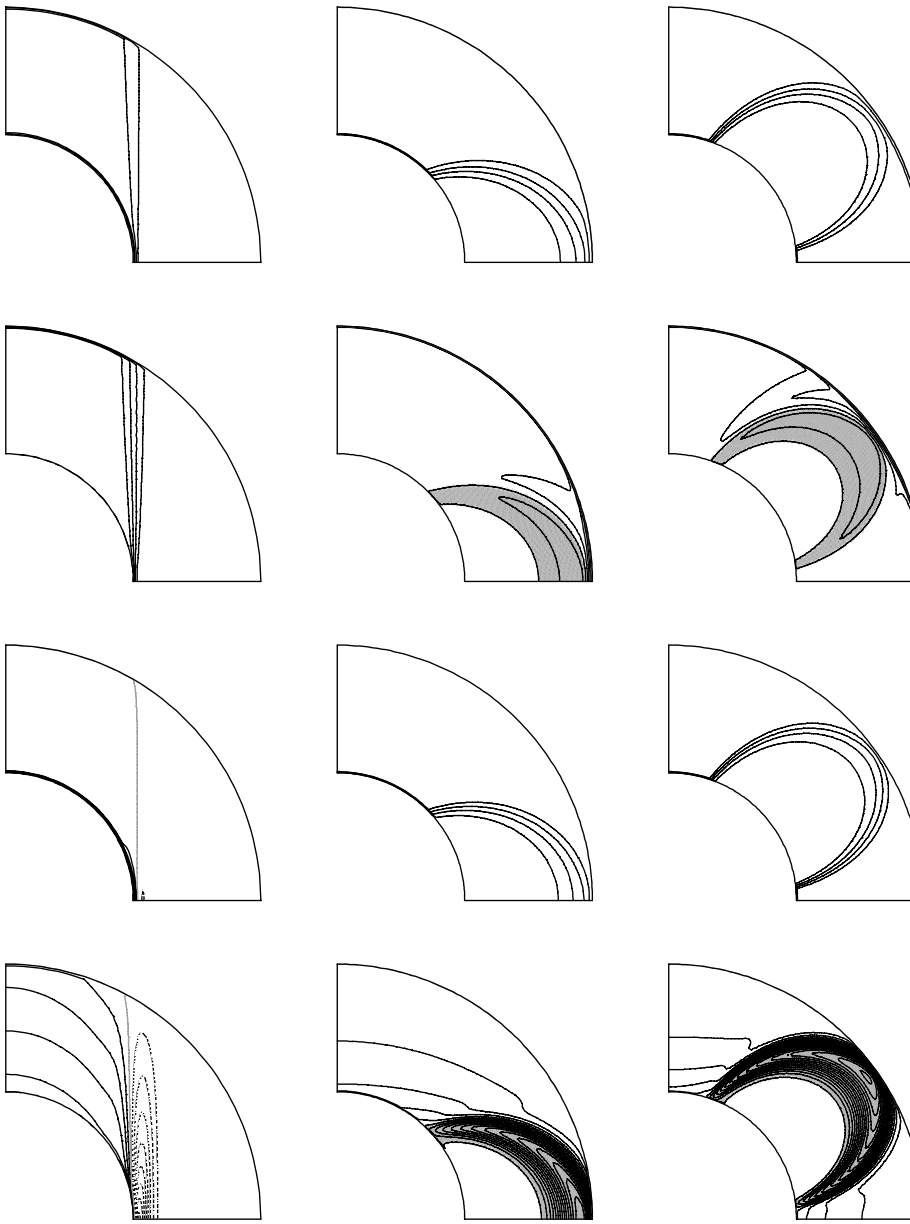

Fig. 1. Contours of the angular velocity, for the three field configurations A, D and Q (from left to right), and the four boundary configurations II, CI, IC, and CC (from top to bottom). $M^2 = 10^5$, $Re = 0$, and a contour interval of $0.2\,\Omega_i$ throughout. The regions of counter-rotation are indicated by the dashed contour lines; the regions of super-rotation by the gray-shading. The maximum values in the bottom row are -1.67, 3.87, and 4.06, respectively. Finally, all of these solutions are symmetric about the equator

Focussing attention on II first, we note that these results are exactly as we expected, with the shear layers occurring on precisely those field lines separating regions magnetically coupled only to one boundary or the other from those coupled to both. Furthermore, if we were to vary M^2, we would find that the thickness of these layers does indeed scale as $M^{-1/2}$. We can already see some hint of this in the D and Q results, where the field strengths, and hence the local Hartmann numbers, vary considerably throughout the shell, and sure enough the shear layers are much thinner at r_i than at r_o.

Turning next to CI and IC, we note that the primary effect of switching either boundary from insulating to conducting is to lock the fluid to that boundary. This is particularly apparent for the axial field, where all the fluid inside the tangent cylinder, which was rotating at a rate $\Omega_i/2$ for II, is now completely locked to the inner boundary for CI, and to the outer boundary for IC. The reason for this behaviour is that across an insulating boundary forces can only be transmitted viscously, whereas across a conducting boundary they can also be transmitted magnetically, and since the Hartmann number measuring magnetic to viscous forces is large, one should expect the coupling across a conducting boundary to be so much stronger that it completely overwhelms the coupling across an insulating boundary.

We also note two other curious effects in the CI and IC configurations: For $\mathrm{D_{CI}}$ and $\mathrm{Q_{CI}}$, there are small regions of *super-rotating* fluid, fluid rotating faster than Ω_i. This super-rotation, which at this aspect ratio amounts to $\sim$40% in both cases, has previously been obtained numerically by [41] and analytically by [45], and is largely independent of M^2 (although the region in which it occurs becomes thinner and thinner as M^2 increases). Similarly, for $\mathrm{A_{IC}}$, there is a very small region of *counter-rotating* fluid, fluid rotating in the opposite direction from Ω_i. This $\sim$25% counter-rotation has not previously been obtained, but it too is largely independent of M^2. Both of these phenomena obviously require explanation. However, because we will encounter far more dramatic examples of both in the CC configuration, we defer discussion until after presenting those results.

Turning to CC then, we note that one reason why one might be interested in considering it is that it is not so obvious where the adjustment to the imposed rotation will now occur. That is, we was previously that switching either boundary from I to C will completely suppress the Hartmann layer at that boundary, so presumably CC shouldn't have any boundary layers at all, and yet somewhere in the fluid the adjustment from a rotation rate of Ω_i at r_i to 0 at r_o must take place. The results in the bottom row of Fig. 1 show that there are indeed no Hartmann layers now; the adjustment occurs throughout the whole of the interior instead.

Far more dramatically, though, what was previously a relatively weak counter- or super-rotation is now a powerful jet far exceeding Ω_i. Furthermore, the strength of these jets is no longer independent of M^2, but instead *increases* with increasing Hartmann number, roughly as $M^{0.6}$ for all three. These jets, reported here for the first time, clearly do require explanation now. In order to

understand the origin of both, we need to consider not the angular velocity, but the meridional electric current instead. Figure 2 shows this, just for the II and CC configurations now.

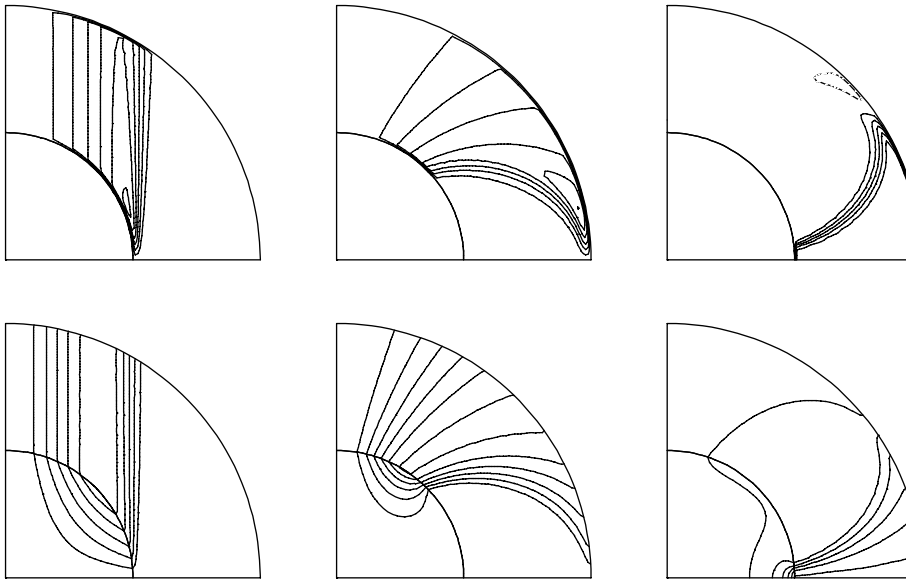

Fig. 2. Streamlines of the meridional electric current, for the three field configurations A, D and Q (from left to right), and the boundary configurations II (top row) and CC (bottom row). The sense of circulation is counter-clockwise for A and D, clockwise for Q, with the recirculation through the outer boundary not shown in the bottom row. Finally, A and D are antisymmetric about the equator, Q is symmetric.

Focussing attention on A first, we note that the overall pattern is strikingly similar for both II and CC, consisting of a broad downward flow inside $\mathcal{C}$ and a narrow upward flow just outside $\mathcal{C}$. The most obvious difference of course is that for II the current must recirculate through the Hartmann layers, whereas for CC it may recirculate through the interior and exterior regions. This difference turns out to be crucial in terms of its effect on the amplitude of the current; having it recirculate through the boundaries is so much easier than having it recirculate through the boundary layers that the CC current is 24 times greater than the II current. Indeed, the scalings with M are completely different; if both boundaries are conducting, the current is independent of M, whereas if either boundary is insulating, it becomes increasingly difficult to recirculate the current through an increasingly thin — scaling as M^{-1} — Hartmann layer, with the result that it then also scales as M^{-1}. And this difference in current amplitudes is precisely what explains the counter-rotating jet for CC but not for II; we note that in both cases the current right at the equator of the inner sphere is radially outward, so

in both cases the Lorentz force $\mathbf{j} \times \mathbf{B}_0$ is in the $-\hat{\mathbf{e}}_\phi$ direction, but only in one case is it sufficiently strong to overwhelm the effect of the rotation in the $+\hat{\mathbf{e}}_\phi$ direction.

Turning to D and Q next, the overall current patterns are again similar for II and CC, but the amplitudes are completely different, with CC independent of M but II scaling as M^{-1}. By working out which way $\mathbf{j}$ and $\mathbf{B}_0$ are oriented, one can show that the Lorentz force at the appropriate places is in the $+\hat{\mathbf{e}}_\phi$ direction now, but once again it is only for CC that it is sufficiently strong to induce such a powerful super-rotating jet. Finally, the reason we already had a slight super-rotation for CI is that the much smaller and thinner inner Hartmann layer poses a far greater limitation to the recirculation of current than the larger and thicker outer layer does, so switching it alone already increases the current by close to an order of magnitude. However, because the existence of the outer layer still limits the scaling of the current to M^{-1}, this slight super-rotation does not increase with M.

We thus realize that switching the boundary conditions from insulating to conducting has very substantial — and initially completely unexpected — effects, but that once we explore all aspects of the solutions, we can make sense of the results. Nevertheless, there are still a great many questions to be answered, such as, why do these jets scale as $M^{0.6}$? The detailed scalings in the regions where they are tangential to the boundary clearly enter into this, but how precisely? And is this $M^{0.6}$ scaling a general result, or does it depend on these specific choices of $\mathbf{B}_0$? Indeed, what is it about these choices of $\mathbf{B}_0$ that yielded counter-rotation for one but super-rotation for the other two? Is it possible, for example, to impose a $\mathbf{B}_0$ that will simultaneously yield counter-rotation in some regions and super-rotation in others? So although we understand the results presented here, there is still a great deal of work to be done on these shear layers and jets.

All of the results presented so far were in the limit of infinitesimally weak rotation, so we might consider next what happens as we gradually increase Re. (Incidentally, we note that one can go to quite large Re before the above assumption of small Rm breaks down, because the ratio of the two, $Rm/Re = \nu/\eta = O(10^{-6})$ for most liquid metals.) At some point inertial effects must surely lead to instabilities of some kind. The (non-axisymmetric) instabilities of the $\mathrm{A_{II}}$ and $\mathrm{A_{CC}}$ configurations have been computed by Hollerbach & Skinner [46], who found that the critical Reynolds number for onset scales as $M^{0.66}$ for $\mathrm{A_{II}}$ and as $M^{0.16}$ for $\mathrm{A_{CC}}$. But again, there is a great deal more work to be done on the instabilities of some of the other configurations.

Instead of considering only very large Hartmann numbers, we could also consider more moderate values. In particular, the limit $M^2 = 0$ corresponds to non-magnetic spherical Couette flow, and given the huge range of interesting phenomena found in that problem (see, for example, the contribution by Junk & Egbers in this volume), it might be worthwhile to see what effect including a moderate magnetic field would have. For example, Fig. 3 shows an initially non-magnetic Taylor vortex pair being distorted by imposing a D or Q field. The effects of the two fields are evidently quite different, with the (predominantly

vertical) D field suppressing the vortices, but the (predominantly horizontal) Q field enhancing them. And perhaps not surprisingly, applying CC boundary conditions again has a greater influence than II. Of course, these are just sample calculations, and no significance should be attached to these particular parameter values, but the magnetohydrodynamic extension of classical spherical Couette flow is clearly another promising area of research, both theoretically and ideally also experimentally.

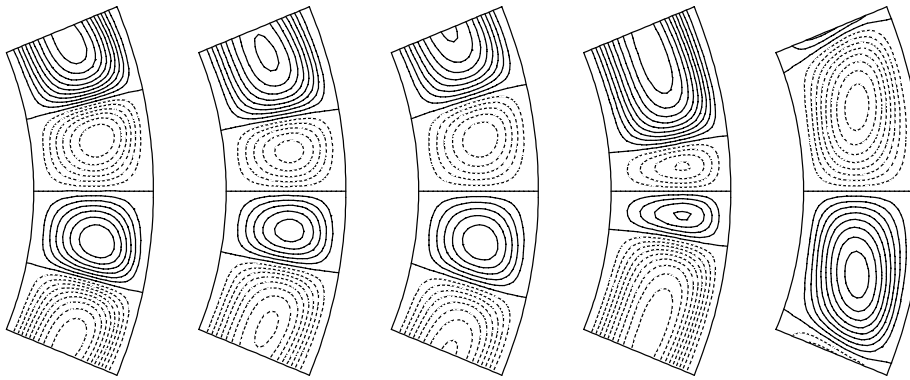

Fig. 3. Streamlines of the meridional circulation, showing the effect of various field configurations on a Taylor vortex pair. From left to right, the initial non-magnetic solution, then $\mathrm{D_{II}}$, $\mathrm{Q_{II}}$, $\mathrm{D_{CC}}$, $\mathrm{Q_{CC}}$. All at an aspect ratio $(r_o - r_i)/r_i = 1/3$, $Re = 1000$, and $M^2 = 250$ for the four magnetic solutions

Finally, uniting the two thus far largely separate aspects of this review, one might wonder whether spherical Couette flow could act as a dynamo. Well, remembering first that dynamo action requires Rm to exceed $O(10)$, and remembering also that $Rm/Re = O(10^{-6})$, we realize that Re would have to exceed $O(10^7)$. While that might just be feasible experimentally, numerically it is not, as such a flow would be fully turbulent. It certainly would be interesting to see how the Lorentz force would ultimately equilibrate such a dynamo though. For example, would the field also be largely small-scale, or would large-scale structures emerge, perhaps aligned with the rotation axis? And would the tension in the field lines perhaps suppress some of the turbulence again? The one thing we can be sure of is that something interesting would emerge!

References

1. R. Hollerbach: Phys. Earth Planet Inter. **98**, 163 (1996)
2. D.R. Fearn: Rep. Prog. Phys. **61**, 175 (1998)
3. G.A. Glatzmaier, P.H. Roberts: Int. J. Eng. Sci. **36**, 1325 (1998)
4. L. Mestel: *Stellar Magnetism* (Oxford University Press, Oxford 1999)

5. M. Núñez, A. Ferriz-Mas, eds.: *Stellar Dynamos: Nonlinearity and Chaotic Flows* (Astronomical Society of the Pacific Conference Series **178**, 1999)
6. W.H. Press, B.P. Flannery, S.A. Teukolsky, W.T. Vetterling: *Numerical Recipes: The Art of Scientific Computing* (Cambridge University Press, Cambridge 1986)
7. P.H. Roberts: *An Introduction to Magnetohydrodynamics* (Elsevier, New York 1967)
8. H.K. Moffatt: *Magnetic Field Generation in Electrically Conducting Fluids* (Cambridge University Press, Cambridge 1978)
9. E.N. Parker: *Cosmical Magnetic Fields: their Origin and their Activity* (Clarendon Press, Oxford 1979)
10. H. Bondi, T. Gold: Mon. Not. R. Astr. Soc. **110**, 607 (1950)
11. E.C. Bullard, H. Gellman: Phil. Trans. R. Soc. Lond. A **247**, 213 (1954)
12. R. Hollerbach: Int. J. Num. Meth. Fluids, in press
13. T.G. Cowling: Mon. Not. R. Astr. Soc. **94**, 39 (1934)
14. S.I. Braginsky: Sov. Phys. JETP **20**, 726 (1965)
15. R. Hide, T.N. Palmer: Geophys. Astrophys. Fluid Dyn. **19**, 301 (1982)
16. D. Lortz, R. Meyer-Spasche: Math. Meth. Appl. Sci. **4**, 91 (1982); Z. Naturforsch. A **37**, 736 (1982)
17. D.J. Ivers, R.W. James: Phil. Trans. R. Soc. Lond. A **312**, 179 (1984)
18. W.M. Elsasser: Phys. Rev. **69**, 106 (1946)
19. F.H. Busse: J. Geophys. Res. **80**, 278 (1975)
20. R. Kaiser, B.J. Schmitt, F.H. Busse: Geophys. Astrophys. Fluid Dyn. **77**, 93 (1994)
21. G.E. Backus: Ann. Phys. **4**, 372 (1958)
22. S. Childress: Théorie magnetohydrodynamique de l'effet dynamo. Report, Department of Mechanics, Faculty of Science, University of Paris (1969)
23. M.R.E. Proctor: Geophys. Astrophys. Fluid Dyn. **9**, 89 (1977)
24. H.K. Moffatt, M.R.E. Proctor: J. Fluid Mech. **154**, 493 (1985)
25. F.E.M. Lilley: Proc. R. Soc. Lond. A **316**, 153 (1970)
26. D. Gubbins: Phil. Trans. R. Soc. Lond. A **274**, 493 (1973)
27. J.J. Love, D. Gubbins: Geophys. Res. Lett **23**, 857 (1996)
28. D. Gubbins, C.N. Barber, S. Gibbons, J.J. Love: Proc. R. Soc. Lond. A, in press
29. J.J. Love, D. Gubbins: Geophys. J. Int. **124**, 787 (1996)
30. R. Hollerbach, D.J. Galloway, M.R.E. Proctor: Phys. Rev. Lett **74**, 3145 (1995); Geophys. Astrophys. Fluid Dyn. **87**, 111 (1998)
31. K.-H. Rädler: Geophys. Astrophys. Fluid Dyn. **20**, 191 (1982)
32. K.-H. Rädler, U. Geppert: In [5], 151 (1999)
33. F. Krause, K.-H. Rädler: *Mean-Field Magnetohydrodynamics and Dynamo Theory* (Pergamon Press, Berlin 1980)
34. E.N. Parker: Astrophys. J. **281**, 839 (1984)
35. C.A. Jones: Phil. Trans. R. Soc. Lond. A, in press
36. K. Zhang, D. Gubbins: Geophys. J. Int., in press; Phil. Trans. R. Soc. Lond. A, in press
37. H. Fuchs, K.-H. Rädler, M. Rheinhardt: Astr. Nach. **320**, 129 (1999)
38. S. Chandrasekhar: Hydrodynamic and Hydromagnetic Stability (Dover, New York 1961)
39. K. Stewartson: J. Fluid Mech. **26**, 131 (1966)
40. R. Hollerbach: Proc. R. Soc. Lond. A **444**, 333 (1994)
41. E. Dormy, P. Cardin, D. Jault: Earth Planet Sci. Lett. **160**, 15 (1998)
42. D.B. Ingham: Phys. Fluids **12**, 389 (1969)
43. S. Vempaty, D.E. Loper: Phys. Fluids **18**, 1678 (1975); Z. Angew. Math. Phys. **29**, 450 (1978)

44. N. Kleeorin, I. Rogachevskii, A. Ruzmaikin, A. Soward, S. Starchenko: J. Fluid Mech. **344**, 213 (1997)
45. S.V. Starchenko: J. Exp. Theor. Phys. **85**, 1125 (1997); Phys. Fluids **10**, 2414 (1998); Studia Geophys. Geodaet. **42**, 314 (1998)
46. R. Hollerbach, S. Skinner: in preparation

Intermittency at onset of convection in a slowly rotating, self-gravitating spherical shell

Pascal Chossat

I.N.L.N. (CNRS and Université de Nice)
1361 Route des Lucioles
Sophia-Antipolis-06560 Valbonne, France

Abstract. I present a joint work with Guyard and Lauterbach [4] which shows the existence and stability of a robust heteroclinic cycle near onset of convection in a self-gravitating, slowly rotating spherical shell filled with a fluid. The consequence of this is the existence of a regime characterized by long periods of time spent near an axisymmetric steady-state followed by sudden bursts of "turbulent flow" which settles down to another axisymmetric state with fluid flow moving in the opposite direction to the previous one. The process repeats indefinitely but non-periodically.

1 Introduction

Can thermal convection in a rotating spherical shell sustain flows whose dynamics is characterised by long periods of time of quasi-stationary and axisymmetric pattern aligned with the axis of rotation, followed by sudden bursts of "turbulence" which relax after a while to a quasi-stationary, axisymmetric pattern, however with reversed direction of flow? A positive answer to this question may have some implications in geo- and astrophysics. It has been recently shown by Chossat and Guyard[3] that it is indeed the case, at least when the rate of rotation of the system is low, that is, when the buoyancy forces dominate the inertial ones. This behaviour is associated with the existence of a dynamically invariant object for the model equations which is specific to systems with symmetry and which is called a "robust heteroclinic cycle". The occurrence of such objects and their experimental interpretation are now well-known in hydrodynamics. The first and most famous example was found by (Busse and Clever[2], in the problem of the intermittent exchange of roll patterns in rotating planar convection (the so-called Küpper-Lortz instability). The simple - but illuminating - mathematical analysis of Guckenheimer and Holmes[7]) for this problem, led to a new and quite successful activity in bifurcation theory and its applications for systems with symmetry. We shall explain below what is meant by "robust heteroclinic cycles".

The symmetries which are responsible for such a behaviour in fluid flows can be quite simple (like $O(2)$, the symmetry group of the circle). In our case of interest, however, the situation is more intricate. We are interested by the onset of convection in a spherical, self-gravitating fluid layer. As a first approximation, the domain is set at rest and perfectly spherical. Then, the standard model (Navier–Stokes and heat equations coupled in the Boussinesq approximation)

C. Egbers and G. Pfister (Eds.): LNP 549, pp. 317–324, 2000.

is invariant under any orthogonal transformation of the domain (invariance by the action of the group $O(3)$). This implies a high degree of degeneracy which makes the analysis more involved, but also which gives a much richer bifurcation diagram and dynamics. When the domain is allowed to rotate around an axis, the Coriolis force which enters in the momentum equation breaks part of that symmetry. The strategy will then be to look first for the existence (bifurcation) and stability of robust heteroclinic cycles in the non-rotating case, then to study their perturbation as slow rotation is set in. The methods are those of equivariant bifurcation theory (see Chossat and Lauterbach[5]). Numerical simulations on the center manifold confirm this dynamics.

2 Heteroclinic cycles in systems with $O(3)$ symmetry and the spherical Bénard problem

In a paper which appeared in 1986, Friedrich and Haken[6] reported on a thorough numerical investigation of the dynamics on an approximate center manifold for the onset of convection in a fixed spherical, self-gravitating shell of fluid. They considered the classical model in Boussinesq approximation, which assumes that the density of the fluid is an affine function of the temperature difference across the domain in the term of buoyancy force, but is constant everywhere else. Their model was set to the case when the radius ratio η of the inner boundary sphere by the outer one is close to a critical value η_c at which the linear center manifold is the sum of the irreducible representations of dimensions 3 and 5 of the group $SO(3)$. We shall denote these spaces by V_1 and V_2 respectively. These can be viewed as the linear spans of the spherical harmonics $Y_{1k}(\vartheta, \varphi)$, $-1 \leq k \leq 1$, and $Y_{2m}(\vartheta, \varphi)$, $-2 \leq m \leq 2$ respectively. The exact value of η_c depends on the physical parameters in the model, especially on the boundary conditions (which are assumed to be homogeneous in order to have a spherically symmetric basic state of pure conduction). Typically, $\eta \sim 0.15$. Friedrich and Haken used a set of equations truncated at order 3 in the "amplitudes" to approximate the dynamics on the center manifold. The dependence of these equations with respect to the various parameters in the problem can be found in their paper. The typical bifurcation parameter is the Rayleigh number which characterises the strength of buoyancy forces. The other important parameters in the mathematical analysis are η and the Taylor number, proportional to the square of the angular speed Ω of rotation of the domain. In Friedrich and Haken's paper, Ω is set equal to 0. The other characteristic quantities (like e.g. the Prandtl number) are supposed fixed.

In their simulations they found, for a "wide" range of parameter values, an intermittent-like dynamics between two different kinds of steady axisymmetric states which they named α-cells and β-cells and which correspond to solutions of the amplitude equations with a vanishing component on the space V_1.

In Chossat and Armbruster[1], I proposed in 1990 an explanation for this behaviour, which I will expose below. However it turns out that this was not sufficient to fully explain the phenomenon observed by Friedrich and Haken. The

complete explanation will be given in the next section.
The following facts are well-known.

(i) The reduction to the center manifold can be set up so that the resulting ODE in $V = V_1 \oplus V_2$ is invariant under the action of the symmetry group (namely $O(3)$ in our case). Therefore we are dealing with an equation

$$\dot{z} = F(z, \mu) \tag{1}$$

where $z = (x, y) \in V_1 \times V_2$ and μ is a multi-parameter. We allow to freely vary the Rayleigh number (proportional to the temperature difference across the shell and responsible for the convective instability) and the radius ratio η which we assume close to η_c. Moreover, if we denote by

$$T(g)z = (T^1(g)x, T^2(g)y), \quad g \in O(3)$$

the representation of $O(3)$ in V, then $F(T(g)z, \mu) = T(g)F(z, \mu)$ for all $g \in O(3)$, $(z, \mu) \in V \times R^2$. F is said $O(3)$-*equivariant*.

(ii) Given a $z \in V$, the subgroup G_z of $O(3)$ which consists of all the elements in $O(3)$ which let z fixed, is called the *isotropy group* of z. Given an isotropy group H, we can define the subspace $Fix(H)$ of V which consists of all points in V which are fixed by H (this is a linear space because the action of the group is linear). Notice that certain elements of $Fix(H)$ may have isotropy group larger than H. If H and H' are isotropy groups such that $H \subset H'$, then $Fix(H) \supset Fix(H')$. Now the basic property of symmetric ODE's is that if z_0 is an initial condition in some $Fix(H)$, then the corresponding trajectory $z(t)$ lies in $Fix(H)$ for all t. This is because F is $O(3)$-equivariant. Clearly, if $H' = gHg^{-1}$ for some $g \in O(3)$, then $Fix(H') = gFix(H)$, and if $z(t)$ is a solution in $Fix(H)$, then $z'(t) = gz(t)$ is another solution lying in $Fix(H')$. We say that z and z' belong to the same *group orbit*. Physically these solutions are identical.

Up to group conjugation, Fig. 1 shows the containment relations between isotropy groups and corresponding fixed-point subspaces for the action of $O(3)$ in V. The coordinates in the spaces V_1 and V_2 are defined as follows. We note $x = (x_{-1}, x_0, x_1) \in V_1$, where x_j is the coordinate along the spherical harmonic $Y_{1,j}$. Note that $x_{-1} = \bar{x}_1$. In particular the "axisymmetric component" x_0 is real. Similarly, we note $y = (y_{-2}, \ldots, y_2) \in V_2$, where y_k is the coordinate along the spherical harmonic $Y_{2,k}$. Note that $y_{-k} = (-1)^k \bar{y}_k$. Also, y_0 is "axisymmetric" and real.

We denote by L the axis $\{y_0\}$, by P_1 the plane $\{y_0, y_2 + y_{-2}\}$, by P_2 the plane $\{x_0, y_0\}$ and by S the 3-space $P_1 + P_2$. All these subspaces are flow-invariant. Another important fact about these subspaces is that P_1 contains overall three copies of L: L itself plus L' and L'', where L' is obtained from L by a rotation by $2\pi/3$ in P_1, and L'' is obtained from L by a rotation of angle $4\pi/3$. These rotations in the space P_1 correspond to physical rotations of the spherical shell

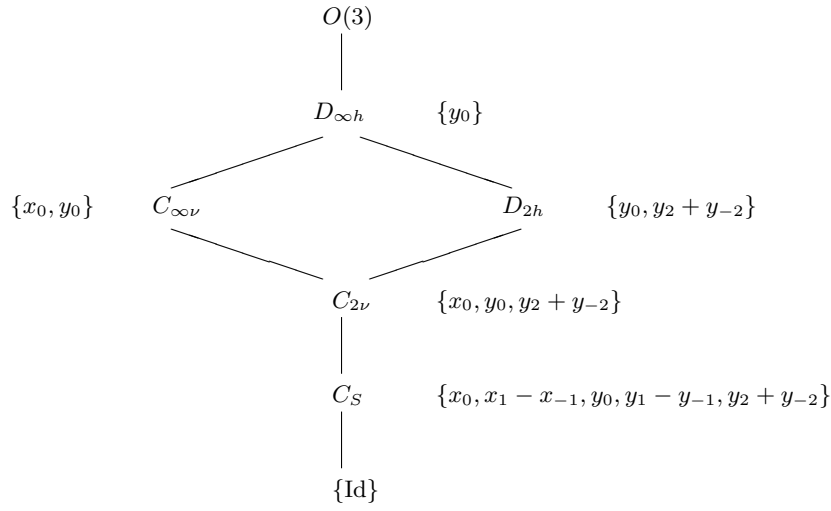

Fig. 1. Containment relations of the isotropy subgroups for the action of $O(3)$ in V (Schönflies notation for the subgroups of $O(3)$)

by $\pm\pi/2$ along the vertical axis and by $\pi/2$ along an axis in the equatorial plane (the first coordinate axis). On the other hand, there is only one copy of L in P_2 and only one copy of P_1 and P_2 in S.
The following bifurcation and dynamical features were proved to exist for an open set of parameter values. The proofs rely on the knowledge of the equivariant structure of the map $F(z, \mu)$ and the fact that coefficients of the linear, quadratic and cubic terms (in the Taylor expansion in z) satisfy certain relations thanks to the special form of the nonlinearity in the Bénard problem (see CHOSSAT AND GUYARD[3]).

(i) Two equilibria bifurcate in L, one with negative y_0 is called α and the other with positive y_0 is called β. These two states are axisymmetric and consist of two identical "cells" separated by the equatorial plane (Fig. 2).
They are stable along the axis L, but they do not belong to the same group orbit: they are not mapped one onto the other by an orthogonal transformation. Corresponding to these equilibria in L, there are two other pairs of equilibria in P_1, lying respectively in L' and in L''. We note them α', β' and α'', β'' respectively. Hence α' and α'' belong to the group orbit of α while β' and β'' belong to the group orbit of β.

(ii) The α, α' and α'' equilibria are stable in P_1, while the β, β' and β'' equilibria are unstable in P_1. Moreover there exist heteroclinic connections from the β's to the α's as shown in Fig. 3.

(iii) α is unstable in P_2 while β is stable. Moreover there exists heteroclinic trajectories in P_2 from α to β (see Fig. 3).

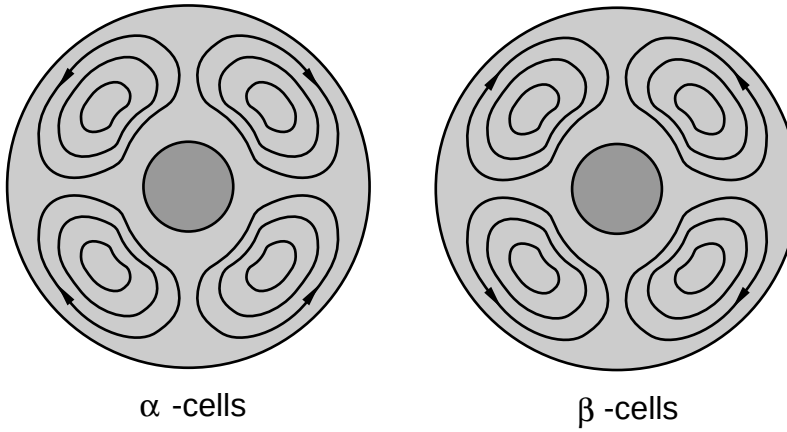

Fig. 2. The α and β-cells (schematic view in a meridian plane).

There are two crucial observations to be made here. Firstly, the heteroclinic trajectories in P_1 and P_2 are *robust* against $O(3)$-equivariant perturbations, because these are saddle-sink connections in flow-invariant subspaces. Secondly, these connections realize a *cycle*. Indeed, starting for example from α, we have a succession of connections to β in P_2, then to α' and α'' in P_1. However α' and α'' belong to the group orbit of α, hence by symmetry they must connect to β' and to β'' by robust heteroclinic trajectories which are the symmetric to those trajectories in P_2, but now lying in planes P_2' and P_2''. Now, β' and β'' themselves are connected back to α in P_1. The invariant set so realized is called a *heteroclinic cycle*.

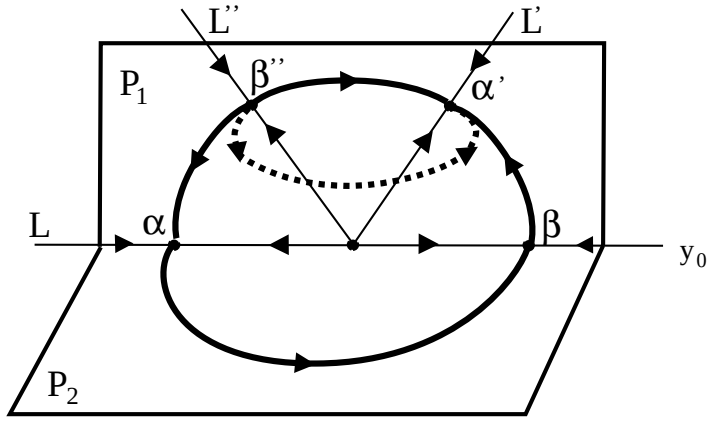

Fig. 3. Dynamics in the space S (an example of trajectory connecting α to α' in S is shown in dashed line).

The interesting property of a heteroclinic cycle is the following. Suppose this invariant set is asymptotically stable. Starting in some neighbourhood of the cycle, a forward trajectory will therefore get closer and closer to the equilibria in the cycle as t grows, and therefore it will spend more and more time in the vicinity of these equilibria. Ideally, this time will grow to infinity so that the dynamics dies out. However in physical applications, small and unpredictable fluctuations are always present, so that a state which is inside a very small neighbourhood of an equilibrium will undergo some excursion (slightly) away from this neighbourhood and involving components along the unstable manifold of that equilibrium. These components will grow exponentially and after finite time, the solution will therefore follow the corresponding heteroclinic connection and jump to the next equilibrium. Asymptotic stability insures that the solution will not diverge outside some neighbourhood of the heteroclinic cycle. The resulting dynamics will exhibit intermittency, with jumps from one equilibrium to the next at times which typically follow a random statistical distribution (see Stone and Holmes[9]).

Unfortunately the usual conditions of asymptotic stability for this kind of heteroclinic cycles are not met in this case (see krupa and Melbourne[8] or Chossat and Lauterbach[5] for an exposition of the stability analysis of robust heteroclinic cycles). This is due to the fact that at the equilibrium point β'' for example, the direction transverse to the plane P_1 in S is unstable. Moreover a closer look at their report shows that in fact the trajectories they have computed do not exactly follow our heteroclinic cycle. Therefore a more careful analysis must be undergone in order to understand this behaviour. This task was achieved by Chossat et al.[4]. They showed that all the unstable directions at β (and at its symmetric images under $O(3)$) correspond to heteroclinic orbits which connect β to the $O(3)$-orbit of α. For example a two dimensional manifold of trajectories connects β'' to α' in S (see one such trajectory in Fig. 3). The resulting set of connections realises a "generalised" heteroclinic cycle. It was shown that this rather complicated object was asymptotically stable under the conditions of Friedrich and Haken numerical set-up.

3 Perturbation induced by a slow rotation of the domain

The relevant effect of the rotation on the model is to induce a Coriolis force. This force has the form $\boldsymbol{k} \times v$, where $\boldsymbol{k} = (0, 0, 1)$, and it is easy to check that it commutes with rotations of axis $\boldsymbol{k}$ and reflection through the plane perpendicular to $\boldsymbol{k}$. Therefore the perturbation provokes a forced symmetry-breaking $O(3) \to C_{\infty h}$. We assume that the speed of rotation is close to 0, so that the center manifold reduction is still valid. We also assume that the generalized heteroclinic cycle exists (the bifurcation parameters are fixed), and moreover that the stability condition derived in the previous section is satisfied.

The first question to ask is what happens to the flow-invariant subspaces? The answer is that some of them persist, like the plane P_2 and the space W, S disappears completely, and P_1 disappears too, but it is important to notice that

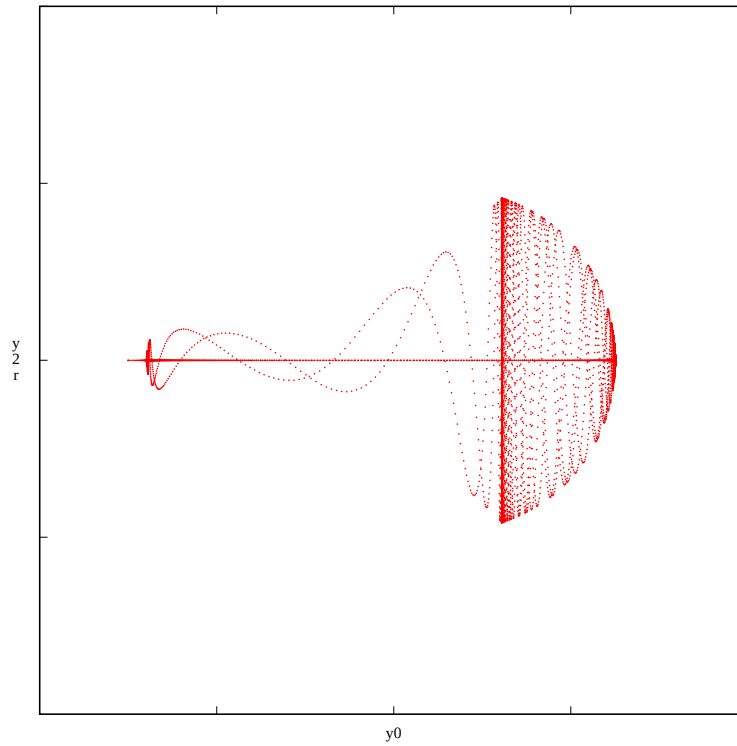

Fig. 4. Projection on P_1 of a trajectory near the heteroclinic cycle for the perturbed system

P_1 is a slice, under the action of $C_{\infty h}$, of the space $\tilde{S} = \{(y_0, y_2, \bar{y}_2)$. Hence $\tilde{S}$ is now a fixed-point subspace for the isotropy group $C_{2h} = D_{2h} \cap C_{\infty h}$ and is therefore flow-invariant.

Clearly α and β are fixed under $C_{\infty h}$ and therefore, by hyperbolicity argument in $\tilde{S}$, these equilibria persist after perturbation. On the other hand, the $C_{\infty h}$-orbits of α' and β' are circles inside $\tilde{S}$, and it can be shown that the flow on these circles is non trivial (rotating waves with a slow drift frequency when the perturbation is not zero). Hence part of the equilibria that we had before the perturbation have disappeared and are replaced by periodic orbits, which we denote by RW_α and RW_β.

It remains to see which heteroclinic connections persist. The connection $\alpha \to \beta$ in P_2 persists because this plane persists. The connection $\beta \to \alpha'$ (or α'') in P_1 is replaced by a robust connection $\beta \to RW_\alpha$ in S. It can be shown that the connection $\alpha' \to \beta'$ (and similarly with $''$ replacing $'$) is generically not replaced by robust connections $RW_\alpha \to RW_\beta$. However, in the persisting invariant space W, the unstable manifold of RW_α is included into the stable manifold of the equilibrium α (see Chossat et al.[4] for a more precise statement and for a proof). This insures the existence of a heteroclinic cycle which now follows the

following path:

$$\alpha \to \beta \to RW_\alpha \to \alpha.$$

An additional argument allows us to insure that this object is asymptotically stable if the generalized heteroclinic cycle was so before perturbation. Figure 4 shows a trajectory following this heteroclinic cycle in projection on the plane P_1. The rotating wave RW_α is visualized by the thick vertical segment (it is seen from the side).

References

1. D. Armbruster, P. Chossat. *Heteroclinic orbits in a spherically invariant system*, *Physica* D 50 (1991) 155-176.
2. F. H. Busse and R.M. Clever. *Nonstationary convection in a rotating system*, in *Recent Development in Theoretical and Experimental Fluid Mechanics*, Eds U. Müller and K. G. Roesner and B. Schmidt, Springer Verlag, Berlin (1979), 376-385.
3. P. Chossat, F. Guyard. *Heteroclinic cycles in bifurcation problems with O(3) symmetry, J. of Nonlin. Sci.*, **6**, 201-238 (1996).
4. P. Chossat, F. Guyard and R. Lauterbach. *Generalized Heteroclinic Cycles in Spherically Invariant Systems and their Perturbations*, J. Nonlinear Sci. **9**, p. 479-524 (1999).
5. P. Chossat, R. Lauterbach. *Methods in equivariant Bifurcation and Dynamical Systems*, to appear in Advanced Series in Nonlinear Dynamics, World Scientific Publishing, Singapur (1999).
6. R. Friedrich, H. Haken. *Static, wavelike and chaotic thermal convection in spherical geometries*, *Phys. Rev. A* **34** (1986), 2100-2120.
7. J. Guckenheimer and P. Holmes. *Structurally stable heteroclinic cycles*, *Math. proc. Cambridge Phil. Soc.* **103** (1988), 189-192.
8. M. Krupa, I. Melbourne. *Asymptotic stability of heteroclinic cycles in systems with symmetry*, *Ergod. Th. Dyn. Sys.* **15**, 1 (1995), 121-147.
9. E. Stone, P. Holmes. *Noise induced Intermittency in a Model of a Turbulent Boundary Layer*, *Physica D* **37** (1989), 20-32.

Control of secondary instability of the crossflow and Görtler-like vortices (Success and problems)

Viktor V. Kozlov and Genrich R. Grek

Institute of Theoretical and Applied Mechanics,
Russian Academy of Sciences, Siberian Branch,
Novosibirsk 630090, Russia

Abstract. The secondary instability on a group of crossflow vortices developing in a swept wing boundary layer is described. It is shown that, for travelling waves, there is a region of linear development, and the growth rate of disturbances appreciably depends on the separation between the vortices. Methods of controlling the secondary instability of the vortices by a controlled wave and local suction are proposed and substantiated. The stability of a flat plate boundary layer modulated by Görtler-like stationary vortices is described. Vortices were generated inside the boundary layer by means of roughness elements arranged in a regular array along the spanwise (z) direction. Transition is not caused directly by these structures, but by the growth of small amplitude travelling waves riding on top of the steady vortices. This situation is analogous to the transition process in Görtler and cross-flows. The waves were found to amplify up to a stage where higher harmonics are generated, leading to turbulent breakdown and disintegration of the spanwise boundary layer structure. For strong modulations, the observed instability is quite powerful, and can be excited "naturally" by small uncontrollable background disturbances. Controlled oscillations were then introduced by means of a vibrating ribbon, allowing a detailed investigation of the wave characteristics. The instability seems to be associated with the spanwise gradients of the mean flow, $\partial U/\partial z$, and at all z-positions, the maximum wave amplitude was found at a wall-normal position where the mean velocity is equal to the phase velocity of the wave, $U(y) = c$, i.e., at the local critical layer. Unstable waves were observed at frequency well above those for which Tollmien-Schlichting (TS) waves amplify in the Blasius boundary layer. Excitation at lower frequencies and milder basic flow modulation showed that TS-type waves may also develop. Study of the transition control in that flow by means of riblets shows that the effect of the riblets is to suppress longitudinal vortex structures in a boundary layer. The boundary layer becomes stable with respect to high-frequency travelling waves, which cause the transition in the absence of the riblets.

Part I. Active control over secondary instability in a swept wing boundary layer

1. Introduction

Most methods of controlling the laminar-turbulent transition in near-wall flows, which are well developed for two-dimensional flows, are passive, since, as they are used, there is no feedback path for monitoring and varying the flow structure, i.e., there is no possibility to change the degree of the action exerted on the flow. The best known among these methods are boundary-layer suction, wall

C. Egbers and G. Pfister (Eds.): LNP 549, pp. 327–351, 2000.

cooling or heating, and employing favourable pressure gradients. Thus, it was shown in [1] that the slot suction is able to considerably decrease the amplitude of a two-dimensional instability wave, the TS wave, and delay the transition to turbulence. The influence of suction was found to be appreciable only at the stage of linear growth of the waves; and if nonlinear interactions are observed and three-dimensional structures form in the flow, the slot suction appears to be less effective. Riblet-type devices are also often used [2–4], they are placed into the boundary layer to suppress formation of or interaction between ordered three-dimensional structures, for example, Λ-vortices [4]. An immediate action on the TS waves arising in the flow is an alternative method for solving the problem of interest. In this approach, the disturbances are to be cancelled or, at least, suppressed due to superposition of linear waves. Various methods of generation of controlling waves in a boundary layer can be used. For this purpose, it is required to construct an actuating device which is able to effectively generate another wave of the same amplitude but the opposite phase. For example, in [5–8] the disturbances in a boundary layer are generated by a vibrating ribbon or wire, a system of heating elements, sound, blowing-suction through perforated holes, etc. The cancelling wave generated by either a second wave generator located downstream or a vibrating surface is used to minimize the amplitude of the initial TS wave. These experiments proved it possible to break two-dimensional TS waves in a boundary layer by generation of a controlling wave of an appropriate amplitude. However, in a number of cases, the stage of development of a two-dimensional instability can be too short or even absent. Three-dimensional flows over a swept wing, a rotating disk, or a concave surface serve as examples. In these cases, the developing instability strongly depends on the local conditions in the stationary vortices arising: the waves originating in neighbouring vortices can differ in amplitudes [9]. The nonuniformity of the field of disturbances results in that, normally, the laminar-turbulent transition occurs in each of the vortices independently, which gives rise to a typical tooth-shaped transition line. For such flows, the use of two-dimensional passive methods proved to be ineffective since it results in different effects for different points in the flow. To exert the control over instability in such three-dimensional flows, active methods can be also used. The schematic diagram illustrating the active control over instability consists in the following [10]. Receiving signals from sensitive elements placed in the flow, an analyzing device processes them and determines the amplitudes, phases and other parameters of the disturbances. Next, an actuating device either generates in the flow three-dimensional disturbances of the same characteristics but of the opposite phase, or implements local suction or other spatially local actions on the flow. The sensitive elements and the actuating devices should be installed close to each other to avoid as completely as possible any variation of flow properties in the gap between them.

Elaboration of such control methods necessitates a special, e.g., microfabrication technology to be used [10,11], which permits fabrication of separate devices or even integral aggregates of extremely small dimensions. Moreover, an inter-

active distributed control is possible over an assembly which combines on one surface sensitive elements, actuating devices and microprocessors.

The study [12] presented below continues previous studies [2,13,14] of the properties of waves and mechanisms of origination of secondary instability of crossflow stationary vortices in a swept wing boundary layer. Two methods are proposed to actively control the transition to turbulence in this flow: mutual suppression of waves and local suction. This study presents also the characteristics of disturbances that arise in the system of crossflow vortices.

2. Experimental procedure and equipment

The experiments were carried out in a subsonic, low-turbulent closed-layout wind tunnel. The wind tunnel had a 4 m-long test section with the cross-sectional area 1x1 m. The turbulence level of the flow in the test section of the tunnel did not exceed 0.04% of the free-stream velocity ($U_0 = 8.5$ m/s).

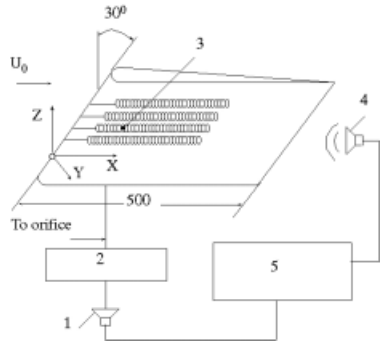

Fig. 1. Schematic of the experiment.1 - loudspeaker for wave generation by blowing-suction; 2 - phase rotation; 3 - orifice; 4 - loudspeaker for wave generation by sound; 5 - audio-signal generator

As a test model (see Fig.1), a C-12 high-lift airfoil was chosen, which had the slip angle of 30° and the wing chord length of 500 mm. The airfoil consisted of a 56 mm-long symmetrical ogival nose with the largest thickness amounting to 16% of the chord. The nose gradually transformed into two equal converging plane surfaces. Special tests [12,13] showed that, in the measurement region ($X > 130$ mm), the streamwise velocity gradient was absent, and the mean velocity profile $U(Y)$ was close to the Blasius form. All measurements of the mean velocity as well as of its fluctuations were carried out in the region of linear development of travelling waves.

Stationary disturbances were generated by roughness elements fixed to the surface. Their arrangement on the wing is shown in Fig.1, and their shape and dimensions were the same as in [13]. In the majority of the measurements, the distance between the roughness elements was 13 mm, which, as special tests showed, was close to the characteristic scale of natural vortices arising over this oblique airfoil under the conditions adopted.

To generate travelling waves within the range of instability of stationary vortices with controlled amplitude and phases, the sound was used produced by

a dynamic loudspeaker installed downstream of the model. The frequency and amplitude of the sound were set by an audio-signal generator.

To introduce a suppressing signal, wave generation by blowing-suction through a round orifice 0.8 mm in diameter was used, the orifice being located at a distance $X = 170$ mm along the crossflow coordinate, under one of the vortices. Through a pneumatic pipeline, the orifice was connected to the loudspeaker, which produced periodic pressure oscillations. The amplitude of these signals was set by the same audio-signal generator, with the possibility provided to vary the phase of the disturbances being introduced, by varying the length of the pipeline within certain limits. The same orifice was used to organize local suction. The mean (U) and fluctuating (u') streamwise velocities were measured by a single-wire probe of the constant-temperature type connected with hot-wire anemometer. To measure the V-component of the mean-velocity vector, an X-shaped double-wire probe was used. In this case, the voltages across the wires were determined by a pair of independent hot-wire anemometers.

3. Measurement results

3.1. Characteristics of waves developing on a group of vortices

As noted above, a stationary streamwise vortex formed behind each roughness element, on which travelling waves developed. The distributions of the streamwise-velocity defect as compared to the undisturbed boundary layer $\Delta U/U_0$ and those of oscillations at the frequency of the sound excited are shown in Fig.2.

The solid curve shows conventional contours of the vortices, the distance between which amounted to 13 mm. The distribution of the streamwise-velocity

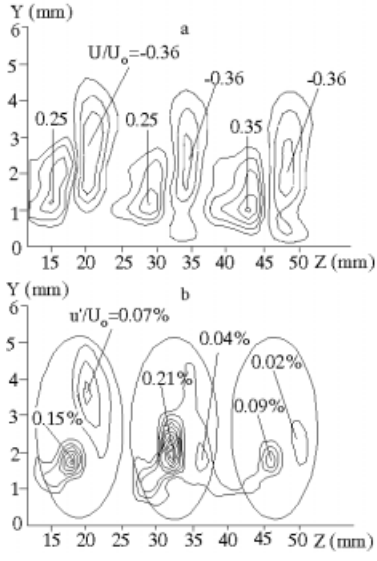

Fig. 2. Distributions of the streamwise-velocity defect (a) and those of oscillations at the frequency of excitation by sound (b) in a system of vortices. The ovals schematically outline the vortices.

defect consists of pairs of an excess and deficit of the velocity, each pair characterizing one stationary vortex. Their amplitudes $\Delta U = (U_{max} - U_{min})/U_0$ fall in the range 0.30–0.35, the values of the defects for different vortices being nearly the same. Nevertheless, the intensities of the oscillations in the neighbouring vortices differ appreciably (Fig. 2, b). This difference can be explained by different conditions brought about by stationary vortices, the difference being in qualitative agreement with previously reported experimental results [9]. The question of the linearity of the waves arising on a set of vortices was studied under controlled wave excitation [12]. The curves of growth of the wave intensity for the wave excitation amplitude at the end of measurements equal to 0.87 and 0.27% were measured. In both cases the curves of growth coincide, which is indicative of the amplitude independence of the growth. No evidence for origination of the difference harmonics or occurrence of other nonlinear effects was obtained. From the distribution of the fluctuating-velocity phases, it was shown that, for the both amplitudes of the induced sound, the propagation velocity of natural disturbances along the vortex remains unchanged (as in the case of an isolated vortex), amounting to 0.6 of the free-stream velocity. The growth rate of the disturbances was found to be sensitive to the change of the crossflow shift of the mean velocity depending on the distance between the stationary vortices. Results of measurements showed that, a s the vortices approach one another, the amplitude of oscillations decreases throughout the whole spectrum of instability. For example, when the distance between the stationary vortices (ΔZ) changes from 16 to 8 mm, the growth factor of the most unstable wave in the packet decreases from 0.08 down to 0.03. It should be noted that, despite this change in the amplitude, the packet of disturbances behaves as an integrity, and the change in the growth amplitude is observed in the whole range of instability.

3.2. Interaction between the neighbouring vortices

To analyze the obtained dependence of the increments on ΔZ, double-wire measurements were carried out. The X-shaped probe measured the U and V velocity components in a system of vortices. The measurements were conducted by the probe, which travelled parallel to the surface (at constant Y) along the Z axis with a 1-mm step for ten values of Y. The intermediate values were obtained by interpolation of the data by cubic splines. Figure 3 shows distributions of the defect of the mean streamwise velocity U (a) and those of the normal velocity V (b) for $\Delta Z = 13$ and 16 mm in the cross-section $X = 245$ mm. The velocity V is seen to decrease as the vortices come close together. For instance, for $\Delta Z = 16$ and 13 mm, its maximum equals 2.98 and 1.76%, respectively. This suppression of the velocity V results in a decreased defect of the velocity U_0, or, in other words, as the vortices approach each other, they begin to interact. However, the approach of t he vortices to each other only slightly influences the shape of the distributions of the velocity defect.

A comparison between Figs.3,I,a and 3,II,b shows nearly identical distributions of the maxima and minima of the velocity U_0, which characterize the vortices, as well as the ascending and descending fluxes of the velocity V that give

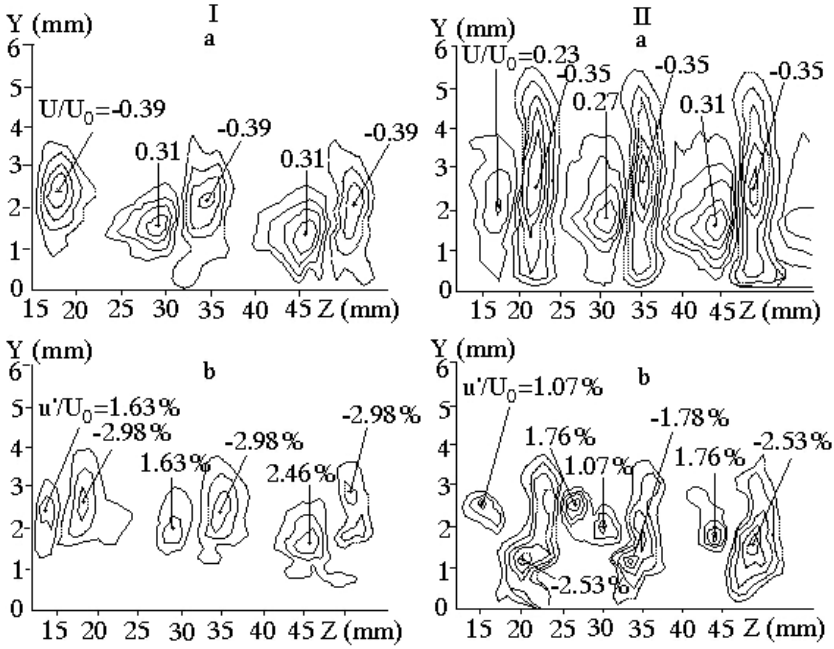

Fig. 3. Distributions of the defects of the U (a) and V (b) velocities in a set of stationary vortices in the cross-section $X = 245$ mm for $\Delta Z = 13$ mm (I) and 16 mm (II).

rise to the extrema at the preserved general shape of the isolines. For instance, for $\Delta Z = 16$ mm, the negative velocity defect (a maximum) amounts to 0.31, whereas for $\Delta Z = 13$ mm it equals 0.27 of the free-stream velocity. When the vortices come as close tog ether as ($\Delta Z = 8$ mm, this quantity decreases down to $0.23U_0$. Thus, the amplitude of the vortex decreases and, hence, the "intense" velocity shear layers, which have a predominant influence on the evolution of instability in the flow, diminish. The latter impedes the growth of secondary disturbances at the preserved general pattern of the flow, which can appreciably delay the transition. In view of the above, it can be concluded that a change in the distance between the neighbouring vortices in a "natural" case can play an important part in the development of secondary waves.

3.3. Propagation of travelling disturbances in a system of vortices

The possibility of passage of disturbances from one vortex to another and interaction between the waves that develop on different vortices are important aspects of the instability pattern. To study this matter, the generation of instability waves with the help of a periodic blowing-suction was used and compared with the case of wave generation by sound. The measurements were carried out in the cross-section $X = 270$ mm, 100 mm away from the orifice. The distributions of the fluctuating velocity in the system of vortices at the frequency of

wave excitation upon wave generation by an acoustic field and by a periodic blowing-suction are shown in Fig.4. It is seen that an instability wave during blowing-suction arises only on one (central) vortex, under which the orifice is located. The distribution fluctuations for the two method of wave generation is identical to the case of an isolated vortex [14].

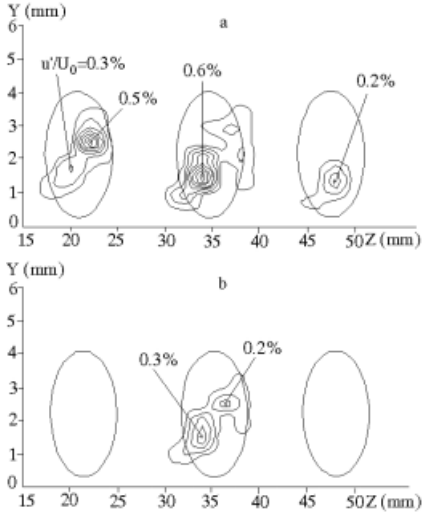

Fig. 4. Distributions of disturbances in a set of vortices at wave excitation by sound (a) and by blowing-suction (b). The ovals schematically outline the vortices.

4. Study of mutual cancellation of the waves

Based on the wave properties studied in the previous section, a method of exerting local control over the instability on one of the vortices can be proposed: with a proper choice of the phase and amplitude of a disturbance generated by a periodic blowing-suction, one can control the development of waves excited by an external factor, e.g., sound.

The measured spectra of the fluctuating velocity in the central part of one of the vortices studied are illustrated the possibility of changing the amplitude of disturbances for interfering waves of equal frequencies generated by different sources. The spectra of disturbances for the waves generated at the frequency f=320 Hz by sound and periodic blowing–suction through the orifice separately and in combination for antiphasal and cophasal excitation showed that at the antiphasal generation, the amplitude of the resulting signal is 0.14%, which is lower than its initial value (0.2 and 0.23% for the cases of generation by sound and by blowing-suction, respectively), i.e., the amplitude of the sound-induced waves is seen to have decreased. And, on the contrary, in the case of cophasal generation, the resulting amplitude increases noticeably to 0.45% (the amplitudes of the waves generated by sound and by blowing-suction were 0.2 and 0.27%, respectively) [12].

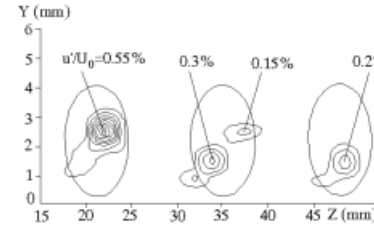

Fig. 5. Distribution of disturbances in a set of vortices during a combined excitation of waves with opposite phases: by sound and by blowing-suction. The ovals schematically outline the vortices.

A more detailed interaction pattern for the waves generated by the two sources for the case of antiphasal generation is depicted in Fig.5. The parameters of the waves generated singly were identical to those in Fig.4. The amplitude of the sound-induced waves, which was equal to 0.6% (see Fig.4,a), has decreased throughout the entire region occupied by the vortex in accordance with the 0.3%-amplitude of the suppressing signal (see Fig.4,b) and was found to equal 0.3% (see Fig.5). It is worth noting that t he subtraction of the waves occurs throughout the entire region occupied by the vortex, which is clear from inspection of the second side maximum. The amplitude of this maximum has also decreased from 0.2% at blowing-suction down to 0.15% at the combined generation. At the same time, the amplitude of the disturbances on the neighbouring vortices remained unchanged, since no disturbances on them were generated by blowing-suction. With a more exact adjustment of the phases, one can gain a more pronounced suppression of disturbances. Thus, in the three-dimensional flow under study, it was shown possible to control the instability through mutual cancellation of the disturbances by an additional generation of waves with opposite phases. Provided that the source to be used can reproduce the whole wave packet with preset amplitude-frequency characteristics, full suppression of waves is possible, and the laminar-turbulent transition can be delayed.

5. Localized continuous suction

In all the experiments described below the measurements were carried out for the suction run immediately behind one of the vortices. The dependence of the amplitude of waves of secondary instability on the suction rate showed that the suction to noticeably affect the amplitude of the oscillations in the vortex core, and the more intense the suction, the stronger the action (see Fig.9 [12]). Even for the weakest suction, when its rate was comparable with the suction used in a two-dimensional flow [1], the difference in the wave amplitudes was quite appreciable. This shows that even weak suction can be successfully implemented in the case when several successive orifices are used.

Spectral measurements in the vortex core showed that suction affects the entire spectrum of wave instability. For this reason, it is apparent that the action of suction, as in the case of a Blasius boundary layer, is exerted indirectly, through changes in the characteristics of the flow in stationary vortices. The experimental results for the case with suction are shown in Fig.6.

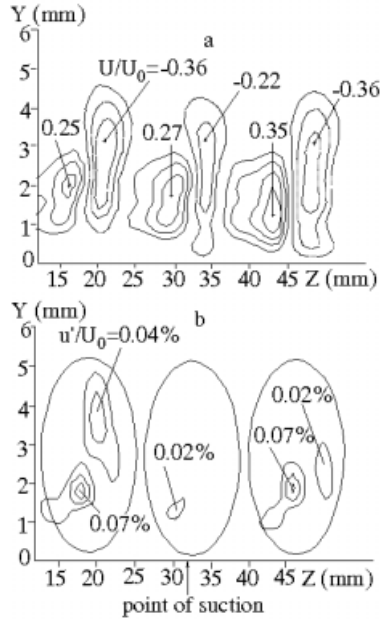

Fig. 6. Distribution of the mean-velocity defect (a) and that of travelling disturbances (b) in a system of vortices during suction. The mean mass-low velocity $\Delta U/U_0$ in the orifice is 1.2.

Comparing them with Fig.2, which shows the experimental results without suction, one can see that the local action of suction results in a tenfold decrease in the amplitude of oscillations on the middle vortex. At the same time, the action on the neighbouring vortices proved to be insignificant, being comparable with the overall measurement error or with the action exerted on the vortices situated in the neighbourhood at a high intensity of suction.

As expected, the suction strongly affects the mean-velocity distribution in the vortex situated just over the orifice, the effect on the vortex structure being asymmetric. The largest effect is exerted on the value of the negative velocity defect, which decreases by $0.15U_0$, whereas the positive defect decreases only by $0.02U_0$. This asymmetry can be explained, for example, by a more intense action on the crossflow velocity component in the near-wall region than in the outside zone. The resulting velocity shift caused by the vortex decreases from $0.61U_0$. down to $0.49U_0$, i.e., by 25% of its initial value.

Thus, the vortex structure can be strongly influenced at the stage of linear development of travelling waves. As in the two-dimensional case [1], this leads to changing conditions of stability in the flow and, as a result, to a decreased level of oscillations. This dependence of the growth rate of disturbances on the velocity shift caused by a vortex was studied in [14]. It is clearly seen that the most pronounced effect is observed for the central vortex, and it is practically undetectable in the neighbouring vortices, being smaller than $0.02U_0$. As a result, as Fig. 6 shows, the influence on the disturbances in neighbouring vortices appears to be insignificant even for such a high rate of suction.

The above-described locality of the effect of suction necessitates studying the effect of suction location on the reduction of disturbances. Such measurements were conducted for the point of suction displaced by half the transversal period of the sequence of vortices and thus falling in the gap between them. The results of these measurements showed that although the mean velocity field remained distorted, the amplitude of the travelling waves was found to be practically unchanged (see Fig.11 [12]). It seems that the action exerted on the vortices does not affect the part of the flow responsible for the origination of instability [14]. In particular, the value of the velocity shift at the centre of the vortex remained unchanged, despite a certain distortion of the flow observed at its periphery.

Thus, for a group of vortices developing in a boundary layer, it is found that the travelling waves, growing in amplitude, possess the same amplitude and phase characteristics as the waves on an isolated vortex; in addition, there is a region of linear development of the waves. It is also shown that the growth rate is largely dependent on the distance between vortices, which can be explained by interaction between them. Secondary-instability control methods for stationary streamwise vortices are proposed and substantiated. It is shown that, with the help of a controlled wave generated by a periodic blowing-suction through an orifice, one can actively influence the evolution of natural waves at the stage of their linear development or to prolong their growth, which is indicative of the possibility to employ the MEMS technology; this influence is localized within one of the vortices. The suction is shown to be able to suppress the secondary instability through a localized action exerted on the flow structure. The effect depends on the location of suction relative to the core of the vortex system; the strongest influence is observed for the location of suction just in front of the vortex.

Part II. Transition and control experiments in a boundary layer with Görtler-like vortices

1. Introduction

Spanwise modulation of the boundary layer flow may result in a variety of flow situations of practical interest. In flat plate boundary layers, localized three-dimensional (3D) disturbances, such as surface roughness [15] or transient disturbances, [16,17] give rise to longitudinal vortex structures which locally alter the spanwise structure of the flow, and provide conditions for the instability [15,17,18]. In the presence of free stream turbulence, the continuous impingement of transient disturbances onto the boundary layer generates longitudinal structures, which locally modulate the boundary layer [19]. The transition to turbulence in this flow is significantly promoted by the presence of TS waves [20]. Other examples are the regular array of streamwise vortices generated by body forces, such as Görtler vortices, rotation-induced vortices or crossflow vortices. In these cases, transition is initiated by the appearance of finite-dependent

waves, which travel along the steady vortices. Few details have so far been reported about their characteristics, the mechanism by which they are generated on critical conditions for onset of a time-dependent instability. The objective of the present study is to cast some light over the characteristics of time-dependent instabilities and their role in the transition to turbulence.

The flow past a single roughness element with a half-spherical shape has been studied extensively in the literature. It is dominated by a large scale vortex which wraps around the element and extends its legs downstream of it. Flow visualizations [15], show that transition is caused by arc-shaped eddies, which appear in the wake past the element. The onset of transition seems to depend critically on the appearance of such eddies. By correlating frequencies observed for different roughness sizes, shapes , and Reynolds numbers, authors [21] showed that the vortex shedding frequency, scaled with the displacement thickness and the local mean velocity at the roughness, was 0.3. For most flow cases, this corresponds to a frequency well above unstable TS-waves frequencies.

Cross-flow vortices occur in accelerated flows over swept wings, and on rotating axisymmetric bodies, such as spheres, cones, and disks (see [22] for a review). The primary vortices are inclined in the direction of the cross-flow component, and they may co-rotate or counter-rotate, depending on the strength of the centrifugal force [23,24]. Flow visualizations [25,26] have shown that transition to turbulence is preceded by the appearance of secondary vortices, which seem to spiral around the primary ones, as they propagate along them. In hot-wire measurements, this is seen as a high-frequency oscillations. This instability is believed to be caused by an inflectional instability in the core of the primary vortex [27]. However, quantitative information on the wave characteristics is so far scarce.

In boundary layers along curved walls, or boundary layers subjected to system rotation, the centrifugal and/or Coriolis forces induce steady streamwise vortices which develop a symmetric mushroom-like shape in the cross-stream plane [28]. Transition is preceded by travelling high frequency instabilities which appear locally at each vortex pair, without being visibly affected by neighbouring vortices. Two types of instabilities have so far been pin-pointed. The so-called varicose mode is seen in flow visualizations as small, horseshoe-like eddies which form between two neighbouring vortices. Another type, called the sinuous mode, manifests itself as an unsteady meandering of the basic vortices. The latter is believed to be most important in the transition to turbulence. Both types were observed in the experiments [9], and have reproduced numerically by performing stability analysis based on simulations of the experiment [29,30]. The varicose mode coincides with the regions of large $(\partial U/\partial y)$ at the mushroom hat, whereas the sinuous mode instability is driven by the spanwise gradients $(\partial U/\partial z)$ near the mushroom stem. Both modes propagate at speed of about 0.65 U_0. The dominant frequency is proportional to $\partial U/\partial z$ [30], and is in the range $F = 10^6 2\pi\nu/U_0^2 = 200 - 800$, well above typical TS wave frequencies. However, waves at lower frequencies may also cause transition in the Görtler flow. In the work [31] used a vibrating ribbon to excite waves at F=135. Initially, the y

distribution of the wave was the similar at all spanwise positions and displayed some TS-type features, but further downstream, the amplitude increased most rapidly near the outflow regions (stems), and the y maximum in the wave amplitude shifted further out into the boundary layer. Similar observations have been made in flat plate boundary layers in works [32–34]. In these studies, travelling waves were excited with a vibrating ribbon at frequencies we re TS-waves would be unstable in the Blasius boundary layer (F between 85 and 170), and waves with TS-type mode shapes were found to propagate at 0.35–0.4U_0. However, these waves did not amplify. When they increased the intensity of the basic flow modulation, they observed the rapid amplification at the middle position between the high- and low-velocity regions, i.e., at the maximum in $|\partial U/\partial z|$ Subsequent nonlinear phenomena in the transition to turbulence [33] lead to a further concentration of travelling vorticity layers near the spanwise gradients in U.

Thus, the laminar-turbulent transition in boundary layers is in many instances caused by the breakdown of longitudinal streak or vortex structures, such as Görtler vortices, crossflow vortices, or vortices caused by roughness elements or free-stream disturbances. An important factor that promotes this mechanism is the strength of the spanwise of the mean velocity in the boundary layer, i.e., the normal vorticity. A recent experimental study presented above shows that such flows are unstable with respect to high-frequency travelling waves, which can cause rapid transition.

As for the effect of riblets, many studies [35–37] performed in turbulent boundary layers show that riblets can give drag reduction. One reason for this may be that the riblets prevent the lateral motion of so-called coherent structures in the near wall region of the boundary layer. A similar effect may also be found in the transitional boundary layer. A recent works shows that riblets can delay the development of so-called Λ structures in the transitional regime [3] and to stabilize f low in the wake behind the roughness element [4].

The aim of the present work, is investigations of the transition in a boundary layer with Görtler-like vortices and its riblets control.

2. Transition experiments in a boundary layer with Görtler-like vortices

2.1. Experimental setup and flow parameters

The experiments were performed in a closed circuit low-turbulence wind tunnel, which is identical to that used in PART I . The free stream turbulence level in the test section is 0.03–0.04%, measured in the band 0.5-500 Hz at velocities near 10 m/s.

The general outline of the experimental setup is shown in Fig.7. A rectangular 100x150 cm^2 flat plate made of 10 mm thick Plexiglas was mounted. Fourteen 10 mm long roughness elements, with a rectangular cross section of 1.8x2.0 mm, were pasted on the flat plate surface periodically in the spanwise direction at a distance of 285 mm from the leading edge. The spanwise spacing of the elements was 10 mm (see Fig.1). Controlled oscillations were introduced into the flow by

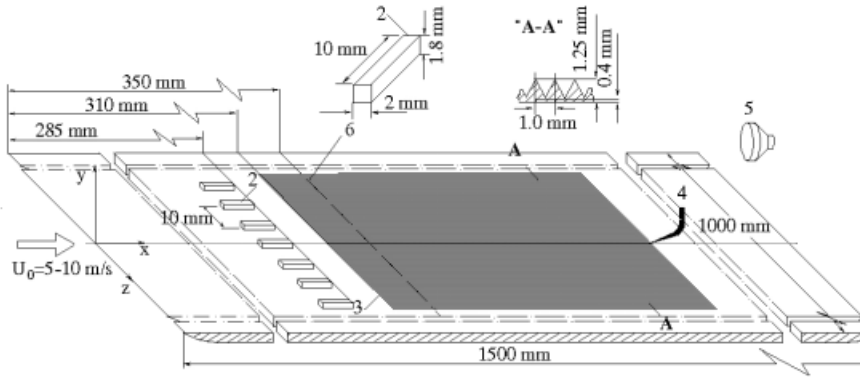

Fig. 7. Experimental set-up: (1) flat plate; (2) roughness elements; (3) riblet plate - 150x150 mm; (4) hot-wire probe; (5) loud speaker; (6) vibrating ribbon position.

means of a vibrating ribbon (0.05 mm thick and 3 mm wide), mounted 0.15 mm from the wall at 350 mm downstream of the leading edge. The streamwise velocity component was measured with a hot-wire anemometer and a single hot wire probe. Measurements were undertaken between x=395 and 750 mm, along wall normal (y) and spanwise (z) directions, at free stream velocities between 5 and 10 m/s.

For reference, critical values of Re_k for transition caused by single roughness elements range between 300 and 1000, depending on roughness shape and wind tunnel conditions [21]. By decreasing U_0, δ in increased and the effective roughness height becomes smaller, giving a milder spanwise modulation of the boundary layer flow. An increase in U_0 has the opposite effect.

If, as suggested above, the instability is associated with $\partial U/\partial z$, another relevant parameter is the spanwise spacing of the elements [30]. In the present setup, the distance between the elements was kept fix at $\lambda = 10$ mm, giving a nondimensional wave number β (defined as $2\pi\delta/\lambda$) of 0.45 at the position of the roughness elements. This value approximately matches typical spanwise wavelengths in Görtler flows [9,38], and is also in the same order as the spanwise scale of boundary layer fluctuations in the presence of free stream turbulence [19].

3. The effect of roughness–induced vortices

In the absence of the roughness elements, a Blasius-type boundary layer with stability characteristics in close agreement with 2-D linear theory developed over the plate. With the elements installed, the boundary layer was seen to become unstable with respect to "natural" background disturbances at free stream velocities above 8 m/s. Upon increasing U_0, the oscillations rapidly amplified and caused breakdown of the flow to a turbulence state. Transition could be observed within the downstream range of measurements at free stream velocities above 9 m/s. These observations will be described in more detail in the following subsec-

tions. The undisturbed flow was studied at the free stream velocity 8.2 m/s in detail in work [39]. The maximum growth of TS waves within the studied region occurs at F between 100 and 150, however the amplification rates are rather small , with maximum N factors of about 1. Note that for frequencies above F=130, the ribbon lies downstream of the unstable region.

The roughness elements give rise to a spanwise modulation of U with the same period as the spacing between the elements. Whereas single roughness elements usually gives a significant wake past the element [15,21], the roughness array in the present case gives wakes which are limited to a small region in the immediate vicinity of the elements. Within the region x=350–700 mm, both the spanwise and the normal U distributions were fairly self-similar.

Fig.8(a) shows the spanwise distribution of U, measured at η=2.5, at R=525, with a free stream velocity U_0=8.2 m/s. The spanwise position of the elements is also shown for reference. The velocity is highest at positions downstream of the elements (in the following termed z_{max} positions) and lowest at z positions between the elements (z_{min} positions). Similar U distributions as in Fig.8(a) have been observed far downstream of a single roughness element, when the wake immediately past the element has relaxed [21]. This situation may be thought of as caused by a downrush of velocity at the edges of the elements and an upwelling in the regions between them.

A conceptual picture of the vortices induced by the elements is shown in Fig.2(b), suggesting that each element sets up a pair of counter-rotating longi-

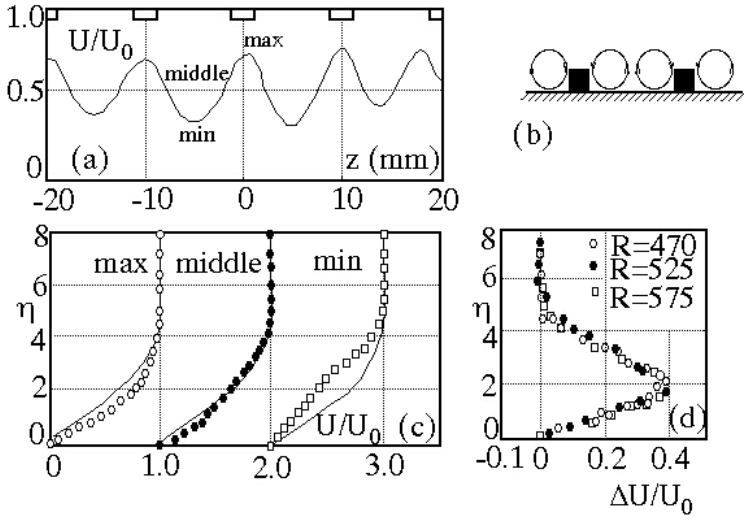

Fig. 8. Boundary layer at the presence of the roughness elements: (a) Spanwise velocity distribution at $\eta = 2.5$, $R = 525$ ($x = 505$ mm, $U_0 = 8.2$ m/s); (b) Conceptual view of roughness-induced vortices; (c) Velocity profiles at $R = 525$, different z positions; (d) Velocity difference (ΔU) between z_{min} and z_{max} positions at $R = 470$, 525 and 575.

tudinal vortices. The profiles of $U(\eta)$ are shown in Fig.2(c). The profile at z_{max} is more full than the undisturbed boundary layer profile, whereas the wall shear is lower at z_{min} positions, and the profile has a clearly visible inflection point in the middle part of the boundary layer. The profile is less distorted at z_{middle} positions , although it also has a minor inflection point in the middle part of the boundary layer. The difference (ΔU) between profiles measured at z_{min} and z_{max}, is shown in Fig.2(d) for three different x positions. The shape of $\Delta U(\eta)$ is seen to be roughly self-similar at all x positions its maximum amounts to about 0.35 U_0 at $\eta = 2.2$. This distribution is strikingly similar to that observed for the root mean square (RMS) of the streamwise velocity in boundary layers subjected to free stream turbulence [19]. The similarity is maybe not surprising, if one considers that the fluctuation velocity in the latter case produced by passage of similar longitudinal structures, generated randomly in time and space. A RMS value of 10% would in that case correspond to a maximum velocity difference of $\Delta U = 0.28$, which is of a similar magnitude as that in Fig.2(a).

3.1. Instability and breakdown to turbulence

The downstream development of "natural" background disturbances is demonstrated in the spectra (see Fig. 5. in [39]). They were obtained at z_{middle}, and at y position corresponding approximately to $\eta = 2.5$. At 8.2 m/s, a broad wave packet with frequencies between 100 and 200 Hz can be seen. As the wave packet amplifies downstream, it shifts towards slightly lower frequencies. The development of high frequency waves is even stronger when U_0 is increased. At 10 m/s, waves in a band between 1 50 and 300 Hz are seen to amplify. Also in this case, a downstream shift towards lower frequencies can be observed. The spectra contain some distinct spectral peaks (e.g., at f=125, 135, 165 Hz for 8 m/s, and f=165, 260 Hz for 10 m/s) which do not appear in the absence of the roughness elements. The frequency which gives a value of 0.3 for the parameter $f\delta^*/U_k$ is 160 Hz at 8.2 m/s and 215 Hz at 10 m/s, which coincides quite well with the central frequencies of the wave packets observed in Fig.5. In the absence of the elements, the boundary layer is stable with respect to these frequencies. It can be noticed that most of the observed unstable frequencies are in a range well above those at which TS waves are unstable in the Blasius boundary layer. If the waves can initially be thought of as small perturbations superimposed on the modulated boundary layer, their strong amplification leads to a stage where nonlinear interactions generate higher harmonics. This is followed by an increase of energy in all spectral components, and finally breakdown to turbulence and disintegration of the basic spanwise structure. In Fig.5, the amplification of the second harmonic (400–450 Hz) is clearly seen. The wave amplitude is largest at z_{middle}, however, higher harmonics are seen at all three z positions. Downstream of x=500 mm, the spectrum becomes broader, and at x=735 mm, it reflects a fully turbulent signal.

This process could also be provoked by forcing oscillations with the vibrating ribbon at a lower velocity. For U_0=8.2 m/s, where the forcing amplitude was intentionally raised so as to produce the nonlinear phenomenon. The non-

linear development also affects the basic flow. A gradual increase of the ribbon amplitude gave a gradual increase of U at z_{min} and z_{middle}.

4. Controlled excitation of the instability

In this section we will give some quantitative characteristics of the time-dependent instability, when the waves are excited in a controlled way. The waves were generated with the vibrating ribbon technique. The filtered RMS amplitude is denoted u'_f, and the phase is denoted by φ. Different forcing frequencies and free stream velocities were investigated. In all cases, the forcing amplitude was chosen small enough to keep the maximum amplitude of u'_f well below 1% at all studied x stations.

4.1. Development of small amplitude travelling waves

Fig.3 shows the spanwise distributions of U, and u'_f , measured in the middle of the boundary layer. The free stream velocity was 8.2 m/s and the forcing frequency 165 Hz, giving F=230, close to the central frequency of the natural wave packet. Near the roughness elements (Fig.9), u'_f is largest at z_{min}, and its spanwise periodicity is the same as that of U. There are distinct phase shifts near each zero crossing of u'_f (see [39]). Further downstream, this distribution undergoes a change, so that the maxima in u'_f coincide with the gradients $|\partial U/\partial z|$. The phase becomes less regular [39]. Another interesting observation to be made from Fig.3 is that the waves grow faster at z-positions where $|\partial U/\partial z|$ is enhanced by minor irregularities in the size and/or arrangement of the roughness elements, e.g., between z=0 and 10 mm, where the variation in U is somewhat larger than at the neighbouring elements, the wave amplification is also larger.

Amplitude profiles across the boundary layer are shown in Fig.10, for different z-positions. The amplitude of the wave is relatively small at z_{max}, and no downstream amplification is observed there. At z_{min}, the amplitude starts to grow past R=500, and it increases rapidly at z_{middle}. The maximum is located at different y, depending on the z position – it is at $\eta \approx 1.5$, 2 and 3 at z_{min}, z_{middle}, and z_{max}, respectively. An interesting observation which can be made by comparing Fig.10 with Fig.8(d), is that at all three z positions the y maxima in u'_f occur where $U/U_0 = 0.6$.

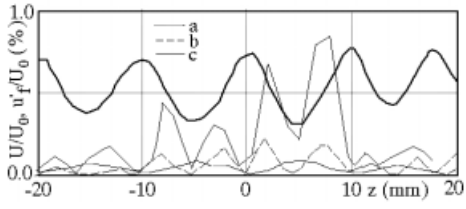

Fig. 9. Spanwise velocity distribution at different downstream positions: (a) x = 400 mm (R = 470); (b) x = 505 mm (R = 525); (c) x = 640 mm (R = 590); solid lines represent U/U_0, dotted lines represent u'_f/U_0 (%).

Near the boundary layer edge, there is a phase shift by about π at z_{min} and z_{middle} (see [39]). The phase then smoothly shifts back inside the boundary

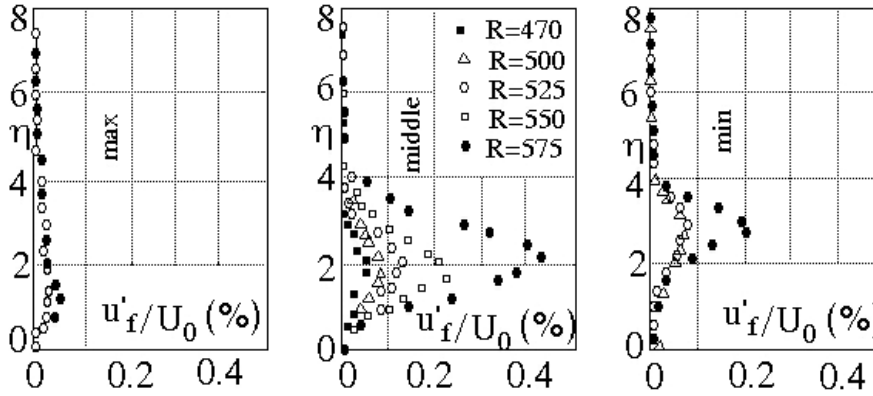

Fig. 10. Amplitude profiles for oscillation forced at $F = 230$, $U_0 = 8.2$ m/s, $x = 400$ mm ($R = 470$), $x = 505$ mm ($R = 525$), $x = 610$ mm ($R = 575$).

layer. Amplitude and phase distributions at a lower frequency (F=95) and the same free stream velocity (U_0 =8.2 m/s) are presented in [39] (see Fig.10). This frequency is in the range where TS waves would b e unstable in the absence of the roughness elements, but below that of the naturally amplifying wave packet. At all three z positions, there is a near-wall part, which is possibly a contribution from a 2-D TS wave, and a part which has its maximum near the *middle* of the boundary layer. Far downstream, the latter clearly dominates. The amplitude grows at z_{middle} and z_{max}, whereas it decreases at z_{min}. This might be interpreted as a competition between a TS-type mode and a "center" mode , a view which is supported by the fact that the near-wall peak is represented at all z positions.

A few measurements were also carried out at a lower velocity (U_0 =5.4 m/s), with the aim of bringing out some features of TS-type waves excited in the modulated boundary layer. In this case, the roughness Reynolds number is only half as large as for 8.2 m/s, and the maximum difference between z_{min} and z_{max} positions amounts to 15% of U_0. The mode shapes were obtained at forcing frequency of 47 Hz (F=150). At z_{max}, the mode shape (both amplitude and phase) is quite similar to that of a 2-D TS wave, but at z_{min}, the profile also has maximum further out in the boundary layer, and the phase shift occurs closer to the boundary layer edge. The mode shape at z_{middle} is similar to that at z_{min}. As in Fig.10 [39] the amplitude increases at z_{max}, and decreases at z_{min}. We may note that these observations are in agreement with previous observations [32,34].

4.2. Amplification and phase characteristics

The 3-D structure of the excited waves makes it necessary to define a way of measuring the wave amplification. Amplification curves for F=230 and U_0=8.2 m/s (see [39]), obtained in the different ways showed that the measured wave

amplitude was approximately proportional to forcing amplitude, and did not exceed 0.6% of U_0 at any of the x stations (from 400 to 610 mm). Similar curves for other frequencies corresponding to F=125–270, and U_0=8.2 m/s showed that initially, at $R < 525$, there is no amplitude increase (at low F, it actually decreases), however, all frequencies give a strong amplification past R=525. In the absence of the roughness elements, these frequencies are either damped or much less amplified (cf. Fig.3 in [39]). The corresponding phase evolution demonstrated that initially, the phase velocity is between 0.4, and $0.5U_0$ but it increases downstream, and $R < 525$, it has a constant value near $0.6U_0$. This value coincides with the value of U/U_0 at the y position of maximum amplitude, showing that the instability may be connected with the critical layer at each local z position.

In an attempt to capture the downstream development of TS-type waves, the near wall evolution was followed for waves excited at low frequencies. Amplitude evolution for F=95, U_0=8.2 m/s and F=150, U_0=5.4 m/s, were obtained. The amplitudes for F=95, U_0=8.2 m/s are evaluated at the near wall maximum ($\eta = 0.85$) of y profiles at different x. The phase velocity at 5.4 m/s was $0.52U_0$ at all z. In both cases the amplitude slowly decreases at z_{min}, but at z_{max} it increases at l east as rapidly as a 2-D TS wave. This behaviour is quite remarkable, since from the point of view of 2-D linear stability, the $U(y)$ profiles at z_{max} are more stable than those at z_{min}. Evidently, such a quasi-2-D approach is not applicable. The fact that different growth rates are obtained at different z positions can not be explained by linear stability arguments, but may rather point towards a three-wave interaction as described in [40].

Discussion

In summary, when the boundary layer flow is modified periodically along the span, its stability characteristics are altered, and new instabilities appear, which are not present in the 2-D boundary layer. The detailed measurements reported above give some indications on the nature of instability waves excited both naturally and in a controlled way. In some cases, there seems to be a competition between simultaneously excited instabilities, of which the strongest one way be assumed to dominate far downstream. At least two different types of modes can be distinguished in the present experiment; one which is similar to TS waves in a 2-D boundary layer, and one which occurs at higher frequencies.

The first type develops at similar frequencies and amplification rates as TS-waves in a 2-D boundary layer, and was here found to propagate with c=0.5. The wave front has the same spanwise periodicity as the basic flow, and the amplitude appears to grow faster at z_{max} than at z_{min}, which is in contrast to what might be expected one the basis of quasi-2-D linear stability. These observations are in agreement with those made by both in [32] and [34]. The similarity to TS-waves in a 2-D boundary layer becomes clearly, the more mildly the flow is modulated [32,34]. Far downstream, the TS-type mode was overtaken by an instability with features which are clearly different from both 2-D and 3-D TS waves – it occurs at higher frequencies, the phase velocity is higher, and it seems to be of a local, inviscid character associated with the spanwise

gradients of U. The shift from one type of instability to the other is indicated by a spanwise shift of the amplitude maximum towards z_{middle}, a change in the spanwise periodicity (see Fig.8a), and an increase in the phase velocity. Such a shift can also be seen in other experiments, both on a flat plate [32] and in the Görtler flow [31]. The experiments in [32], in which the vortex spacing was varied, indicates that the high frequency instability is favoured by a narrow spacing. It should be pointed out, however, that in their experiment the wave amplitude was $> 1\%$. In the present study, the amplitudes were kept well below 1%, and the amplification of the high frequency instability did not depend on the forcing amplitude, indicating that it can develop within the linear regime, i.e., not as a product of nonlinear wave interactions.

The high-frequency instability observed here is similar to the meandering (or sinuous) mode of the time-dependent instability in the Görtler flow [9,29] (e.g., the phase velocity is similar, and it is associated with the spanwise gradients of U), and is also compatible with the conceptual view of the secondary instability in cross flows given in [26]. Some studies [17,18] indicate that a high-frequency instability can develop in flows modulated by a controlled transient disturbance. Also in these cases, the instability is associated with $\partial U/\partial z$, and propagates faster than TS wave. In boundary layers subjected to free stream turbulence [19,20], this has not been observed, however, TS waves seem to play an important role in the transition process. The present experiments show that spanwise-modulated boundary layers may be unstable with respect to TS-type waves, and it is reasonable to believe that this occurs also in flows modulated by transient disturbances. This matter certainly deserves further investigation.

The present study demonstrates a relatively simple method by which the transition mechanisms in spanwise-modulated flows can be studied, and provides data for a flow case which may serve as a model for a variety of similar flow situations. The basic flow studied here has a smooth periodic distribution of U along the span, which is invariant in the downstream direction. This flow is subjected to a powerful instability in the form of high-frequency travelling waves, which cause the transition to turbulence. Schematic diagram of a boundary layer transition with embedded streamwise vortices investigated here is presented in Fig.11.

Thus, the characteristics of the high-frequency instability are presented above can be summarized as follows:

1. The wave amplifies rapidly at z positions between the high- and low- velocity regions (z_{middle}), i.e., where $|\partial U/\partial z|$ is maximum.
2. The phase velocity of the wave is $0.6U_0$. At all z positions, the maximum of u'_f with respect to y occurs where $U(y) = c$. This adjustment of the mode shapes to the local critical layer may indicate that the underlying mechanism is inviscid.
3. The observed range of unstable frequencies is between F=100 and 300. Naturally developing frequencies are centered at $f\delta^*/U_k$=0.3, in agreement with the correlation studies in [21] for instabilities past a single roughness element.

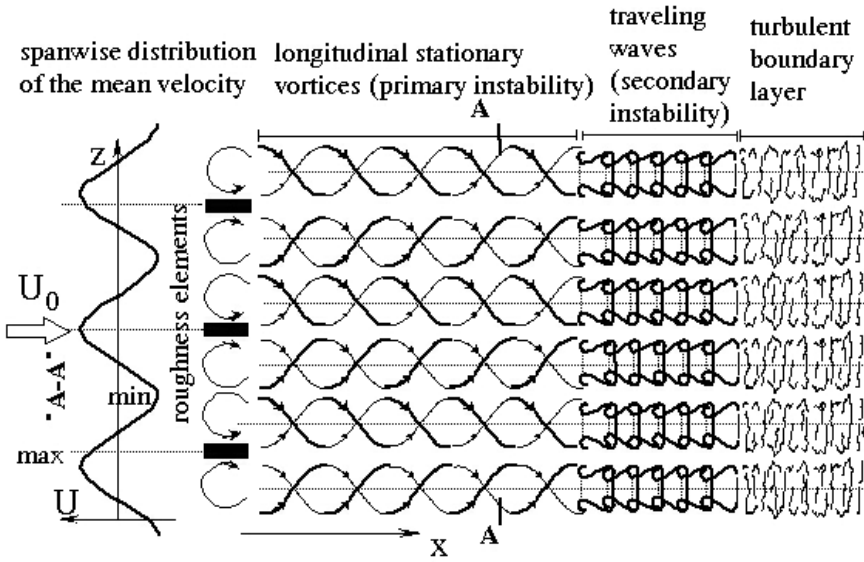

Fig. 11. Schematic diagram of a boundary layer transition with embedded streamwise vortices.

4. The breakdown to turbulence is initiated by the appearance of higher harmonics of the fundamental wave frequency, which gradually fill the spectrum. The spanwise structure of the mean flow is dissolved in this process.

PART III. Influence of riblets on a boundary layer with Görtler-like vortices

The experimental setup is identical to that used above or in [39], the only new feature being a removal riblet surface, which was mounted, as shown in Fig.7. Triangular riblets with a square section, as shown in Fig.7 were used. These are identical to the ones used in [3,4]. Longitudinal vortices were generated by periodically arranged roughness elements. Fourteen 10 mm long elements with a rectangular cross section of 1.8x2.0 mm^2 were distributed along the spanwise direction, as shown in Fig.7. A dynamic loudspeaker placed after the plate was used to generate controlled high-frequency travelling waves. The streamwise velocity was measured with constant temperature anemometer using a single hot wire probe. All results presented in here were obtained at free-stream velocity of U=9 m/s, which is the lowest velocity could be observed within the studied region [39]. The roughness array gives a strong modulation of the boundary layer mean velocity (U) in the z direction. With the present arrangement, U is maximum at z position downstream of an element, and minimum between

two elements. These two position are in the following termed z_{max} and z_{min}, respectively.

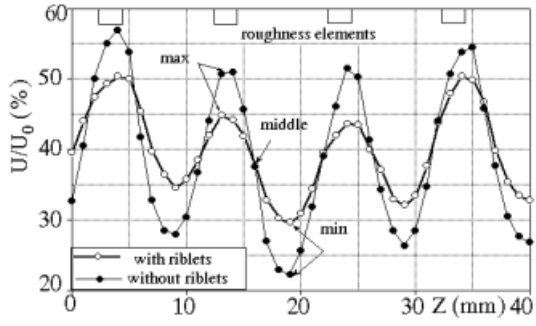

Fig. 12. Mean velocity distribution along the spanwise (z) direction at $x = 473$ mm.

Fig.12 shows how the riblet surface affects the spanwise modulation. Here we compare the cases with and without riblets at two different downstream position, corresponding to the upstream end ($x = 320$ mm) and a position just downstream (x=473 mm) of the riblet surface. The y position is approximately in the middle of the boundary layer. The effect of the riblets cannot be distinguished at x=320 mm, while it is quite clear at $x = 473$ mm; after introducing the riblet surface, the amplitude of the spanwise modulation of U is reduced to half its size. This effect can also be seen in Figs.9(a) and 9(b) [41], which show velocity profiles in the y direction at x=473 mm, with and without riblets, respectively. The y coordinate is normalized with the boundary layer thickness (δ), while δ is the y position where U=0.99 (different δ's are used for the cases with and without riblets). y is taken to be zero at the level of the smooth surface. Each figure shows the profiles at z_{max} and z_{min}. The difference in u between z_{min} and z_{max}, Δu, is plotted in Fig.9(c). Without the riblets, Δu amounts to, at most, 35% at y/δ=0.2. With the riblets, the profiles are shifted away from the wall by a distance of about 0.15δ, due to the blocking effect of the riblet surface near the wall (see Fig.6 in [3]). In this case, the maximum difference between the min and max positions is less than 20%.

The spectra presented in Fig.5 of [39] show that the fluctuations are dominated by low frequencies, but there are also contributions in a band of higher frequencies (at 9 m/s, the naturally excited frequency band is centered at about 200 Hz). The low- frequency band can be thought of as an irregular meandering of the basic vortex structure, while the high frequencies are due to travelling waves that grow in the downstream direction and eventually cause the breakdown to turbulence.

Figure 10 (see Fig.6 in [41]) shows the broadband fluctuations (u_{RMS} along the span at x=473 mm, with and without riblets, respectively). In both cases, the u_{RMS} is maximum at positions between z_{min} and z_{max} , i.e., where $\partial U/\partial z$ has its maximum. In the case with riblets, the RMS level is at least two times

lower in the case without riblets: the u_{RMS} maximum is about 0.5% in the case without riblets.

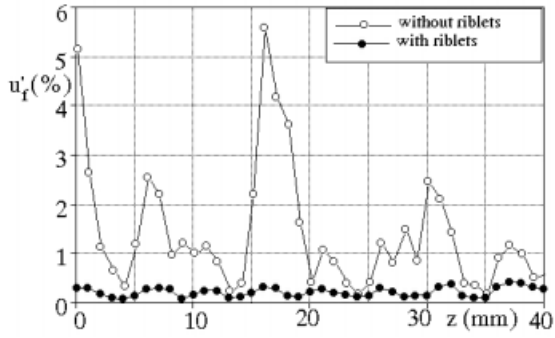

Fig. 13. The z distribution of u'_f at $x = 473$ mm, $f = 225Hz$.

Travelling waves with an easily detectable amplitude were generated using the loudspeaker, using a frequency of 225 Hz. This is approximately the frequency where maximum amplification occurs in the case without riblets. After calibration, the hot wire signal was digitally filtered in a narrow band near the forcing frequency. The filtered signal is denoted u_f. Fig.13 compares the spanwise distribution of u_f at $x = 473$ mm, with and without riblets. In both cases, the amplitude maxima coincide with the maxima in $\partial U/\partial z$, the waves are clearly damped by the presence of the riblets. Without riblets, the amplitude is rather irregular in the spanwise direction. It was observed in [39] that this is due to the sensitivity of the amplification to small irregularities in $\partial U/\partial z$.

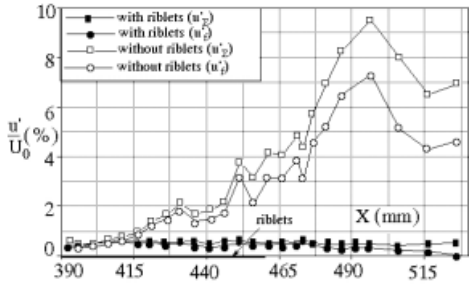

Fig. 14. Downstream development of u'_Σ and u'_f at $z = 17$ mm (cf.Fig.13.).

The downstream development of the waves was studied in great detail in [39] and presented above. It was found that the wave amplitude has a smooth y profile with a maximum slightly below the middle of the boundary layer. The downstream development of u' with and without riblets is shown in Fig.14.

The signals were collected at the z position, where u'_f is maximum (see Fig.13), and were followed downstream at y constant y position. The figure shows both the broadband RMS (u'_Σ) and the signal when it is filtered near the

forcing frequency (u'_f). In the case without riblets, the waves amplify by a factor of 10 between x=390 and 500 mm, in the region downstream of 450 mm, the growing difference between u'_Σ and u'_f indicates the growth of harmonics of the forcing frequency, as observed above and in [39]. The decrease downstream of 500 mm is due to transition to turbulence. In the case with riblets, on the other hand, the waves are slowly damped, and the flow remains laminar throughout the studied region.

Thus, the present study shows that the effect of the riblets is to suppress longitudinal vortex structures in a boundary layer. The boundary layer becomes stable with respect to high-frequency traveling waves, which cause the transition in the absence of the riblets. This finding should also be relevant for other boundary layers with embedded longitudinal vortices, in particular crossflow and Görtler-like flow [39]. In these flows, it is known that transition to turbulence is caused by high-frequency traveling waves, much as in the case studied here. The present result opens the interesting perspective of being able to control the transition in such flows by means of surface manipulation.

In summary, it is necessary to note, that results of the given researches on transition in flows with Görtler and crossflow vortices have shown, that it is connected to development secondary, high-frequency disturbances on the given stationary vortices, modulated boundary layer flow in spanwise direction. The secondary disturbances development depends on a spanwise velocity gradient ($\partial U/\partial z$), i.e., from vortices intensity. The various methods of control by transition in such flows showed above, allow to delay the transition suppressing the vortices intensity or decreasing of the secondary, high-frequency waves amplitude. Possibilities of as of both the given control methods and new (for example, use of active control methods with using of the MEMS technology) is obvious. It is obvious as well necessity of more detailed study of the transition mechanism for the given flows as from the point of view of its clearer understanding, and, hence, opportunity to control them.

This study was supported by Russian Foundation for Basic Research under Grants No.96-15-96310 and No.99-01-00591.

References

1. V.V. Kozlov, V.Ya. Levchenko, V.A. Shcherbakov: Development of disturbances in a boundary layer with slot suction, Uch.Zap.TsAGI **IX**, 2 (1978), pp. 99–105 (In Russian)
2. A.V. Boiko, V.V. Kozlov, V.V. Syzrantsev, V.A. Shcherbakov: Transition control by riblets in swept wing boundary layer with embedded streamwise vortex, Eur. J. Mechanics **16**, 3, (1997)
3. G.R. Grek, V.V. Kozlov, S.V. Titarenko: Effects of riblets on vortex development in the wake behind a single roughness element in the laminar boundary layer on a flat plate, La Recherche Aerospatiale **1** (1996) pp. 1–9
4. G.R. Grek, V.V. Kozlov, S.V. Titarenko: An experimental study on the influence of riblets on transition J.Fluid Mech. **315** (1996) pp. 31–49
5. R.W. Milling: Tollmien–Schlichting wave cancellation Phys.Fluids **24** 1981 pp. 979–981

6. V.M. Gilev: Tollmien–Schlichting wave excitation on the vibrator and laminar-turbulent transition control, ed. by V.V.Kozlov, Springer-Verlag, Berlin, 1985, pp. 243–248
7. V.V. Kozlov, V.Ya. Levchenko: 'Laminar-turbulent transition control by localized disturbances'. In: Turbulence Management and Relaminarization IUTAM Symp. at Bangalore, 1987, ed. By H.W. Liepmann, R. Narasimha
8. V.M. Gilev, V.V. Kozlov: Effect of a periodic blowing-suction on the boundary-layer transition, Preprint No.1, Inst. Theor. Appl. Mech., Sib. Branch, USSR Acad. Sci., Novosibirsk, (1985) (In Russian)
9. J.D. Swearinger, R.F. Blackwelder: The growth and breakdown of streamwise vortices in the presence of the wall J. Fluid Mech. **182** (1987) pp. 255–290
10. A.V. Boiko, V.V. Kozlov: Strategy of the flow MEMS control at laminar-turbulent transition in a boundary layer, IUTAM Symposium on Mechanics of Passive and Active Flow Control, G.F.A. Meier and P.R. Viswanath (eds.), 1999, Kluwer Academic Publishers, pp. 203-208.
11. Ch.-M. Ho, Yu-Ch. Tan: MEMS: Science and Technology, Application of Microfabrication to Fluid Mech., **197** (1994) pp. 39–48
12. A.V. Boiko, V.V. Kozlov, V.V. Syzrantsev, V.A. Shcherbakov: Active control over secondary instability in a three-dimensional boundary layer, Thermophysics and Aeromechanics, **6** 2 (1999) pp. 167–177
13. A.V. Boiko, V.V. Kozlov, V.V. Syzrantsev, V.A. Shcherbakov: An experimental study of the laminar-turbulent transition on an isolated stationary disturbance in a swept wing boundary layer, Appl. Mech. Tech. Phys. 1 (1995) pp. 72–84
14. A.V. Boiko, V.V. Kozlov, V.V. Syzrantsev, V.A. Shcherbakov: Investigation of the effect of internal structure of a streamwise vortex on the development of travelling disturbances in it, Thermophysics and Aeromechanics, **4** 3 (1997) pp. 369–380
15. M.S. Acarlar, C.R. Smith: A study of hairpin vortices in a laminar boundary layer. Part 2. Hairpin vortices generated by fluid injection, J.Fluid Mech. **175** (1987) pp. 43–83
16. G.R. Grek, V.V. Kozlov, M.P. Ramasanov: Three types of disturbances from the point source in the boundary layer, Laminar-Turbulent Transition (Ed. V.V. Kozlov), Springer-Verlag, 1985 pp. 267–272
17. K.S. Breuer, M.T. Landahl: The evolution of a localized disturbance in a laminar boundary layer. Part 2. Strong disturbances, J.Fluid Mech. **220** (1990) p. 595
18. B.G.B. Klingmann: On transition due to 3-D disturbances in plane Poiseuille flow, J.Fluid Mech. **240** (1992) p. 161
19. K.J.A. Westin, A.V. Boiko, B.G.B. Klingmann, V.V. Kozlov, P.H. Alfredsson: Experiments in a boundary layer subjected to free stream turbulence. Part I: Boundary layer structure and receptivity, J. Fluid Mech. **281** (1994) pp. 193–218
20. A.V. Boiko, K.J.A. Westin, B.G.B. Klingmann, V.V. Kozlov, P.H. Alfredsson: Experiments in a boundary layer subjected to free stream turbulence. Part II: The role of TS-waves in transition, J.Fluid Mech. **281** (1994) pp. 219–245
21. P.S. Klebanoff, W.G. Cleveland, K.D. Tidstrom: On evolution of a turbulent boundary layer induced by a three-dimensional roughness element, J.Fluid Mech. **237** (1992) p. 101
22. H.L. Reed, W.S. Saric: Stability of three-dimensional boundary layers, Annu.Rev. Fluid Mech., **21** (1989) p. 235
23. R. Kobayashi: Critical review of three-dimensional boundary layer transition, In Boundary Layer Stability and transition to Turbulence (Ed. D. C. Reda, H. L.Reed, R. Kobayashi) ASME FED 114, 1 (1991).

24. R. Kobayashi, Y. Kohama, T. Arai, M. Ukaku: The boundary layer transition on rotating cones in axial flow with free stream turbulence, JSME, **261** (1987) p. 423
25. Y. Kohama: Behavior of spiral vortices on a rotating cone in axial flow, Acta Mech. **51** (1984) p. 105
26. Y. Kohama: Some expectation on the mechanism of cross-flow instability in a swept wing Flow, Acta Mech. **66** (1987) p. 21
27. Y. Kohama, W.S. Saric, J.A. Hoos: A high-frequency, secondary instability of crossflow vortices that leads to transition, Proc.R.Aero.Soc.Conf. Boundary Layer Transition and Control XX, XXXX (1991)
28. W.S. Saric: Görtler vortices, Annu.Rev.Fluid Mech. **26** (1994) P/ 379
29. W. Liu, J.A. Domaradzky: Direct numerical simulation of transition to turbulence in Görtler flow, J.Fluid Mech. **246** (1993) p. 267
30. A. Bottaro, B.G.B. Klingmann: On the linear breakdown of Görtler vortices, Eur. J. Mechanics **15** 3 (1996) pp. 301–330
31. I. Tani, Y. Aihara: Görtler vortices and boundary layer transition, ZAMP, **20** (1969) p. 609
32. I. Tani, H. Komoda: Boundary layer transition in the presence of streamwise vortices, J.Aerospace Sci. **29** (1962) p. 440
33. H. Komoda: Nonlinear development of disturbance in a laminar boundary layer, Physic. Fluids Suppl. **10** (1967) p. S87
34. Y.S. Kachanov, O.I. Tararykin: Experimental investigations of an relaxating boundary layer, Izv. SO AN SSSR, Ser. Tech. Nauk, 1987, 18, 5, 9; see also The development of 3-D separated flows and their influence on laminar-turbulent transition, // in Separated Flows and Jets, edited by V.V. Kozlov and A.V. Dovgal (Springer-Verlag, Berlin, (1991), pp. 373–740
35. M.S. Walsh: Drag characteristics of V-groove and transverse curvature riblets in "Viscous flow and drag reduction", Progress in Astronautics and Aeronautics, (Ed. G.R. Hough) 1979, V.72, presented at the AIAA Symposium on Viscous Drag Reduction, Dallas, Texas, November .
36. D. Wbechert, M. Bartenwerfer: The viscous flow on surfaces with longitudinal ribs, J.Fluid Mech, **206** (1989) pp. 105-129
37. P. Luchini, F. Manzo, A. Pozzi: Resistance of a grooved surfaces to parallel and crossflow, J.Fluid Mech, **228** (1991) pp. 87–107
38. H. Bippes: Experimental study of the laminar to turbulent transition on a concave wall in parallel flow, NASA TM 75243, (1978)
39. A.A. Bakchinov, H.R. Grek, B.G.B. Klingmann, V.V. Kozlov: Transition experiments in a boundary layer with embedded streamwise vortices, Phys. Fluids. **7** 4 (1995) pp. 820–832
40. M.R. Malik, M.Y. Hussaini: Numerical simulation of interactions between Görtler vortices and Tollmien-Schlichting waves, J. Fluid Mech. **210** (1990) p. 183
41. G.R. Grek, V.V. Kozlov, B.G.B. Klingmann, S.V. Titarenko: The influence of riblets on a boundary layer with embedded streamwise vortices, Phys. Fluids, **7** 10 (1995) pp. 2504–2506

Higher order dynamics of baroclinic waves

Bernd Sitte and Christoph Egbers

Center of Applied Space Technology and Microgravity
University of Bremen, Germany

Abstract. Instabilities in the form of baroclinic waves occur in a rotating cylindrical annulus cooled from within. Flow visualisation studies and LDV-measurements of the radial velocity component were carried out in an annulus with an aspect ratio of 4.4. The flow undergoes transitions from the laminar stable state through baroclinic waves, both stable and time-varying, to an irregular state. Based on the time series of the radial velocity at fixed point in the rotating annulus, the attractors of the flow match previous results based on temperature measurements. The bifurcation diagram of extrema in the radial velocity shows the existence of low dimensional chaos at the transition from the axisymmetric flow to periodic baroclinic waves. This bifurcation scenario at low rotation rates is substantially different from the nonlinear behaviour of Taylor–Couette flow.

1 Introduction

In the last decades, rotating cylindrical annulus experiments have been carried out to obtain laboratory simulations of the large-scale circulation of the atmosphere, with the cool polar regions at the center of rotation. In contrast to Taylor–Couette flow, the flow in the cylindrical gap is driven by a temperature difference between the inner and the outer cylinder. Both cylinders are co-rotating at the same speed. The flow is caused by a baroclinic instability, the planes of constant pressure are not parallel to the planes of constant density. The resulting waves are called baroclinic waves, sometimes also thermal Rossby waves.

As an example for atmospheric and oceanographic flows and since a lot of basic research was done in the last 40 years, baroclinic waves are a topic in standard literature of fluid mechanics, e.g. [28] [16].

In 1958, Hide [13] visualised baroclinic waves in a rotating cylindrical annulus cooled from within. He confined a fluid in a rotating, cylindrical gap with a free surface, cooled the inner wall and heated the outer one. With an aspect ratio of $\Gamma = 2.9$, a stable axisymmetric basic flow is guaranteed. The axisymmetric basic flow is characterized by an upward flow of the warm fluid at the outer wall and a downward flow at the cooler inner wall. The resulting radial flow, mainly close to surface and bottom, is deflected by the Coriolis force (see Fig. 1 a,b). At higher rotation rates, this azimuthal flow becomes dominant. If the rotation rate is increased, the azimuthal flow shows a wavy behaviour, the axial symmetry is broken. Hide observed waves with different wave numbers m, traveling slowly around the cylinder (see Fig. 1 c). Basically, with increasing rotation rates higher

C. Egbers and G. Pfister (Eds.): LNP 549, pp. 355–375, 2000.

wave numbers are stable. At high rotation rates, the transition to turbulence takes place.

In 1965, Bowden and Eden [2] were able to measure the temperature field and the heat flux for the axisymmetric case in an experiment very similar to Hides. They used ink to visualize the flow structures.

In the following years a lot of work was done to investigate the complex behaviour of the waves in various geometries and under different boundary conditions. Fowlis and Hide [10] investigated the effect of the Prandtl-number on the stability of the waves. They also closed the free upper surface with a plate. This did not change the basic flow types, but shifted the stability diagram and slowed down the drift speed of the waves. Fein and Pfeffer [9] also varied the viscosity. In 1970, Hide and Mason [14] were able to do experiments with internal heating. With alternating currents, the fluid itself is heated. This is a better analogy to heating processes in the atmosphere. Busse and Carrigan [3] tried conical upper and lower end walls. Pfeffer et al. [22] measured the temperature gradients for different flow types.

With the development of analyzing methods which are powerful enough to describe bifurcation scenarios and chaotic properties of fluid flows, in the last decade new investigations have been carried out and new insight into the complex behaviour of baroclinic instabilities was gained.

In 1989, Morita and Uryu [19] were able to examine the transition from baroclinic waves to geostrophic turbulence in an experiment very similar to Hide's. They found the characteristic decay of the energy spectrum proportional to f^{-3}, where f is the frequency. Lorenzen et al. [17] made LDV measurements and described the Hopf bifurcation from the basic flow to baroclinic waves. Read et al. [25] used the method of time delayed coordinates to analyse their thermocouple data. By taking long temperature time series with a temperature sensor in the

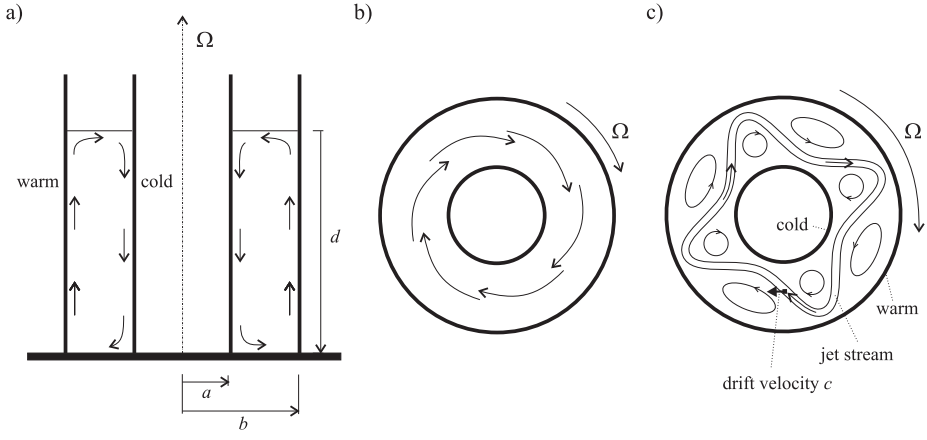

Fig. 1. Sketch of (a) lateral view and (b) top view of the axisymmetric basic flow, (c) top view of a $m = 4$ wave pattern.

middle of the cylindrical gap they were able to reconstruct the phase space of the system and to analyse the nonlinear behaviour. Früh and Read [11] deepened these investigations. Different flow types of baroclinic waves were found. At the transition from the axisymmetric basic flow to stable baroclinic waves so called 'amplitude vacillation' (AV) waves occur. The AV waves have an oscillating amplitude. Further on, 'modulated amplitude vacillation' (MAV) waves have been found, where the amplitude oscillation does not have a constant frequency. In this terminology, the structural disturbance of the waves towards the transition into turbulence is called 'structural vacillation' (SV). Früh and Read [11] were able to show that low dimensional chaotic states occur not only at the transition to turbulence, but also slightly above the critical point in the MAV waves. The transition to turbulence has been examined by Pfeffer et al. [23] for the case of a wide gap. They used the data of earlier experiments by Buzyna et al. [5] to calculate the Lyapunov exponents. In contrast to the experiments of Früh and Read, they did not find chaotic behaviour in the wide gap case.

In the beginning, theoretical work was based on Eadys theory of baroclinic instability, published in 1949 [7], before the first experiments were made. Eadys linear stability analysis neglected viscosity, but is, transfered to the rotating cylinder, valid for the transition from the axisymmetric flow to baroclinic waves in the case $Ta \to \infty$. Davies [6] made a linear stability analysis of the waves. In an expanded Eady model, Hide and Mason were able to calculate the correct shape of the two dimensional stability diagram [15].

Pedlosky was in 1970 the first to do an analysis with nonlinear aspects. He enhanced his theory subsequently in the following years [21]. In his simulations, he was able to show, that the amplitude of baroclinic waves can oscillate. He also found parameter regions, where these oscillations are aperiodic. For a simpler geometry, Mundt et al. [20] did a nonlinear stability analysis using a two layer model with no-slip boundary conditions at the sidewalls. They were the first to find aperiodic waves at parameters which might correspond to the MAV waves described by Früh and Read. Herrmann and Busse [12] integrated the full nonlinear equations for the case of conical endwalls, with periodic varying fluid depth d. They also found pulsating waves in this case and, further on, standing waves which have not been found in experiments with constant depth d.

Beside the special case of the rotating annulus, a lot of numerical work has been done to understand the basic mechanisms of baroclinic instabilities, mostly in direct application to atmospheric or oceanographic scales, see [24] for an overview.

2 The rotating annulus experiment

The flow in the rotating annulus cooled from within can be characterized by the following control parameters: The geometry can be described by the radius ratio $\eta = a/b$ and the aspect ratio $\Gamma = d/(b-a)$, where a and b are the inner and the outer radii of the cylindrical gap, d is the depth. Further parameters may be

defined, such as the Taylor number

$$Ta = \frac{4\,\Omega^2\,(b-a)^5}{\nu^2\,d} \tag{1}$$

and

$$Ro = \frac{g\,d\,\Delta\rho}{\bar{\rho}\;\Omega^2\;(b-a)^2} \tag{2}$$

which is known as the thermal Rossby number. Ω is the angular velocity, ν is the kinematic viscosity and ρ the density of the fluid. The Taylor number describes the rotational influence while the thermal Rossby number characterises the influence of the density gradient due to temperature differences and the influence of rotation.

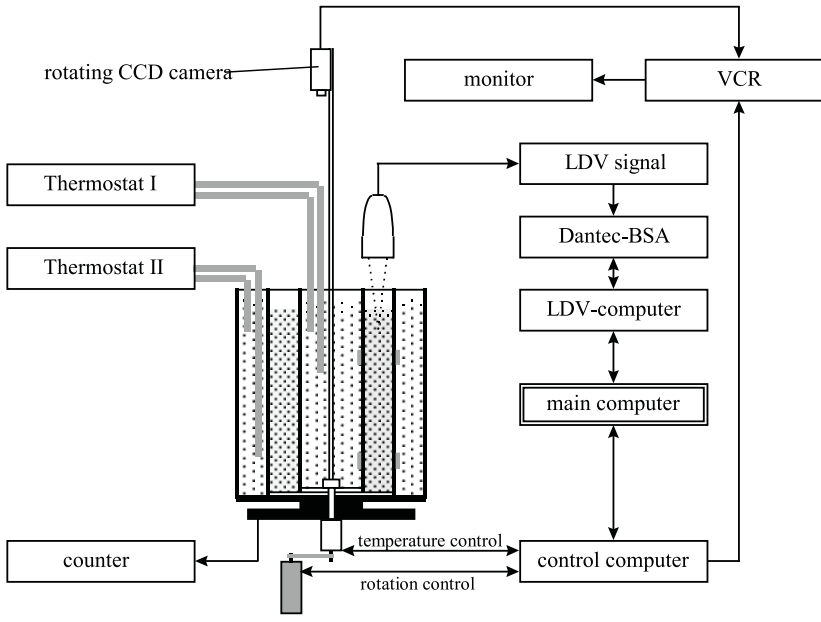

Fig. 2. Experimental setup

Figure 2 shows the experimental setup. The cylindrical tank has three concentric chambers. The inner and outer chambers are filled with water and connected with two thermostats. They control the wall temperatures of the cylindrical gap between these two chambers. Both temperature baths are strongly mixed during rotation, to avoid vertical temperature differences. The surfaces of all chambers are free. The outer two walls are made of acrylic glass to enable visual investigations and LDV measurements from lateral directions. The temperature is controlled by thermocouples at both walls of the gap. A co-rotating camera

Table 1. Parameters of the experiment

$a = 45$ mm	Inner radius of the cylindrical gap
$b = 95$ mm	Outer radius of the cylindrical gap
$d = 220$ mm	Depth of the fluid
$\eta = a/b = 0.47$	Radius ratio
$\Gamma = \frac{d}{b-a} = 4.4$	Aspect ratio
$T_a = 19.0°\mathrm{C}$	Temperature of the inner wall
$T_b = 22.8°\mathrm{C}$	Temperature of the outer wall
$\nu = 1.004$ mm^2/s	Kinetic viscosity (water, 21° Celsius)
$\bar{\rho} = 0.998$ kg/l	Average density (water, 21° Celsius)
$\Delta\rho = 0.000823$ kg/l	Maximum density difference
$Pr = 8.0$	Prandtl number
0.25 rad/s $< \Omega < 6.0$ rad/s	Variation of the angular velocity
$Ro = \frac{g\,d\,\Delta\rho}{\bar{\rho}\,\Omega^2\,(b-a)^2} > 0.004$	Variation of the thermal Rossby number
$10^6 < Ta = \frac{4\,\Omega^2\,(b-a)^5}{\nu^2\,d} < 10^8$	Variation of the Taylor number

is mounted on top of the experiment. The whole experiment is installed on a turntable, the maximum rotation frequency is 1 Hz. As the time scales of baroclinic waves are of the order of 10^3 seconds, automation of the experiment is necessary. Therefore all components and parameters of the setup, including rotation rate, the LDV system, thermostats and VCR, are controlled by a main computer. LDV time series measurements took about 7 to 9 hours for one parameter point.

The parameters of the experiment are given in table 1. Distilled water was used as the fluid. The temperature difference between the inner and the outer walls was kept constant for all measurements. This reduces the parameter space to a line, with the rotation speed Ω left as the only free parameter.

3 Stability

The fluid motion on the free surface of the annulus is visualised by aluminium flakes suspended in the working fluid. The reflecting flakes allow no LDV measurements during the visual investigations.

Beside the axialsymmetric basic flow of wave number $m = 0$, waves of different wave numbers $m \neq 0$ occur in the non-axisymmetric flow regime. However, m is limited. Hide and Mason [14] determined the lowest and highest existing

wave numbers $m_{min} \leq m \leq m_{max}$ for different geometries of the annulus and found the empirical law

$$m_{min} = 0.25\,\frac{\pi(b+a)}{(b-a)}\,, \qquad m_{max} = 0.75\,\frac{\pi(b+a)}{(b-a)}\,. \tag{3}$$

For this geometry, $m_{min} = 2$ and $m_{max} = 6$. However, $m = 6$ did not occur if Ω is increased or decreased quasi-stationarily. $m = 6$ waves only emerge in case of rapid speed changes. Therefore the following investigations are only focused on $m = 2, 3, 4, 5$.

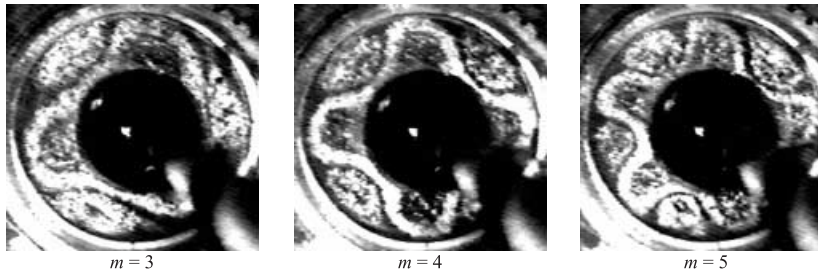

Fig. 3. Different wave numbers $m = 3, 4, 5$ at identical Parameters $f = 0.167$ Hz, $Ta = 6.32 \cdot 10^6$, $Ro = 0.585$

The flow shows a very strong hysteresis. Figure 3 shows three different wave numbers at identical parameters. Each of the flow patterns is stable, no spontaneous jumps between wave numbers occured within the investigated region of the parameter space. The wave patterns are propagating around the cylindrical gap, with a positive drift velocity c relative to the rotating system. The drift velocities are two orders of magnitude smaller than the rotational velocity and are very sensitive to small variations of the boundary conditions. Basically, c decreases with increasing Taylor number. At low Taylor numbers, waves with a higher wavenumber are slightly faster than waves of lower mode. At higher Taylor numbers this relation is inverse [26].

Figure 4 shows the different flow regimes as a function of the Taylor number Ta. At the critical point $Ta = 1.76 \cdot 10^6$, $Ro = 2.11$, the axisymmetric basic flow becomes unstable. This critical point is very close to the results of Hide and Mason [14] and their measurements with water as a fluid. Since only one of two possible parameters was varied, Figure 4 is not a complete stability diagram, because the temperature difference was kept constant. It represents a straight line in the two dimensional stability diagram of Hide and Mason, that crosses the regions where we hoped to find interesting transitions between different regimes.

At Taylor numbers slightly above the critical point the amplitude of the waves begins to oscillate. These are the AV and MAV waves described by Read et al. and Früh & Read. Figure 5 shows an example of an amplitude oscillation. While the wave slowly drifts with a velocity $c = 0.013$ rad/s faster than the

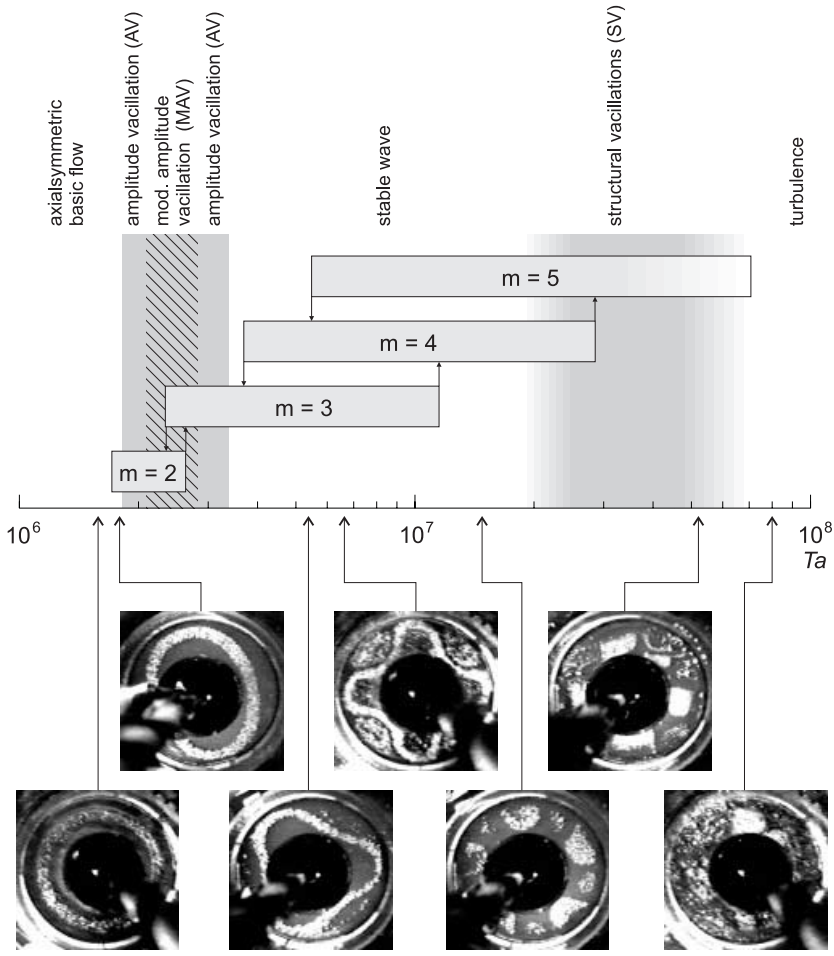

Fig. 4. Stability diagramm for $\Delta T = 3,5°\mathrm{C}$, stable wave numbers at different Taylor numbers Ta and videoprints of the surface flow.

rotating annulus, its amplitude oscillates with a period of $t \approx 1000$ s. In case of a MAV wave this period and the amplitude of the oscillation itself is not constant. At medium Taylor numbers, the waves show no fluctuations. The amplitude is constant, their structure is stable. With higher Taylor numbers, structural vacillations occur. The onset of the structural vacillations at Taylor numbers $Ta > 2 \cdot 10^7$ mark the begin of the transition to turbulence. The vacillations grow stronger with increasing Ta. Finally, at Taylor numbers $Ta > 7 \cdot 10^7$, no periodic structure can be identified.

Visual investigations alone are not sufficient to classify these flow regimes. Therefore an extensive time series analysis of the different flows is presented in the next section.

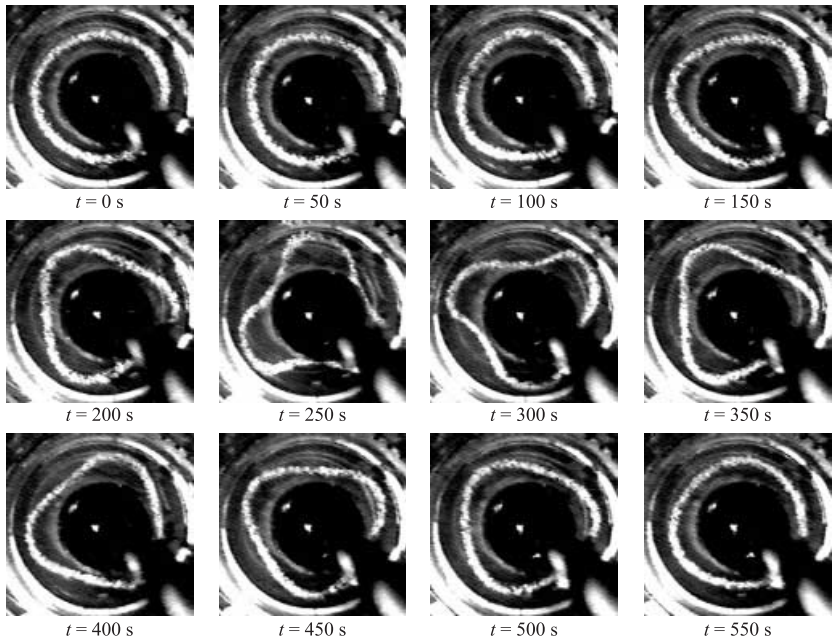

Fig. 5. Amplitude vacillation (AV) wave, $m = 3$, $Ta = 2.86 \cdot 10^6$, $Ro = 1.29$. The videoprints were taken at different times t.

4 Nonlinear dynamics

4.1 Measurement technique

To analyse the flow described in section 3, Laser Doppler velocimetry (LDV) was used to measure the flow velocities. The same LDV-techniques were used as described in a previous work of our group [8]. To detect the dynamic behaviour of the occuring waves in the rotating annulus using linear signal processing techniques, the most common and very useful way is to analyse the time series of a representative velocity component. In this case, the radial component is chosen. The Fourier spectrum and the autocorrelation are constructed. The spectrum gives a measure of the amount of power in a given frequency band over a selected frequency range. The autocorrelation function for a periodic signal is itself periodic and can often give a less confusing representation of the data. Irregularity in the data gives rise to a decay in the autocorrelation function, and the rate of decay gives a measure of the degree of irregularity.

However, in case of chaotic dynamic behaviour of the system, these linear methods are not sufficient to describe the complex flows. Therefore, the attractor of the system is reconstructed by the method of Takens [27]. In the reconstructed phase space, the topological properties of the attractor can be calculated. The methods used for this nonlinear time series analysis are described in more detail in the work of Wulf [29] and Wulf et al. [30].

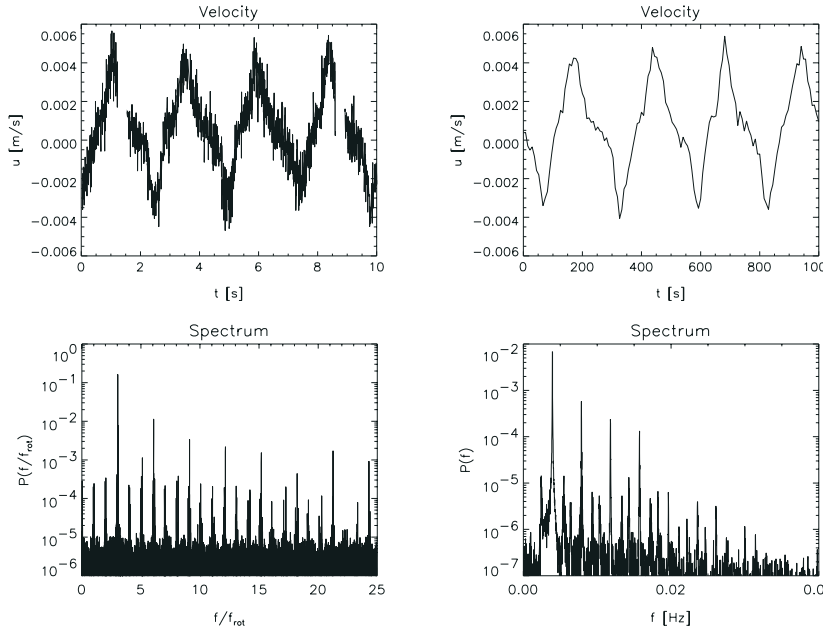

Fig. 6. LDA-data time series and its power spectrum (left) and the and the calculated time series in the co-rotating system and its spectrum (right), $m = 3$, $Ta = 4.1 \cdot 10^6$, $Ro = 0.91$, $f_{rot} = 0.135$ Hz.

The LDV measurement system is not co-rotating with the cylinder. Therefore, the raw data is collected at a circle in the rotating annulus. It is not possible to analyse the dynamic behaviour of the baroclinic waves directly from this series. However, one can determine the dominant modes of the waves from its power spectrum (see i.e. [1]), due to the fact, that the drift velocity c of the waves is very small compared to the rotation velocity. The spectrum of the LDV-data shown in figure 6 has the dominant peak at $f = 3 \cdot f_{rot}$, the dominant wave number is $m = 3$. To analyse the full dynamic motion of the wave, one needs to investigate a time series at a fixed point in the rotating coordinate frame. This information is embedded in the LDV-data. If the rotation rate is known precisely, a series at a fixed point can be calculated from the raw data using only the data points at the beginning of a new rotation cycle.

Figure 6 shows the unfiltered LDV-data, the calculated time series in the co-rotating system and their Fourier spectra. One should note the different time scales, the time scale of the time series in the co-rotating system is two orders of magnitude larger than that of the raw LDV-data. This big difference in the time scales is a stringent condition for this kind of transformation.

The method demonstrated above is limited in two ways. First, by the rotation frequency, because $\Delta t = 1/f_{rot}$ is the minimum time step between two points in the calculated time series. Therefore, $f_{rot}/2$ is the upper limit of frequency detection. However, the time scales of the baroclinic waves are large compared

to $1/f_{rot}$ in this case, so the detectable frequency domain is sufficient. Second, the rotation frequency has to be known very precisely. A small error results in a large distortion of the calculated time series. In the experimental setup, a counter registers 1500 pulses per rotation cycle and allows to determine the mean rotation frequency f_{rot} over a longer time period with nearly arbitrary precision. But small variations of f_{rot} during the measurements broaden the frequency peaks in the power spectrum. In this setup the variation is limited to 0.05%. To take care of this effect, artificial breaks are inserted into the LDV data, marking each rotation period. These breaks can be seen in the LDV data time series of figure 6 (top, left), they are used to calculate the time series in the co-rotating system. Nevertheless, the effect of small errors in f_{rot} is not negligible. The frequency peaks of the co-rotating time series in figure 6 are broadened compared to the spectrum of the raw LDV-data.

For the LDV analysis of the time series, as many data points as possible are needed for exact results. The LDV-data time series was taken for at least 7 hours. In the co-rotating system this time series has about 3000 up to 10000 data points, depending on the rotation rate. The radial velocity component is measured 20 mm under the surface.

4.2 Flow characterization

The phase space was reconstructed using time delayed coordinates. The fill-factor method and the integral local deformation method were used to estimate the time delay and the embedding dimension [4], [30]. A low pass filter and a singular value filter were applied to smoothen the data.

In phase space, the correlation integrals and the correlation dimension D_2 were calculated for different embedding dimensions. In the following figures, the dimensions are calculated for the embedding dimensions 1-10 as a function of $\epsilon = R/R_{max}$, where R is the radius of a hypersphere in phase space and R_{max} is the extension of the attractor. In addition, the pointwise dimension D_p and the largest Lyapunov exponent λ_1 were determined.

Figure 7 shows the development of λ_1 for different Taylor numbers at constant temperature difference between inner and outer cylinder (Compare with the stability diagram in figure 4). In the area of the modulated amplitude vacillation, small, but significantly positive Lyapunov exponents occur. For the stable baroclinic waves, represented by a limit cycle in phase space, the largest exponent decreases to zero. With the onset of the structural vacillations, λ_1 increases to relatively high values, indicating the transition to turbulence.

The pointwise dimension D_p shows the same dependency (see figure 8). At low Taylor numbers, just above the critical point in the regime of AV and MAV waves, dimensions $D_p > 2$ occur. For the limit cycle of stable waves the pointwise dimension D_p has values just above 1. At the onset of structural vacillation, the values of D_p increase significantly. Values of $D_p = 4$ mark the upper limit of the analysing method; higher dimensions cannot be determined, because of the restricted number of points in the velocity time series.

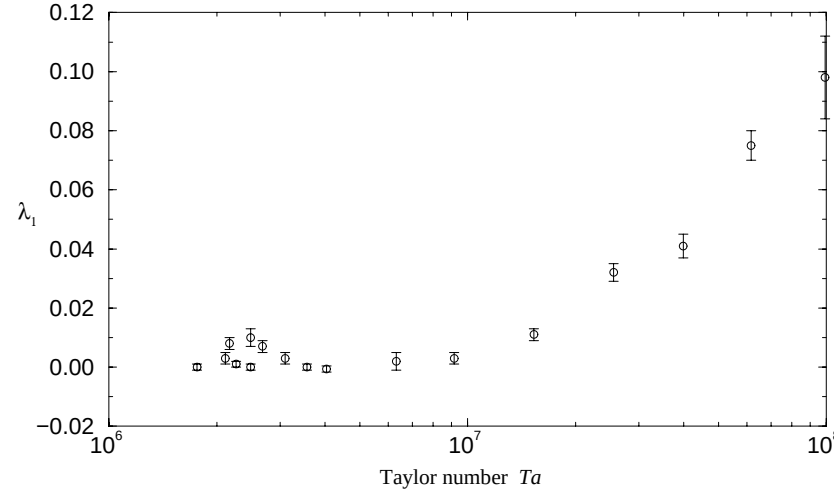

Fig. 7. Lyapunov exponent λ_1 for different Taylor numbers Ta, $\Delta T = 3.5°\mathrm{C}$.

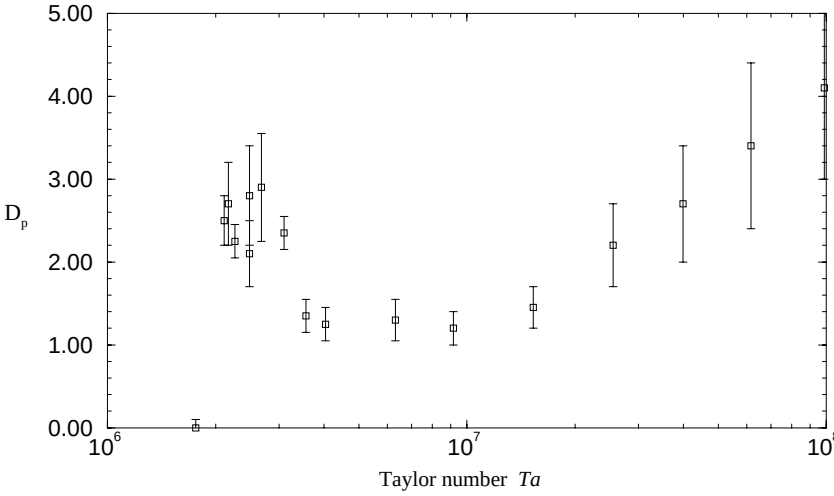

Fig. 8. Pointwise dimension D_2 for different Taylor numbers Ta, $\Delta T = 3.5°\mathrm{C}$.

Figure 9 shows a $m = 3$ AV wave, where the amplitude vacillation frequency is coupled to the drift frequency. The drift frequency f_c is the main peak in the power spectrum, corresponding to a drift velocity of $c = 0.13$ rad/s, which is in good agreement with visual measurements (see [26]). This peak is surrounded by harmonics of $1/5 \cdot f_c$. Fr/"uh and Read [11] observed this coupling between the two frequencies in their experiments, too. However, since the coupling has not been encountered in numerical simulations, they could not rule out the possibility that their temperature sensors in the fluid or irregularities of the tank itself might be the reason for this weak coupling. This LDV measurement shows

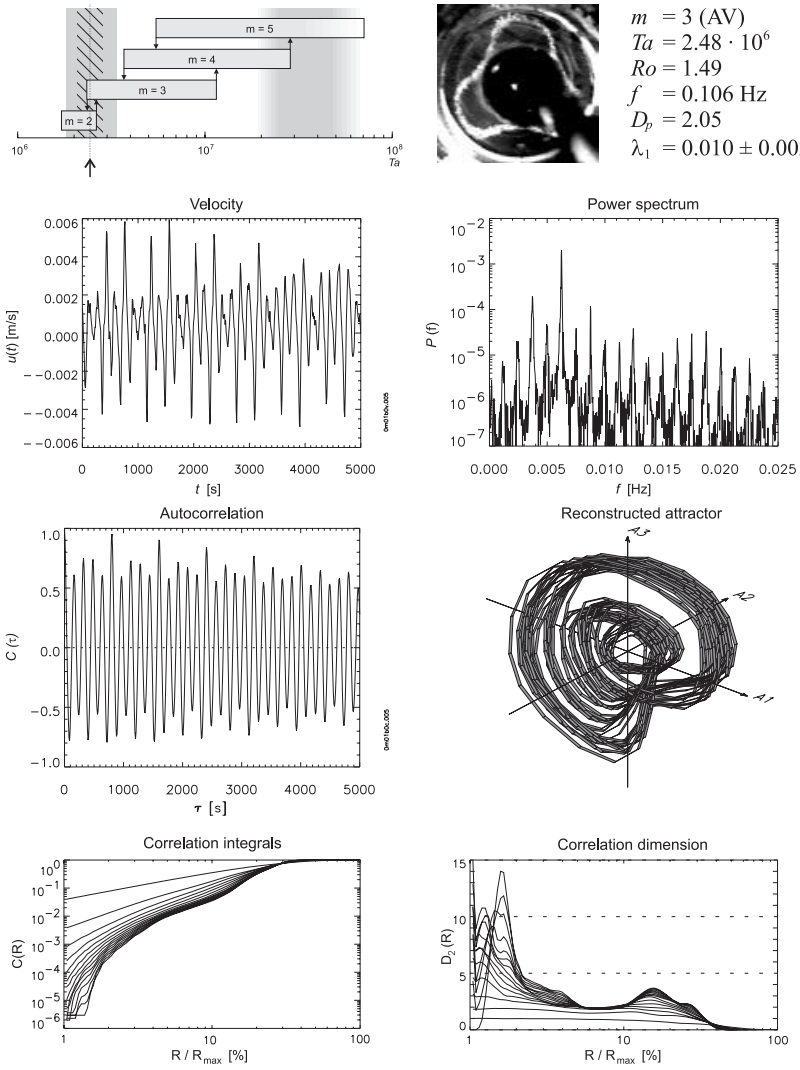

Fig. 9. Wave with amplitude vacillation, the vacillation frequency is coupled to the drift frequency.

at least that the temperature sensors are not responsible for the coupling. The largest Lyapunov exponent is significantly greater than zero, indicating chaotic fluctuations in the periodic flow.

Figure 10 shows a totally different behaviour than the flow in figure 9, though the parameters are exactly the same. First, it is a $m = 2$ wave instead of $m = 3$. Second, the vacillation frequency is decoupled from the drift frequency. Therefore, the attractor is a torus and $D_p \approx 2$. The largest Lyapunov exponent is 0. Both of these two flows are very sensitive to small changes of the boundary

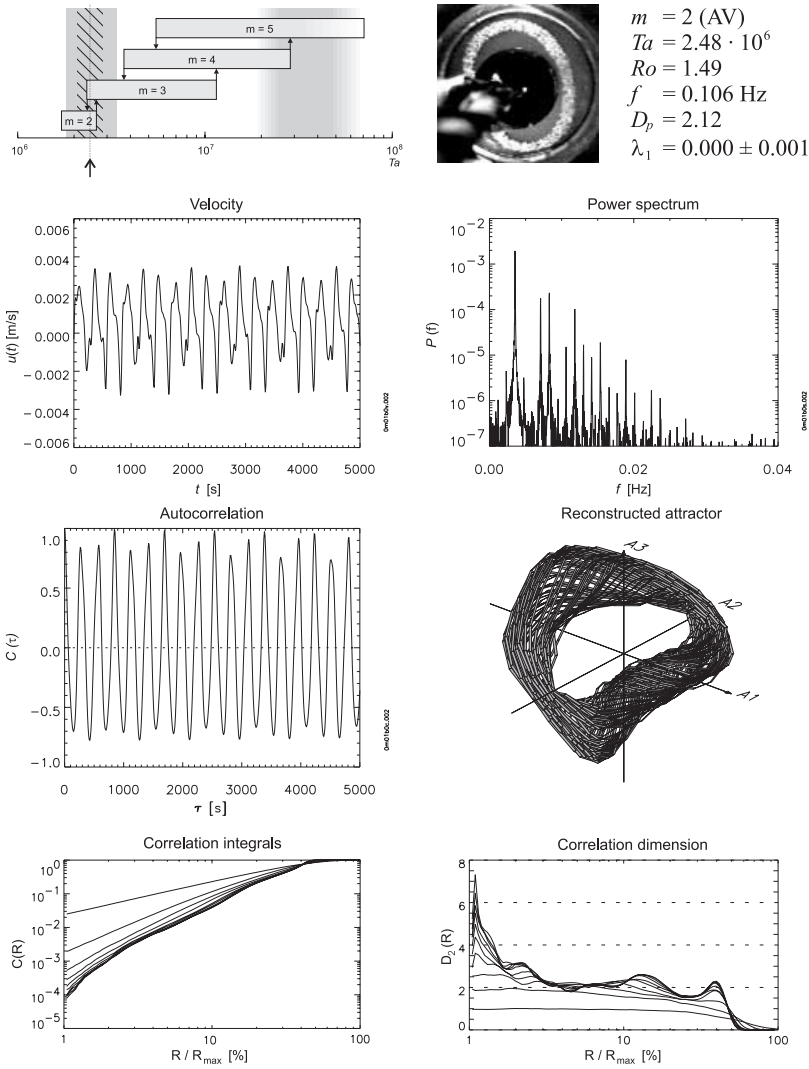

Fig. 10. Wave with amplitude vacillation, the vacillation frequency is decoupled from the drift frequency.

conditions. Small disturbances (e.g. a small variation of the rotation frequency) can cause a transition from one flow to the other. This is the main indicator, that the coupling observed in figure 9 is a weak effect. We did not find a pulsing state with coupled frequencies and $\lambda_1 = 0$. This, too, might be a hint that the coupling is just strong enough to overcome the steady disturbances within the error tolerances of our system.

At slightly different parameters than in figures 9 and 10, figure 11 shows a more complex flow. The autocorrelation function decays. The spectrum shows

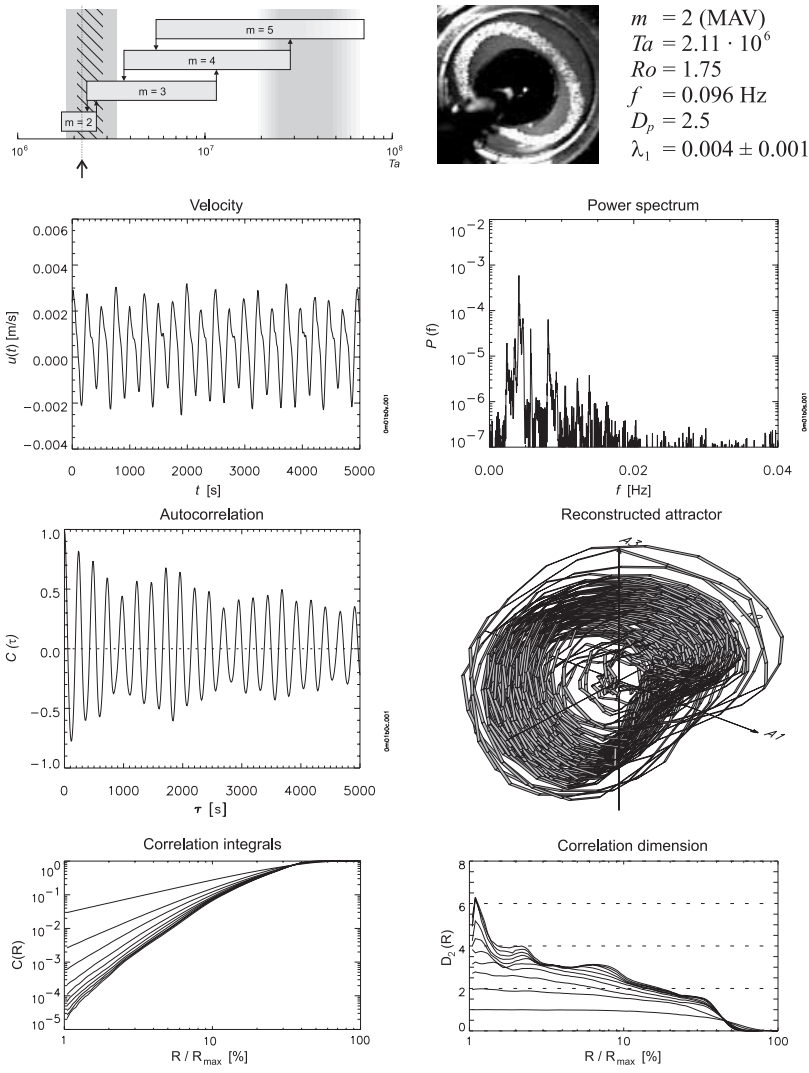

Fig. 11. Modulated amplitude vacillation wave.

broadened peaks, the Lyapunov exponent is greater than zero, indicating chaotic flow. The correlation dimension has a plateau at $D_c = 3$, indicating low dimensional chaos.

Figure 12 exhibits a stable $m = 3$ baroclinic wave, the attractor shows just the dominant drift frequency and the upper harmonics. The Lyapunov exponent is 0 within the error tolerance.

With higher Taylor numbers, the steady waves of figure 12 become unstable. The $m = 4$ wave in figure 13 shows the onset of structural vacillations. These vacillations have a small amplitude compared to the steady baroclinic wave and

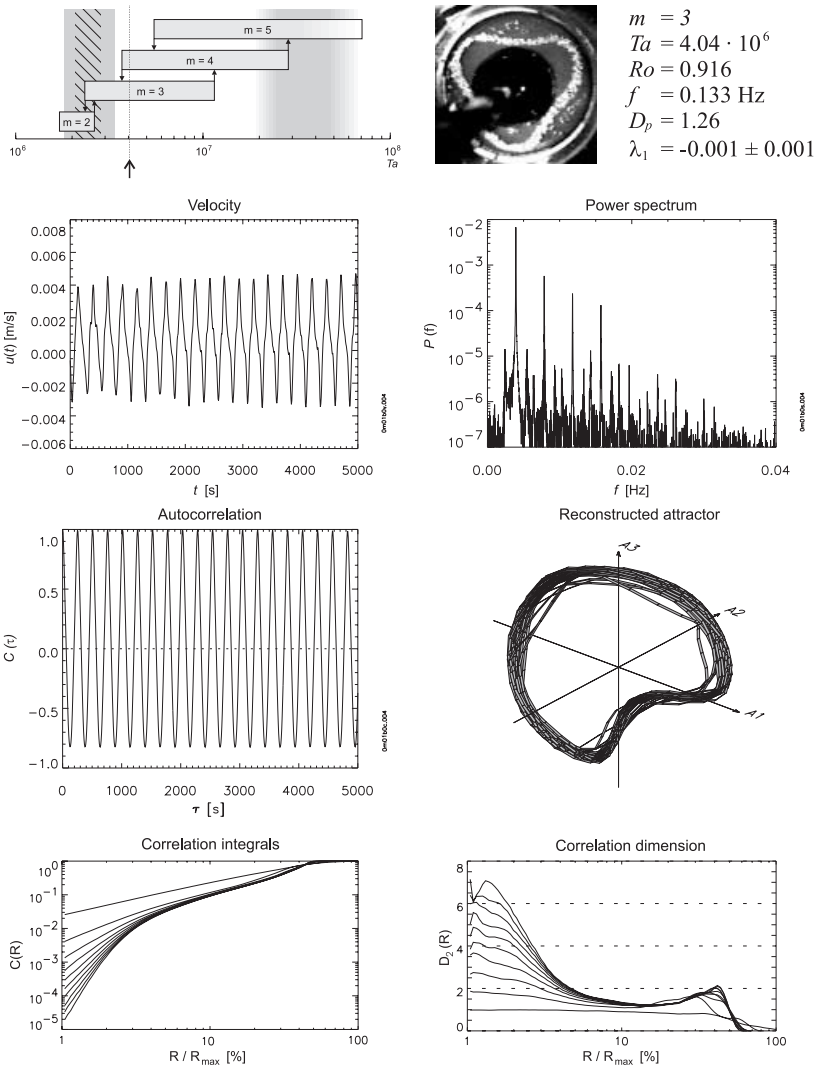

Fig. 12. Stable baroclinic wave.

are not large enough to be seen in the visual investigations. They can hardly be seen in the Fourier spectrum nor in the autocorrelation function, because of their very local nature. But the attractor shows the vacillations, their amplitude is significantly higher than the noise level. They cause a divergence of the correlation dimension for small $\epsilon = R/R_{max}$. The Lyapunov exponent is greater than zero, showing the chaotic nature of the fluctuations.

Figure 14 shows strong vacillations. Still, the periodic nature is evident in the Fourier spectrum. The fluctuations result in a higher 'noise' level in the spectrum, compared to a stable wave (see figure 12). The attractor is a highly

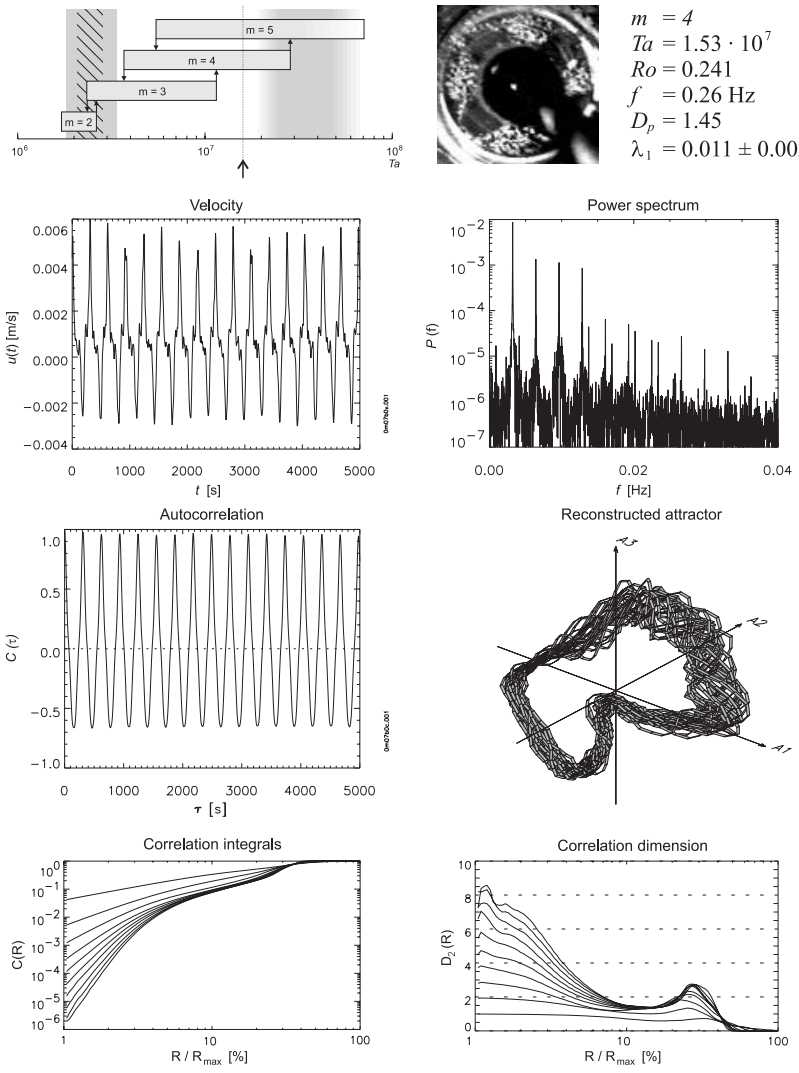

Fig. 13. Wave at the onset of structural vacillations.

disturbed limit cycle. The dimensions and the high Lyapunov exponent underline the chaotic nature of the vacillations.

With increasing Taylor numbers, the structural vacillations result in turbulent flow, shown in figure 15. No single significant peaks can be identified in the spectrum, the Lyapunov exponent is high, the correlation dimension does not converge.

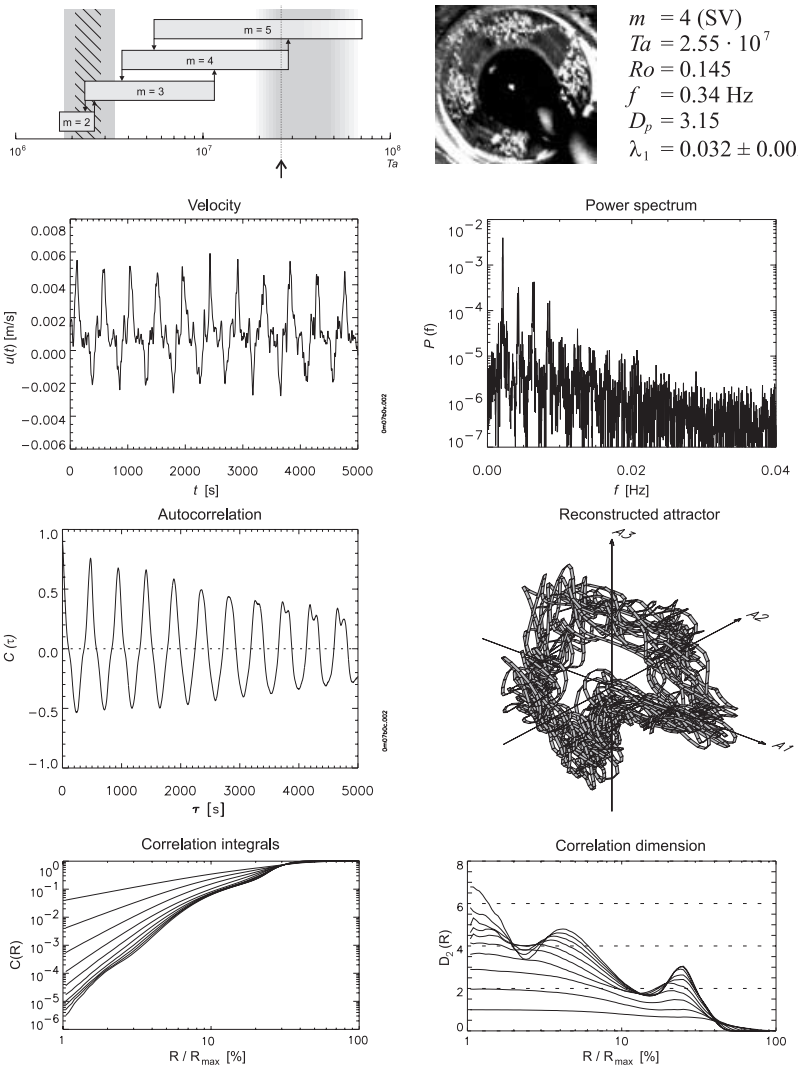

Fig. 14. Wave with structural vacillations.

4.3 Bifurcation scenario

The bifurcation diagrams were taken to investigate the interesting transition from the axisymmetric basic flow (a fixed point in phase space) to stable baroclinic waves (a limit cycle). One might think of an ordinary Hopf bifurcation, but the the different flow patterns at Taylor numbers just above the critical point (see section 4.2) make this transition more complex.

From the filtered LDV data, the local minima and maxima values of the radial velocity time series were determined. For each Taylor number, the histogram

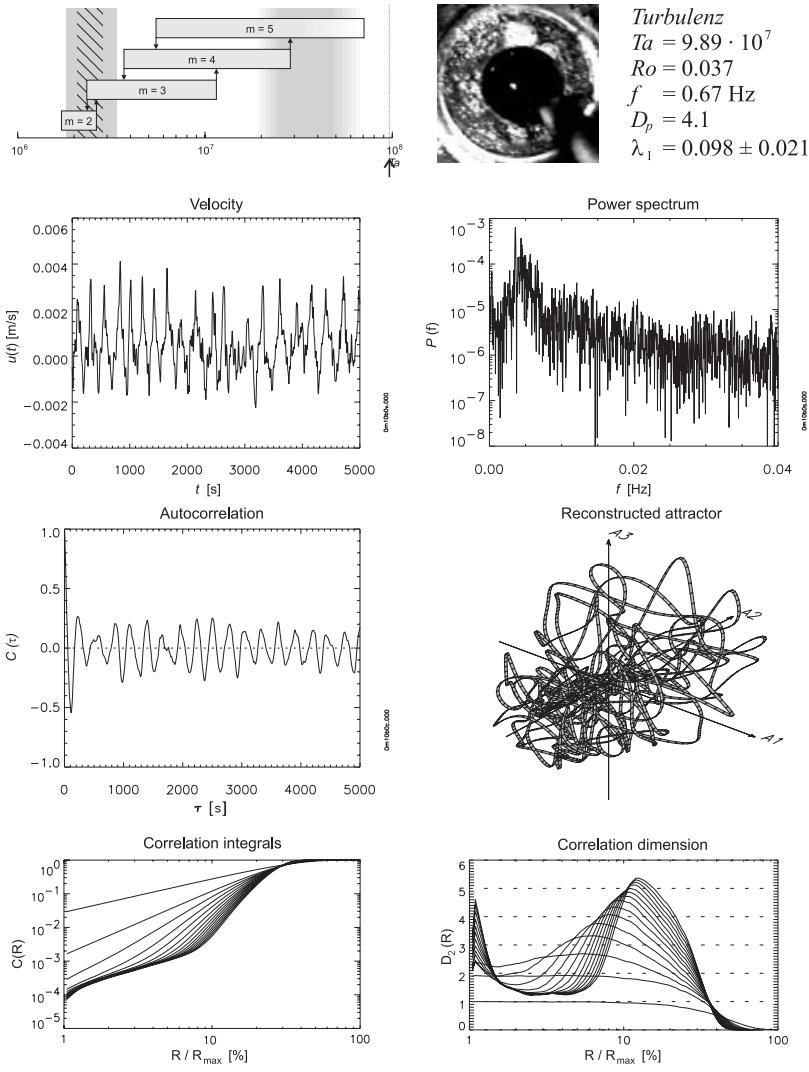

Fig. 15. The onset of turbulence

distributions of these extrema were fitted with Gauss curves. The medians of the Gauss curves are plotted in the diagramms shown in figure 16. The time series for a steady baroclinic wave has saddle points at $v(t) = 0$ (see figure 12). These saddle points are the reason for the line at $v = 0$ in the bifurcation diagrams.

The first dotted line in figure 16 denotes the transition from the axisymmetric basic flow to baroclinic waves with wave number $m = 2$. The critical Taylor number is the same, both for the increasing and the decreasing case, it shows no hysteresis. This is a supercritical Hopf bifurcation from a fixed point in phase

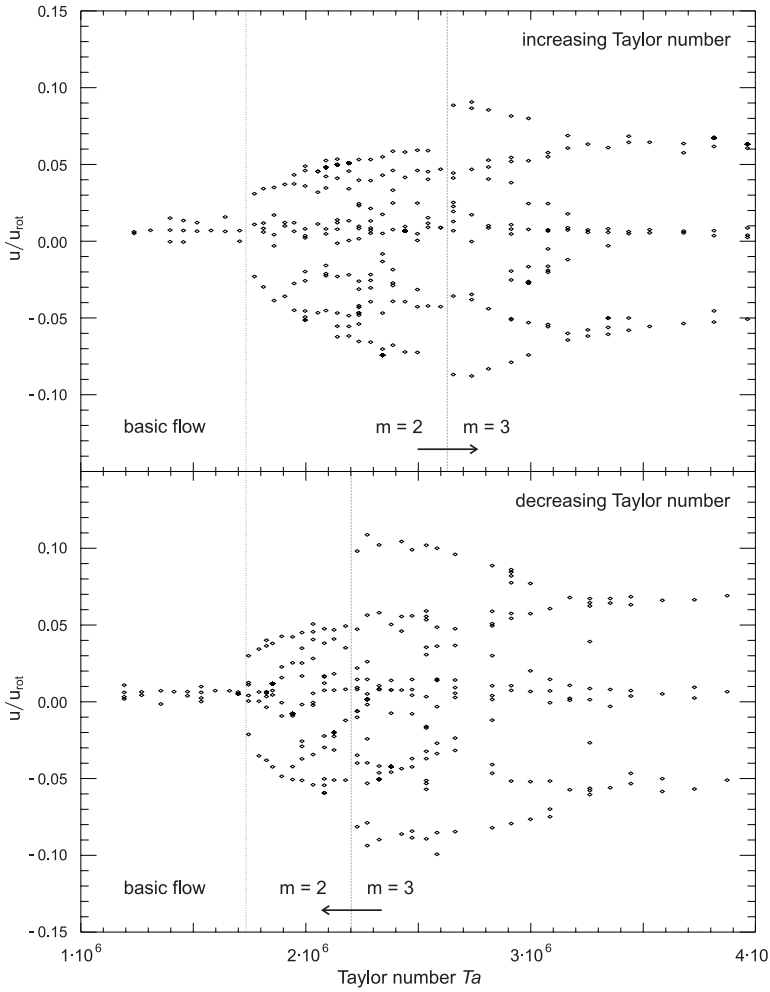

Fig. 16. Bifurcation diagram of the extrema of the velocity time series, for increasing (top) and decreasing Taylor number (bottom).

space (the axisymmetric basic flow) to a limit cycle (steady waves). However, with increasing Taylor number, the amplitude of the wave begins to oscillate.

The dotted lines at the right denote the transition between the wave numbers $m = 2$ and $m = 3$, determined by the dominant mode in the Fourier spectra of the LDV data. The hysteresis between the diagram for increasing (figure 16, top) and decreasing Taylor numbers (figure 16, bottom) is clearly visible in the difference between the two lines. The amplitude of the flow has a significant jump at this point, because the jetstream crosses the r-direction at a different angle if the wave number jumps from $m = 2$ to $m = 3$.

At high Taylor numbers, two subcritical Hopf bifurcations occur, this is the transition from AV waves to steady waves. The dynamical characteristics of

the flow in between the supercritical bifurcation on the left and the subcritical bifurcation on the right is not completely resolved by the diagrams. In this area, periodic flow (see figure 10) occurs as well as low dimensional chaotic flow (see figure 11).

4.4 Comparison to Taylor–Couette flow

Similar experiments on bifurcation scenarios in the classical Taylor–Couette system (rotating inner cylinder, fixed end plates) with corresponding geometrical data to the baroclinic wave tank were carried out for a radius ratio of $\eta = 0.5$ (wide gap) and $\Gamma = 3.97$ (short annulus). Flow visualization studies and investigations on the different routes into chaos of the isothermal Taylor–Couette flow with increasing Reynolds numbers for $\eta = 0.5$ were carried out in comparison to $\eta = 0.85$ [18]. In contrast to small cylindrical gaps, the experiments on bifurcation scenarios in the wide gap Taylor–Couette system $\eta = 0.5$ show another bifurcation scenario and another route into chaos as illustrated in the article "Taylor–Couette system with asymmetric boundary conditions" by Meincke et al. in this volume. In small gaps the flow becomes wavy, modulated wavy and then chaotic with increasing Reynolds number. In wide cylindrical gaps with small aspect ratios the Taylor vortex flow shows small scale disturbances and a much smaller modulated wavy flow regime due to the strong influence of the end plates and then it becomes chaotic.

The basic flow bifurcates via a Pitchfork bifurcation to Taylor vortex flow. There is no complex transition process comparable to the bifurcation diagrams in figure 16. In this point, the two systems are substantially different. This is no surprise, because the underlying mechanisms, heat transfer on the one hand and momentum transport on the other hand, are different. But, however, both systems show a similar variety of flow regimes, e.g. the periodicity, quasi-periodicity and stochastic regions.

5 Conclusions

Supplemental to the temperature measurements of Read et al. [25] and Früh and Read [11], contact free LDV measurements on baroclinic instabilities have been carried out. The LDV measurement method is good enough to apply nonlinear methods to the velocity time series. The results confirm the temperature measurements of Früh and Read [11] and Read et al. [25], in particular, the coupling between the amplitude vacillation frequency and the drift frequency was observed, too. The locality of the onset of the structural vacillations is evident.

The transition from the axisymmetric basic flow to steady baroclinic waves is documented by bifurcation diagrams of the extrema of the velocity time series. The diagrams prove the complexity of this transition. Supercritical and subcritical Hopf bifurcations occur during the transition to steady waves. But though the topological properties of some of the flow patterns are very similar

to the flow types found in Taylor–Couette systems, the bifurcation scenario is not comparable.

Acknowledgements. The financial support of Deutsche Forschungsgemeinschaft (DFG) under grant no. Eg100/3-1 is gratefully acknowledged. The authors wish to thank Wolfgang Beyer and Rüdiger Maier for their assistance during the preparation of the experiments.

References

1. P. Bernardet, A. Butet, M. Déqué: J. Atmos. Sci., **47**, No 24, 3023–3043 (1990)
2. M. Bowden, H. F. Eden: J. Atmos. Sci, **22**, 185–195 (1965)
3. F. H. Busse, C. R. Carrigan: J. Fluid Mech., **62**, 579–592 (1972)
4. T. Buzug, G. Pfister: Phys. Rev. A, **45** (10), 7073–7098 (1992)
5. G. Buzyna, R. L. Pfeffer, R. Kung: J. FLuid Mech., **145**, 377–403 (1984)
6. T. V. Davies: Phil. Trans. R. Soc. Lond. A, **249**, 27–64 (1956)
7. E. T. Eady: Tellus, **1**, 33-52 (1949)
8. C. Egbers, H. J. Rath: 'LDV-measurements on wide gap instabilities in spherical Couette flow'. In: *Developments in Laser Techniques and Applications to Fluid Mechanics*, ed. by R. J. Adrian, D. F. G. Durao, F. Durst, M. V. Heitor, M. Maeda, J. H. Whitelaw (Springer, Berlin Heidelberg 1996), pp. 45–66
9. J. S. Fein, R. L. Pfeffer: J. Fluid Mech., **22**, 541–558 (1976)
10. W. W. Fowlis, R. Hide: J. Atmos. Sci., **22**, 541–558 (1965)
11. W.-G. Früh, P. L. Read: Phil. Trans. R. Soc. Lond. A, **355**, 101–153 (1997)
12. J. Herrmann, F. H. Busse: Physics of Fluids, **10**, No. 7, 1611–1620 (1998)
13. R. Hide: Phil. Trans. R. Soc. Lond. A, **250**,441–478 (1958)
14. R. Hide, P.-J. Mason: Phil. Trans. Roy. Soc. Lond. A, **268**, 201–232 (1970)
15. R. Hide, P.-J. Mason: Adv. Physics, **24**, No. 1, 47–100 (1975)
16. P. K. Kundu: *Fluid Mechanics* (Academic Press, San Diego 1990)
17. A. Lorenzen, G. E. A. Meier, M. Assenheimer, E.-A. Müller: Experiments in Fluids, **8**, 286–290 (1990)
18. O. Meincke, C. Egbers: Phys. Chem. Earth (B), **24**, no. 5, 467–471 (1999)
19. O. Morita, M. Uryu: J. Atmos. Sci., **46**, No. 15, 2349–2355
20. M. D. Mundt, N. H. Brummell, J. E. Hart: J. Fluid Mech., **291**, 109–138 (1995)
21. J. Pedlosky: *Geophysical Fluid Dynamics* (Springer, New York 1987)
22. R. L. Pfeffer, G. Buzyna, R. Kung: J. Atmos. Sci., **37**, 2129–2149 (1980)
23. R. L. Pfeffer, S. Applequist, R. Kung, C. Long, G. Buzyna: Theoret. Comput. Fluid Dynamics, **9**, 253–267 (1997)
24. R. T. Pierrehumbert, K. L. Swanson: Annu. Rev. Fluid. Mech., **27**, 419–467 (1995)
25. P. L. Read, M. J. Bell, D. W. Johnson, R, M. Small: J. Fluid Mech., **238**, 599–632, (1992)
26. B. Sitte, C. Egbers: Phys. Chem. Earth (B), **24**, No. 5, 473–476 (1999)
27. F. Takens: 'Detecting strange attractors in turbulence'. In: *Lecture Notes in Mathematics: Dynamical Systems and Turbulence*, **898**, ed. by D. Rand and L. S. Young (Springer, Berlin Heidelberg 1980), pp. 366–381
28. D. J. Tritton: *Physical Fluid Dynamics*, 2nd edition (Oxford University Press, Oxford 1988)
29. P. Wulf: *VDI Fortschrittberichte Strömungstechnik: Untersuchungen zum laminar-turbulenten Übergang im konzentrischen Kugelspalt*, Band **333** (VDI-Verlag, Düsseldorf 1997)
30. P. Wulf, C. Egbers, H. J. Rath: Phys. Fluids, **11**, No. 6, 1359–1372 (1999)

Superfluid Couette flow

Carlo F. Barenghi

Mathematics Department, University of Newcastle upon Tyne,
Newcastle upon Tyne, NE1 7RU England

Abstract. The stability of the Couette flow of superfluid helium is discussed using a generalized form of Landau's two-fluid model. It is showed that the tension of the superfluid vortex lines has a great influence in determining the critical wavenumber and the critical Reynolds number of the transition from azimuthal Couette flow to Taylor vortex flow. The resulting Taylor vortex flow pattern is different from ordinary Taylor vortex flow and tends to be very elongated in the axial direction. Since the vortex tension is proportional to Planck's constant, the observed difference is a manifestation of quantum effects on the macroscopic scale. The aim of this article is to review the current understanding of superfluid Couette flow and point to the issues which are still unsolved, the directions of future development and the new link with current turbulence research.

1 Liquid helium

Helium is a gas at room temperature and becomes liquid only if it is cooled to temperatures of few Kelvin degrees (the boiling point is 4.2 K). At these low temperatures any other substance is solid, while helium remains liquid even if the temperature is further reduced to absolute zero. Liquid helium is thus essential in engineering applications in which a liquid is required to make good contact with another body to cool it. Some examples are: cooling samples in solid state physics, cooling infrared detectors in astrophysics, cooling superconducting magnets in hospitals and particle physics accelerators. Fluid dynamicists use liquid helium to perform experiments which exploit some of its physical properties which make it attractive in the study of ultra-high turbulence [1] [2]. For example, the kinematic viscosity of liquid helium ($\nu \approx 10^{-4}\ cm^2/sec$) is two orders of magnitude smaller than water's, so, for given speed U and size L, it is possible to achieve a much higher Reynolds number $Re = UL/\nu$. Similarly, the quantity $\alpha/\nu\kappa$ in liquid helium is more then three orders of magnitude larger than in water, so it is possible to study convection at very large Rayleigh numbers $Ra = g\alpha\Delta T L^3/\nu\kappa$, where g is the acceleration due to gravity, α is the thermal expansion coefficient, κ is the thermal diffusivity and ΔT is the imposed temperature gradient.

2 Helium II and Landau's two-fluid model

What makes liquid helium particularly interesting, however, are the phenomena which take place in the temperature range $0 \leq T \leq T_\lambda$ where T_λ is the

C. Egbers and G. Pfister (Eds.): LNP 549, pp. 379–398, 2000.

temperature of a phase transition called the *lambda transition* ($T_\lambda = 2.17\ K$ at saturated vapour pressure). Below T_λ liquid helium stops being just an ordinary (albeit cold) liquid and acquires the remarkable physical property of *superfluidity* (motion without friction) and a new name, *helium II*. What causes the peculiar behaviour of helium II is Bose–Einstein condensation, the macroscopic quantum ordering which is also responsible for superconductivity. Liquid helium above T_λ is called helium I. Hereafter we shall be concerned only with helium II.

The relation between fluid dynamics and helium II dates back to the times of Landau and Tisza who developed the so called *two -fluid model* [3]. The model describes helium II as the intimate mixture of two separate but compenetrating fluid components, the normal fluid and the superfluid. Each fluid component has its own density and velocity field, ρ_n and $\mathbf{v}_n$ for the normal fluid and ρ_s and $\mathbf{v}_s$ for the superfluid. The total density of helium II is $\rho = \rho_n + \rho_s$. The superfluid is related to the quantum ground state and has zero viscosity. The normal fluid consists of thermally excited states (called phonons and rotons) and is viscous. Essentially, the superfluid is like a classical, inviscid Euler fluid and the normal fluid is like a classical, viscous Navier–Stokes fluid. The relative proportion of normal fluid and superfluid depends on the temperature. At absolute zero helium II is entirely superfluid ($\rho_s/\rho = 1$, $\rho_n/\rho = 0$). If the temperature is raised the superfluid fraction decreases and the normal fluid fraction increases until, at $T = T_\lambda$, $\rho_s/\rho = 0$ and $\rho_n/\rho = 1$ and helium II becomes helium I. It is important to remark that the temperature dependence of ρ_n and ρ_s is nonlinear, and for $T < 1\ K$ helium is almost entirely superfluid, see Figure 1.

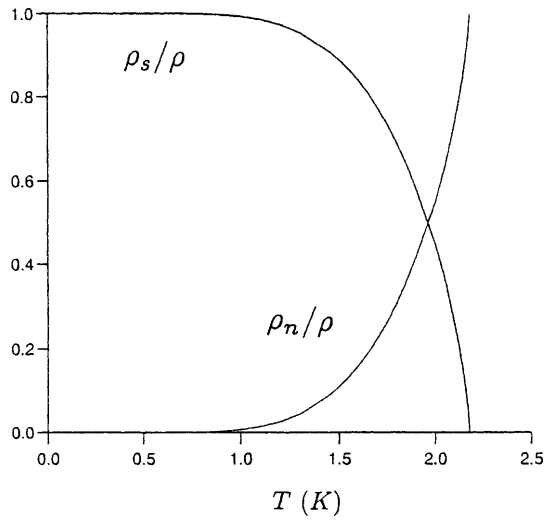

Fig. 1. Relative proportion of superfluid and normal fluid as a function of temperature.

Finally, Landau's model assumes that the motion of the superfluid is potential, $\boldsymbol{\omega}_s = \nabla \times \mathbf{v}_s = 0$. This property follows from the fact that the superfluid velocity is proportional to the gradient of the phase of the quantum mechanical wave function.

Landau's model predicts many observed nonclassical phenomena such as the existence of *first sound*, *second sound* and *thermal counterflow*. It is useful to review these phenomena briefly, since they are examples of the rich hydrodynamics of helium II and are relevant to what follows. First sound corresponds to ordinary sound in a classical liquid: it is a wave in which normal fluid and superfluid move together in phase, entropy and temperature remain approximately constant and density and pressure oscillate. Viceversa second sound is a wave in which the normal fluid and the superfluid move in antiphase, density and pressure remain approximately constant and temperature and entropy oscillate. Second sound can be easily generated by applying an AC voltage to a resistor and can be detected using a thermometer. Another popular way to generate second sound is to vibrate a membrane which is covered by microscopic holes: the normal fluid, clamped by its own viscosity, cannot move through the holes and is pushed back and forth by the membrane; on the contrary the superfluid, which is inviscid, moves through the holes. In this way a relative motion between normal fluid and superfluid is set up. Second sound is important in superfluid Couette flow because it is used to detect directly the superfluid vortex lines. Finally, thermal counterflow is linked to the special heat transfer properties of helium II. In an ordinary liquid, if care is taken to prevent convection, heat is transfered by conduction, so the heat flux W is proportional to the temperature gradient ΔT and there is a well defined thermal conductivity. In helium II the heat is carried away by the normal fluid only ($W = \rho S T v_n$ where S is the entropy per unit mass) and the condition of zero mass flux $\rho_n v_n + \rho_s v_s = 0$ makes the superfluid to flow towards the source of heat, $v_s = -(\rho_n/\rho_s)v_n$. In this way a relative velocity $v_n - v_s = W/\rho_s S T$ is set up between the two fluids which is proportional to the applied heat flux W. An example of this ability to transfer heat is the following. Consider a sample of helium I which is cooled by pumping the vapour above the surface; when the lambda point is crossed and helium I becomes helium II the violent boiling ceases because thermal gradients cannot be set up any longer. The presence of vortex lines in turbulent flows however limits this perfect heat conducting property [4], with implications for the engineering applications.

3 Vortex lines and the breakdown of Landau's model

If the heat flux W in thermal counterflow exceeds a critical value then helium II's ability to conduct heat breaks down with the appearance of superfluid vortex lines. Vortex lines also appear when helium II rotates at angular velocities which exceed a critical value, or when it flows in a pipe faster than some critical speed [5]. A superfluid vortex line is characterized by the Onsager–Feynman condition that the circulation around its axis is quantized:

$$\int_{\mathcal{C}} \mathbf{v}_s \cdot \mathbf{dl} = \Gamma, \tag{1}$$

where $\Gamma = h/2\pi m = 9.97 \times 10^{-4}\ cm^2/sec$ is the quantum of circulation, h is Planck's constant, m is the mass of one helium atom and $\mathcal{C}$ is a path around the core of the vortex line. Using cylindrical coordinates r, ϕ and z and assuming that the vortex line is set on the z axis, it follows from equation (1) that the superfluid velocity field around the vortex line is

$$\mathbf{v}_s = \frac{\Gamma}{2\pi r}\hat{\mathbf{e}}_\phi, \tag{2}$$

where $\hat{\mathbf{e}}_\phi$ is the unit vector in the azimuthal direction. The singularity at $r \to 0$ is only apparent because the superfluid density decreases from its bulk value to zero as $r \to 0$, thus keeping the momentum finite. The characteristic length scale over which $\rho_s \to 0$ as $r \to 0$ near the vortex core is called the *vortex core radius* $a_0 \approx 10^{-8}\ cm$. Since the length of a vortex line can be few centimeters (the height of a Couette apparatus for example), the aspect ratio of the vortex line can be of nine orders of magnitude: no other vortex structure in Nature has such a relatively thin core.

The existence of vortex lines was first established by studying the motion of helium II in a vessel which rotates at constant angular velocity Ω. It was found that the vortex lines form an uniform array aligned along the axis of rotation, and that the number of vortex lines per unit area is

$$n = \frac{2\Omega}{\Gamma}, \tag{3}$$

a relation called Feynman's rule. The vortex line density is typically high ($n \approx$ 2000 vortices per square centimeter at the angular velocity of 1 radiant per second). The superfluid velocity field which results from the presence of so many vortex lines is *microscopically* complex. However, if one averages over the individual vortices, one finds a *macroscopic* superfluid velocity field which is the same velocity $\mathbf{v} = \Omega r\hat{\mathbf{e}}_\phi$ of classical solid body rotation. The creation of vortex lines is therefore the superfluid's way to mimic classical rotation. Note also that, since the vortex core is hollow, the superfluid becomes multiply connected when in rotation. In conclusion, although Landau's condition that $\nabla \times \mathbf{v}_s = 0$ holds true at the microscopic level, at the macroscopic level the rotating superfluid has the same average vorticity 2Ω of an ordinary rotating fluid; the superfluid vorticity is discretized and consists of $n\Gamma$ vortices per unit area, each vortex carrying one quantum of circulation.

As mentioned in the previous section, second sound absorption is a sensitive technique to measure the length L of superfluid vortex lines per unit volume. The average superfluid vorticity is then defined as $\omega_s = \Gamma L$. The technique can detect values of L as low as $L \approx 10\ cm^{-2}$. Values as high as $L \approx 5 \times 10^5\ cm^{-2}$ are observed in turbulent helium II.

4 The generalized Landau equations

The breakdown of the original two-fluid model led to the development of a new theory which generalizes the two-fluid equations to situations in which a large number of superfluid vortex lines are present in the flow [6] [7] [8]. This theory is essentially a continuum approximation in which a fluid particle is a small but macroscopic region of volume Δ^3 centered around a point $\mathbf{r}$ and threaded by a high density of superfluid vortex lines which are almost parallel to each others. The number of superfluid vortex lines pointing in a given direction defines that component of the average superfluid vorticity field $\boldsymbol{\omega}_s$ at the point $\mathbf{r}$. The theory is limited to situations in which $\Delta_{lines} << \Delta << \Delta_{flow}$ where Δ_{lines} is the average distance between the vortex lines, Δ is the size of the fluid particle and Δ_{flow} is the smallest scale of interest in the flow. Assuming incompressibility, the theory consists of the following Hall–Vinen–Bekharevich– Khalatnikov (HVBK) equations:

$$\rho_n(\frac{\partial \mathbf{v}_n}{\partial t} + \mathbf{v}_n \cdot \nabla \mathbf{v}_n) = -\frac{\rho_n}{\rho}\nabla p - \rho_s S \nabla T + \mu \nabla^2 \mathbf{v}_n + \mathbf{F}_{mf}, \tag{4}$$

$$\rho_s(\frac{\partial \mathbf{v}_s}{\partial t} + \mathbf{v}_s \cdot \nabla \mathbf{v}_s) = -\frac{\rho_s}{\rho}\nabla p + \rho_s S \nabla T + \mathbf{F}_{ten} - \mathbf{F}_{mf}, \tag{5}$$

$$\nabla \cdot \mathbf{v}_n = 0, \tag{6}$$

$$\nabla \cdot \mathbf{v}_s = 0, \tag{7}$$

where p is the pressure and μ is the viscosity. Hereafter we define the kinematic viscosity as $\nu_n = \mu/\rho_n$, using the normal fluid density rather than the total density.

Equations (4) and (5) differ from the original two-fluid equations of Landau in two ways. The first difference is the interpretation of the fields $\mathbf{v}_n$, $\mathbf{v}_s$ and $\boldsymbol{\omega}_s = \nabla \times \mathbf{v}_s$ as macroscopic rather than microscopic. The second difference is the presence of two extra forces per unit volume, the *mutual friction force* $\mathbf{F}_{mf}$, and the *tension force* $\mathbf{F}_{ten}$. Microscopically, the mutual friction force arises from the fact that the superfluid vortex lines scatter the phonons and the rotons which make up the normal fluid [9]; macroscopically, $\mathbf{F}_{mf}$ is essentially a drag which acts simultaneously on the two fluids [10]. Its actual form is

$$\begin{aligned}\mathbf{F}_{mf} = &\frac{\rho_s \rho_n B}{2\rho}\widehat{\boldsymbol{\omega}}_s \times (\boldsymbol{\omega}_s \times (\mathbf{v}_n - \mathbf{v}_s - \nu_s \nabla \times \widehat{\boldsymbol{\omega}}_s)) \\ &+\frac{\rho_s \rho_n B'}{2\rho}\boldsymbol{\omega}_s \times (\mathbf{v}_n - \mathbf{v}_s - \nu_s \nabla \times \widehat{\boldsymbol{\omega}}_s),\end{aligned} \tag{8}$$

where B and B' are known temperature dependent coefficients. The tension force is present if the vortex lines are bent and has the form

$$\mathbf{F}_{ten} = -\nu_s \rho_s \boldsymbol{\omega}_s \times (\nabla \times \widehat{\boldsymbol{\omega}}_s), \tag{9}$$

where

$$\widehat{\boldsymbol{\omega}}_s = \frac{1}{|\boldsymbol{\omega}_s|}\boldsymbol{\omega}_s, \tag{10}$$

is the unit vector in the direction of the superfluid vorticity and

$$\nu_s = \frac{\Gamma}{4\pi}\log\left(\frac{\Delta_{lines}}{a_0}\right), \tag{11}$$

is the vortex tension parameter. Note that ν_s is proportional to the quantum of circulation, hence to Planck's constant.

Equations (4) and (5) have three interesting limits. If $T \to T_\lambda$ then $\rho_s \to 0$ and the normal fluid equation (4) becomes the Navier–Stokes equation for a classical viscous fluid:

$$\frac{\partial \mathbf{v}_n}{\partial t} + \mathbf{v}_n \cdot \nabla \mathbf{v}_n = -\frac{1}{\rho}\nabla p + \nu_n \nabla^2 \mathbf{v}_n, \tag{12}$$

If $T \to 0$ then $\rho_n \to 0$ and the superfluid equation (5) becomes the equation of motion of a pure superfluid:

$$\frac{\partial \mathbf{v}_s}{\partial t} + \mathbf{v}_s \cdot \nabla \mathbf{v}_s = -\nabla p_s - \nu_s \boldsymbol{\omega}_s \times (\nabla \times \widehat{\boldsymbol{\omega}}_s), \tag{13}$$

where $-\nabla p_s = -1/\rho \nabla p + S\nabla T$. Finally, if Planck's constant h is set equal to zero, then $\nu_s = 0$ and the superflow equation (13) becomes Euler's equation for a classical inviscid fluid:

$$\frac{\partial \mathbf{v}_s}{\partial t} + \mathbf{v}_s \cdot \nabla \mathbf{v}_s = -\nabla p_s, \tag{14}$$

Since the vortex tension force plays an important role in the stability of Couette flow, it is worth discussing its physical meaning [11] in more detail. A superfluid vortex line is stiff because it has energy per unit length, that is to say tension. Let us assume first that $T = 0\ K$. If the vortex line is straight along the z axis then the tension is the kinetic energy per unit length

$$E = \frac{1}{2}\rho_s \int_0^{2\pi} d\phi \int_{a_0}^{\Delta_{lines}} dr r v_s^2, \tag{15}$$

where the cutoffs a_0 and Δ_{lines} prevent a singularity at $r \to 0$ and a divergence at $r \to \infty$. Using equation (2) it follows that

$$E = \frac{\rho_s \Gamma^2}{4\pi}\log\left(\frac{\Delta_{lines}}{a_0}\right), \tag{16}$$

A vortex line which is bent with radius of curvature r suffers a straightening force per unit length $\mathbf{F'}_{ten}$ which has magnitude $F_{ten} = E/r$. For example, for a vortex ring of radius r, $\mathbf{F'}_{ten} = E(\widehat{\boldsymbol{\omega}}_s \cdot \nabla)\widehat{\boldsymbol{\omega}}_s$ where $\widehat{\boldsymbol{\omega}}_s$ is the unit vector along the vortex ring, hence $\mathbf{F'}_{ten}$ has magnitude E/r in the negative radial direction towards the centre of the ring.

Suppose now that instead of a single superfluid vortex we have a tube containing many vortices, and that the number of vortices per unit area of the tube is ω_s/Γ. Then the straightening force per unit volume of superfluid is $\mathbf{F}_{ten} = (\omega_s/\Gamma)\mathbf{F}'_{ten}$

$$\mathbf{F}_{ten} = \frac{\omega_s}{\Gamma} E(\widehat{\boldsymbol{\omega}}_s \cdot \nabla \widehat{\boldsymbol{\omega}}_s) = -\nu_s \rho_s \boldsymbol{\omega}_s \times (\nabla \times \widehat{\boldsymbol{\omega}}_s), \tag{17}$$

which agrees with (9).

If the temperature is not zero then the normal fluid must be taken into account. Let us consider the conservation law for vortex lines

$$\frac{\partial \boldsymbol{\omega}_s}{\partial t} + \nabla \times (\boldsymbol{\omega}_s \times \mathbf{v}_L) = 0, \tag{18}$$

where $\mathbf{v}_L$ is the velocity of a tube containing vortex lines of average vorticity $\boldsymbol{\omega}_s$. Since $\boldsymbol{\omega}_s = \nabla \times \mathbf{v}_s$ we have

$$\frac{\partial \mathbf{v}_s}{\partial t} + \boldsymbol{\omega}_s \times \mathbf{v}_L = \nabla \Phi, \tag{19}$$

where Φ is some scalar function. The velocity $\mathbf{v}_L$ of the tube is obtained by neglecting the inertia of the vortex core and setting equal to zero all forces acting on the superfluid tube: we get

$$\mathbf{F}_{drag} + \mathbf{F}_{ten} + \mathbf{F}_{Mag} = 0, \tag{20}$$

where the drag force on the superfluid is

$$\mathbf{F}_{drag} = -\mathbf{F}_{mf}, \tag{21}$$

the tension force $\mathbf{F}_{ten}$ is given by equation (9), and the Magnus force arises from the superfluid circulation about the tube:

$$\mathbf{F}_{Mag} = \rho_s \boldsymbol{\omega}_s \times (\mathbf{v}_L - \mathbf{v}_s), \tag{22}$$

Since $\widehat{\boldsymbol{\omega}}_s \times (\boldsymbol{\omega}_s \times \mathbf{c}) = -\boldsymbol{\omega}_s \times (\mathbf{c} \times \widehat{\boldsymbol{\omega}}_s)$ it follows that

$$\rho_s \boldsymbol{\omega}_s \times (\mathbf{v}_L - \mathbf{v}_s - \nu_s \nabla \times \widehat{\boldsymbol{\omega}}_s + \frac{B}{2}\frac{\rho_n}{\rho}\mathbf{c} \times \widehat{\boldsymbol{\omega}}_s - \frac{B'}{2}\frac{\rho_n}{\rho}\mathbf{c}) = 0, \tag{23}$$

where we have defined

$$\mathbf{c} = \mathbf{v}_n - \mathbf{v}_s - \nu_s \nabla \times \widehat{\boldsymbol{\omega}}_s, \tag{24}$$

Therefore the velocity of the tube is

$$\mathbf{v}_L = \mathbf{v}_s + \nu_s \nabla \times \widehat{\boldsymbol{\omega}}_s - \frac{B\rho_n}{2\rho}\mathbf{c} \times \widehat{\boldsymbol{\omega}}_s + \frac{B'\rho_n}{2\rho}\mathbf{c}, \tag{25}$$

From (25) we get

$$\boldsymbol{\omega}_s \times \mathbf{v}_L = -\nabla(\frac{v_s^2}{2}) + \mathbf{v}_s \cdot \nabla \mathbf{v}_s - \frac{1}{\rho_s}\mathbf{F}_{ten} + \frac{1}{\rho_s}\mathbf{F}_{mf}, \tag{26}$$

hence equation (19) becomes

$$\frac{\partial \mathbf{v}_s}{\partial t} + \mathbf{v}_s \cdot \nabla \mathbf{v}_s = -\nabla(\Phi + \frac{v_s^2}{2}) + \frac{1}{\rho_s}\mathbf{F}_{ten} - \frac{1}{\rho_s}\mathbf{F}_{mf}, \tag{27}$$

which is equation (5) after a suitable identification of Φ.

A very strict test which can be performed on proposed fluid equations is the prediction of a hydrodynamical instability. The transition from azimuthal Couette flow to Taylor vortices is therefore an ideal test of the HVBK equations. Some of the early experiments were performed in order to measure the viscosity of helium II - the Couette apparatus is indeed a viscometer. These experiments showed that the stability of helium II is very different from the stability of a classical fluid, but no clear picture emerged from the experiments [12]. This is partly because the experiments were performed at a number of different temperatures, and helium's properties vary greatly with temperature. More important was the lack of a theoretical framework to interpret the results, despite the pioneering attempts of Chandrasekhar and Donnelly [13] and later of Snyder [14]. As described in Section 6, contact between the HVBK equations and the experiments was only achieved when Barenghi and Jones [15] discovered the temperature dependence of the critical wavenumber and Swanson and Donnelly [16] confirmed the predictions of Barenghi [17]. This progress opened the way to the study of the nonlinear Couette flow of helium II.

5 The basic state

We consider liquid helium II contained between two concentric cylinders of height h, inner radius R_1 and outer radius R_2. We call $\delta = R_2 - R_1$ the width of the gap between the cylinders and assume that the inner and outer cylinder rotate at constant angular velocities Ω_1 and Ω_2 around the z axis. We call $\eta = R_1/R_2$ the radius ratio and h/δ the aspect ratio of the cylinders. Hereafter, unless otherwise indicated, we make the infinite cylinder approximation that $h >> \delta$. Most experiments and calculations are done in the narrow gap limit ($\eta \to 1$), so this is the typical situation which we discuss unless otherwise stated. Finally, for the sake of simplicity, in the following discussion we assume that the outer cylinder is held fixed ($\Omega_2 = 0$). The case of rotations of the outer cylinder is discussed separately in Sections 9 and 10.

Superfluid vortex lines represent vorticity in discrete amounts, so if helium II does not rotate fast enough to create the first vortex line (or, more precisely, to create by symmetry the first *row* of vortices in the middle of the gap), then the flow of the superfluid is potential. The nucleation of the first quantized vortex line is a major problem of condensed matter physics which is still not well understood and requires a quantum description, but some progress has been made using general arguments. Two theories exist. The first theory was

developed by Fetter [18] and is based on thermodynamics and the minimization of the free energy. Fetter's theory was extended to the Couette problem by Swanson and Donnelly [19] who determined that the critical velocity Ω_1^* at which the first row of vortices appears is

$$\Omega_1^* = \frac{(1-\eta^2)\Gamma}{\eta^2 \pi \delta^2} \log\left(\frac{2\delta}{\pi a}\right), \tag{28}$$

Using a very different approach (local conservation of momentum rather than minimization of free energy) Jones et al [20] developed a second theory which yields the critical velocity $(1+\rho_s/\rho_n)\Omega_1^*$. The second theory is in quantitative agreement with the observation of metastability (which is not explained by the theory of Fetter) and differs from the Fetter–Swanson–Donnelly theory because of the presence of the factor $(1+\rho_s/\rho_n)$ which gives better agreement with the experiments at temperatures $T > 2\ K$. The second theory however fails if the temperature is reduced below $T \approx 1.85\ K$. Jones et al also investigated whether the first row of vortices (once it has appeared) is also linearly stable. They found that for $T < 1.85\ K$ the vortices are unstable, in disagreement with the observations. The theoretical issues of the appearance of the first row of vortices and of its stability in the presence of normal fluid azimuthal Couette flow is thus still open.

If Ω_1 is increased past Ω_1^* more and more rows of superfluid vortices are quickly created, until a uniform array of vortices aligned along the z direction fills the gap, see Figure 2.

/noindent At this point both the normal fluid and the superfluid are in the Couette state

$$\mathbf{v}_n = \mathbf{v}_s = (Ar + \frac{B}{r})\hat{\mathbf{e}}_\phi, \tag{29}$$

where the usual Couette parameters A and B are

$$A = \frac{R_2^2\Omega_2 - R_1^2\Omega_1}{R_2^2 - R_1^2}, \tag{30}$$

$$B = \frac{R_1^2 R_2^2(\Omega_1 - \Omega_2)}{R_2^2 - R_1^2}, \tag{31}$$

The existence of the Couette state for the normal fluid is verified experimentally by measuring the torque induced on the stationary cylinder, which, for consistency, must yield the correct viscosity of helium II as determined by another method (eg using the vibrating wire technique).

The Couette state of the superfluid is checked by measuring the attenuation of second sound (hence the vortex line density) across the gap and testing that it is proportional to Ω_1, hence to the axial vorticity $2A$. It is also possible to make the measurement of superfluid vorticity absolute by calibration against the case of solid body rotation ($\Omega_2 = \Omega_1$) and using Feynman's rule (3). Barenghi and Jones [15] found a solution of (3) and (4) in which the normal fluid is in the

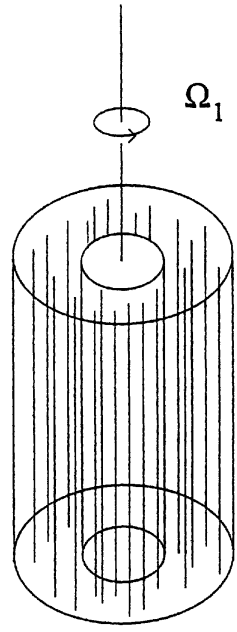

Fig. 2. Schematic representation of superfluid vortex lines in the Couette state.

Couette state but the superfluid is not; this solution corresponds to potential flow for $\mathbf{v}_s$ but is not isothermal, unlike the Couette solution. Since no radial temperature gradient has yet been detected, it is justified to assume the basic state (29).

In using the HVBK equations to study Couette flow there are some assumptions which one should bear in mind. The HVBK equations are based on a continuum approximation in which the intervortex spacing is small compared with length scales of the apparatus (eg δ) and the flow. For some experiments this approximation is satisfactory, but for some others there may be only two or three rows of vortices across the gap when the instability takes place, which may be too few for the continuum approximation to be valid. Another problem is the uncertainty about the effects of the endwalls. In classical Couette flow the top and bottom walls create a weak meridional Ekman circulation which is always present even at very low angular velocities. The same effect must be present in helium II. The effects of this circulation are neglected using the infinite cylinder approximation.

Before applying the HVBK equations to Couette flow it is important to review the boundary conditions. The normal fluid is viscous and obeys no-slip boundary conditions at the walls: $v_{nr} = v_{nz} = 0$ at $r = R_1$ and $r = R_2$, $v_{n\phi} = \Omega_1 R_1$ at $r = R_1$, $v_{n\phi} = \Omega_2 R_2$ at $r = R_2$. The superfluid's boundary conditions are more delicate. Evidently $\mathbf{v}_s$ must satisfy $v_{sr} = 0$ at $r = R_1$ and

$r = R_2$. In the absence of vortices (the original Landau model) there are no other boundary conditions and the superfluid is free to slip at the walls.

6 Rotations of the inner cylinder: absolute zero

Despite the fact that no experiment can achieve absolute zero, the study of the stability of pure superfluid Couette flow ($T = 0\ K$) is the key to understand the role played by the quantized vortex lines. Barenghi and Jones [21] studied the linear stability of the Couette state (29) with respect to axisymmetric ($m = 0$) and nonaxisymmetric ($m \neq 0$) perturbations of the form $exp(im\phi + ikz)$ governed by equation (13) where m and k are respectively the azimuthal and axial wavenumbers. The superfluid boundary conditions required in this calculation is that there is no flow into the walls ($v_{sr} = 0$ at $r = R_1$ and R_2). Figure 3 shows the calculated stability boundary, where the Donnelly number $D_1 = \Omega_1 R_1 \delta / \nu_s$ is the dimensionless velocity of the inner cylinder and the wavenumber k is made dimensionless using the gap δ. The figure shows that axisymmetric perturbations are stable below a certain critical velocity, but nonaxisymmetric perturbations are always unstable to long wavelength ($k \to 0$) instabilities. Barenghi and Jones discussed the results in terms of the combined effects of rotation and vortex tension: the vortex tension plays a key role as it makes bent vortex lines to rotate at angular velocity $\nu_s k^2$ in the direction opposite to the vorticity. The conclusion of their work is that a pure superfluid follows Rayleigh's criterion of a classical inviscid fluid in the sense that any rotation of the inner cylinder is destabilizing. This result clarifies the relation between equation (13) and equation (14).

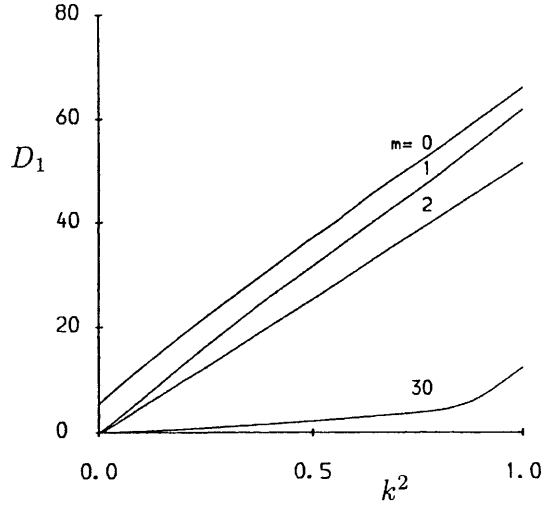

Fig. 3. Stability boundaries for rotations of the inner cylinder: Donnelly number D_1 versus square of the wavenumber k^2 for $m = 0, 1, 2, 30$ at radius ratio $\eta = 0.99$.

7 Rotations of the inner cylinder: finite temperatures

We now consider what happens at nonzero temperatures. It is known from the experiments that if Ω_1 is increased from Ω_1^* and exceeds some critical value Ω_{1c} then a transition takes place. Typically, what is observed in the experiments is a break in the linear relation between Ω_1 and the torque induced on the outer stationary cylinder, or a break in the relation between Ω_1 and the attenuation of second sound.

The transition from azimuthal Couette flow to Taylor vortex flow at nonzero temperature was studied by Barenghi and Jones [15] and Barenghi [17]. They found that the $m = 0$ mode is the first to become unstable. The main result of their investigation is that, if the temperature is reduced below T_λ, the critical wavenumber k_c decreases from its classical value and tends to zero in the limit $T \to 0$, which is consistent with the result described in the previous section. Figure 4 shows the stability boundaries of the $m = 0$ mode at various temperatures (only the bottom part of each curve is showed for clarity). The velocity of rotation of the inner cylinder is expressed as a Taylor number

$$Ta = \frac{2\Omega_1^2 \delta^4}{\nu_n^2} \frac{\eta^2}{(1-\eta^2)}, \tag{32}$$

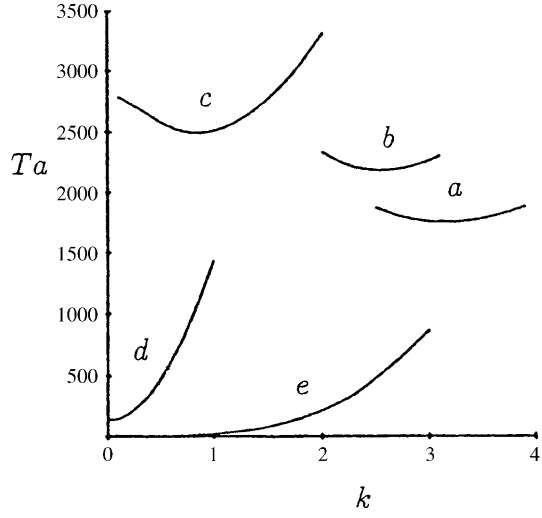

Fig. 4. Stability boundaries of the $m = 0$ mode for rotations of the inner cylinder at $\eta = 0.95$: critical Taylor number Ta versus wavenumber k; (a): the classical Taylor–Couette case; (b): $T = 2.16\ K$; (c): $T = 2.1\ K$; (d): $T = 2.05\ K$; (e): $T = 1.5\ K$

Note that the critical wavenumber (the value of k which corresponds to the minimum of each curve of Figure 4) moves to the left at decreasing temperature.

In the classical Taylor–Couette problem the critical wavenumber is $k_{class} \approx \pi/\delta$, as showed by curve (a) of Figure 4. Therefore the axial extension of the classical Taylor vortex cell is the same as the gap's width. The smaller wavenumbers in helium II mean that the Taylor cells are elongated in the axial direction. Barenghi and Jones found that the effect is due to the vortex tension. Figure 5 shows the dramatic effect on the stability boundary caused by the reduction of the vortex tension parameter ν_s to half of its value - see curve (b) - or to zero - see curve (c). These arbitrary changes are equivalent to halving Planck's constant h or setting $h = 0$ respectively.

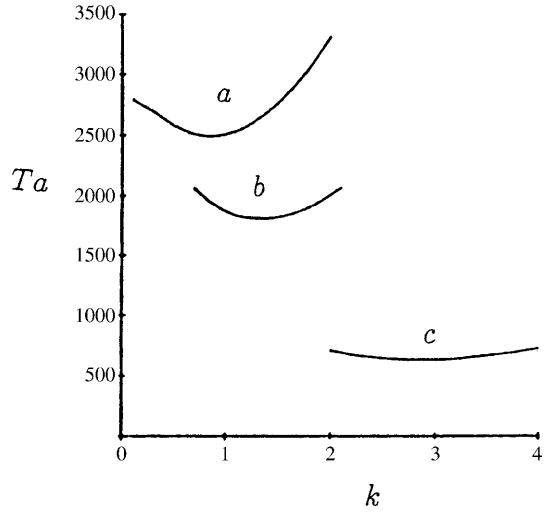

Fig. 5. Effects of artificially changing the vortex tension ν_s: Taylor number Ta versus wavenumber k. (a): stability curve of the $m = 0$ mode at $T = 2.1\ K$ and $\eta = 0.95$; (b): same curve as in (a) but ν_s is halved; (c): same curve as in (a) but ν_s is set equal to zero.

The elongation of the Taylor cells in helium II is so strong that many early experiments were dominated by ill defined and temperature dependent end effects, so it is not surprising that results were not very consistent with each others. To appreciate this issue it is important to remark that the flow of helium II cannot be visualized easily (the Couette cylinders are hidden inside a low temperature apparatus), so, by default, the early investigators incorrectly assumed that the pattern of the Taylor vortex flow had the same wavelength of the pattern in a classical fluid.

Once the issue of the wavenumber was understood, Swanson and Donnelly [19] performed an experiment which confirmed the theoretical prediction of Barenghi [17] of the critical angular velocity Ω_{1c} at which the Taylor transition takes place. Figure 6 compares the experimental and theoretical values of Ω_{1c} as a function of reduced temperature $log_{10}((T_\lambda - T)/T_\lambda))$. The reduced temperature is used

to make the figure more clear, since the properties of helium II change rapidly with temperature and the effect is concentrated in the temperature region above $T = 2\ K$. The critical angular velocity of the figure is expressed in terms of the Reynolds number $Re_1 = \Omega_1 R_1 \delta / \nu_n$. The agreement between the theory (which makes the infinite cylinder approximation) and the data is good at high temperatures but worsen at low temperatures, which is expected since fewer and fewer Taylor cells are present in the apparatus and end effects become important. The dashed line represents the critical Reynolds number $Re_{class} = 268$ in a classical fluid at the same radius ratio. Note that the critical Reynolds number in helium II, Re_{1c}, tends to the classical limit Re_{class} as $T \to T_\lambda$, as expected.

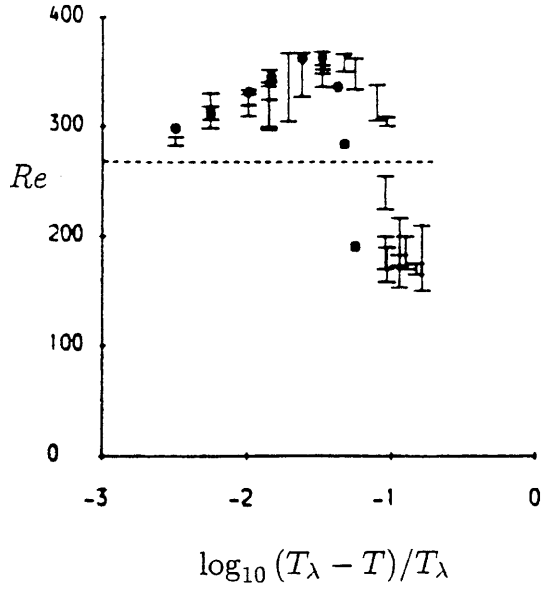

Fig. 6. Critical Reynolds number Re_{1c} versus reduced temperature at $\eta = 0.976$. Dashed line: critical Reynolds number $Re_{class} = 268$ of the classical Couette problem at this radius ratio. Error bars: experimental data of Swanson and Donnelly. Solid dots: theory of Barenghi

Figure 6 shows that, if the temperature is reduced (that is to say, if we move from left to right), the Couette flow of helium II is more stable than classical Couette flow. At lower temperature however helium II is less stable than an ordinary fluid. The same temperature dependence was also observed by Bielert and Stamm [22]. Figure 7 shows how the flow pattern changes with the temperature: as T becomes smaller k_c becomes smaller, hence the wavelength becomes larger.

A physical explanation for the temperature dependence of the transition is the following. We have seen in Section 6 that in the limit of a pure superflow

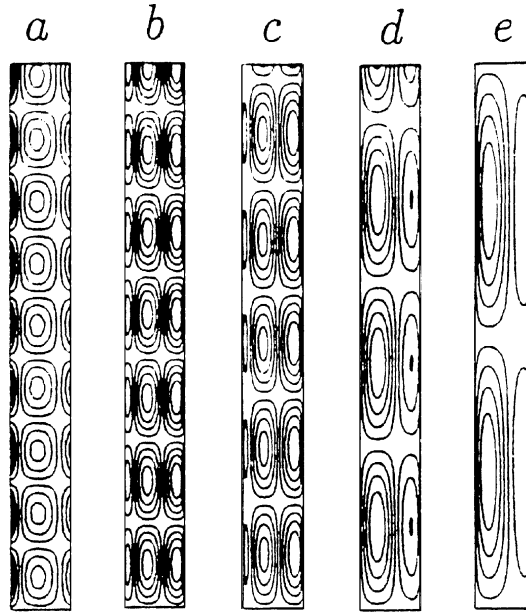

Fig. 7. Contour plots of the vorticities $\omega_{n\phi}$ at $T = T_\lambda$ (a) and of $\omega_{s\phi}$ at $T = 2.16\ K$ (b), $T = 2.14\ K$ (c), $T = 2.10\ K$ (d) and $T = 2.08\ K$ (e).

($T \to 0$) Couette flow is unstable to long wavelength ($k \to 0$) perturbations; the stability boundary is a curve with vertex at the origin and the critical velocity increases rapidly if k is increased (see Figure 3). Viceversa, in the limit of pure normal flow ($T \to T_\lambda$), Couette flow is unstable to perturbations of wavelength comparable to the gap's width. What happens between $T = 0$ and $T = T_\lambda$ depends on the relative amount of superfluid and normal fluid. Just below T_λ the dynamics of helium II is dominated by the normal fluid, which is like a classical viscous fluid. If $Re_1 \approx Re_{class}$ then the normal fluid would like to overturn on the length scale $2\pi/k_{class} \approx 2\delta$, but the superfluid vortex lines are very stiff on this short scale - their stability boundary increases rapidly with k. A compromise is reached between the two effects and the instability sets in at higher velocity than in the classical case, $Re_{1c} > Re_{class}$, but at shorter wavenumber, $k_c < k_{class}$, hence helium II is more stable than a classical fluid. If the temperature is reduced the superfluid becomes more important and the balance is struck at smaller Re_{1c} and smaller k_c so the Taylor cells become more elongated. The rapid drop of the critical Reynolds number for $T < 2\ K$ is due to the rapidly decreasing normal fluid fraction ($\rho_n/\rho \approx 0.5$ at $T = 2\ K$).

8 Rotations of the inner cylinder: nonlinear effects

Henderson, Barenghi and Jones [23] studied the nonlinear development of axisymmetric Taylor vortex flow for $Re_1 > Re_{1c}$ in the weakly nonlinear regime. The major difficulty in their study was the identification of the extra boundary conditions required to determine the superfluid velocity $\mathbf{v}_s$: the linearized superfluid equations are of the second order in r, while the fully nonlinear equations are of the sixth order. The extra conditions are not determined by the HVBK equations themselves, and there is no general agreement about what these conditions should be. Ultimately the correct boundary conditions are a matter to be decided by better understanding of the physics involved and by the experiments. The choice of boundary conditions made by Henderson et al, namely $\omega_{s\phi} = v_{s\phi} = 0$ at $r = R_1$ and $r = R_2$, implies vanishing mutual friction at the boundary and is consistent with the Couette state since the vorticity is purely axial at the walls. However other boundary conditions have been proposed in the literature [8] [11]: smooth boundary conditions in which the superfluid vortices slide freely at the walls' surfaces, rough boundary conditions, in which the vortices are pinned to the walls' imperfections, and partially sliding boundary conditions in which the vortices are partially pinned. Until now there is no experimental evidence for any of these conditions, but the issue clearly requires further work. In particular it would be interesting to analyze the nonlinear boundary layer which must form near the Taylor transition, whose length scale depends on the amplitude of the solution.

Henderson et al then compared their nonlinear steady state solution against measurements of the attenuation of second sound and obtained order of magnitude agreement. They were however able to explain why the second sound attenuation of an axial resonance mode was observed to be greater than the attenuation of an azimuthal mode. Later Henderson and Barenghi [24] computed the torque which is induced on the outer cylinder and compared it with the measured torque, finding quantitative agreement, within the experimental errors.

9 Rotations of the outer cylinder

The stability of the Couette flow of helium II under rotations of the outer cylinder ($\Omega_1 = 0$, $\Omega_2 \neq 0$) is still an unsolved problem. The experiments show that, unlike what happens in classical Couette flow, for which rotations of the outer cylinder are centrifugally stable, helium II becomes *unstable* if Ω_2 exceeds a critical value. Figure 8 shows the viscosity obtained by Heikkila and Hollis Hallet [25] using the torque method: the departure from the linear relation marks the critical velocity.

Attempting to explain this result, Barenghi and Jones[21] studied the linear stability of pure superfluid Couette flow ($T = 0$ K). They found that the vortex tension makes any rotation of the outer cylinders always unstable to long wavelength nonaxisymmetric perturbations $k \to 0$, so that the critical velocity is $\Omega_2 = 0$, as showed in Figure 9. The result of Barenghi and Jones is therefore consistent with the experimental finding of Heikkila and Hollis Hallet.

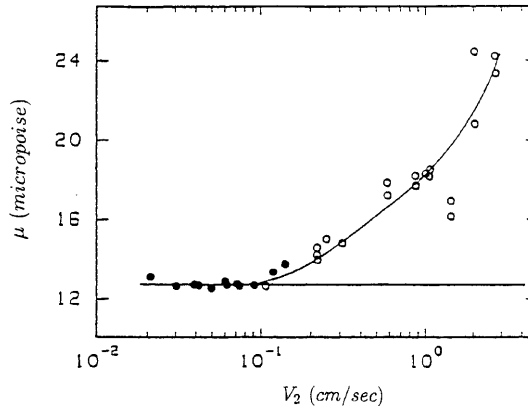

Fig. 8. Rotations of the outer cylinder: experiments of Heikkila and Hollis Hallet at $T = 1.82\ K$. Effective viscosity μ versus velocity V_2 of the outer cylinder with the inner cylinder at rest.

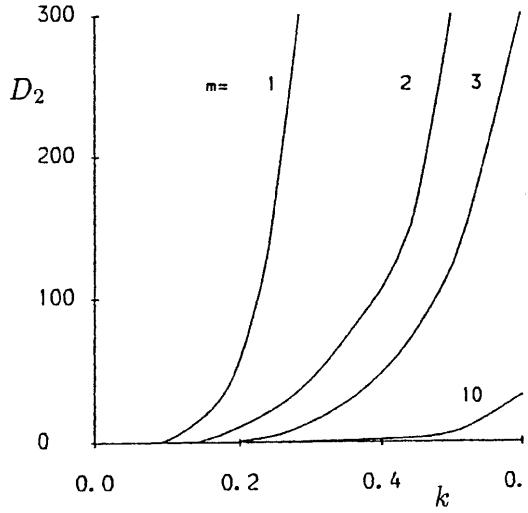

Fig. 9. Rotations of the outer cylinder: theory of Barenghi and Jones at $T = 0\ K$. Stability boundaries for the $m = 1, 2, 3$ and $m = 10$ mode at $\eta = 0.99$ expressed as Donnelly number $D_2 = \Omega_2 R_2 \delta / \nu_s$ versus dimensionless axial wavenumber k.

It can be speculated then the transition observed at nonzero temperature by Heikkila and Hollis Hallet at nonzero value of Ω_2 is a compromise between the nature of the normal fluid (which, by itself, is always stable under rotations of the outer cylinder)) and the nature of the superfluid (which, by itself, is always unstable as showed by Barenghi and Jones). The stability of helium II when the outer cylinder rotates is clearly still a major issue open to investigation.

10 Co-rotations and counter-rotations of the cylinders

The stability of Couette flow under counter-rotations was studied experimentally and theoretically by Barenghi, Swanson and Donnelly [26]. At fixed rotation of the outer cylinder (measured by the Reynolds number $Re_2 = \Omega_2 R_2 \delta / \nu_n$) they determined the critical rotation Re_{1c} of the inner cylinder at which Couette flow becomes unstable using the second sound technique. Theory and experiments agreed very well over the range $-4000 \leq Re_2 \leq 0$, $0 \leq Re_{1c} \leq 1250$ explored. The critical wavenumbers ranged from $k_c = 1.7$ at $Re_2 = -250$ to $k_c = 4.5$ at $Re_2 = -4000$. They found that helium II is more stable than a classical fluid.

Co-rotations of the cylinders were explored theoretically by Barenghi [27] at the temperature $T = 2.16\ K$. He found that at this temperature helium II is always more stable than a classical fluid, but the difference decreases if Re_2 increases. The first mode to become unstable is always $m = 0$.

11 Finite aspect ratios and end effects

It is apparent from the previous discussion that end effects in the Couette flow of helium II can be more important than in the ordinary classical Couette problem because the Taylor vortex cells in helium II tend to be elongated axially. It is therefore interesting to study Couette flow at small aspect ratio in order to understand the effects induced by the ends. Henderson and Barenghi [28] considered unit aspect ratio ($h/\delta = 1$) and made comparison with the classical work of Pfister et al [29]. They found two surprising results. The first result is that, because of the vortex tension, the superfluid tends to rotate in the azimuthal direction almost like a column of liquid. The superfluid azimuthal velocity component $v_{s\phi}$, in fact, slips at the top and bottom ends, while the superfluid vortices, which are stiff and do not like to bend too much on short scale, keep the superfluid motion almost z independent.

The second finding was the discovery of the anomalous direction of the motion of helium II when compared with the motion of a classical liquid. In the classical case the Ekman circulation induced by the ends has an outflow jet at the midplane and two inflow jets near $z = 0$ and $z = h$. In the case of helium II the circulation can be reversed by the action of the mutual friction force.

12 Discussion and outlook

Couette flow has proved to be a useful benchmark to test the HVBK equations which generalize Landau's model to the general situation in which vortex lines are present in the flow. Because of the existence of two separate, coupled fluids, the fluid dynamics of helium II is particularly rich and there are still phenomena which are not understood. In our view the major issues which are worth investigating are:

1. **Wavy modes** Using the second sound technique, Wolf et al [30] observed many transitions for $Re_1 > Re_{1c}$. It is natural to assume that these transitions refer to the onset of various wavy modes. The linear analysis of Barenghi and Jones show that nonaxisymmetric modes become unstable if Re_1 is made sufficiently large. What is needed is clearly more theoretical work in the nonlinear regime to interpret the existing experimental data.
2. **Rotations of the outer cylinder** The observation of Heikkila and Hollis Hallet that the Couette flow of helium II is unstable when $\Omega_1 = 0$ and Ω_2 is sufficiently large is striking, because it is in total contrast to what happens in a classical fluid. At the moment the only theoretical explanation is offered by the theory of Barenghi and Jones, which unfortunately refers only to the case of zero temperature. What is necessary is to study what happens to the transition at nonzero temperature, in the presence of the normal fluid.
3. **Appearance and stability of the first row of vortices** The issue of the appearance of the first row of vortices is still open as the current theories do not agree quantitatively with the experimental data. The problem of the appearance of the vortices may require a more fundamental quantum approach, but the issue of the stability of a row of superfluid vortices at temperatures $T < 1.85\ K$ should be understandable using the methods of classical hydrodynamics.
4. **Axial flow** The study of what happens to the Taylor instability when an axial flow is superimposed to the rotation is a classical variation of the Taylor–Couette problem [31]. In the case of helium II the case of axial flow is particularly important in the view of the current developments in the study of turbulence. It is known that waves on superfluid vortex lines become unstable in the presence of a sufficiently large normal flow parallel to the superfluid vorticity. If vortex waves become unstable then a superfluid vortex tangle is generated [32] which mimics the vorticity of the normal fluid [33]. This phenomenon was first noticed experimentally by Cheng, Cromar and Donnelly [34], and it was explained by Ostermeier and Glaberson [35]. It is now thought that this Ostermeir– Glaberson instability is important [36] in turbulence. Couette flow with superimposed axial flow is therefore an ideal configuration to study this instability, because the basic state consists exactly of superfluid vortices set parallel to the normal flow.

References

1. R.J. Donnelly: *High Reynolds number flows using liquid and gaseous helium.* (Springer, New York 1991)
2. C.F. Barenghi, C.J. Swanson and R.J. Donnelly: J. Low Temp. Phys. **100**, 385 (1995)
3. L. Landau, E. Lifchitz: *Mécanique des fluides.* (Editions MIR, Moscow 1971)
4. J.T. Tough: 'Superfluid turbulence '. In: *Progress in Low Temperature Physics* vol. VIII, ed. D. F. Brewer, North Holland, Amsterdam page 133 (1987).
5. R.J. Donnelly: *Quantized vortices in helium II.* (Cambridge University Press, Cambridge 1991)
6. H.E. Hall, W.F. Vinen: Proc. Roy. Soc. London **A238**, 215 (1954)
7. I.M. Khalatnikov: *An introduction to the theory of superfluidity.* (Benjamin, New York 1965)
8. R.N. Hills, P.H. Roberts: Arch. Ration. Mech. Analysis **66**, 43 (1971)
9. D.C. Samuels, R.J. Donnelly: Phys. Rev. Lett. **65**, 187 (1990)
10. C.F. Barenghi, R.J. Donnelly, W.F. Vinen: J. Low Temp. Phys. **32**, 189 (1983)
11. E.L. Adronikashvili, Y.G. Mamaladze: Rev. Modern Phys.**38**, 567 (1966).
12. R.J. Donnelly, M.M. LaMar: J. Fluid Mech. **186**, 163 (1988)
13. S. Chandrasekhar, R.J. Donnelly: Proc. Roy. Soc. London **A241**, 9 (1957)
14. H. Snyder: In *Proceedings of the* 13^{th} *International Conference of Low Temperature Physics (LT13)*, vol. 1, p. 283 (Plenum Press, New York, 1974)
15. C.F. Barenghi, C.A. Jones: J. Fluid Mech. **197**, 551 (1988)
16. C.J. Swanson, R.J. Donnelly: Phys. Rev. Lett. **67**, 1568 (1991)
17. C.F. Barenghi: Phys. Rev. B **45**, 2290 (1992)
18. A. L. Fetter: Phys. Rev. **153**, 285 (1967)
19. C.E. Swanson, R.J. Donnelly: J. Low Temp. Phys. **67**, 185 (1987)
20. C.A. Jones, K.B. Khan, C.F. Barenghi, K.L. Henderson: Phys. Rev. B **51**, 16174 (1995)
21. C.F. Barenghi, C.A. Jones: Phys. Lett. **122**, 425 (1987)
22. F. Bielert, G. Stamm: Physica B **194**, 561 (1994)
23. K.L. Henderson, C.F. Barenghi, C.A. Jones: J. Fluid Mech. **283**, 329 (1995i)
24. K.L. Henderson, C.F. Barenghi: Phys. Lett. A **191**, 438 (1994)
25. W.J. Heikkila, A.C. Hollis Hallet, Can. J. Phys. **33**, 420 (1955)
26. C.F. Barenghi, C.J. Swanson, R.J. Donnelly: J. Low Temp. Phys. **99**, 143 (1995)
27. C.F. Barenghi, Phys. Rev. B **52**, 3596 (1995)
28. K.L. Henderson, C.F. Barenghi: to be published in J. Fluid Mech.
29. G. Pfister, H. Schmidt, K.A. Cliffe, T. Mullin: J. Fluid Mech. **191**, 1 (1988)
30. P.L. Wolf, B. Perrin,B. Hulin,J.P. Elleaume: J. Low Temp. Phys. **44**, 569 (1981)
31. S. Chandrasekhar: *Hydrodynamics and hydromagnetic stability.* (Oxford University Press, Oxford 1961).
32. D.C. Samuels: Phys. Rev. B **47**, 1107 (1993)
33. C.F. Barenghi, G. Bauer, D.C. Samuels, R.J. Donnelly: Phys. Fluids **9**, 2631 (1997)
34. D.K. Cheng, M.W. Cromar and R.J. Donnelly: Phys. Rev. Lett. **31**, 433 (1973)
35. R.M. Ostermeier, W.I. Glaberson: J. Low Temp. Phys. **21**, 191 (1975)
36. D. Kivotides, D.C. Samuels: to be published in Phys. Rev. Lett.

Tertiary and quaternary solutions for plane Couette flow with thermal stratification

R.M. Clever[1 3] and Friedrich H. Busse[1 2]

[1] Institute of Geophysics and Planetary Physics, UCLA,
[2] Institute of Physics, University of Bayreuth, D-95440 Bayreuth
[3] deceased

Abstract. Numerical solutions describing steady wavy rolls are obtained for a horizontal Couette layer heated from above. Two different Prandtl numbers have been investigated, $P = 0.71$ and $P = 7$, but most of the results depend only on the Grashof number G. The stability of wavy solutions is analyzed with respect to disturbances that do not change the horizontal periodicity interval. Oscillatory quaternary solutions bifurcating from the steady wavy rolls have been obtained through forward integrations in time.

1 Introduction

The shear layers of a fluid between two parallel plates moving in opposite directions corresponds to the simplest configuration described by the Navier–Stokes equations. Despite its conceptional simplicity it has given rise to some of the most challenging problems of theoretical fluid dynamics. The basic or primary solution in the form of a constant shear has been found to be stable with respect to infinitesimal three-dimensional disturbances for all Reynolds numbers (see, for example, [10]). The existence of states of flow which are not connected through a bifurcation with the basic state of plane Couette flow has thus received considerable attention. Three-dimensional solutions describing such states of flow can be obtained through a bifurcation analysis if more general problems are considered which include the plane Couette configuration as a special case. Nagata [11,12] obtained steady solutions in this way through the consideration of the problem in a system that is rotating with the angular velocity Ω about an axis parallel to the plates but perpendicular to their direction of motion. In this case two-dimensional Taylor vortices are obtained at finite values of Ω from which wavy vortices are bifurcating which continue to exist in the limit of vanishing Ω. Clever and Busse [6] obtained the same solutions when a Rayleigh number Ra is introduced as additional parameter. They considered a horizontal Couette layer heated from below and cooled from above for which convection in the form of longitudinal rolls bifurcates from the basic state of constant shear when Ra exceeds the critical value Ra_c of about 1708. Steady solutions describing wavy rolls bifurcate from the longitudinal rolls when the shear Reynolds number Re exceeds a critical value depending on the Rayleigh- and the Prandtl number. While this bifurcation of a tertiary solution from the secondary solution is supercritical for relatively low Reynolds numbers it becomes subcritical as Re increases. As

C. Egbers and G. Pfister (Eds.): LNP 549, pp. 399–416, 2000.

the sub-criticality strengthens, wavy roll solutions become possible for $Ra = 0$. A schematic diagram of the bifurcation structure is shown in figure 1.

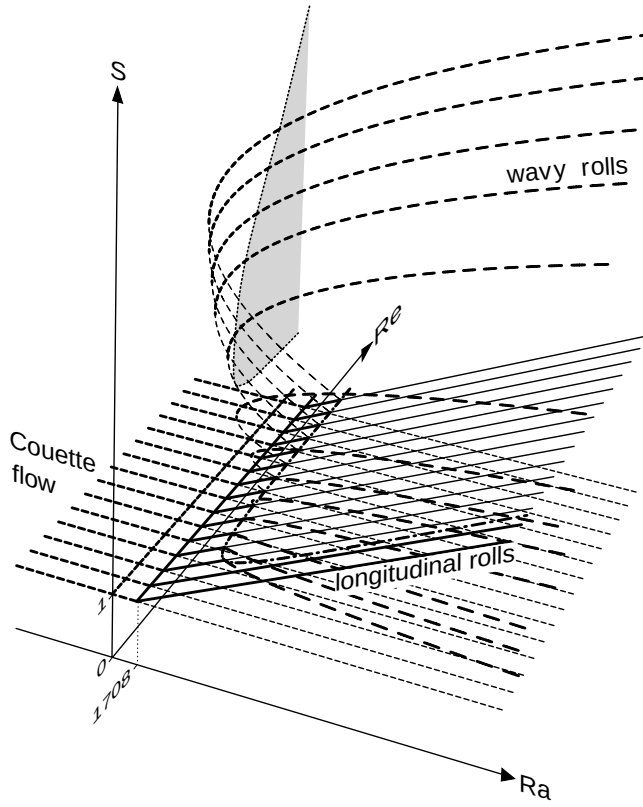

Fig. 1. Sketch of the bifurcation diagram for the thermally stratified plane Couette system. The shear Nusselt number S is shown as a function of the Rayleigh number Ra and the Reynolds number Re. The primary solution of plane Couette flow, the secondary solution in the form of longitudinal rolls and the tertiary solution in the form of wavy rolls are indicated by thick (thin) lines where they are stable (unstable). Wavy rolls are also unstable, however, in part in the region where they are indicated by thick dashed lines. The shaded region indicates the plane $Ra = 0$.

It should be mentioned that besides the tertiary solutions of the form of wavy rolls or wavy vortices there also exist two-dimensional solutions for the plane Couette layer problem as has been shown by Cherhabili and Ehrenstein [4]. In a more recent paper these authors have extended their analysis to solutions with a dependence on the spanwise coordinate [5]. But the Reynolds numbers for these types of solutions are much higher than those for which the bifurcations illustrated in figure 1 occur.

Clever and Busse [6,7] also studied the stability of the tertiary wavy roll solutions and followed the steady and time dependent quaternary solutions that evolve from them. Similar work has been done by Nagata [13]. Neither experiments (Dauchot and Daviaud, [9]; Bottin et al., [1]) nor general numerical simulations (Schmiegel and Eckhardt, [14]) have exhibited stable tertiary or quaternary states of flow. The tertiary solutions are unstable with respect to infinitesimal disturbances in most of their domain of existence if not in the entire domain and the same property is likely to hold for the quaternary solutions as well. There exists the possibility, however, that these solutions could be stabilized in the case of a stably stratified layer. With this possibility in mind the analysis of Clever and Busse [6,7] is extended in this paper to the case of a horizontal shear layer heated from above and cooled from below.

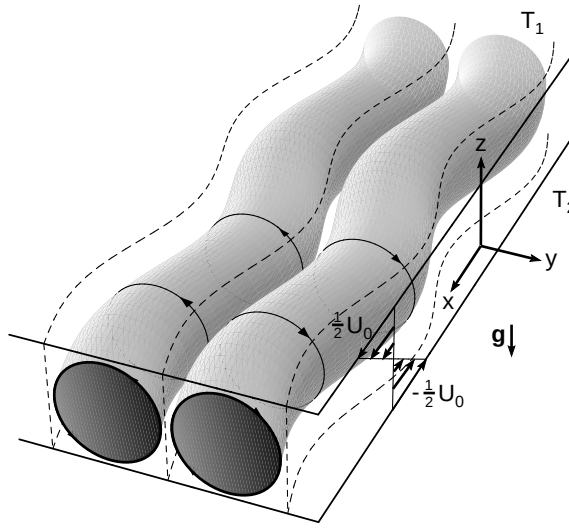

Fig. 2. Sketch of the wavy roll solution in the thermally stratified plane Couette layer.

2 Mathematical formulation of the problem

We consider a horizontal fluid layer between two horizontal rigid plates separated by the distance d and moving in opposite directions with the relative velocity U_0. Constant temperatures T_1 and T_2 are prescribed at the upper and at the lower boundary. Using d as length scale, d^2/ν as timescale where ν is the kinematic viscosity, and $(T_2 - T_1)Ra^{-1}$ as scale for the temperature we write the Navier–Stokes equations in the Boussinesq approximation for the velocity vector $\boldsymbol{u}$ and the heat equation for the deviation Θ from the temperature distribution of pure

conduction in dimensionless form:

$$\nabla^2 \boldsymbol{u} + \boldsymbol{k}\Theta - \nabla\pi = \boldsymbol{u}\cdot\nabla\boldsymbol{u} + \frac{\partial}{\partial t}\boldsymbol{u}, \tag{1a}$$

$$\nabla\cdot\boldsymbol{u} = 0, \tag{1b}$$

$$\nabla^2\Theta + Ra\boldsymbol{k}\cdot\boldsymbol{u} = (\boldsymbol{u}\cdot\nabla + \frac{\partial}{\partial t})\Theta, \tag{1c}$$

where $\boldsymbol{k}$ is the unit vector in the vertical direction and the Rayleigh, Prandtl and Reynolds number are defined by

$$Ra = \frac{\gamma g(T_2 - T_1)d^3}{\kappa\nu}, \quad P = \frac{\nu}{\kappa}, \quad Re = \frac{U_0 d}{\nu} \tag{2}$$

γ is the thermal expansivity, g is the acceleration of gravity and κ is the thermal diffusivity. The solution of pure conduction is compatible with the solution of plane Couette flow of equations (1a,b),

$$\boldsymbol{u}_0 = Rez\boldsymbol{i} \tag{3}$$

As indicated in figure 2, we are assuming a Cartesian system of coordinates with the z-coordinate in the direction of the applied shear, and the origin of the midplane of the layer. For more general solutions of (1) we introduce the representation

$$\boldsymbol{u} = Rez\boldsymbol{i} + U_x\boldsymbol{i} + U_y\boldsymbol{j} + \nabla\times(\nabla\times\boldsymbol{k}\phi) + \nabla\times\boldsymbol{k}\psi \equiv \boldsymbol{U} + \boldsymbol{\delta}\phi + \boldsymbol{\varepsilon}\psi \text{ with } \bar{\boldsymbol{u}} = \boldsymbol{U}, \tag{4}$$

where the bar indicates the average over the (x,y)-plane. The component $\boldsymbol{\delta}\phi$ of the velocity field is called the poloidal part while $\boldsymbol{\varepsilon}\psi$ is referred to as the toroidal part of the velocity field. By operating with $\boldsymbol{\delta}$ and $\boldsymbol{\varepsilon}$ onto equation (1a) we obtain equations for ϕ and ψ:

$$\nabla^4\Delta_2\phi - \Delta_2\Theta = \boldsymbol{\delta}\cdot[(\boldsymbol{\delta}\phi+\boldsymbol{\varepsilon}\psi)\cdot\nabla(\boldsymbol{\delta}\phi+\boldsymbol{\varepsilon}\psi)] + (\boldsymbol{U}\cdot\nabla+\partial_t)\nabla^2\Delta_2\phi - \partial_{zz}^2\boldsymbol{U}\cdot\nabla\Delta_2\phi, \tag{5a}$$

$$\nabla^2\Delta_2\psi = \boldsymbol{\varepsilon}\cdot[(\boldsymbol{\delta}\phi+\boldsymbol{\varepsilon}\psi)\cdot\nabla(\boldsymbol{\delta}\phi+\boldsymbol{\varepsilon}\psi)] + (\boldsymbol{U}\cdot\nabla+\partial_t)\Delta_2\psi - \partial_z\boldsymbol{U}\cdot\boldsymbol{\varepsilon}\Delta_2\phi, \tag{5b}$$

$$\nabla^2\Theta - Ra\Delta_2\phi = [(\boldsymbol{\delta}\phi+\boldsymbol{\varepsilon}\psi)\cdot\nabla\Theta + (\boldsymbol{U}\cdot\nabla+\partial_t)\Theta]P, \tag{5c}$$

We have also rewritten equation (1c) in the form (5c). In addition equations for the components $U_{x,y}$ of the mean flow $\boldsymbol{U}(z,t)$ are needed,

$$(\partial_{zz}^2 - \partial_t)U_x = -\partial_z\overline{(\Delta_2\phi(\partial_{xz}^2\phi + \partial_y\psi))}, \tag{5d}$$

$$(\partial_{zz}^2 - \partial_t)U_y = -\partial_z\overline{(\Delta_2\phi(\partial_{yz}^2\phi - \partial_x\psi))}, \tag{5e}$$

where the bar indicates the horizontal average and the symbol Δ_2 stands for $\nabla^2 - \partial_{zz}^2$. The boundary conditions for the variables ϕ, ψ, Θ and $U_{x,y}$ are given by

$$\phi = \partial_z\phi = \psi = \Theta = U_x = U_y = 0 \text{ at } z = \pm\frac{1}{2}. \tag{6}$$

For the solution of equations (5) the Galerkin method will be employed. The dependent variables are expanded in complete systems of functions satisfying the respective boundary conditions,

$$\phi = \sum_{l,m,n} a_{lmn}(t) \exp\{il\alpha_x x + im\alpha_y y\} g_n(z), \tag{7a}$$

$$\psi = \sum_{l,m,n} c_{lmn}(t) \exp\{il\alpha_x x + im\alpha_y y\} \sin n\pi(z + \frac{1}{2}), \tag{7b}$$

$$\Theta = \sum_{l,m,n} b_{lmn}(t) \exp\{il\alpha_x x + im\alpha_y y\} \sin n\pi(z + \frac{1}{2}), \tag{7c}$$

$$U_{x,y} = \sum_{n} U_n^{(x,y)}(t) \sin n\pi(z + \frac{1}{2}), \tag{7d}$$

where the Chandrasekhar (1961) functions $g_n(z)$ are defined by

$$g_n = \frac{\cosh\lambda_n z}{\cosh\lambda_n \frac{1}{2}} - \frac{\cos\lambda_n z}{\cos\lambda_n \frac{1}{2}} \text{ for odd } n, \quad g_n = \frac{\sinh\lambda_n z}{\sinh\lambda_n \frac{1}{2}} - \frac{\sin\lambda_n z}{\sin\lambda_n \frac{1}{2}} \text{ for even } n, \tag{8a}$$

and the numbers λ_n are determined such that the conditions $g(z) = g'(z) = 0$ at $z = \pm\frac{1}{2}$ are satisfied,

$$\tanh\frac{1}{2}\lambda_n + \tan\frac{1}{2}\lambda_n = 0 \text{ for odd } n, \quad \coth\frac{1}{2}\lambda_n - \cot\frac{1}{2}\lambda_n = 0 \text{ for even } n. \tag{8b}$$

In order that real expressions (7) are obtained, the conditions $a_{lmn} = a^*_{-l-mn}$, $b_{lmn} = b^*_{-l-mn}$, $c_{lmn} = c^*_{-l-mn}$ must be imposed where the asterisk indicates the complex conjugate. After representations (7) have been inserted into equations (5) and these are multiplied by the expansion functions and averaged over the fluid layer, a system of ordinary differential equations in time is obtained for the coefficients $a_{lmn}, b_{lmn}, c_{lmn}$ and $U_n^{(x,y)}$. These equations can be solved after a truncation scheme has been established. We shall neglect all coefficients and corresponding equations for which

$$l + m + n \geq N_T \tag{9}$$

holds, where N_T is a natural number which will be chosen sufficiently high such that the physically relevant properties of the solution do not change significantly when N_T is replaced by $N_T - 2$. A typical value of N_T which has been used for most of the computations reported in the following is 18.

Steady solutions of equations (5) with constant coefficients a_{lmn}, b_{lmn}, c_{lmn}, $U_n^{(x)}$ are of special interest since they can be obtained through the use of a Newton-Raphson method. The coefficients $U_n^{(y)}$ vanish for these steady solutions. The stability of the steady three-dimensional solutions can then be studied through the superposition of infinitesimal disturbances of the form

$$\tilde{\phi} = \exp\{idx + iby + \sigma t\} \sum_{l,m,n} \tilde{a}_{lmn} \exp\{il\alpha_x x + im\alpha_y y\} g_n(z), \tag{10a}$$

$$\tilde{\psi} = \exp\{idx + iby + \sigma t\} \sum_{l,m,n} \tilde{c}_{lmn} \exp\{il\alpha_x x + im\alpha_y y\} \sin n\pi(z + \frac{1}{2}), \quad (10b)$$

$$\tilde{\Theta} = \exp\{idx + iby + \sigma t\} \sum_{l,m,n} \tilde{b}_{lmn} \exp\{il\alpha_x x + im\alpha_y y\} \sin n\pi(z + \frac{1}{2}). \quad (10c)$$

When equations (5) are linearized in the disturbances $\tilde{\phi}, \tilde{\psi}, \tilde{\Theta}$, a homogeneous system of linear algebraic equations for the unknown coefficients $\tilde{a}_{lmn}, \tilde{c}_{lmn}, \tilde{b}_{lmn}$ is obtained with the growth rate σ as eigenvalue. Whenever there exists an eigenvalue σ with positive real part as a function of b and d for a given steady solution of the form (7) with constant coefficients $a_{lmn}, b_{lmn}, c_{lmn}, U_n^{(x)}$, then the latter is regarded as unstable. Otherwise it will be considered as stable. There is no need to consider a disturbance of the mean flow since the righthand side of (5d,e) vanishes when the terms linear in $\tilde{\phi}, \tilde{\psi}$ are considered as long as d or b is finite. In fact the disturbances of the mean flow are included in the representation (10a,b) where the sum includes the case $l = m = 0$ in contrast to the summation in (7a,b). Because of a smooth dependence of σ on the Floquet wavenumbers b, d, there is no need to consider the special case $d = b = 0$ separately.

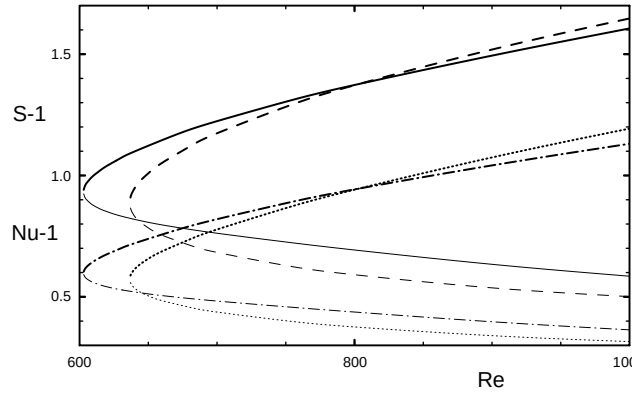

Fig. 3. Shear Nusselt number S [solid (dashed) line in the case A(B)] and Nusselt number Nu [dash-dotted (dotted) line in the case A(B)] as a function of Re for $Ra = -2000, P = 0.71$ with case A(B) corresponding to $\alpha_x = 1.2(1.6)$, $\alpha_y = 2.2(3.0)$.

3 Steady three-dimensional wavy roll solutions in an air layer

In the Bénard-Couette problem longitudinal rolls are the preferred solution bifurcating from the basic solution in the form of a constant shear when the Rayleigh number Ra exceeds the critical value, $Ra_c = 1708$. When the Rayleigh number is increased, the longitudinal rolls become unstable to wavy disturbances as the

Reynolds number Re exceeds a critical value. Steady solutions in the form of wavy rolls bifurcate from the two-dimensional secondary solutions (Clever et al., [8]). As has already been pointed out in the introduction, this bifurcation is supercritical if the Reynolds number is not too high, but for increasing values of Re the bifurcation becomes subcritical [6]. For Reynolds numbers of the order 500 and higher the wavy roll solutions extend to $Ra = 0$ and to negative values of Ra as indicated in figure 1. A sketch of the steady wavy roll solution is shown in figure 2. This solution can be represented in the form (7) with constant coefficients $a_{lmn}, b_{lmn}, c_{lmn}$ which exhibit the following symmetry properties:

$$a_{lmn} = (-1)^{m+n} a_{-lmn}, \quad a_{lmn} = (-1)^{l} a_{l-mn}, \tag{11a}$$

$$b_{lmn} = (-1)^{m+n} b_{-lmn}, \quad b_{lmn} = (-1)^{l} b_{l-mn}, \tag{11b}$$

$$c_{lmn} = (-1)^{m+n} c_{-lmn}, \quad c_{lmn} = (-1)^{l+1} c_{l-mn}, \tag{11c}$$

Among the physical properties that characterize this solution the shear Nusselt number S is of primary interest since it measures the ratio between the momentum transport in the presence of the wavy rolls and in their absence. In terms of the representation (7) its definition is given by

$$S \equiv 1 + Re^{-1} \sum_{n} n\pi U_n^{(x)} \tag{12}$$

which is analogous to the definition of the heat transport Nusselt number

$$Nu = 1 + Ra^{-1} \sum_{n} n\pi b_{00n} \tag{13}$$

In figure 3 the shear Nusselt number S and the ordinary Nusselt number Nu have been plotted in the particular case $Ra = -2000$, $P = 0.71$ which corresponds to a stratified layer of air. As must be expected on the basis of the schematic figure 1, there exist an upper and a lower branch of wavy roll solutions. The wavy rolls on the upper branch show a higher amplitude in terms of the Nusselt numbers than those on the lower branch and the contrast between the two solutions increases with distance from the saddle node where the two branches merge. The kinetic energies E_{mf} of the mean flow and E_{tor} of the toroidal component of the velocity field, however, are lower on the upper branch as can be seen in figure 4. The kinetic energies E_{mf}, E_{tor} and E_{pol} are defined by

$$E_{mf} = \frac{1}{2}\langle (Re\, z + U_x(z))^2 \rangle, \quad E_{tor} = \frac{1}{2}\langle |\, \nabla \times \boldsymbol{k}\psi\, |^2 \rangle, \quad E_{pol} = \frac{1}{2}\langle |\, \nabla \times (\nabla \times \boldsymbol{k}\phi\, |^2 \rangle \tag{14}$$

where the angular brackets indicate the average over the fluid layer. As the vigor of the roll motion increases the shear in the interior of the layer decreases and with it the energy of the mean flow. The strength of the toroidal component of motion decreases at the same time since it is generated through the advection of the mean shear by the vertical component of the velocity field.

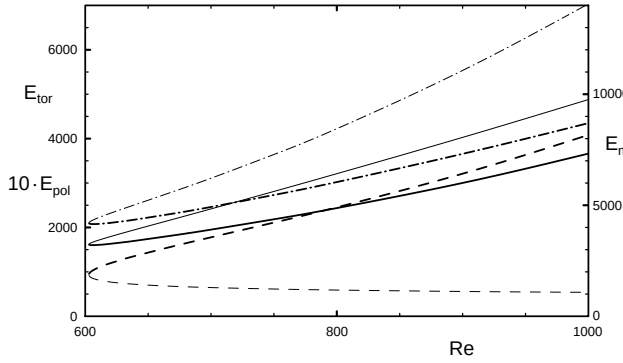

Fig. 4. Energies E_{pol}, E_{tor}, E_{mf} of the poloidal (dashed), toroidal (dash-dotted) and mean flow (solid) components of the velocity field, respectively, as function of Re in the case $Ra = -2000, P = 0.71$, $\alpha_x = 1.2, \alpha_y = 2.2$. Thin (thick) lines correspond to the lower (upper) branch.

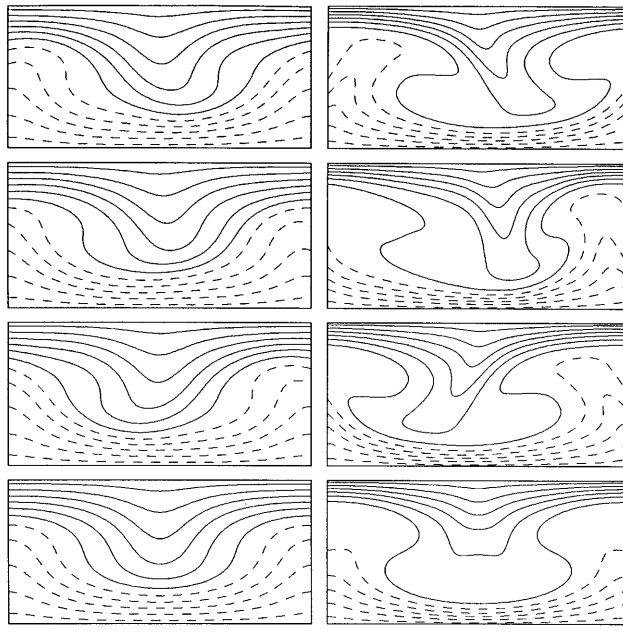

Fig. 5. Lines of constant velocity u_x in the planes $x = 0, x = \pi/2\alpha_x$, $x = \pi/\alpha_x$ (from top to bottom). The lowermost plots show the average of u_x over x. The z-coordinate is the direction of the ordinate, y increases from left to right. The left (right) plots correspond to the lower (upper) branch solution in the case $Re = 1000, Ra = -2000, P = 0.71, \alpha_x = 1.6, \alpha_y = 3.0$. Positive (negative) values of u_x are indicated by solid (dashed) lines. The solid line next to the dashed lines corresponds to $u_x = 0$.

Figures 5, 6 and 7 show the typical differences between the two solution branches. While the basic Couette flow is only somewhat distorted in the case of the lower branch solution, the distortions caused by the upper branch solutions are so strong, that the shear is nearly confined to the boundary layers at the planes $z = \pm 0.5$ as shown in figure 5. The difference in the profiles of the mean flow for the lower and the upper branch solutions is also clearly exhibited in figures 8a and 8b. As is evident from figure 8b the mean shear even reverses in the interior of the layer in the case $Re = 1000$. The profile of the mean temperature shows a similar structure as the mean flow. Since the Prandtl number is less than unity, thermal diffusion exceeds viscous friction and as a result the mean temperature profile deviates less from the linear slope than the mean flow profile. In general, it is remarkable to see how little the structure of the wavy roll solution in the stably stratified case is changed in comparison with the isothermal case studied by Clever and Busse [7]. Only the Reynolds number is increased a bit through the effects of stratification.

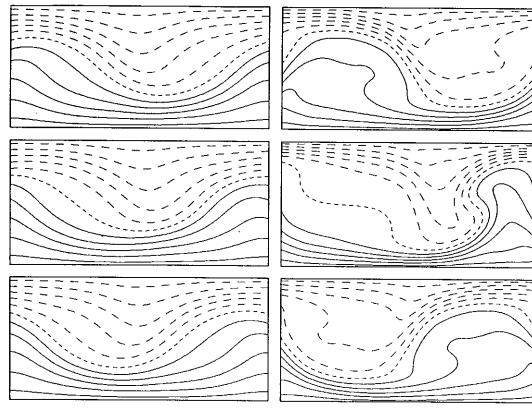

Fig. 6. Isotherms in the planes $x = 0, x = \pi/2\alpha_x, x = \pi/\alpha_x$ (from top to bottom) in the same case as in figure 5. Positive (negative) isotherms are indicated by dashed (solid) lines. The short-dashed line indicates the zero isotherm.

The lowest Reynolds numbers that can be reached in the particular case $Ra = -2000, P = 0.71$ have been plotted in figure 9 in dependence on the two wavenumbers, α_x and α_y, that characterize wavy rolls. The absolute minimum $Re_{min} \approx 600$ is reached near $\alpha_x = 1.1$, $\alpha_y = 2.2$. These values can be compared with the corresponding values $Re_{min} \approx 512$, at $\alpha_x = 1.15$, $\alpha_y = 2.3$, in the case $Ra = 0$. As in the latter case, the lowest values of Re are reached along a valley stretching along the line $\alpha_x \approx 0.5 \cdot \alpha_y$. A plot analogous to figure 9 for the case $Ra = 0$ has been published as figure 3 in [2]. Inadvertently α_x and α_y are exchanged in that figure. In order to give an impression of the wavenumber range for which steady wavy roll solutions can be obtained, we have plotted the shear Nusselt number S for upper and lower solutions for fixed values of Re, Ra

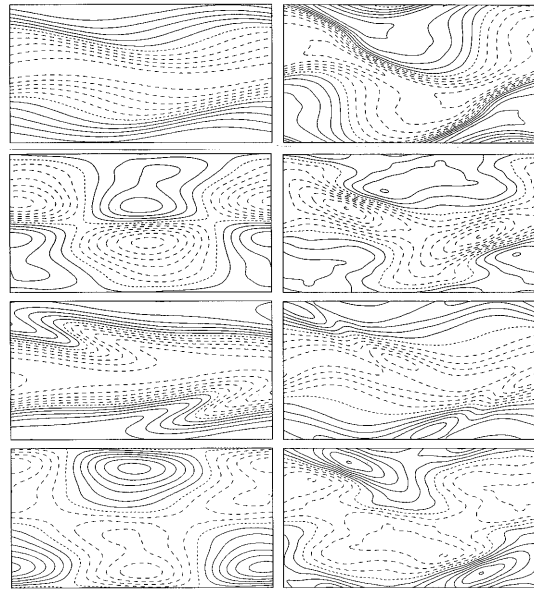

Fig. 7. Isotherms in the plane $z = 0$ (uppermost plots) and lines of constant vertical velocity in the planes $z = -0.4, z = 0$, and $z = 0.4$ (second through fourth plots from top) for the same solutions as in figure 5. Solid (dashed) lines indicate positive (negative) values of the vertical velocity u_z and negative (positive) isotherms. The ordinate corresponds to the y-coordinate, x increases towards the right.

and P in figure 10. It is clear from this figure that solutions exist on a ellipsoidal surface stretched from left to right of which only two perpendicular cross sections are shown in the figure.

4 Wavy roll solutions in dependence on the Grashof number

A remarkable property of the steady wavy roll solutions is that the influence of stratification depends mainly on the combination $G \equiv Ra/P$ of parameters where G is the Grashof number. In figure 11a through 11e the results obtained for $Ra = -2000, P = 0.71$ are plotted together with those obtained for $Ra = -2 \cdot 10^4, P = 7$ in the case of two different Reynolds numbers. As can be seen, the curves for the kinetic energies are always close together for negative as well as positive Rayleigh numbers. At the point $Ra = G = 0$ the results obtained for the different Prandtl numbers coincide as must be expected for the case of an isothermal Couette layer.

The Nusselt number plotted in figure 11b differs strongly for the two Prandtl numbers, however, in that much higher values are attained in the high Prandtl number fluid than in the low P fluid. Actually for given values of Ra and Re

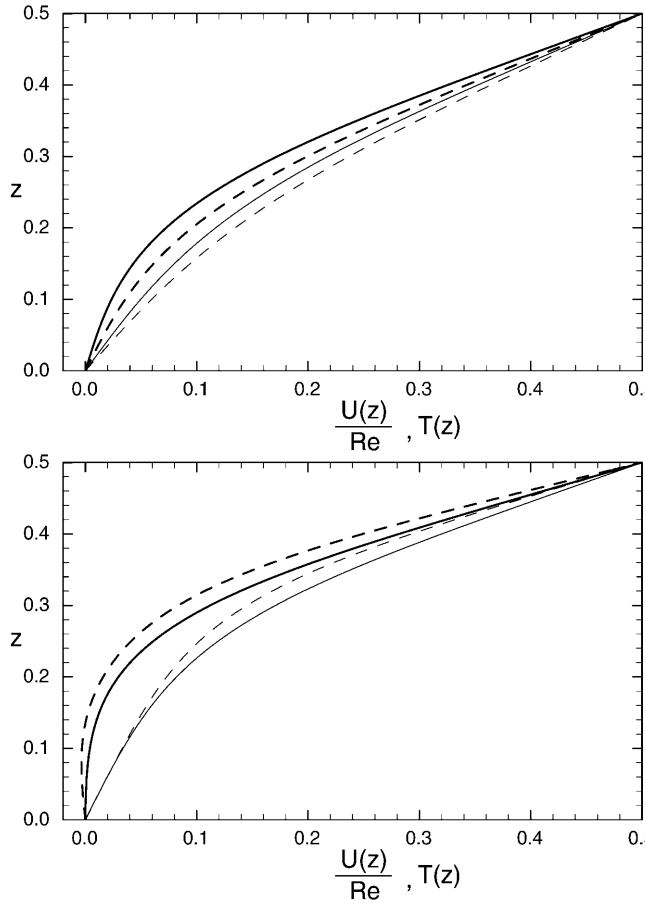

Fig. 8. Profiles of the mean flow $U(z)$ (thick lines) and of the mean temperature $T(z)$ (thin lines) for $Re = 700$ (solid lines) and $Re = 1000$ (dashed lines) for the lower (upper) branch solution in upper (lower) figure 8a(b). The values $\alpha_x = 1.2, \alpha_y = 2.2, P = 0.71, Ra = -2000$ have been used in all cases.

the convective heat transport is nearly independent of P. But since the heat transport by conduction varies in proportion to P^{-1}, $Nu-1$ varies approximately like P. There is no coincidence for the Nusselt numbers at $G = 0$, because the Nusselt number looses its meaning for an isothermal layer. But since the Nusselt number is defined as the ratio between two heat transports it depends smoothly on G through the point $G = 0$ as shown in figure 11b. The low influence of thermal diffusion in the case $P = 7$ manifests itself also in the mean temperature profile as shown in figure 12. While the profiles of the mean flow do not differ much from those plotted in figure 8b, the temperature profile has now become close to an isothermal one in the interior of the layer.

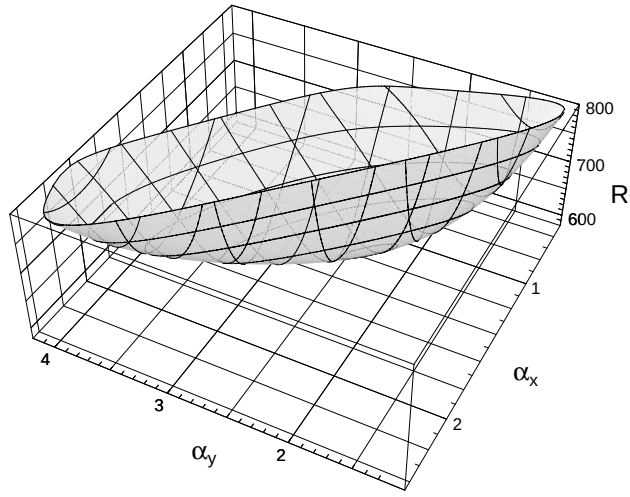

Fig. 9. Lowest Reynolds numbers for which steady wavy roll solutions can be obtained as a function of the horizontal wavenumbers α_x and α_y in the case $Ra = -2000$, $P = 0.71$.

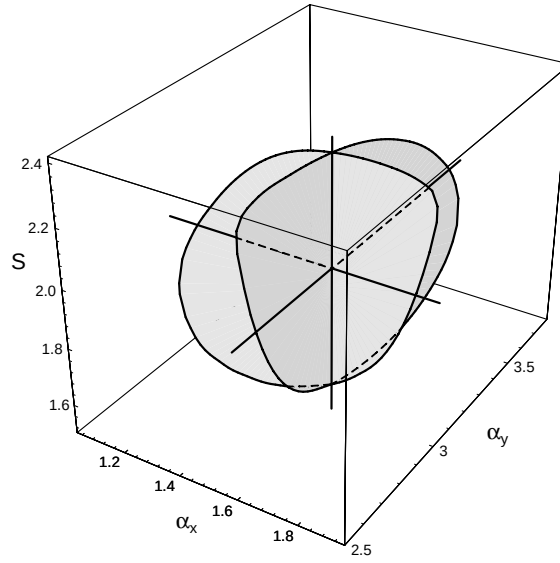

Fig. 10. Shear Nusselt number S as a function of the wavenumbers α_x and α_y in the case $Re = 800, Ra = -2000, P = 0.71$. The origin of the coordinate cross in the center of the figure is located at $S = 2.0, \alpha_x = 1.6, \alpha_y = 3.0$.

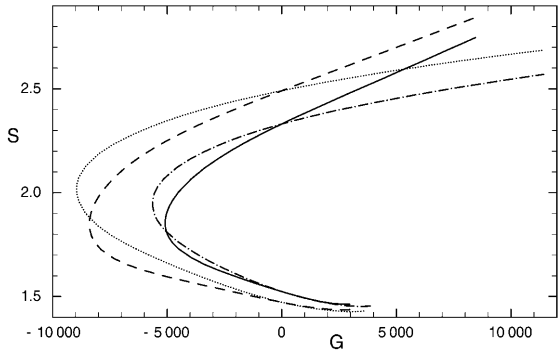

Fig. 11. a) Shear Nusselt number S as a function of the Grashof number $G = Ra/P$ in the cases $P = 7, R = 800$ (dotted curve); $P = 7, R = 700$ (dash-dotted); $P = 0.71, R = 800$ (dashed) and $P = 0.71, R = 700$ (solid) with $\alpha_x = 1.4$, $\alpha_y = 2.8$ in all cases.

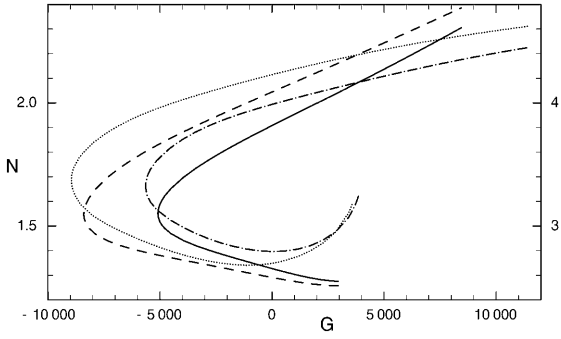

Fig. 11. b) Nusselt number Nu as function of G for the same cases as in figure 11a. The left (right) ordinate applies in the case $P = 0.71$ (7).

The Grashof number can be introduced into equations (5) through the multiplication of (5c) by P^{-1}. As a result Ra is replaced by G and P drops from the equation except that the term $\nabla^2\Theta$ is now multiplied by P^{-1}. The fact that the results displayed in figures 11 are nearly independent of P except for the Nusselt number indicates that thermal diffusion plays a rather minor role, at least for values of P of the order unity of larger.

It is also of interest to interprete the results displayed in the plots of figure 11 in terms of the Richardson number J which is defined by

$$J = -GRe^{-2} = -Ra/PRe^2 \tag{15}$$

in terms of the dimensionless parameters of the present analysis. The minimum values of G for which wavy roll solutions exist in the cases $Re = 700$ and 800 correspond to the following values of J

$$J = 1.04 \cdot 10^{-2}(\text{ or } 1.31 \cdot 10^{-2}) \text{ for } Re = 700(\text{ or } 800) \text{ in the case } P = 7 \tag{16a}$$

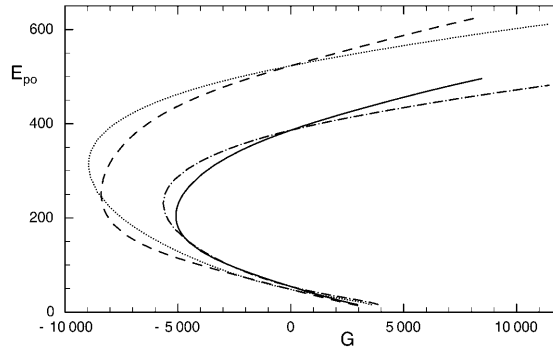

Fig. 11. c) Energy E_{pol} of the poloidal component of the velocity field as a function of G for the same cases as in figure 11a.

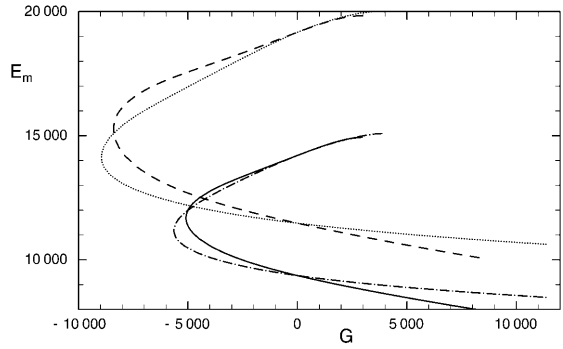

Fig. 11. d) Energy E_{mf} of the mean flow component of the velocity field as a function of G for the same cases as in figure 11a.

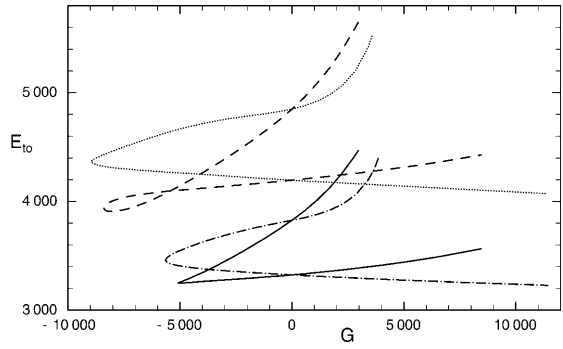

Fig. 11. e) Energy E_{tor} of the toroidal component of the velocity field as a function of G for the same cases as in figure 11a.

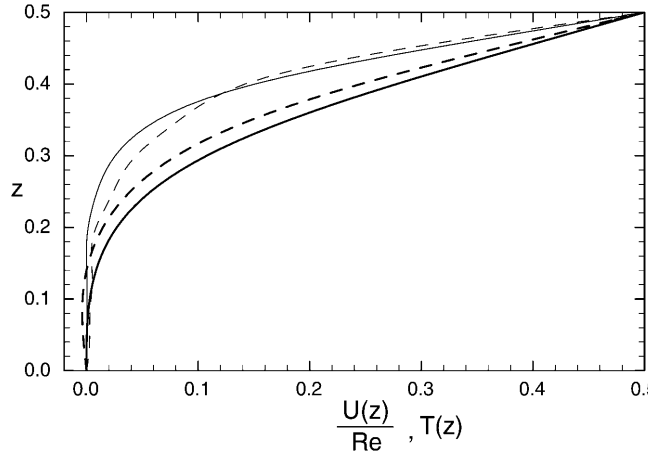

Fig. 12. Profiles of the mean flow $U(z)$ (thick lines) and of the mean temperature $T(z)$ (thin lines) in the cases $Re = 700$ (solid lines) and $Re = 1000$ (dashed lines). $Ra = -2 \cdot 10^4, P = 7, \alpha_x = 1.2, \alpha_y = 2.2$ have been used in all cases.

$$J = 1.16 \cdot 10^{-2} (\text{ or } 1.40 \cdot 10^{-2}) \text{ for } Re = 700 (\text{ or } 800) \text{ in the case } P = 0.71 \quad (16b)$$

These values are rather small compared to the limiting value for J of the order 0.25 [10]. Undoubtedly the attainable values for J will increase with increasing values of Re. But because of the limits posed by the numerical resolution this aspect of the problem has not been pursued any further.

5 Transition to quaternary states of fluid flow

An analysis of the stability of the steady solutions discussed in the preceding sections has been performed based on the representation (10) for general infinitesimal disturbances. But for reasons of limited computer capacity only the case of disturbances preserving the horizontal periodicity interval of the steady solutions has been investigated, i.e. $d = b = 0$ has been assumed in representation (10). In this particular case the general class (10) of disturbances can be separated into four subclasses which either exhibit the same or the opposite of each of the two symmetries (11) of the steady wavy roll solutions. Growing disturbances are found for almost all steady solutions. The lower branch solutions are always unstable with respect to symmetry preserving disturbances, i.e. the coefficients in the representation (10) exhibit the same symmetry

$$\tilde{a}_{lmn} = (-1)^{m+n} \tilde{a}_{-lmn}, \quad \tilde{a}_{lmn} = (-1)^l a_{l-mn} \quad (17a)$$

$$\tilde{b}_{lmn} = (-1)^{m+n} \tilde{b}_{-lmn}, \quad \tilde{b}_{lmn} = (-1)^l b_{l-mn} \quad (17b)$$

$$\tilde{c}_{lmn} = (-1)^{m+n} \tilde{c}_{-lmn}, \quad \tilde{c}_{lmn} = (-1)^{l+1} c_{l-mn} \quad (17c)$$

as the steady solution. The imaginary part of the growthrate vanishes in this case. As must be expected the lower branch thus acts as a repellor in the solution space of the problem. The upper branch solutions are stable with respect to disturbances of the restricted set with $b = d = 0$ considered here if Re and G are not too far from their minimum values in the parameter space. Otherwise an oscillatory instability with the symmetry (16) grows or an instability with vanishing imaginary part σ_i of the growthrate occurs which is characterized by the property that both symmetries are opposite to that of the steady solution, i.e.

$$\tilde{a}_{lmn} = (-1)^{m+n+1}\tilde{a}_{-lmn}, \quad \tilde{a}_{lmn} = (-1)^{l+1}a_{l-mn} \tag{18a}$$

$$\tilde{b}_{lmn} = (-1)^{m+n+1}\tilde{b}_{-lmn}, \quad \tilde{b}_{lmn} = (-1)^{l+1}b_{l-mn} \tag{18b}$$

$$\tilde{c}_{lmn} = (-1)^{m+n+1}\tilde{c}_{-lmn}, \quad \tilde{c}_{lmn} = (-1)^{l}c_{l-mn} \tag{18c}$$

In order to follow the evolution of disturbances of this kind, integrations in time have been performed with time dependent coefficients in the representation (7) and with the admission of coefficients that obey the symmetries (17) and (18). The results of the integrations show, however, that all coefficients with the latter property (18) decay and that a time periodic state is reached asymptotically. In these integrations in time it is important that the noise that is superimposed onto the steady solution is of sufficiently low amplitude since otherwise the integration in time may lead to the vanishing solution, i.e. asymptotically the primary state of plane Couette flow is reached.

An example of the time periodic state is shown in figure 13. Even though the measures of the amplitude, $S - 1$ and $Nu - 1$, vary approximately sinusoidally by more than 10 percent around their mean value, the structure of the oscillating wavy roll hardly changes at all. This oscillation appears to be similar to the amplitude oscillations discussed in [7] where the solution tends to oscillate between the steady solutions on the upper and lower branches. Since upper and lower branch solutions are close to the saddle node in the case of the parameters of figure 13, the changes in the structure of the solution is rather minimal. The amplitude of oscillation increases with increasing Reynolds number. When the computations of figure 13 are repeated for $Re = 805$ a period doubling bifurcation has taken place, but variations in the structure of the solution can still hardly be discerned.

6 Concluding remarks

The analysis of this paper has been performed with the goal of finding even simpler tertiary and quaternary solutions than in the case of an isothermal plane Couette layer. Although the computations of steady wavy roll solutions have been extended far into the regime of negative Rayleigh numbers, the structure of the flow field does not differ much from the case of an isothermal Couette layer. But the temperature field offers a new way of identifying states of fluid

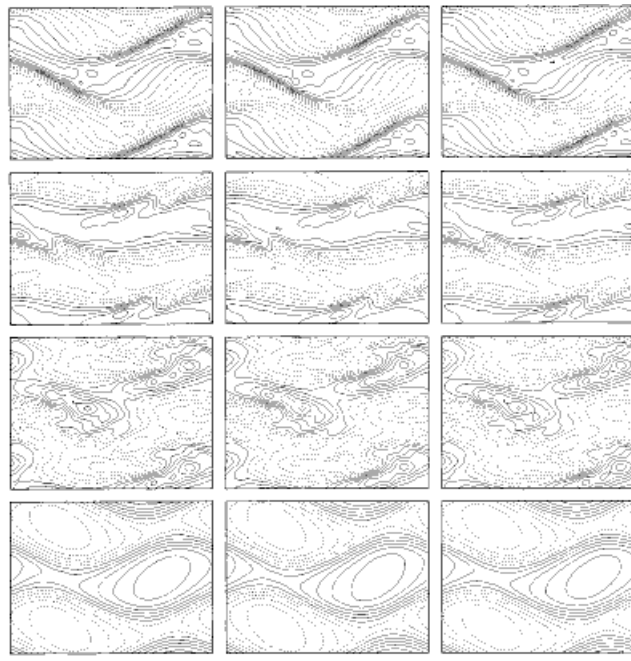

Fig. 13. Time sequence of plots (from left to right) for oscillating wavy rolls in the case $Re = 800, Ra = -5600, P = 0.71$, $\alpha_x = 1.4$, $\alpha_y = 2.8$. The uppermost row of plots shows the isotherms in the plane $z = 0$, the second and third rows show lines of constant vertical velocity in the plane $z = 0$ and $z = 0.4$, respectively, and the lowest row shows lines of constant ψ in the plane $z = 0$. The time interval between the plots is one third of the period $T_p = 0.39$ of oscillation such that a fourth plot would be identical to the first one. The x-direction is to the left, the y-direction is upward.

motion which is not available in the case of an isothermal layer. The shadowgraph method (see, for example, [3]) could be used for the experimental visualisation of flow states in a horizontal plane Couette layer heated from above and cooled from below. This method would eliminate some of the problems associated with suspensions of ceramic powder which have been used in experiments on isothermal Couette flow [9,2]. Experiments on stratified plane Couette flow have not been performed up to now in the parameter regime of the analysis of this paper.

Since a stably stratified fluid layer supports the propagation of internal waves it could have been expected that some instabilities of the steady wavy roll solutions would lead to propagation of disturbances in the form of traveling internal waves. Such a mechanism does not seem to operate in the parameter regime that has been studied in this paper. The possibility exists, however, that traveling internal waves are associated with larger horizontal scales which are not included in the stability analysis carried out in this paper.

References

1. S. Bottin, O. Dauchot, F. Daviaud, P. Manneville: Phys. Fluids **10**, 2597 (1998)
2. F.H. Busse, R.M. Clever: ZAMM **78**, S323 (1998)
3. F.H. Busse, J.A. Whitehead: J. Fluid Mech. **47**, 305 (1971)
4. A. Cherhabili, U. Ehrenstein: Eur. J. Mech. B/Fluids **14**, 677 (1995)
5. A. Cherhabili, U. Ehrenstein: J. Fluid Mech. **342**, 159 (1997)
6. R.M. Clever, F.H. Busse: J. Fluid Mech. **234**, 511 (1992)
7. R.M. Clever, F.H. Busse: J. Fluid Mech. **344**, 137 (1997)
8. R.M. Clever, F.H. Busse, R.E. Kelly: J. Appl. Math. Phys. (ZAMP) **28**, 771 (1977)
9. O. Dauchot, F. Daviaud: Phys. Fluids. **7**, 901 (1995)
10. P. Drazin, W. Reid: *Hydrodynamic stability*, (Cambridge University Press 1981)
11. M. Nagata: J. Fluid Mech. **188**, 585 (1988)
12. M. Nagata: J. Fluid Mech. **217**, 519 (1990)
13. M. Nagata: 'Stability of non-axisymmetric flows in the Taylor–Couette system'. In: *Unstable and Turbulent Motion of Fluid*, ed. by S. Kida (World Scientific 1993)
14. A. Schmiegel, B. Eckhardt: Phys. Rev. Letts. **79**, 5250 (1997)

On the rotationally symmetric laminar flow of Newtonian fluids induced by rotating disks

Antonio Delgado

Technische Universität München, Weihenstephaner Steig 23, D-85350 Freising, Germany

Abstract. This paper deals with the flow induced by rotating disks. Such flows are subject of a large number of contributions in the twentieth century. Most of them are based on the famous von Kármán transform. In the last three decades the applicability of this transform has been proved in sophisticated experimental and theoretical investigations. The present paper focuses on theoretical investigations treating a pair of disks rotating concentrically. In addition to classical solutions given by Batchelor and Stewartson, the problem of solutions being multiple, unstable and even aphysical is briefly addressed. Furthermore, some approaches dealing with moderate Reynolds-numbers are presented for which the equations of motion are linearized starting from a known creeping flow solution. A comparison of the results with those obtained from the solution of the complete Navier–Stokes equation is carried out.

1 Introduction

Fluid driven by rotating flows have represented a major field of study in fluid mechanics for a large part of the twentieth century. This results from the fact that they are not only of special interest in research but also of high relevance for a large number of applications. This is the case e.g. in rotating machines, lubrication, droplet generators, filtering systems, rheometry, computer storage devices and operation units for heat and mass transfer, as well as in the simulation of astro- and geophysical phenomena. Most of these applications can be considered classical ones. But, further fields of application became increasingly important with the progress in space technology, i.e. with the increasing in importance of processes in a gravity compensated environment. In the absence of gravity effects the centrifugal forces induced by the rotating disks can be used very efficiently e.g. for positioning and handling fluids, removing gas bubbles from molten materials, spinning and despinning of orbital vehicles, crystal growth processes and control of thermocapillarity effects.

From the theoretical point of view, rotating disk flows represent one of the few examples for which there is an exact solution to the Navier–Stokes equations. This was recognised very early for flows with a relatively simple kinematics such as the rigid body motion which occurs in the steady, isothermal case, when the fluid is enclosed by two concentrical infinite disks rotating with the same angular velocity ω. Thus, the boundary conditions are homogeneous. In this case there is no movement of the fluid relative to the disks and, therefore, no effects due to fluid friction take place. The flow kinematics is described completely by the

C. Egbers and G. Pfister (Eds.): LNP 549, pp. 417–439, 2000.

circumferential velocity component and the centripetal acceleration. The latter produces a centrifugal field which generates a radial pressure distribution.

When friction occurs the flow field is substantially more complex. Thus, solutions for the equations of motion were found only in special cases. For example, Hort [34] studied the flow in a bounded cylindrical region whereby the parallel circular areas limiting the cylinder in the axial direction z as well the cylindrical surface $r = r_0$ are allowed to rotate with different velocities. By neglecting inertial effects this author was able to give some analytical solutions on the basis of Bessel functions.

When considering inertial effects in a viscous fluid the full equations of motion must be treated. But even in this case exact solutions of the Navier–Stokes equations can be found. This was recognised first by von Kármán [1] who studied the problem of a disk of infinite radius rotating with a constant angular velocity ω in a unbounded, quiescent fluid. By applying his celebrated transform this author was able to reduce the full equation of motion to a pair of non-linear ordinary differential equations.

But, solving these non-linear equations is a non-trivial problem. Thus, Cochran [2] was the first investigator who was able to obtain an accurate numerical solution to von Kármán's equations. Later Batchelor [3] and Stewartson [4] pointed out that the same transform can be applied to the problem of steady flow between two infinite rotating disks. Batchelor [3] argued that for infinite Reynolds numbers the main body of the fluid would rotate with constant angular velocity, and that boundary layers would develop at both disks. In contrast to this Stewartson [4] predicted that the main body of the fluid outside the friction dominated layers at the disks would be at rest for the case of counterrotating disks. This would be also the case when one disk remains at rest. This means that the velocity vector outside the friction dominated layers has only an axial component.

Picha & Eckers [5] obtained experimental results very similar to that predicted by Stewartson for disks rotating in opposite direction but with the same angular velocity. But most remarkable they found that for a disk being at rest the experimental velocity distribution corresponds to the Batchelor solution when a housing is available. In contrast to this, they observed a Stewartson flow when the disks are free.

From a academic point of view the interest on rotating disks flows has even increased significantly in the last three decades. This is certainly due to the fact, that the non-linear behaviour of the flow admits a large variety of solutions. Besides so-called multiple-cell solutions, branching of solution, instable and even aphysical solutions [13,14,18,23] have been found. However, some authors didn't observe experimentally certain solutions predicted theoretically, see e.g. Dijkstra & van Heijst [9].

Therefore, some authors have focused their interest on solutions which appear to be physical. Furthermore, some efforts have been made to reduce significantly the very high efforts required when using classical numerical methods.

In [10,11,19–21] a method is proposed which allows to reduce the numerical work to be done or even to find full analytical solutions.

Very concise overviews on the field of rotating fluids are given by Greenspan [12], van Wijngaarden [13], Zandbergen & Dijkstra [14] and Parter [15]. Thus, some well-known features of the flow induced by rotating disks are treated here only in a way that they can be understood basically. However, the present paper focuses on theoretical investigations done more recently in the field of rotating disks. New applications of rotating disks flow such as mentioned above have influenced recent research work significantly, including considerations on permeable disks, turbulence, non-isothermal flows, free surface flows and non-newtonian fluid flow, but they are considered to be outside of the framework of the present survey.

2 Isotherm, steady flow of a Newtonian fluid

Here, the motion of a pure, single-phase, incompressible, non-polar, and newtonian fluid induced by rotating impermeable disks is considered. The flow field is assumed to be steady, isotherm, laminar and rotational symmetric.

2.1 Governing equations

For convenience, the flow field in question is treated in cylindrical co-ordinates, where r indicates the radial, φ the circumferential and z the axial direction. The fluid motion is described by the Navier–Stokes equation

$$\varrho \frac{\mathrm{D}\,\boldsymbol{v}}{\mathrm{D}\,t} = -\operatorname{grad} p + \operatorname{div} \mathbf{T} + \boldsymbol{f} \tag{1}$$

and the continuity equation

$$\operatorname{div} \boldsymbol{v} = 0 \ . \tag{2}$$

Hereby, ϱ denotes the density, p the pressure, t the time, $\boldsymbol{v} = u\boldsymbol{e}_r + v\boldsymbol{e}_\varphi + w\boldsymbol{e}_z$ the velocity vector, $\mathbf{T}$ the stress tensor, and $\boldsymbol{f}$ a conservative volume force. The term $\mathrm{D}\boldsymbol{v}/\mathrm{D}\,t$ is the total derivation of the velocity, which expresses only the convective acceleration in the steady case assumed. In the Navier–Stokes equation the fluid is postulated to be newtonian and, therefore, depends linearly from the velocity gradient tensor $\mathbf{L} = \operatorname{grad} \boldsymbol{v}$ according to the relation $\mathbf{T} = \mu\,(\mathbf{L}+\mathbf{L}^T)$. The symbol μ represents the dynamic viscosity.

A general solution of the equations of motion has not been found yet. Therefore, the solutions available in literature correspond to the specific physical cases considered. Here, the boundary conditions are formulated in the section in question, for convenience.

The basic features of the large diversity of rotating disks flows reported in literature are dominated either by inertial effects or the boundary conditions. With increasing inertial effects the non-linear character of the Navier–Stokes

equations becomes more and more important. Therefore, typical non-linear phenomena such as multiple or bifurcating solutions appear. On the other hand, the observable flow type depends strongly on the conditions pre-described at the boundaries of the fluid domain. In this context it is of crucial importance that the Navier–Stokes equations are not only non-linear but also of elliptical type in space.

2.2 Von Kármán's solution for a single rotating disk

Though the single infinite disk flow is not considered here extensively it is of interest because it behaves - in some cases - very similar to the flow between two infinite disks. It is e.g. very remarkable that Reshotko & Rosenthal [27] were able to construct a large Reynolds number solution for the flow in the gap between a rotating and a quiescent disk by matching together two single infinite disk solutions.

As argued by Batchelor [3], the single impermeable disk flow is characterised by a single parameter $s = \omega_2/\omega_1$ which describes the ratio of the angular velocity of the disk to that of the flow for large values of z. For convenience ω_1 is the higher angular in question. This allows to consider only the bounded domain $|s| \leq 1$.

The von Kármán's transform assumes the flow motion to be axisymmetric with respect to the axial co-ordinate z. Furthermore, von Kármán postulates that the axial velocity component w depends on z only. As a consequence of this, the radial velocity component v depends linearly on the radial co-ordinate r when mass continuity holds. Furthermore, fulfilling the non-slip condition requires the circumferential velocity component to be a linear and the pressure a quadratic function in r. Thus, in accordance to von Kármán the equations of motion can be transformed to a set of non-linear, ordinary differential equations by the ansatz:

$$\boldsymbol{v} = u\,\boldsymbol{e}_r + v\,\boldsymbol{e}_\varphi + w\,\boldsymbol{e}_z = r\omega G(z)\,\boldsymbol{e}_r + r\omega H(z)\,\boldsymbol{e}_\varphi + \delta\omega F(z)\,\boldsymbol{e}_z \tag{3}$$

$$p = \varrho\omega^2 \left(\delta^2 Q(z) + \frac{\lambda}{2} r^2\right) . \tag{4}$$

Herein, $\delta = \sqrt{\nu/\omega}$ represents a scale for the thickness of the shear dominated layer in the vicinity of the rotating disk. $G(z)$, $H(z)$ and $F(z)$ can be considered as dimensionless velocity components which depends only on z. The parameter λ characterises the radial pressure distribution. In the case of a single disk rotating in an unbounded, quiescent fluid it can be shown that it has to vanish, i.e. $\lambda = 0$.

The von Kármán solution is depicted graphically in Fig. 1. As a result of wall adhesion and friction the fluid in the vicinity of the disk is pumped outwards by the centrifugal force. Due to continuity fluid suction towards the disk occurs. The flow is fully threedimensional but rotationally symmetric.

It is not appropriate to present the transformed equations here (see for example [25]). But instead, some interesting consequences which follow from the transform are discussed. First the transform from partial to ordinary differential equations is only possible when the solutions are self-similar. This means for the

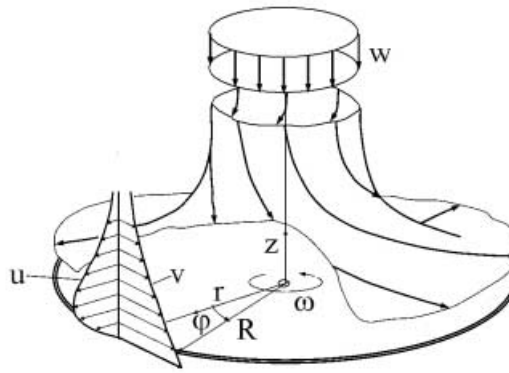

Fig. 1. Flow in a close region around an impermeable disk rotating in a fluid at rest. Velocity components: u - radial; v - azimuthal; w - axial, see also equation (3)

flow induced by a single disk that the velocity distribution for two different values of the radial co-ordinate only differs by a constant mapping factor. From this, it follows that the von Kármán transform holds only for an infinite disk radius R. But this poses a substantial theoretical problem as the conditions to be fulfilled for $R \to \infty$ can not be pre-described a priori. And apart from this they must be compatible with the kinematics of the flow. Furthermore, mass conservation is required. Thus, at infinity the existence of an adequate distribution of sinks and sources must be postulated (of course, self-similarity can be also achieved when the distribution of sinks for a given, finite value of R is compatible to the kinematics of the flow as described by the von Kármán solution).

Furthermore, when considering a single infinite disk the problem arises that the radius R can not be considered as the characteristic length of the flow field. As a consequence of this the commonly used definition of the Reynolds number ($\nu = \mu/\varrho$: kinematic viscosity)

$$Re = \frac{u_c \cdot L_c}{\nu} \ , \tag{5}$$

which requires a characteristic velocity u_c and length L_c, can not be applied. Here, an analogy to flows with boundary layer character is obvious. For example, the Blasius solution for the flat plate (see e.g. [25]) is based on a transform which provides a self-similar solution, too. But physically a self-similarity of the flow can be expected only for a plate of infinite length or, at least, when for a given finite length L the boundary conditions at L are fulfilled identically by the Blasius solution.

Usually, it is postulated that the self - similar solution (see Fig.1) is valid also for finite disk radii R when $R \gg \delta$ (this is in agreement with the similar assumption done in the case of the flat plate). However, this can be only an approximation in which the elliptical type of the Navier–Stokes equations are

altered in a parabolic type. In fact the von Kármán transform has the same effect on the friction term $\operatorname{div}\mathbf{T}$ in the Navier–Stokes equations as the basic assumption in boundary layer theory that for $Re \to \infty$ any changes of the shear stress in the main flow direction can be neglected as compared to those in a perpendicular direction. This is very particular as the boundary layer considerations hold only for very large Reynolds numbers, but the von Kármán transform does not prescribe any similar requirement. Furthermore, the von Kármán solution is valid even for very slowly rotating disks or high viscosity and, thus, when the extension of the friction dominated layer δ is very large.

The effect of the parabolisation of the Navier–Stokes equation in the case of a single disk by application the von Kármán transform are treated sparsely in literature in contrast to the situation for the case of two co-rotating disks (see below). But one-parameter flows have been studied extensively analysing regions of uniqueness, non-existence and multiplicity of solutions [13,18,23].

Roger & Lance [16] obtained solutions for each positive value of s (fluid at infinity ($z \to \infty$) rotating in the same sense as the disk), but they were not able to find results for $s < -0.2$. A further remarkable observation of these authors was that their solutions were oscillatory with the exception of that for $s = 0$. This was in agreement with the findings of Bödewadt [17] who calculated oscillating solutions for the flow above a stationary disk with the outer flow in solid body rotation.

Zandbergen & Dijkstra [14] gave an explanation for the non-existence of solutions for $s < -0.2$. These authors find not only a limit point in s at $s = -0.1605$ but also at $s = 0.07453$. After this basic finding several authors extended the investigations of [14]. Of decisive importance was the understanding achieved that for $s = 0$ there is an infinite number of solutions.

From this it became obvious that some solutions should be unstable or even aphysical. Bodonyi & Ng [18] showed that only the classical von Kármán solution is temporally stable.

In the next sections the behaviour of the flow between two co-rotating disks is discussed, which is the main subject of this paper.

2.3 Flow between co-rotating disks

There is also a large amount of publications regarding this case [3–12,19–24]. Most of them consider impermeable disks of infinite radii whereby the flow motion is described by the non-linear von Kármán equations. In contrast to the case of a single disk with the gap width b a characteristic length is available. Therefore, the fluid motion is described by a two-parameter family of solutions. In addition to the ratio of the angular velocities s, a Reynolds number

$$Re = \frac{\omega \cdot b^2}{\nu} \tag{6}$$

appears.

The discussion given in section 2.2 regarding the required kinematic compatibility of boundary conditions to the von Kármán transform can be extended to

the flow between co-rotating disks. But the analogy to boundary layer theory is not obvious, although the von Kármán transform leads to a similar parabolisation of the Navier–Stokes equations as in the case of the single disk.

Similarity to boundary layer flows, but also the effects on the non-linear character of the fluid motion such as multiplicity, non-existence and stability of solutions become more pronounced for high values of Re. On the other hand, some applications i.e. in viscometry and space technology make it necessary to have access to the physics of flows at moderate Reynolds numbers and, therefore, there are some new publications in this field [10,11,20,21].

In contrast to the single disk flow, in literature more interest has been devoted to the influence of boundary conditions existing at the outer region of disks with finite radii. Usually finite disks are assumed to be closed by a cylindrical container being at rest or moving with a constant angular velocity ω_E. In this case further parameters $s_E = \omega_E/\omega_1$ and $\hat{b} = b/R$ which characterise the ratio of the angular velocities and the aspect ratio, respectively, must be taken into consideration. Therefore, it is convenient to present also some results in this field, whereby the discussion will focus on the validity of self-similar two-parameter solutions.

Self-similar solutions for infinite co-rotating disks at high values of *Re*

Two disks of infinite extension R are separated by a gap of the width b. In order to guarantee $|s| < 1$, ω_1 should correspond to the faster rotating disk. The considered problem is illustrated in Fig. 2. Mellor et al. [7] found solution

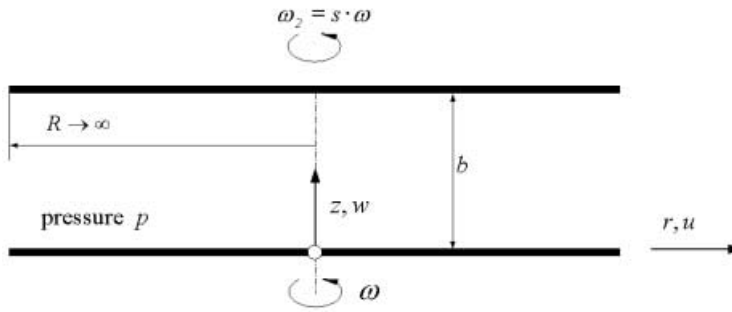

Fig. 2. Schematic representation of coaxially rotating disks with infinite radius

multiplicity for $s = 0$ and high Reynolds numbers. They demonstrate that both the Batchelor and the Stewartson solution, as well as many others, exist. The Batchelor solution evolves from the creeping flow solution. At $Re \approx 217$, two new solutions appear and both extend to high Reynolds numbers, one of these being the Stewartson flow. Furthermore Mellor et al. [7] observed an alternation in the sign of the axial velocity in the gap. This corresponds to the existence

of multiple cell flows in the meridional plane. Robert & Shipman [6] generated numerically up to five cells. It is remarkable, that they found at high values of Re regions of uniqueness, non-existence and multiplicity of solution.

Holodniok et al. [8] showed with the help of the Newton-Raphson method, that the non-linear von Kármán equations accept for $s = 0.8$ only one solution for small Reynolds numbers ($Re < 205$). But with increasing Re the number of solutions found by these authors becomes three ($205 < Re < 330$), and, finally, five ($Re > 330$).

In Fig. 3(a) results of these authors for $s = 0.8$ and Re up to 10^4 are depicted graphically. As can be seen the radial pressure coefficient λ obtains different values depending on Re. In this context multiplicity in solution is characterised by the fact that different values of λ are obtained for the same Re.

Coming back to the von Kármán ansatz for the pressure (4) it should be stated that the value of λ is not known a priori. Instead, it must be calculated from the boundary conditions which are for the infinite, co-rotating, impermeable disks considered here:

$$z = 0 : \boldsymbol{v} = r\omega\, \boldsymbol{e}_\varphi \ , \tag{7}$$

$$z = b : \boldsymbol{v} = sr\omega\, \boldsymbol{e}_\varphi \ . \tag{8}$$

Taking into consideration the three components of the velocity vector $\boldsymbol{v}$ these are

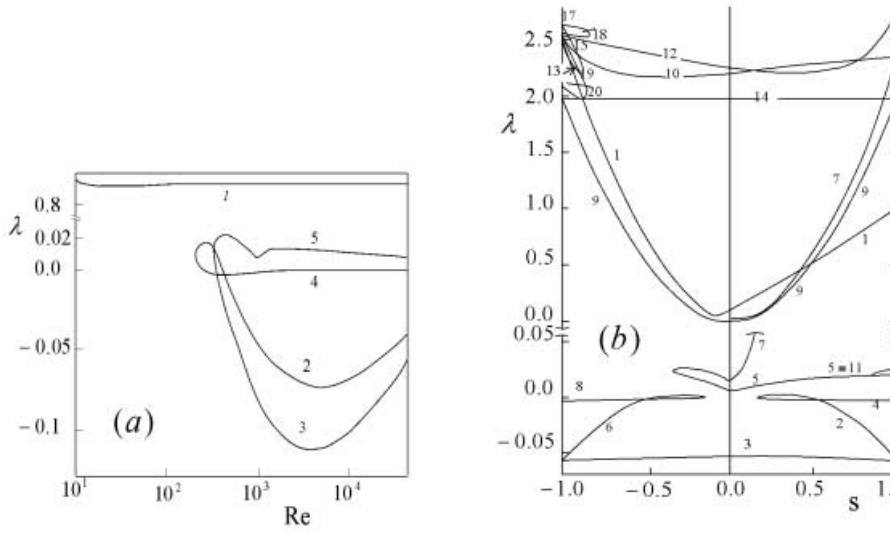

Fig. 3. Dependence of λ (a) on the Reynolds number Re for $s = 0.8$ and (b) on the parameter s for $Re = 625$

six boundary conditions. Five of them are required for completing the non-linear von Kármán equations. The sixth is used for determining λ.

In a further work Holodniok et al [26] investigated the influence of s on λ. For $Re = 625$ they found up to 20 solution branches each corresponding to a different number of cells, see Fig. 3(b).

These authors did not investigate the stability of the solution they found. Most of them appear to be unstable or even aphysical. However, Holodniok et al. [26] were able to show that most of the results published in literature were consistent with those of the own numerical calculation.

On the other hand, Dijkstra & van Heijst [9] investigate the flow generated by a pair of finite, impermeable disks enclosed by a cylindrical surface. They found that in such a case the solution is unique for all value of the parameters studied. From this it can be concluded, that the diversity of the theoretical results obtained is at least partly connected to the use of the von Kármán transform.

Self-similar solutions for disks rotating at moderate Reynolds numbers

As already mentioned in the introduction this case is of substantial importance for example in rheometry and space technology where slowly rotating disks or highly viscous fluids are considered. But, additionally, studying the case of moderate Re numbers some basic features of the flow induced by the disks become obvious. Furthermore, the costs required for calculating the flow field can be reduced substantially when restricting to moderate Reynolds numbers. Last but not least, it can be stated that flows which develop from the kinematics obtained for small Reynolds numbers are free from the uncertainties discussed above such as multiple, unstable or aphysical solutions.

In [10,11,20,21] a method is proposed which allows to calculate the flow field for moderate Reynolds numbers very efficiently. The basic ideas of this method is

(i) to linearise the Navier–Stokes equations by perturbing a known solution for the creeping flow ($Re \to 0$) by means of low order perturbations p^+, u^+, v^+ and w^+;
(ii) to transform the perturbed equations of motion into a set of linear, ordinary differential equations with the help of the von Kármán ansatz;
(iii) to integrate these set of differential equations numerically or analytically.

The first step is in agreement to the linearisation method proposed by Oseen for the treatment of the flow around a sphere for small Reynolds numbers, see i.e. [25]. It is based on the assumption that the magnitude of the perturbing velocities u^+, v^+, and w^+ is much smaller than that of a reference azimuthal velocity v^0 , i.e.

$$v^0 \gg u^+, v^+, w^+ \ . \tag{9}$$

The perturbed solution is introduced into the equations of motion. The linearised equations of motion are obtained by neglecting the second order terms consisting of products of the perturbing velocities and their derivatives.

In accordance to the non-linear case the transform from the linearised equations of motion (which are partial differential equations) to a set of ordinary differential equations holds only for self-similar flows. This is not given generally but the von Kármán transform fulfils the perturbed equations of motion when a suitable creeping flow is used.

Such a creeping flow field is described by

$$\boldsymbol{v} = r\omega\Phi(z)\boldsymbol{e}_\varphi \tag{10}$$

$$p = p_0 \tag{11}$$

$$\text{with} \quad \Phi(z) = 1 + \frac{s-1}{b} \cdot z \quad . \tag{12}$$

This flow can be considered as a member of the family of steady, pure shear flows characterised by the fact that the kinematics depend only on a measure for the deformation rate (shear rate). Furthermore, the Rivlin-Ericsen tensors

$$\mathbf{A}_{n+1} = \mathbf{L}^T\mathbf{A}_n + \mathbf{A}_n\mathbf{L} \quad \text{with } \mathbf{A}_1 = \mathbf{L} + \mathbf{L}^T \tag{13}$$

of the order $n \geq 3$ have to vanish.

Regarding the restriction (9) it should be mentioned that it can be kept in a large number of flows induced by generated disks but it is violated by the classical von Kármán single disk case. This is due to the fact that in von Kármán's problem the flow far from the disk is assumed to be normal to the disks and to be induced by the rotation of the disk. Therefore, from a physical point of view the only creeping flow situation compatible is such of a vanishing axial component. From this follows that $v = v^+$. But it is well known that there is an extended region in the neighbourhood of the axis of rotation in which the order of magnitude of the axial velocity component is similar to that of the circumferential velocity v and, thus, restriction (9) does not hold.

Returning to the method proposed in [10,11] the perturbation of the creeping flow (10) - (12) and the linearisation of the momentum equations lead to the expression (p^+ and $\mathbf{T}^+$ denote the perturbing pressure and stress tensor):

$$(-r\omega^2\Phi^2 - 2\omega\Phi v^+)\boldsymbol{e}_r + (2\omega\Phi u^+ + r\omega\Phi' w^+)\boldsymbol{e}_\varphi = -\frac{1}{\varrho}\operatorname{grad} p^+ + \frac{1}{\varrho}\operatorname{div}\mathbf{T}^+ \tag{14}$$

Herein, the stroke ($'$) denotes differentiation with respect to z. In the mass balance (2) the velocity vector $\boldsymbol{v}$ can be simply substituted by the perturbing vector $\boldsymbol{v}^+$ as from (10) it follows $u^+ = u$ and $w^+ = w$. The azimuthal velocity component does not appear in (2) for rotationally symmetric flows. The application of the von Kármán ansatz

$$\boldsymbol{v}^+ = r\omega g(z)\boldsymbol{e}_r + r\omega h(z)\boldsymbol{e}_\varphi + \delta\omega f(z)\boldsymbol{e}_z \tag{15}$$

$$p^+ = \varrho\omega^2\left(\delta^2 q(z) + \frac{\lambda}{2}r^2\right) \;;\; \lambda = \frac{1}{r}\frac{\partial p^+}{\partial r} \tag{16}$$

to (14) and (2) leads to the following set of linear, ordinary differential equations

$$-\Phi^2 - 2\Phi h = -\lambda + g'' \tag{17}$$
$$2g\Phi + f\Phi' = h'' \tag{18}$$
$$0 = f'' - q' \tag{19}$$
$$0 = 2g + f' \ . \tag{20}$$

For convenience the axial co-ordinate z has been made non-dimensional by dividing it by δ, and, therefore, the stroke ($'$) denotes differentiation with respect to $\zeta = z/\delta$. For the impermeable disks considered here the boundary conditions (7) and (8) transform to

$$\zeta = 0 : \qquad g = h = f = 0 \tag{21}$$
$$\zeta = \zeta_b := b/\delta : g = h = f = 0 \ . \tag{22}$$

From the set (17) - (22) some basic statements on the behaviour of the flow can be derived. From the continuity equation (20) and the boundary conditions (21) and (22) it can be deduced that not only the transformed axial perturbing velocity f but also its first derivative f' must vanish at the impermeable disks. The axial perturbation pressure coefficient q can be directly determined when the distribution of the transformed axial perturbing velocity f is known. On the other hand calculating f requires the simultaneous solution of the momentum equations in circumferential (18) and radial direction (17) as well as the continuity equation (20). This interdependence expresses the redistribution of momentum in the flow. The momentum is generated by the rotating disks. The wall adhesion of the fluid is responsible for the momentum transfer to the perturbing velocity component h. The momentum connected to this component is the source of the formation of the radial pressure gradient λ (see also (16)). This can be directly deduced from the radial momentum (17) but more concisely from

$$-4\Phi^3 h + \phi' h''' - \Phi h^{IV} = 2\Phi^4 - 2\lambda\Phi^2 \ , \tag{23}$$

which is equivalent to (17), (18) and (20). Unfortunately, no analytical solution of (23) has been found yet (compare [10,11]). On the other hand it can be solved numerically whereby five boundary conditions have to be fulfiled since λ is unknown, too.

It appears not convenient to give details of the numerical solution of (23) here. Instead, the discussion of the set (17) - (21) is continued. Assuming h and λ to be known, the redistribution of momentum can be traced easily from these equations. Obviously, (17) and (18) expresses respectively the transfer of momentum from the mainflow component h to the dimensionless radial and axial perturbing velocities g and f. For elucidating more concisely the transfer to f the term $2g$ on the left hand of (18) can be replaced by $-f'$ in accordance to the mass balance (20). Doing so the direct interdependence of f and h becomes evident.

Starting the linearisation of the equations of motion from the creeping flow (10) - (12) has the advantage that a good approximation can be expected for very different values of the angular velocity ratio s. This is due to the fact that the basic assumption (9) is preserved. On the other hand a significant numerical work has to be carried out when treating the system (17) - (22). However, in [10,11] full analytical solutions are presented for some special cases and, therefore, it seems to be of high educational value to analyse them before presenting some numerical results from (17) - (22).

As shown in [10,11] full analytical solutions of the equations of motion can be obtained starting the linearisation from a rigid body flow. Formally this flow is obtained by setting $s = 1$ in (12) whereby (becomes equals to unity. Then the radial and circumferential momentum balances (17) and (18) simplify to:

$$-1 - 2h = -\lambda + g'' \tag{24}$$

$$2g \qquad = h'' \ . \tag{25}$$

The boundary condition (21) remains unchanged but (22) translates into

$$\zeta = \zeta_b \ : \ g = f = 0 \ ; \ h = s - 1. \tag{26}$$

Doing so, it becomes obvious that (24) and (25) can be treated separately from the axial momentum balance (19) and mass conservation (20). This represents a substantial simplification in finding solutions describing the fluid movement induced by the co-rotating disks. After some algebraic manipulations (24) and (25) can be reduced even to a single linear differential equation (which can be also found by setting $\Phi = 1$ in (23), of course)

$$h^{IV} + 4h = 2\lambda - 2 \ . \tag{27}$$

In [10,11] it is shown that the set (24), (25), (19) - (21), and (26) accepts the general solution

$$g(\zeta) = e^{\zeta}(C_1 \cos\zeta - C_2 \sin\zeta) + e^{-\zeta}(C_3 \cos\zeta + C_4 \sin\zeta) \tag{28}$$

$$h(\zeta) = e^{\zeta}(C_2 \cos\zeta + C_1 \sin\zeta) + e^{-\zeta}(C_4 \cos\zeta - C_3 \sin\zeta) + \frac{\lambda}{2} - \frac{1}{2} \tag{29}$$

$$\begin{aligned} f(\zeta) = {} & -C_1 e^{\zeta}(\sin\zeta + \cos\zeta) + C_2 e^{\zeta}(\sin\zeta - \cos\zeta) \\ & -C_3 e^{-\zeta}(-\cos\zeta + \sin\zeta) + C_4 e^{-\zeta}(\sin\zeta + \cos\zeta) + C_5 \end{aligned} \tag{30}$$

$$q(\zeta) = -2g(\zeta) + C_6 \ . \tag{31}$$

It is important to mention that h is antisymmetric with respect to a co-ordinate system with the origin at $(\zeta/\zeta_b = 0.5\,;\, h = h_m = (s-1)/2)$ whereby h_m denotes the average perturbating circumferential velocity. Furthermore, g and f are, respectively, antisymmetric and symmetric with respect to a horizontal axis going through $(\zeta/\zeta_b = 0.5\,;\, 0)$. In the general solution (28) -(31), C_1 - C_6 represent constants; C_6 can be set to zero without the loss of generality . The values of these constants are given in [10,11]. But it is of importance to emphasise that they depend on ζ_b.

As a consequence of this the solution (28)-(31) are functions of ζ and ζ_b or in other words functions of the global and the local Reynolds numbers Re and Re_z, as

$$\zeta = \frac{z}{\delta} = \sqrt{\frac{z^2 \cdot \omega}{\nu}} = \sqrt{Re_z} \; . \tag{32}$$

In [10,11] it is shown that the solution (28) - (31) agrees excellently with those calculated by Holodniok et al. [8] for $Re = 275$ and $s = 0.8$ starting from the non-linear von Kármán equations. This results from two different facts. At first the isorotation ($\Phi = 1$, i.e. $s = 1$) is a solution of the full Navier–Stokes equation. Therefore, it is valid for arbitrary Reynolds numbers. Thus, a low order perturbation of the isorotation must be expected to provide a good approximation of the flow field at least in laminar flow regime as far as the flow remains stable. The second reason is connected to the s-value studied in [8]. As long as the deviation from $s = 1$ is only moderate the basic assumption (9) is preserved. In [11] it is estimated that even when the deviation of s is 0.5 the error to be expected should be not larger than $12,5\,\%$.

The influence of Re on the velocity components for $s = 0.6$ is illustrated in Fig. 4. For convenience, the velocity distributions are depicted graphically as functions of ζ/ζ_b. In Fig. 4 the lower, faster rotating disk is represented by the velocity co-ordinate axis characterised by $\zeta/\zeta_b = 0$. The parallel line intersecting the ζ/ζ_b-axis at 1 is considered to describe the surface of the upper disk. In accordance to the results of different authors [8,22] the solution (28)-(31) describes a flow of Batchelor type. In [8] it has been observed that the Batchelor flow develops continuously from the flow at low Reynolds numbers. This is confirmed by Fig. 4(b). But in contrast to the prediction of Batchelor, a core region rotating at a nearly constant angular velocity $(1 - s)\omega/2$ is only available for sufficiently large Re. This can be deduced from Fig. 4. This figure shows the characteristic core rotation only for $Re \geq 49$.

For very low Re numbers the distribution of the circumferential velocity component h is nearly linear in ζ. This can be deduced immediately from the solution (29). The order of magnitude of Re determines also that of Re_z and ζ, see (32). This allows to replace in (29) e^{ζ} and $\cos\zeta$ by unity and $\sin\zeta$ by ζ. As a consequence of this, h can be rewritten as (B_1, B_2 are constants)

$$h(\zeta) = B_1 + B_2 \cdot \zeta \; . \tag{33}$$

Similar considerations require the radial and axial perturbing velocity components to vanish for very low Re numbers, compare Fig. 4(b).

The nearly linear dependence of h on ζ/ζ_b can only hold up to a flow situation in which the inertia and shear forces are of the same order of magnitude, i.e. up to $Re = 1$. For higher values of Re the momentum transfer due to inertia dominates and the velocity distributions change not only quantitatively but also qualitatively. As shown in Fig. 4(b), for $Re = 9$ the circumferential perturbing velocity h decreases monotonously with ζ/ζ_b. At $\zeta/\zeta_b = 0.5$ the graph shows a point of inflexion the existence of which can be derived from the circumferential

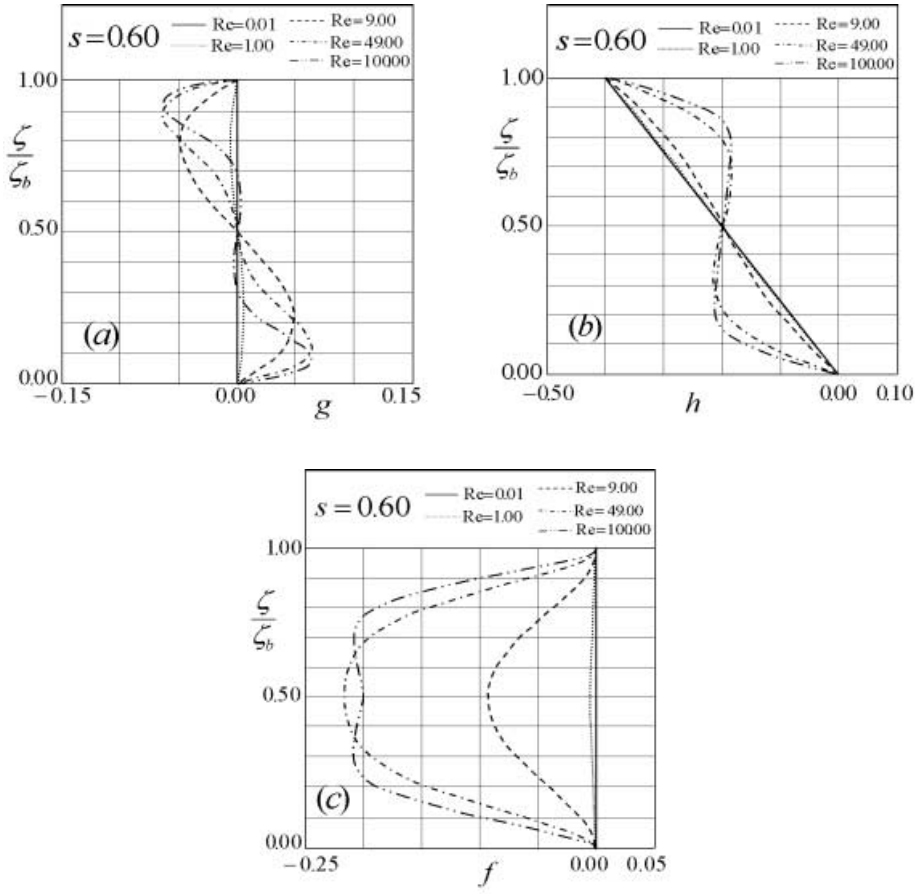

Fig. 4. Influence of Re on the transformed axial perturbing velocity component $g(\zeta/\zeta_b)$ (radial), $h(\zeta/\zeta_b)$ (azimuthal) and $f(\zeta/\zeta_b)$ (axial)

momentum (25) when taking also into consideration the symmetry properties of g mentioned above which requires g to vanish but not its first derivative.

When Re is further increased the graph of h shows additional extrema, as demonstrated in Fig. 4(b) for $Re = 49$. Obviously, in a large distance away from the rotating disks the friction forces are not longer able to balance the inertial forces. Similar to the single disk, shearing effects dominate only in a layer of the magnitude of $\sqrt{\nu/\omega}$. This behaviour becomes more pronounced with increasing Re. But, as shown in Fig.4(b) for $Re = 100$, not only the thickness of the shear dominated layer becomes smaller but also the core region in which the flow rotates nearly with the mean velocity $v_m = r\omega(1 + h_m) = r(1 + (s - 1)/2)$ extends for large values of Re.

This is typical for the Stewartson flow type which is also supported by the behaviour of the radial and axial velocity components, see Fig. 4(a),(c). In agree-

ment with the prediction of Stewartson the lower, faster rotating disk acts as a fan which carries the fluid in the radial direction outwards. This is connected to positive values of g in the neighbourhood of this disk. Continuity requires a suction of the fluid at the upper, slower rotating disk, i.e. negative values of g. Increasing values of Re generate high velocity gradients in the vicinity of the disks whereby the local velocity extrema are shifted towards the disks. When the inertia effects dominate absolutely (see the data for $Re = 100$ in Fig. 4)(a) the radial perturbing velocity component tends to zero in the core region, too. Stewartson [4] argued that in spite of the mass transport taking place along the disks in opposite direction the secondary flow generated in the meridional section is characterised by the presence of a single cell in the sense as defined by Mellor et al. [7]. This can be deduced also from the behaviour of the axial perturbing velocity component f as depicted graphically in Fig. 4(c). The axial velocity has on negatives values in the whole gap, i.e. it does not change its sign. This indicates the existence of a single cell whereby the fluid moves from the slower disk to the faster one.

This can be shown more conclusively when introducing a perturbing stream function Ψ^+ which fulfils identically the continuity equation (20) (but also (2) as $u^+ = u$ and $w^+ = w$) when the linearisation is started from isorotation:

$$u^+ = -\frac{1}{r}\frac{\partial \Psi^+}{\partial z} \tag{34}$$

$$w^+ = \frac{1}{r}\frac{\partial \Psi^+}{\partial r} \ . \tag{35}$$

When using the von Kármán transform for u^+ and w^+ mass conservation leads to (dimensionless) transformed stream function

$$\xi = \frac{\Psi^+}{\delta \omega r^2} = \frac{f}{2} \ . \tag{36}$$

This relationship shows that the sign of the stream function ξ agrees to that of f. As it remains unaltered in the whole gap it is obvious that in the meridional section only one movement cell exists.

Studying the interdependence of the perturbing velocity components in a more detailed manner provides a better insight in the basic features of the flow. In this context it appears convenient to come back to the interdependence between the axial and the radial component resulting from the continuity equation as already used in the discussion above. The relation between g and the derivative of f expresses that the number of extrema of f must be equal to the number of roots of g. This can be also seen immediately when comparing in Fig. 4. While for small values of Re g becomes zero only at $\zeta/\zeta_b = 0.5$ zero in the gap (apart from the disks at which wall adhesion requires vanishing values of g), the graph of g intersects the ζ/ζ_b-axis three times for $Re = 100$ this generating an equivalent number of extrema in the distribution of f.

There is also a similar closed relationship between the circumferential and the axial component. From an algebraic manipulation of (20) and (25) one obtains

$$f + h' = B_3 \ . \tag{37}$$

This means that the sum of f and the first derivative h' is equal to a constant value B_3 in the whole gap. In [11] it is shown that for large values of Re

$$B_3 = h'(0) = h_m \ . \tag{38}$$

Both equations are of great importance when discussing the behaviour of f as shown in Fig. 4(c). At first it must be stated that the symmetry of f mentioned above demands $f' = 0$ and in accordance to (37) $h'' = 0$ at $\zeta/\zeta_b = 0.5$. This is a necessary and, obviously, a sufficient condition for the inflection point appearing at half the gap width as demonstrated in Fig. 4(b). Furthermore, from (37) it can be deduced that the existence of maxima of h requires the condition to be fulfiled that the local value of f must exceed that of h_m. For the angular velocity ratio $s = 0.6$ considered in Fig. 4 this condition is already preserved when a characteristic Reynolds number of $Re_c \approx 22.3$ is achieved. Though this value is relatively small the difference between B_3 and h_m is smaller that 2 %. Thus for $Re > Re_c$ the validity of (37) can be assumed to be given. This also means in accordance to (37) and (38) that

$$f_c \approx h_m \tag{39}$$

and, therefore, that the position of the maxima of azimuthal perturbing velocity are located at those points at which the line parallel to the ζ/ζ_b-axis going through f_c intersects the function $f(\zeta/\zeta_b)$. For completeness, it should be mentioned that due to (38) $B_3 = h_m$ represents also the wall shear rate of the circumferential velocity component. Thus, in accordance to the discussion above, local extrema of h can only exist if the wall shear rate exceeds the values corresponding to that available at Re_c.

As demonstrated in this section, linearising the equations of motion starting from the isorotational flow proposed in [10,11,19,20] permits to get an detailed insight into the basic features of the flow induced by co-rotating, impermeable disks with a comparably small effort. On the other hand, the restriction (9) permits to study flows in which the ratio of the angular velocities deviates only slightly from $s = 1$. For other values of s, specially for the case of counter-rotating and for disk at rest it is necessary - and somewhere physically evident - to start the linearisation from the creeping flow described by (10)-(12). Therefore, it appears more appropriate not to discuss the dependence of the flow dynamics on s with the aid of the full analytical solution (28) - (31) but with numerical results obtained for the set (17) - (21).

Details on the numerical method used for solving this system are given in [10,11,19]. Here, it should be mentioned, that due to linearisation the numerical work is substantially smaller than when solving the non-linear von Kármán equations. Fig. 5 shows data for the case of the upper disk being at rest ($s = 0$). As already discussed this flow was studied by Batchelor [3] first. He argued by qualitative reasoning that for high values of Re the core region should rotate with a constant angular velocity. Furthermore, the fluid should move axially towards the rotating disk, but a formation of boundary layer should occurs at both disks. In contradiction to this Stewartson [4] concluded on the base of a series

expansion for small Re numbers that the boundary layer formation should take place only on the rotating disk. Other authors [2,7] have shown that both flow types fulfil the non-linear von Kármán equations.

The experimental results of Mellor et al. [7] as well as of Schulz-Grunow [7,28] but also the theoretical results found in [22,24] give strong evidence that the flow is of Batchelor type for $s = 0$. In [10,11] it is shown that also for a steady disk only a single cell is present in the gap. Furthermore, in the neighbourhood of the rotating disk the meridional flow is nearly radial as the (big) peak in the radial velocity distribution, see Fig. 5, is relatively close to the wall but not the (low) peak (not shown in the present survey) of the axial velocity component. The first derivative is additionally zero at the wall due to mass conservation.

As discussed in [10,11] (see also Fig. 5) the deviation from the creeping flow (10) - (12) is very small for values of Re up to unity. With increasing Re numbers substantial velocity gradients arise at both disks. This indicates the formation of boundary layers. The largest gradients appear at the rotating disk. When comparing the behaviour of the function $g(\zeta/\zeta_b)$ for $Re = 49$ and $Re = 100$ in Fig. 5(a), it is evident that the gradient of g becomes smaller for $Re = 100$. Furthermore, for this Re number a flow zone ($0.45 < \zeta/\zeta_b < 0.75$) appears, in which g depends only very slightly on ζ/ζ_b. This can be attributed to the linear dependence of f on ζ/ζ_b observed in this region by [10,11] as mass conservation requires g to be constant in this case. From this it can be deduced that g does not participate on the momentum balance (17) in this region. In other words any shear effect due to gradients of g vanishes there due to $g'' = 0$. As a consequence of this, the inertia terms on the left side of (17) must provide a constant value at each position ζ/ζ_b, as λ is constant, too, for given s and Re. Considering that Φ is linear in ζ/ζ_b this condition is satisfied only if h is also a linear function in the region in question. Furthermore, the graphs of Φ^2 and $-2\Phi h$ must be parallel this being only possible if

$$\frac{d\,h}{d(\zeta/\zeta_b)} = \frac{1}{2}\frac{d\,\Phi}{d(\zeta/\zeta_b)} = \frac{1}{2}\ . \tag{40}$$

As Fig. 5(b) demonstrates this represents in fact a good approximation of the $h(\zeta/\zeta_b)$.

In connection to the contradictory predictions of Batchelor and Stewartson the appearance of a point of inflection for $Re = 100$ in the core region as shown in Fig. 5(b) seems to be essential. Taking $v = r\omega\, H = r\omega(\Phi + h)$ into account, this means that the dependence of the circumferential velocity on ζ/ζ_b diminishes when Re is sufficiently large. This in connection to the discussed behaviour of g indicates that the flow tends to rotate with a constant angular velocity as predicted by Batchelor. Stewartson [4] was not able to find this point of inflection as his serial expansion diverges for $Re > 10$. For completeness, the case of counter-rotating disks is discussed briefly here. The results found in [10,11,21] for moderate Reynolds number up to 100 agree excellently with those of other authors who used the non-linear von Kármán equation, see for example [22,24]. In literature the prediction of Stewartson [4] is well accepted. In accordance

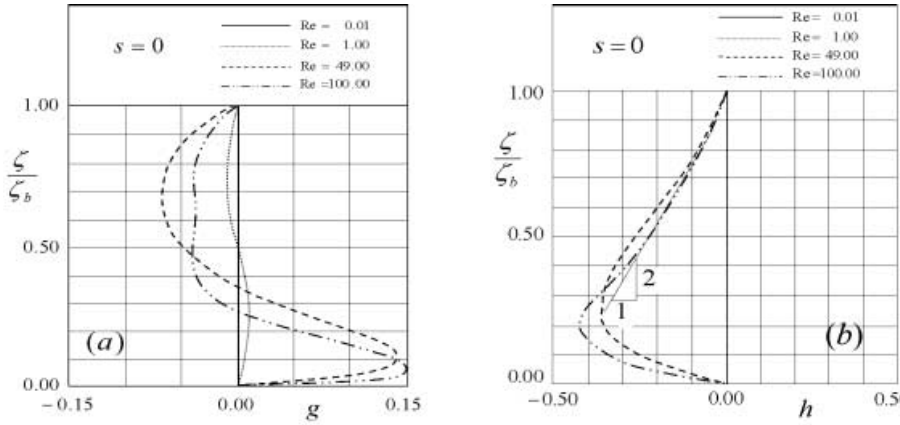

Fig. 5. The transformed perturbing velocity components g (radial) and h (azimuthal) for the flow induced by co-rotating disks one those being at rest ($s = 0$) for different values of Re

with this author boundary layers are formed at both disks which carries the fluid outwards. Due to mass conservation an inflow occurs in the core region from which the disks are supplied with the same flow rate this requiring the axial component to flow into opposite directions. Thus, the perturbing stream function Ψ^+ changes its sign (compare also (36)). A two-cell flow is available in the meridional section. Szeto [29] shows that a solution of the non-linear von Kármán equation (Branch 1 in [29]) with similar characteristics develops continuously from the creeping flow and extends to $Re \to \infty$ (this author does not study the appearance of turbulence!). This solution is found to be temporally stable. For $Re = 199.8$ it bifurcates supercritically into two asymmetrical solutions (Branches 2 and 3 in [29]).

Finite disks and limitations of self-similar solutions

The influence of a housing of the flow field induced by rotating disks or, more general, of boundary conditions at $r = 1$ has been subject of intensive investigations, as yet [5,21–23,28]. Furthermore, the number of parameters which affects the flow is so large, that the considerations given here can not be more than just an example.

When studying theoretically the flow induced by disks of the finite radius R three main ideas are followed in literature. Among others, Brady and Durlofsky [22] calculate the flow numerically on the base of a parabolisation of the equations of motion. Furthermore, for moderate values of Re in [20,21] it is suggested to solve directly the linearised equations of motion (14) and (2). Other authors - especially those of most recent investigations - [9,11,21,30] seek solutions of the full Navier–Stokes equations with the aid of sophisticated numerical algorithms.

At the beginning of the present section it was mentioned that in the presence of a housing the influence of s_E must be taken into consideration additionally to the Re and s. Furthermore, the flow depends on R. This encourages some authors to introduce a further Re_R number with R as characteristic length. However, the meaning of Re_R is obviously restricted as e.g. for very small gap width the flow will remain shear dominated even when Re is large due to a large values of R. In fact, the flow is influenced directly by the aspect ratio $\hat{b} = b/R$. Furthermore, for simplification it is convenient to introduce $\hat{r} = r/R$.

Parabolising the equations of motion requires formulating conditions at R which match the flow in the gap. Finding such conditions is not trivial. In most cases they can not be connected directly to a real physical case [24].

When treating finite disks the question is often addressed how reliable self-similar solutions can describe the flow induced by finite disks enclosed by a cylindrical wall [11,22,24,30]. This question arose originally from the experimental findings of Picha & Eckert [5] that a housing performs a selection in the sense that only certain self-similar solutions are observable. Dijkstra & van Heijst [9] found in similar experiments and in numerical simulations only a unique flow type in the presence of a housing.

Fig. 6 shows a comparison of results of the method proposed in [10,11] for moderate Reynolds numbers, of Brady & Durlofsky [22] for parabolised equations of motion, and those calculated by Bhattacharyya & Pal [30] by treating the full Navier–Stokes equations. In this figure the radial pressure gradient coefficient, see (16) is depicted graphically as a function of Re for the case of counter-rotating disks. Brady and Durlofsky [22] evaluated the results of the non-linear

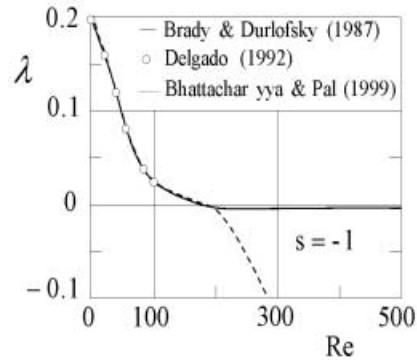

Fig. 6. Comparison of the radial pressure coefficient data given in literature for counter-rotating disks, $r = 0.1$ and half the gap width (Stewartson flow type)

von Kármán equation with those provided by the parabolisation of the equations of motion for disks of the radius R. These authors investigate among others so-called "open end" boundary conditions at R which have to match the flow field in the gap. This boundary conditions prescribe an angular velocity of zero, an radial

outflow in the vicinity of the disks due to the effects of the boundary and a mass conserving flow which transports fluid with an uniform radial component in the negative r-direction. Concerning the radial velocity component they found that the discrepancies in the solutions based on the parabolisation and the non-linear von Kármán equations were not greater than 2 % in the region $0 \leq \hat{r} \leq 0.85$ when $Re = 40$ and in the region $0 \leq \hat{r} \leq 0.7$ for $Re = 100$.

The data shown in Fig. 6 are valid for $\hat{r} = 0.1$ and $\hat{b} = 0.2$. Brady and Durlofsky [22] demonstrated that the values of λ for different boundary conditions they investigated when using the parabolised equations of motion and those of the self-similar Stewartson flow type coincide within a small error range. Therefore, the data of these authors are depicted graphically by a single curve for simplification. The results of Bhattacharyya & Pal [30] were calculated by assuming the housing rigid and steady, i.e. $s_E = 0$.

As can be seen, the data presented in Fig. 6 are in excellent agreement for values of Re up to 200. Bhattacharyya & Pal [30] make the end effects at higher Reynolds numbers responsible for the deviation occurring at higher Reynolds numbers. Fig. 7 illustrates these end effects for the case of counter-rotating disks for large values of $\hat{b}$. It demonstrates stream lines of the meridional flow found by [30] for different Re numbers. At the housing re-circulation zones exist which are symmetrical regarding the half gap width for each Re number depicted grahically, but the streamline contours exhibit waviness. This could lead to the formation of a new flow system with a higher number of cells. The

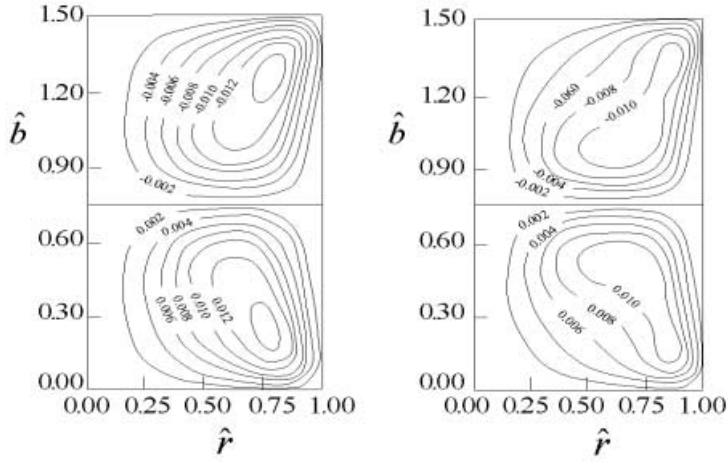

Fig. 7. End effects for disks with small radius R and large gap width b

data shown in Fig. 8 illustrate that for small values of $\hat{b}$ the end effects influence significantly the axial velocity component which even changes its sign for large values of $\hat{r}$ but not the radial component ($Re = 100$; $\hat{b} = 0.2$). This permits different interpretations. At first, the radial transport effect due to the shear

layers remains nearly unaltered in the case of a housing in a large region of $\hat{r}$. In fact, the radial flow is deviated only in the vicinity of the cylinder enclosing the disks. Concerning the von Kármán ansatz this fact is of substantial importance, as it holds even for large values of $\hat{r}$, see Fig. 8. In contrast to this, a basic assumption of the von Kármán ansatz which requires the axial velocity f to be a function of z only is violated at relatively small values of $\hat{r}$.

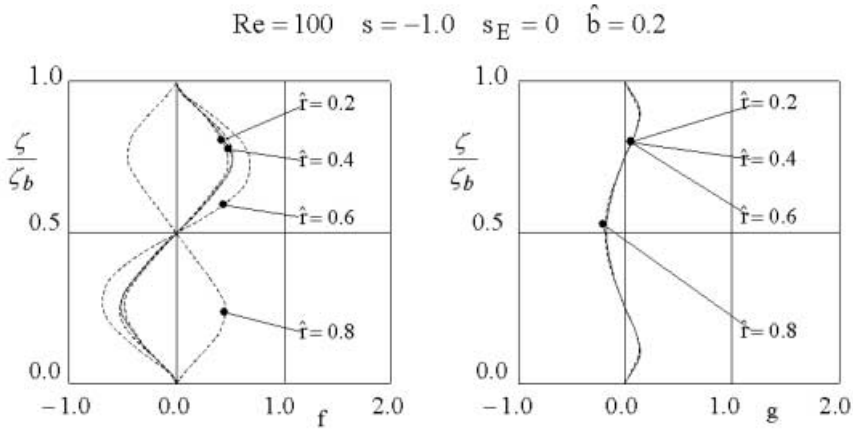

Fig. 8. Velocity of self-similar solution in a gap with the aspect ratio $\hat{b} = 0.2$ (counter-rotating disks)

3 Conclusions and future investigations

Although rotating disk flows can be considered as classical subject of research in fluid mechanics, the understanding of the physics of the fluid is far from be complete. For the newtonian, one-phase fluids in a steady, laminar flow field treated here, the variety of the problems arising when treating co-rotating disks is due to inertia effects and the boundary conditions available in the physical case in question. In other words, non-linearity and the elliptical character of the Navier–Stokes equations are the sources for a large number of problems occurring in the mathematical description of the flow.

The von Kármán transform [1] has been applied to a large number of flow situations up to now. In this context stable as well as unstable, multiple and even aphysical solutions have been calculated. For the validation of these solutions one must consider especially that the boundary conditions for $\hat{r} = 1$ can not be

prescribed a priori. This is a consequence of the transformation of the equations of motion with the aid of the von Kármán ansatz: the equations of motion are not only parabolised but also they provide self-similar solutions which accept only such boundary conditions at $\hat{r} = 1$ which are compatible to their kinematics.

In the last three decades of theoretical and experimental investigations the potential as well as the limitations of self-similar solutions became substantially clearer [5,8,9,11,22,29]. Furthermore, most of the investigations have been driven by the increasing number of applications for rotating disks flows. For applications in which a pair of disks rotates slowly or a high viscosity fluid is used the application of the von Kármán ansatz on the linearised equations of motion represents a powerful mean of investigation [10,11,20,21] which facilitates a better access to the physics of the flow with less mathematical work. In certain cases even full analytical solutions have been found.

On the other hand, in the most recent literature [21,30] there is a trend to solve the full Navier–Stokes equations by using sophisticated numerical methods where also turbulence is considered. This represent a huge work but avoids some uncertainties connected to the simplification of the equations of motion such as when parabolising them.

The author of the present contribution foresees that at least in the near future the use of numerical algorithms will increase substantially but the more "classical" methods of solution will keep their relevance, too. This has been deduced from the known and expected fields of applications of rotating disks which are specially characterised by a large spectrum of chemo-physical processes to be studied [11,31–33,35–38]. Poly-phases as well as -components fluids, rheological substances and last, but not least, flow with chemical reactions will require the availability of well suitable means.

References

1. T. von Kármán: ZAMM **1**, 233-254 (1921)
2. W.G. Cochran: Proc. Camb. Phil. Soc. **30**, 365-375 (1934)
3. K.G Batchelor: Q. J. Mech. Maths **4**, 29-41 (1951)
4. K. Stewartson: Proc. Camb. Phil. Soc. **49**, 333-341 (1953)
5. K.G. Picha, E.R.G. Eckert: 'Study of the air flow between coaxial disks rotating with arbitrary velocities in an open or enclosed space'. In: *Proc. Third U.S. Natl. Cong. Appl. Mech.*, 791-798 (1958)
6. S.M. Roberts, J.S. Shipman: J. Fluid Mech. **73**, 53-63 (1976)
7. G.L. Mellor, P.J. Chapple, V.J. Stokes: J. Fluid Mech. **68**, 95-112 (1968)
8. M. Holodniok, M. Kubicek, V. Hlavácek: J. Fluid Mech. **81**, 689-699 (1977)
9. D. Dijkstra, G.J.F. van Heijst: J. Fluid Mech. **128**, 123-154 (1983)
10. A. Delgado, H.J. Rath: Archives of Mech. **42**, 4-5, 443-462 (1990)
11. A. Delgado: 'Gravitationskompensierte Strömungen rotierender newtonscher und nichtnewtonscher Fluide'. In: *Fortschr.-Ber. VDI Reihe 7 Nr. 264*, VDI-Verlag (1995)
12. H.P. Greenspan: 'The theory of rotating fluids'. In: *Cambridge University Press*, Cambridge (1980)
13. L. van Wijngaarden: Fluid Dynamics Transactions **12**, 157-179 (1985)

14. P.J Zandbergen, D. Dijkstra: Annual Rev. Fluid Mech. **19**, 465-491 (1987)
15. S.V. Parter: 'On the swirling flow between coaxial rotating disks: a survey'. In: *MCR Technical Report 2332 (1982)*
16. M.H. Rogers, G.N. Lance: J. Fluid Mech. **7**, 617-631 (1960)
17. U.T. Bödewadt: ZAMM **20**, 241-253 (1940)
18. R.J. Bodonyi, B.S. Ng: J. Fluid Mech. **144**, 311-328 (1984)
19. A. Delgado, H.J. Rath: ZAMM **69/6**, T614-T616 (1989)
20. A. Delgado, B. Petri, H.J. Rath: Appl. Microgravity Technology **1,4**, 188-201 (1988)
21. J. Wu, A. Delgado, H.J. Rath: 'Linearized numerical solution method for rotating coaxial disk flows at moderate Reynolds numbers'. In: *Proc. 7th Int. Conf. Numerical Methods in Laminar and Turbulent Flows, 15.-19. July 1991*, Stanford, CA, USA, Vol VII,1, pp. 480-490 (1991)
22. J.F. Brady, L.J. Durlofsky: J. Fluid Mech. **175**, 363-394 (1987)
23. A.Z. Szeri, A. Giron, S.J. Schneider, H.N. Kaufman: J. Fluid Mech. **134**, 133-154 (1983)
24. L.J Durlofsky: Topics in fluid mechanics: I. Flow between finite rotating disks, II. Simulation of hydrodynamically interacting particles in Stokes flow. Ph.D. Thesis, Massachussets Institute of Technology (1986)
25. H. Schlichting: *Grenzschicht-Theorie*, 8nd edn. (Braun, Karlsruhe 1982)
26. M. Holodniok, M. Kubicek, V. Hlavácek: J. Fluid Mech. **108**, 227-240 (1981)
27. E. Reshotko, R.L. Rosenthal: Israel J. Tech. **9**, 93-103 (1971)
28. F. Schultz-Grunow: ZAMM **14**, 191-204 (1935)
29. R.K.-H. Szeto: The flow between rotating coaxial disks. Ph.D. Thesis, California Institute of Technology (1978)
30. S. Bhattacharyya, A. Pal: Acta Mechanica **135/1**, 27-40 (1999)
31. A. Delgado, H.J. Rath: 'Theoretical investigation of the rotating disks flow of one- and two-phase fluids in microgravity'. In. *Proc. IUTAM Symp. Microgravity Fluid Mech., 2.-6. September 1991*, Springer, Heidelberg, pp.185-193 (1992)
32. W.M. Yan, C.Y. Soong: International J. of Heat and Mass Transfer **40/4**, 773-784 (1997)
33. G. Leneweit, K.G. Roesner, R. Koehler: Exp. Fluids **26**, 75-85 (1999)
34. W. Hort: Zeitschrift für Technische Physik **1/10**, 213-221 (1920)
35. P.C. Ray, B.S. Dandapat: The quarterly J. of Mech. and appl. Math. **47/1**, 297-304 (1994)
36. M. Kilic, X. Gan, J.M. Owen: J. of Fluid Mech. **281**, 119-135 (1994)
37. J.S. Roy, S. Padhy, L.K. Bhopa: Acta Mechanica **108/1-4**, 111-120 (1995)
38. C.Y. Soong, H.L. Ma: International J. of Heat and Mass Transfer **38**, 1865-1878 (1995)
39. C.Y. Soong, W.M. Yan: J. of Thermophysics and Heat Transfer **7/1**, 165-170 (1993)